The Dissertation Committee for Megan Rachel Mehaffey Certifies that this is the approved version of the following Dissertation:

Leveraging Native Mass Spectrometry and 193 nm Ultraviolet Photodissociation as Structural Biology Tools

Committee:

Jennifer S. Brodbelt, Supervisor

Eric V. Anslyn

Livia S. Eberlin

Walter Fast

Leveraging Native Mass Spectrometry and 193 nm Ultraviolet Photodissociation as Structural Biology Tools

by

Megan Rachel Mehaffey

Dissertation

Presented to the Faculty of the Graduate School of

The University of Texas at Austin

in Partial Fulfillment

of the Requirements

for the Degree of

Doctor of Philosophy

The University of Texas at Austin

December 2020

Dedication

To my family (Dad, Mom, Hunter, & Caitlin), and the absolute best pup, Rylie.

Acknowledgements

This academic journey was by no means taken alone and certainly would not have been possible without the support of many people in my life. I would first like to acknowledge my graduate advisor, Dr. Jenny Brodbelt, for affording me the opportunity to pursue my degree in her research lab and providing abundant support during my graduate career. She works tirelessly to establish meaningful collaborations, obtain funding, and create a productive environment conducive to top-notch research. I am forever grateful to my undergraduate advisor and mentor, Dr. Allison Danell, who introduced me to the world of mass spectrometry and encouraged me to apply to graduate school. I owe many thanks to the talented scientists with whom I had the privilege to collaborate with, particularly Dr. Walt Fast and Dr. George Georgiou, for providing pristine samples and invaluable biological insights without which the work presented here would not have been possible.

I must gratefully acknowledge the current and former members of the Brodbelt group. All of you have my utmost appreciation for troubleshooting and maintaining the myriad of instruments throughout the lab, providing a constant source of insightful discussion, sharing your expertise, and generally challenging me to become a better scientist. Especially, Dr. Michael Cammarata, who taught me everything I know about native mass spectrometry, as well as Dr. Dustin Klein, Molly Blevins, and Edwin Escobar, who always lent me an ear whether it was to talk about science or gossip about life.

To the many friends I have made while living in Austin, thank you for providing a much needed escape from the rigors and stress of research. I will forever cherish the sunny days at the pool and unforgettable nights on 6th Street. Specifically, I would like to thank the Dream Team (Mackenzie Meece-Rayle, Juan Flores, Sophia Beyer) and Rahul Kadakia

for being my “ride or die” friends and providing a source of healthy distractions. I will be forever grateful to Matt Boullt for tolerating me over the years and being such an important part of my life. Thanks to John Leopard for the many study nights in the library at ECU and entertaining phone calls that have made our friendship last over the years. Also, I owe Morgan Kelley a thank you for being the best dog aunt to Rylie and saving my life that one time.

Lastly, I would like to thank my family for their unwavering love and support. My parents, Jim and Missy Mehaffey, worked hard to provide me with every possible opportunity and raised me to value the importance of diligence. My brother, Hunter Mehaffey, through his many achievements, set an excellent example for me to follow. My sister and best friend, Caitlin Mehaffey, has been there for me countless times, always providing good advice, a shoulder to cry on, and plenty of laughs. I am abundantly grateful for the person they molded me in to and the constant encouragement they offered throughout my career, without which I undoubtedly could not have completed this doctorate work.

Abstract

Leveraging Native Mass Spectrometry and 193 nm Ultraviolet Photodissociation as Structural Biology Tools

Megan Rachel Mehaffey, Ph.D.

The University of Texas at Austin, 2020

Supervisor: Jennifer S. Brodbelt

Structural biology studies aimed at the elucidation of protein-dependent disease mechanisms have traditionally relied on high-resolution techniques, including X-ray crystallography, nuclear magnetic resonance, and cryogenic electron microscopy. While such methodologies remain standard for gaining information on the core structure of proteins, specific drawbacks including time or large sample quantities associated with these approaches have spawned the development of other pipelines. Mass spectrometry (MS) is one such tool that has gained traction as a rapid and sensitive low-resolution structural biology technique. Routinely protein complexes of interest are reacted in solution with covalent chemical probes to preserve structural information prior to enzymatic digestion and mass spectrometric read-out. However, with the advent of native MS, protein complexes can now be efficiently transferred intact into the gas phase using high ionic strength solutions while retaining structures reminiscent of their solution conformations, and directly interrogated using MS/MS methods. Ultraviolet photodissociation (UVPD) is one such ion activation method that has been extensively developed to break apart protein complexes in a manner that allows conclusions about structure to be drawn based on the

fragmentation behavior. The work presented here leverages native mass spectrometry in conjunction with 193 nm UVPD to probe a variety of biologically important protein-ligand and protein-protein complexes.

The utility in a native UVPD-MS approach for structural examination of protein-ligand complexes is demonstrated through characterization of conformational changes associated with the catalytic cycle of a phosphotransferase enzyme as well as elucidation of structural changes resulting from mutation or inhibition of an enzyme responsible for conferring antibiotic resistance to bacteria. An oncogenic protein and several clinical variants bound to a downstream effector protein provides an example of the capabilities of native MS and UVPD to characterize the structure of a protein-protein complex. Native UVPD-MS is also used for epitope mapping of the main antigenic determinant of the influenza virus. Aimed at improving analysis of larger complexes, multistage native UVPD-MS is developed to probe the structure of a protein implicated in chemotherapeutic resistance in glioblastoma tumors. Lastly, uniting on-line capillary electrophoresis (CE) with multistage native UVPD-MS offers a high-throughput workflow for structural characterization of ribosomal protein complexes.

Table of Contents

Chapter 1: Introduction

1.1 Motivation and Scope of Research

Structural biology, or the study of the molecular structures of proteins and nucleic acids, relies on the key principle that structure determines function. As such, studies are aimed at mapping the dynamic movements and noncovalent interactions of such biological macromolecules to gain insight into their complex interplay that sustains life.[1] Arguably even more important is understanding the mechanisms by which these processes go awry, leading to dysfunction or disease. Although molecular modelling is useful for refining and visualizing certain aspects of biomolecular assemblies,[2] the foundation of the structural biology toolbox used to probe macromolecular structures is comprised of high-resolution experimental methods including X-ray crystallography (XRC),[3,4] nuclear magnetic resonance (NMR),[5,6] and more recently, cryogenic electron microscopy (cryo-EM).[7] These "gold standard" techniques provide information on the structures of macromolecules with single amino acid residue resolution that translate directly into three-dimensional representations of side chain positions from which specific function can be inferred. However, each of these approaches is not without specific drawbacks. XRC and NMR both require relatively large sample quantities (up to milligram amounts or millimolar concentrations) that are often not representative of biologically relevant concentrations. This can result in packing artifacts of important loops during crystallization or protein precipitation during NMR analysis.[8–10] Additionally, both of these methods require complex and time-consuming data interpretation approaches, hampering them from being amenable to high-throughput screening of small molecule drugs or interacting partners. Although cryo-EM addresses these issues while still delivering high-resolution data, low signal-to-noise ratios can complicate data acquisition.[11] These specific shortcomings have

spawned the development of alternative structural biology tools more fitting for certain tasks.

Mass spectrometry (MS) is one such method that has solidified a spot in the structural biology toolbox with its unparalleled sensitivity and speed making it an attractive option for analyzing protein architectures.[12–14] Typically, sub-microgram quantities of proteins are enough for structural characterization by MS. Additionally, in conjunction with on-line sample introduction or separation methods, many combinations of protein sequences and ligands can be quickly screened with the resulting data comparatively easy to interpret. Although the structural information gained by MS is typically low-resolution, these attributes often counterbalance the lack of position information on the single amino acid level. The work presented in this dissertation focuses on the application of native MS in conjunction with ultraviolet photodissociation (UVPD) to characterize the structure of increasingly large proteins and complex biological samples. However, a brief review of the advent and development of MS for structural biology applications is first necessary to appreciate recent advancements.

1.2 Mass Spectrometry as a Structural Biology Tool

Over the past two decades, MS has come of age as a structural biology method capable of informing on all levels of protein organization and tracking dynamic interactions.[12,15,16] The first applications of MS to probe macromolecular structures involved the attachment of covalent modifications or chemical probes to preserve structural information during proteolytic digestion and MS detection.[17] A shift to transferring intact protein assemblies into the gas phase for direct analysis was enabled with the arrival of native MS.[18,19] Coupling ion-mobility spectrometry (IMS) with native MS (termed IM-MS) can provide further information on the topology of protein complexes.[20]

1.2.1 Covalent Labeling

Building on classical MS-based proteomics approaches utilizing proteolytic digestion and on-line liquid chromatography with tandem MS (LC-MS/MS) to identify and quantify proteins and their interaction partners, the introduction of covalent labeling to the general workflow added "structural biology tool" to the MS resume. Specifically, covalent labeling refers to the covalent addition of chemical probes to reactive and accessible amino acids on the surfaces of proteins.[17] The position of attachment of such tags can be localized by tracking the resulting mass shift after subsequent proteolytic digestion of the protein and LC-MS/MS analysis of resulting peptides. Low-resolution structural information is then inferred from a map of the modified residues. Although MS involves detection of analytes in the gas phase, the modification reactions typically occur in buffered solutions, as such the native solution behavior is probed.[17] Commonly used covalent labeling techniques fall into three main categories that are each described below: solvent accessibility, hydrogen/deuterium exchange (HDX), and chemical cross-linking.

Taking advantage of a variety of specific side chain chemistries, solvent accessibility labeling refers to the decoration exclusively of exposed amino acid side chains along the protein surface by small, reactive molecules.[21] The extent to which each amino acid is labelled can be determined from the number of unmodified and modified sites along constituent peptides resulting from digestion and LC-MS/MS analysis. By far the most common target for solvent accessibility studies are primary amines, present on side chain lysine residues and the N-terminus of the protein.[21] Typically found on the outer surfaces of folded proteins and acting as strong nucleophiles, solvent accessible free amines are easily targeted by N-hydroxysuccinimidyl (NHS) leaving group chemistries.[22] Other side chain groups that have been successfully targeted include arginine, cysteine, histidine, tyrosine, tryptophan, aspartic acid, and glutamic acid.[21] Additionally, less specific labels

have been developed (*i.e.* ones that target multiple side chain groups at once) to increase the number of sites probed per experiment but this results in more complex samples and data analysis.[23] Emerging covalent labeling approaches typically rely on laser activation to attach photoreactive groups with minimal side chain identity bias of solvent accessible residues. One such method, termed fast photochemical oxidation for proteins (FPOP) involves addition of millimolar concentrations of peroxide and exposure to laser irradiation (250 nm – 270 nm) resulting in the creation of radical OH species that can oxidize most amino acid side chain moieties (excluding alanine, asparagine, aspartic acid, glycine, glutamine, and glutamic acid).[24] Similarly, carbene footprinting utilizes a sterically strained, UV photoreactive diazirine ring. Exposure to 355 nm laser light activates the reagent to covalently attach at any surface accessible amino acids and even the protein backbone itself.[25] Not only do these solvent accessibility approaches maximize the information gained on exposed sites, the reactions occur on rapid timescales, preventing any structural disruption to the protein that can result from slower labeling techniques.[26]

While solvent accessibility approaches offer insight into the surface exposure of individual side chain residues, hydrogen/deuterium exchange (HDX) instead monitors protein structure by probing the dynamic reactivity of amide sites along the protein backbone.[17] Exposure of proteins to deuterium oxide-containing solvents induces the replacement of backbone hydrogen with deuterium. Exchange events can then be tracked using the multiple resulting ~1 Da mass shifts in resulting peptides by LC-MS/MS.[27] Typically deuterium uptake per residue is compared for different HDX reaction times or across different solution conditions to track dynamic movements of the protein backbone. Although HDX-MS offers the highest resolution of any covalent labeling MS technique, the main challenge with this type of experiment is preventing back exchange during proteolysis and MS analysis.[27] Owing to the reversibility of the HDX process, returning

the protein to a non-deuterated solvent causes the loss of some structural information as hydrogen exchanges back into the backbone. Back-exchange of side chain heteroatoms (O-H, N-H, S-H) is so rapid that HDX events at these sites are not measured.[17] Nevertheless, several precautions can be taken to mitigate this process along the backbone including acid quenching and freezing after D_2O exposure, digestion with pepsin, a rapid and non-specific protease that cleaves under conditions ideal for preventing back-exchange (0 °C, pH 2), and shortened reversed-phase LC gradients, often using cryogenically-cooled systems.[27] Despite these challenges, HDX-MS has been fully developed and even commercialized as a robust method[28] routinely used in academia and industry alike to characterize protein structures such as studying conformational changes in amyloid beta peptides during aggregation[29] and mapping epitopes of antibody-antigen complexes.[30]

As opposed to probing the surface accessibility of side chains or the backbone, chemical cross-linkers instead act as molecular rulers that covalently attach residues within a specified distance constraint of each other in space.[31] Such information aids in structural modeling of complexes[32] as well as in identifying interaction networks of individual proteins.[33] Similar to solvent accessibility probes, the reactivity of cross-linking reagents can be tuned to target specific side chain moieties.[31] Primary amines are again the most attractive target for cross-linking reagents containing NHS leaving groups at each end with a carbon chain in between to set the distance constrain of the linker (typically in the range of 10 – 30 Å). Such reagents with identical reactive groups on each side are referred to as homobifunctional. However, heterobifunctional cross-linkers have also been developed for applications in which targeting two different side chain groups is desirable.[31] Photoreactive cross-linkers containing diazirine or benzophenone groups represent a specific class of heterobifunctional reagents that allow for promiscuity in the residues targeted by one side of the linker.[34] Aimed at identifying residues that are spatially close or directly interacting,

zero-length cross-linkers utilize 1-ethyl-3-(3-dimethylaminopropyl)carbodiimide (EDC) coupling reactions to form a new peptide bond between acidic and basic side chains.[35] Other classes of chemical cross-linking reagents continue to be developed to address the two main challenges with this approach: low reaction yields and complex fragmentation patterns resulting from MS/MS of cross-linked peptides.[31] Including groups along the cross-linker structure susceptible to enrichment procedures after the reaction can improve the signal of desired cross-link products orders of magnitude during LC-MS/MS analysis.[36] Similarly, using cross-linking reagents whose structure has been modified to dissociate in a more predictable, simplified manner during MS/MS streamlines data analysis.[37] Other recent advancements have centered on skipping the digestion step and directly probing intact cross-linked protein complexes by MS/MS, referred to as top-down cross-linking MS,[38,39] but this approach has numerous other technical hurdles which has limited widespread adoption.

1.2.2 Native MS

A significant shift in the paradigm of MS for structural biology analysis occurred with the introduction of native MS.[14,18,19] This approach negates the need for protein labeling and subsequent digestion through the use of high ionic strength solution (*i.e.* "salty" solutions) during the electrospray ionization (ESI) process to gently transfer intact protein complexes into the gas phase while maintaining noncovalent interactions with metal cofactors, ligands, or other proteins.[19,40] Thus, protein architectures can now be directly probed within the mass spectrometer instead of relying on the preservation of structural information through covalent tags. In addition to conserving noncovalent interactions into the gas phase, native MS solution conditions also alter the ESI charging process.[41] In contrast to denaturing MS conditions (typically defined as > 50% organic

solvent and up to 2% acid) which yield a wide range of high charge states, native MS solutions lead to a narrow range of low charge states as proteins are ionized from nearly 100% aqueous solvents with high concentrations (5 mM up to 2 M) of volatile salts, most commonly ammonium acetate but ammonium formate and ammonium bicarbonate are also options.[41,42] **Figure 1.1** demonstrates this observed principle for two standard protein complexes: myoglobin and concanavalin A. Native MS conditions allow the retention of a noncovalent heme ligand for myoglobin (**Figure 1.1A**) and preserves the preferred homotetrameric oligomeric state of concanavalin A (**Figure 1.1B**). Conversely, denaturing MS conditions cause ejection of the ligand (evident in **Figure 1.1A** as a separate peak at *m/z* 616) and monomerization of concanavalin A as well as the observation a wider distribution of higher charge states (relative to the mass of the species) for both proteins.

The observed differences in resulting charge states for denaturing and native MS are thought to the be result of divergent ionization mechanisms termed the chain ejection model (CEM) and charge residue model (CRM).[41] The former describes the ionization of proteins under denaturing conditions while the latter details the proposed mechanism of gas phase transfer for native MS conditions. Following the CEM, unfolding protein structures reveals hydrophobic side chains typically buried deep in the folded structure that cause the proteins to arrange around the outer edge of a charged, hydrophilic ESI droplet. As coulombic explosions and solvent evaporation lead the droplet to shrink, the hydrophobic groups further drive the protein to extrude from the outer barrier of the droplet and pick up many of the charges that reside along the outer surface of the relatively large ESI droplet as it exits.[41] Alternatively, the CRM proposes for native MS conditions that owing to the conservation of a folded protein structure, the hydrophobic effect no longer pushes the protein to the outskirts of the droplet and instead it remains near the center for the duration of ionization. Continuous evaporation of the droplet leads to the deposition of

what little charge remains on the surface of the evaporated droplet along the outside of the folded protein.[41]

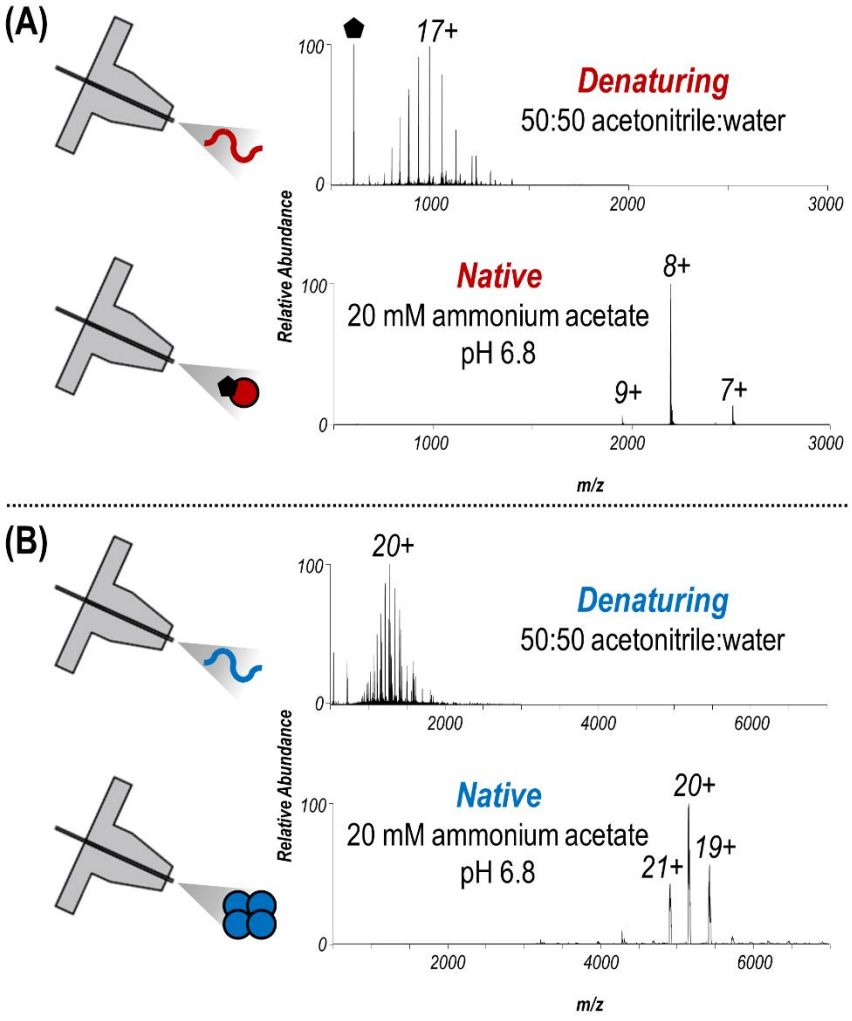

Figure 1.1: ESI-MS of (A) myoglobin and (B) concanavalin A each sprayed under denaturing (50:50 acetonitrile:water) and native (20 mM ammonium acetate, pH 6.8) MS conditions. The heme ligand in myoglobin is represented as a black pentagon. Select charge states are labelled.

The preservation of noncovalent interactions and production of lower charge states observed with native MS initially presented limitations in instrumentation that prohibited

widespread adoption of this technique. Not only are the analytes typically larger, the ESI process imparts less charge meaning even small proteins and protein-ligand complexes show up above the normal scan range maximum of *m/z* 2000. Until recent years, a limited number of mass spectrometers were capable of guiding such large ions through the instrument optics and scanning up to the higher *m/z* regions in which native protein complexes are observed (typically 2500 – 8000 *m/z*).[43] Mass spectrometers utilizing time-of-flight (TOF) mass analyzers were among the first used for native MS studies owing to their mid-range resolving powers and high *m/z* scan ranges.[43,44] Fourier-transform ion cyclotron resonance (FT-ICR) instruments afford the highest resolutions for native MS experiments, but prohibitively expensive maintenance continues to make them the least commonly used.[43,45,46] Instead, Orbitrap mass analyzers introduced in the early 2000's offer relatively high resolving powers and the ability to scan high *m/z* regions, making them the top choice for native mass spectrometrists.[43,47,48] Recently a commercial Orbitrap instrument was developed aimed specifically at extending the scannable mass range for improving native MS capabilities.[48]

The application of native MS to elucidate subunit stoichiometry and connectivity has become increasingly routine for ever larger protein complexes.[49] Ranging in size from kDa protein oligomers such as ATP-synthase,[50] to MDa assemblies including intact ribosomal particles[51] and virus capsids,[52,53] the speed and sensitivity of native MS make it an attractive technique for such analysis. Additionally, native MS has demonstrated utility in monitoring a wide range of protein-ligand interactions[54] including screening small molecule drug candidates,[55] determining optimal lipid compositions for membrane protein analysis,[56,57] measuring dissociation constants,[58] and defining kinetic and thermodynamic binding parameters.[59,60] Although native MS itself can provide some structural information, it is far more powerful for gaining detailed structural biology insight when

used in conjunction with other gas phase techniques, particularly ion mobility spectrometry (IMS) or tandem MS (MS/MS) methods.

1.2.3 Ion Mobility-MS

In short, ion mobility spectrometry (IMS) involves the separation of gas-phase ions by size and shape based on their differential mobility through a buffer gas.[61] For proteins this drift time is represented as a rotationally averaged cross-sectional area, referred to as a collision cross section (CCS) value, that can be used to correlate structures and conformations.[20,62–64] Depending on the desired resolution or information, in practice three primary IM-MS techniques are used: drift-time (DT) IMS, travelling-wave ion mobility spectrometry (TWIMS), and field-asymmetric ion mobility spectrometry (FAIMS).[61] DT-IMS represents the oldest and conceptually simple version of IMS utilizing a uniform static electric field across drift tube filled with a buffer gas.[61] Owing to the higher number of interactions with the drift gas, elongated structures travel the length of the tube slower than more compact ions. TWIMS removes the need for a high drift voltage across the entire tube by instead successively applying a direct current (DC) voltage to a series of stacked rings that outline the drift region to propel the ions axially and create a "travelling wave". Opposite phase radio-frequency (RF) potentials applied to adjacent electrodes confine the ions radially.[61] This method has been commercialized in the popular Waters Synapt Q-TOF platform. FAIMS devices utilize two electrodes with a voltage across them that deflects ions introduced perpendicular towards the walls. A second voltage is manipulated to selectively permit ions of interest to pass through the electrodes while removing ions of differing mobility. While FAIMS does not measure CCS values, it can filter out unwanted species and improve the signal of desired species up to several orders of magnitude.[61] As

such, FAIMS devices are typically integrated to the front end of a mass spectrometer, prior to mass analysis.

Coupling IMS with native MS (referred to as native IM-MS) provides an avenue for more detailed structural analysis of large or heterogenous protein assemblies by providing a type of shape/size-based sieving. Measurement of the CCS values of the individual *m/z* values related to these complexes and their composite subunits offers a new dimension of information on the flexibility and conformational dynamics of a system, in addition to the stoichiometry and topology.[20,61,62,65] Such characteristics make IMS a complementary tool to native MS in the context of structural biology.[66] One particular area in which native IM-MS has provided critical insight is defining protein folding/unfolding, in which changes in ion mobility as a function of gentle collisional activation or partial solvent denaturation serve as an indicator of conformational disruption.[61,62] In fact, IM-MS experiments offer the most compelling evidence that proteins ionized by native MS do retain architectures in the gas phase reminiscent of their solution phase structures, a topic still hotly debated.[67–69] Additionally, native IM-MS has been applied to study a wide variety of biologically important topics including the structural impact of single point mutants of human hemoglobin,[70] disorders related to glycosylation state that alter protein conformation,[71] and diseases caused by protein conformers or aggregates.[72,73] Databases of CCS values help to calibrate drift time measurements and maintain uniformity across IM-MS platforms, especially following the commercialization of TWIMS and subsequent increase in widespread application to studying structural biology questions.[74] Also common is the use of native IM-MS in conjunction with tandem MS (MS/MS) approaches to further probe secondary and tertiary structures of single protein subunits within complexes.[75,76]

1.3 Tandem Mass Spectrometry of Intact Protein Complexes

Tandem MS (MS/MS) in basic terms refers to the addition of energy to gas phase ions of interest to cause dissociation into smaller fragment ions. Activation of intact proteins or protein complexes is referred to as top-down MS in contrast to the bottom-up MS approach which must include a proteolytic step yielding peptides for MS/MS analysis.[77] Upon ion activation of a protein-ligand or protein-protein complex several dissociation pathways are possible, the most common of which include ejection or unfolding of the ligand/single subunits, disassembly of the oligomeric assembly into smaller sub-complexes, or cleavage of the covalent bonds comprising the protein backbone.[78,79] The amount of energy and timescale of deposition both impact which of these outcomes are favored.[78,79] As such, traditional collisional activation typically falls short in producing fragment ions that provide structural information so several alternative MS/MS approaches have been tested. Following is a brief review of the merits and specific applications of common MS/MS activation methods (collisional dissociation, electron-based dissociation, surface-induced dissociation, and ultraviolet photodissociation) with regards to dissociating the intact protein-ligand and protein-protein complexes resulting from native MS.

1.3.1 Polypeptide Fragmentation Nomenclature

Disassembly of the noncovalent bonds within a protein complex after ion activation yields intact protein subunits or ligands whose *m/z* values are easily labelled as such in the resulting MS/MS spectra.[78] Conversely, cleavage of the covalent bonds along the polypeptide backbone within a single subunit, herein referred to as sequence ions, requires its own systematic nomenclature to categorize the resulting fragments.[80] Together the location of the bond cleavage within the repeating unit of the protein backbone and the

terminus which is retained (N- or C-) define the type of sequence ion, while the number denotes the position in the overall sequence. Sequence ions containing the N-terminus are classified as *a*-, *b*-, or *c*-type ions depending on whether the cleavage occurs across the C_α-C bond, C-N amide bond, or N-C_α bond, respectively. The corresponding ion types containing instead the C-terminal end of the protein are *x*-, *y*-, and *z*-type ions.[81] As such, *a/x*, *b/y*, and *c/z* ions make complementary pairs resulting from cleavage of the same bond along the backbone (although both partners in the pairs are not necessarily detected). A graphical illustration representing this sequence ion nomenclature is shown in **Figure 1.2**. Owing to the differences in energy and timescale of depositions, each ion activation method favors the production of certain ion types.[78,79] Briefly, threshold-based methods, including collisional dissociation and infrared wavelength photodissociation, result in predominantly *b*- and *y*-type ions following cleavage of the lowest energy peptide bond. Electron-based dissociation methods that rely on radical-directed mechanisms typically yield *c*- and *z*-type ions. Ultraviolet photodissociation (UVPD), a higher energy activation method, produces all six ion types with a slight preference for *a/x*-type ions for intact proteins or *b/y*-type ions for peptides.[78,79]

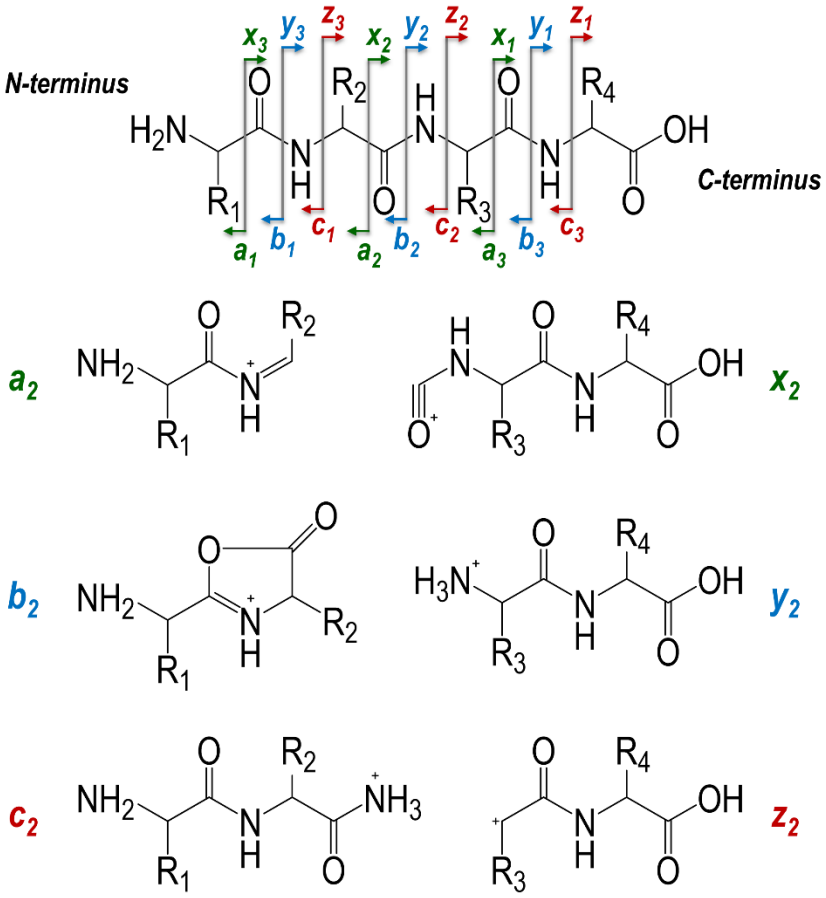

Figure 1.2: Representation of the nomenclature proposed by Roepstorff *et al.* to classify sequence ions resulting from fragmentation of the polypeptide backbone of a protein subunit, illustrated for a peptide containing four amino acids.

1.3.2 Collisional Dissociation

Collisional dissociation refers to low-energy collision-induced dissociation (CID) or collisionally activated dissociation (CAD) involving the acceleration of ions to low kinetic energies (< 1 keV) causing inelastic collisions with an inert gas, typically helium or nitrogen, and converting kinetic energy into internal vibrational energy. Owing to the low energy deposition of this process, multiple collisions are typically required to reach the dissociation threshold of the precursor ion and cause fragmentation (*i.e.* referred to as

slow heating), resulting in preferential cleavage of only the most labile bonds.[82] On modern mass spectrometers, collisional dissociation is implemented either within an ion trap through resonant excitation using a supplemental RF waveform at the secular frequency of the precursor ion, or by acceleration of precursor ions through a higher-pressure collision cell, referred to as beam-type activation.[82] The latter is termed higher-energy collisional dissociation (HCD) on Thermo Scientific commercial MS platforms, not be confused with true high-energy collisional dissociation (> 1 keV collision energies on TOF or sector instruments). Collisional dissociation remains the most established and widely utilized ion activation method due to its robust performance and implementation on virtually all commercially available mass spectrometers.

In regards to collisional activation of protein-ligand or protein-protein complexes introduced by native MS, it predominantly results in disruption of labile noncovalent interactions.[78,79,83] For protein-ligand complexes, this corresponds to ejection of the ligand as the protein unfolds during the inelastic collisions before reaching the threshold of backbone fragmentation and producing sequence ions.[78,79] As such, information on the binding site is not reflected in observed fragment ions. Although there have been a limited number of studies in which collisional dissociation was used to determine binding sites of adenosine phosphate ligands through the retention of one or two phosphate groups noncovalently bound to the protein during dissociation (*i.e.* likely due to the enhanced strength of electrostatic interactions in the gas phase) or the entire ligand when supercharging reagents were added.[84,85] Similarly, collisional activation of protein-protein complexes primarily results in unfolding of a single subunit that sequesters a disproportionately high amount of the charge as it is ejected.[78,79] A typical MS/MS spectrum then contains, in addition to a limited number of sequence ions, a highly charged monomer in the lower *m/z* region and the remaining low charge (*n*-1)-mer in the higher *m/z*

region. To gain structural information from this type of favored dissociation pathway, typically MS/MS spectra are collected over a range of collision energies. Briefly, collision energy refers to the amount of kinetic energy added to the precursor during collisional activation. Tracking the production of subunits and eventually sequence ions across activation energies allows relative gas-phase stabilities to be established and offers some insights on protein structure with regards to salt bridges, charge density, or subunit flexibility.[83] This approach is even more powerful when combined with IMS measurement, termed collision-induced unfolding (CIU) footprinting. Measuring the CCS value of a protein or protein complex as a function of collision energy creates an unfolding "footprint", allows visualization of unfolding intermediates, and enables rapid differentiation of protein isoforms with subtle differences based on their unfolding patterns.[86] Despite the widespread availably of collisional dissociation methods, its limitations in providing structural information on proteins make alternative approaches worthwhile for structural biology applications.

1.3.3 Electron-based Dissociation

Electron-based ion activation methods rely on the gas phase interaction of electrons or radical reagents with ions of interest to promote fragmentation. The energy range of such electrons defines the fundamental difference between the variety of electron-based dissociation methods. Electron capture dissociation (ECD) induces fragmentation of multiply charged protein cations by exothermic capture of low energy electrons (< 1 eV).[87,88] This technique was originally limited to FT-ICR instrument platforms on which a magnetic field facilitates the simultaneous trapping of electrons and analyte cations, but ECD has more recently been implemented on other platforms via a modular drop-in electron filament device from eMSion. Electron transfer dissociation (ETD), the ion trap

instrument analogue of ECD, instead transfers an electron to a multiply charged polypeptide cation via reaction with a radical anion reagent (*i.e*. fluoranthene or anthracene).[89] Higher energy electrons (~30 kV) have also been used to activate protein complexes, termed electron ionization dissociation (EID).[90] The formation of odd-electron radical species represents a primary advantage of electron-based ion activation methods as fragmentation occurs through hydrogen radical migration prior to energy redistribution through vibrational relaxation. This presumed non-ergodic dissociation behavior allows certain challenges associated with collisional activation to be overcome including preferential cleavages and loss of labile modifications.[91–93]

Although originally aimed at improving the sequence characterization of denatured peptides and proteins for proteomics applications, ECD and ETD have been widely applied for structural analysis of protein-protein complexes. In stark contrast to collisional activation of protein complexes, electron-based methods result predominantly in the production of sequence ions and limited disassembly of noncovalent higher order structure. The resulting sequence ions typically originate exclusively from surface exposed regions of a folded protein structure.[94] Maps of sequence ions by residue resulting from ECD/ETD of proteins introduced by native MS have been correlated with crystallographic B-factors, a measure of flexibility in XRC experiments. As such, electron-based dissociation approaches can be used to directly probe secondary and tertiary structure of proteins.[94] To date, the higher order structures of increasingly large multimeric protein complexes including hemoglobin (64 kDa),[95] alcohol dehydrogenase (147 kDa),[95–97] and GroEL (802 kDa)[46] have been probed using ECD or ETD. Additionally, the extra electron energy imparted during EID can yield significantly more informative sequence ions compared to ECD while retaining sensitivity to higher order protein structure.[90]

1.3.4 Surface-Induced Dissociation

As the name suggests, surface-induced dissociation (SID) involves the fast, energetic collision of protein ions with a surface. The rapid and high deposition of energy results in disassembly of noncovalent protein complexes into constituent subcomplexes with little to no backbone cleavage nor unfolding of individual subunits, as evidenced by symmetric partitioning of charge during dissociation (*i.e.* the precursor charge splits evenly by mass among the observed subcomplexes).[98] As such, SID is exceptionally useful for probing the quaternary structure of protein-protein complexes. Specifically, tracking observed subcomplexes as the SID energy is increased offers insight into the relative strength of protein interfaces. IMS separation of complexes before SID allows different protein conformations to be activated individually while IMS of subcomplexes resulting from SID greatly improves the resolving power of this approach by eliminating overlapping *m/z* peaks (*e.g.* a 10+ dimer and 5+ monomer).[98] The SID-IM-MS methodology has been used to study a variety of protein complexes including rapidly screening 48 computationally designed heterocomplexes to confirm stoichiometry, intersubunit connectivity, and complex topology.[99] Also, recently the capability of SID to localize small ligand binding for multimeric protein-ligand complexes to either within a subunit or between adjacent subunits was demonstrated.[100]

1.3.5 Ultraviolet Photodissociation

Although a laser was first coupled to a mass spectrometer for the purpose of photoactivation of gas phase ions almost 50 years ago,[101,102] only within the last decade have photodissociation methods evolved into powerful and versatile tools for identification and structural characterization of various classes of biomolecules.[78,79] Continuous wave CO_2 lasers have been used to probe protein complexes with IR wavelength photons,

referred to as infrared multiphoton photodissociation (IRMPD), but the low energy deposition yields similar fragmentation trends as collisional activation.[46] Instead, irradiation of proteins with photons in the ultraviolet range, termed ultraviolet photodissociation (UVPD), has proven highly effective for the structural characterization of protein-ligand and protein-protein complexes. Coordinating commercially available laser technology with specific wavelengths strongly absorbed by the polypeptide backbone make coupling excimer lasers operated at 157 nm or 193 nm to mass spectrometers the optimal choice for UVPD applications.[78,79] While the general utility of UVPD as a frontier strategy for generating informative fragmentation patterns of proteins, nucleic acids, lipids, and carbohydrates alike has been showcased, the work presented in this dissertation focuses specifically on using 193 nm photons to characterize protein-ligand and protein-protein complexes introduced by native MS.

Despite the lack of a detailed understanding of the complex mechanisms governing photodissociation of intact protein complexes, several specific attributes posit UVPD as an all-inclusive approach for the analysis of protein complexes across all structural levels. Regarding primary structure, UVPD of intact proteins under denaturing or native conditions yields the full array of backbone cleavages (*a*-, *b*-, *c*-, *x*-, *y*-, and *z*-type ions).[103–105] Absorption of photons by the protein backbone is a fast, high energy process thought to result in both electronic excitation as well as intermolecular vibrational redistribution allowing access to both higher energy direct dissociation and lower energy internal conversion pathways.[106–108] The observation of a diverse set of ion types and access to higher energy dissociation pathways translates to sequence coverages of intact proteins unsurpassed by other ion activation methods.[104,105] For example, UVPD of model membrane protein complexes sprayed by native MS resulted in significantly improved sequence coverages compared to collisional activation.[109] Sequence coverage is defined as

the percentage of residues for which backbone cleavage is observed adjacent to that residue in a given protein sequence.

Additionally, direct dissociation pathways allow significant retention of labile covalent and noncovalent modifications along UVPD sequence ions (*i.e.* covalent bonds along the polypeptide backbone break before vibrational redistribution occurs to instead dissociate lower energy covalent or noncovalent bonds).[105,110–112] For peptides or denatured intact proteins, this has allowed improved localization of biologically relevant covalent post-translational modifications, including phosphorylation and sulfation sites.[110–112] In the context of native MS, small molecule ligand or metal cofactor binding sites can be determined from UVPD spectra of protein-ligand complexes.[105] Specifically, the location within the protein sequence of fragment ions noncovalently bound to the ligand/metal (referred to as holo ions) are mapped based on the corresponding mass shift of these ions from sequence ions that do not retain the ligand/metal (termed apo ions). Such analysis has allowed confirmation of the putative binding sites for a wide variety of protein-ligand complexes including: the heme group bound to myoglobin,[105] an NADPH cofactor and inhibitor methotrexate bound to dihydrofolate reductase (DHFR),[113] and GDP or a GTP-analogue bound to the oncogenic rat sarcoma protein K-Ras.[114]

Information on the secondary and tertiary structure of protein complexes is gained from examination of the abundances of observed sequence ions as well as the sequence position.[115,116] Subtraction of the intensities of backbone cleavages upon UVPD for a protein in different conformational states creates a difference plot that highlights regions of enhancement or suppression.[115] Observed variations in UVPD behavior reflect changes in stabilizing noncovalent interactions and protein flexibility. Specifically, enhancement of backbone fragmentation signifies fewer interactions and more flexibility, which in turn leads to the greater production of sequence ions; whereas suppression indicates

engagement in more extensive interactions, which limits the separation and detection of fragment ions.[115,117] This native UVPD-MS approach has been applied to probe the structure of myoglobin across several ESI charge states,[115] detect loop movements induced by ligand binding to DHFR,[113] define conformational changes upon ligand exchange for sequence variants of K-Ras and DHFR,[114,118] and evaluate metal binding regions of calmodulin and azurin.[119] In addition to a variety of protein-ligand complexes, UVPD-MS has also been used to analyze protein-protein complexes.[116,120–123] Favored dissociation pathways resulting from UV photoactivation of multimeric proteins include both subunit disassembly (with limited subunit unfolding during ejection) and sequence ion production. As such, information on the quaternary structure of protein-protein complexes can be gained by tracking resulting subcomplexes as a function of pulse energy or the number of pulses, in addition to the primary, secondary, and tertiary structural insight available from sequence ion identification.[120,121] Much of the work presented in this dissertation builds on these previous studies and further develops native UVPD-MS for structural analysis of biologically important protein-ligand complexes as well as scales it up to increasingly large protein-protein complexes. However, other technical developments with regards to on-line separations and multistage MS/MS approaches are first necessary to make possible the analysis of the higher order structures within more biologically complex samples.

1.4 High-Throughput Analysis of Native Protein Complexes

A logical step towards the overarching goal of analyzing increasingly complex mixtures by native MS approaches is enabling higher-throughput analysis of native protein complexes. Such developments are aimed at facilitating the idea of "native" proteomics which would entail structural characterization of every protein within a cell, identification of its interacting partners, and quantitative analysis of the dynamics of the states in which

it exists.[124,125] This type of detailed information is necessary to paint the complete picture of processes governing most disease mechanisms owing to their reliance on non-covalent interactions and networks of binding partners.[126] In practice, much work remains to optimize a reliable on-line separation method that is compatible with native MS conditions, as well as improve MS/MS approaches with regards to when and how energy is deposited into proteins of interest.

1.4.1 On-line Separation Methods Compatible with Native MS

While the large majority of native MS studies to date involve the direct infusion of a single purified protein, efforts to analyze more complex mixtures rely on coupling separation techniques to allow sequential detailed analysis of all species present.[127] For bottom-up and top-down proteomics applications reverse-phase liquid chromatography (RPLC) acts as a robust and high-resolution separation approach that is easily coupled with MS. However, the denaturing solvents required by the separation principles governing RPLC make this method incompatible with native MS. Among conventional separation techniques that can be adapted to native conditions and act as possible alternatives are size exclusion chromatography (SEC),[128,129] ion exchange chromatography (IEX),[99,130] hydrophobic interaction chromatography (HIC),[131] and capillary zone electrophoresis (CZE).[127,132–134] SEC allows separation of proteins and protein complexes based on decreasing size as larger analytes are excluded from pores and travel faster than smaller analytes that can fit within the particle cavities. As such, the pore size can be tuned to separate a desired mass range. An isocratic mobile phase is used to introduce analytes and SEC columns are notoriously tolerant of salts or detergents making it relatively easy to maintain native conditions during separation and couple on-line with MS. However, the simplicity in principle and implementation of SEC result in relatively low-resolution

separations insufficient for the distinction of species with subtle differences. IEX and HIC have each afforded slightly higher resolving power but IEX can require several columns (*i.e.* separate columns are necessary for cation and anion exchange), and both of these approaches require high salt concentrations (up to 1 M) which can disrupt weak noncovalent interactions and foul MS interfaces. Additionally, these separation methods (SEC, IEX, HIC) are not particularly amenable to nanoscale flow rates (< 1 μL/min) and instead are more routinely carried out at microbore (10 – 500 μL/min) or capillary (1 – 10 μL/min) flow rates, thus requiring significantly larger sample quantities. The improved sensitivity characteristic of nanoflow rates is highly desirable for native analysis of protein structures due to the division of the MS signal into multiple channels corresponding to different oligomeric, modification, or ESI charge states.[127]

In contrast to the above techniques, electrophoresis approaches that rely on an electric field instead of solution phase interactions with a solid phase to separate analytes based on charge and size (*i.e.* electrophoretic mobilities which are dependent on analyte charge and hydrodynamic volume) have become exciting avenues for native separations.[134,135] Capillary isoelectric focusing (cIEF) and native gel-eluted liquid fraction entrapment electrophoresis (GELFrEE) have both been used for separation of native protein complexes.[136,137] However, so far cIEF is limited to relatively stable complexes due to concerns of unfolding at a given protein's isoelectric point and the need for denaturing sheath flow buffers to maintain stable ESI. Additionally, native GELFrEE is limited to off-line separations as it has yet to be coupled on-line to a mass spectrometer owing to the use of non-MS compatible detergents and salts. Instead recently capillary zone electrophoresis (abbreviated as CE in this dissertation) has become the front-runner as an MS compatible separation method (under both denaturing and native conditions) based on its ability to achieve high-resolution separations in 0-30 kV electric fields using negligible sample and

buffer quantities.[134,135] Native MS-friendly salts are easily substituted for more harsh buffers typically used in CE as the background electrolyte (BGE). Initial challenges with coupling CE on-line with MS stemmed from the difficulty in completing the electrical circuit for separation while simultaneously providing voltage for ESI. However, several commercial solutions for interfacing CE on-line to MS exist including sheath flow, sheathless, and liquid junction.[134,135] A sheath flow interface involves directing BGE flow into a sheath liquid junction at which a separate ESI voltage is applied allowing ionization of eluting analytes from the sheath liquid. In practice this entails coupling the CE capillary coaxially with a glass emitter, similar to that used for direct infusion experiments. Another important advance in the application of CE-MS was the introduction of neutral capillary coatings, particularly linear polyacrylamide (LPA).[134,135] Coating procedures cover the inner walls of the capillary, eliminating the electroosmotic flow (EOF) to afford wider separation windows and suppress protein adsorption to the bare silica. Both sheath flow and sheathless interfaces have been used along with LPA-coated capillaries for the separation of fractionated lysate samples under native MS conditions.[127,133] Similar CE conditions using a sheath flow interface are employed in this dissertation for the separation of ribosomal proteins. Advances in CE interfaces now offer the possibility of separating proteins based on injections containing as little as 50 nL, albeit at higher concentrations (10-30 μM) than typically used with nanoscale LC separations (typically using 1-5 μL injections at 1 μM concentrations).

1.4.2 Multistage MS/MS Approach

As separations technologies inch closer to full compatibility with native MS, simultaneous development of MS/MS approaches is still necessary to enable comprehensive structural characterization of protein complexes on a high-throughput

timescale. Alternative ion activation methods, in particular ECD/ETD and UVPD, have demonstrated great utility in probing the higher order structures of relatively large protein complexes. However, with increasing protein size, these techniques require more scans to acquire quality MS/MS spectra. As such, amenability to the structural analysis of large protein complexes introduced by on-line separation methods is questionable. Instead, multistage MS/MS approaches have been introduced that involve the introduction of intact protein complexes into the gas phase by native MS, subunit disassembly of the protein complexes into monomers using front-end collisional activation, isolation of a specific monomeric subunit for subsequent activation by higher-energy collisional dissociation (HCD), and detection of the resulting sequence ions.[138] A schematic outlining the multistage MS/MS approach is shown in **Figure 1.3**. The main benefit of this method lies in simplification of the species being probed during the MS/MS event (*i.e.* monomer instead of oligomer) without sacrificing information on the quaternary structure of the protein complex, which is still obtained from the full MS scan. The benefits of employing a multistage MS/MS approach for the analysis of several model protein complexes,[138] a biologically important metabolic enzyme,[139] and off-line separated endogenous protein complexes[124] have already been demonstrated. In this dissertation, the multistage approach is further developed in this for improved structural characterization protein complexes by utilizing UVPD instead of HCD as the MS/MS step.

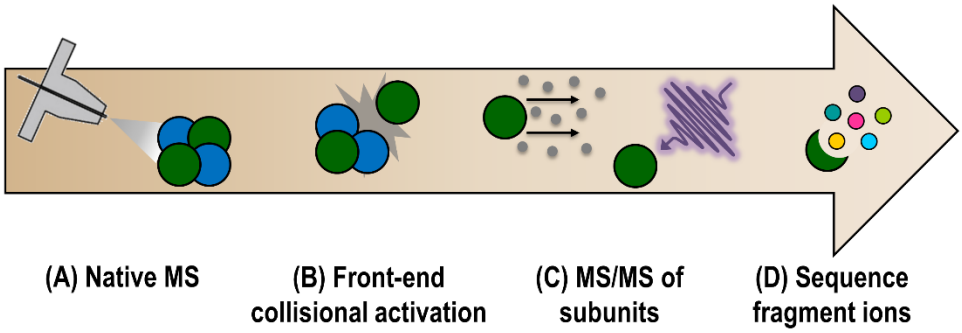

Figure 1.3: Schematic illustrating a typical multistage MS/MS approach for the improved analysis of intact protein complexes.

1.5 Overview of Chapters

As increasingly complex disease mechanisms remain to be unraveled and new ones arise, MS has already solidified its place in the structural biology toolbox owing to the speed and sensitivity it offers as an analytical technique. Although a solid groundwork for applying native MS with 193 nm UVPD to probe the structure of proteins has previously been laid, further development is still necessary to scale up this approach to larger and more complex protein samples. The work presented here is aimed at applying native UVPD-MS to characterize increasingly larger protein complexes, as well as at employing an on-line separation method in conjunction with a multistage MS/MS approach to improve the throughput of the analysis.

In Chapter 3, the utility of UVPD-MS for providing structural information on several different scales from large loop movements down to fluctuations of single residues is demonstrated by tracking the conformation of the phosphate transferase enzyme adenylate kinase during its entire catalytic cycle. Each step in the reaction is probed including binding one each of a monophosphate and triphosphate ligand, addition of a Mg^{2+} cofactor, and production of two diphosphate ligands. Variations in the efficiencies of UVPD backbone cleavage efficiencies for each protein-ligand complex provide snapshots

highlighting specific regions that undergo local fluctuations to facilitate the global transitions responsible for the catalytic function of the enzyme.

Chapter 4 details the application of UVPD-MS to characterize structural variations due to the inhibition or mutation of New Delhi metallo-β-lactamase (NDM), an enzyme responsible for conferring antibiotic resistance to bacteria. Native MS of the protein bound separately to three different covalent inhibitors provides information on the enzyme metalation state, while mapping the differences in UVPD fragment ion distributions for the three protein-ligand complexes allows closure of a beta hairpin loop to be tracked. Similarly probing the metal affinity of three clinical variants for two active site zinc ions provides insight on how zinc scarcity is driving evolution of this antibiotic resistance determinant.

The first application of UVPD-MS to investigate conformational changes in a protein-protein complex is described in Chapter 5. Native MS offers insight into the guanosine-ligand dependent homodimerization of the GTP-ase rat sarcoma (K-Ras), an important oncogene in human cancers, and three G12X clinical mutants. Additionally, heterodimerization with the downstream effector kinase rapidly accelerated fibrosarcoma (Raf) was monitored for each K-Ras variant by UVPD-MS. The stabilization of two different heterodimer interfaces were related to each of the specific variants, offering insight on how different G12X mutations impact downstream signaling and cause oncogenic upregulation.

In Chapter 6, UVPD-MS shows promise as a rapid and sensitive method to map the epitope regions of an intact model antibody-antigen complex. The workflow involves comparison of sequence coverage afforded by UV photoactivation of hemagglutinin A (HA), the main immunogenic antigen of the influenza virus, to that of HA in complex with the D1 H1-17/H3-14 antibody which has shown to confer potent protection to infection.

Specifically, the presence of the antibody results in a suppression of UVPD backbone cleavages exclusively along the putative antigenic determinant regions of HA. Plotting the number and type of sequence ions observed per residue highlights the epitope regions as stretches of HA in which fewer and less diverse sequence ions are observed for the HA:antibody complex compared to HA.

Chapter 7 introduces a multistage UVPD-MS approach aimed at more thorough structural characterization of increasingly larger noncovalent protein assemblies. Front-end collisional activation is used to break apart multimeric protein complexes into monomeric subunits that can be subsequently interrogated individually with UVPD-MS. Using this approach, two single amino acid variants of human mitochondrial enzyme branched-chain amino acid transferase 2 (BCAT2), a protein implicated in chemotherapeutic resistance in glioblastoma tumors, are each characterized from the higher-order structure down to specific interactions with a small molecule cofactor in a single experiment.

Uniting capillary electrophoresis (CE) on-line with multistage UVPD-MS allows for the high-throughput analysis of proteins comprising the *E. coli* ribosome in Chapter 8. Lowering the magnesium concentration in solution and removing the RNA that holds the ribosome unit together allows subcomplexes and individual ribosomal proteins to be observed, even under native CE-MS conditions. Implementing a multistage UVPD-MS approach for the analysis of ribosomal protein complexes separated by CE affords higher sequence coverages and improved structural characterization of protein-metal, protein-ligand, and protein-protein complexes alike. This strategy represents a significant advance towards the structural characterization of complex endogenous protein samples using UVPD-MS.

1.6 REFERENCES

(1) Baker, D.; Sali, A. Protein Structure Prediction and Structural Genomics. *Science* **2001**, *294*, 93–96.

(2) Forster, M. J. Molecular Modelling in Structural Biology. *Micron* **2002**, *33*, 365–384.

(3) Shi, Y. A Glimpse of Structural Biology through X-Ray Crystallography. *Cell* **2014**, *159*, 995–1014.

(4) Ameh, E. S. A Review of Basic Crystallography and X-Ray Diffraction Applications. *Int. J. Adv. Manuf. Technol.* **2019**, *105*, 3289–3302.

(5) Wüthrich, K. The Way to NMR Structures of Proteins. *Nat. Struct. Mol. Biol.* **2001**, *8*, 923–925.

(6) Cavalli, A.; Salvatella, X.; Dobson, C. M.; Vendruscolo, M. Protein Structure Determination from NMR Chemical Shifts. *Proc. Natl. Acad. Sci.* **2007**, *104*, 9615–9620.

(7) Bai, X.; McMullan, G.; Scheres, S. H. W. How Cryo-EM Is Revolutionizing Structural Biology. *Trends Biochem. Sci.* **2015**, *40*, 49–57.

(8) Fernández, C.; Jahnke, W. New Approaches for NMR Screening in Drug Discovery. *Drug Discov. Today Technol.* **2004**, *1*, 277–283.

(9) Søndergaard, C. R.; Garrett, A. E.; Carstensen, T.; Pollastri, G.; Nielsen, J. E. Structural Artifacts in Protein−Ligand X-Ray Structures: Implications for the Development of Docking Scoring Functions. *J. Med. Chem.* **2009**, *52*, 5673–5684.

(10) Niedzialkowska, E.; Gasiorowska, O.; Handing, K. B.; Majorek, K. A.; Porebski, P. J.; Shabalin, I. G.; Zasadzinska, E.; Cymborowski, M.; Minor, W. Protein Purification and Crystallization Artifacts: The Tale Usually Not Told. *Protein Sci.* **2016**, *25*, 720–733.

(11) Glaeser, R. M.; Hall, R. J. Reaching the Information Limit in Cryo-EM of Biological Macromolecules: Experimental Aspects. *Biophys. J.* **2011**, *100*, 2331–2337.

(12) Benesch, J. L.; Ruotolo, B. T. Mass Spectrometry: Come of Age for Structural and Dynamical Biology. *Curr. Opin. Struct. Biol.* **2011**, *21*, 641–649.

(13) Liko, I.; Allison, T. M.; Hopper, J. T.; Robinson, C. V. Mass Spectrometry Guided Structural Biology. *Curr. Opin. Struct. Biol.* **2016**, *40*, 136–144.

(14) Allison, T. M.; Bechara, C. Structural Mass Spectrometry Comes of Age: New Insight into Protein Structure, Function and Interactions. *Biochem. Soc. Trans.* **2019**, *47*, 317–327.

(15) Marcoux, J.; Robinson, C. V. Twenty Years of Gas Phase Structural Biology. *Structure* **2013**, *21*, 1541–1550.

(16) Lössl, P.; Waterbeemd, M. van de; Heck, A. J. The Diverse and Expanding Role of Mass Spectrometry in Structural and Molecular Biology. *EMBO J.* **2016**, *35*, 2634–2657.

(17) Konermann, L.; Vahidi, S.; Sowole, M. A. Mass Spectrometry Methods for Studying Structure and Dynamics of Biological Macromolecules. *Anal. Chem.* **2014**, *86*, 213–232.

(18) Heck, A. J. R. Native Mass Spectrometry: A Bridge between Interactomics and Structural Biology. *Nat. Methods* **2008**, *5*, 927–933.
(19) Leney, A. C.; Heck, A. J. R. Native Mass Spectrometry: What Is in the Name? *J. Am. Soc. Mass Spectrom.* **2017**, *28*, 5–13.
(20) Zhong, Y.; Hyung, S.-J.; Ruotolo, B. T. Ion Mobility–Mass Spectrometry for Structural Proteomics. *Expert Rev. Proteomics* **2012**, *9*, 47–58.
(21) Mendoza, V. L.; Vachet, R. W. Probing Protein Structure by Amino Acid-Specific Covalent Labeling and Mass Spectrometry. *Mass Spectrom. Rev.* **2009**, *28*, 785–815.
(22) O'Brien, J. P.; Pruet, J. M.; Brodbelt, J. S. Chromogenic Chemical Probe for Protein Structural Characterization via Ultraviolet Photodissociation Mass Spectrometry. *Anal. Chem.* **2013**, *85*, 7391–7397.
(23) Zhou, Y.; Vachet, R. W. Increased Protein Structural Resolution from Diethylpyrocarbonate-Based Covalent Labeling and Mass Spectrometric Detection. *J. Am. Soc. Mass Spectrom.* **2012**, *23*, 708–717.
(24) Zhang, H.; Gau, B. C.; Jones, L. M.; Vidavsky, I.; Gross, M. L. Fast Photochemical Oxidation of Proteins for Comparing Structures of Protein−Ligand Complexes: The Calmodulin−Peptide Model System. *Anal. Chem.* **2011**, *83*, 311–318.
(25) Zhang, B.; Rempel, D. L.; Gross, M. L. Protein Footprinting by Carbenes on a Fast Photochemical Oxidation of Proteins (FPOP) Platform. *J. Am. Soc. Mass Spectrom.* **2016**, *27*, 552–555.
(26) Madsen, J. A.; Yin, Y.; Qiao, J.; Gill, V.; Renganathan, K.; Fu, W.-Y.; Smith, S.; Anderson, J. Covalent Labeling Denaturation Mass Spectrometry for Sensitive Localized Higher Order Structure Comparisons. *Anal. Chem.* **2016**, *88*, 2478–2488.
(27) Benhaim, M.; Lee, K. K.; Guttman, M. Tracking Higher Order Protein Structure by Hydrogen-Deuterium Exchange Mass Spectrometry. *Protein Pept. Lett.* **2019**, *26*, 16–26.
(28) Pirrone, G. F.; Iacob, R. E.; Engen, J. R. Applications of Hydrogen/Deuterium Exchange MS from 2012 to 2014. *Anal. Chem.* **2014**, *87*, 99–118.
(29) Zhang, Y.; Rempel, D. L.; Zhang, J.; Sharma, A. K.; Mirica, L. M.; Gross, M. L. Pulsed Hydrogen–Deuterium Exchange Mass Spectrometry Probes Conformational Changes in Amyloid Beta (Aβ) Peptide Aggregation. *Proc. Natl. Acad. Sci.* **2013**, *110*, 14604–14609.
(30) Malito, E.; Faleri, A.; Surdo, P. L.; Veggi, D.; Maruggi, G.; Grassi, E.; Cartocci, E.; Bertoldi, I.; Genovese, A.; Santini, L.; Romagnoli, G.; Borgogni, E.; Brier, S.; Passo, C. L.; Domina, M.; Castellino, F.; Felici, F.; Veen, S. van der; Johnson, S.; Lea, S. M.; Tang, C. M.; Pizza, M.; Savino, S.; Norais, N.; Rappuoli, R.; Bottomley, M. J.; Masignani, V. Defining a Protective Epitope on Factor H Binding Protein, a Key Meningococcal Virulence Factor and Vaccine Antigen. *Proc. Natl. Acad. Sci.* **2013**, *110*, 3304–3309.
(31) Sinz, A. Chemical Cross-Linking and Mass Spectrometry to Map Three-Dimensional Protein Structures and Protein–Protein Interactions. *Mass Spectrom. Rev.* **2006**, *25*, 663–682.

(32) Schmidt, C.; Robinson, C. V. A Comparative Cross-Linking Strategy to Probe Conformational Changes in Protein Complexes. *Nat. Protoc.* **2014**, *9*, 2224–2236.
(33) Liu, F.; Rijkers, D. T. S.; Post, H.; Heck, A. J. R. Proteome-Wide Profiling of Protein Assemblies by Cross-Linking Mass Spectrometry. *Nat. Methods* **2015**, *12*, 1179–1184.
(34) Pham, N. D.; Parker, R. B.; Kohler, J. J. Photocrosslinking Approaches to Interactome Mapping. *Curr. Opin. Chem. Biol.* **2013**, *17*, 90–101.
(35) Hage, C.; Iacobucci, C.; Rehkamp, A.; Arlt, C.; Sinz, A. The First Zero-Length Mass Spectrometry-Cleavable Cross-Linker for Protein Structure Analysis. *Angew. Chem.* **2017**, *129*, 14743–14747.
(36) Trester-Zedlitz, M.; Kamada, K.; Burley, S. K.; Fenyö, D.; Chait, B. T.; Muir, T. W. A Modular Cross-Linking Approach for Exploring Protein Interactions. *J. Am. Chem. Soc.* **2003**, *125*, 2416–2425.
(37) Kao, A.; Chiu, C.; Vellucci, D.; Yang, Y.; Patel, V. R.; Guan, S.; Randall, A.; Baldi, P.; Rychnovsky, S. D.; Huang, L. Development of a Novel Cross-Linking Strategy for Fast and Accurate Identification of Cross-Linked Peptides of Protein Complexes. *Mol. Cell. Proteomics* **2011**, *10*, M110.002212.
(38) Kruppa, G. H.; Schoeniger, J.; Young, M. M. A Top down Approach to Protein Structural Studies Using Chemical Cross-Linking and Fourier Transform Mass Spectrometry. *Rapid Commun. Mass Spectrom.* **2003**, *17*, 155–162.
(39) Cammarata, M. B.; Brodbelt, J. S. Characterization of Intra- and Intermolecular Protein Crosslinking by Top Down Ultraviolet Photodissociation Mass Spectrometry. *ChemistrySelect* **2016**, *1*, 590–593.
(40) Loo, J. A. Studying Noncovalent Protein Complexes by Electrospray Ionization Mass Spectrometry. *Mass Spectrom. Rev.* **1997**, *16*, 1–23.
(41) Konermann, L.; Ahadi, E.; Rodriguez, A. D.; Vahidi, S. Unraveling the Mechanism of Electrospray Ionization. *Anal. Chem.* **2013**, *85*, 2–9.
(42) Konermann, L. Addressing a Common Misconception: Ammonium Acetate as Neutral PH "Buffer" for Native Electrospray Mass Spectrometry. *J. Am. Soc. Mass Spectrom.* **2017**, *28*, 1827–1835.
(43) Lössl, P.; Snijder, J.; Heck, A. J. R. Boundaries of Mass Resolution in Native Mass Spectrometry. *J. Am. Soc. Mass Spectrom.* **2014**, *25*, 906–917.
(44) Robinson, C. V.; Chung, E. W.; Kragelund, B. B.; Knudsen, J.; Aplin, R. T.; Poulsen, F. M.; Dobson, C. M. Probing the Nature of Noncovalent Interactions by Mass Spectrometry. A Study of Protein−CoA Ligand Binding and Assembly. *J. Am. Chem. Soc.* **1996**, *118*, 8646–8653.
(45) Li, H.; Wolff, J. J.; Van Orden, S. L.; Loo, J. A. Native Top-Down Electrospray Ionization-Mass Spectrometry of 158 KDa Protein Complex by High-Resolution Fourier Transform Ion Cyclotron Resonance Mass Spectrometry. *Anal. Chem.* **2014**, *86*, 317–320.
(46) Li, H.; Nguyen, H. H.; Ogorzalek Loo, R. R.; Campuzano, I. D. G.; Loo, J. A. An Integrated Native Mass Spectrometry and Top-down Proteomics Method That

Connects Sequence to Structure and Function of Macromolecular Complexes. *Nat. Chem.* **2018**, *10*, 139–148.
(47) Rose, R. J.; Damoc, E.; Denisov, E.; Makarov, A.; Heck, A. J. R. High-Sensitivity Orbitrap Mass Analysis of Intact Macromolecular Assemblies. *Nat. Methods* **2012**, *9*, 1084–1086.
(48) Fort, K. L.; Waterbeemd, M. van de; Boll, D.; Reinhardt-Szyba, M.; Belov, M. E.; Sasaki, E.; Zschoche, R.; Hilvert, D.; Makarov, A. A.; Heck, A. J. R. Expanding the Structural Analysis Capabilities on an Orbitrap-Based Mass Spectrometer for Large Macromolecular Complexes. *Analyst* **2017**, *143*, 100–105.
(49) Sharon, M.; Robinson, C. V. The Role of Mass Spectrometry in Structure Elucidation of Dynamic Protein Complexes. *Annu. Rev. Biochem.* **2007**, *76*, 167–193.
(50) Schmidt, C.; Zhou, M.; Marriott, H.; Morgner, N.; Politis, A.; Robinson, C. V. Comparative Cross-Linking and Mass Spectrometry of an Intact F-Type ATPase Suggest a Role for Phosphorylation. *Nat. Commun.* **2013**, *4*, 1985.
(51) Waterbeemd, M. van de; Fort, K. L.; Boll, D.; Reinhardt-Szyba, M.; Routh, A.; Makarov, A.; Heck, A. J. R. High-Fidelity Mass Analysis Unveils Heterogeneity in Intact Ribosomal Particles. *Nat. Methods* **2017**, *14*, 283.
(52) Snijder, J.; Rose, R. J.; Veesler, D.; Johnson, J. E.; Heck, A. J. R. Studying 18 Mega Dalton Virus Assemblies with Native Mass Spectrometry. *Angew. Chem. Int. Ed Engl.* **2013**, *52*, 4020–4023.
(53) Snijder, J.; van de Waterbeemd, M.; Damoc, E.; Denisov, E.; Grinfeld, D.; Bennett, A.; Agbandje-McKenna, M.; Makarov, A.; Heck, A. J. R. Defining the Stoichiometry and Cargo Load of Viral and Bacterial Nanoparticles by Orbitrap Mass Spectrometry. *J. Am. Chem. Soc.* **2014**, *136*, 7295–7299.
(54) Schmidt, C.; Robinson, C. V. Dynamic Protein Ligand Interactions – Insights from MS. *FEBS J.* **2014**, *281*, 1950–1964.
(55) Kitova, E. N.; El-Hawiet, A.; Schnier, P. D.; Klassen, J. S. Reliable Determinations of Protein–Ligand Interactions by Direct ESI-MS Measurements. Are We There Yet? *J. Am. Soc. Mass Spectrom.* **2012**, *23*, 431–441.
(56) Laganowsky, A.; Reading, E.; Allison, T. M.; Ulmschneider, M. B.; Degiacomi, M. T.; Baldwin, A. J.; Robinson, C. V. Membrane Proteins Bind Lipids Selectively to Modulate Their Structure and Function. *Nature* **2014**, *510*, 172–175.
(57) Gault, J.; Donlan, J. A. C.; Liko, I.; Hopper, J. T. S.; Gupta, K.; Housden, N. G.; Struwe, W. B.; Marty, M. T.; Mize, T.; Bechara, C.; Zhu, Y.; Wu, B.; Kleanthous, C.; Belov, M.; Damoc, E.; Makarov, A.; Robinson, C. V. High-Resolution Mass Spectrometry of Small Molecules Bound to Membrane Proteins. *Nat. Methods* **2016**, *13*, 333–336.
(58) Cubrilovic, D.; Haap, W.; Barylyuk, K.; Ruf, A.; Badertscher, M.; Gubler, M.; Tetaz, T.; Joseph, C.; Benz, J.; Zenobi, R. Determination of Protein–Ligand Binding Constants of a Cooperatively Regulated Tetrameric Enzyme Using Electrospray Mass Spectrometry. *ACS Chem. Biol.* **2014**, *9*, 218–226.

(59) Cong, X.; Liu, Y.; Liu, W.; Liang, X.; Russell, D. H.; Laganowsky, A. Determining Membrane Protein–Lipid Binding Thermodynamics Using Native Mass Spectrometry. *J. Am. Chem. Soc.* **2016**, *138*, 4346–4349.
(60) Moghadamchargari, Z.; Huddleston, J.; Shirzadeh, M.; Zheng, X.; Clemmer, D. E.; M. Raushel, F.; Russell, D. H.; Laganowsky, A. Intrinsic GTPase Activity of K-RAS Monitored by Native Mass Spectrometry. *Biochemistry* **2019**, *58*, 3396–3405.
(61) Lanucara, F.; Holman, S. W.; Gray, C. J.; Eyers, C. E. The Power of Ion Mobility-Mass Spectrometry for Structural Characterization and the Study of Conformational Dynamics. *Nat. Chem.* **2014**, *6*, 281–294.
(62) Uetrecht, C.; Rose, R. J.; Duijn, E. van; Lorenzen, K.; Heck, A. J. R. Ion Mobility Mass Spectrometry of Proteins and Protein Assemblies. *Chem. Soc. Rev.* **2010**, *39*, 1633–1655.
(63) Jurneczko, E.; E. Barran, P. How Useful Is Ion Mobility Mass Spectrometry for Structural Biology? The Relationship between Protein Crystal Structures and Their Collision Cross Sections in the Gas Phase. *Analyst* **2011**, *136*, 20–28.
(64) Konijnenberg, A.; Butterer, A.; Sobott, F. Native Ion Mobility-Mass Spectrometry and Related Methods in Structural Biology. *Biochim. Biophys. Acta BBA - Proteins Proteomics* **2013**, *1834*, 1239–1256.
(65) Ben-Nissan, G.; Sharon, M. The Application of Ion-Mobility Mass Spectrometry for Structure/Function Investigation of Protein Complexes. *Curr. Opin. Chem. Biol.* **2018**, *42*, 25–33.
(66) Eschweiler, J. D.; Frank, A. T.; Ruotolo, B. T. Coming to Grips with Ambiguity: Ion Mobility-Mass Spectrometry for Protein Quaternary Structure Assignment. *J. Am. Soc. Mass Spectrom.* **2017**, *28*, 1991–2000.
(67) Breuker, K.; McLafferty, F. W. Stepwise Evolution of Protein Native Structure with Electrospray into the Gas Phase, 10−12 to 102 S. *Proc. Natl. Acad. Sci.* **2008**, *105*, 18145–18152.
(68) Vahidi, S.; Stocks, B. B.; Konermann, L. Partially Disordered Proteins Studied by Ion Mobility-Mass Spectrometry: Implications for the Preservation of Solution Phase Structure in the Gas Phase. *Anal. Chem.* **2013**, *85*, 10471–10478.
(69) Devine, P. W. A.; Fisher, H. C.; Calabrese, A. N.; Whelan, F.; Higazi, D. R.; Potts, J. R.; Lowe, D. C.; Radford, S. E.; Ashcroft, A. E. Investigating the Structural Compaction of Biomolecules Upon Transition to the Gas-Phase Using ESI-TWIMS-MS. *J. Am. Soc. Mass Spectrom.* **2017**, *28*, 1855–1862.
(70) Williams, J. P.; Giles, K.; Green, B. N.; Scrivens, J. H.; Bateman, R. H. Ion Mobility Augments the Utility of Mass Spectrometry in the Identification of Human Hemoglobin Variants. *Rapid Commun. Mass Spectrom.* **2008**, *22*, 3179–3186.
(71) Vakhrushev, S. Y.; Langridge, J.; Campuzano, I.; Hughes, C.; Peter-Katalinić, J. Ion Mobility Mass Spectrometry Analysis of Human Glycourinome. *Anal. Chem.* **2008**, *80*, 2506–2513.
(72) Smith, D. P.; Giles, K.; Bateman, R. H.; Radford, S. E.; Ashcroft, A. E. Monitoring Copopulated Conformational States during Protein Folding Events Using

Electrospray Ionization-Ion Mobility Spectrometry-Mass Spectrometry. *J. Am. Soc. Mass Spectrom.* **2007**, *18*, 2180–2190.
(73) Ashcroft, A. E. Mass Spectrometry and the Amyloid Problem—How Far Can We Go in the Gas Phase? *J. Am. Soc. Mass Spectrom.* **2010**, *21*, 1087–1096.
(74) Bush, M. F.; Hall, Z.; Giles, K.; Hoyes, J.; Robinson, C. V.; Ruotolo, B. T. Collision Cross Sections of Proteins and Their Complexes: A Calibration Framework and Database for Gas-Phase Structural Biology. *Anal. Chem.* **2010**, *82*, 9557–9565.
(75) Shepherd, D. A.; Marty, M. T.; Giles, K.; Baldwin, A. J.; Benesch, J. L. P. Combining Tandem Mass Spectrometry with Ion Mobility Separation to Determine the Architecture of Polydisperse Proteins. *Int. J. Mass Spectrom.* **2015**, *377*, 663–671.
(76) Zheng, X.; Wojcik, R.; Zhang, X.; Ibrahim, Y. M.; Burnum-Johnson, K. E.; Orton, D. J.; Monroe, M. E.; Moore, R. J.; Smith, R. D.; Baker, E. S. Coupling Front-End Separations, Ion Mobility Spectrometry, and Mass Spectrometry For Enhanced Multidimensional Biological and Environmental Analyses. *Annu. Rev. Anal. Chem.* **2017**, *10*, 71–92.
(77) Lermyte, F.; Tsybin, Y. O.; O'Connor, P. B.; Loo, J. A. Top or Middle? Up or Down? Toward a Standard Lexicon for Protein Top-Down and Allied Mass Spectrometry Approaches. *J. Am. Soc. Mass Spectrom.* **2019**, *30*, 1149–1157.
(78) Brodbelt, J. S.; Morrison, L. J.; Santos, I. Ultraviolet Photodissociation Mass Spectrometry for Analysis of Biological Molecules. *Chem. Rev.* **2019**.
(79) Macias, L. A.; Santos, I. C.; Brodbelt, J. S. Ion Activation Methods for Peptides and Proteins. *Anal. Chem.* **2020**, *92*, 227–251.
(80) Roepstorff, P.; Fohlman, J. Proposal for a Common Nomenclature for Sequence Ions in Mass Spectra of Peptides. *Biomed. Mass Spectrom.* **1984**, *11*, 601.
(81) Paizs, B.; Suhai, S. Fragmentation Pathways of Protonated Peptides. *Mass Spectrom. Rev.* **2005**, *24*, 508–548.
(82) McLuckey, S. A. Principles of Collisional Activation in Analytical Mass Spectrometry. *J. Am. Soc. Mass Spectrom.* **1992**, *3*, 599–614.
(83) Hall, Z.; Hernández, H.; Marsh, J. A.; Teichmann, S. A.; Robinson, C. V. The Role of Salt Bridges, Charge Density, and Subunit Flexibility in Determining Disassembly Routes of Protein Complexes. *Structure* **2013**, *21*, 1325–1337.
(84) Yin, S.; Loo, J. A. Elucidating the Site of Protein-ATP Binding by Top-Down Mass Spectrometry. *J. Am. Soc. Mass Spectrom.* **2010**, *21*, 899–907.
(85) Yin, S.; Loo, J. A. Top-down Mass Spectrometry of Supercharged Native Protein–Ligand Complexes. *Int. J. Mass Spectrom.* **2011**, *300*, 118–122.
(86) Dixit, S. M.; Polasky, D. A.; Ruotolo, B. T. Collision Induced Unfolding of Isolated Proteins in the Gas Phase: Past, Present, and Future. *Curr. Opin. Chem. Biol.* **2018**, *42*, 93–100.
(87) Zubarev, R. A.; Horn, D. M.; Fridriksson, E. K.; Kelleher, N. L.; Kruger, N. A.; Lewis, M. A.; Carpenter, B. K.; McLafferty, F. W. Electron Capture Dissociation for Structural Characterization of Multiply Charged Protein Cations. *Anal. Chem.* **2000**, *72*, 563–573.

(88) Zubarev, R. A. Electron-Capture Dissociation Tandem Mass Spectrometry. *Curr. Opin. Biotechnol.* **2004**, *15*, 12–16.
(89) Syka, J. E. P.; Coon, J. J.; Schroeder, M. J.; Shabanowitz, J.; Hunt, D. F. Peptide and Protein Sequence Analysis by Electron Transfer Dissociation Mass Spectrometry. *Proc. Natl. Acad. Sci.* **2004**, *101*, 9528–9533.
(90) Li, H.; Sheng, Y.; McGee, W.; Cammarata, M.; Holden, D.; Loo, J. A. Structural Characterization of Native Proteins and Protein Complexes by Electron Ionization Dissociation-Mass Spectrometry. *Anal. Chem.* **2017**, *89*, 2731–2738.
(91) Zubarev, R. A.; Kelleher, N. L.; McLafferty, F. W. Electron Capture Dissociation of Multiply Charged Protein Cations. A Nonergodic Process. *J. Am. Chem. Soc.* **1998**, *120*, 3265–3266.
(92) Breuker, K.; Oh, H.; Horn, D. M.; Cerda, B. A.; McLafferty, F. W. Detailed Unfolding and Folding of Gaseous Ubiquitin Ions Characterized by Electron Capture Dissociation. *J. Am. Chem. Soc.* **2002**, *124*, 6407–6420.
(93) Breuker, K.; Oh, H.; Lin, C.; Carpenter, B. K.; McLafferty, F. W. Nonergodic and Conformational Control of the Electron Capture Dissociation of Protein Cations. *Proc. Natl. Acad. Sci.* **2004**, *101*, 14011–14016.
(94) Lermyte, F.; Valkenborg, D.; Loo, J. A.; Sobott, F. Radical Solutions: Principles and Application of Electron-Based Dissociation in Mass Spectrometry-Based Analysis of Protein Structure. *Mass Spectrom. Rev.* **2018**, *37*, 750–771.
(95) Lermyte, F.; Sobott, F. Electron Transfer Dissociation Provides Higher-Order Structural Information of Native and Partially Unfolded Protein Complexes. *PROTEOMICS* **2015**, *15*, 2813–2822.
(96) Zhang, H.; Cui, W.; Wen, J.; Blankenship, R. E.; Gross, M. L. Native Electrospray and Electron-Capture Dissociation FTICR Mass Spectrometry for Top-down Studies of Protein Assemblies. *Anal. Chem.* **2011**, *83*, 5598–5606.
(97) Li, H.; Wongkongkathep, P.; Van Orden, S. L.; Ogorzalek Loo, R. R.; Loo, J. A. Revealing Ligand Binding Sites and Quantifying Subunit Variants of Noncovalent Protein Complexes in a Single Native Top-Down FTICR MS Experiment. *J. Am. Soc. Mass Spectrom.* **2014**, *25*, 2060–2068.
(98) Zhou, M.; Wysocki, V. H. Surface Induced Dissociation: Dissecting Noncovalent Protein Complexes in the Gas Phase. *Acc. Chem. Res.* **2014**, *47*, 1010–1018.
(99) Sahasrabuddhe, A.; Hsia, Y.; Busch, F.; Sheffler, W.; King, N. P.; Baker, D.; Wysocki, V. H. Confirmation of Intersubunit Connectivity and Topology of Designed Protein Complexes by Native MS. *Proc. Natl. Acad. Sci.* **2018**, *115*, 1268–1273.
(100) Busch, F.; VanAernum, Z. L.; Ju, Y.; Yan, J.; Gilbert, J. D.; Quintyn, R. S.; Bern, M.; Wysocki, V. H. Localization of Protein Complex Bound Ligands by Surface-Induced Dissociation High-Resolution Mass Spectrometry. *Anal. Chem.* **2018**, *90*, 12796–12801.
(101) Dunbar, R. C. Photodissociation of the Methyl Chloride (CH3Cl+) and Nitrous Oxide (N2O+) Cations. *J. Am. Chem. Soc.* **1971**, *93*, 4354–4358.

(102) Tecklenburg, R. E.; Miller, M. N.; Russell, D. H. Laser Ion Beam Photodissociation Studies of Model Amino Acids and Peptides. *J. Am. Chem. Soc.* **1989**, *111*, 1161–1171.
(103) Canon, F.; Milosavljević, A. R.; van der Rest, G.; Réfrégiers, M.; Nahon, L.; Sarni-Manchado, P.; Cheynier, V.; Giuliani, A. Photodissociation and Dissociative Photoionization Mass Spectrometry of Proteins and Noncovalent Protein–Ligand Complexes. *Angew. Chem. Int. Ed.* **2013**, *52*, 8377–8381.
(104) Shaw, J. B.; Li, W.; Holden, D. D.; Zhang, Y.; Griep-Raming, J.; Fellers, R. T.; Early, B. P.; Thomas, P. M.; Kelleher, N. L.; Brodbelt, J. S. Complete Protein Characterization Using Top-Down Mass Spectrometry and Ultraviolet Photodissociation. *J. Am. Chem. Soc.* **2013**, *135*, 12646–12651.
(105) O'Brien, J. P.; Li, W.; Zhang, Y.; Brodbelt, J. S. Characterization of Native Protein Complexes Using Ultraviolet Photodissociation Mass Spectrometry. *J. Am. Chem. Soc.* **2014**, *136*, 12920–12928.
(106) Zabuga, A. V.; Kamrath, M. Z.; Boyarkin, O. V.; Rizzo, T. R. Fragmentation Mechanism of UV-Excited Peptides in the Gas Phase. *J. Chem. Phys.* **2014**, *141*, 154309.
(107) R. Julian, R. The Mechanism Behind Top-Down UVPD Experiments: Making Sense of Apparent Contradictions. *J. Am. Soc. Mass Spectrom.* **2017**, *28*, 1823–1826.
(108) Pereverzev, A. Y.; Koczor-Benda, Z.; Saparbaev, E.; Kopysov, V. N.; Rosta, E.; Boyarkin, O. V. Spectroscopic Evidence for Peptide-Bond-Selective Ultraviolet Photodissociation. *J. Phys. Chem. Lett.* **2020**, *11*, 206–209.
(109) Sipe, S. N.; Patrick, J. W.; Laganowsky, A.; Brodbelt, J. S. Enhanced Characterization of Membrane Protein Complexes by Ultraviolet Photodissociation Mass Spectrometry. *Anal. Chem.* **2020**, *92*, 899–907.
(110) Robinson, M. R.; Moore, K. L.; Brodbelt, B. Direct Identification of Tyrosine Sulfation by Using Ultraviolet Photodissociation Mass Spectrometry. *J. Am. Soc. Mass Spectrom.* **2014**, *25*, 1461–1471.
(111) Fort, K. L.; Dyachenko, A.; Potel, C. M.; Corradini, E.; Marino, F.; Barendregt, A.; Makarov, A. A.; Scheltema, R. A.; Heck, A. J. R. Implementation of Ultraviolet Photodissociation on a Benchtop Q Exactive Mass Spectrometer and Its Application to Phosphoproteomics. *Anal. Chem.* **2016**, *88*, 2303–2310.
(112) Robinson, M. R.; Taliaferro, J. M.; Dalby, K. N.; Brodbelt, J. S. 193 Nm Ultraviolet Photodissociation Mass Spectrometry for Phosphopeptide Characterization in the Positive and Negative Ion Modes. *J. Proteome Res.* **2016**, *15*, 2739–2748.
(113) Cammarata, M. B.; Thyer, R.; Rosenberg, J.; Ellington, A.; Brodbelt, J. S. Structural Characterization of Dihydrofolate Reductase Complexes by Top-Down Ultraviolet Photodissociation Mass Spectrometry. *J. Am. Chem. Soc.* **2015**, *137*, 9128–9135.
(114) Cammarata, M. B.; Schardon, C. L.; Mehaffey, M. R.; Rosenberg, J.; Singleton, J.; Fast, W.; Brodbelt, J. S. Impact of G12 Mutations on the Structure of K-Ras Probed by Ultraviolet Photodissociation Mass Spectrometry. *J. Am. Chem. Soc.* **2016**, *138*, 13187–13196.

(115) Cammarata, M. B.; Brodbelt, J. S. Structural Characterization of Holo- and Apo-Myoglobin in the Gas Phase by Ultraviolet Photodissociation Mass Spectrometry. *Chem. Sci.* **2015**, *6*, 1324–1333.
(116) Zhou, M.; Liu, W.; Shaw, J. B. Charge Movement and Structural Changes in the Gas-Phase Unfolding of Multimeric Protein Complexes Captured by Native Top-Down Mass Spectrometry. *Anal. Chem.* **2020**, *92*, 1788–1795.
(117) Warnke, S.; von Helden, G.; Pagel, K. Analyzing the Higher Order Structure of Proteins with Conformer-Selective Ultraviolet Photodissociation. *PROTEOMICS* **2015**, *15*, 2804–2812.
(118) Cammarata, M.; Thyer, R.; Lombardo, M.; Anderson, A.; Wright, D.; Ellington, A.; Brodbelt, J. S. Characterization of Trimethoprim Resistant E. Coli Dihydrofolate Reductase Mutants by Mass Spectrometry and Inhibition by Propargyl-Linked Antifolates. *Chem. Sci.* **2017**, *8*, 4062–4072.
(119) Crittenden, C. M.; Novelli, E. T.; Mehaffey, M. R.; Xu, G. N.; Giles, D. H.; Fies, W. A.; Dalby, K. N.; Webb, L. J.; Brodbelt, J. S. Structural Evaluation of Protein/Metal Complexes via Native Electrospray Ultraviolet Photodissociation Mass Spectrometry. *J. Am. Soc. Mass Spectrom.* **2020**, *31*, 1140–1150.
(120) Morrison, L. J.; Brodbelt, J. S. 193 Nm Ultraviolet Photodissociation Mass Spectrometry of Tetrameric Protein Complexes Provides Insight into Quaternary and Secondary Protein Topology. *J. Am. Chem. Soc.* **2016**, *138*, 10849–10859.
(121) Tamara, S.; Dyachenko, A.; Fort, K. L.; Makarov, A. A.; Scheltema, R. A.; Heck, A. J. R. Symmetry of Charge Partitioning in Collisional and UV Photon-Induced Dissociation of Protein Assemblies. *J. Am. Chem. Soc.* **2016**, *138*, 10860–10868.
(122) Greisch, J.-F.; Tamara, S.; Scheltema, R. A.; Maxwell, H. W. R.; Fagerlund, R. D.; Fineran, P. C.; Tetter, S.; Hilvert, D.; Heck, A. J. R. Expanding the Mass Range for UVPD-Based Native Top-down Mass Spectrometry. *Chem. Sci.* **2019**, *10*, 7163–7171.
(123) Sipe, S. N.; Brodbelt, J. S. Impact of Charge State on 193 Nm Ultraviolet Photodissociation of Protein Complexes. *Phys. Chem. Chem. Phys.* **2019**, *21*, 9265–9276.
(124) Skinner, O. S.; Haverland, N. A.; Fornelli, L.; Melani, R. D.; Do Vale, L. H. F.; Seckler, H. S.; Doubleday, P. F.; Schachner, L. F.; Srzentić, K.; Kelleher, N. L.; Compton, P. D. Top-down Characterization of Endogenous Protein Complexes with Native Proteomics. *Nat. Chem. Biol.* **2018**, *14*, 36–41.
(125) Gault, J.; Liko, I.; Landreh, M.; Shutin, D.; Bolla, J. R.; Jefferies, D.; Agasid, M.; Yen, H.-Y.; Ladds, M. J. G. W.; Lane, D. P.; Khalid, S.; Mullen, C.; Remes, P. M.; Huguet, R.; McAlister, G.; Goodwin, M.; Viner, R.; Syka, J. E. P.; Robinson, C. V. Combining Native and 'Omics' Mass Spectrometry to Identify Endogenous Ligands Bound to Membrane Proteins. *Nat. Methods* **2020**, *17*, 505–508.
(126) Savaryn, J. P.; Catherman, A. D.; Thomas, P. M.; Abecassis, M. M.; Kelleher, N. L. The Emergence of Top-down Proteomics in Clinical Research. *Genome Med.* **2013**, *5*, 53.

(127) Belov, A. M.; Viner, R.; Santos, M. R.; Horn, D. M.; Bern, M.; Karger, B. L.; Ivanov, A. R. Analysis of Proteins, Protein Complexes, and Organellar Proteomes Using Sheathless Capillary Zone Electrophoresis - Native Mass Spectrometry. *J. Am. Soc. Mass Spectrom.* **2017**, *28*, 2614–2634.
(128) Kükrer, B.; Filipe, V.; van Duijn, E.; Kasper, P. T.; Vreeken, R. J.; Heck, A. J. R.; Jiskoot, W. Mass Spectrometric Analysis of Intact Human Monoclonal Antibody Aggregates Fractionated by Size-Exclusion Chromatography. *Pharm. Res.* **2010**, *27*, 2197–2204.
(129) Muneeruddin, K.; Thomas, J. J.; Salinas, P. A.; Kaltashov, I. A. Characterization of Small Protein Aggregates and Oligomers Using Size Exclusion Chromatography with Online Detection by Native Electrospray Ionization Mass Spectrometry. *Anal. Chem.* **2014**, *86*, 10692–10699.
(130) Muneeruddin, K.; Nazzaro, M.; Kaltashov, I. A. Characterization of Intact Protein Conjugates and Biopharmaceuticals Using Ion-Exchange Chromatography with Online Detection by Native Electrospray Ionization Mass Spectrometry and Top-Down Tandem Mass Spectrometry. *Anal. Chem.* **2015**, *87*, 10138–10145.
(131) Debaene, F.; Bœuf, A.; Wagner-Rousset, E.; Colas, O.; Ayoub, D.; Corvaïa, N.; Van Dorsselaer, A.; Beck, A.; Cianférani, S. Innovative Native MS Methodologies for Antibody Drug Conjugate Characterization: High Resolution Native MS and IM-MS for Average DAR and DAR Distribution Assessment. *Anal. Chem.* **2014**, *86*, 10674–10683.
(132) Han, X.; Wang, Y.; Aslanian, A.; Fonslow, B.; Graczyk, B.; Davis, T. N.; Yates, J. R. In-Line Separation by Capillary Electrophoresis Prior to Analysis by Top-Down Mass Spectrometry Enables Sensitive Characterization of Protein Complexes. *J. Proteome Res.* **2014**, *13*, 6078–6086.
(133) Shen, X.; Kou, Q.; Guo, R.; Yang, Z.; Chen, D.; Liu, X.; Hong, H.; Sun, L. Native Proteomics in Discovery Mode Using Size-Exclusion Chromatography–Capillary Zone Electrophoresis–Tandem Mass Spectrometry. *Anal. Chem.* **2018**, *90*, 10095–10099.
(134) Shen, X.; Yang, Z.; McCool, E. N.; Lubeckyj, R. A.; Chen, D.; Sun, L. Capillary Zone Electrophoresis-Mass Spectrometry for Top-down Proteomics. *TrAC Trends Anal. Chem.* **2019**, *120*, 115644.
(135) Kristoff, C. J.; Bwanali, L.; Veltri, L. M.; Gautam, G. P.; Rutto, P. K.; Newton, E. O.; Holland, L. A. Challenging Bioanalyses with Capillary Electrophoresis. *Anal. Chem.* **2020**, *92*, 49–66.
(136) Fonslow, B. R.; Kang, S. A.; Gestaut, D. R.; Graczyk, B.; Davis, T. N.; Sabatini, D. M.; Yates III, J. R. Native Capillary Isoelectric Focusing for the Separation of Protein Complex Isoforms and Subcomplexes. *Anal. Chem.* **2010**, *82*, 6643–6651.
(137) Skinner, O. S.; Do Vale, L. H. F.; Catherman, A. D.; Havugimana, P. C.; Sousa, M. V. de; Compton, P. D.; Kelleher, N. L. Native GELFrEE: A New Separation Technique for Biomolecular Assemblies. *Anal. Chem.* **2015**, *87*, 3032–3038.
(138) Belov, M. E.; Damoc, E.; Denisov, E.; Compton, P. D.; Horning, S.; Makarov, A. A.; Kelleher, N. L. From Protein Complexes to Subunit Backbone Fragments: A

Multi-Stage Approach to Native Mass Spectrometry. *Anal. Chem.* **2013**, *85*, 11163–11173.

(139) Ben-Nissan, G.; Belov, M. E.; Morgenstern, D.; Levin, Y.; Dym, O.; Arkind, G.; Lipson, C.; Makarov, A. A.; Sharon, M. Triple-Stage Mass Spectrometry Unravels the Heterogeneity of an Endogenous Protein Complex. *Anal. Chem.* **2017**, *89*, 4708–4715.

Chapter 2: Experimental Methods

2.1 Overview

Exploiting the methods described below allows significant improvements in the versatility and throughput for the structural characterization of protein-ligand and protein-protein complexes by MS. Key developments include coupling native MS compatible separation methods with existing UVPD technology in a multistage tandem MS approach as well as streamlining the data analysis workflow by utilizing several MS/MS interpretation pipelines.

2.2 Mass Spectrometry

Either a Fourier transform (FT) hybrid linear quadrupole ion trap-Orbitrap mass spectrometer or an ultra-high mass range Orbitrap mass spectrometer were used for all experiments detailed in this dissertation. Each of these instruments was equipped with an electrospray ionization (ESI) source to ionize proteins under native conditions and modified to perform UVPD in the HCD collision cell.

2.2.1 Native Electrospray Ionization

A basic requirement of any MS-based approach is the creation of gas-phase ions from analytes of interest. As such, an alphabet soup of ionization techniques already exists (*e.g.* EI, MALDI, APCI, DESI, etc.) while more are still being developed for specialized applications. Nevertheless, the field of biological MS has specifically relied on those methods capable of maintaining the integrity of biomolecules as they are charged and transferred to the gas phase. Among such soft ionization techniques, electrospray ionization (ESI) remains the most widely used owing to the deposition of multiple charges and orthogonality in on-line coupling of solution-phase separations. First reported in 1984 by

Fenn and Yamishita, ESI is best depicted as a controlled current electrolytic cell (**Figure 2.1**).[1,2] Under the influence of an electric field, charge accumulates at the surface of a solution containing the analytes of interest. For denaturing MS conditions (> 50% organic solvent, typically acetonitrile or methanol) low percentages of formic or acetic acid (< 1%) are added to aid in this process. However, for native MS conditions, spray solvents only contain volatile salts (ammonium acetate, ammonium bicarbonate, or ammonium formate) at near-neutral pH values to mimic physiological conditions. With sufficiently high voltage conditions, a Taylor cone is formed at the tip of the spray needle from which highly charged droplets are ejected. As these droplets travel towards the mass spectrometer inlet, they undergo rapid evaporation of the surrounding solvent. As coulombic repulsion forces of the ions surpass the surface tension of the shrinking droplets, referred to as the Rayleigh stability limit, numerous fission events occur and eventually yield completely desolvated, gas-phase ions that can enter the mass spectrometer for analysis.

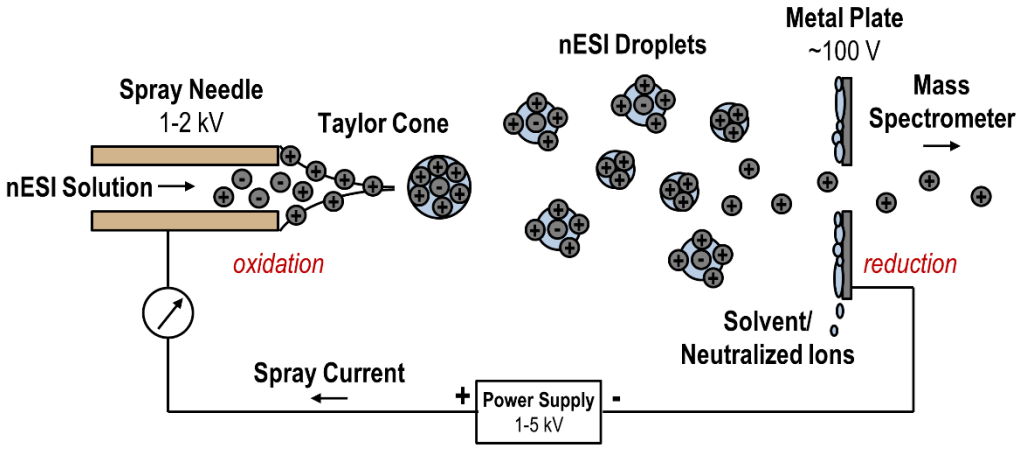

Figure 2.1: The electrospray ionization process as a schematic representation with values corresponding to nESI conditions (adapted from Cech and Enke).[2]

For native MS applications, typically this process is scaled down to nano ESI (nESI) in which, instead of introducing the sample with an ESI source and syringe pump, metal-coated borosilicate emitters (20-50 μm inner diameter) are filled with ~5 μL of solution for offline ionization. A ring electrode acts to hold the emitter tip in proximity to the mass spectrometer inlet and apply a voltage along the metal coating (20:80 Au:Pd), which in turn induces electroosmotic flow of the nESI solution. In addition to lower sample volumes, nESI requires lower spray voltages compared to standard ESI (1-2 kV vs. 3-5 kV, respectively). This is advantageous for lowering the internal energy imparted to analytes during ionization and minimizing protein unfolding. In the same vein, the mass spectrometer inlet temperature is typically lowered from 275 °C to 50-200 °C for native MS experiments. In general, native MS ionization parameters are tuned to be as "gentle" as possible, often at the expense of sensitivity compared to denaturing MS.

2.2.2 Mass Analyzers

Schematic representations of the two mass spectrometric platforms used for all work detailed in this dissertation are shown in **Figure 2.2**. The Orbitrap Elite (Thermo Fisher Scientific, Bremen Germany) is a hybrid ion trap-Orbitrap mass spectrometer. Following ionization in the nESI source region, several optics are used to guide ions to the dual linear ion traps (LITs). Composed of two pairs of hyperbolic rods arranged orthogonally and radially equidistant from each other (referred to as a quadrupole) as well as static lens elements at both terminal ends of the rods, LITs can be used for low-resolution mass analysis, ion isolation, and collisional ion activation.[3] RF voltages applied to each pair of rods 180 degrees out of phase confine ion motion radially while DC offset voltages on the static lens elements at the front and back control the ions axially and gate flow of the ions into the trap. Broadband waveforms and auxiliary RF voltages are applied to one

pair of rods to enable ion isolation and activation in a secular frequency-dependent manner. For mass analysis, instead an RF amplitude ramp causes sequential, mass-selective ejection of ions through slits in the center electrodes. Typically, dual LITs are present, allowing the first to be maintained at a higher pressure (~5 mTorr) of helium bath gas for improved ion trapping and collisional activation efficiency, while the second is kept at a lower pressure (0.3 mTorr) and used exclusively for mass analysis scans. For native MS experiments, LITs are useful for ion isolation, but activation by beam-type collisional activation in the HCD cell and high-resolution mass analysis in the Orbitrap are more informative.

First introduced almost 20 years ago by Makarov, Orbitraps provide high resolving power, part per million mass accuracies, and short acquisition times without the need for the expensive superconducting magnets required by FT-ICR instruments.[4,5] Instead an Orbitrap is composed of a barrel-shaped electrode with two different segments that enclose an inner spindle-like electrode. Packets of ions are pulsed into the analyzer and undergo harmonic oscillations along the axis of the inner electrode under the influence of a quadro-logarithmic field. The frequency of this motion, which is proportional to $(m/z)^{-1/2}$ for a given ion, is detected as an image current between the two segments comprising the outer electrode. In the context of native MS, Orbitrap mass analyzers can scan high *m/z* regions (currently up to *m/z* 80,000 on some instruments) but still fail to routinely provide isotopic resolution for complexes larger than ~30 kDa. As such, native MS spectra of large complexes are typically collected at lower resolving powers (< 25K) as the overall signal decreases quickly at higher resolving power values.

While the other mass spectrometer in **Figure 2.2** similarly contains an Orbitrap for mass analysis, several modifications were made to the ion optics at the front-end to improve the transfer of higher *m/z* ions (these modifications are detailed in Chapter 7). As such it is referred to as a Q Exactive UHMR (ultra-high mass range) mass spectrometer (Thermo

Fisher Scientific, Bremen, Germany). Additionally, a quadrupole mass filter is used for ion isolation instead of a LIT. Consisting of two pairs of hyperbolic rods with RF voltages 180 degrees out of phase applied to opposite pairs (similar to the middle section of a LIT), quadrupoles can operate as RF-only ion guides allowing all ions to pass or as narrow isolation width filters for specific *m/z* values by application of DC offset voltages to each pair of electrodes. Both instrument platforms contain an HCD collision cell for ion activation by HCD or UVPD prior to Orbitrap mass analysis. The specific values of all MS parameters used to acquire data are detailed in each Chapter.

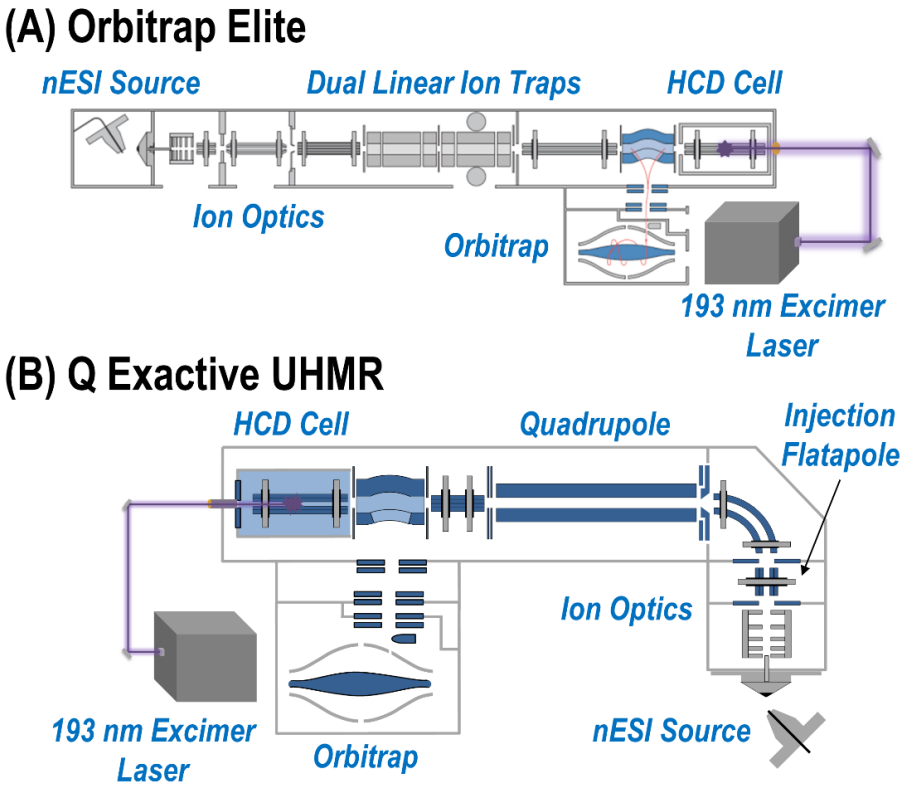

Figure 2.2: Schematic representations of a Thermo Fisher Scientific (A) Orbitrap Elite and (B) Q Exactive UHMR mass spectrometer with important regions labelled. Modifications to enable UVPD in the HCD cell of each instrument are detailed in section 2.3.3.

2.3 Ion Activation

For the protein-ligand and protein-protein complexes probed herein, either HCD or UVPD were employed for ion activation. Additionally, in-source trapping (IST) provided front-end collisional activation during the analysis of some complexes. Subsequent sections detail relevant acquisition parameters and any modifications necessary to implement these MS/MS approaches.

2.3.1 In-Source Trapping

Exclusive to the Q Exactive UHMR is a type of broadband front-end collisional activation enabled in the ion optics region of the instrument (specifically in the injection flatapole) and termed in-source trapping (IST).[6] Since there is no precursor isolation of a specific *m/z* value, this type of activation is not technically considered an MS/MS technique. Increasing the positive potential on the lens following this multipole while simultaneously dropping the injection flatapole bias to a negative voltage, referred to as the desolvation voltage (up to -250 V), blocks ions from exiting and traps them in a potential well for a set amount of desolvation time (4 – 10 msec). This process is depicted in **Figure 2.3**. While trapped, ions collide with background gas in the injection flatapole causing collisional activation. A 200 µs release event returns the injection flatapole and following lens biases to their previous operating values and allows the resulting ions to proceed through the instrument. The makeup of the resulting ion population following IST is dependent on the desolvation voltage as well as protein size and flexibility, with lower desolvation voltage values (-50 to -150 V) simply aiding in desolvation and maintaining intact complexes, while higher desolvation voltages (> -150 V) typically causing disassembly of complexes into constituent subunits or even production of sequence ions.

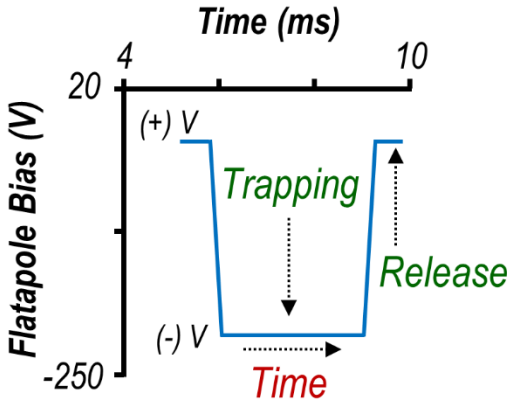

Figure 2.3: Graph schematically representing the injection flatapole bias as a function of time during an IST event. The depth of the potential well is determined by the desolvation voltage while the width is controlled by the desolvation time.

2.3.2 Higher-energy Collisional Dissociation

Throughout this dissertation, beam-type higher-energy collisional dissociation (HCD) is used as a collisional activation method for protein-ligand and protein-protein complexes. The metrics (sequence coverage, localization of modifications, etc.) of HCD provide a baseline to which UVPD can be compared, making evident specific advantages of using an alternative ion activation method. Both instrument platforms used in this work have an HCD cell so no instrument modifications were necessary. On the Orbitrap Elite, HCD is controlled as a % normalized collision energy (% NCE) that is normalized to the charge state of the precursor while on the Q Exactive UHMR, instead the collision energy is set as a direct value in electronvolts.

2.3.3 Ultraviolet Photodissociation

As depicted in **Figure 2.2**, both mass spectrometers required modifications to enable ultraviolet photodissociation (UVPD) in the HCD cell via coupling Coherent ExciStar XS 500 (Santa Clara, CA) pulsed excimer lasers using ArF to operate at 193 nm.

For the Orbitrap Elite, these changes have been previously described.[7] Briefly, a CaF_2 optical window was added coaxially to the vacuum manifold of the HCD collision cell to allow transmission of the laser beam. Firmware modifications allowed the creation of a custom UVPD flag that sends an external trigger to the laser using a Berkeley Nucleonics Corp. pulse generator (San Rafael, CA) as ions are transferred into the HCD cell using 1% NCE. The laser was similarly incorporated through the HCD cell on the Q Exactive UHMR. Further detailed in Chapter 7, a fused silica window was incorporated using a stainless-steel tube, allowing the laser beam to pass coaxially through the HCD cell. An Arduino Uno microcontroller controlled by a custom script creates transistor-transistor logic (TTL) signals to trigger emission of the laser based on a rise in the HCD multipole DC offset. On both instruments, the laser is operated at the maximum repetition rate (500 Hz) to generate one 5 nsec pulse every 2 msec. Unless otherwise noted, UVPD spectra are the result of 1 pulse at 3 mJ.

2.4 On-line Separation Methods

Two separation methods were coupled on-line with MS in this dissertation to enable another dimension of analysis. The first, size-exclusion chromatography (SEC), was used to gain information on the solution phase oligomeric states of protein-protein complexes. The second, capillary zone electrophoresis (CE), allowed separation of a more complex biological mixture for high-throughput analysis by UVPD-MS.

2.4.1 Size-Exclusion Chromatography

A Dionex LC system (Thermo Fisher Scientific) interfaced on-line with the mass spectrometers in **Figure 2.2** was used to carry out size-exclusion chromatography (SEC) experiments. Owing to the higher flow rates (80 – 100 μL/min) required for SEC, an ESI

source with spray voltages of 3-4 kV and nitrogen sweep gas was used to ionize proteins. Unless otherwise stated, samples were prepared at 1 μg/μL for 5 μL injections. Isocratic mobile phases of 20-50 mM ammonium acetate (pH 6.8) pushed proteins along a 2.1 mm × 300 mm ACQUITY UPLC Protein BEH SEC column with a 200 Å pore size and 1.7 μm particle size (Waters, Milford, MA), or a 2.1 mm × 300 mm Zenix-C column with an 80 Å pore size and 3 μm particle size (Sepax Technologies, Newark, DE). ESI-MS spectra were collected at a resolving power of 240K (Orbitrap Elite) or 12500 (Q Exactive UHMR) as proteins eluted.

2.4.2 Capillary Zone Electrophoresis

For the CE-MS analysis described in Chapter 8, a CMP Scientific (Brooklyn, NY) ECE-001 capillary electrophoresis autosampler and electrokinetically pumped sheath flow interface were coupled on-line to the Q Exactive UHMR mass spectrometer. Samples were prepared at ~30 μg/μL and hydrodynamically injected (using 5 psi for 45 sec) into a 100 cm LPA-coated capillary (50 μm inner diameter). Briefly, as previously described,[8] the capillary coating process involved successively flushing a bare fused silica capillary with 1 M hydrochloric acid, water, 1 M sodium hydroxide, water, and methanol. Subsequent exposure to 3-(trimethoxysilyl) propyl methacrylate introduced carbon-carbon double bonds along the inner wall of the capillary. The treated capillary was filled with an acrylamide solution in water containing ammonium persulfate and incubated at 50 ˚C for 1 hour. Unreacted reagents were flushed with water. The background electrolyte (BGE) for CE was 25 mM ammonium acetate (pH 6.8) containing up to 100 μM magnesium acetate, and the sheath liquid used for ESI was 10 mM ammonium acetate (pH 6.8). CE separation was achieved using a +30 kV separation voltage and 0.5 psi pressure was applied for the duration of the separation. A Sutter Instrument (Novato, CA) P-1000 micropipette puller

was used to fabricate ESI emitters (~20 μm tip opening, 4 cm length) for the CE-MS interface from borosilicate capillaries (1.0 mm outer dimeter, 0.75 mm inner diameter). ESI spray voltages of 2.4-2.6 kV were used for on-line ionization of proteins following CE separation.

2.5 DATA ANALYSIS

Several MS data analysis programs are used in conjunction throughout this dissertation to aid in the interpretation of MS/MS spectra. Specifically, ProSight Lite and ProSight Native are used to identify sequence ions or monomeric subunits resulting from HCD or UVPD of protein-ligand or protein-protein complexes. Adding expected mass shifts to the search parameters in these programs allows for the identification of ligand-bound holo fragment ions. For UVPD spectra, UV-POSIT streamlines summation of sequence ion intensities by residue. Statistical analysis is performed for measured differences in UVPD fragment ion intensities to establish a confidence threshold for claims about structural changes.

2.5.1 ProSight Lite and ProSight Native

Obtaining structural information from MS/MS spectra requires identifying up to hundreds of sequence ions from a single spectrum. As this would be a tedious and time-consuming task to carry out by hand, programs exist to generate a theoretical mass list resulting from cleavage along every single backbone site. The experimental mass list can then be cross-referenced and identifications of sequence ions made within a mass tolerance. ProSight Lite is one such program that matches experimental fragment ions to the list of theoretical sequence ion masses and visualizes the results along the entered protein sequence.[9] Specifically, all HCD and UVPD MS/MS spectra in this dissertation were first

deconvoluted using the Xtract algorithm (Thermo Fisher Scientific) using a signal-to-noise ratio of 3, fit factor of 44%, and remainder of 25% to create a list of monoisotopic fragment ion masses. Based on the protein sequence input into ProSight Lite, sequence ion matches were made within a ±10 ppm mass tolerance. For HCD spectra, only *b*- and *y*-type ions were considered while for UVPD spectra, nine possible ion types (*a*, *a + 1*, *b*, *c*, *x*, *x + 1*, *y*, *y – 1*, *z*) were searched. More recently developed, ProSight Native facilitates deconvolution and sequence ion identification for MS/MS spectra of protein-protein complexes collected in a high-throughput manner. This software helps assign peaks that correspond to intact subunits resulting from disassembly of oligomeric complexes in addition to backbone cleavages. ProSight Native was used to identify ribosomal protein complexes analyzed by CE-MS/MS in Chapter 8.

2.5.2 Identifying Holo Fragment Ions

UVPD of a protein non-covalently bound to a ligand typically yields a significant number of backbone fragment ions that retain the ligand. Termed holo fragment ions, identification of these mass shifted sequence ions facilitates the localization of ligand binding sites and improves sequence coverages. **Figure 2.4** shows an example of a holo fragment ion in the UVPD MS/MS spectrum of holo myoglobin (non-covalently bound to a heme ligand). In addition to the heme-free, apo x_{120}^{6+} sequence ion, also observed is the heme-bound, holo x_{120}^{6+} sequence ion that is shifted by the corresponding mass of the heme group (+615.1695 Da). Throughout this dissertation, holo fragment identifications are made by adding expected mass shift values at the N- and C-termini in ProSight Lite search. Once identified, holo fragment ions contribute to reported sequence coverages and can be mapped along the sequence to gain structural insights or highlight binding sites.

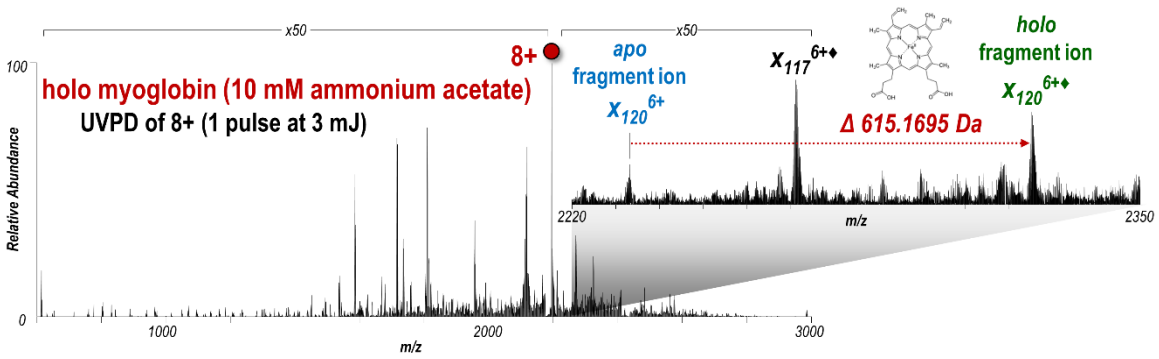

Figure 2.4: UVPD MS/MS spectrum (1 pulse at 3 mJ) of the 8+ charge state of holo myoglobin sprayed by native MS. The apo (heme-free) and holo (heme-bound) versions of the x_{120}^{6+} fragment ion are both labelled, separated by a mass shift corresponding to the heme group (+615.1695 Da).

2.5.3 UV-POSIT

Information on the structure of protein-ligand and protein-protein complexes is gleaned through comparison of the relative abundances of UVPD fragment ions for different conformational states. As such, fragment ion intensities must be summed in a manner that accurately represents the propensity for cleavage adjacent to each residue in a protein sequence. The fragment ion abundance utility of the web-based program UV-POSIT automates this process based on the exported list of deconvoluted masses and intensities that comprise a given UVPD spectrum.[10] The program reports a UVPD backbone cleavage yield normalized to the total ion current of the spectrum for each amino acid. Specifically, for a given residue *n* in a protein containing *R* amino acids numbered 1 (N-terminus) to *R* (C-terminus), UV-POSIT collectively sums the intensities of N-terminal apo and holo sequence ions (a_n, b_n, c_n) arising from backbone cleavage C-terminal to position *n* with C-terminal fragment ions (x_{R-n+1}, y_{R-n+1}, z_{R-n+1}) resulting from cleavage N-terminal to residue *n*. These calculated values were used to represent UVPD backbone cleavage efficiency adjacent to each amino acid in the protein sequence and compared

between different conformational states for a given protein to highlight regions exhibiting suppression or enhancement.

2.5.4 Statistical Analysis

Owing to the reliance of UVPD-MS on measuring differences in backbone cleavage efficiencies to gain structural information, statistical analysis is necessary to ensure significance and establish a confidence threshold. UVPD MS/MS spectra were collected in triplicate which allowed calculation of standard deviations for all backbone cleavage efficiency values. For comparison of the cleavage yield at a given residue for two different protein states, Student's *t*-test was used to ensure that the variation in the measurements (*i.e.* standard deviation) was significantly smaller than the difference between the two values. Briefly, pooled standard deviations were used to calculate *t*-values which were converted to *p*-values, assuming a two-tailed test. Only those residues with values exceeding the confidence threshold 99% (corresponding to a p-value < 0.01) were considered statistically significant and discussed as structural changes in the protein.

2.6 REFERENCES

(1) Fenn, J. B.; Mann, M.; Meng, C. K.; Wong, S. F.; Whitehouse, C. M. Electrospray Ionization for Mass Spectrometry of Large Biomolecules. *Science* **1989**, *246*, 64–71.

(2) Cech, N. B.; Enke, C. G. Practical Implications of Some Recent Studies in Electrospray Ionization Fundamentals. *Mass Spectrom. Rev.* **2001**, *20*, 362–387.

(3) Schwartz, J. C.; Senko, M. W.; Syka, J. E. P. A Two-Dimensional Quadrupole Ion Trap Mass Spectrometer. *J. Am. Soc. Mass Spectrom.* **2002**, *13*, 659–669.

(4) Makarov, A. Electrostatic Axially Harmonic Orbital Trapping: A High-Performance Technique of Mass Analysis. *Anal. Chem.* **2000**, *72*, 1156–1162.

(5) Michalski, A.; Damoc, E.; Lange, O.; Denisov, E.; Nolting, D.; Müller, M.; Viner, R.; Schwartz, J.; Remes, P.; Belford, M.; Dunyach, J.-J.; Cox, J.; Horning, S.; Mann, M.; Makarov, A. Ultra High Resolution Linear Ion Trap Orbitrap Mass Spectrometer (Orbitrap Elite) Facilitates Top Down LC MS/MS and Versatile Peptide Fragmentation Modes. *Mol. Cell. Proteomics* **2012**, *11*.

(6) Fort, K. L.; Waterbeemd, M. van de; Boll, D.; Reinhardt-Szyba, M.; Belov, M. E.; Sasaki, E.; Zschoche, R.; Hilvert, D.; Makarov, A. A.; Heck, A. J. R. Expanding the Structural Analysis Capabilities on an Orbitrap-Based Mass Spectrometer for Large Macromolecular Complexes. *Analyst* **2017**, *143*, 100–105.

(7) Shaw, J. B.; Li, W.; Holden, D. D.; Zhang, Y.; Griep-Raming, J.; Fellers, R. T.; Early, B. P.; Thomas, P. M.; Kelleher, N. L.; Brodbelt, J. S. Complete Protein Characterization Using Top-Down Mass Spectrometry and Ultraviolet Photodissociation. *J. Am. Chem. Soc.* **2013**, *135*, 12646–12651.

(8) Shen, X.; Kou, Q.; Guo, R.; Yang, Z.; Chen, D.; Liu, X.; Hong, H.; Sun, L. Native Proteomics in Discovery Mode Using Size-Exclusion Chromatography–Capillary Zone Electrophoresis–Tandem Mass Spectrometry. *Anal. Chem.* **2018**, *90*, 10095–10099.

(9) Fellers, R. T.; Greer, J. B.; Early, B. P.; Yu, X.; LeDuc, R. D.; Kelleher, N. L.; Thomas, P. M. ProSight Lite: Graphical Software to Analyze Top-down Mass Spectrometry Data. *PROTEOMICS* **2015**, *15*, 1235–1238.

(10) Rosenberg, J.; Parker, W. R.; Cammarata, M. B.; Brodbelt, J. S. UV-POSIT: Web-Based Tools for Rapid and Facile Structural Interpretation of Ultraviolet Photodissociation (UVPD) Mass Spectra. *J. Am. Soc. Mass Spectrom.* **2018**, *29*, 1323–1326.

Chapter 3: Tracking the Catalytic Cycle of Adenylate Kinase by Ultraviolet Photodissociation Mass Spectrometry*

3.1 Overview

The complex interplay of dynamic protein plasticity and specific side-chain interactions with substrate molecules that allows enzymes to catalyze reactions has yet to be fully unraveled. Herein the phosphotransferase adenylate kinase (AK) provides a tractable framework for development of native mass spectrometry and top-down ultraviolet photodissociation (UVPD) as a new tool for tracking conformational fluctuations of active enzymes throughout a given reaction cycle. Complexes containing AK and one of four adenosine phosphate ligands were transferred to the gas-phase using nano-electrospray ionization and subsequently characterized with UVPD-MS. Ligand-containing holo fragment ions were mapped to establish the locations of the substrates in their respective binding pockets. Variations in efficiencies of UVPD backbone cleavages were consistently observed for three α-helices and the adenosine binding regions for AK complexes representing different steps of the catalytic cycle, implying that these stretches of the protein sample various structural microstates as the enzyme undergoes global open-to-closed transitions. Focusing on the conformational impact of recruiting or releasing the Mg^{2+} cofactor highlights two loop regions for which fragmentation increases upon UVPD, signaling an increase in loop flexibility as the metal cation disrupts the loop interactions with the substrate ligands. Additionally, the observation of holo ions and variations in UVPD backbone cleavage efficiency at R138 implicate this conserved active site residue in stabilizing the donor phosphoryl group during catalysis. This study establishes the utility

*Mehaffey, M. R.; Cammarata, M. B.; Brodbelt, J. S. Tracking the Catalytic Cycle of Adenylate Kinase by Ultraviolet Photodissociation Mass Spectrometry. *Anal. Chem.* **2018**, *90*, 839-846.

MBC largely contributed to the project idea and implementation. JSB provided mentorship and reviewed the manuscript prior to publication.

of UVPD-MS for providing information on several different scales ranging from global movements down to conformational fluctuations of single residues for active enzymes.

3.2 INTRODUCTION

Enzymes are powerful catalysts capable of accelerating chemical reaction rates several orders of magnitude allowing biochemical processes to take place on biologically relevant timescales. Despite the enormous headway in deciphering the interplay of side-chain residues, cofactors, and overall protein plasticity that contributes to a suitable electrostatic environment amenable for promoting a given chemical reaction, a comprehensive understanding of enzymatic catalysis is still lacking.[1–4] One well-studied enzyme known to undergo a large conformational change from an open inactive state to a closed active state is adenylate kinase (AK).[5] Acting to maintain the energy balance in cells, this protein catalyzes the reversible phosphoryl transfer reaction starting with adenosine 5'-monophosphate (AMP) and adenosine 5'-triphosphate (ATP) which results in production of two adenosine 5'-diphosphate (ADP) molecules.[6] Strategies involving elaborate computer simulations and ultrafast laser spectroscopy have complemented the static three-dimensional structures provided by crystallography and NMR studies to identify the specific residues of AK, in concert with a divalent Mg cofactor, which play key roles in the acceleration of phosphoryl transfer.[7–22] However, controversy still remains over whether individual high-frequency local fluctuations in the enzyme's structure facilitate large conformational transitions on the timescale of catalytic turnover and significantly contribute to an increase in efficiency of transferring the phosphoryl moiety.[2,3,12,14,15,22–24] Given that catalytic mechanisms often involve several microscopic steps occurring over a hierarchy of time and distance, development of novel tools for unraveling these complex processes would represent a compelling advance.[3,22]

Mass spectrometry (MS) has shown promise in recent years for the development of sensitive, higher-throughput approaches to addressing structural biology questions.[25] Bottom-up strategies involving covalent chemical probes, including hydrogen/deuterium exchange (HDX) and cross-linking of reactive residues, have cemented the pivotal role of tandem mass spectrometry (MS/MS) in examining the native structures of proteins.[26–29] Although these covalent labeling techniques have been successfully applied to evaluate solvent accessibilities, reveal distance restraints, and determine transient protein-protein interactions, the development of less chemically intensive top-down MS methods has provided an alternative non-proteolytic strategy.[29] Native MS methods allow the efficient transfer of proteins and protein complexes into the gas phase in low charge states via electrospray ionization of buffered solutions that contain volatile salts, most commonly ammonium acetate.[30,31] Despite the questions that still remain concerning the specific mechanism of native electrospray ionization (ESI), measurements of collisional cross sections by ion mobility MS suggest the charged proteins and protein complexes maintain to a large extent the folded tertiary and quaternary structures adopted in solution.[32–34] Applications of native MS to determination of stoichiometries and binding/dissociation constants of protein-ligand and protein-protein complexes continue to grow. Moreover, even the ability to elucidate conformational changes occurring during ligand interactions and/or unfolding has been demonstrated.[30,31,35–41] Time-resolved electrospray ionization (ESI) and HDX MS experiments have been previously used to directly monitor enzymatic reactions on millisecond time scales and detect transient covalent intermediates.[42–44]

The development of MS/MS methods sensitive to protein structure has further advanced the utility of native MS. Electron-based activation techniques, including electron transfer dissociation (ETD)[45] and electron capture dissociation (ECD),[46–50] yield significant sequence coverage with abundances of the resulting fragments correlating with

crystallographic B-factors.[49,50] Fragments reflecting the degree of flexibility of certain regions are thought to arise from salt bridges in proteins that may be strong enough in the gas phase to survive exothermic electron-transfer reactions.[45] Surface-induced dissociation (SID) is another activation method that has found great utility for decoding the quaternary structures of protein-protein complexes.[51] A third activation method, ultraviolet photodissociation (UVPD), offers unsurpassed levels of diagnostic backbone fragmentation for both denatured and natively sprayed proteins via fast high-energy excitation caused by absorption of 193 nm photons.[38–41,52–54] UVPD yields both holo (ligand-bound) and apo (free of ligand) product ions with ion abundances that reflect secondary or tertiary protein structure, thus offering both localization of non-covalent protein-ligand interaction sites and structural characterization of complexes.[38–41] Suppression or enhancement in UVPD cleavage efficiencies at certain positions along the protein backbone may result from variations in secondary or tertiary features occurring in other regions of the protein structure.[40] Furthermore, ion mobility MS measurements of ubiquitin have demonstrated that UVPD fragmentation patterns vary for different gas-phase conformers, a particularly interesting outcome that demonstrates the sensitivity of UVPD to protein structure.[55,56] Most recently UVPD fragmentation patterns were used to monitor stepwise loop movements of dihydrofolate reductase (DHFR) upon binding of co-factor NADPH and inhibitor methotrexate, and to delineate conformational changes caused by clinically relevant single point G12X mutants of K-Ras bound to guanosine phosphate ligands.[40,41] These previous studies have demonstrated the versatility of UVPD-MS for monitoring conformational changes in proteins arising from binding different ligands or from subtle mutations in protein sequence. The aim of the present work is to evaluate the utility of UVPD for tracking the conformational dynamics of an active enzyme throughout its catalytic cycle.

Here we present native MS and top-down UVPD of binary and ternary complexes of AK with AMP, ADP, ATP, and P^1, P^4-di(adenosine-5')tetraphosphate (AP4A) inhibitor, mirroring the steps of its enzymatic cycle. Previously native MS has been used to screen metal-chelating to AKs and quantify association constants with various noncovalent inhibitors.[57,58] More recently, phosphate-bound fragment ions observed upon ECD and collision-induced dissociation (CID) were used to elucidate ATP binding sites of the enzyme sequence.[59] Comprehensive studies of the AK energy landscape along the reaction pathway at the molecular level point to the precise placement of a divalent Mg cofactor, conserved Arg residue, and conformational fluctuations in the protein as possible explanations for the efficient phosphoryl transfer and suppression of detrimental hydrolysis.[2,3,12,16,19,22] These studies using traditional structural biology methods provide a comparative framework for the gas-phase UVPD approach used in the present work. Building on these results, we track variations in UVPD of AK throughout its catalytic cycle to shed light on the roles of local unfolding during a global open-to-closed transition, a divalent metal cofactor, and interactions of the ligands with a conserved residue in assembling the pre-organized active site essential for catalysis. Our work highlights the utility in developing novel approaches that may provide a deeper understanding of the general mechanism of enzyme catalysis.

3.3 EXPERIMENTAL

3.3.1 Materials and Reagents

Adenosine 5'-monophosphate (AMP) monohydrate, adenosine 5'-diphosphate (ADP), adenosine 5'-triphosphate (ATP) disodium salt hydrate, P^1, P^4-di(adenosine-5')tetraphosphate (AP4A) ammonium salt, ammonium acetate, magnesium acetate tetrahydrate, and adenylate kinase (AK) (myokinase from chicken muscle) were purchased

from Sigma-Aldrich (St. Louis, MO). Protein samples were desalted and concentrated to 10 µM at pH 6.5 buffered with 10 mM ammonium acetate containing 10 µM magnesium acetate using 10 kDa molecular weight cutoff filter devices (Millipore, Billerica, MA). Adenosine phosphate ligands were added to the protein solution at a 1:1 ratio after desalting.

3.3.2 Mass Spectrometry

Equimolar protein-ligand solutions were infused with a gold-coated static tip electrospray setup operated at an applied voltage of 1.0-1.2 kV. A heated capillary set at 200°C aided in desolvation of protein-ligand complexes. All experiments were performed on a Thermo Scientific Orbitrap Elite mass spectrometer (Bremen, Germany) modified as previously described[52] with a Coherent Excistar 193 nm ArF excimer laser (Santa Cruz, CA) to perform photodissociation in the HCD cell. All spectra were collected with a resolving power of 240 K at *m/z* 400. For MS1 spectra, sixty scans were averaged with an automatic gain control (AGC) set to achieve a signal level of 1E6. MS/MS analysis involved selection of the 9+ charge state of each protein-ligand complex using an isolation width of 15-20 *m/z* and activation by exposure to a single 3 mJ pulse. For UVPD experiments, the AGC value was set to 5E5 with a maximum ion time of 2 s. Each UVPD mass spectrum represents the average of 500 scans of the Orbitrap mass analyzer over a range from *m/z* 220-4000. Three replicates of MS/MS spectra were collected for each protein-ligand complex.

3.3.3 Data Analysis

Xtract was used to de-charge and de-isotope UVPD MS/MS spectra with a signal-to-noise ratio of 2, fit factor of 44%, and remainder of 25%. Monoisotopic fragment ions

were then searched against the AK amino acid sequence using a version of ProSight PC 3.0 modified to account for the nine ion types observed with UVPD (*a*, *a*•, *b*, *c*, *x*, *x*•, *y*, *y*-1, *z*). **Figure 3.1** gives the sequence of AK (*Gallus gallus*) and the structures of the adenosine phosphate ligands. Residues are numbered from the first serine (S) in subsequent figures and all N-terminal fragment ions were identified containing an N-terminal acetylation (+42.0106 Da).

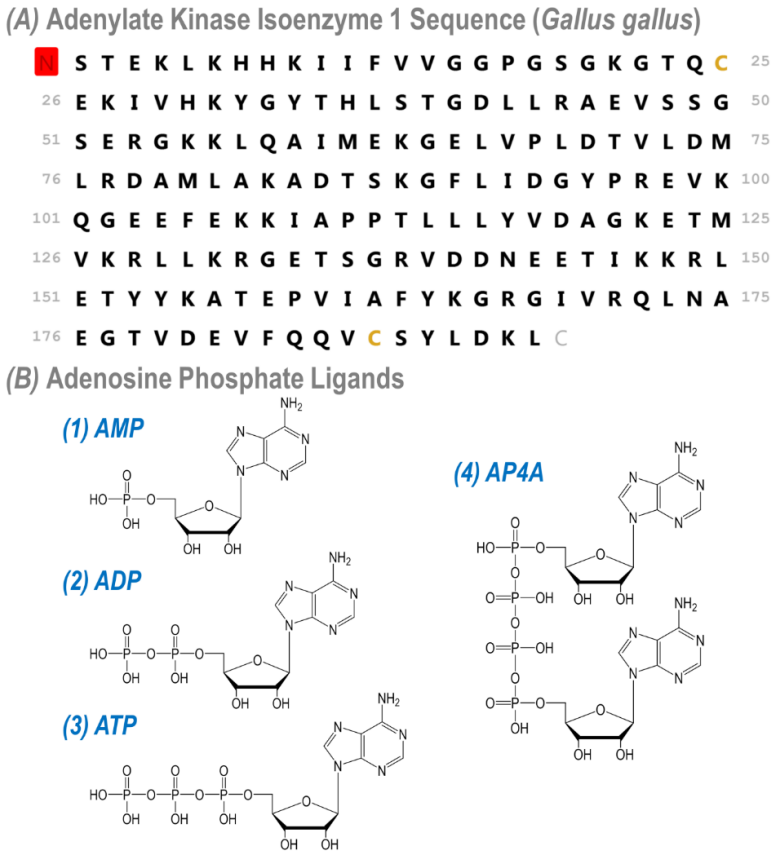

Figure 3.1: (A) Sequence of adenylate kinase (AK) isoenzyme 1 (*Gallus gallus*). Residues are numbered from the first serine (S) in subsequent figures. All N-terminal fragment ions were identified containing an N-terminal acetylation (+42.0106 Da). (B) Structures of the adenosine phosphate ligands: (1) AMP, (2) ADP, (3) ATP, and (4) AP4A.

Holo ions were also considered by searching the spectra for fragment ions with a mass shift corresponding to the mass of the bound adenosine phosphate ligand and coordinating Mg^{2+}. Plots of the number of holo fragment ions identified versus the mass shift searched relative to the apo fragment ions for each of the AK•ligand complexes examined are given in **Figure 3.2**. Specifically, mass shifts included in the searches are: 345.0474-347.0631 Da for AMP, 425.0138-427.0294 Da for ADP, 504.9800-506.9957 Da for ATP, 834.0326-836.0483 Da for AP4A, and 852.0432-854.0588 Da for AMP + ATP/ADP + ADP. A +21.9694 Da shift was used to account for the presence of the Mg^{2+} cofactor (*e.g.*, addition of one Mg atom and loss of two hydrogen atoms).

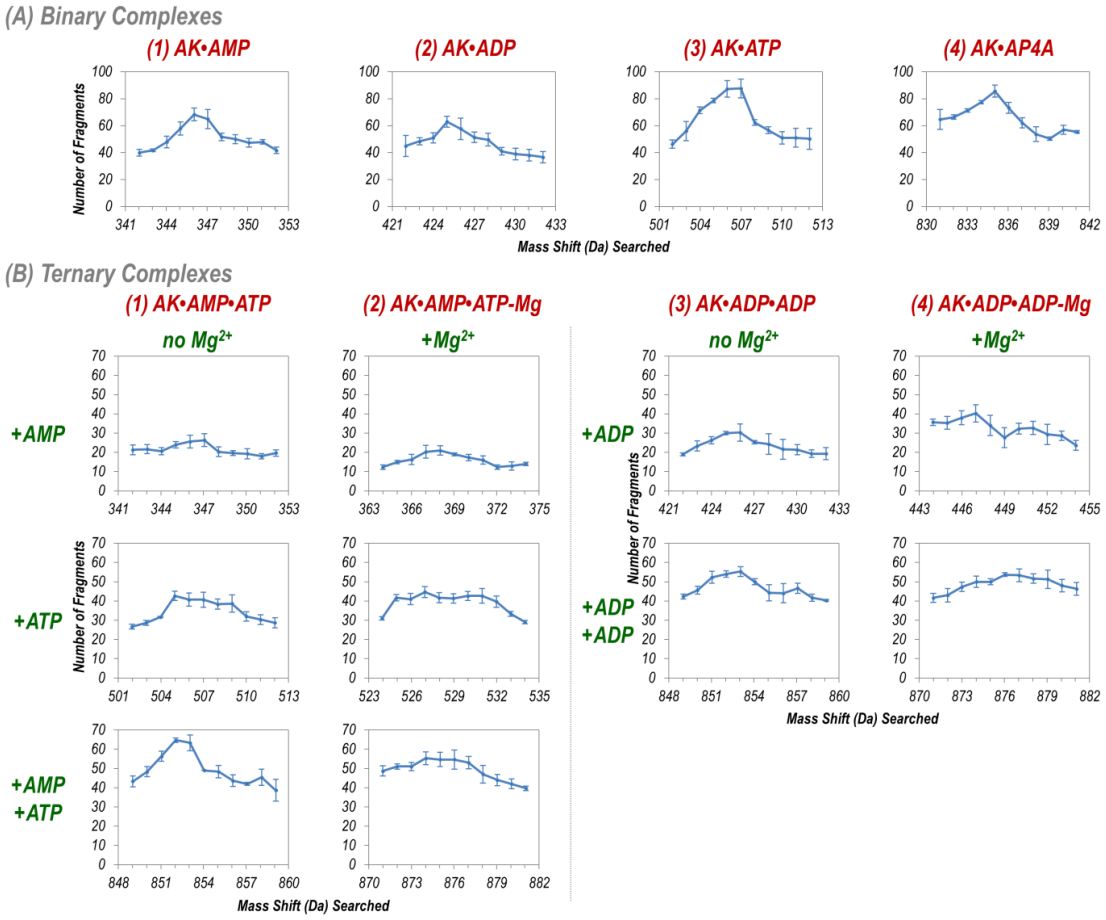

Figure 3.2: Number of holo (ligand-containing) fragment ions identified plotted versus the mass shift searched relative to the apo fragment ions for each of the (A) binary and (B) ternary (with and without the Mg^{2+} cofactor) AK•ligand complexes examined. The mass shifts specifically included in the searches are: 345.0474-347.0631 Da for AMP, 425.0138-427.0294 Da for ADP, 504.9800-506.9957 Da for ATP, 834.0326-836.0483 Da for AP4A, and 852.0432-854.0588 Da for AMP + ATP/ADP + ADP. A +21.9694 Da shift was used to account for the presence of the Mg^{2+} cofactor.

To determine cleavage yields at each backbone position upon UVPD, the abundances of identified holo and corresponding apo ions were normalized to the total ion current of the spectrum and summed per residue along the protein backbone as previously described.[40,41] Briefly, N-terminal fragment ions (a_n, b_n, c_n) resulting from cleavage of the backbone C-

terminal to a given amino acid were collectively summed with C-terminal product ions (x_{R-n+1}, y_{R-n+1}, z_{R-n+1}) arising from fragmentation N-terminal to that same amino acid to represent the UVPD cleavage efficiency for a specific residue, *n*, in a protein sequence with *R* amino acids. **Figure 3.3** gives the normalized TIC abundances of summed holo and apo product ions plotted per residue for the AK•ligand complexes examined. Statistical significance of a change in backbone cleavage efficiency upon UVPD between steps of the catalytic cycle was determined using student's *t*-test with pooled standard deviations. *P*-values were determined from calculated *t*-values assuming a two-tailed test. Consequently, for a given residue, a *p*-value smaller than 0.01 indicates that the average measured UVPD intensity within a triplicate measurement is statistically different from the measured average in the subsequent step of the catalytic cycle at the 99% confidence level. Calculated *p*-values per residue corresponding to the differences in UVPD cleavage efficiency throughout the catalytic cycle are given in **Figure 3.4**. A histogram of calculated *p*-values over the entire data set reveals that over 32% of all measured differences in backbone cleavage efficiency are significant at the 99% confidence level (**Figure 3.4B**). An overlay of the UVPD cleavage efficiency plot for each of five separate replicates collected for the AK•ATP complex demonstrates the high reproducibility of the measurements (**Figure 3.5**).

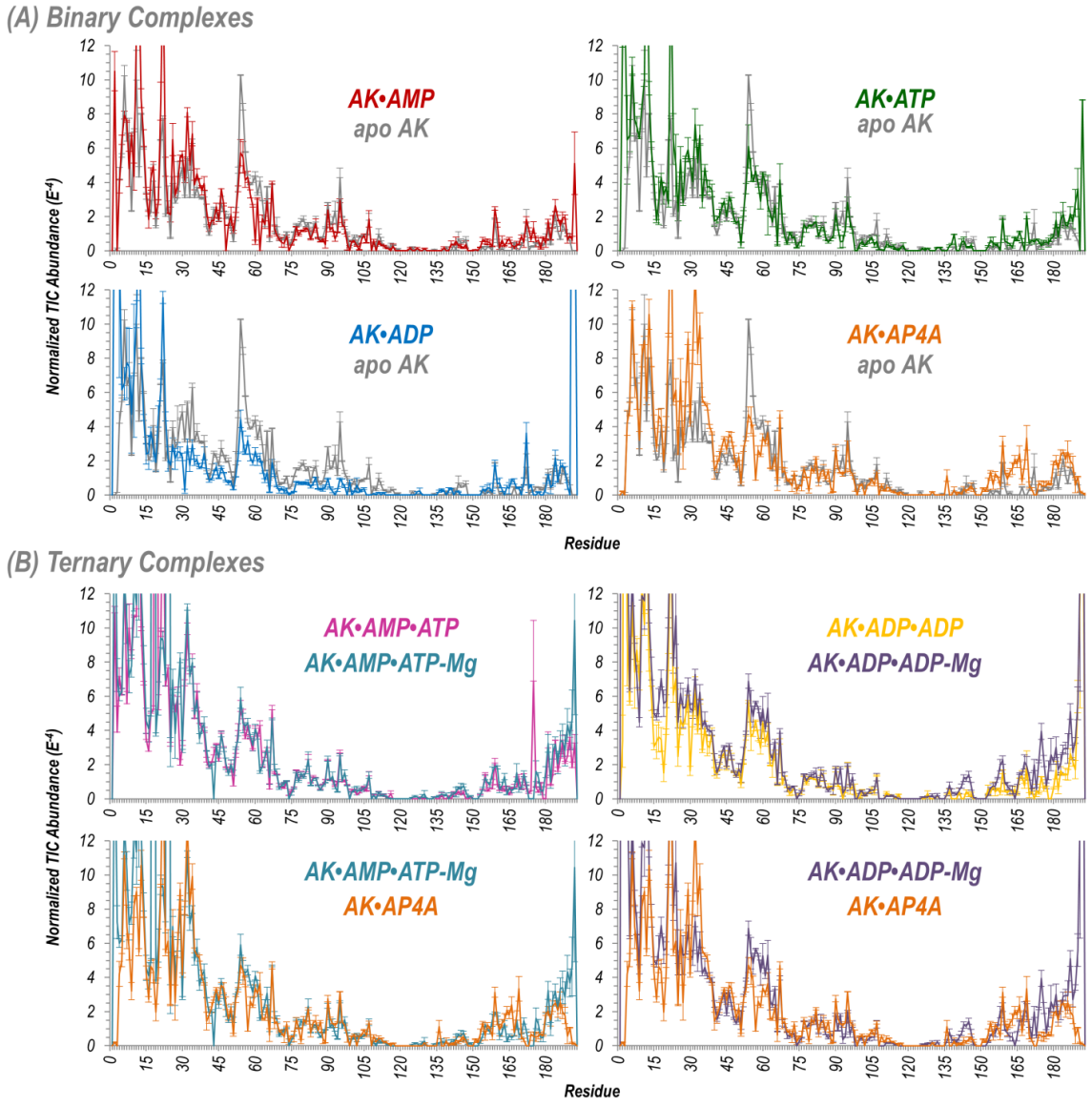

Figure 3.3: Normalized TIC abundance of summed holo and apo product ions plotted per residue for the (A) binary and (B) ternary AK•ligand complexes examined. These plots were used to create the difference plots shown in Figure 3.15. For each binary complex in (A), the UVPD data for apo AK is shown as a reference. For each ternary complex in (B), the UVPD data for a second binary or ternary complex of interest is shown as a reference.

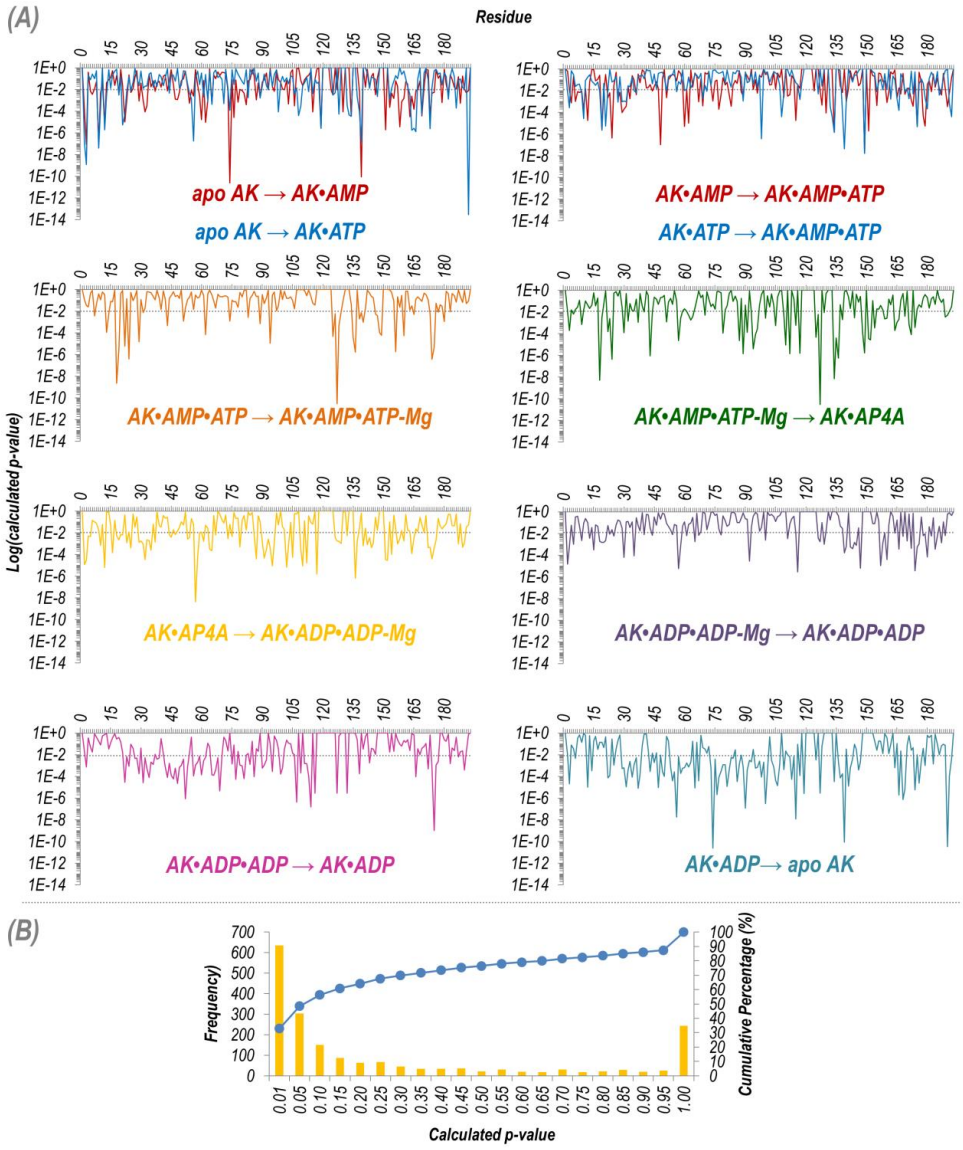

Figure 3.4: (A) Calculated *p*-values per residue corresponding to the differences plotted in Figure 3.15 with a confidence threshold at 99% shown as a gray dotted line. (B) Histogram of calculated *p*-values over the entire data set with the cumulative percentage shown in blue. Student's *t*-test was performed for each comparison of UVPD between the steps of the catalytic cycle using pooled standard deviations. *P*-values were determined from calculated *t*-values assuming a two-tailed hypothesis. Consequently, for a given residue, a *p*-value smaller than 0.01 indicates that the average measured UVPD intensity within a triplicate measurement is statistically different from the measured average in the subsequent step of the catalytic cycle at the 99% confidence level.

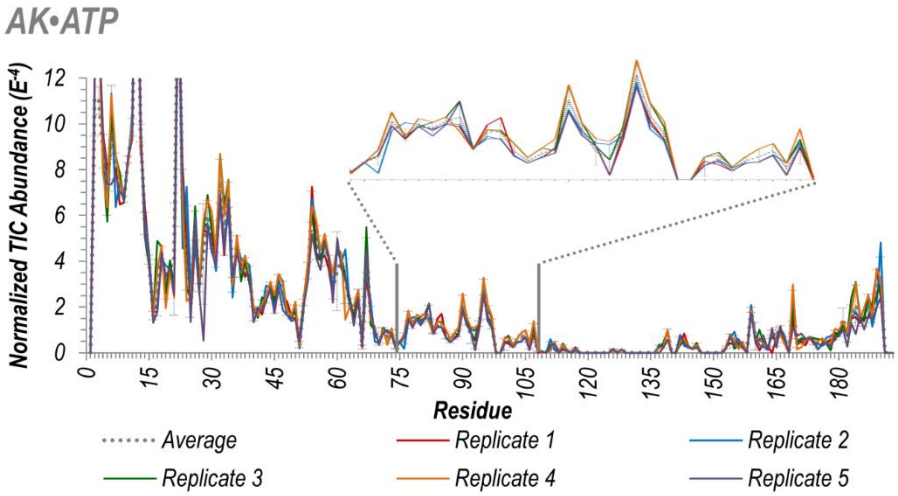

Figure 3.5: Overlay of the normalized TIC abundances of summed holo and apo product ions plotted per residue for five separate replicates of UVPD activation of the AK•ATP complex. The average of the five replicates is given as a gray dotted line with the error bars corresponding to the standard deviation. Inset shows an expanded view for residues 74-108.

A diagram of the crystal structure of AK•AP4A (PDB ID: 2C95)[60] used as a model is given in **Figure 3.6** with the three domains (CORE, AMP binding domain (bd), and ATP lid) color coded and the conserved residue R138 shown in stick format closing over the active site.

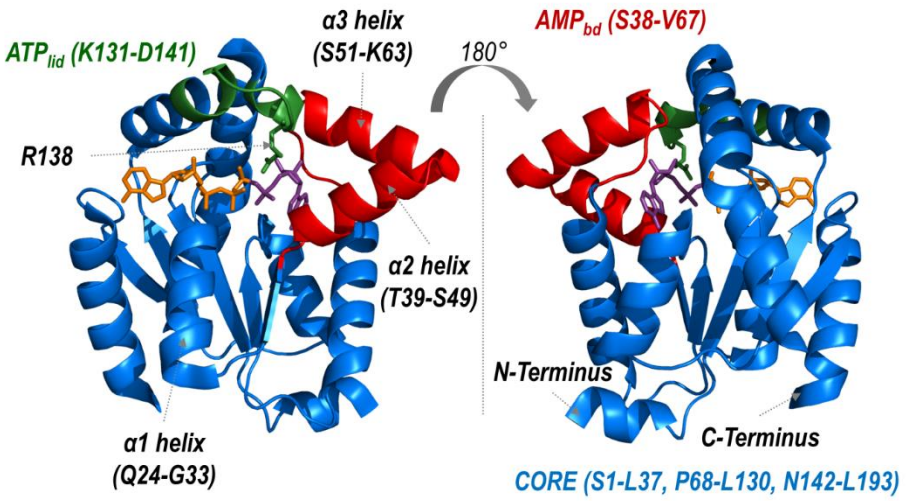

Figure 3.6: The three domains of AK (CORE, AMP binding domain, and ATP lid) color coded on the crystal structure of the protein bound to AP4A (PDB ID: 2C95). The bound ligand is represented as sticks with the AMP portion shown in purple and ATP portion in orange. Conserved residue R138 is also shown as sticks closing over the active site.

3.4 Results and Discussion

3.4.1 Native MS and UVPD of AK-Ligand Complexes

Mirroring the steps of the catalytic cycle, native MS conditions were used to transfer complexes containing AK non-covalently bound to AMP, ADP, ATP, or AP4A into the gas phase by electrospray ionization. Low charge states (8+, 9+, 10+) characteristic of native-like proteins were observed for each protein-ligand complex (**Figure 3.7A-F**, including AK, AK•AMP, AK•ADP, AK•ATP, AK•AP4A, AK•AMP•ATP, AK•AMP•ATP-Mg, AK•ADP•ADP, and AK•ADP•ADP-Mg). Although present in each solution, the divalent Mg cofactor only bound to the ternary complexes (**Figure 3.7G-I**). Catalytic products (AMP, ADP, ATP-Mg) were observed in the ESI mass spectra for the ternary complexes containing Mg but not when bound to the AP4A inhibitor, thus

indicating that the protein adopted an enzymatically active conformation during analysis (**Figure 3.8**).

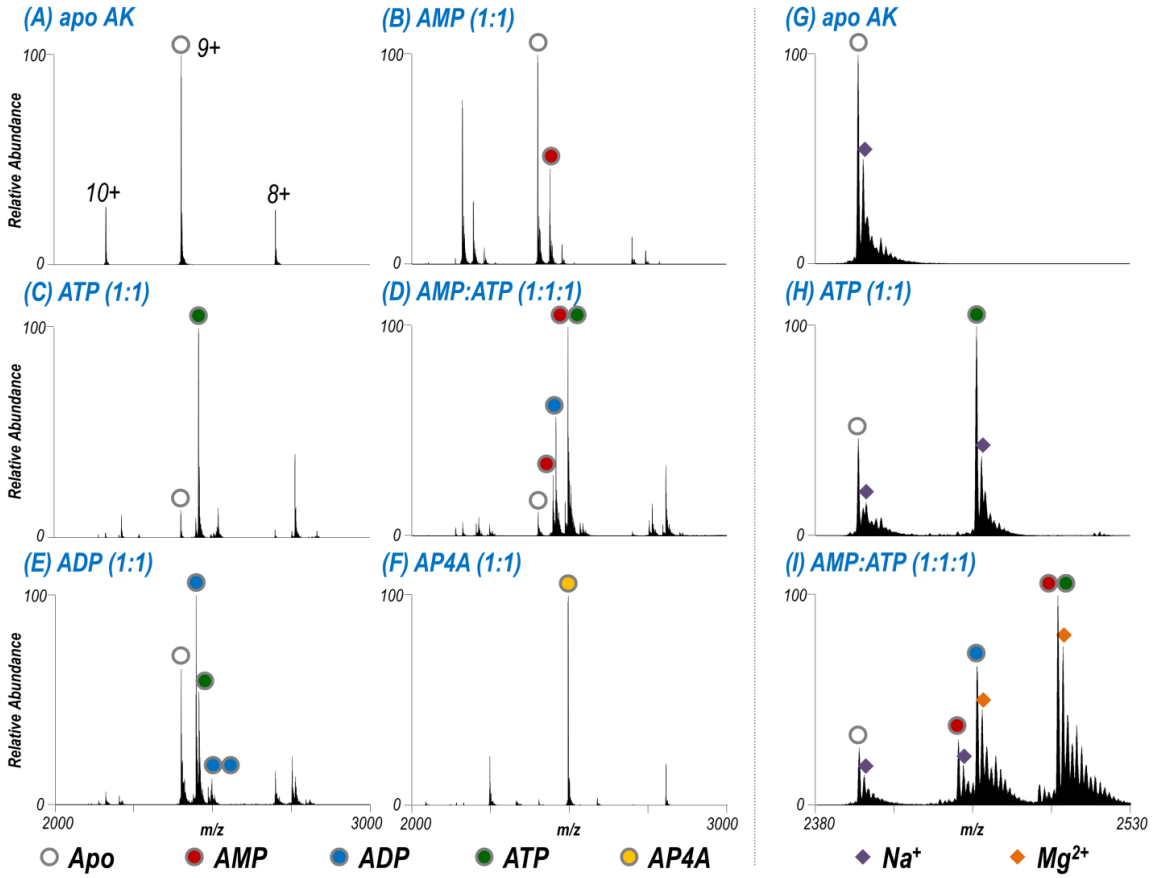

Figure 3.7: ESI mass spectra (2000-3000 *m/z*) of natively sprayed (A) apo AK with a 1:1 ratio of (B) AMP, (C) ATP, (D) AMP + ATP, (E) ADP, and (F) AP4A present in solution. The colored circles identify the species observed in each spectrum for the 9+ charge state. An expanded view of mass range 2380-2530 *m/z* demonstrates that only Na^+ adducts were observed for (G) apo AK and binary complexes including (H) AK•ATP while one Mg^{2+} was bound to the ternary complexes as shown for (I) AK•AMP•ATP (and also for AK•ADP•ADP, spectrum not shown). Mg^{2+} was present in each solution at a 1:1 ratio with AK.

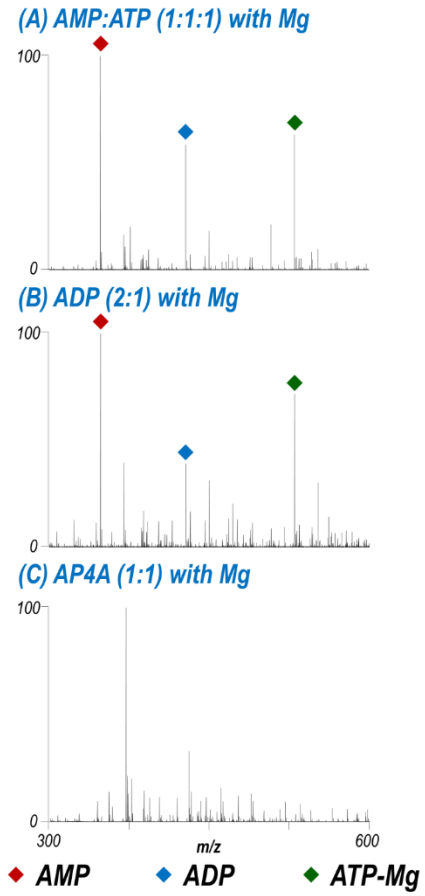

Figure 3.8: Mass range 300-600 *m/z* of ESI mass spectra for complexes of AK sprayed with Mg and (A) AMP:ATP (1:1:1), (B) ADP (2:1), or (C) AP4A (1:1) demonstrating that the enzyme was catalytically active during analysis except when bound to the AP4A inhibitor.

For each complex examined, the most abundant charge state (9+) was subsequently isolated and subjected to 193 nm UVPD to yield the informative fragmentation patterns in **Figure 3.9**. Although the spectra appear congested, expansions of specific segments of the *m/z* range show isotopically resolvable fragment ions that are readily assigned as diagnostic sequence ions (**Figure 3.9J**).

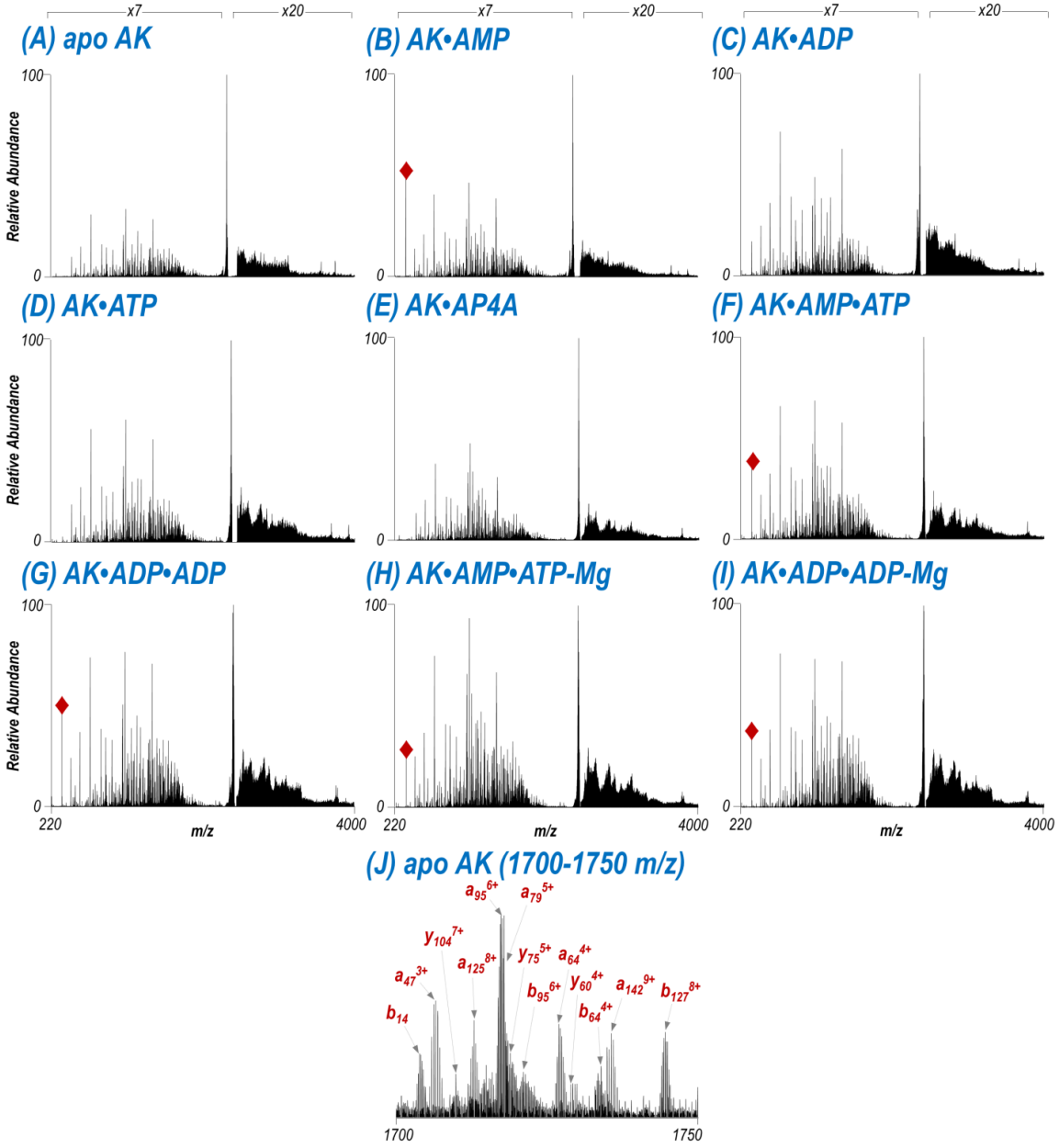

Figure 3.9: (A-I) UVPD mass spectra of the 9+ charge state of AK•ligand complexes activated using a single 3 mJ pulse. (J) Expanded view (1700-1750 *m/z*) of panel (A) with selected fragment ions labelled. The sequence coverage obtained was between 74-83% for all complexes examined. The red diamond (B, F-I) indicates loss of intact AMP during activation.

Deconvoluted spectra were created from raw UVPD spectra using Xtract to decharge the fragment ions (**Figure 3.10**). High sequence coverage (74-83%) was obtained for all nine complexes examined. More extensive details on assignment of apo (without ligand) and holo (ligand-containing) fragment ions, and data interpretation are given in the Experimental section.

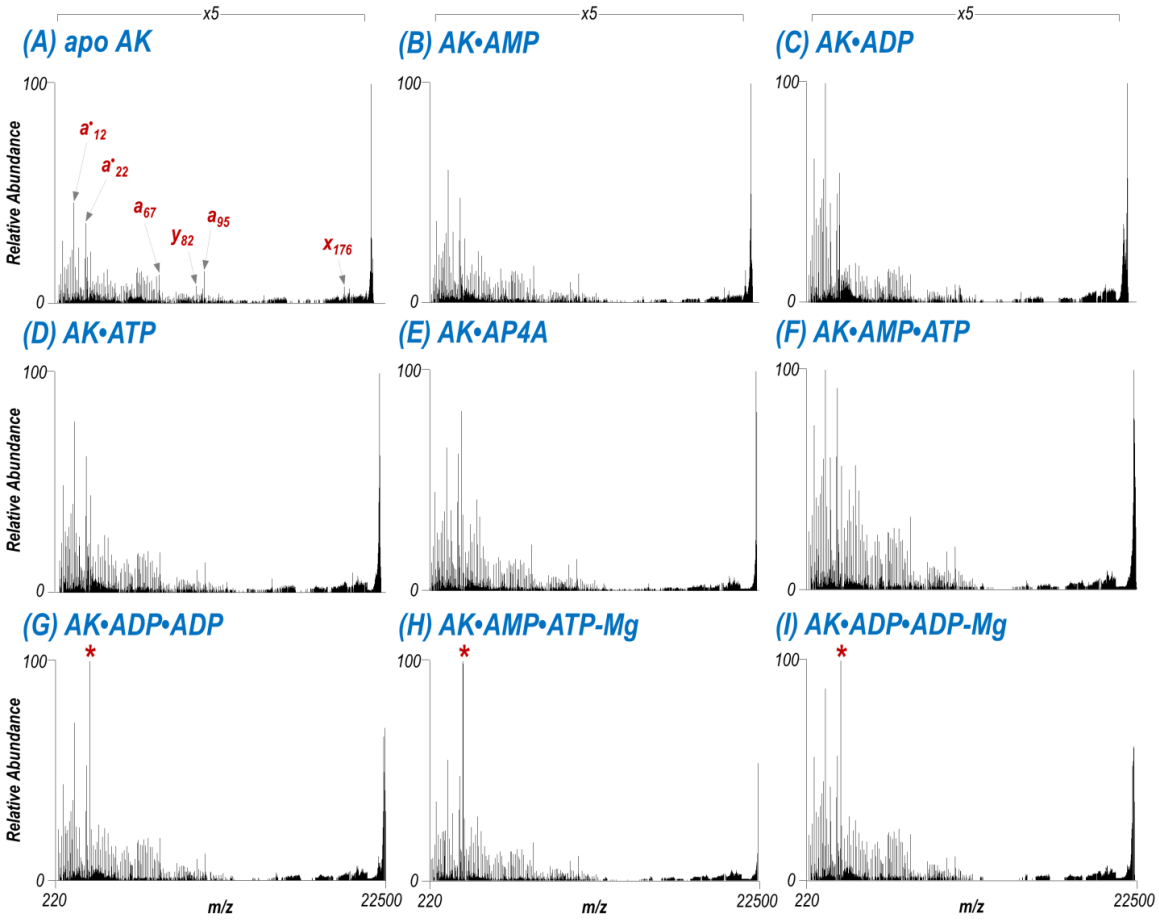

Figure 3.10: (A-I) Deconvoluted UVPD mass spectra (corresponding to the spectra in Figure 3.9) of all AK•ligand complexes examined (9+ charge state) performed using one 193 nm pulse at 3 mJ. Several abundant fragment ions are labelled in (A). The asterisks (G-I) represent surviving precursor that resulted as an artifact during deconvolution.

3.4.2 Mapping UVPD Holo Fragment Ions to Examine Ligand Binding Sites

Previously it was reported that the intrinsic stability of electrostatic interactions governing the binding of adenosine phosphate ligands allowed the survival and detection of protein fragment ions containing mono- and diphosphate groups and release of the truncated adenosine monophosphate upon CAD or ECD of AK•ATP complexes in the gas phase.[59] A subsequent study found that using supercharging reagents, such as *m*-nitrobenzyl alcohol and sulfolane, to increase the charge state of the precursor allowed production of AK fragment ions bound non-covalently to intact ATP upon ECD.[61] Interestingly, UVPD has been shown to produce fragment ions retaining intact nucleotide phosphate ligands without the need for supercharging reagents for eIF4E•m^{7}GTP, DHFR•NADPH, and K-Ras•GDP/GTP complexes.[38,40,41] The retention of entire nucleotide phosphate ligands upon UVPD rather than retention of individual phosphate groups upon CAD or ECD[59] is attributed to the higher energy deposition upon absorption of 193 nm photons which presumably favor cleavage of backbone bonds of the protein rather than cleavage of labile phosphate bonds.[38,40,41] Classifications of the patterns and relative abundances of the extensive array of N- and C-terminal holo (ligand-containing) sequence ions resulting from UVPD as a function of backbone cleavage site has shown to be predictive for ligand binding sites.[38,40,41] In particular regions with overlapping N- and C-terminal holo fragment ions are anticipated to be directly involved in non-covalent interactions with the bound ligand.[40,41] In the present study, holo fragment ions containing the intact adenosine phosphate ligands were observed for each of the complexes examined. **Figure 3.11** displays the distribution of holo fragment ions for the binary and ternary AK complexes with the specific residues containing bidirectional holo ions (*e.g.*, bidirectional holo ions are those for which both N-terminal and C-terminal fragment ions retain the ligands and share overlapping residues) highlighted in red. These regions demarcated by

the holo fragment ions are represented as red spheres on space-filled models on the crystal structure of the protein (PDB ID: 2C95)[60] in **Figure 3.12** to aid in visualization of the putative binding locations of the adenosine phosphate ligands.

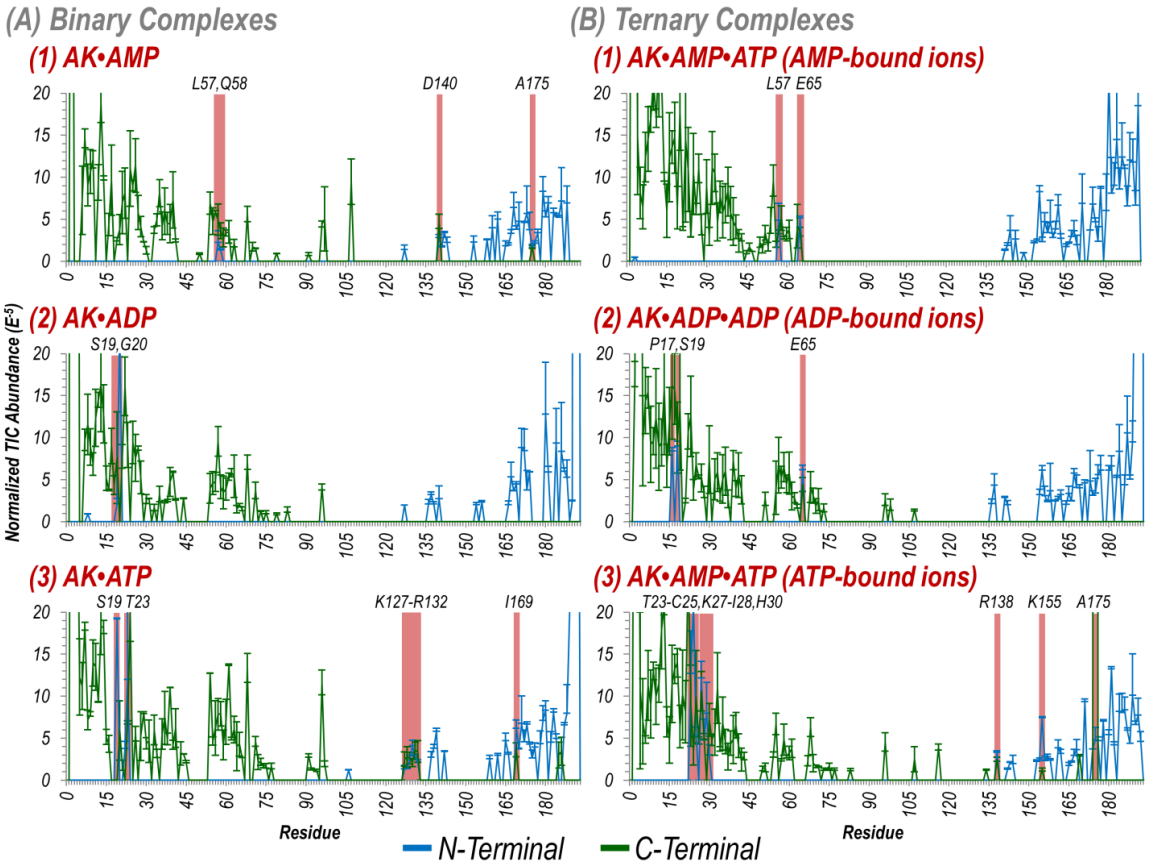

Figure 3.11: Plots of the normalized abundances of N-terminal (blue) and C-terminal (green) holo fragment ions produced upon UVPD per residue for the (A) binary and (B) ternary AK•ligand complexes examined. For the ternary complexes, the plots reflect product ions that retain only a single ligand (either AMP in B(1), ADP in B(2), or ATP in B(3)). The complementary plots showing retention of both ligands upon UVPD of the ternary complexes are displayed in Figure 3.13. Residues with overlapping N- and C-terminal holo ions are shaded in red.

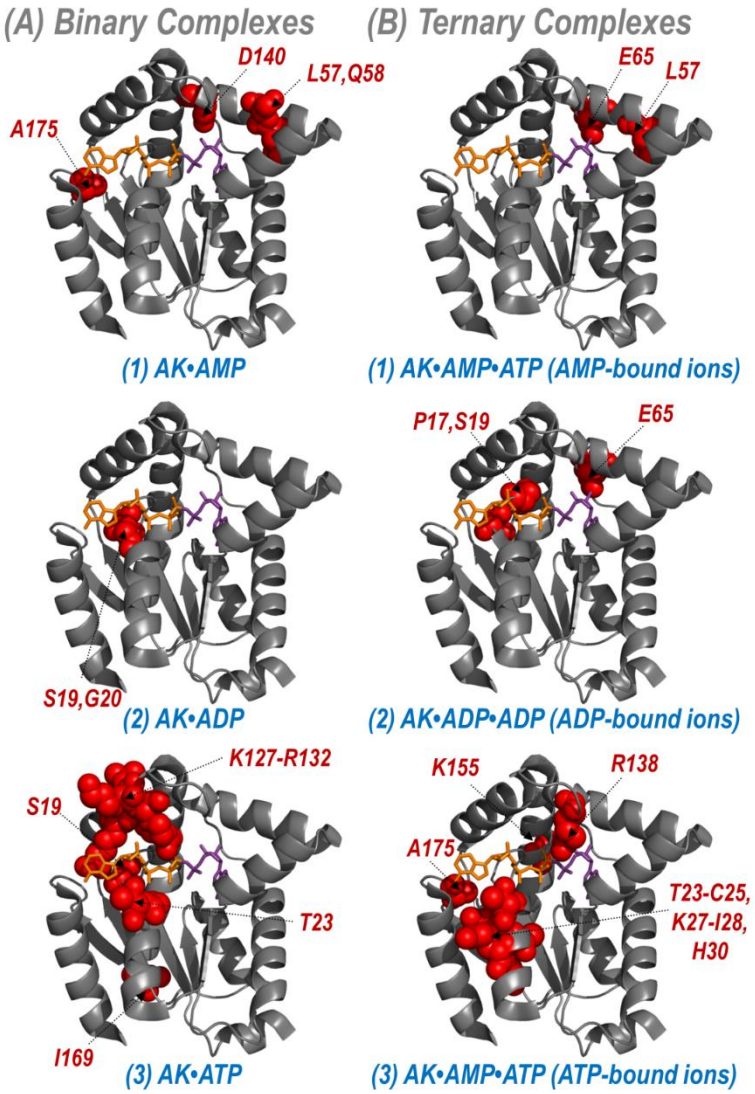

Figure 3.12: Potential adenosine phosphate ligand binding residues derived from overlapping N- and C-terminal holo fragment ions produced by UVPD of (A) binary and (B) ternary AK•ligand complexes represented as red spheres in space-filling models of the crystal structure of the protein bound to AP4A (PDB ID: 2C95).

For the binary complexes, ATP was retained preferentially compared to either AMP or ADP as evidenced by the overall greater number and higher abundance of holo ions (88, 71, and 164 unique holo fragment ions for AK•AMP, AK•ADP, and AK•ATP respectively)

(**Figure 3.11A**). This outcome correlates well with crystallographic data and molecular modelling that suggest the phosphate groups of ATP are more strongly bound to the enzyme than the adenosine moiety while the converse is true for AMP.[11,62] In essence, the hydrogen bonding network established between protein side-chains and the adenosine ring of AMP, a network that allows high nucleotide monophosphate specificity in the binding pocket, is less stable in the gas phase and more likely to disassemble during photoactivation than the strong electrostatic interactions formed between the phosphate portion of ATP and positively polarized side-chains of the protein.

For two of the ternary complexes (AK•AMP•ATP and AK•ADP•ADP), the majority of holo fragment ions contained both ligands (*e.g.*, 93 unique fragment ions contained both AMP and ATP for AK•AMP•ATP and 79 unique fragment ions contained both ADP molecules for AK•ADP•ADP) (**Figure 3.13**).

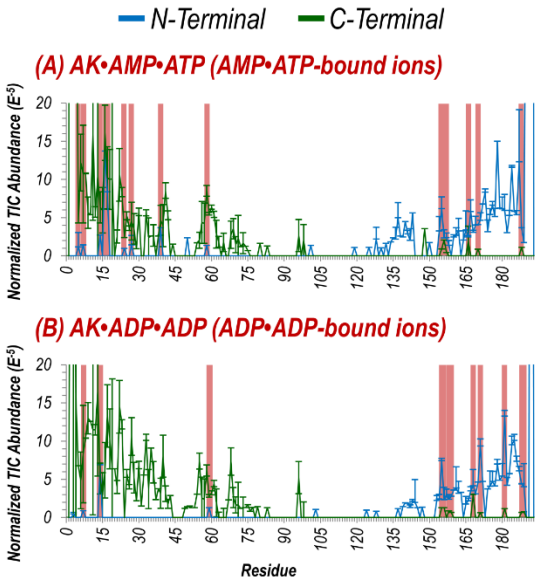

Figure 3.13: Plots of the normalized abundances of N-terminal (blue) and C-terminal (green) holo fragment ions retaining both ligands upon UVPD for the (A) AK•AMP•ATP and (B) AK•ADP•ADP ternary complexes. Residues with overlapping N- and C-terminal holo ions are shaded in red.

To streamline deciphering the location of each ligand within the binding pocket, it is most informative to search for holo fragment ions originating from the ternary complex but only retaining one of the ligands (**Figure 3.11B**). AMP and ATP were traced back to their respective binding sites in AK while evidence of ADP binding was found for both regions. As an example, analysis of the AK•AMP complex yielded overlapping holo fragment ions from both the N- and C- terminus for residues in the AMP_{bd} (L57, Q58) and ATP_{lid} (D140) regions suggesting that this ligand is promiscuous in the absence of ATP (**Figure 3.12A(1)** AK•AMP). However in the presence of ATP, only residues in the AMP adenosine binding region (L57, E65) yielded bidirectional AMP-bound holo fragment ions for the ternary complex (**Figure 3.12B(1)** AK•AMP•ATP). Evidence of ADP interactions were only found involving residues in the ATP adenosine binding region (S19, G20) for the binary AK•ADP complex, further supporting the high monophosphate nucleotide specificity of the AMP binding pocket (**Figure 3.12A(2)** AK•ADP).[11,62–64] For the ternary complex containing two ADP molecules, N- and C-terminal holo fragment ions incorporating residues in the adenosine binding regions of both AMP (E65) and ATP (P17, S19) were identified (**Figure 3.12B(2)** AK•ADP•ADP). For both the binary and ternary complexes involving ATP, both N- and C-terminal fragment ions retaining ATP spanned residues from the ATP adenosine binding (S19, G22, T23) and ATP_{lid} (K131, R132, R138) regions (**Figure 3.12A(3)** AK•ATP, and **3.12B(3)** AK•AMP•ATP). This finding correlates well with previous top-down MS data that identified amino acids G121-D140 in the ATP_{lid} region as the primary binding site of ATP as well as an additional minor site at residues D141-D180.[59] Prior data supported the role of several conserved arginines (R44, R97, R132, R138, R149) in binding ATP; however, the Gly-loop making up the ATP adenosine binding region (G18-T23) was not previously implicated[59] but is identified in the current study. Even though these interactions were too labile to survive collisional activation, in

the present study UVPD did not disrupt these interactions and key ATP-bound holo ions were observed from this region for both the binary and ternary complexes.

3.4.3 Conformational Changes throughout the Catalytic Cycle

Enzymatic activity is often governed by a dynamic interplay between structure and stability but understanding this linkage between plasticity and activity is still in its infancy. For AK, which is known to undergo a large conformational transition from an open inactive to a closed active state, it has been established that dynamic sampling of several structural microstates limits the rate of substrate molecule turnover.[10,12,14–19] Unlike other protein kinases that require specific protein-protein interactions or covalent modifications to enable catalytic activity, the presence of two adenosine phosphate substrates is all that is necessary for AK to catalyze a reversible reaction; thus making it amenable to experimental and theoretical studies aimed at identifying specific residues that contribute to opening and closing, and the timescale of these events. Based on these previous studies, almost exclusively focused on AK from *E. coli*, the AMP_{bd} and ATP_{lid} regions are implicated as undergoing the largest conformational changes and the rate of catalytic turnover is limited by opening of these regions after phosphoryl transfer to release product molecules.[12,14,16–19,22] One aim of the current study is to assess the sensitivity of UVPD-MS to some of the more subtle structural changes AK undergoes during its catalytic cycle. In an effort to identify these we focused on AK from *Gallus gallus* (PDB ID: 2C95)[60] which has abbreviated AMP_{bd} and ATP_{lid} regions compared to AK from *E. coli* (PDB ID: 1AKE)[65] (**Figure 3.14**). These two regions still close over the active site to align the substrates for phosphoryl transfer and prevent hydrolysis, but owing to the shortened active site loops, dynamic fluctuations throughout the remainder of the enzyme during catalysis have a more significant impact.

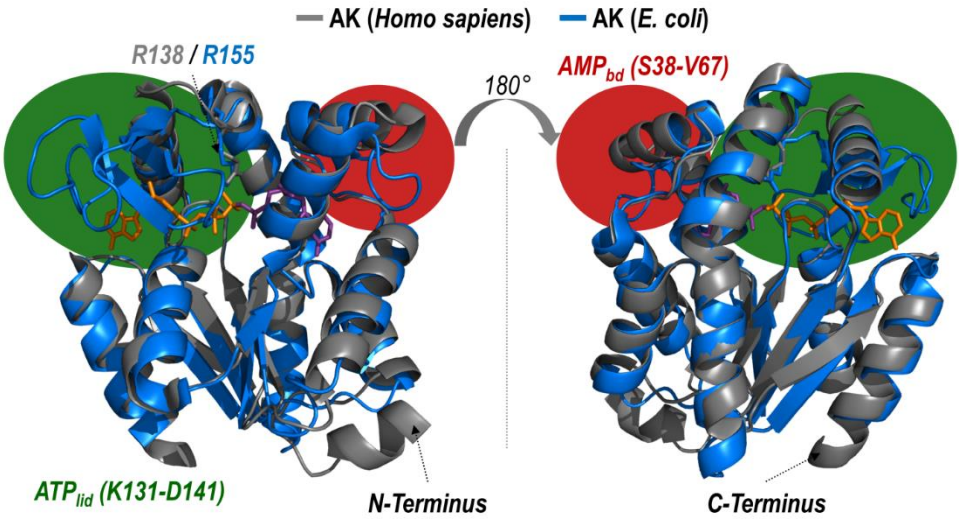

Figure 3.14: Overlay of the crystal structures of AK from *Homo sapiens* (gray; PDB ID: 2C95) and *E. coli* (blue; PDB ID: 1AKE) bound to AP4A (92% and 55% sequence homology, respectively, with AK from *Gallus gallus*). The bound ligand is represented as sticks with the AMP portion shown in purple and ATP portion in orange. The most significant differences in structure are highlighted with ovals and occur in the ATP_{lid} and AMP_{bd} regions that are abbreviated in AK from *Homo sapiens* and *Gallus gallus*. As such, AK from *Gallus gallus* is smaller in size (21.5 kDa, 193 amino acids) than AK from *E. coli* (23.4 kDa, 213 amino acids).

Conformational information was inferred from backbone cleavage efficiencies across the protein determined by analysis of both holo and apo fragment ions upon UVPD.[39–41] In particular, we are interested in the changes in UVPD backbone cleavage efficiencies that occur during each step of the reaction cycle. Enhancement or suppression of backbone cleavages upon UVPD depend on the flexibility, *e.g.*, the extent to which a given region is involved in stabilizing intramolecular interactions.[39–41] Cumulative evidence suggests that regions where UVPD fragmentation of a protein or protein complex is suppressed (relative to an analogous protein or protein complex in another state) indicates enhanced stabilization owing to conformational changes, variations in

intramolecular interactions, or other factors.[39–41] The efficiency of backbone cleavage upon UVPD relative to each amino acid for each AK•ligand complex is represented graphically in **Figure 3.3**. To visualize these changes in backbone cleavage efficiency for each of the eight steps of the AK catalytic cycle, difference plots were constructed by subtraction of the summed holo and apo fragment ion abundances for a given step in the cycle from the previous step (**Figure 3.15**). As shown in **Figure 3.15**, values that fall below the zero axis indicate a decrease or suppression of UVPD, whereas values that lie above the zero axis indicate an increase or enhancement of fragmentation. Considering all of the steps of the reaction cycle, most of the significant variations in backbone cleavage efficiency upon UVPD occur in the adenosine binding region of ATP and α-helices of the AMP_{bd}. Those amino acids (representing backbone cleavage sites along the sequence of AK) for which reproducible and statistically significant variations were observed are highlighted on the structure of AK•AP4A in **Figure 3.16** for each step of the catalytic cycle. Red-colored residues designate an increase in backbone cleavage upon UVPD compared to the previous step in the cycle, thus implying weakened or reduced intramolecular interactions. Conversely blue-colored residues denote a decrease in cleavage efficiency suggesting engagement in new intramolecular interactions that stabilize the structure. **Figure 3.17** showcases five regions of the enzyme (α1, α2, α3 helices, AMP and ATP adenosine binding regions) found to consistently undergo significant conformational changes throughout the enzymatic cycle (based on the UVPD data) highlighted on the crystal structure of AK bound to AP4A.

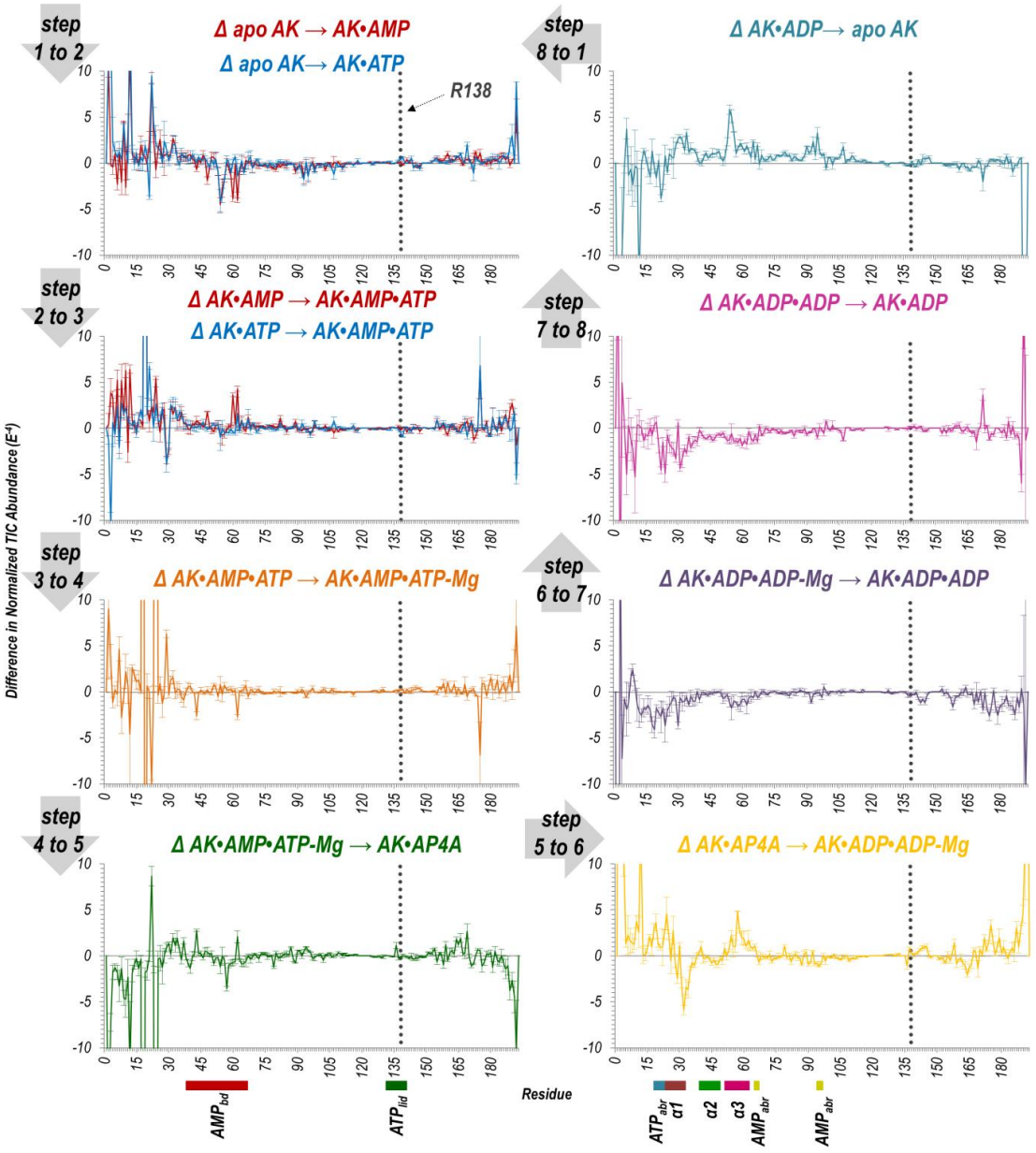

Figure 3.15: Difference plots showing the change in summed abundances of holo and apo fragment ions produced upon UVPD of each AK•ligand complex throughout the entire catalytic cycle of the enzyme. The UVPD fragmentation plot for each individual complex is shown in Figure 3.3. The dotted line indicates the position of R138. Relevant helices (α1, α2, α3) and regions (adenosine binding regions of AMP and ATP, AMP_{bd}, ATP_{lid}) are labelled underneath the *x*-axis using colors corresponding to Figure 3.16.

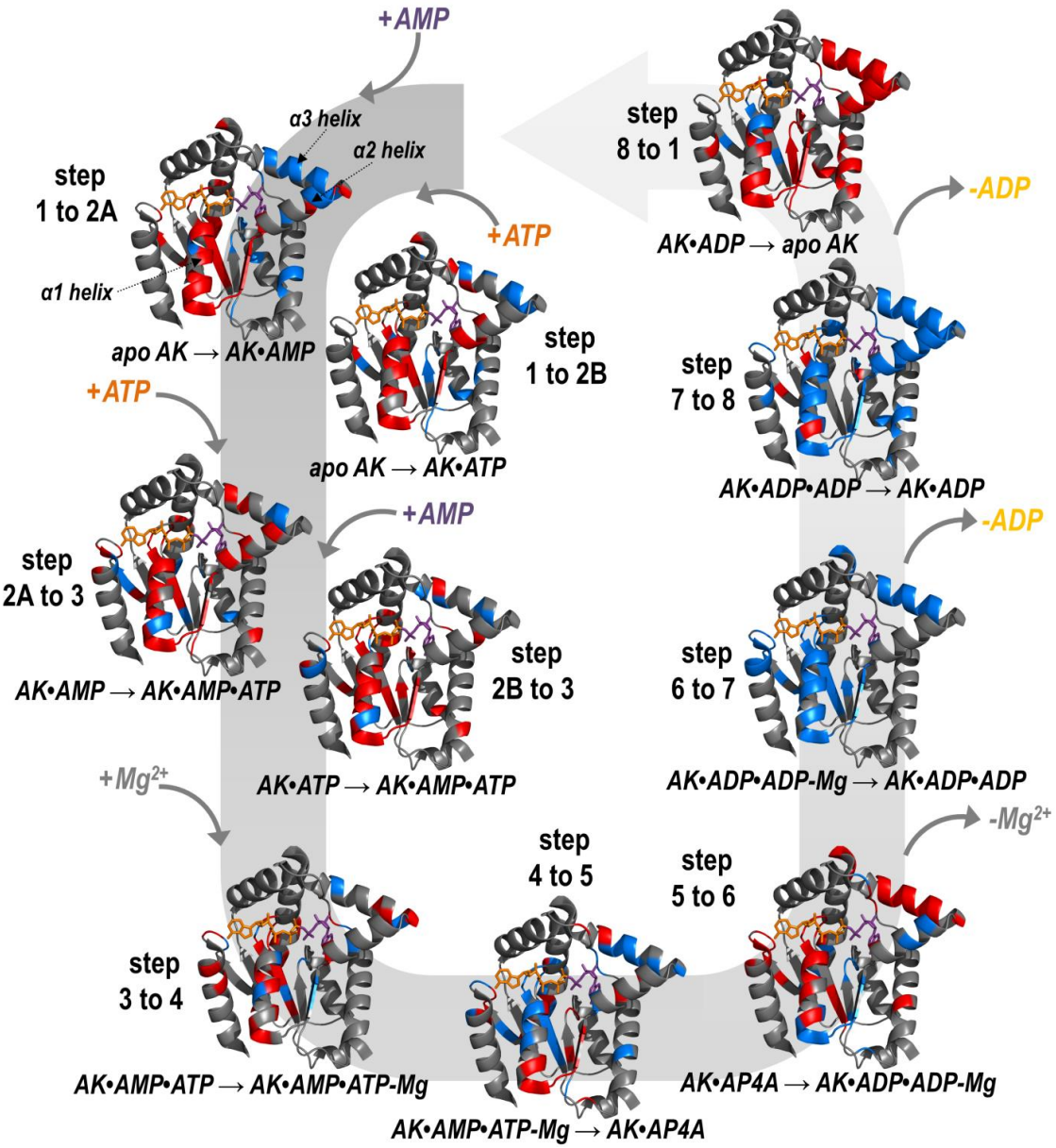

Figure 3.16: Tracking the enhancement (red) and suppression (blue) of UVPD throughout the entire catalytic cycle impressed on a crystal structure of AK bound to AP4A (PDB ID: 2C95): apo AK binding to form binary complexes (step 1 to 2A,B), each transitioning to the ternary complex (step 2A,B to 3), recruiting the Mg^{2+} cofactor (step 3 to 4), closing into the transition state (step 4 to 5), producing two ADP molecules (step 5 to 6), losing the cofactor (step 6 to 7), and releasing ADP (step 8 to 1). The colored regions reflect statistically significant changes in UVPD backbone cleavage efficiency for the difference plots shown in Figure 3.15. Three key helices are labelled in step 1 to 2A.

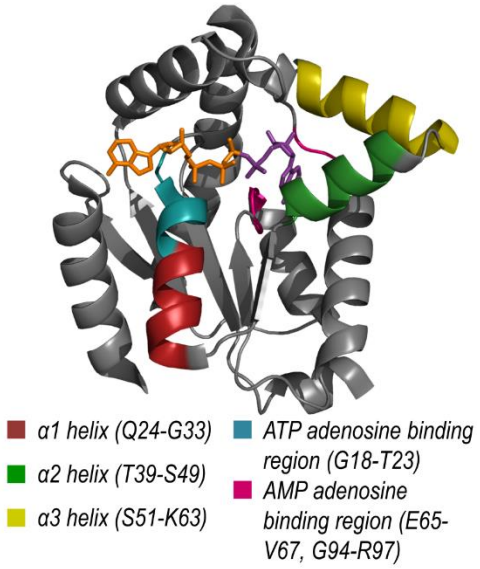

Figure 3.17: Five regions of the protein consistently undergoing significant fragmentation changes based on UVPD, indicative of conformational changes throughout the enzymatic cycle highlighted on the crystal structure of AK bound to AP4A (PDB ID: 2C95).

In detail, following a random bi-bi mechanism during catalysis (*i.e.*, two substrates on, two substrates off), either AMP or ATP can bind apo AK and cause suppression of backbone cleavage in the AMP_{bd} and AMP adenosine binding region (**Figure 3.16(step 1 to 2A)**) or K21 of the ATP adenosine binding region (**Figure 3.16(step 1 to 2B)**). Enhancement in the degree of fragmentation of the α1 helix for both states suggests a global opening of the protein during binary complex formation. Addition of the second cognate ligand to each of the binary complexes to form the ternary AK•AMP•ATP complex results in similar changes in UVPD cleavage efficiencies: most notably significant enhancement of fragmentation in the α1, α2, and α3 helices (**Figure 3.16(steps 2A, 2B to 3)**). This outcome is consistent with further opening of AK to accommodate a second ligand as well as local conformational fluctuations of these three helices to align the reactive atoms of the substrate ligands during catalysis. Recruitment of the Mg^{2+} cofactor leads to further

enhancement of fragmentation in these helical regions, a result that parallels the increased catalytic efficiency of AK as these regions dynamically sample different microstates to carry out the enzymatic function (**Figure 3.16(step 3 to 4)**). Locking the protein in the transition state with inhibitor AP4A causes significant suppression of UVPD backbone cleavage efficiency in the α1 and α3 helices. As expected this supports that the protein is trapped in a closed but catalytically inactive conformation (**Figure 3.16(step 4 to 5)**). Fragmentation throughout the α1 and α3 helices is again enhanced transitioning to the catalytically active ternary complex containing two ADP products and the Mg^{2+} cofactor (**Figure 3.16(step 5 to 6)**). Removal of the cofactor causes significant suppression of fragmentation throughout the entire protein, especially in the α1 and α3 helices; this corresponds to the step in which the catalytic efficiency of the protein is markedly decreased (**Figure 3.16(step 6 to 7)**). Similar suppression of UVPD is observed as one ADP product molecule is released implying local unfolding of these regions has ceased (**Figure 3.16(step 7 to 8)**). Loss of the second product ADP molecule to yield apo AK returns the protein to an open, inactive conformation, suggested by the significant enhancement in UVPD cleavage efficiency throughout the three α-helices (**Figure 3.16(step 8 to 1)**). In general, tracking the variations in UVPD fragmentation during the catalytic cycle specifically implicates the α-helices of the AMP_{bd} and the adenosine binding regions of AMP and ATP as key features that undergo significant reorganization during the catalytic reaction trajectory of AK (**Figure 3.17**).

Given that the catalytic efficiency is not being measured during ESI-UVPD-MS analysis, conclusions about whether the apparent conformational fluctuations play a role in the chemical step of enzyme catalysis or to what extent they assist in pre-organizing active site residues in the configuration needed to facilitate the phosphoryl transfer cannot be drawn. However, it has been previously demonstrated that addition of a small amount

of denaturant, specifically urea, to AK complexes redistributes preexisting structural microstates and stabilizes a substrate-bound open state at the expense of a substrate-bound closed state. This urea-dependent structural redistribution resulted in an increase in catalytic activity of AK and was attributed to an increased rate for the rate-limiting lid opening step.[66] Additionally, previous in vacuum molecular dynamics simulations of AK conclude that although the absolute magnitude of the fluctuations is different in the gas phase (as would be expected without solvent present), the same regions of the protein (AMP_{bd} and ATP_{LID}) have the highest rms deviation values from the crystal structure during ligand binding and catalysis for both solution and the gas phase.[67–69] In summary, UVPD-MS appears to be sensitive to the dynamic conformational equilibria that exist as AK samples various structural microstates in the presence of substrates to align reactive atoms during catalysis.

3.4.4 Examining the Impact of the Mg^{2+} Cofactor

Metal ion cofactors are often required for enzyme catalysis but controversies regarding the specific role of Mg cofactors in kinase catalysis remain. Specifically, some kinases are activated by a single Mg^{2+} ion while for others binding of additional Mg^{2+} might be necessary or may result in inhibition of the enzyme.[22] A recent comprehensive study of the energy landscape of AK during its reaction cycle investigated the mechanism of transition state stabilization and demonstrated a single divalent Mg^{2+} ion as a key player in both orienting active site groups on the ligands for efficient phosphoryl transfer and facilitating opening of the AMP_{bd} and ATP_{lid} after reaction catalysis.[22] In addition to balancing the negative charge of the adenosine phosphate ligands in the active site, the positively charged Mg^{2+} maintains its position during the transition state and acts as an electrostatic pivot to anchor the donor phosphoryl group for a more favorable nucleophilic

attack by the oxygen of the acceptor ligand.[22,70] Additionally the cation serves to weaken strong electrostatic interactions that coordinate the Arg side-chains and phosphates of the adenosine ligands to accelerate opening of the complex, the rate-limiting step of catalysis for this enzyme.[22] UVPD-MS can provide complementary insight into changes of the protein conformation in response to the recruitment or release of the Mg^{2+} cofactor during the catalytic cycle.

Specifically, examining the variations in AK fragmentation after binding and release of the metal ion reveals residues that may be engaging in new interactions (suppressed backbone cleavage) or are situated in regions that become flexible after weakening of previous interactions (enhanced backbone cleavage).[39–41] **Figure 3.18** gives an expanded view of steps 3-7 from **Figure 3.16** demonstrating the enhancement (red) and suppression (blue) of UVPD upon addition of the Mg^{2+} cofactor (step 3 to 4), locking into the transition state (step 4 to 5), yielding two ADP molecules (step 5 to 6), and releasing the Mg^{2+} cofactor (step 6 to 7).

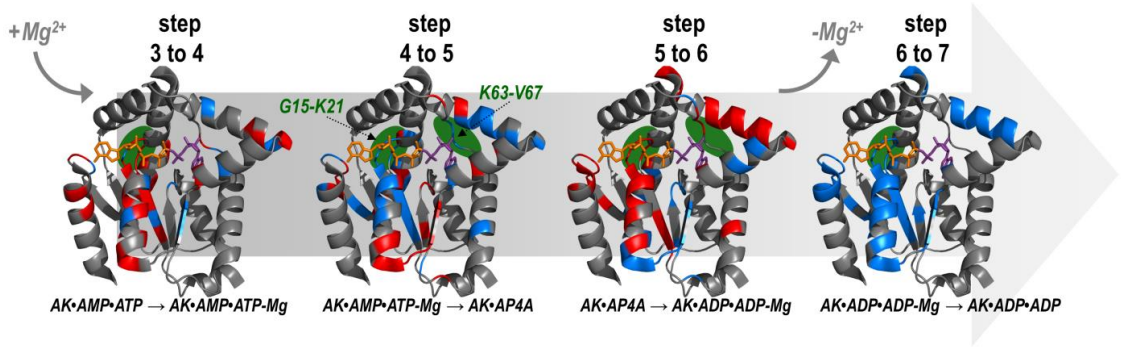

Figure 3.18: Expanded view of steps 3-7 from Figure 3.16 demonstrating the enhancement (red) and suppression (blue) of UVPD (step 3 to 4) upon addition of the Mg^{2+} cofactor, (step 4 to 5) locking into the transition state, (step 5 to 6) yielding two ADP molecules, and (step 6 to 7) releasing the cofactor. The green ovals highlight two regions that are engaged in stabilizing interactions with the phosphate groups of the adenosine substrates and where significant variations in UVPD backbone efficiency are observed as the Mg^{2+} cation is recruited and released.

The green ovals in **Figure 3.18** highlight two regions that are engaged in stabilizing interactions with the phosphate groups of the adenosine substrates and exhibit significant variation in UVPD backbone cleavage efficiency as the Mg^{2+} cation is recruited and released. In particular, enhancement in fragmentation of the loop binding the phosphates of ATP (G15-K21) is observed upon Mg^{2+} binding (**Figure 3.18(step 3 to 4)** and **Figure 3.16(step 3 to 4)**). This result supports the role of Mg^{2+} in interrupting intramolecular interactions between the side-chains of the protein and the phosphates of the ligand to accelerate opening the AMP_{bd} and ATP_{lid} regions after catalysis of the phosphoryl transfer. Conversely locking the enzyme in a transition-like state with the AP4A inhibitor causes suppression of fragmentation in that same loop region (G15-K21) as well as a second loop region (K63-V67) engaged in interactions with the phosphate of AMP (**Figure 3.18(step 4 to 5)** and **Figure 3.16(step 4 to 5)**), suggesting that for this complex these stabilizing interactions have been re-established. Returning the enzyme to its catalytically active state

with Mg^{2+} present once again yields enhanced backbone cleavage in these two loop regions (**Figure 3.18(step 5 to 6)** and **Figure 3.16(step 5 to 6)**). Removal of the Mg^{2+} cofactor results in suppression of fragmentation of the loop adjacent to the phosphate groups of ATP (G15-K21) as the cation is no longer present to disrupt these interactions (**Figure 3.18(step 6 to 7)** and **Figure 3.16(step 6 to 7)**). The conformational impact of addition and removal of the Mg^{2+} cofactor on AK revealed by UVPD-MS correlates well with previous findings of the important role of the cation in stabilizing groups involved in the phosphoryl transfer and accelerating opening of the enzyme after catalysis.[22]

3.4.5 Tracking Conserved Residue R138 during the Catalytic Cycle

The active site residue R138, conserved across all species of AK, has previously been implicated as a significant factor for catalysis by this enzyme. Specifically, mutation of this residue, even to a similarly positively charged Lys, drastically inhibits the rate of enzyme turnover for AK.[71] This finding implies that the specific guanidinium interaction with the β-phosphate of the donor substrate is necessary, an interaction not replicated by a surrogate positively charged group.[22] Additionally, x-ray crystallographic analysis of transition-state AK structures reveals that R138 shifts in concert to mirror the position of the donor phosphoryl group.[22] However previous quantification of phosphoryl transfer and lid opening rates for an R138K mutant revealed that the R to K mutation only influenced the rate of transfer of the phosphoryl group, but not the rate of opening of the ATP_{lid} region after catalysis.[22]

Tracking the variations in UVPD backbone cleavage efficiency specifically for R138 supports these findings. The position of R138 is indicated by a gray dotted line in **Figure 3.15**. The most notable variations in fragmentation at this amino acid backbone position occur during steps 4 to 5, 5 to 6, and 6 to 7. As the enzyme is locked into a

catalytically inactive state bound to AP4A (**Figure 3.15(step 4 to 5)**), the backbone cleavage efficiency is suppressed suggesting that the residue is strongly interacting with the phosphate of the donor substrate. Return of the enzyme to a catalytically active state (**Figure 3.15(step 5 to 6)**) results in significantly enhanced cleavage at R138 implying that the segment containing this residue regains flexibility, engaging in only transient interactions as it mirrors the movement of the donor phosphoryl group. Loss of the Mg^{2+} cofactor (**Figure 3.15(step 6 to 7)**) lowers the catalytic activity of the enzyme, and once again cleavage at R138 is suppressed suggesting a loss of dynamic flexibility and engagement in interactions with the donor phosphoryl group. Upon examination of the holo ions produced upon UVPD of the ternary AK•AMP•ATP complex, R138 was directly identified as interacting strongly with ATP. This result implies that the enhancement and suppression of the cleavage at this residue arises from its interaction with the phosphoryl group of the donor ligand and not some other stabilizing interaction (**Figure 3.11B(3)**). Additionally, if R138 was directly involved in lid opening, suppression of cleavage at this residue for the catalytically inactive complex (AK•AP4A) would be expected instead of the observed enhancement (**Figure 3.16(step 4 to 5)**).

3.5 CONCLUSION

UVPD-MS was successfully used to probe structural changes of the phosphotransferase AK during its reaction cycle. Mapping holo fragment ions for binary and ternary AK•ligand complexes allowed both AMP and ATP to be traced back to their putative binding sites and offered insight into the preference of each substrate for their respective binding pockets. Variations in UVPD backbone cleavage efficiencies were tracked to examine the dynamic plasticity of the enzyme throughout its catalytic cycle. The changes in fragmentation efficiencies are attributed to differences in the intra- and

intermolecular interactions in which the residues of AK engage as the protein binds each of the substrates, recruits a divalent cofactor (Mg^{2+}), carries out the phosphoryl-transfer reaction, and releases the product molecules. Specifically, three α-helices of the AMP_{bd} and the adenosine binding regions of AMP and ATP were implicated as undergoing conformational fluctuations during a global open-to-closed transition as the protein samples various structural microstates to optimize the environment for phosphoryl transfer and suppress hydrolysis. Additionally, closer examination of the changes in UVPD fragmentation efficiency for amino acids in the active site of the enzyme upon recruitment and removal of a divalent Mg^{2+} cofactor by the ternary complex highlights two loop regions known to engage in interactions with the phosphate groups of the substrates. This finding supports the role of Mg^{2+} in accelerating opening of the AMP_{bd} and ATP_{lid} regions by disrupting electrostatic interactions between the side-chains and bound ligands. Lastly, UVPD-MS allowed the conformational variations of the conserved active site residue R138, known to aid in transfer of the phosphoryl group from the donor to the acceptor ligand, to be tracked. Suppression of cleavage efficiency when the enzyme is catalytically active and observation of ATP-bound holo ions at this residue echo the role of R138 in aiding the catalysis of the phosphoryl transfer. Pairing UVPD-MS with more extensive molecular dynamics simulations and integrating complementary data from other biophysical tools, such as vibrational Stark effect spectroscopy,[72] will allow further validation of UVPD as a probe of protein conformation and help unravel the fundamental underpinnings of the UVPD mechanism with respect to the dominant structural or chemical factors that influence the variations in protein fragmentation caused by UVPD.UVPD-MS has shown to be a promising new tool that can provide multiple layers of information on the individual contributions of structural dynamics, metal cofactors, and side-chain chemistries during enzyme catalysis.

3.6 REFERENCES

(1) Daniel, R. M.; Dunn, R. V.; Finney, J. L.; Smith, J. C. The Role of Dynamics in Enzyme Activity. *Annu. Rev. Biophys. Biomol. Struct.* **2003**, *32*, 69–92.

(2) Henzler-Wildman, K. A.; Thai, V.; Lei, M.; Ott, M.; Wolf-Watz, M.; Fenn, T.; Pozharski, E.; Wilson, M. A.; Petsko, G. A.; Karplus, M.; Hübner, C. G.; Kern, D. Intrinsic Motions along an Enzymatic Reaction Trajectory. *Nature* **2007**, *450*, 838–844.

(3) Henzler-Wildman, K. A.; Lei, M.; Thai, V.; Kerns, S. J.; Karplus, M.; Kern, D. A Hierarchy of Timescales in Protein Dynamics Is Linked to Enzyme Catalysis. *Nature* **2007**, *450*, 913–916.

(4) Kamerlin, S. C. L.; Warshel, A. At the Dawn of the 21st Century: Is Dynamics the Missing Link for Understanding Enzyme Catalysis? *Proteins Struct. Funct. Bioinforma.* **2010**, *78*, 1339–1375.

(5) Vonrhein, C.; Schlauderer, G. J.; Schulz, G. E. Movie of the Structural Changes during a Catalytic Cycle of Nucleoside Monophosphate Kinases. *Structure* **1995**, *3*, 483–490.

(6) Noda, L. Adenosine Triphosphate-Adenosine Monophosphate Transphosphorylase Iii. Kinetic Studies. *J. Biol. Chem.* **1958**, *232*, 237–250.

(7) Abele, U.; Schulz, G. E. High-Resolution Structures of Adenylate Kinase from Yeast Ligated with Inhibitor Ap5A, Showing the Pathway of Phosphoryl Transfer. *Protein Sci.* **1995**, *4*, 1262–1271.

(8) Sinev, M. A.; Sineva, E. V.; Ittah, V.; Haas, E. Domain Closure in Adenylate Kinase. *Biochemistry* **1996**, *35*, 6425–6437.

(9) Sheng, X. R.; Li, X.; Pan, X. M. An Iso-Random Bi Bi Mechanism for Adenylate Kinase. *J. Biol. Chem.* **1999**, *274*, 22238–22242.

(10) Miyashita, O.; Onuchic, J. N.; Wolynes, P. G. Nonlinear Elasticity, Proteinquakes, and the Energy Landscapes of Functional Transitions in Proteins. *Proc. Natl. Acad. Sci.* **2003**, *100*, 12570–12575.

(11) Krishnamurthy, H.; Lou, H.; Kimple, A.; Vieille, C.; Cukier, R. I. Associative Mechanism for Phosphoryl Transfer: A Molecular Dynamics Simulation of Escherichia Coli Adenylate Kinase Complexed with Its Substrates. *Proteins Struct. Funct. Bioinforma.* **2005**, *58*, 88–100.

(12) Bae, E.; Phillips, G. N. Roles of Static and Dynamic Domains in Stability and Catalysis of Adenylate Kinase. *Proc. Natl. Acad. Sci. U. S. A.* **2006**, *103*, 2132–2137.

(13) Ådén, J.; Wolf-Watz, M. NMR Identification of Transient Complexes Critical to Adenylate Kinase Catalysis. *J. Am. Chem. Soc.* **2007**, *129*, 14003–14012.

(14) Arora, K.; Brooks, C. L. Large-Scale Allosteric Conformational Transitions of Adenylate Kinase Appear to Involve a Population-Shift Mechanism. *Proc. Natl. Acad. Sci.* **2007**, *104*, 18496–18501.

(15) Hanson, J. A.; Duderstadt, K.; Watkins, L. P.; Bhattacharyya, S.; Brokaw, J.; Chu, J.-W.; Yang, H. Illuminating the Mechanistic Roles of Enzyme Conformational Dynamics. *Proc. Natl. Acad. Sci.* **2007**, *104*, 18055–18060.

(16) Whitford, P. C.; Miyashita, O.; Levy, Y.; Onuchic, J. N. Conformational Transitions of Adenylate Kinase: Switching by Cracking. *J. Mol. Biol.* **2007**, *366*, 1661–1671.
(17) Schrank, T. P.; Bolen, D. W.; Hilser, V. J. Rational Modulation of Conformational Fluctuations in Adenylate Kinase Reveals a Local Unfolding Mechanism for Allostery and Functional Adaptation in Proteins. *Proc. Natl. Acad. Sci.* **2009**, *106*, 16984–16989.
(18) Daily, M. D.; Phillips Jr., G. N.; Cui, Q. Many Local Motions Cooperate to Produce the Adenylate Kinase Conformational Transition. *J. Mol. Biol.* **2010**, *400*, 618–631.
(19) Olsson, U.; Wolf-Watz, M. Overlap between Folding and Functional Energy Landscapes for Adenylate Kinase Conformational Change. *Nat. Commun.* **2010**, *1*, 111.
(20) Ådén, J.; Verma, A.; Schug, A.; Wolf-Watz, M. Modulation of a Pre-Existing Conformational Equilibrium Tunes Adenylate Kinase Activity. *J. Am. Chem. Soc.* **2012**, *134*, 16562–16570.
(21) Rao, V. V. H. G.; Gosavi, S. In the Multi-Domain Protein Adenylate Kinase, Domain Insertion Facilitates Cooperative Folding While Accommodating Function at Domain Interfaces. *PLOS Comput. Biol.* **2014**, *10*, e1003938.
(22) Kerns, S. J.; Agafonov, R. V.; Cho, Y.-J.; Pontiggia, F.; Otten, R.; Pachov, D. V.; Kutter, S.; Phung, L. A.; Murphy, P. N.; Thai, V.; Alber, T.; Hagan, M. F.; Kern, D. The Energy Landscape of Adenylate Kinase during Catalysis. *Nat. Struct. Mol. Biol.* **2015**, *22*, 124–131.
(23) Ferreiro, D. U.; Hegler, J. A.; Komives, E. A.; Wolynes, P. G. On the Role of Frustration in the Energy Landscapes of Allosteric Proteins. *Proc. Natl. Acad. Sci.* **2011**, *108*, 3499–3503.
(24) Warshel, A.; Bora, R. P. Perspective: Defining and Quantifying the Role of Dynamics in Enzyme Catalysis. *J. Chem. Phys.* **2016**, *144*, 180901.
(25) Konermann, L.; Vahidi, S.; Sowole, M. A. Mass Spectrometry Methods for Studying Structure and Dynamics of Biological Macromolecules. *Anal. Chem.* **2014**, *86*, 213–232.
(26) Konermann, L.; Tong, X.; Pan, Y. Protein Structure and Dynamics Studied by Mass Spectrometry: H/D Exchange, Hydroxyl Radical Labeling, and Related Approaches. *J. Mass Spectrom.* **2008**, *43*, 1021–1036.
(27) Fitzgerald, M. C.; West, G. M. Painting Proteins with Covalent Labels: What's In the Picture? *J. Am. Soc. Mass Spectrom.* **2009**, *20*, 1193–1206.
(28) Cammarata, M.; Lin, K.-Y.; Pruet, J.; Liu, H.; Brodbelt, J. Probing the Unfolding of Myoglobin and Domain C of PARP-1 with Covalent Labeling and Top-Down Ultraviolet Photodissociation Mass Spectrometry. *Anal. Chem.* **2014**, *86*, 2534–2542.
(29) Pirrone, G. F.; Iacob, R. E.; Engen, J. R. Applications of Hydrogen/Deuterium Exchange MS from 2012 to 2014. *Anal. Chem.* **2014**, *87*, 99–118.
(30) Sharon, M.; Robinson, C. V. The Role of Mass Spectrometry in Structure Elucidation of Dynamic Protein Complexes. *Annu. Rev. Biochem.* **2007**, *76*, 167–193.

(31) Heck, A. J. R. Native Mass Spectrometry: A Bridge between Interactomics and Structural Biology. *Nat. Methods* **2008**, *5*, 927–933.
(32) Hopper, J. T. S.; Oldham, N. J. Collision Induced Unfolding of Protein Ions in the Gas Phase Studied by Ion Mobility-Mass Spectrometry: The Effect of Ligand Binding on Conformational Stability. *J. Am. Soc. Mass Spectrom.* **2009**, *20*, 1851–1858.
(33) Konermann, L.; Ahadi, E.; Rodriguez, A. D.; Vahidi, S. Unraveling the Mechanism of Electrospray Ionization. *Anal. Chem.* **2012**, *85*, 2–9.
(34) Schennach, M.; Breuker, K. Proteins with Highly Similar Native Folds Can Show Vastly Dissimilar Folding Behavior When Desolvated. *Angew. Chem. Int. Ed.* **2014**, *53*, 164–168.
(35) Cubrilovic, D.; Haap, W.; Barylyuk, K.; Ruf, A.; Badertscher, M.; Gubler, M.; Tetaz, T.; Joseph, C.; Benz, J.; Zenobi, R. Determination of Protein–Ligand Binding Constants of a Cooperatively Regulated Tetrameric Enzyme Using Electrospray Mass Spectrometry. *ACS Chem. Biol.* **2014**, *9*, 218–226.
(36) Li, H.; Wongkongkathep, P.; Orden, S. L. V.; Loo, R. R. O.; Loo, J. A. Revealing Ligand Binding Sites and Quantifying Subunit Variants of Noncovalent Protein Complexes in a Single Native Top-Down FTICR MS Experiment. *J. Am. Soc. Mass Spectrom.* **2014**, *25*, 2060–2068.
(37) Li, H.; Wolff, J. J.; Van Orden, S. L.; Loo, J. A. Native Top-Down Electrospray Ionization-Mass Spectrometry of 158 KDa Protein Complex by High-Resolution Fourier Transform Ion Cyclotron Resonance Mass Spectrometry. *Anal. Chem.* **2014**, *86*, 317–320.
(38) O'Brien, J. P.; Li, W.; Zhang, Y.; Brodbelt, J. S. Characterization of Native Protein Complexes Using Ultraviolet Photodissociation Mass Spectrometry. *J. Am. Chem. Soc.* **2014**, *136*, 12920–12928.
(39) Cammarata, M. B.; Brodbelt, J. S. Structural Characterization of Holo- and Apo-Myoglobin in the Gas Phase by Ultraviolet Photodissociation Mass Spectrometry. *Chem. Sci.* **2015**, *6*, 1324–1333.
(40) Cammarata, M. B.; Thyer, R.; Rosenberg, J.; Ellington, A.; Brodbelt, J. S. Structural Characterization of Dihydrofolate Reductase Complexes by Top-Down Ultraviolet Photodissociation Mass Spectrometry. *J. Am. Chem. Soc.* **2015**, *137*, 9128–9135.
(41) Cammarata, M. B.; Schardon, C. L.; Mehaffey, M. R.; Rosenberg, J.; Singleton, J.; Fast, W.; Brodbelt, J. S. Impact of G12 Mutations on the Structure of K-Ras Probed by Ultraviolet Photodissociation Mass Spectrometry. *J. Am. Chem. Soc.* **2016**, *138*, 13187–13196.
(42) Zechel, D. L.; Konermann, L.; Withers, S. G.; Douglas, D. J. Pre-Steady State Kinetic Analysis of an Enzymatic Reaction Monitored by Time-Resolved Electrospray Ionization Mass Spectrometry. *Biochemistry* **1998**, *37*, 7664–7669.
(43) Li, Z.; Sau, A. K.; Shen, S.; Whitehouse, C.; Baasov, T.; Anderson, K. S. A Snapshot of Enzyme Catalysis Using Electrospray Ionization Mass Spectrometry. *J. Am. Chem. Soc.* **2003**, *125*, 9938–9939.

(44) Liuni, P.; Jeganathan, A.; Wilson, D. J. Conformer Selection and Intensified Dynamics During Catalytic Turnover in Chymotrypsin. *Angew. Chem. Int. Ed.* **2012**, *51*, 9666–9669.
(45) Lermyte, F.; Sobott, F. Electron Transfer Dissociation Provides Higher-Order Structural Information of Native and Partially Unfolded Protein Complexes. *PROTEOMICS* **2015**, *15*, 2813–2822.
(46) Breuker, K.; Oh, H.; Horn, D. M.; Cerda, B. A.; McLafferty, F. W. Detailed Unfolding and Folding of Gaseous Ubiquitin Ions Characterized by Electron Capture Dissociation. *J. Am. Chem. Soc.* **2002**, *124*, 6407–6420.
(47) Breuker, K.; McLafferty, F. W. Stepwise Evolution of Protein Native Structure with Electrospray into the Gas Phase, 10−12 to 102 S. *Proc. Natl. Acad. Sci.* **2008**, *105*, 18145–18152.
(48) Zhang, H.; Cui, W.; Wen, J.; Blankenship, R. E.; Gross, M. L. Native Electrospray and Electron-Capture Dissociation in FTICR Mass Spectrometry Provide Top-down Sequencing of a Protein Component in an Intact Protein Assembly. *J. Am. Soc. Mass Spectrom.* **2010**, *21*, 1966–1968.
(49) Zhang, H.; Cui, W.; Gross, M. L.; Blankenship, R. E. Native Mass Spectrometry of Photosynthetic Pigment–Protein Complexes. *FEBS Lett.* **2013**, *587*, 1012–1020.
(50) Zhang, H.; Cui, W.; Gross, M. L. Native Electrospray Ionization and Electron-Capture Dissociation for Comparison of Protein Structure in Solution and the Gas Phase. *Int. J. Mass Spectrom.* **2013**, *354–355*, 288–291.
(51) Zhou, M.; Wysocki, V. H. Surface Induced Dissociation: Dissecting Noncovalent Protein Complexes in the Gas Phase. *Acc. Chem. Res.* **2014**, *47*, 1010–1018.
(52) Shaw, J. B.; Li, W.; Holden, D. D.; Zhang, Y.; Griep-Raming, J.; Fellers, R. T.; Early, B. P.; Thomas, P. M.; Kelleher, N. L.; Brodbelt, J. S. Complete Protein Characterization Using Top-Down Mass Spectrometry and Ultraviolet Photodissociation. *J. Am. Chem. Soc.* **2013**, *135*, 12646–12651.
(53) Cannon, J. R.; Cammarata, M. B.; Robotham, S. A.; Cotham, V. C.; Shaw, J. B.; Fellers, R. T.; Early, B. P.; Thomas, P. M.; Kelleher, N. L.; Brodbelt, J. S. Ultraviolet Photodissociation for Characterization of Whole Proteins on a Chromatographic Time Scale. *Anal. Chem.* **2014**, *86*, 2185–2192.
(54) Brodbelt, J. S. Ion Activation Methods for Peptides and Proteins. *Anal. Chem.* **2016**, *88*, 30–51.
(55) Warnke, S.; Baldauf, C.; Bowers, M. T.; Pagel, K.; von Helden, G. Photodissociation of Conformer-Selected Ubiquitin Ions Reveals Site-Specific Cis/Trans Isomerization of Proline Peptide Bonds. *J. Am. Chem. Soc.* **2014**, *136*, 10308–10314.
(56) Warnke, S.; von Helden, G.; Pagel, K. Analyzing the Higher Order Structure of Proteins with Conformer-Selective Ultraviolet Photodissociation. *PROTEOMICS* **2015**, *15*, 2804–2812.
(57) Briand, G.; Perrier, V.; Kouach, M.; Takahashi, M.; Gilles, A. M.; Bârzu, O. Characterization of Metal and Nucleotide Liganded Forms of Adenylate Kinase by Electrospray Ionization Mass Spectrometry. *Arch. Biochem. Biophys.* **1997**, *339*, 291–297.

(58) Daniel, J. M.; McCombie, G.; Wendt, S.; Zenobi, R. Mass Spectrometric Determination of Association Constants of Adenylate Kinase with Two Noncovalent Inhibitors. *J. Am. Soc. Mass Spectrom.* **2003**, *14*, 442–448.
(59) Yin, S.; Loo, J. A. Elucidating the Site of Protein-ATP Binding by Top-Down Mass Spectrometry. *J. Am. Soc. Mass Spectrom.* **2010**, *21*, 899–907.
(60) Bunkoczi, G.; Filippakopoulos, P.; Jansson, A.; Longman, E.; Von Delft, F.; Edwards, A.; Arrowsmith, C.; Sundstrom, M.; Weigelt, J.; Knapp, S. Structure of Adenylate Kinase 1 in Complex with P1, P4-Di(Adenosine)Tetraphosphate, **2017**, to be submitted for publication.
(61) Yin, S.; Loo, J. A. Top-Down Mass Spectrometry of Supercharged Native Protein-Ligand Complexes. *Int. J. Mass Spectrom.* **2011**, *300*, 118–122.
(62) Pai, E. F.; Sachsenheimer, W.; Schirmer, R. H.; Schulz, G. E. Substrate Positions and Induced-Fit in Crystalline Adenylate Kinase. *J. Mol. Biol.* **1977**, *114*, 37–45.
(63) Schulz, G. E.; Müller, C. W.; Diederichs, K. Induced-Fit Movements in Adenylate Kinases. *J. Mol. Biol.* **1990**, *213*, 627–630.
(64) Tsai, M. D.; Yan, H. Mechanism of Adenylate Kinase: Site-Directed Mutagenesis versus x-Ray and NMR. *Biochemistry* **1991**, *30*, 6806–6818.
(65) Müller, C. W.; Schulz, G. E. Structure of the Complex between Adenylate Kinase from Escherichia Coli and the Inhibitor Ap5A Refined at 1.9 Å Resolution. *J. Mol. Biol.* **1992**, *224*, 159–177.
(66) Rogne, P.; Wolf-Watz, M. Urea-Dependent Adenylate Kinase Activation Following Redistribution of Structural States. *Biophys. J.* **2016**, *111*, 1385–1395.
(67) Kern, P.; Brunne, R. M.; Folkers, G. Nucleotide-Binding Properties of Adenylate Kinase from Escherichia Coli: A Molecular Dynamics Study in Aqueous and Vacuum Environments. *J. Comput. Aided Mol. Des.* **1994**, *8*, 367–388.
(68) Elamrani, S.; Berry, M. B.; Phillips, G. N.; McCammon, J. A. Study of Global Motions in Proteins by Weighted Masses Molecular Dynamics: Adenylate Kinase as a Test Case. *Proteins Struct. Funct. Bioinforma.* **1996**, *25*, 79–88.
(69) Orzechowski, M.; Tama, F. Flexible Fitting of High-Resolution X-Ray Structures into Cryoelectron Microscopy Maps Using Biased Molecular Dynamics Simulations. *Biophys. J.* **2008**, *95*, 5692–5705.
(70) Baxter, N. J.; Blackburn, G. M.; Marston, J. P.; Hounslow, A. M.; Cliff, M. J.; Bermel, W.; Williams, N. H.; Hollfelder, F.; Wemmer, D. E.; Waltho, J. P. Anionic Charge Is Prioritized over Geometry in Aluminum and Magnesium Fluoride Transition State Analogs of Phosphoryl Transfer Enzymes. *J. Am. Chem. Soc.* **2008**, *130*, 3952–3958.
(71) Yan, H.; Tsai, M.-D. Nucleoside Monophosphate Kinases: Structure, Mechanism, and Substrate Specificity. In *Advances in Enzymology and Related Areas of Molecular Biology*; Purich, D. L., Ed.; John Wiley & Sons, Inc.: Hoboken, NJ, USA, 1999; pp 103–134.
(72) Fried, S. D.; Boxer, S. G. Measuring Electric Fields and Noncovalent Interactions Using the Vibrational Stark Effect. *Acc. Chem. Res.* **2015**, *48*, 998–1006.

Chapter 4: Elusive Structural Changes of New Delhi Metallo-β-Lactamase Revealed by Ultraviolet Photodissociation Mass Spectrometry[†]

4.1 Overview

We use mass spectrometry (MS), under denaturing and non-denaturing solution conditions, along with ultraviolet photodissociation (UVPD) to characterize structural variations in New Delhi metallo-β-lactamase (NDM) upon perturbation by ligands or mutation. Mapping changes in the abundances and distributions of fragment ions enables sensitive detection of structural alterations throughout the protein. Binding of three covalent inhibitors were characterized: a pentafluorphenyl ester, an *O*-aryloxycarbonyl hydroxamate, and ebselen. The first two inhibitors modify Lys211 and maintain dizinc binding, although the pentafluorophenyl ester is not selective (Lys214 and Lys216 are also modified). Ebselen reacts with the sole Cys (Cys208) and ejects Zn2 from the active site. For each inhibitor, native UVPD-MS enabled simultaneous detection of the closing of a substrate-binding beta-hairpin loop, identification of covalently-modified residue(s), reporting of the metalation state of the enzyme, and in the case of ebselen, induced partial disorder in the C-terminus of the protein. Owing to the ability of native UVPD-MS to track structural changes and metalation state with high sensitivity, we further used this method to evaluate the impact of mutations found in NDM clinical variants. Changes introduced by NDM-4 (M154L) and NDM-6 (A233V) are revealed to propagate through separate networks of interactions to direct zinc ligands, and the combination of these two mutations

[†]Mehaffey, M. R.; Ahn, Y. C.; Rivera, D. D.; Thomas, P. W.; Cheng, Z.; Crowder, M. W.; Pratt, R. F.; Fast, W.; Brodbelt, J. S. Elusive structural changes of New Delhi metallo-β-lactamase revealed by ultraviolet photodissociation mass spectrometry. *Chem. Sci.* **2020**, doi: 10.1039/d0sc02503h.

YCA and DDR synthesized a small molecule inhibitor to bind the protein. PWT and ZC expressed and purified the proteins for the study. MWC, RFP, WF, and JSB provided mentorship and reviewed the manuscript prior to publication.

in NDM-15 (M154L, A233V) results in additive as well as additional structural changes. Insight from UVPD-MS helps to elucidate how distant mutations impact zinc affinity in the evolution of this antibiotic resistance determinant. UVPD-MS is a powerful tool capable of simultaneous reporting of ligand binding, conformational changes and metalation state of NDM, revealing structural aspects of ligand recognition and clinical variants that have proven difficult to probe.

4.2 INTRODUCTION

Infection by antibiotic resistant organisms remains a serious health threat. A 2019 report from the Centers for Disease Control and Prevention (CDC) indicates that in the U.S., bacteria and fungi cause over 2.8 million antibiotic resistant infections each year and that 35,000 people die due to these infections.[1] The CDC ranks carbapenem-resistant Enterobacteriaceae in the top tier of "Urgent Threats." Resistance against carbapenems is particularly dangerous because these β-lactam drugs are often held in reserve as life-saving "drugs of last resort" for patients with complicated infections.[2] Some carbapenems can serve two purposes: dual inhibition of peptidoglycan biosynthesis and activity of some serine-β-lactamases. However, these drugs do not inhibit metallo-β-lactamases (MBLs), which instead use active-site zinc ion(s) to catalyze efficient hydrolysis and inactivation of carbapenems. For example, New Delhi metallo-β-lactamase (NDM) readily catalyzes hydrolysis of meropenem and imipenem with specificity constants (k_{cat}/K_M) $>10^6$ $M^{-1}s^{-1}$.[3] Currently, there are no FDA approved drugs that counter the activity of NDM, or any other MBL, so NDM inhibitors are an unmet clinical need.[4]

Despite more than 100 structural models of NDM deposited in the protein data bank, there are still significant gaps in our knowledge about NDM structure. NDM drug development efforts would greatly benefit from specific information detailing how ligands

bind to active site loops and how clinical variants of the enzyme impact structure, but aspects of these structural differences often remain elusive. For example, MBLs similar to NDM have a flexible beta-hairpin loop containing a hydrophobic amino acid at the apex that closes down over a ligand upon inhibitor binding or during catalysis, making important binding interactions with the ligand as revealed by mutagenesis, kinetic analysis, X-ray crystallography, and protein NMR studies.[5–9] However, the conformation of the homologous beta-hairpin loop in NDM is often obscured or artifactually constrained in X-ray studies owing to interactions with a neighboring NDM monomer during crystal formation.[10] Mutagenesis and kinetic studies indicate an important role for this NDM loop in ligand binding and substrate turnover that may differ somewhat from its role in homologous MBLs, underscoring the need to better characterize structural changes upon ligand binding.[11,12] Two spectroscopic methods (^{19}F NMR and RFQ-DEER) have been used along with covalent incorporation of labels into the NDM loop to detect conformational changes upon ligand binding.[13,14] The conformations that this loop adopts appear to be ligand dependent and ligand binding may even trigger loop opening, although the covalent incorporation of these labels may perturb the system and complicate interpretation.[13,14] Alternative methods are needed to better understand the structural implications of ligand-binding, preferably using unlabeled proteins.

A second example of inadequate structural information relates to clinical variants of NDM. Almost 30 different protein sequences have been reported for NDM clinical variants (NDM-1 through NDM-29). Many of these variants improve thermostability and the affinity of Zn2 (some variants have 10-fold lower K_d values) and appear to be emerging due to the combined selective pressures of antibiotic treatment and zinc scarcity at infection sites brought on by the host innate immune response.[3,15–18] The structural models of seven different NDM variants (NDM-1, 3, 4, 5, 8, 9, 12) are deposited in the protein data bank,

but the structural differences observed among these variants by X-ray crystallography are small and the mechanisms whereby mutations lead to improvements in zinc affinity are difficult to discern.[15] Alternative strategies that can better detect the impact of mutation on NDM structure would help elucidate how clinical variants achieve improved resistance and aid in predicting the impact of newly sequenced variants.

The development of native mass spectrometry (MS) represents an alternative technique to probe protein structure by enabling the transfer of intact protein complexes with bound ligands into the gas phase using electrospray ionization (ESI) of high ionic strength solutions.[19,20] While traditional collisional activation provides some sequence information on native protein complexes in the gas phase, typically this MS/MS approach disrupts non-covalent interactions and ejects ligands and individual protein constituents. As such, alternative MS/MS methods are necessary to probe the structure of intact protein complexes.[21,22] The ability of electron-based activation methods, including electron transfer dissociation (ETD),[23] electron capture dissociation (ECD),[24–26] and electron ionization dissociation (EID),[27] to allow retention of noncovalent ligands and metal cofactors on fragment ions, referred to as holo ions, has been used to identify structural differences between ligand-bound (holo) and ligand-free (apo) ions. The propensity of these electron-based strategies for fragmenting a given region correlates with protein flexibility (*i.e.* B-factors), enabling aspects of tertiary structure to be determined.[23,28] In many ways mirroring the scope of electron-based activation methods, ultraviolet photodissociation (UVPD) at 193 nm has proven capable of providing sequence information, localizing ligand binding sites, and probing conformational changes of ligand:protein complexes.[29–31] Retention of noncovalent ligands during photoactivation yields ligand-bound "holo" fragment ions that can be mapped along the sequence to elucidate binding sites.[30] Tracking enhancement or suppression of backbone cleavages

upon UVPD highlights regions where there are changes in stabilizing noncovalent interactions and in protein flexibility (*i.e.* enhancement of backbone fragmentation indicates fewer interactions, more flexibility, and typically leads to greater production of sequence ions; whereas suppression signifies more extensive interactions that limit the separation and detection of fragment ions).[31] Additionally, UVPD affords unsurpassed sequence coverage[29,30] and retention of labile covalent moieties[32] with little dependence on precursor charge state.[33] This native UVPD-MS approach has previously been applied for detecting conformational changes induced by ligand binding to dihydrofolate reductase (DHFR),[34] sequence variants of rat sarcoma GTPase K-Ras[35,36] and DHFR,[37] and structural re-organization of the phosphotransferase enzyme adenylate kinase during its catalytic cycle.[38]

Here, we use native UVPD-MS to track changes in fragmentation patterns as a means to infer changes in the active site loop conformation, zinc binding, and conformations of surrounding residues in NDM-1 upon binding to three different small molecule inhibitors known to covalently modify the enzyme. Combining a native MS strategy with UVPD allows us to simultaneously define changes in protein conformation and zinc binding arising from interaction with inhibitors. We also compare four representative clinical NDM variants: NDM-1 (the reference sequence), NDM-4 (M154L), NDM-6 (A233V), and NDM-15 (M154L, A233V), specifically focusing on variations in backbone fragmentation adjacent to the six zinc-coordinating residues. Application of this method reveals structural differences not easily monitored by other approaches and provides information useful for NDM inhibitor development and better understanding how clinical variants lead to increased zinc affinity and enhanced drug resistance.

4.3 EXPERIMENTAL

4.3.1 Sample Preparation

The reference sequence (NDM-1) and three clinical variants (NDM-4, NDM-6, and NDM-15) of recombinant NDM were expressed and purified as previously described, all of which include an *N*-terminal truncation to remove a lipidation signal sequence to make soluble versions of each protein.[3,17] The expressed protein sequence with mutated sites highlighted and structures of the small molecule inhibitors are shown in **Figure 4.1**. The numbering scheme includes the initial 35 residues although the coding region for this sequence is omitted in the expression constructs. The three covalent inhibitors (**1**-**3**) were synthesized or purchased.

A covalent inhibitor of imipenemase-1 (IMP-1), the pentafluorophenyl ester of 3-mercaptopropionic acid (**1**), was synthesized as described elsewhere[39] and reconstituted in dimethyl sulfoxide stock solutions immediately prior to incubation with NDM-1 [^{1}H NMR (400 MHz, $CDCl_3$): δ 3.01 (2H, t), 2.91 (2H, dt), 1.75 (1H, t); ESI-MS (m/z): 273.0014 $(M+H)^+$]. Inhibitor **1** and NDM-1 were combined at various stoichiometric ratios (1:1, 5:1, and 100:1 inhibitor:NDM-1) in 20 mM ammonium acetate (pH 6.8) and incubated at 25 °C for 1 h. The synthesis of a covalent inhibitor of NDM-1, *N*-(benzyloxycarbonyl)-*O*-[(phenyoxycarbonyl)]hydroxylamine, which is an *O*-aryloxycarbonyl hydroxamate (**2**), was previously described,[40,41] and a 125:1 stoichiometric ratio (inhibitor:NDM-1) was incubated with NDM-1 at 2 °C for 18 h in 50 mM HEPES (pH 7.0). The covalent NDM-1 inhibitor ebselen,[42] a benzisoselenazol (**3**), was purchased from Sigma-Aldrich (St. Louis, MO) and incubated at a 1:1 stochiometric ratio (inhibitor:NDM-1) at 25 °C for 30 min in 20 mM ammonium acetate (pH 6.8). Prior to use in MS experiments, these incubation solutions, as well as stock solutions of the variants NDM-1, -4, -6, and -15, were desalted

and exchanged into water or 20 mM ammonium acetate using 10 kDa molecular weight cutoff filter devices (MilliporeSigma, Burlington, MA). Samples were subsequently diluted for MS analysis to 10 μM protein concentration in 50/49.5/0.5 (v/v/v) acetonitrile/water/formic acid for denaturing experiments or 20 mM ammonium acetate (pH 6.8) for native conditions.

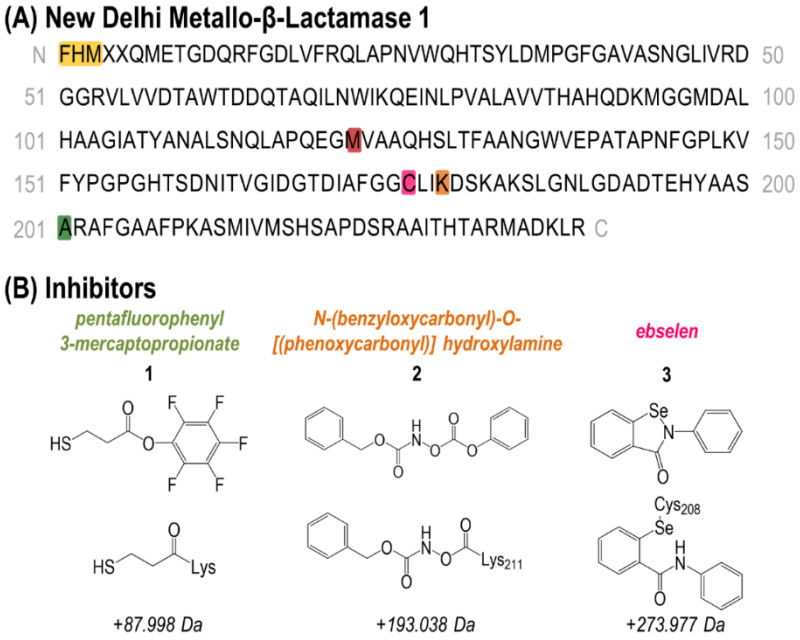

Figure 4.1: Sequence of (A) New Delhi Metallo-β-Lactamase-1. In subsequent figures, residues are numbered accounting for a 29 (no FHM) or 32 (with FHM) residue N-terminal region that is absent in the expressed sequence. Some of the proteins used in this study contain the FHM residues shaded in yellow owing to differences in cleavage of the expression tag. Use of two different NDM expression and purification systems resulted in variation in the 4 and 5 positions with X4X5 = GM or GQ. The two positions mutated resulting in clinical variants are shaded: M154L (red) and A233V (green). The two reaction sites for covalent inhibitors, C208 and K211, are shaded in pink or orange, respectively. (B) Structures of covalent inhibitors of NDM-1 (**1**) pentafluorophenyl 3-mercaptopropionate, (**2**) N-(benzyloxycarbonyl)-O-[(phenoxycarbonyl)] hydroxylamine, and (**3**) ebselen. The chemical structure of the resulting modification of an amino acid side-chain is shown along with the expected mass shift.

4.3.2 Mass Spectrometry

An offline nano-ESI source with borosilicate emitters fabricated in-house and coated in Au/Pd was used to ionize proteins and protein complexes. The source was operated at applied voltages of 1.0 – 1.1 kV and set at a temperature of 200 °C to transfer proteins into a Thermo Scientific Orbitrap Elite mass spectrometer (Bremen, Germany). This instrument was modified previously by aligning an Excistar 193 nm ArF excimer laser (Coherent, Santa Cruz, CA) with the HCD cell to perform UV photodissociation.[29] MS/MS experiments involved ion trap isolation of a single charge state of the protein species of interest using isolation widths of 10-20 *m/z* and subsequent collisional activation using 15-20% NCE or a single 3 mJ pulse for UVPD. MS1 spectra represent sixty scans, while MS/MS spectra contain 500 transients with a scan range of *m/z* 220-4000. Using a resolving power of 240K at 400 *m/z* and a maximum ion time of 2 s, the automatic gain control was set at 1×10^6 for MS1 and 5×10^5 for MS/MS spectra. All MS/MS spectra were collected in triplicate.

4.3.3 Data Analysis

The Thermo Xtract algorithm was used to de-charge and de-isotope all ESI mass spectra and HCD or UVPD mass spectra (S/N ratio of 3, fit factor of 44%, remainder of 25%). ProSight Lite v1.4 assigned monoisotopic fragment ions from the MS/MS spectra as apo sequence ions by searching against the NDM sequence. For HCD mass spectra, only *b*- and *y*-type ions were considered, while for UVPD mass spectra all nine ion types were considered (*a, a+1, b, c, x, x+1, y, y-1, z*). Holo fragment ions bound to zinc(II) resulting from photodissociation were also identified for the clinical variants and protein-inhibitor complexes by including the corresponding mass shifts at the termini: 61.913 – 63.929 Da for one zinc(II) or 123.827 – 127.858 Da for two zinc(II) ions. Covalently attached

inhibitors were considered static modifications and included in searches using the expected mass shifts listed in **Figure 4.1**.

The relative efficiencies of backbone cleavages induced upon UVPD were calculated for clinical variants and protein-inhibitor complexes using the fragment abundance tab of the Web-based utility UV-POSIT.[43] Briefly, in a protein with *R* residues (numbered 1 to *R* from N-terminus to C-terminus), this program sums the abundances of all the fragment ions resulting from backbone cleavages adjacent to each individual amino acid and calculates a backbone cleavage yield for each amino acid position. In essence, the total backbone cleavage yield of amino acid *n* is the sum of all N-terminal sequence ions (a_n, b_n, c_n) resulting from cleavage C-terminal to the n^{th} residue and all C-terminal product ions (x_{R-n+1}, y_{R-n+1}, z_{R-n+1}) produced by backbone cleavage N-terminal to the n^{th} residue. The summed values for each backbone position are then normalized to the total ion current of the spectrum and reported as the cleavage "efficiencies" (*i.e.* relative propensities) adjacent to each amino acid.[43] This method provides a semi-quantitative way to evaluate variations in fragmentation throughout the protein sequence. Two protein states are compared (*e.g.* NDM-1 versus clinical variant, or unmodified versus inhibitor-bound) by subtraction of corresponding backbone cleavage efficiencies and represented as difference plots or heatmaps. Statistical significance of observed differences is established by pooling standard deviations and calculating *p*-values using a two-tailed Student's *t*-test. The log of these values is plotted for each protein:inhibitor complex compared to the corresponding unmodified protein (**Figure 4.2A,B**) or for each clinical variant compared to the reference NDM-1 protein (**Figure 4.2C(1,2,3)**). A histogram of *p*-values for the entire clinical variant data set is included in **Figure 4.2C(4)**. The ~25% of residues with *p*-values of 1.00 correspond to those with no adjacent backbone cleavages (*i.e.* no sequence coverage). The *p*-values less than 1.00 (~75% of the values which also correlates to the observed 75%

sequence coverage) correspond to those residues for which bracketing backbone cleavages were observed for both NDM-1 and an NDM-1:inhibitor complex or for both NDM-1 and a variant, thus allowing comparison of the abundances and calculation of a statistical significance. All differences in backbone fragmentation efficiencies discussed below are significant at a confidence threshold of 99% (*i.e.* *p*-value < 0.01), with this cutoff represented as a black line for each of the five difference graphs in **Figure 4.2** and collectively represented by the left-most blue bar in **Figure 4.2C(4)** (highest significance). A crystal structure of NDM-1 (PDB ID: 3SPU)[44] with important regions labelled is included to aid in visualization and detail the residues involved in the defined active site loops (ASLs) (**Figure 4.3**).

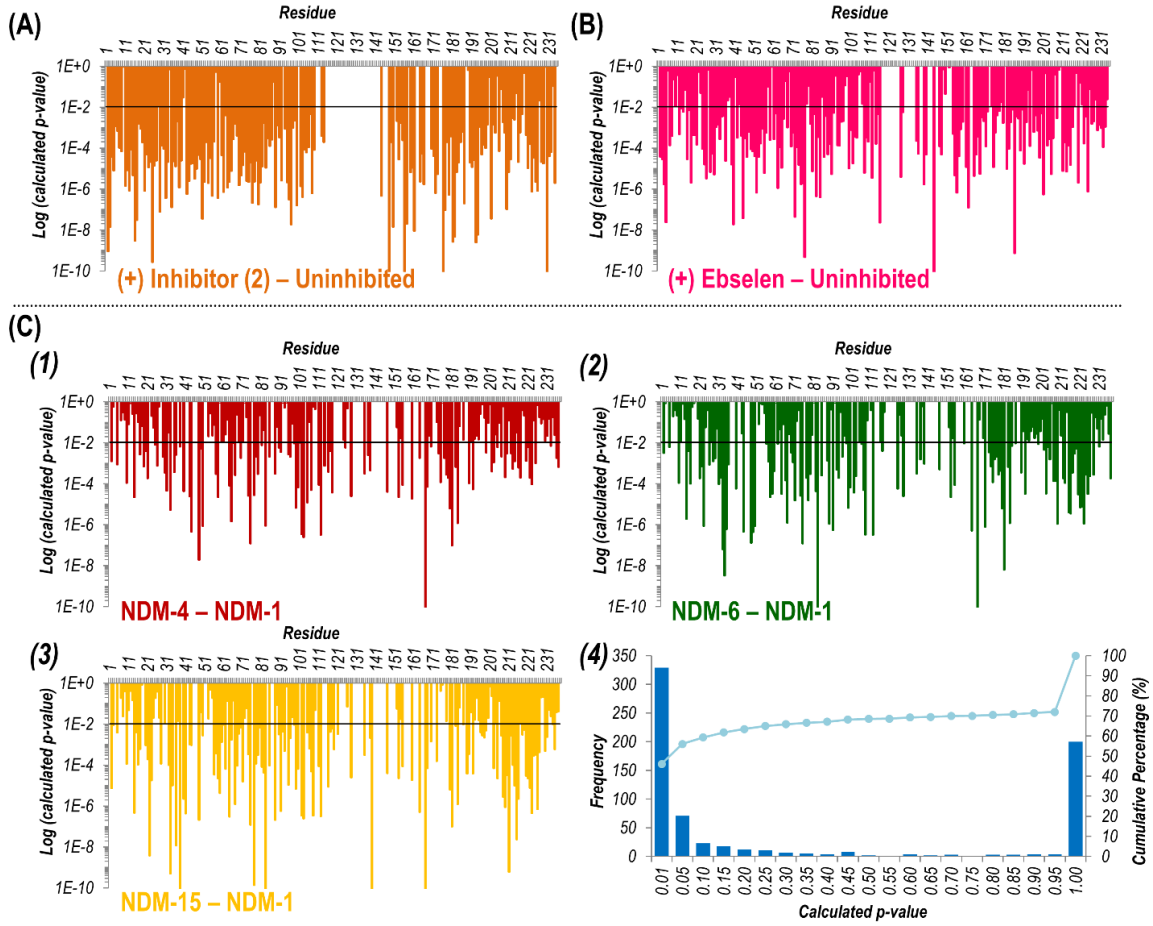

Figure 4.2: Log of *p*-values plotted per residue calculated from the differences for (A) NDM-1 bound to inhibitor (**2**) (Figure 4.13), (B) ebselen-bound NDM-1 (Figure 4.20), and (C) clinical variants of NDM (Figure 4.25). Student's *t*-test was used with pooled standard deviations to compare differences in UVPD backbone cleavage efficiencies of each inhibitor-bound protein (A, B) or clinical variant (1-3) to unreacted NDM or the reference NDM-1 sequence. Calculated *t*-values were converted to *p*-values assuming a two-tailed hypothesis. At a given residue for the inhibitor-bound or variant NDM, a *p*-value smaller than 0.01 (assuming a 99% confidence threshold represented as a black solid line) designates that the average of the triplicate measurement of UVPD intensity is statistically different from the corresponding measured average of unreacted NDM or NDM-1. (C) A histogram of calculated *p*-values in (1-3) is shown in (4) with the cumulative percentage plotted.

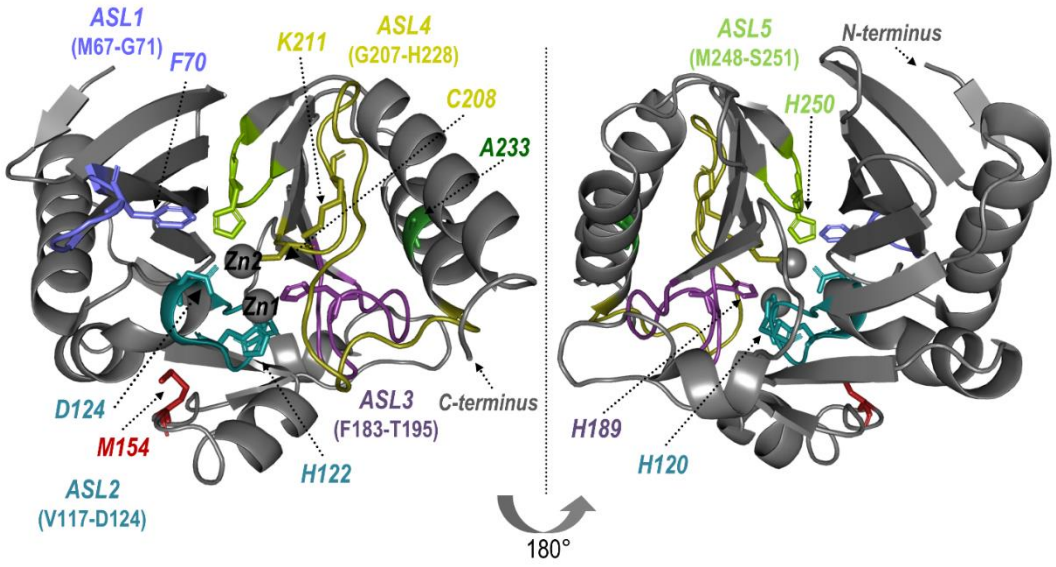

Figure 4.3: Crystal structure and 180° view of NDM-1 (PDB ID: 3SPU) with important loops and residues highlighted and labelled. The five active site loops (ASL) responsible for the broad substrate specificity of the protein are colored as follows: ASL1 (slate), ASL2 (turquoise), ASL3 (purple), ASL4 (olive), ASL5 (lime green). The six residues along these loops known to anchor two Zn(II) ions (shown as gray spheres) in the active site are labelled and shown as sticks (H120, H122, D124, H189, C208, H250). Located on ASL1 and shown as sticks, F70 is important for substrate binding and recognition. An important target for covalent inhibitors, K211 is shown as sticks along ASL4. The two residues mutated in the clinical variants used for this study are shown as sticks as well: M154 (red) and A233 (green).

4.4 Results and Discussion

4.4.1 Inhibitor Selection

We applied a native UVPD-MS approach to simultaneously detect changes in protein structure and zinc content upon inhibitor binding to NDM-1, using two distinct types of MBL covalent inhibitors as examples: lysine 211-modifying inhibitors that retain binding of both zinc ions, and a cysteine 208-modifying inhibitor that ejects one zinc from the active-site. The first Lys-modifying inhibitor, 3-mercaptopropionic acid pentafluorophenylester (**1**), contains a zinc-binding thiol group tethered to a reactive ester

and was previously shown to serve as an affinity label that covalently modifies the Lys244 in IMP-1 (K_I= 3.45 μM; k_{inact} = 4.6 min^{-1}), and retains both zinc ions at the active site after inhibition.[39] Because of the homology between IMP and NDM, we reasoned that **1** would also serve as an affinity label for Lys211 in NDM-1 (**Figure 4.4**). Due to an unexpected lack of selectivity for **1** (*vide infra*), we also investigated a second Lys-modifying affinity label, an *O*-aryloxycarbonyl hydroxamate (**2**), that we previously determined to modify Lys211 in NDM-1 (K_I = 140 μM; k_{inact} =0.045 min^{-1}) and to leave the dizinc active site intact (**Figure 4.4**).[41] For a Cys-modifying inhibitor, we chose a non-selective thiol-modifying reagent ebselen (**3**) that has been previously shown to covalently modify the sole Cys in soluble NDM-1 constructs (Cys208) as an affinity label (K_I = 0.38 μM; k_{inact} =0.034 min^{-1}), and to eject one equivalent of zinc from the dinuclear zinc cluster (**Figure 4.4**).[42]

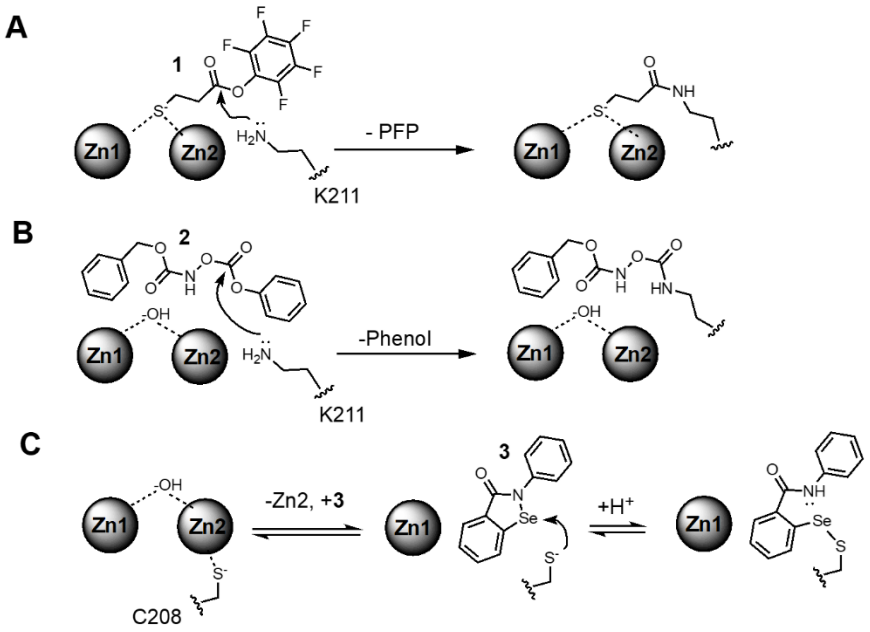

Figure 4.4: Proposed covalent NDM-1 inactivation mechanisms: (A) A reactive pentafluorophenol (PFP) ester (**1**) is bound in proximity to active-site K211 to facilitate reaction and loss of pentafluorophenol (PFP). (B) A reactive *O*-aryloxycarbonyl hydroxamate (**2**) is bound in proximity to active-site K211 to facilitate reaction. (C) Because the C208 thiol is not solvent accessible in the dinuclear zinc form of NDM-1, and Zn2 is bound relatively weakly,[3] a dynamic equilibrium is depicted between dizinc and monozinc metalloforms, enabling binding of the thiol-reactive ebselen (**3**) in proximity to Cys208 to facilitate reaction and loss of Zn2 affinity.

4.4.2 UVPD-MS to Localize a Lysine-Selective Covalent Inhibitor of NDM-1

We found that a Lys-targeted pentafluorophenyl ester affinity label reported for IMP-1 (**1**) can also readily inactivate the homologous NDM-1 enzyme in a manner that is irreversible to dilution into excess substrate (**Figure 4.5**). A full kinetic characterization was not completed owing to unexpected lack of selectivity noted below. ESI-MS data were collected for denaturing and non-denaturing (high ionic strength) solutions containing NDM-1 without or with inhibitor **1** (**Figure 4.6**, inhibitor:protein ratios 1:1, 5:1, 100:1). Even at a 1:1 inhibitor:protein ratio, up to two inhibitors were observed to bind covalently

to NDM-1 with up to three inhibitors per protein for solutions containing higher inhibitor:protein ratios. This outcome indicates that inhibitor **1** is less specific for one particular Lys in NDM-1 as compared to IMP-1.[39] Similar results were observed for spectra collected after various incubation time-points. Using non-denaturing ESI conditions yields similar results with addition of up to three inhibitor molecules to NDM-1 and also confirms that neither of the active site Zn(II) ions are displaced due to the reaction (**Figure 4.6B**).

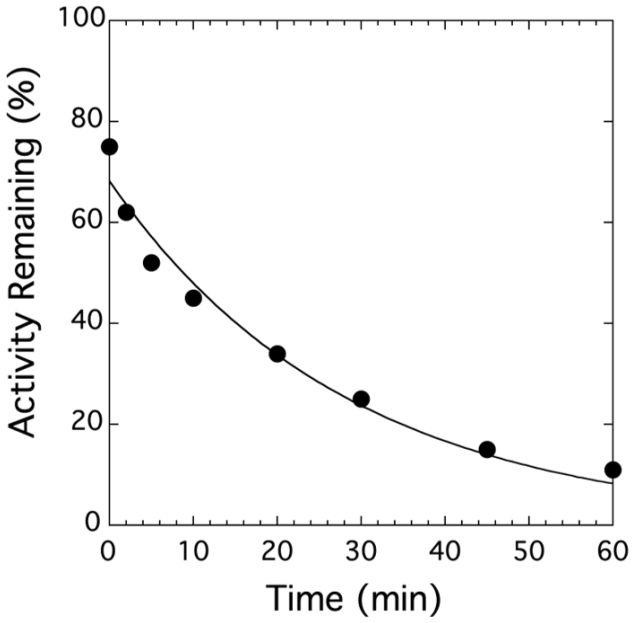

Figure 4.5: Time-dependent Inactivation of NDM-1 by **1**. Purified NDM-1 (0.5 μM) was incubated with inhibitor (**1**) (10 μM) in the presence of $ZnSO_4$ (10 μM), HEPES (50 mM), DMSO (1% v/v) at pH 7.0, 25 °C. At various timepoints, aliquots were diluted 25-fold into a reaction mixture containing chromacef (20 μM), $ZnSO_4$ (10 μM), and HEPES (50 mM) at pH 7.0, 25 °C, and the activity monitored by UV-vis as described previously.[1] Values for activity remaining were calculated as a percent of the uninhibited activity at each timepoint determined using a parallel incubation in which inhibitor was omitted (but 1% DMSO cosolvent included for consistency). The fit shown is to a single exponential decay to yield k_{obs} 0.035 ± 0.003 min^{-1} for this concentration of (**1**).

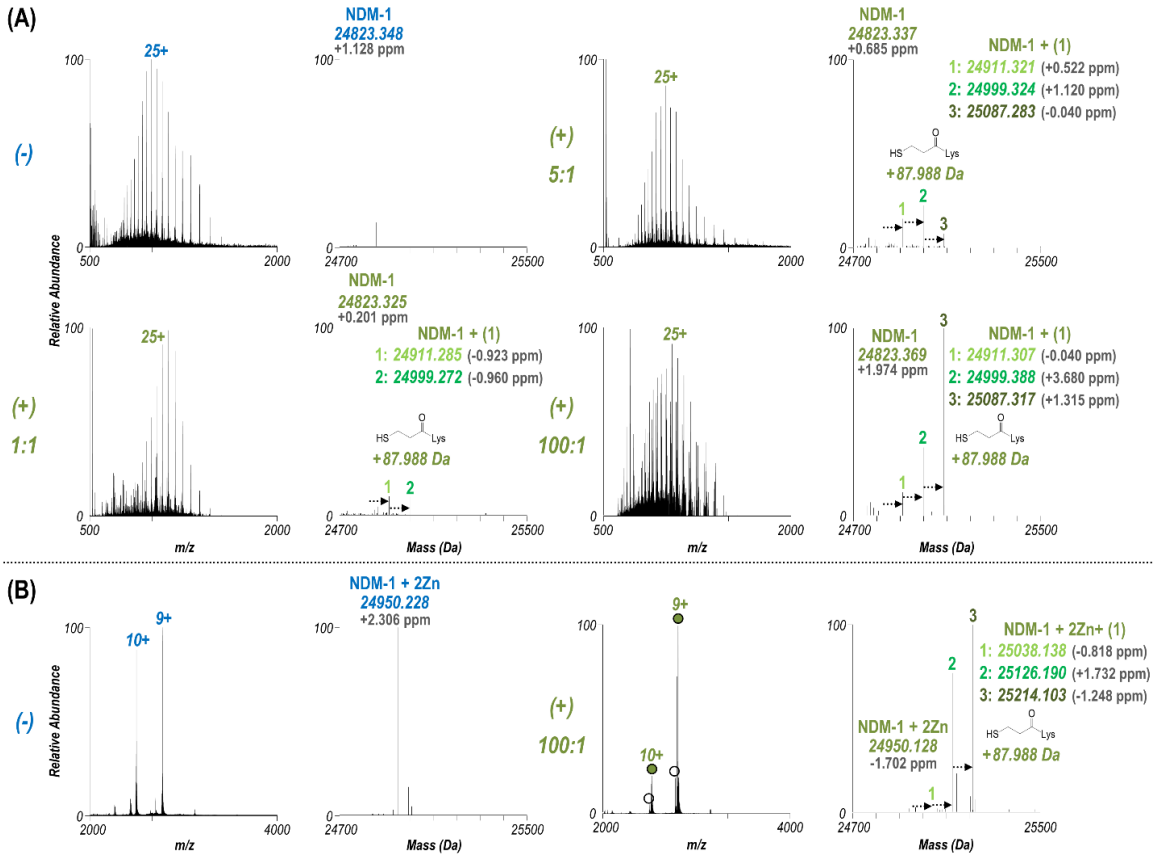

Figure 4.6: ESI mass spectra of (-) NDM-1 and (+) NDM-1 reacted with inhibitor (**1**) at various inhibitor:protein ratios (1:1, 5:1, 100:1) sprayed under (A) denaturing or (B) native conditions. Deconvolution reveals that up to three inhibitors can bind to NDM-1 and, under native conditions, attachment of the inhibitor does not displace the Zn(II) ions. Open circles in (B) denote uninhibited NDM-1 in the reacted sample. Reported mass accuracies (ppm) account for mass shifts due to the covalent inhibitor or Zn(II) cofactors.

To localize the reaction sites of inhibitor **1**, the 25+ charge states of the singly, doubly, and triply modified NDM-1 were individually isolated and characterized using HCD and UVPD (**Figure 4.7**). As opposed to the diverse array of sequence ions produced by UVPD, HCD results in a relatively small number of *b/y* ions dominated by preferential Pro cleavages (*e.g.*, y_{100} and b_{114}). Maps of the backbone cleavage sites corresponding to the observed fragment ions shown in **Figure 4.8** highlight the higher sequence coverage

afforded by UVPD (74-84%) compared to HCD (16-26%). The mass shifts of the y_{100}^{11+} ions observed for both HCD and UVPD in **Figure 4.7** corresponds to addition of one, two, or three equivalents of **1**. In this context, the specific positions of the each adduct can be determined by accounting for the mass shift(s) at each of the eight possible Lys residues of NDM-1. Covalent attachment of inhibitor **1** through disulfide bridging of the thiol end (opposite the expected reactive moiety) to C208 was considered but the retention of both Zn(II) ions (**Figure 4.6B**) after modification as well as the similar HCD and UVPD fragmentation patterns observed even after addition of a reducing agent provide strong evidence against this possibility. Both HCD and UVPD methods indicate that the modification sites are all located along the same loop that borders the active-site (ASL4: G207-H228). Localization of binding sites is summarized in **Figure 4.9** for NDM-1 containing one, two, or three equivalents of inhibitor **1**. Briefly, for the singly-bound species, the UVPD data indicates that reaction occurs at either K211 (expected site) or K214. When two equivalents of **1** are bound, UVPD confidently localizes them to K211 and K214. The UVPD results indicate that the third equivalent is added at K216. There is no evidence for covalent modification by **1** at K125 (buried), or at other solvent accessible Lys residues (K106, K181, K242, K268). The only Lys residues that are modified are contained within a single loop consisting of residues 209-224 that neighbor the active site (ASL4), and none of the other Lys residues are targeted. In comparison, the homologous loop in IMP-1 is considerably shorter and lacks the two Lys residues in NDM-1 that account for additional modifications. Therefore, sequence differences likely underlie the apparent difference in Lys modification selectivity between IMP-1 and NDM-1.

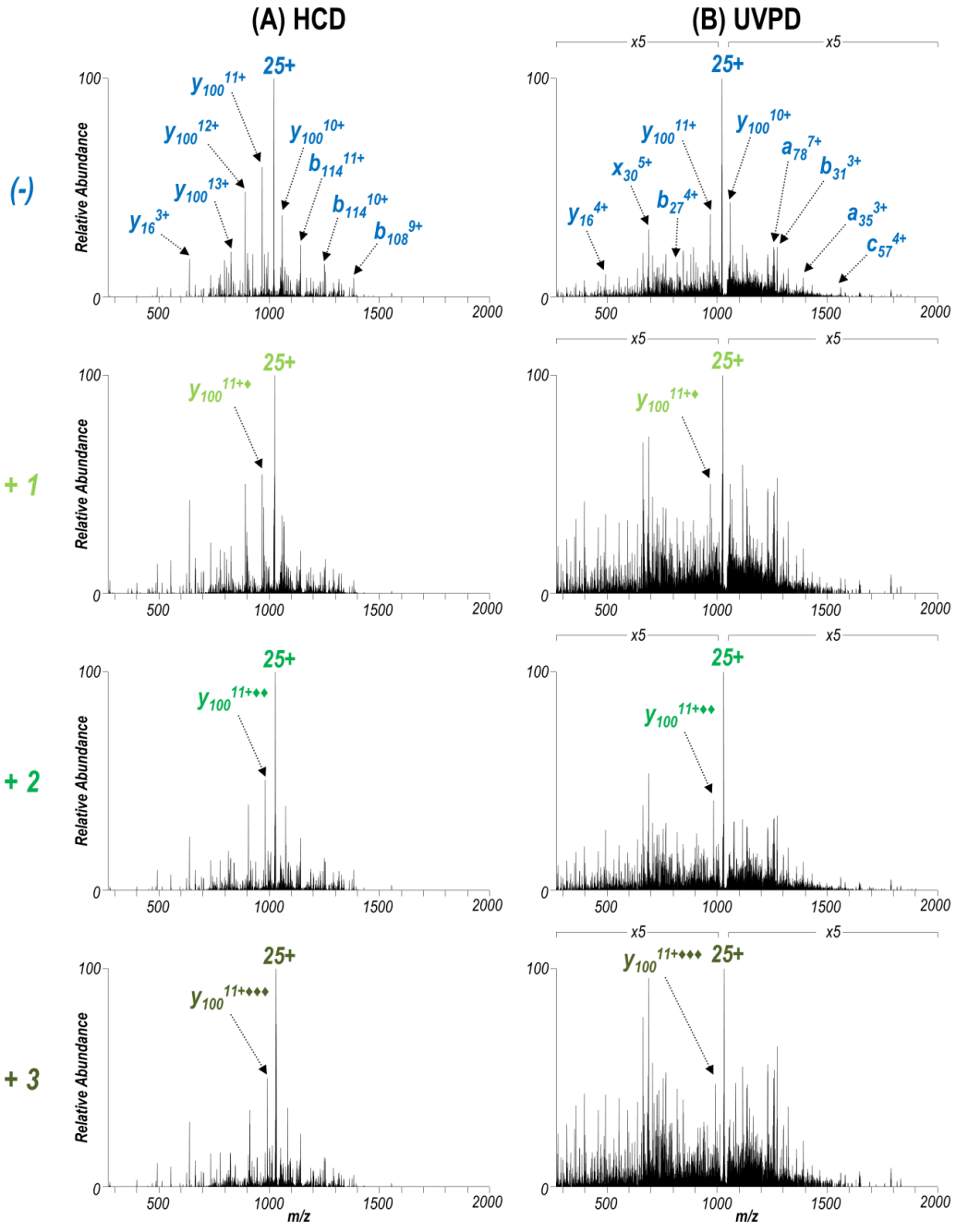

Figure 4.7: (A) HCD and (B) UVPD MS/MS spectra resulting from activation of the 25+ charge state of (-) NDM-1 or (+) NDM-1 covalently bound to one, two, or three of inhibitor (**1**). Abundant fragment ions are labelled for the uninhibited sample. Mass shifts of +88 Da in one of the most abundant fragment ions (y_{100}^{11+}) in both the HCD and UVPD spectra due to sequential addition of inhibitor (**1**) can be observed and is denoted by ♦.

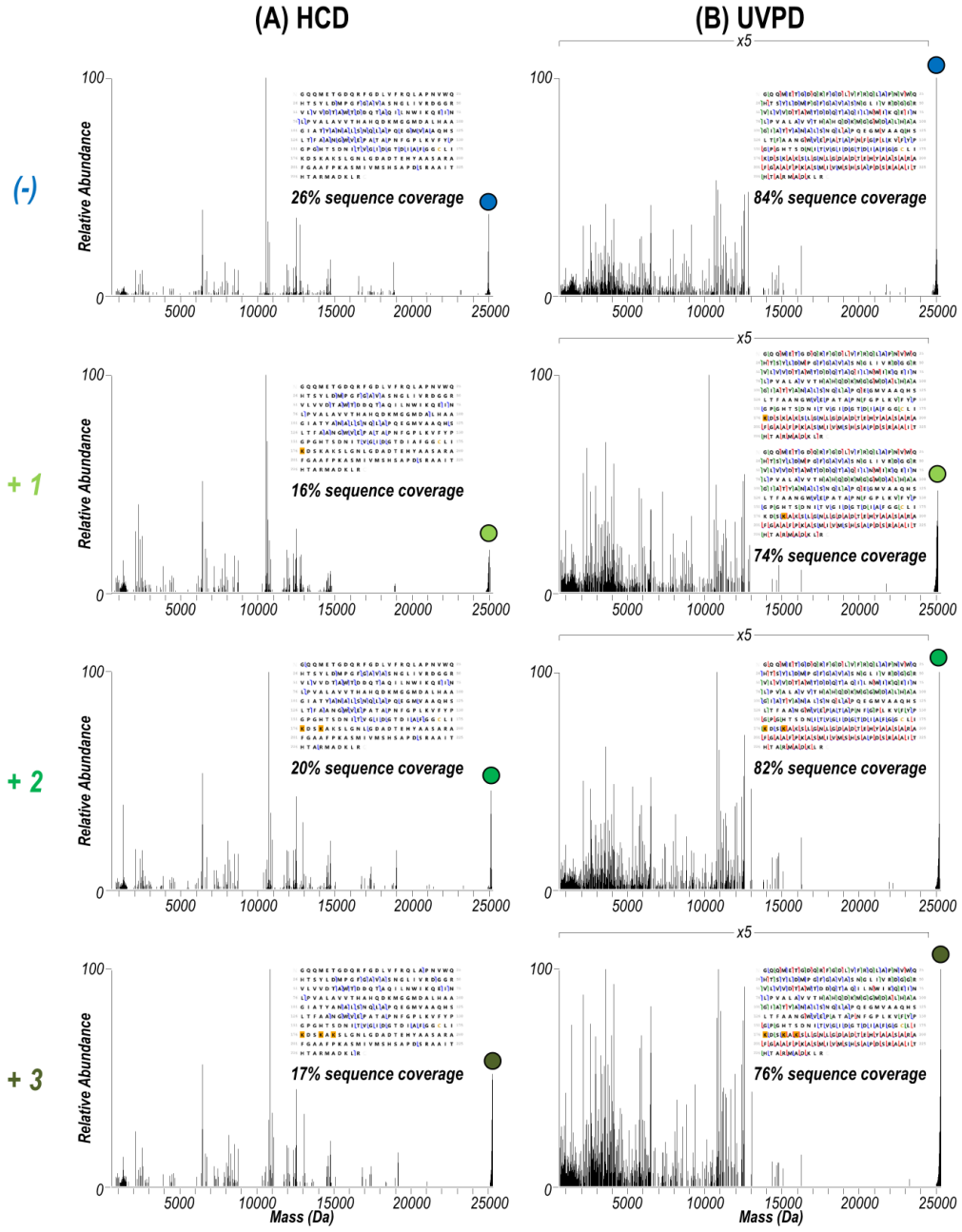

Figure 4.8: Deconvoluted (A) HCD and (B) UVPD spectra produced by activation of (-) NDM-1 or (+) NDM-1 covalently bound to one, two, or three of inhibitor (**1**). The corresponding MS/MS spectra are shown in Figure 4.7. Surviving precursor is labelled with a filled circle. Sequence coverage maps of identified fragment ions are shown with corresponding sequence coverage values. Static modifications of +88 Da were added to highlighted Lys residues. UVPD allowed complete localization of up to three inhibitor (**1**).

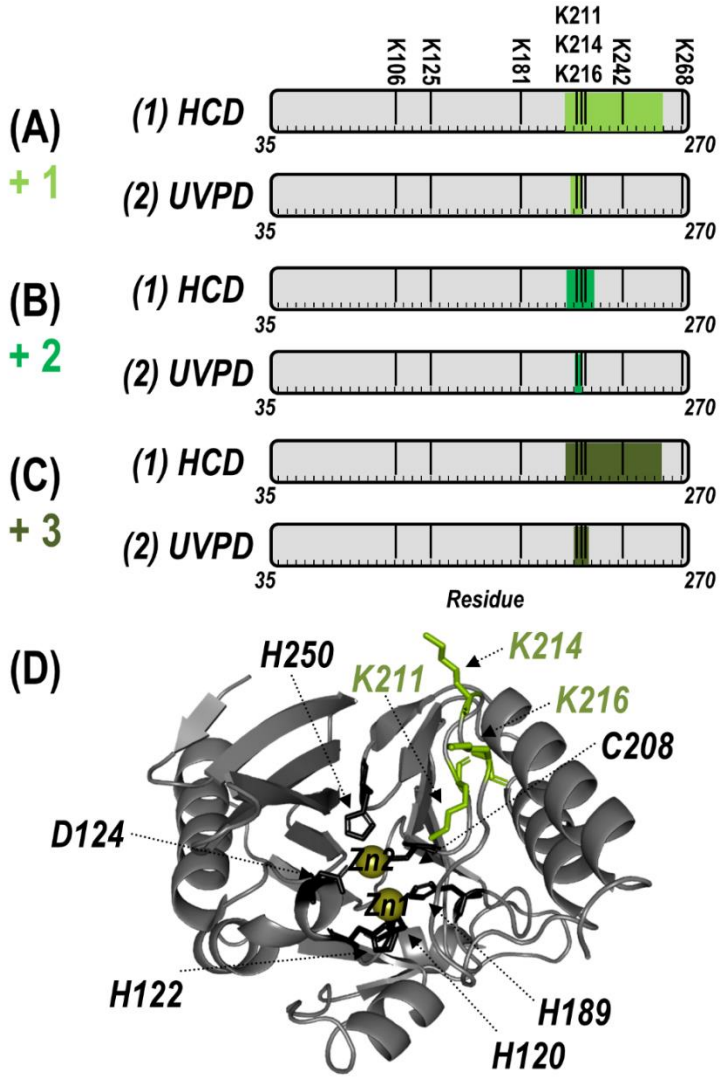

Figure 4.9: Summary of the localization of (A) one, (B) two, or (C) three inhibitor (**1**) moieties (with loss of pentafluorophenol) covalently attached to Lys residues of NDM-1 by using (1) HCD and (2) UVPD. Green shaded regions indicate localization according to the MS/MS spectra in Figure 4.7 and corresponding sequence coverage maps of identified fragment ions in Figure 4.8. The eight possible Lys sites are labelled above the gray residue bar in (A). (D) Sites at which the inhibitor was localized (K211, K214, K216) are labelled and shown as green sticks on the crystal structure of NDM-1 (PDB ID: 3SPU). The six Zn(II) binding residues are also labelled and shown as black sticks.

4.4.3 Tracking Closure of an Active Site Loop over a Lysine-Modifying Covalent NDM-1 Inhibitor

To characterize conformational changes resulting from a more well-defined binding event, we substituted a different affinity label, an *O*-aryloxycarbonyl hydroxamate (**2**), that selectively modifies Lys211 in NDM-1 (although minor amounts of an undefined secondary modification site were reported when excess **2** was used for labeling).[41] In a previous study both X-ray crystallography and MS were used to confirm covalent modification of K211, but the positioning of the substrate-binding beta-hairpin loop was perturbed artifactually by interaction with a second monomer found in the crystal lattice, and by non-enzymatic degradation of the adduct during crystallization.[41] Here, we used native ESI-MS to better characterize structural changes that occur upon incubation of **2** with NDM-1. Even with treatment of excess **2**, only one equivalent of expected adduct was detected on NDM-1 (**Figure 4.10**), with retention of both zinc ions after modification. The degraded adduct (a carbamoylated K211) observed earlier by X-ray crystallography was not observed under these conditions.

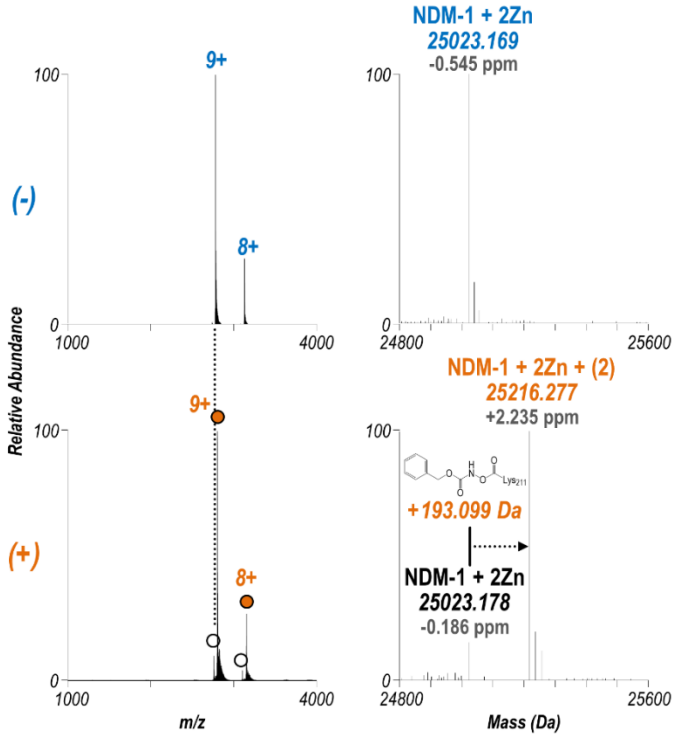

Figure 4.10: Native ESI mass spectra of (-) NDM-1 and (+) NDM-1 reacted with inhibitor (**2**) with observed charge states labelled (8+, 9+). Unreacted NDM was observed in the reacted sample (open circles). The right panel shows the corresponding deconvoluted spectra. Both Zn(II) cofactors were retained after covalent attachment of inhibitor (**2**). Mass shifts for the inhibitor and Zn(II) cofactors are accounted for when calculating accuracies (ppm).

We then used UVPD-MS to characterize the structural impact on NDM-1 caused by inhibition with **2** via changes in observed fragmentation. Specifically, we have consistently found that regions of a protein that exhibit increased flexibility and/or fewer stabilizing interactions frequently result in enhanced fragmentation and thus yield more abundant sequence ions. In contrast, engagement of a region in stabilizing noncovalent interactions may prevent separation of fragment ions, thus hindering their detection and leading to an apparent suppression in the backbone cleavages.[31] UVPD of the 9+ charge state yielded a wide array of sequence ions, including those retaining both the covalently-

bound inhibitor and one or two non-covalently bound Zn(II) ions (**Figure 4.11**). The binding site of the inhibitor was localized to the expected residue, K211 (**Figure 4.11B**, **4.11C**), based on backbone cleavages that confidently bracketed the mass shift of the inhibitor. Summation of all the fragment ions arising from backbone cleavages as described in the Experimental section yielded the graphical displays shown in **Figure 4.12** for unmodified NDM-1 and the inhibitor **2**:NDM-1 complex. A plot of calculated *p*-values per residue in **Figure 4.2A** assigns statistical significance to observed differences from *t*-test calculations. Conversion of the two displays to a difference plot in **Figure 4.13A** or as a heatmap in **Figure 4.13B** facilitates visualization of the variations in fragmentation of NDM-1 after reaction with this affinity label.

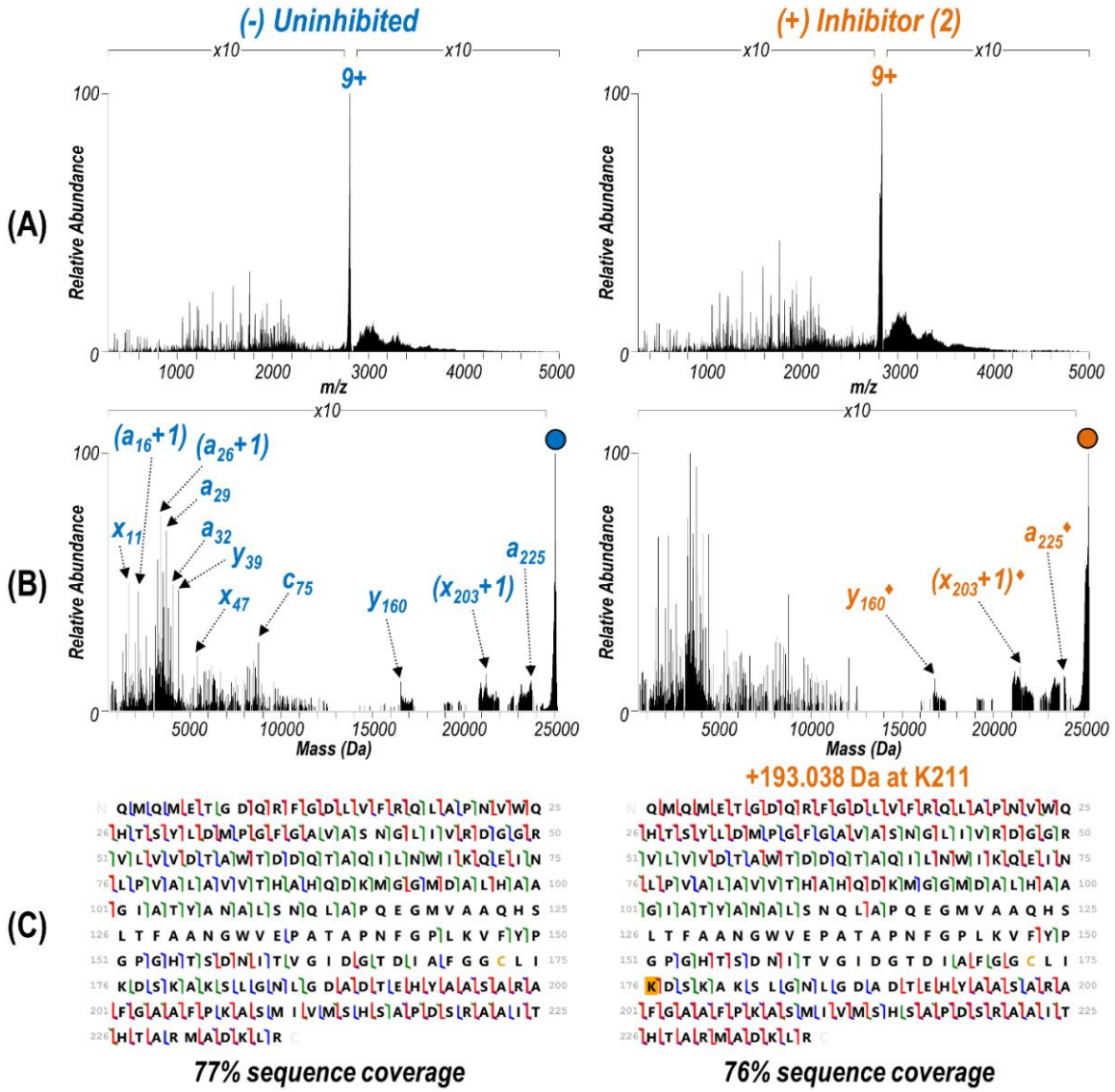

Figure 4.11: (A) UVPD MS/MS spectra of the 9+ charge state of (-) NDM-1 and (+) NDM-1 bound covalently to inhibitor (**2**). Corresponding deconvoluted UVPD spectra are shown in (B) with the precursor identified by a filled circle. Several abundant fragment ions are labelled in which the ♦ denotes a mass shift corresponding to inhibitor (**2**). (C) Apo and holo (Zn-bound) fragment ions produced by UVPD are mapped along the protein sequence. A +193 Da static modification at K211 (highlighted yellow) was considered to localize covalent attachment of the inhibitor.

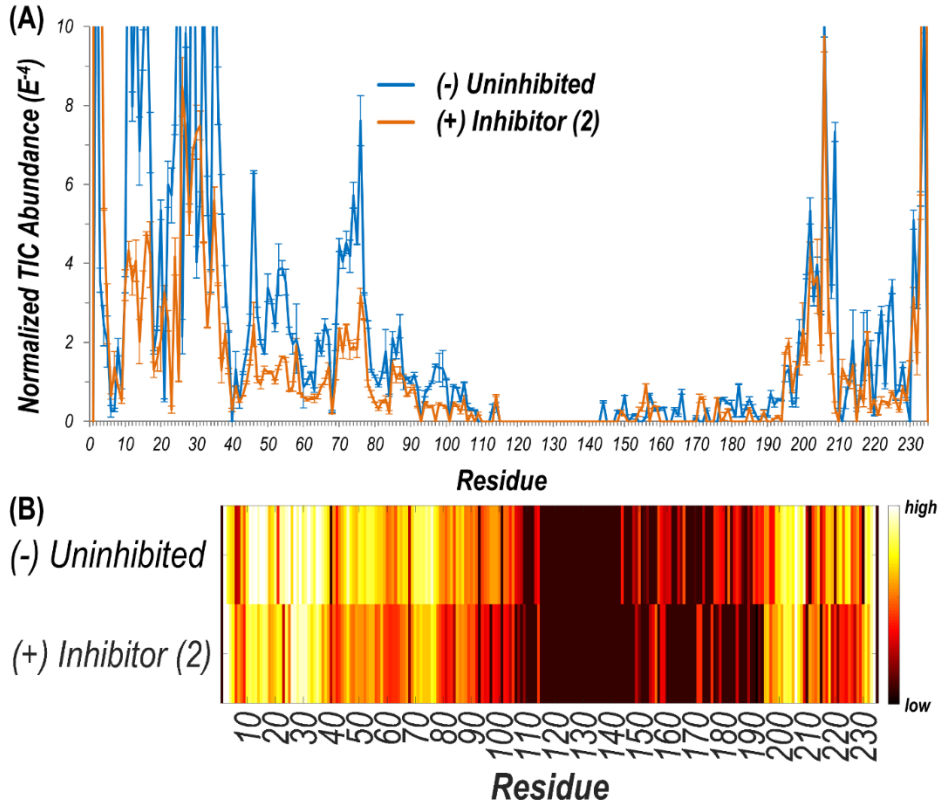

Figure 4.12: (A) Intensities (summed and normalized to the TIC) of identified UVPD fragment ions plotted per residue for uninhibited NDM-1 (blue) and NDM-1 bound to inhibitor (**2**) (orange). Subtracting the values for uninhibited NDM-1 from the corresponding values for inhibitor-bound NDM-1 yields the difference plot in Figure 4.13. (B) Heatmap representing the log of the values in (A) shown along the linear protein sequence.

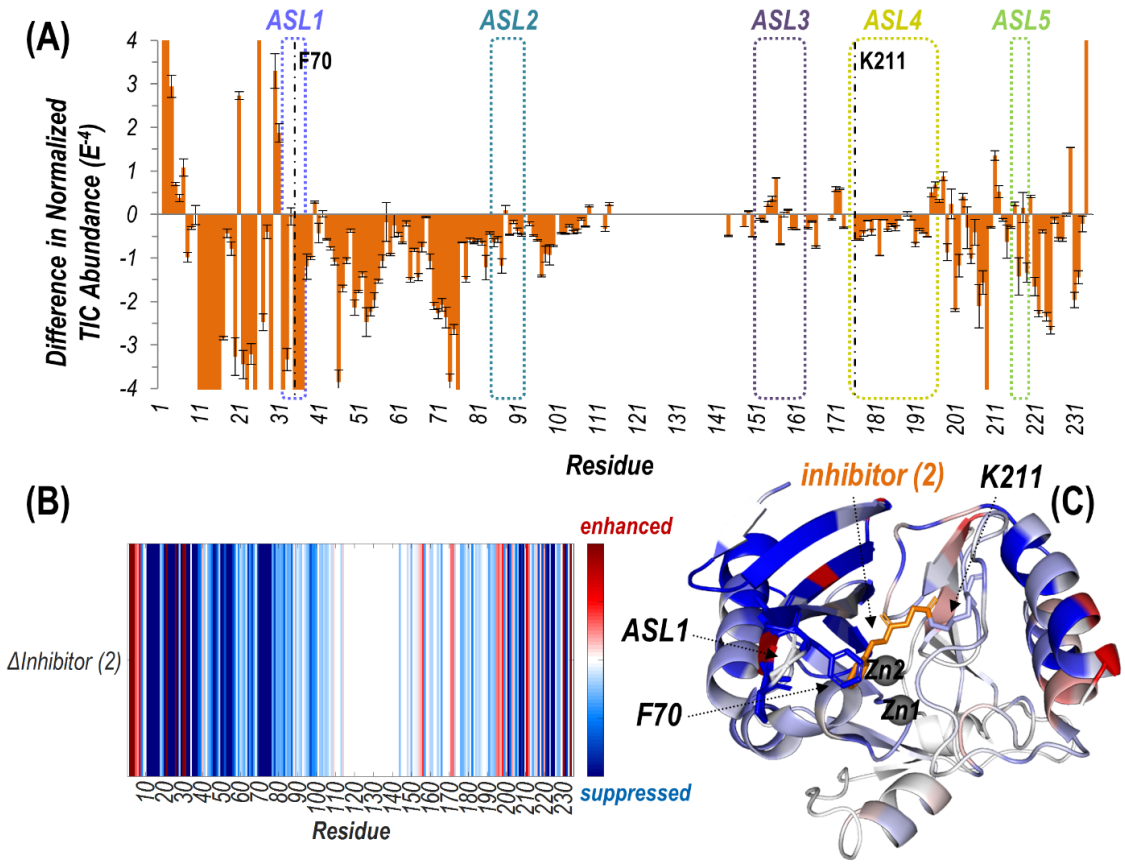

Figure 4.13: (A) Difference plot showing the change in summed abundances of Zn(II) bound holo and apo fragment ions produced upon UVPD of NDM-1 covalently bound to inhibitor (**2**) (with loss of phenol) compared to uninhibited NDM-1. The UVPD fragmentation plots for both samples are shown in Figure 4.12. The five active site loops are outlined with dotted lines while the residue at which the inhibitor attaches (Lys211) is denoted with a dashed line. Heatmaps of these differences are represented (B) linearly along the protein sequence or (C) mapped on the crystal structure of NDM-1 bound to inhibitor (2) (PDB ID: 6OVZ). Red regions correspond to enhancement of backbone cleavage efficiency for the inhibitor bound sample compared to the uninhibited while blue regions indicate suppression. Active site loop 1 (including F70), Lys211, and inhibitor (2) are displayed as sticks, while the Zn(II) ions are shown as spheres in (C).

Suppression of backbone fragmentation (colored blue in the heatmap) is observed throughout large stretches of the protein for inhibitor-bound NDM-1, particularly

encompassing the N-terminal half of the protein that includes two of the active site loops (ASL1: M67-G71 and ASL2: V117-D124) as well as the three other active site loops in the C-terminal region (**Figure 4.13**). ASL3 (F183-T195) and ASL5 (M248-S251) are short loops that form a deep cavity in which the two Zn(II) ions reside. ASL4 (G207-H228) is significantly longer and creates the floor, while ASL2 acts as the ceiling. Notably, ASL1 is the beta-hairpin loop proposed to play an important role in substrate binding (**Figure 4.3**). The suppression of fragmentation indicates a general loss of flexibility in all five active site loops that frame the active site. This observation is consistent with other studies that show a general increase in overall thermostability of NDM-1 upon binding inhibitors.[45] More specifically, our use of native UVPD-MS reveals that fragmentation of the backbone spanning the ASL1 region shows the greatest suppression, specifically bracketing the residue F70, which is positioned at the apex of this substrate-binding beta-hairpin loop (**Figure 4.13**). This observation is a clear indication that the beta-hairpin loop neighboring the active site NDM-1 closes and rigidifies over the bound ligand. The use of UVPD-MS avoids several artifacts in the crystallography of ligand:NDM-1 complexes: commonly observed ASL1 intertwining between neighboring monomers in the crystal lattice and degradation of the covalent adduct made by **2**. Additionally, this MS approach avoids the requirement to covalently install reporter labels in the beta-hairpin loop that could perturb function, and clearly favors a loop closing event upon inhibitor binding. Our result is more consistent with prior ^{19}F NMR results indicating loop closure upon ligand binding and implies that the loop opening previously suggested by RFQ-DEER studies may instead be due to perturbation by the spin label or loop twisting resulting in an apparent distance increase.[13,14]

4.4.4 Detecting Displacement of Zn2 by a Cysteine-Modifying Covalent NDM-1 Inhibitor

Determining the impact of inhibitors on the metalation state of NDM-1 is an important yet often overlooked aspect of developing inhibitors suitable for therapeutic use.[4] Compounds that inhibit by stripping both metal ions from the dinuclear zinc NDM-1 and sequestering them as small molecule complexes are likely to have significant off-target effects making them less suitable as potential therapeutics. Native MS has previously been used to detect changes in the metalation state of NDM-1 upon inhibitor binding.[42,45] Here we apply UVPD-MS and an established Zn2 ejector to more extensively elucidate structural changes that occur throughout the NDM-1 protein upon inhibitor binding.

The non-selective thiol reagent ebselen (**3**) has been examined as a ligand for a wide variety of cysteine-containing proteins by using mass spectrometry.[46] In particular, ebselen is a potent inhibitor of NDM-1 that functions by covalently modifying the sole Cys residue found in soluble NDM-1 constructs (Cys208).[42] Cys208 is a direct ligand to Zn2 (coordinated by D124, C208, H250) and treatment with ebselen (**3**) induces the loss of one zinc ion, previously presumed to be Zn2, from NDM-1 as detected by native MS. Based on using denaturing conditions for initial collection of ESI mass spectra in the present study, we confirmed addition of one ebselen equivalent to NDM-1 (**Figure 4.14A**). Using non-denaturing conditions, a narrow envelope of low charge states (8+ – 11+) is observed for uninhibited NDM-1 with the retention of two Zn(II) ions (**Figure 4.14B**). After reaction with ebselen, NDM-1 yields a much wider distribution of charge states (8+ – 18+) and the net mass shift corresponds to the attachment of a single ebselen along with the loss of one Zn(II) ion (**Figure 4.14B**). These results confirm removal of a metal cofactor after modification by ebselen, and also indicate unfolding of a portion of the NDM-1 protein as evidenced by the extended tail of the charge state distribution.

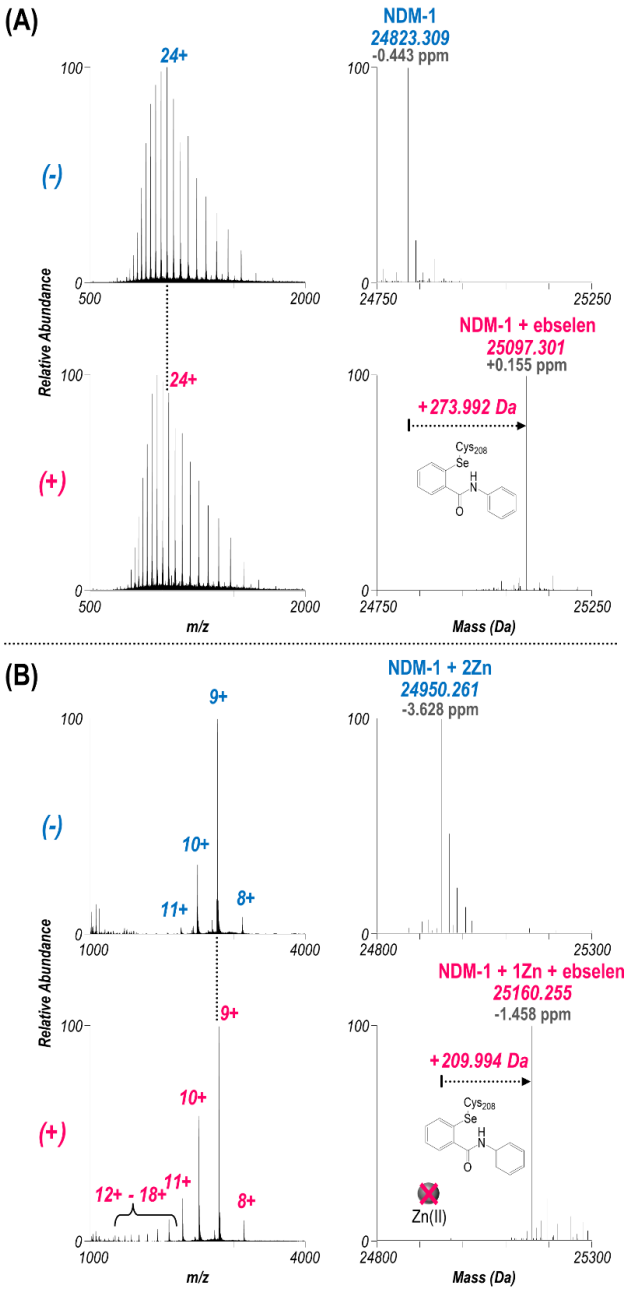

Figure 4.14: ESI mass spectra sprayed under (A) denaturing and (B) native conditions of (-) NDM-1 and (+) NDM-1 reacted with ebselen. The charge states observed in (B) are labelled (uninhibited: 8+ – 11+; reacted: 8+ – 18+). Corresponding deconvoluted spectra are shown to the right. Addition of ebselen causes loss of one of the Zn(II) ions as evidenced in (B). Accuracies (ppm) are calculated accounting for mass shifts due to covalent attachment of the inhibitor or non-covalent retention of metal cofactors.

UVPD of the most abundant charge state (24+ for denaturing conditions; 9+ for non-denaturing conditions) allows the structure of the modified protein to be characterized in more detail. High sequence coverages were obtained for the protein in both the high (denatured) and low (non-denaturing) charge states (78% and 79%, respectively) and allowed confident localization of the inhibitor adduct to Cys208 based on bracketing the mass shift via backbone cleavages (**Figure 4.15** and **Figure 4.16**). Under non-denaturing conditions, zinc-bound holo fragment ions are observed in addition to apo (zinc-free) fragment ions (**Figure 4.16B**). Owing to the high energy deposited during UV photoactivation, backbone bonds are cleaved preferentially over the disruption of non-covalent interactions, resulting in production of holo (containing Zn) fragment ions as well as apo (without Zn) fragment ions that elucidate binding sites.[30,34–36,38] For uninhibited NDM-1, holo fragment ions can contain up to two zinc(II) ions, whereas the ebselen-modified protein only has one remaining Zn(II) that can be retained in fragment ions (in addition to the covalently-bound ebselen moiety). Zn-bound holo ions resulting from UVPD were mapped along the protein sequence and upon the crystal structure for uninhibited NDM-1 (**Figure 4.17**). Corresponding structures for inhibited NDM-1 in which holo ions containing one or two Zn(II) were considered separately are shown in **Figure 4.18**. Based on this analysis, it is evident that it is exclusively Zn2, and not Zn1, that is lost upon binding of ebselen to NDM-1. Specifically, Zn-bound holo fragment ions are no longer observed from backbone cleavages adjacent to the three residues responsible for coordinating Zn2 (D124, C208, H250). Also, N-terminal holo ions are only produced C-terminal to the first Zn1 binding residue (H120) and C-terminal holo ions N-terminal to H189 (**Figure 4.17**). This assessment of the appearance and disappearance of key Zn-containing fragment ions allows the identity of the lost Zn ion to be directly observed as Zn2.

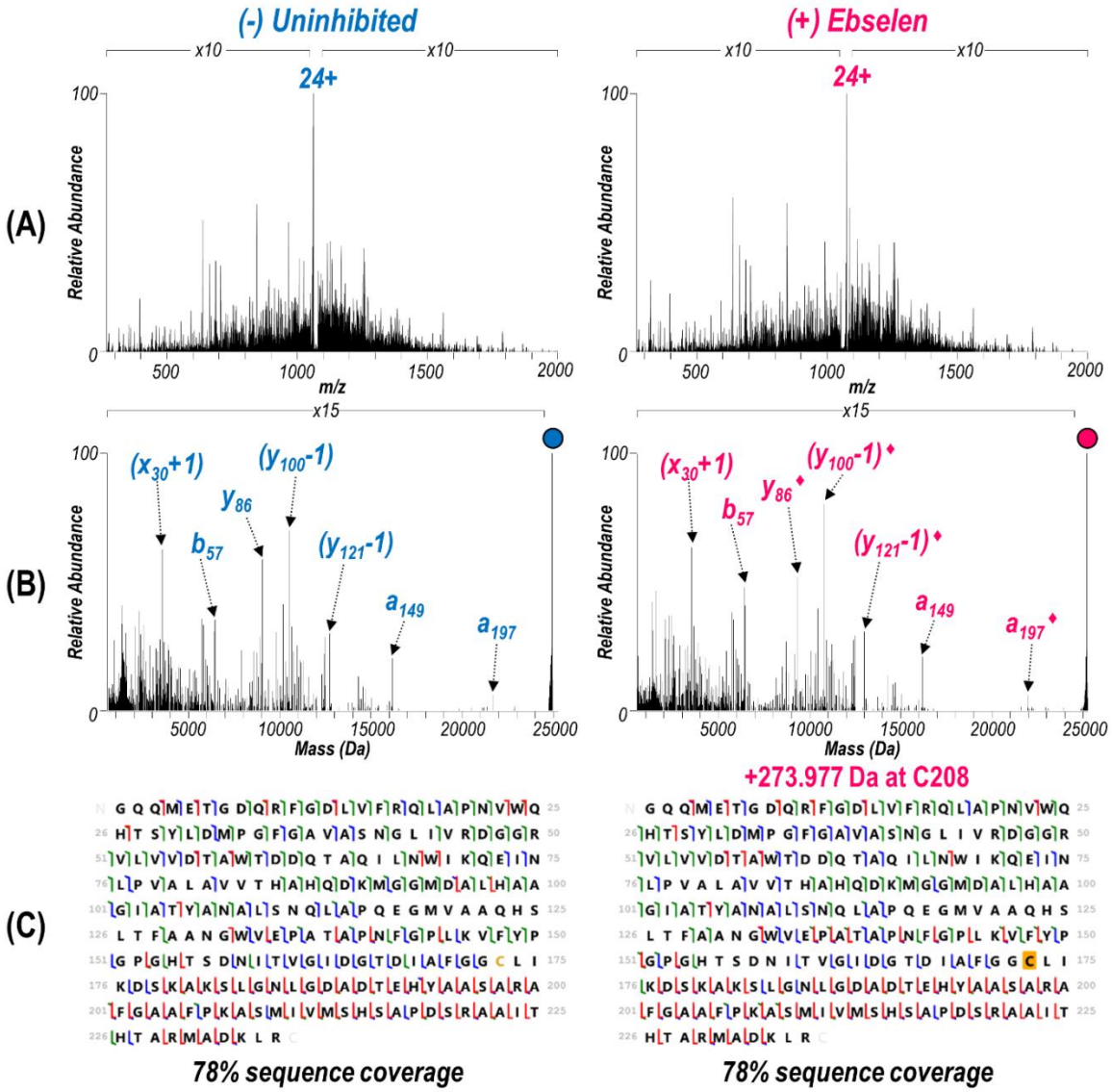

Figure 4.15: (A) UVPD MS/MS spectra collected while spraying under denaturing conditions of the 24+ charge state of (-) NDM-1 and (+) NDM-1 bound covalently to ebselen. The corresponding deconvoluted spectra are shown in (B) with the precursor identified with a filled circle and several abundant fragment ions labelled. Fragment ions labelled with a ♦ are mass shifted +273 Da and contain the inhibitor. (C) Sequence coverage maps of identified fragment ions resulting from UVPD. For the reacted sample, a static modification was added at the highlighted Cys (C208) allowing localization of the inhibitor to that residue.

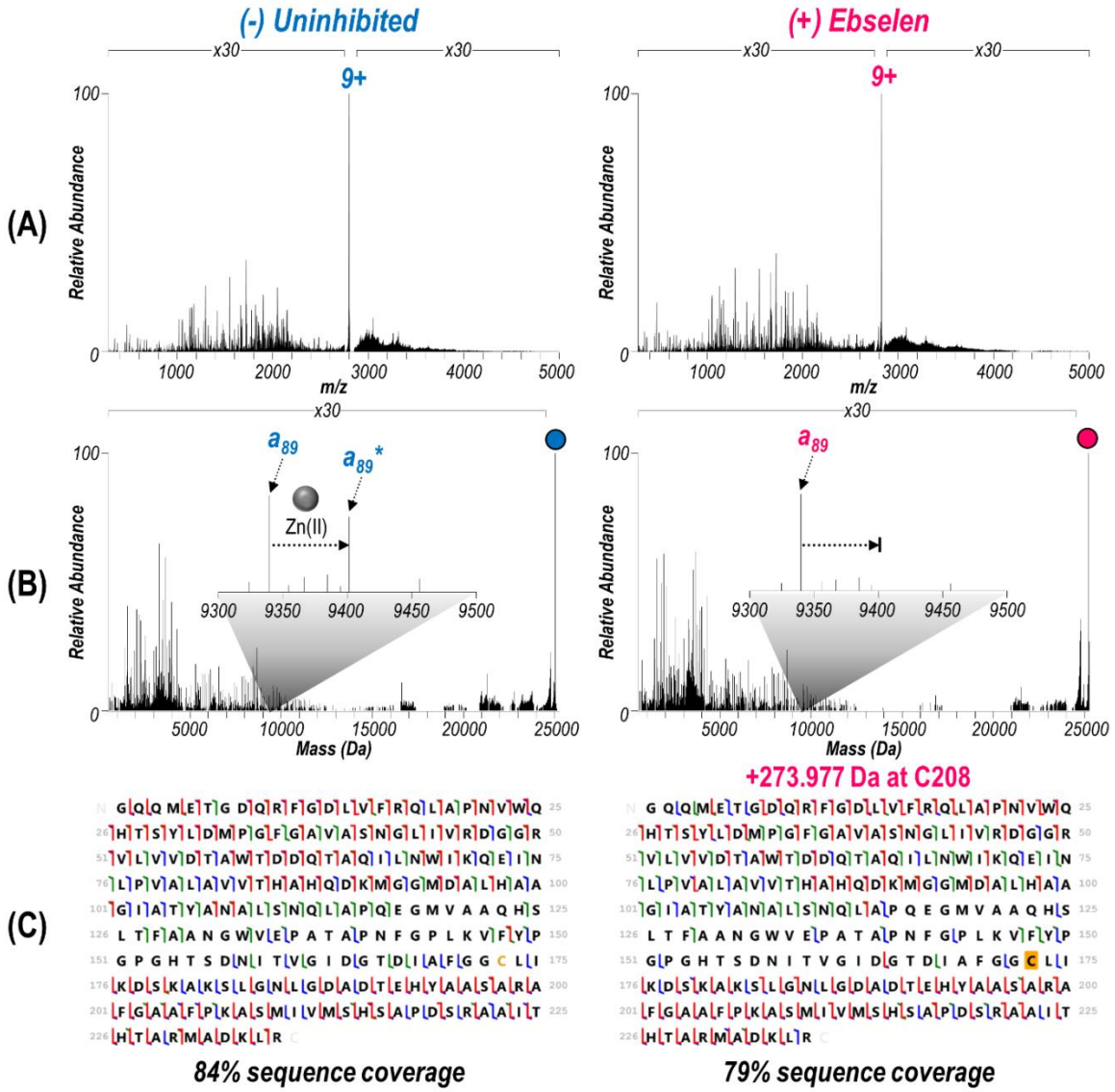

Figure 4.16: (A) MS/MS spectra produced by UV photoactivation of the 9+ charge state of (-) NDM-1 and (+) NDM-1 bound covalently to ebselen sprayed under native conditions. (B) Deconvoluted UVPD spectra corresponding to the MS/MS spectra in (A). The precursor is denoted by a filled circle. The inset (*m/z* 9300-9500) highlights a fragment ion observed in both the apo and holo (Zn-bound; indicated by an *) forms for the uninhibited sample but only in the apo form for the inhibitor bound species. (C) Sequence coverage maps accounting for identified apo and holo (Zn-bound) fragment ions resulting from UVPD. Searching with a +273 Da static modification at C208 (highlighted yellow) allows localization of the inhibitor to that residue.

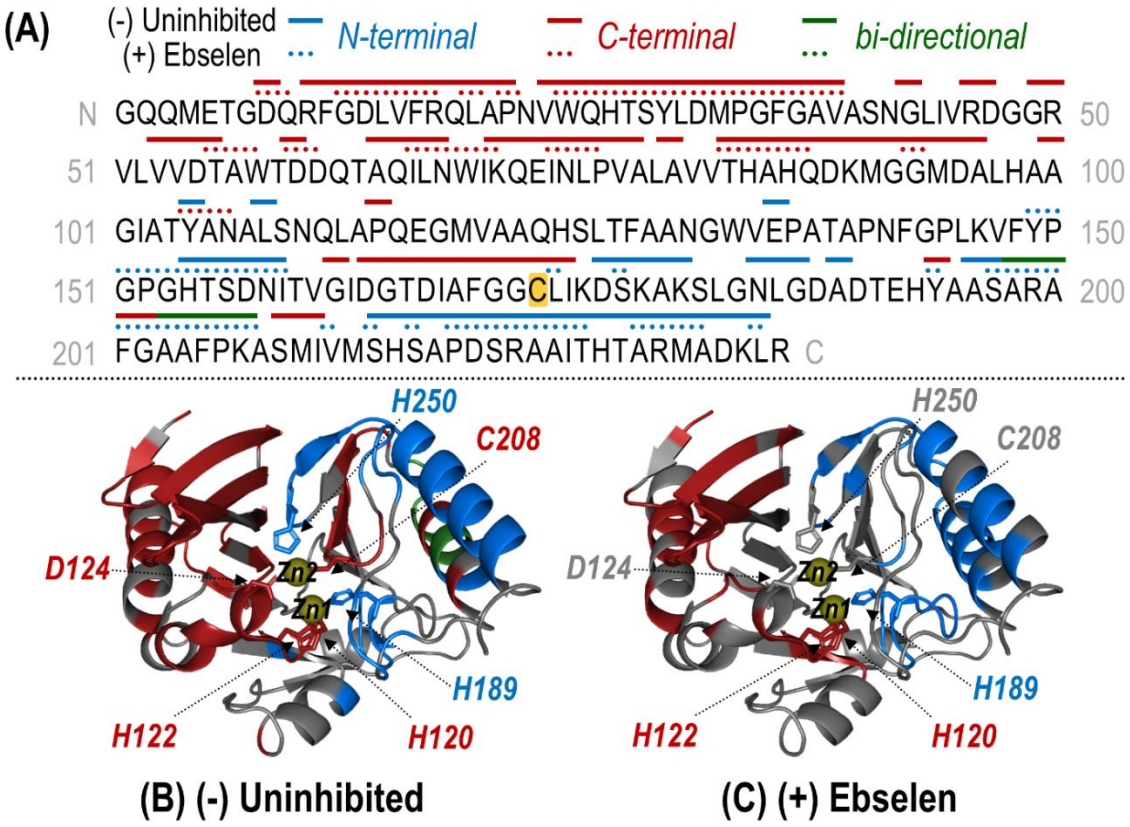

Figure 4.17: (A) Sequence of NDM-1 with Zn(II)-containing holo ions observed during UVPD of the uninhibited (solid line) and ebselen (**3**) reacted (dotted line) samples mapped above as linear segments. Coloring of the lines corresponds to N-terminal (blue), C-terminal (red), or bi-directional (green) Zn(II)-containing holo fragment ions identified from the UVPD spectra of the corresponding 9+ species shown in Figure 4.16. Complementary N- and C-terminal holo ions arising from the same backbone position indicate bi-directional fragmentation. For the uninhibited protein, one or two bound Zn(II) ions were considered while for the reacted protein, only holo ions containing a single Zn(II) were identified. The residue at which ebselen covalently attaches (Cys208) is highlighted in yellow. This information is mapped along the crystal structure of NDM-1 (PDB ID: 3SPU) for the uninhibited (B) and (+) ebselen (C) proteins. Corresponding crystal structure maps for the uninhibited protein separately identifying singly and doubly Zn(II) bound holo ions are given in Figure 4.18. Zn(II) binding residues are shown as sticks and the two Zn(II) ions are represented as yellow spheres.

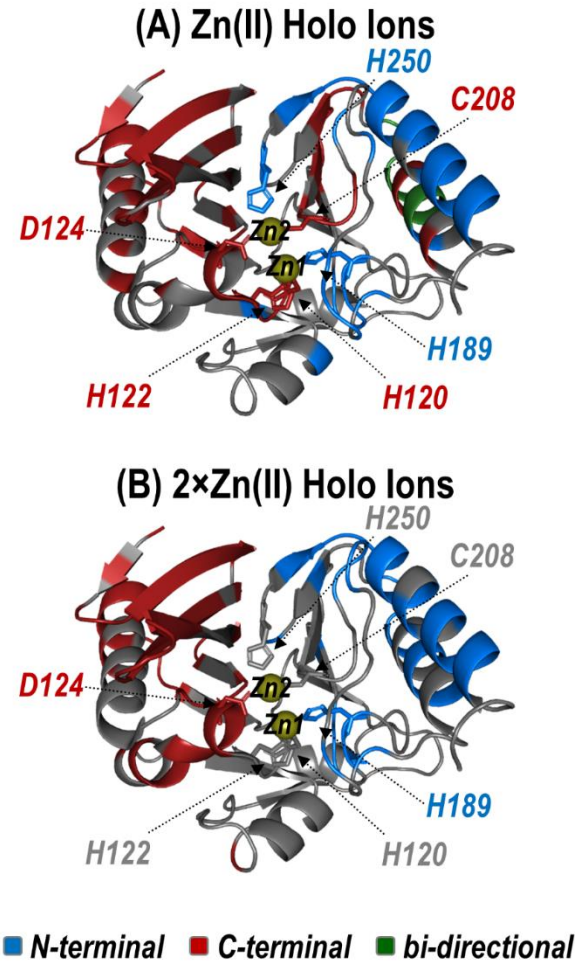

Figure 4.18: Crystal structure map (PDB ID: 3SPU) of (A) singly and (B) doubly Zn(II) bound holo ions for an unreacted NDM-1 sample. A corresponding combined map is shown in Figure 4.17. Residue color indicates whether the holo fragment ion is N-terminal (blue), C-terminal (red), or bi-directional (green). Ions were identified from the UVPD spectra shown in Figure 4.16. Bi-directional fragmentation is defined as complementary N- and C-terminal holo ions resulting from cleavage at the same backbone position. The six residues known to bind the cofactors are represented as sticks.

Lastly, considering both apo and holo fragment ions, variations in the backbone fragmentation efficiencies for ebselen-modified NDM-1 versus uninhibited NDM-1 were charted (**Figure 4.19**) and shown as a difference plot in **Figure 4.20**. Suppression of

backbone cleavages is observed for the ASL1 region (the substrate-binding beta-hairpin loop) as well as for the three residues coordinating Zn1 (H120, H122, H189), suggesting a reorganization that curbs fragmentation throughout the N-terminal region of the protein after modification by ebselen. Interestingly, there is slight suppression of UVPD at D124 suggesting that this residue, no longer coordinated to Zn2, may engage in new interactions with the bound inhibitor, which is expected to be located nearby due to the proximity of Cys208.

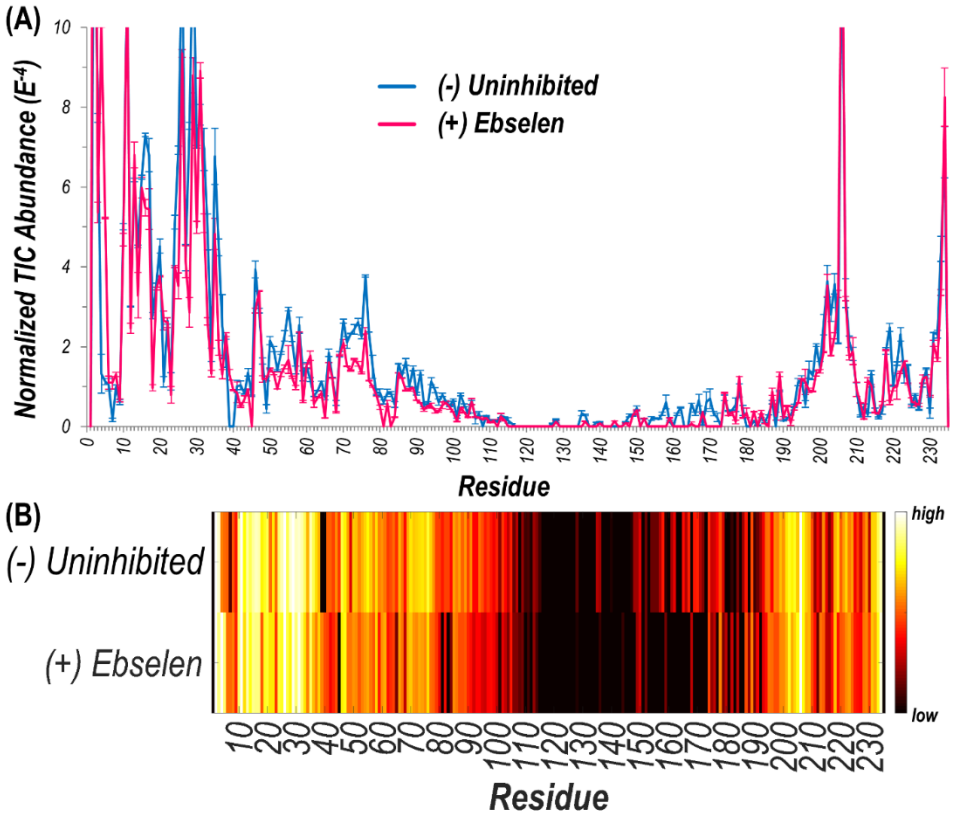

Figure 4.19: (A) Plot per residue of the abundances of identified fragment ions summed and normalized to the TIC for uninhibited NDM-1 (blue) and ebselen-bound NDM-1 (pink). The difference plot in Figure 4.20 was created by subtraction of the values for uninhibited NDM-1 from the corresponding values for ebselen-bound NDM-1. (B) Log of the values in (A) shown as a linear heatmap along the sequence.

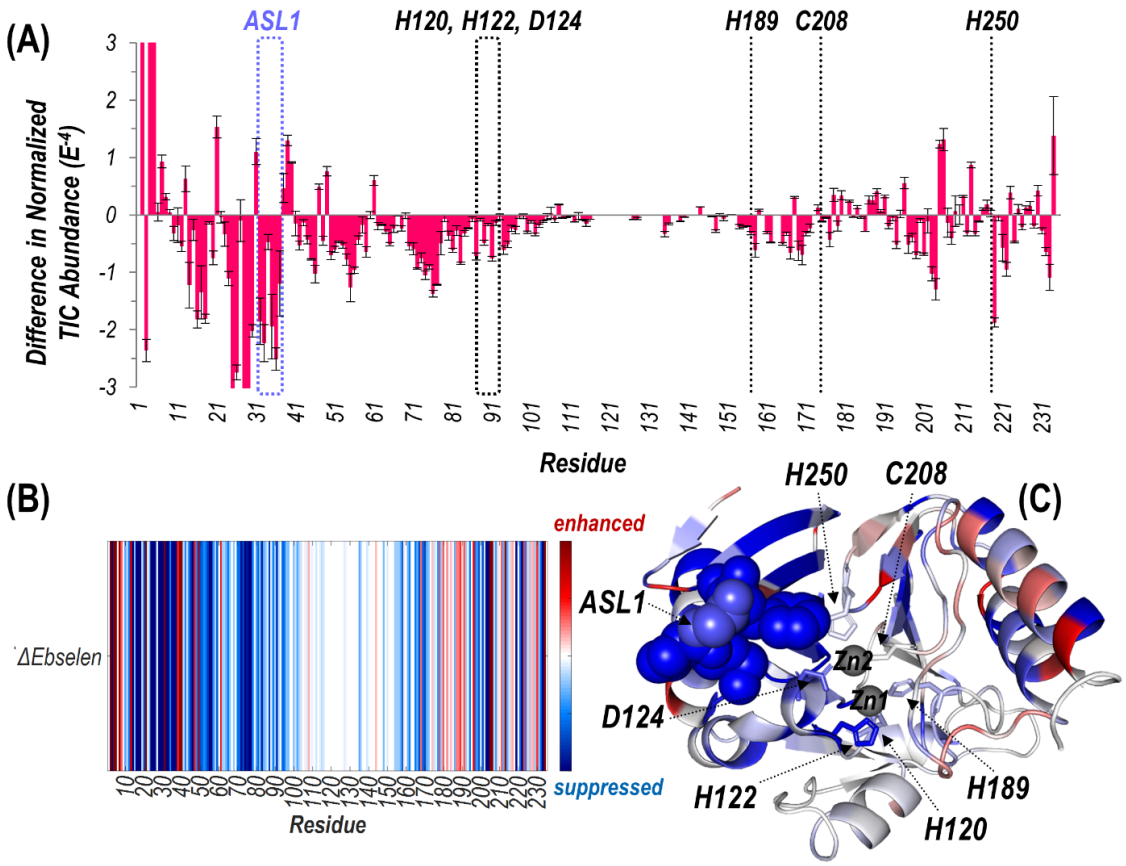

Figure 4.20: (A) Changes in abundances represented as a difference plot of apo and holo UVPD fragment ions between NDM-1 bound covalently to ebselen and an uninhibited sample resulting from subtraction of the UVPD fragmentation plots shown in Figure 4.19. ASL1 is outlined with a dashed slate line while the six residues known to bind the Zn(II) cofactors are highlighted with dashed black lines. (B) Linear and (C) crystal structure (PDB ID: 3SPU) heatmap representations are shown. Suppression in backbone cleavage efficiency of the inhibitor-bound species compared to the uninhibited is indicated by blue regions while enhancement is represented by red regions. In (C), ASL1 is displayed as spheres and the Zn(II)-binding residues are shown as sticks. The inhibitor attaches covalently at C208.

Here we demonstrate the application of UVPD-MS to characterize inhibitor binding, and to simultaneously report on the site of covalent reaction (Cys208), the metalation state of NDM-1 (specifically the loss of Zn2), the closure of the substrate-binding beta-hairpin loop (ASL1), and the partial denaturation of C-terminal domain of the

protein. These results are consistent with prior work that shows loss of one zinc equivalent upon addition of one equivalent of ebselen, and additionally provide direct evidence that Cys208 is adducted and that Zn2 is ejected.[42] Our results are also consistent with prior studies that show an overall decrease in thermostability upon loss of Zn2 and the formation of putative inclusion bodies upon ebselen treatment, but provide more specific structural details about how the structure of Zn2 ligands, surrounding residues, and the C-terminal domain of the protein are impacted by Zn2 ejection.[15,47]

4.4.5 Examining Structural Changes in NDM Clinical Variants Associated with Zn(II) Binding Residues

Given the capability of UVPD-MS to detect structural changes in NDM-1 upon Zn2 ejection by ebselen (**3**), we reasoned that this MS technique may also be useful to detect and better understand the structural implications of sequence differences introduced by clinical variants of NDM. Many of the NDM variants (currently NDM-1 through NDM-29) have increased thermostability and increased affinity for Zn2, presumably indicating that the *bla*$_{\text{NDM}}$ gene is evolving in response to the dual selective pressures of antibiotic treatment and zinc depravation by host innate immune responses.[3,15–18] Here, we compare NDM-1 (the reference sequence) and the double mutant NDM-15 (M154L, A233V), which has a ~10-fold increase in Zn2 K_d value and ~7 °C increase in thermostability, as well as the individual single mutants NDM-4 (M154L) and NDM-6 (A233V) (**Figure 4.3**).[17] X-ray crystallography has revealed only minor structural differences between NDM-1 and NDM-4 (or other variants), and the mechanism whereby these mutations communicate to the Zn2 site to impact affinity is not obvious. Here, we apply UVPD-MS to interrogate structural differences among representative clinical NDM variants.

Upon electrospray ionization, each of the variants was observed to produce intact protein ions in low charge states (9+, 10+, 11+) bound to two Zn(II) (**Figure 4.21**). Isolation and UV photoactivation of the 9+ charge state yielded the fragmentation patterns in **Figure 4.22**. Deconvolution allows the isotopically-resolved fragments to be readily assigned as sequence ions (**Figure 4.23**). In addition to apo (Zn-free) fragment ions, holo (Zn-bound) fragment ions were identified, the latter readily assigned based on inclusion of a mass shift of one or two Zn(II) ions relative to the metal-free fragment ions. Combining the observed metal-free and holo fragment ions accounts for coverage of 69-78% of the protein sequence as shown in the maps in **Figure 4.23**.

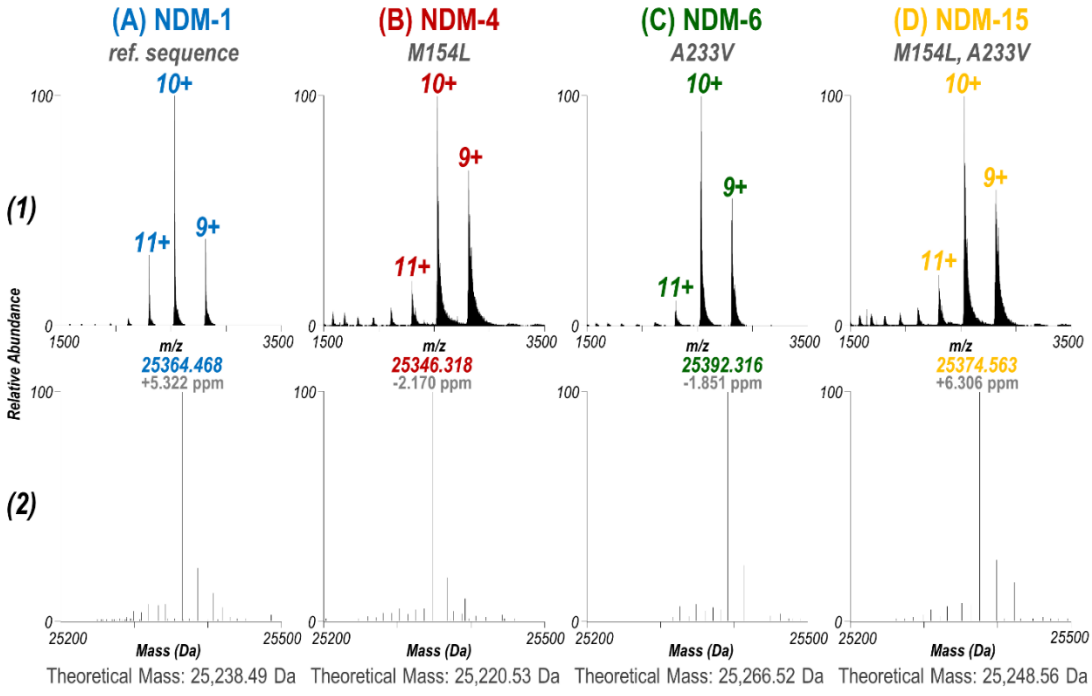

Figure 4.21: (1) Native ESI mass spectra of (A) NDM-1, (B) NDM-4, (C) NDM-6, and (D) NDM-15 with observed charge states labelled (9+, 10+, 11+). Corresponding deconvoluted spectra are shown in (2). Observed masses were +126 Da from theoretical masses based on protein sequence indicating that two Zn(II) ions are retained. Accuracies (ppm) are calculated accounting for the mass shift of the metal cofactors.

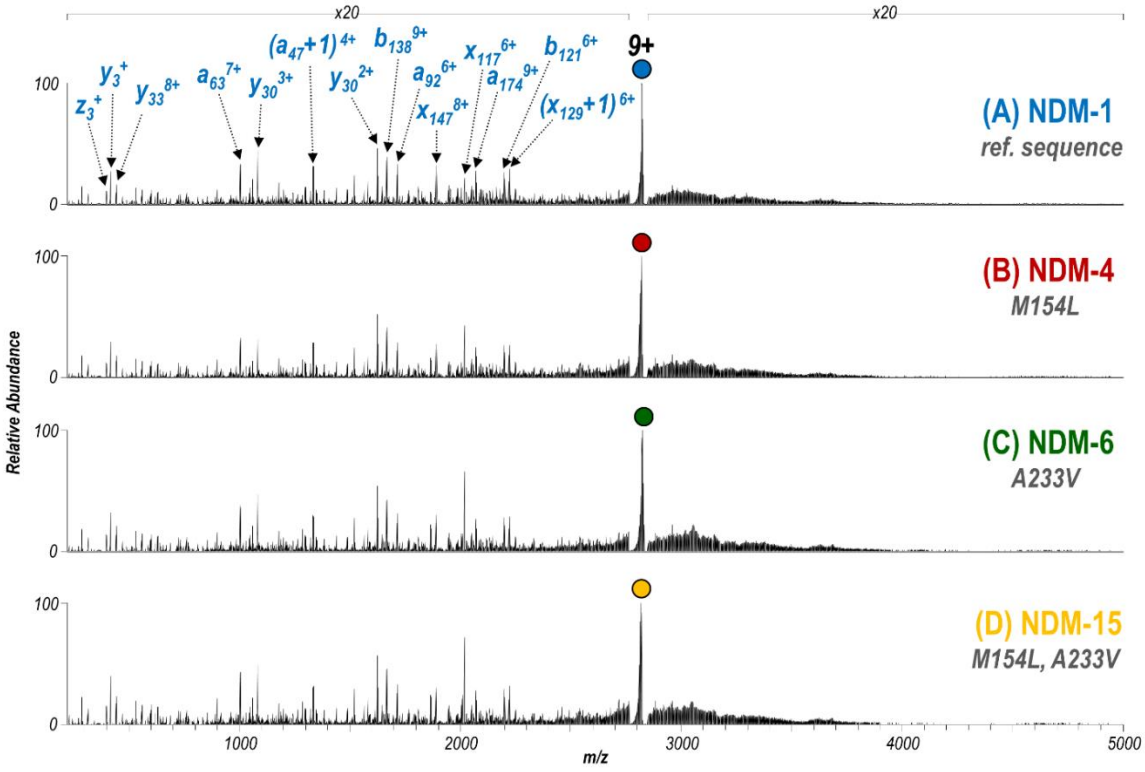

Figure 4.22: UVPD MS/MS spectra (one pulse at 3 mJ) of the 9+ charge state of NDM clinical variants: (A) NDM-1, (B) NDM-4, (C) NDM-6, and (D) NDM-15. In panel (A) several of the most abundant fragment ions are labelled. Surviving precursor is identified with a filled circle.

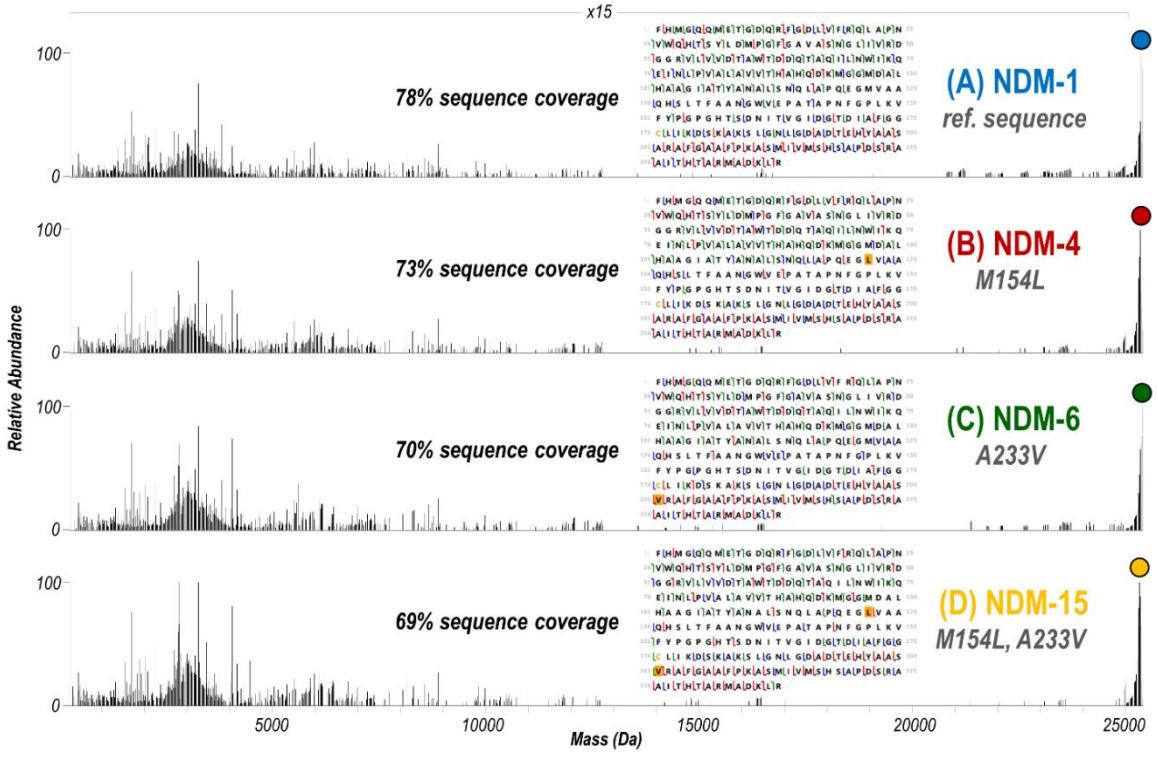

Figure 4.23: (A-D) Deconvoluted UVPD mass spectra of the corresponding spectra shown in Figure 4.22 for activation of the 9+ charge state of four clinical variants of NDM. The precursor is labelled with a filled circle. Sequence coverage maps and values of identified fragment ions are shown for each spectrum. These account for apo (Zn-free) and holo (Zn-bound) fragment ions. For the variants, the mutated residue(s) is highlighted in yellow.

Differences in relative abundances of some of the fragment ions between variants are apparent upon visual inspection of the UVPD mass spectra in **Figure 4.22**. Regions of the protein in which noncovalent interactions or flexibility are impacted by single point mutations can be elucidated by examining the enhancement or suppression of UVPD backbone clevages.[35–37] For each NDM variant, the backbone cleavage efficiency upon UVPD was determined and is represented graphically in **Figure 4.24** as a function of each residue of the protein. The fragmentation behavior of three clinical variants (NDM-4, NDM-6, NDM-15) is compared to that of the reference sequence of NDM-1 by subtraction

of the backbone cleavage values at each residue and visualized as difference plots (**Figure 4.25**). Negative values are indicative of suppression in UVPD backbone cleavages for each clinical variant compared to NDM-1, whereas positive values designate enhancement in backbone cleavages for the clinical variant compared to NDM-1. Statistical significance of the observed differences is determined from *t*-test calculations and represented as *p*-values plotted per residue in **Figure 4.2C**. To aid in visualization, the changes are represented as a heatmap spanning blue (suppression of fragmentation of the clinical variant) to red (enhancement of fragmentation of the clinical variant) along the protein sequence from N-terminus to C-terminus (**Figure 4.26A**). Imprinting the heatmap on the crystal structure allows differences in fragmentation to be related to structural features and specific regions of the protein, as illustrated **Figure 4.26B-D**.

Overall, the variations in backbone fragmentation (enhancement of some regions and suppression of others) observed for NDM-15 (**Figure 4.26D**) generally mirror the collective differences for NDM-4 and NDM-6 (**Figures 4.26B-C**). Specifically, for NDM-15 suppression in UVPD fragmentation is observed along the loop containing H120-D124 (ASL2) and the loop containing C208 (ASL4), with the same modest degree of suppression occurring for both NDM-4 and NDM-6. These two loop regions are shaded in blue on the crystal structure in **Figure 4.26D** to highlight the suppression of backbone fragmentation of NDM-15. The suppression in fragmentation likely represents a rigidification of these domains that is qualitatively consistent with the observed changes in thermostability. Reported melting temperatures (T_m) for NDM-1, -4, -6, and -15 (54.5, 58.4, 56.3, and 61.5 °C, respectively) show increases in stability and the gain for NDM-15 (~7 °C) is only slightly more than the sum of the two individual mutants, which is also consistent with the mostly additive nature of the observed structural changes.[17]

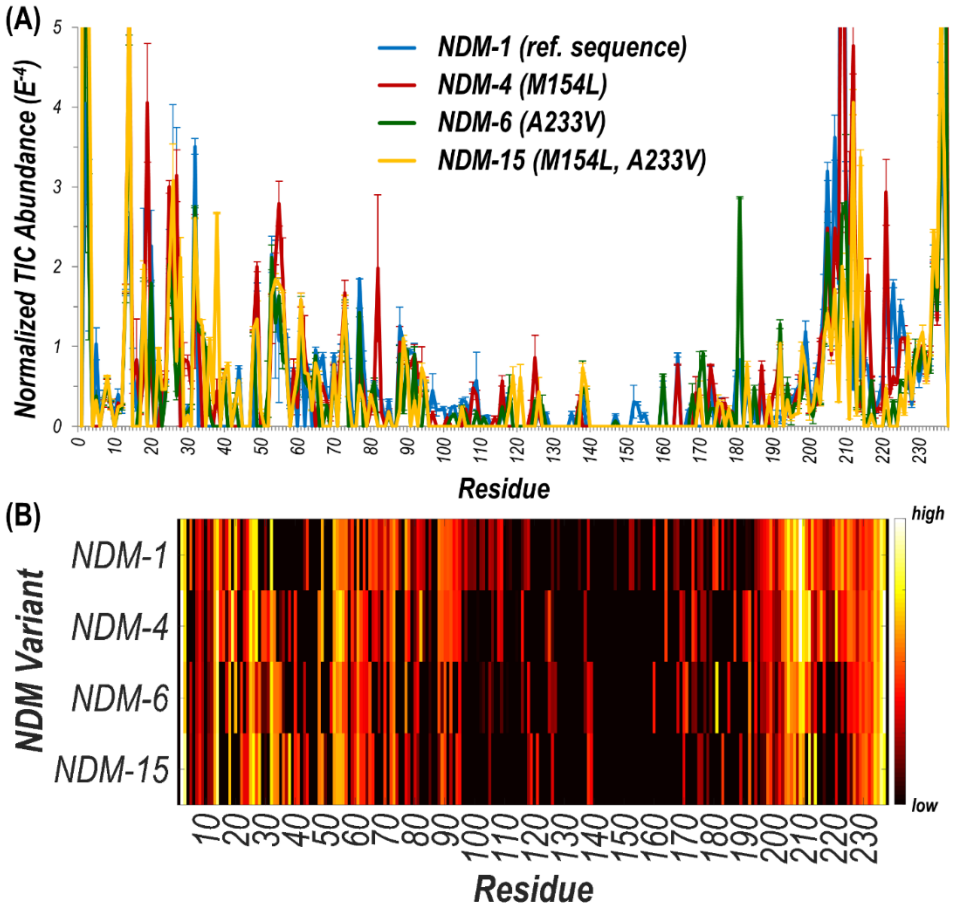

Figure 4.24: (A) Abundance of apo and holo fragment ions (summed and normalized to TIC) plotted per residue for NDM-1 (blue), NDM-4 (red), NDM-6 (green), and NDM-15 (yellow). Larger values indicate greater extents of backbone cleavages adjacent to the amino acid. Subtraction of the values for NDM-1 from the corresponding values for each of the variants was used to create the difference plots in Figure 4.25. (B) Linear heatmap of the log of the values in (A) shown along the sequence.

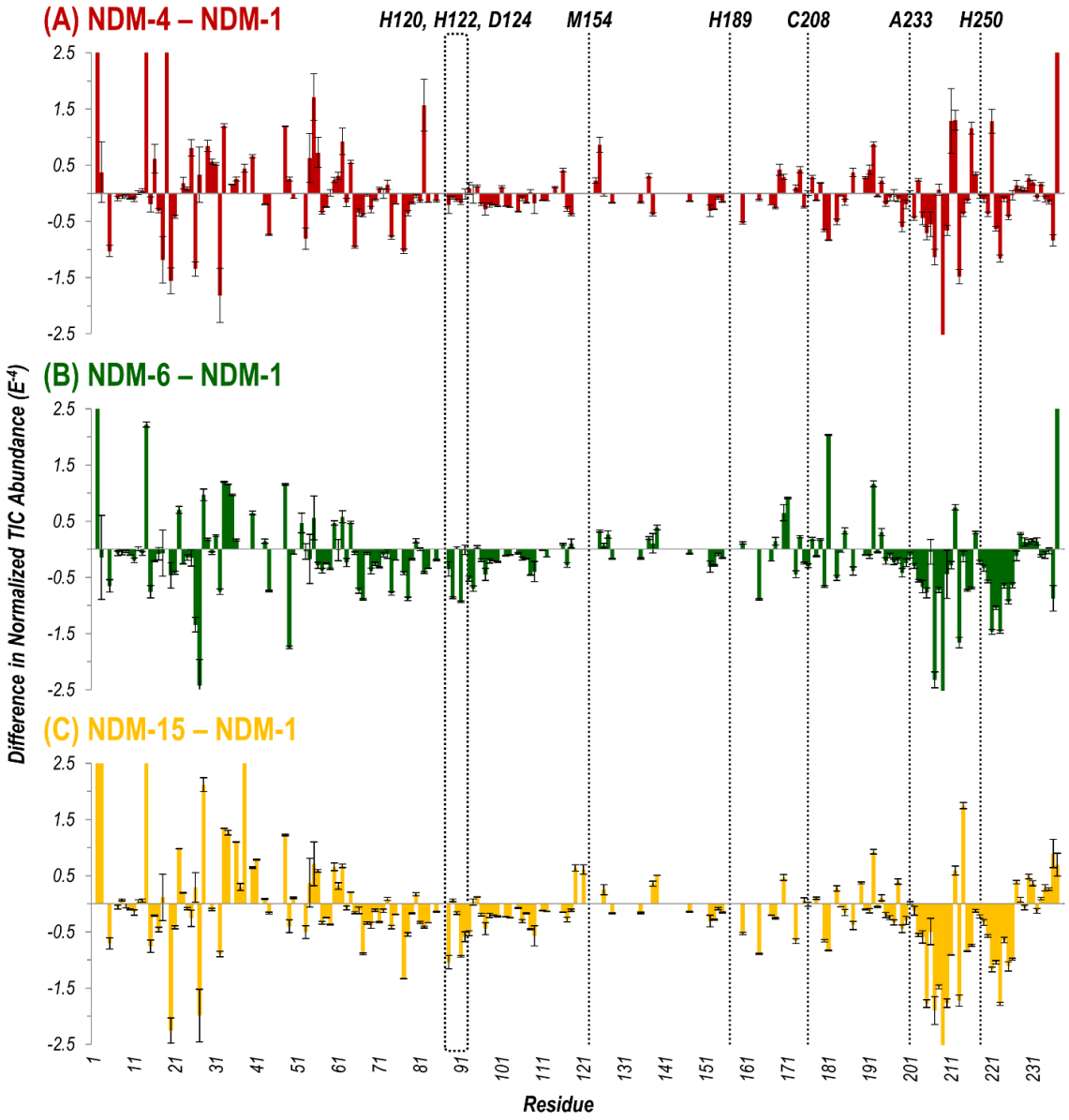

Figure 4.25: (A-C) Changes in the summed abundances of apo and Zn-bound holo fragment ions resulting from UVPD of three clinical variants of NDM compared to the reference NDM-1 sequence represented as difference plots. Values greater than zero indicate that the backbone cleavages are enhanced for the variant relative to NDM-1; values less than zero indicate that the backbone cleavages are suppressed for the variant. A plot of the summed backbone cleavage values used to create these graphs is shown in Figure 4.24. The six Zn-binding residues and two mutated residues (M154, A233) are indicated with dashed lines.

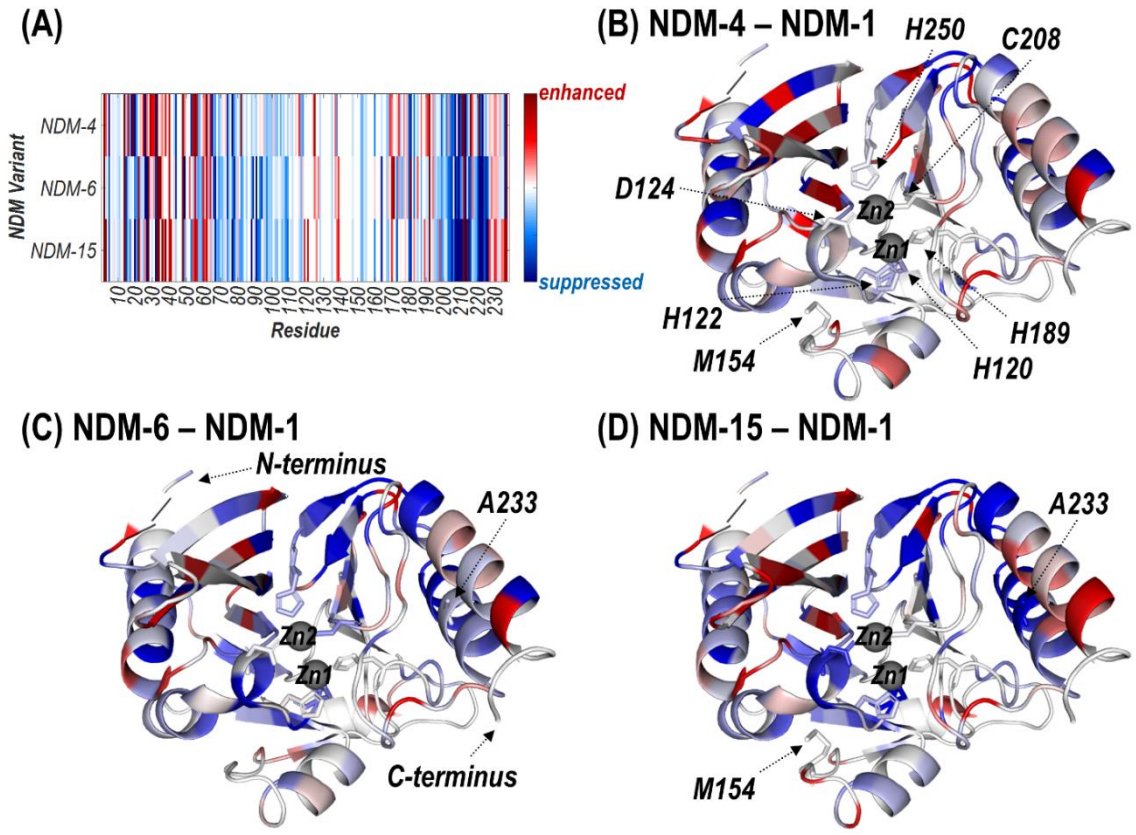

Figure 4.26: Changes in backbone cleavage efficiency during UVPD for three clinical variants of NDM (NDM-4, NDM-6, NDM-15) compared to the reference sequence (NDM-1) represented as heatmaps along the (A) linear sequence or (B-D) crystal structure (PDB ID: 3SPU) of NDM-1. Regions colored red indicate enhancement while blue regions denote suppression in UVPD cleavage efficiency of the variant compared to NDM-1, based on the difference plots shown in Figure 4.25. The mutated sites are shown as sticks (M154L, A233V). The six residues involved in binding the two Zn(II) ions represented as gray spheres are shown as sticks and labelled in (B).

We then focused particularly on the six residues that anchor the dinuclear zinc ion cluster at the active site. The higher affinity Zn1 site consists of H120, H122, and H189 ligands, and the lower-affinity Zn2 site consists of D124, C208, and H250 (**Figure 4.3**).[48] The relative degrees of backbone fragmentation bracketing these six key residues of NDM-1 and each of the other variants are highlighted in **Figure 4.27**. For NDM-4 (M154L)

compared to NDM-1, the only significant differences in fragmentation related to the six targeted Zn-binding residues are suppression of backbone cleavages at H120 and H122. This observation aligns well with the location of M154 near the α-carbon of H122, and with a prior proposal that substitution of Met to Leu shifts the position of H122 to enable more stabilizing interactions with Zn1.[15] Here, we clearly observe the stronger H122:Zn1 interactions experimentally as a suppression in the efficiency of backbone cleavages at H122. This same type of suppression of fragmentation at H122 is not noted for NDM-6 (A233V), indicating a different stabilization mechanism is used for these two variants.

For NDM-6 (A233V), the backbone cleavage efficiency is substantially suppressed at a different Zn1-ligand, H120, as well as at two Zn2-ligands, C208 and H250. The shift of the flexible loop containing C208 owing to the introduction of a bulkier Val for Ala would place C208, H120 and H250 (on neighboring loops) in more ideal positions for stabilizing Zn2. Lastly, for NDM-15 (M154L, A233V), suppression of backbone fragmentation was observed at four of the six zinc-binding residues, representing mostly a sum of the changes observed in individual single mutations. However, backbone fragmentation at C208 was not suppressed for NDM-15, suggesting that the M154L substitution has a greater impact on enhancing Zn(II) affinity compared to A233V when both mutations are present. The use of native UVPD-MS reveals in increased detail how distant structural changes located on each side of the dizinc site are propagated and combine to increase metal ion affinity, helping to elucidate the mechanisms used by clinical variants to overcome zinc scarcity at infection sites.

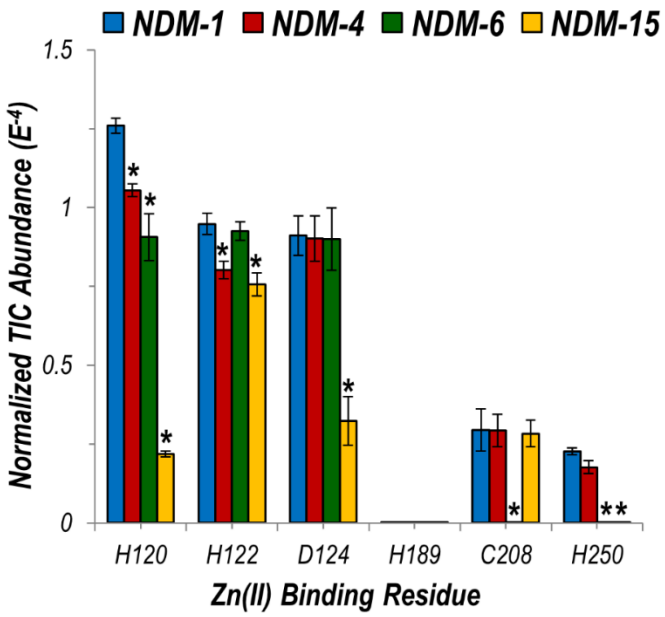

Figure 4.27: Graph displaying summed UVPD fragment ion abundances normalized to the total ion current (TIC) corresponding to fragment ions originating from cleavages occurring proximal to each of the six Zn(II) binding residues for NDM-1 (blue), NDM-4 (red), NDM-6 (green), and NDM-15 (yellow). Corresponding values for the entire protein sequence are given in the UVPD abundance plots in Figure 4.24. Asterisks indicate residues at which the difference in backbone cleavages for the clinical variant compared to the reference NDM-1 protein is statistically significant (99% confidence threshold).

4.5 Conclusion

Structural information detailing ligand:NDM interactions is important for design and optimization of selective and potent inhibitors to serve as probes for chemical biology experiments and as lead compounds for therapeutic development. However, interactions between ligand and the essential substrate-binding beta-hairpin loop are obscured due to method-dependent artifacts. Additionally, structure activity relationships are often difficult to extract from libraries if the mechanisms of inhibition are not determined. Attributes that lead to more effective metal stripping and attributes that lead to more effective ternary complex formation (inhibitor:dizinc cluster:NDM) can both show increased inhibition, but

only the latter category is suitable for developing NDM-selective probes and therapeutic leads. Here, we demonstrate a powerful strategy utilizing native MS along with UVPD relying on observed changes in fragmentation to interrogate structural differences between uninhibited and inhibited NDM-1, simultaneously revealing conformational changes in the substrate-binding beta-hairpin loop, reporting on the metalation state of the enzyme, identifying modified residues (if any), and tracking other changes throughout the protein structure. We characterized two structurally divergent inhibitors, a K211-selective covalent inhibitor and a C208 covalent modifier and found that each induced a similar structural change - closure of the beta-hairpin loop. These cases were characterized using covalent inhibitors, but native UVPD-MS can also be applied to the similar characterization of non-covalent ligands.[31,34–36,38] Previous solution phase studies of NDM led to conflicting conclusions, that ligand binding either induces loop closure or opens the cavity even wider.[13,14] However, the prior studies required mutation and chemical modification of the loop which likely impact both structure and dynamics, and one approach used a non-native metalloform. Here, native UVPD-MS was completed using wild type dizinc NDM to conclusively show loop closing upon ligand binding. This result is particularly significant because optimization of loop:inhibitor interactions is required for NDM drug design, and native UVPD-MS now provides a novel strategy to probe this interaction with minimal perturbation that was not possible with previous methods.

Another advantage of native UVPD-MS as showcased here for NDM is the ability to simultaneously report on modification sites (for covalent inhibitors), metalation state, and structural perturbations in addition to loop closure. Several notable conclusions can be drawn from the study of inactivators **1**-**3**. The pentafluorophenyl ester (**1**) was previously shown to be specific for one Lys residue in IMP-1, but we find it readily modifies three Lys residues neighboring the active site (although no other surface Lys residues). This

finding reveals two additional Lys residues as alternative available targets for design of more effective covalent NDM inhibitors. Simultaneous targeting of multiple Lys residues could be useful in overcoming resistance-causing mutations. Previous characterization of the *O*-aryloxycarbonyl hydroxyamate inactivator (**2**) by X-ray crystallography revealed two covalent adducts, and one was proposed to be a degradation product of the other.[41] Here, native UVPD-MS revealed only the parent modification and not the degradation product, supporting the proposed inactivation mechanism and suggesting that the MS method may give less ambiguous results. Finally, native UVPD-MS of ebselen (**3**)-treated NDM-1 confirms a prior report that one zinc ion is ejected,[15,47] and now reveals the identity of the ejected zinc as Zn2 and provides direct evidence that Cys208 is the modified residue. Unexpectedly, we also detected partial denaturation of the C-terminus of the protein, which provides structural information that helps explain decreased thermostability and inclusion body formation upon Zn2 loss and ebselen treatment. We note that ebselen is a useful probe to show the structural and mechanistic implications of Cys modification and Zn2 loss in NDM-1 that may be more broadly applicable. NDM-1 appears to be less effective than other carbapenemases in some infection models and patients.[49] One possibility is that the weak affinity for Zn2 allows NDM-1 to be more easily inhibited by host zinc sequestering proteins such as calprotectin or Cys oxidation by ROS during inflammation, which would be expected to result in deleterious structural changes similar to those we observed with ebselen using native UVPD-MS.

The ability of native UVPD-MS to report on structural changes related to metalation state prompted us to use this method to characterize select NDM clinical variants. Notably, we were able to track the structural impact of distant mutations to direct zinc ligands. Specifically, the increased Zn2 affinity (with respect to NDM-1) previously measured for NDM-4 (M154L) and NDM-6 (A233V) appear to be due to structural

changes largely propagated through different networks of residues emanating from the distant mutated sites toward the dizinc cluster. Many of the structural changes induced by the individual mutations are conserved when combined in the NDM-15 variant (M154L, A233V), but additional structural changes are also observed, highlighting the structural basis of the small synergism observed in this double mutant. Identification of these networks of residues may enable prediction of how newly emerging clinical variants perturb structure, function and zinc affinity. These structural changes were not easily observed using X-ray crystallography, but native UVPD-MS provides an innovative approach to determine the impact of NDM clinical variants on structure and dynamics and elucidates in greater mechanistic detail how structural changes at distant mutation sites are propagated to the zinc binding site.

In summary, native UVPD-MS is a powerful analytical tool that enables simultaneous detection of inhibitor binding, covalent modification sites, metalation state, and structural changes to NDM, including closing of the active-site beta-hairpin loop and other perturbations owing to ligand binding or mutation, all using unlabeled wild-type dizinc protein. This tool should help to easily distinguish metal stripping agents from ternary complex forming inhibitors, which are preferred for drug design,[4] while providing additional information about inhibitor interactions with the substrate-binding beta-hairpin loop that were not easily obtained previously. Moreover, new insight into the structure and dynamics of emerging NDM clinical variants has been uncovered.

4.6 REFERENCES

(1) Centers for Disease Control and Prevention (CDC). *Antibiotic Resistance Threats in the United States, 2019*; Centers for Disease Control and Prevention (U.S.): Atlanta, 2019.

(2) Papp-Wallace, K. M.; Endimiani, A.; Taracila, M. A.; Bonomo, R. A. Carbapenems: Past, Present, and Future. *Antimicrob. Agents Chemother.* **2011**, *55*, 4943–4960.

(3) Thomas, P. W.; Zheng, M.; Wu, S.; Guo, H.; Liu, D.; Xu, D.; Fast, W. Characterization of Purified New Delhi Metallo-β-Lactamase-1. *Biochemistry* **2011**, *50*, 10102–10113.
(4) Ju, L.-C.; Cheng, Z.; Fast, W.; Bonomo, R. A.; Crowder, M. W. The Continuing Challenge of Metallo-β-Lactamase Inhibition: Mechanism Matters. *Trends Pharmacol. Sci.* **2018**, *39*, 635–647.
(5) Toney, J. H.; Fitzgerald, P. M. D.; Grover-Sharma, N.; Olson, S. H.; May, W. J.; Sundelof, J. G.; Vanderwall, D. E.; Cleary, K. A.; Grant, S. K.; Wu, J. K.; Kozarich, J. W.; Pompliano, D. L.; Hammond, G. G. Antibiotic Sensitization Using Biphenyl Tetrazoles as Potent Inhibitors of Bacteroides Fragilis Metallo-β-Lactamase. *Chem. Biol.* **1998**, *5*, 185–196.
(6) Moali, C.; Anne, C.; Lamotte-Brasseur, J.; Groslambert, S.; Devreese, B.; Van Beeumen, J.; Galleni, M.; Frère, J.-M. Analysis of the Importance of the Metallo-β-Lactamase Active Site Loop in Substrate Binding and Catalysis. *Chem. Biol.* **2003**, *10*, 319–329.
(7) Scrofani, S. D. B.; Chung, J.; Huntley, J. J. A.; Benkovic, S. J.; Wright, P. E.; Dyson, H. J. NMR Characterization of the Metallo-β-Lactamase from Bacteroides Fragilis and Its Interaction with a Tight-Binding Inhibitor: Role of an Active-Site Loop. *Biochemistry* **1999**, *38*, 14507–14514.
(8) Huntley, J. J. A.; Scrofani, S. D. B.; Osborne, M. J.; Wright, P. E.; Dyson, H. J. Dynamics of the Metallo-β-Lactamase from Bacteroides Fragilis in the Presence and Absence of a Tight-Binding Inhibitor. *Biochemistry* **2000**, *39*, 13356–13364.
(9) Huntley, J. J. A.; Fast, W.; Benkovic, S. J.; Wright, P. E.; Dyson, H. J. Role of a Solvent-Exposed Tryptophan in the Recognition and Binding of Antibiotic Substrates for a Metallo-β-Lactamase. *Protein Sci.* **2003**, *12*, 1368–1375.
(10) Fast, W.; Sutton, L. D. Metallo-β-Lactamase: Inhibitors and Reporter Substrates. *Biochim. Biophys. Acta BBA - Proteins Proteomics* **2013**, *1834*, 1648–1659.
(11) Chiou, J.; Leung, T. Y.-C.; Chen, S. Molecular Mechanisms of Substrate Recognition and Specificity of New Delhi Metallo-β-Lactamase. *Antimicrob. Agents Chemother.* **2014**, *58*, 5372–5378.
(12) Palacios, A. R.; Mojica, M. F.; Giannini, E.; Taracila, M. A.; Bethel, C. R.; Alzari, P. M.; Otero, L. H.; Klinke, S.; Llarrull, L. I.; Bonomo, R. A.; Vila, A. J. The Reaction Mechanism of Metallo-β-Lactamases Is Tuned by the Conformation of an Active-Site Mobile Loop. *Antimicrob. Agents Chemother.* **2019**, *63*.
(13) Aitha, M.; Moritz, L.; Sahu, I. D.; Sanyurah, O.; Roche, Z.; McCarrick, R.; Lorigan, G. A.; Bennett, B.; Crowder, M. W. Conformational Dynamics of Metallo-β-Lactamase CcrA during Catalysis Investigated by Using DEER Spectroscopy. *J. Biol. Inorg. Chem.* **2015**, *20*, 585–594.
(14) Rydzik, A. M.; Brem, J.; van Berkel, S. S.; Pfeffer, I.; Makena, A.; Claridge, T. D. W.; Schofield, C. J. Monitoring Conformational Changes in the NDM-1 Metallo-β-Lactamase by 19F NMR Spectroscopy. *Angew. Chem. Int. Ed.* **2014**, *53*, 3129–3133.
(15) Stewart, A. C.; Bethel, C. R.; VanPelt, J.; Bergstrom, A.; Cheng, Z.; Miller, C. G.; Williams, C.; Poth, R.; Morris, M.; Lahey, O.; Nix, J. C.; Tierney, D. L.; Page, R.

C.; Crowder, M. W.; Bonomo, R. A.; Fast, W. Clinical Variants of New Delhi Metallo-β-Lactamase Are Evolving To Overcome Zinc Scarcity. *ACS Infect. Dis.* **2017**, *3*, 927–940.

(16) Bahr, G.; Vitor-Horen, L.; Bethel, C. R.; Bonomo, R. A.; González, L. J.; Vila, A. J. Clinical Evolution of New Delhi Metallo-β-Lactamase (NDM) Optimizes Resistance under Zn(II) Deprivation. *Antimicrob. Agents Chemother.* **2018**, *62*, e01849-17.

(17) Cheng, Z.; Thomas, P. W.; Ju, L.; Bergstrom, A.; Mason, K.; Clayton, D.; Miller, C.; Bethel, C. R.; VanPelt, J.; Tierney, D. L.; Page, R. C.; Bonomo, R. A.; Fast, W.; Crowder, M. W. Evolution of New Delhi Metallo-β-Lactamase (NDM) in the Clinic: Effects of NDM Mutations on Stability, Zinc Affinity, and Mono-Zinc Activity. *J. Biol. Chem.* **2018**, *293*, 12606–12618.

(18) Makena, A.; Brem, J.; Pfeffer, I.; Geffen, R. E. J.; Wilkins, S. E.; Tarhonskaya, H.; Flashman, E.; Phee, L. M.; Wareham, D. W.; Schofield, C. J. Biochemical Characterization of New Delhi Metallo-β-Lactamase Variants Reveals Differences in Protein Stability. *J. Antimicrob. Chemother.* **2015**, *70*, 463–469.

(19) Konermann, L.; Ahadi, E.; Rodriguez, A. D.; Vahidi, S. Unraveling the Mechanism of Electrospray Ionization. *Anal. Chem.* **2013**, *85*, 2–9.

(20) Leney, A. C.; Heck, A. J. R. Native Mass Spectrometry: What Is in the Name? *J. Am. Soc. Mass Spectrom.* **2017**, *28*, 5–13.

(21) Allison, T. M.; Bechara, C. Structural Mass Spectrometry Comes of Age: New Insight into Protein Structure, Function and Interactions. *Biochem. Soc. Trans.* **2019**, *47*, 317–327.

(22) Macias, L. A.; Santos, I. C.; Brodbelt, J. S. Ion Activation Methods for Peptides and Proteins. *Anal. Chem.* **2020**, *92*, 227–251.

(23) Lermyte, F.; Sobott, F. Electron Transfer Dissociation Provides Higher-Order Structural Information of Native and Partially Unfolded Protein Complexes. *PROTEOMICS* **2015**, *15*, 2813–2822.

(24) Zhang, H.; Cui, W.; Wen, J.; Blankenship, R. E.; Gross, M. L. Native Electrospray and Electron-Capture Dissociation FTICR Mass Spectrometry for Top-Down Studies of Protein Assemblies. *Anal. Chem.* **2011**, *83*, 5598–5606.

(25) Zhang, J.; Malmirchegini, G. R.; Clubb, R. T.; Loo, J. A. Native Top-down Mass Spectrometry for the Structural Characterization of Human Hemoglobin. *Eur. J. Mass Spectrom.* **2015**, *21*, 221–231.

(26) Wongkongkathep, P.; Han, J. Y.; Choi, T. S.; Yin, S.; Kim, H. I.; Loo, J. A. Native Top-Down Mass Spectrometry and Ion Mobility MS for Characterizing the Cobalt and Manganese Metal Binding of α-Synuclein Protein. *J. Am. Soc. Mass Spectrom.* **2018**, *29*, 1870–1880.

(27) Li, H.; Sheng, Y.; McGee, W.; Cammarata, M.; Holden, D.; Loo, J. A. Structural Characterization of Native Proteins and Protein Complexes by Electron Ionization Dissociation-Mass Spectrometry. *Anal. Chem.* **2017**, *89*, 2731–2738.

(28) Li, H.; Nguyen, H. H.; Ogorzalek Loo, R. R.; Campuzano, I. D. G.; Loo, J. A. An Integrated Native Mass Spectrometry and Top-down Proteomics Method That

Connects Sequence to Structure and Function of Macromolecular Complexes. *Nat. Chem.* **2018**, *10*, 139–148.
(29) Shaw, J. B.; Li, W.; Holden, D. D.; Zhang, Y.; Griep-Raming, J.; Fellers, R. T.; Early, B. P.; Thomas, P. M.; Kelleher, N. L.; Brodbelt, J. S. Complete Protein Characterization Using Top-Down Mass Spectrometry and Ultraviolet Photodissociation. *J. Am. Chem. Soc.* **2013**, *135*, 12646–12651.
(30) O'Brien, J. P.; Li, W.; Zhang, Y.; Brodbelt, J. S. Characterization of Native Protein Complexes Using Ultraviolet Photodissociation Mass Spectrometry. *J. Am. Chem. Soc.* **2014**, *136*, 12920–12928.
(31) Cammarata, M. B.; Brodbelt, J. S. Structural Characterization of Holo- and Apo-Myoglobin in the Gas Phase by Ultraviolet Photodissociation Mass Spectrometry. *Chem. Sci.* **2015**, *6*, 1324–1333.
(32) Robinson, M. R.; Taliaferro, J. M.; Dalby, K. N.; Brodbelt, J. S. 193 Nm Ultraviolet Photodissociation Mass Spectrometry for Phosphopeptide Characterization in the Positive and Negative Ion Modes. *J. Proteome Res.* **2016**, *15*, 2739–2748.
(33) Sipe, S. N.; Brodbelt, J. S. Impact of Charge State on 193 Nm Ultraviolet Photodissociation of Protein Complexes. *Phys. Chem. Chem. Phys.* **2019**, *21*, 9265–9276.
(34) Cammarata, M. B.; Thyer, R.; Rosenberg, J.; Ellington, A.; Brodbelt, J. S. Structural Characterization of Dihydrofolate Reductase Complexes by Top-Down Ultraviolet Photodissociation Mass Spectrometry. *J. Am. Chem. Soc.* **2015**, *137*, 9128–9135.
(35) Cammarata, M. B.; Schardon, C. L.; Mehaffey, M. R.; Rosenberg, J.; Singleton, J.; Fast, W.; Brodbelt, J. S. Impact of G12 Mutations on the Structure of K-Ras Probed by Ultraviolet Photodissociation Mass Spectrometry. *J. Am. Chem. Soc.* **2016**, *138*, 13187–13196.
(36) Mehaffey, M. R.; Schardon, C. L.; Novelli, E. T.; Cammarata, M. B.; Webb, L. J.; Fast, W.; Brodbelt, J. S. Investigation of GTP-Dependent Dimerization of G12X K-Ras Variants Using Ultraviolet Photodissociation Mass Spectrometry. *Chem. Sci.* **2019**, *10*, 8025–8034.
(37) Cammarata, M.; Thyer, R.; Lombardo, M.; Anderson, A.; Wright, D.; Ellington, A.; Brodbelt, J. S. Characterization of Trimethoprim Resistant E. Coli Dihydrofolate Reductase Mutants by Mass Spectrometry and Inhibition by Propargyl-Linked Antifolates. *Chem. Sci.* **2017**, *8*, 4062–4072.
(38) Mehaffey, M. R.; Cammarata, M. B.; Brodbelt, J. S. Tracking the Catalytic Cycle of Adenylate Kinase by Ultraviolet Photodissociation Mass Spectrometry. *Anal. Chem.* **2018**, *90*, 839–846.
(39) Kurosaki, H.; Yamaguchi, Y.; Higashi, T.; Soga, K.; Matsueda, S.; Yumoto, H.; Misumi, S.; Yamagata, Y.; Arakawa, Y.; Goto, M. Irreversible Inhibition of Metallo-β-Lactamase (IMP-1) by 3-(3-Mercaptopropionylsulfanyl)Propionic Acid Pentafluorophenyl Ester. *Angew. Chem. Int. Ed.* **2005**, *44*, 3861–3864.
(40) Tilvawala, R.; Cammarata, M.; Adediran, S. A.; Brodbelt, J. S.; Pratt, R. F. A New Covalent Inhibitor of Class C β-Lactamases Reveals Extended Active Site Specificity. *Biochemistry* **2015**, *54*, 7375–7384.

(41) Thomas, P. W.; Cammarata, M.; Brodbelt, J. S.; Monzingo, A. F.; Pratt, R. F.; Fast, W. A Lysine-Targeted Affinity Label for Serine-β-Lactamase Also Covalently Modifies New Delhi Metallo-β-Lactamase-1 (NDM-1). *Biochemistry* **2019**, *58*, 2834–2843.
(42) Chiou, J.; Wan, S.; Chan, K.-F.; So, P.-K.; He, D.; Chan, E. W.; Chan, T.; Wong, K.; Tao, J.; Chen, S. Ebselen as a Potent Covalent Inhibitor of New Delhi Metallo-β-Lactamase (NDM-1). *Chem. Commun.* **2015**, *51*, 9543–9546.
(43) Rosenberg, J.; Parker, W. R.; Cammarata, M. B.; Brodbelt, J. S. UV-POSIT: Web-Based Tools for Rapid and Facile Structural Interpretation of Ultraviolet Photodissociation (UVPD) Mass Spectra. *J. Am. Soc. Mass Spectrom.* **2018**, *29*, 1323–1326.
(44) King, D.; Strynadka, N. Crystal Structure of New Delhi Metallo-β-Lactamase Reveals Molecular Basis for Antibiotic Resistance. *Protein Sci.* **2011**, *20*, 1484–1491.
(45) Chen, A. Y.; Thomas, C.; Thomas, P. W.; Yang, K.; Cheng, Z.; Fast, W.; Crowder, M. W.; Cohen, S. M. Iminodiacetic Acid as a Novel Metal-Binding Pharmacophore for New Delhi Metallo-β-Lactamase Inhibitor Development. *ChemMedChem* **2020**, *10.1002/cmdc.202000123*.
(46) Xu, K.; Zhang, Y.; Tang, B.; Laskin, J.; Roach, P. J.; Chen, H. Study of Highly Selective and Efficient Thiol Derivatization Using Selenium Reagents by Mass Spectrometry. *Anal. Chem.* **2010**, *82*, 6926–6932.
(47) Chen, C.; Xiang, Y.; Yang, K.-W.; Zhang, Y.; Wang, W.-M.; Su, J.-P.; Ge, Y.; Liu, Y. A Protein Structure-Guided Covalent Scaffold Selectively Targets the B1 and B2 Subclass Metallo-β-Lactamases. *Chem. Commun.* **2018**, *54*, 4802–4805.
(48) Guo, Y.; Wang, J.; Niu, G.; Shui, W.; Sun, Y.; Zhou, H.; Zhang, Y.; Yang, C.; Lou, Z.; Rao, Z. A Structural View of the Antibiotic Degradation Enzyme NDM-1 from a Superbug. *Protein Cell* **2011**, *2*, 384–394.
(49) Boyd, S. E.; Livermore, D. M.; Hooper, D. C.; Hope, W. W. Metallo-β-Lactamases: Structure, Function, Epidemiology, Treatment Options, and the Development Pipeline. *Antimicrob. Agents Chemother.* **2020**, *10.1128/AAC.00397-20*.

Chapter 5: Investigation of GTP-Dependent Dimerization of G12X K-Ras Variants Using Ultraviolet Photodissociation Mass Spectrometry‡

5.1 Overview

Mutations in the GTPase enzyme K-Ras, specifically at codon G12, remain the most common genetic alterations in human cancers. The mechanisms governing activation of downstream signaling pathways and how they relate back to the identity of the mutation have yet to be completely defined. Here we use native mass spectrometry (MS) combined with ultraviolet photodissociation (UVPD) to investigate the impact of three G12X mutations (G12C, G12V, G12S) on the homodimerization of K-Ras as well as heterodimerization with a downstream effector protein, Raf. Electrospray ionization (ESI) was used to transfer complexes of WT or G12X K-Ras bound to guanosine 5'-diphosphate (GDP) or GppNHp (non-hydrolyzable analogue of GTP) into the gas phase. Relative abundances of homo- or hetero-dimer complexes were estimated from ESI-MS spectra. K-Ras + Raf heterocomplexes were activated with UVPD to probe structural changes responsible for observed differences in the amount of heterocomplex formed for each variant. Holo (ligand-bound) fragment ions resulting from photodissociation suggest the G12X mutants bind Raf along the expected effector binding region (β-interface) but may interact with Raf via an alternative α-interface as well. Variations in backbone cleavage efficiencies during UV photoactivation of each variant were used to relate mutation identity to structural changes that might impact downstream signaling. Specifically, oncogenic upregulation for hydrogen-bonding amino acid substitutions (G12C, G12S) is achieved by

‡Mehaffey, M. R.; Schardon, C. L.; Novelli, E. T.; Cammarata, M. B.; Webb, L. J.; Fast, W.; Brodbelt, J. S. Investigation of GTP-Dependent Dimerization of G12X K-Ras Variants Using Ultraviolet Photodissociation Mass Spectrometry. *Chem. Sci.* **2019**, *10*, 8025-8034.

CLS expressed and purified K-Ras and variants. ETN expressed and purified RBD of Raf. MBC largely contributed to the project idea and implementation. LJW, WF, and JSB provided mentorship and reviewed the manuscript prior to publication.

stabilizing β-interface interactions with Raf, while a bulkier, hydrophobic G12V substitution leads to destabilization of this interface and instead increases the proximity of residues along the α-helical bundles. This study deciphers new pieces of the complex puzzle of how different K-Ras mutations exert influence in downstream signaling.

5.2 INTRODUCTION

The canonical rat sarcoma (Ras) family of GTPases H-, N-, and K-Ras function as molecular switches and key regulators of cell proliferation and survival through effector pathways, including Raf-MAPK, which communicates signals from surface receptors to the cell nucleus.[1,2] The G-domain (GTPase and effector binding regions) of these proteins are highly conserved while their C-terminal hypervariable regions are post-translationally modified in an isoform specific manner.[1,3–5] Ras remains inactive in a GDP-bound state until upstream stimuli cause a switch to the GTP-bound active state, catalyzed by interaction with a guanine-nucleotide exchange factor (GEF). Once activated, Ras binds effector proteins to transmit receptor-initiated signals until it is returned to the inactive state by interaction with a GTPase activating protein (GAP).[1] Single point mutations most commonly in the Gly12 (G12X) position (or less frequently at the residues specified by codons 13 or 61) prevent GTP hydrolysis, causing the protein to stall in the active state and resulting in activation of cell cycle progression and proliferation.[6] Consequently, Ras is the most frequently mutated gene in human cancer and an important oncogene for targeting in cancer therapy.[7,8] Based on the knowledge that Ras requires membrane localization and GTP-loading to be active, previous therapeutic strategies involved prevention of membrane localization by inhibiting isoprenylation[9], targeting the GTP-binding pocket[10–17], or interfering with interaction of upstream and downstream effectors.[18–21] However, these efforts to pharmacologically inhibit mutant Ras have met limited success.[22] Recent

evidence from immuno-EM[23], spectroscopy[24,25], dynamic light scattering[26], and microscopy[27–29] experiments suggest that Ras functions as a dimer (or less likely as a nanocluster[30,31]), not as a monomer. Accordingly, therapeutic efforts have expanded to disruption of the mechanisms modulating Ras oligomerization instead of solely the enzymatic ones.[32–36] The regulation of Ras dimer formation and signaling is still poorly understood, although based on modeling there are two known dimer interfaces along the protein: (1) β-sheet interface at the Switch I/effector binding region and (2) α-helix interface at the C-terminal allosteric lobe of the G domain.[26,36] Studies that reveal integral components of Ras dimers, decipher mechanisms regulating formation of these complexes, and define how oncogenic mutations impact these processes are needed to guide the development of more effective therapeutic strategies.

In recent years, mass spectrometry (MS) has proven to be a useful experimental technique to probe theoretical models and address structural biology questions in a sensitive, rapid manner.[37,38] The use of covalent chemical probes, such as hydrogen/deuterium exchange (HDX) or cross-linking reagents, in conjunction with bottom-up tandem mass spectrometry (MS/MS) is now a standard approach for evaluating solvent accessibilities and mapping protein interfaces.[39–41] Top-down techniques have more recently gained traction for characterization of protein structure with the advent of native MS and advances in MS/MS methods.[37,38] The framework for native MS entails the transfer of intact protein complexes to the gas phase by electrospray ionization of solutions of high ionic strength which largely preserves tertiary and quaternary structures of macromolecules.[42] Consequently, native MS is now routinely used for identification of oligomeric states of proteins and elucidation of binding stoichiometry with other proteins or ligands.[38] To further discern three-dimensional shapes of protein complexes in the gas phase, ion mobility (IM) mass spectrometry has proved to be an indispensable technique

for providing information complementary to static high resolution structures resulting from X-ray crystallography, NMR spectroscopy, or cryo-EM.[43]

MS/MS methods sensitive to protein structure have been developed to study the architecture of protein-protein and protein-ligand complexes. Traditional collisional activation of native-like complexes mainly yields ejection of ligands or subunits,[44,45] which is often uninformative and has spurred the application of alternative activation methods. Electron-based methods, including electron transfer dissociation (ETD) and electron capture dissociation (ECD), and surface induced dissociation (SID) represent the most widely used alternative methods to characterize protein structure.[46–52] ETD and ECD yield mostly diagnostic sequence ions with abundances that can be correlated with crystallographic B-factors and used to probe the topology of protein assemblies for flexible regions, thus revealing insight into the higher order structure of the complexes.[46–51] Conversely, SID causes disassembly of protein-protein complexes into intact subunits in a way that conserves the symmetry of charge distribution among the separating proteins or subunits.[52] Coupled with IM, this MS/MS technique allows for the rapid determination of stoichiometry and topology for computationally designed protein complexes.[53] Ultraviolet photodissociation (UVPD) represents a third alternative MS/MS method that utilizes fast, high-energy excitation via 193 nm photons and yields the widest array of diagnostic sequence ions for protein complexes.[54–58] The abundances of holo (ligand-bound) and apo (ligand-free) product ions resulting from activation of protein-ligand complexes by 193 nm UVPD have been demonstrated to reflect secondary and tertiary structural features.[59–62] The suppression or enhancement of UVPD at each position along the backbone is thought to be modulated by non-covalent interactions that stabilize structural features and prevent separation of fragments after bond cleavage. Recent studies have demonstrated this approach is sensitive to loop movements upon ligand binding in dihydrofolate reductase

(DHFR)[60], dynamic plasticity throughout a catalytic cycle of the active enzyme adenylate kinase[61], and even long-range conformational changes resulting from single residue mutations in K-Ras.[62]

Previously variations in UVPD backbone cleavage efficiencies were monitored for monomeric protein-ligand complexes of K-Ras (wild-type (WT) and three G12X mutants: G12C, G12V, G12S) upon exchange of GDP for a non-hydrolyzable GTP analogue, guanosine 5'-[β,γ-imido]triphosphate (GppNHp).[62] Switching from the inactive diphosphate bound state to the active triphosphate bound protein yielded unique structural changes for each mutant. Based on the examination of monomeric K-Ras and a series of G12X variants, the way each mutation modulated homo- or hetero-dimer formation with downstream effectors was inferred. Given that the G12 position lies on the surface of the protein, longer-range conformational changes in areas of the protein related to dimer formation are likely involved. Specifically, observations included stabilization of the α-helical bundle for G12C K-Ras, stabilization of the β-sheet region for G12V K-Ras, and increased flexibility of the β-sheet region for G12S K-Ras.[62] Although the mechanism is not yet well defined, this supports that the identity of the G12 substitution impacts downstream signaling and patient survival differently.[63–69]

Here we report the use of native MS and UVPD to directly interrogate homo- and hetero-dimers of WT and three clinically relevant G12X mutants of K-Ras (G12C, G12S, G12V). We use native MS to define the relative abundance of homodimer formation for each K-Ras G12X mutant bound to either GDP or GppNHp (the non-hydrolyzable analogue of GTP), and compare the amount of heterodimer formed between each of the K-Ras mutants and the Ras binding domain (RBD) of a downstream effector kinase, rapidly accelerated fibrosarcoma (Raf). Comparing UVPD cleavage efficiencies of K-Ras•GppNHp + Raf_{RBD} heterodimers for each of the mutants to the WT suggests hydrogen-

bonding amino acid substitutions (G12C, G12S) rely on directly stabilizing the β-interface interactions with Raf for oncogenic upregulation, whereas a bulkier, hydrophobic G12V substitution causes destabilization of this interface and instead results in tightened α-helical bundles. Direct structural interrogation of intact dimers by UVPD-MS represents an advance in unraveling the mutation-dependent interplay of structure and binding interactions for K-Ras signaling phenotypes.

5.3 EXPERIMENTAL

5.3.1 Sample Preparation

Four variants of recombinant human K-Ras (WT, G12C, G12V, G12S) were expressed and purified as previously described.[62] The RBD of c-Raf-1 was expressed using a purchased plasmid and purified as follows. A pET 15-b vector containing the gene for the Ras Binding Domain (RBD) of c-Raf-1 with an N-terminal 6X-Histidine tag separated by a thrombin cleavage site was purchased from Genscript. The vector was transformed into BL21(DE3) competent *E. coli* cells (New England Biolabs) for expression. Single colonies of *E. coli* containing the desired plasmid were inoculated in 5 mL of Luria-Bertani (LB) Broth and grown at 37 °C for 14-16 hours. The 5 mL cultures were used to seed 2 L flasks containing Terrific Broth (TB, Millipore) which were incubated with shaking at 37 °C for 4-6 hours until an OD_{600} ~0.6 was obtained. Isopropyl β-D-1-thiogalactopyranoside (IPTG, GoldBio) was added to a final concentration of 1 mM, and protein expression was carried out at 30 °C while shaking for 6 hours.

Cells were collected via centrifugation at 6000 RPM for 15 minutes, and re-suspended in lysis buffer containing 50 mM phosphate, 500 mM NaCl, 40 mM imidazole, and 10% glycerol at pH = 8.0. Re-suspended cells were lysed by sonication with a probe sonicator for 3 rounds consisting of 1 minute of pulsed sonication followed by 5 minutes

of resting on ice, for a total sonication time of 3 minutes. The cell debris was separated via centrifugation at 19000 RPM for 30 minutes, and the supernatant was passed through a 10 μM filter then added to an Ni-nitrilotriacetic acid (Ni-NTA) column pre-equilibrated with lysis buffer for affinity chromatography. The flow through was reapplied to the column and then the column was washed with lysis buffer prior to elution with a buffer containing 50 mM phosphate, 500 mM NaCl, 500 mM imidazole, and 10% glycerol at pH = 8.0. The eluent containing the target protein was exchanged into a cleavage buffer containing 20 mM tris, 150 mM NaCl, 2.5 mM $CaCl_2$, and 10% glycerol at pH = 8.0. Protein concentration was estimated via absorbance at 280 nm and thrombin (Millipore) was added to a concentration of 2 U thrombin per mg Raf and incubated overnight at 4 °C. The cleaved Raf was separated from thrombin by applying the protein solution to a benzamidine column equilibrated in cleavage buffer, and the flow through containing Raf was collected. The protein was then exchanged into a final buffer of 50 mM ammonium acetate (pH 7.8). Typical yield was 20-30 mg per liter of growth. Expressed sequences of K-Ras and Raf, and structures of the guanosine phosphate ligands GDP and GppNHp (the stable GTP analogue) are shown in **Figure 5.1**.

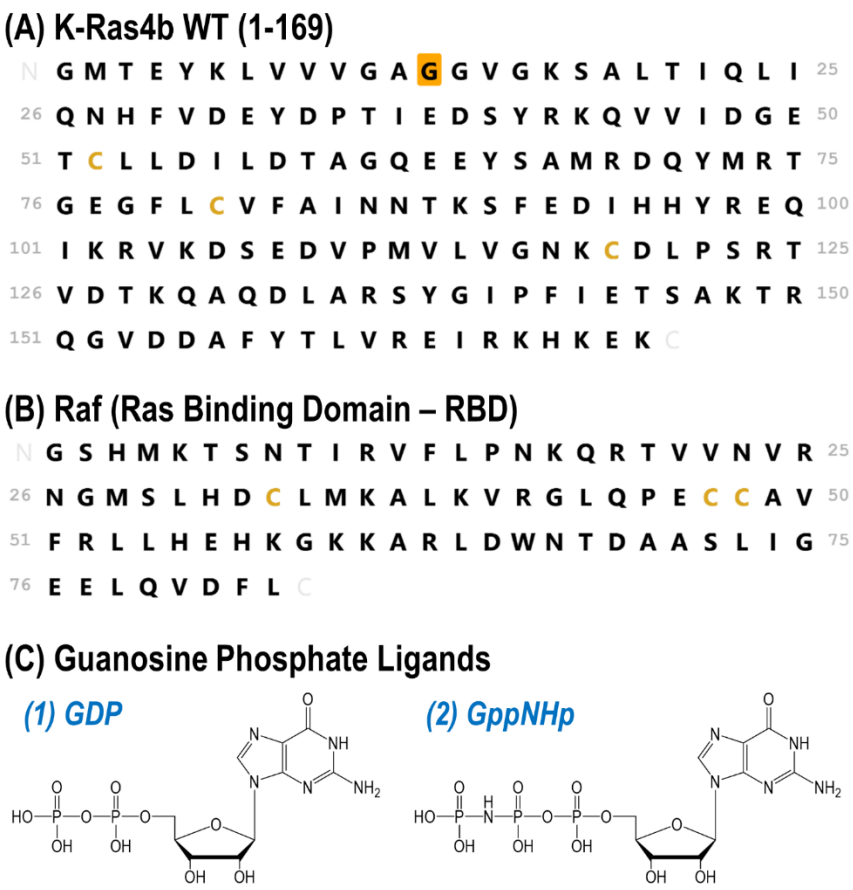

Figure 5.1: Sequence of (A) WT K-Ras4b (1-169) and (B) the Ras binding domain (RBD) of Raf. Residues are numbered from the first glycine (G) of K-Ras4b in subsequent figures. The G12X position mutated to Cys, Val, or Ser is shaded in a gold box. (C) Structures of the guanosine phosphate ligands (1) guanosine 5'-diphosphate (GDP) and (2) guanosine 5'-[β,γ-imido]triphosphate (GppNHp).

Given that purified K-Ras was already bound to GDP, the procedure for nucleotide exchange to GppNHp is described here. To remove GDP and load K-Ras with the non-hydrolyzable GTP mimic GppNHP, variants were diluted to 30 μM in an exchange buffer (pH 8.0) consisting of 25 mM Tris, 10 mM EDTA, 1 mM dithiothreitol (DTT), and 1.5 mM guanosine 5'-[β,γ-imido]triphosphate (GppNHp, Sigma Aldrich, St. Louis, MO). This solution was incubated on ice for 1 hour. Subsequently magnesium acetate was added at a

final concentration of 25 mM and the mixture was incubated on ice for an additional 30 min. These steps were repeated once after using a 10 kDa molecular weight cutoff filter device (EMD Millipore, Billerica, MA) to put the protein back into exchange buffer. Afterwards, a final buffer exchange was performed to put the GppNHp-loaded protein into MS spray buffer (50 mM ammonium acetate with 5 μM magnesium acetate, pH 7.8). Protein samples were diluted to 20 μM or 80 μM dimer concentration in 50 mM ammonium acetate containing 5 μM magnesium acetate (pH 7.8) and desalted for MS analysis using 3 kDa molecular weight cutoff filter devices (EMD Millipore, Billerica, MA). For heterodimer experiments, K-Ras (~19.3 kDa) and Raf (~9.4 kDa) were combined at a 1:1 ratio before desalting.

5.3.2 Mass Spectrometry

Experiments were performed on a Thermo Scientific Orbitrap Elite mass spectrometer (Bremen, Germany) modified with a 193 nm Coherent Excistar excimer laser (Santa Cruz, CA) to allow photodissociation in the HCD cell.[54] An offline nano-ESI source with Au-coated borosilicate emitters ionized the native complexes using source voltages of 1.0-1.1 kV and a source temperature of 200 °C. A resolving power of 240K at *m*/*z* 400 was used to collect all MS spectra. MS1 spectra represent sixty scans with an automated gain control (AGC) setting of 1E6. On-line size-exclusion chromatography experiments of K-Ras•GppNHp + Raf_{RBD} complexes were performed by interfacing a Dionex LC system to the modified Thermo Scientific Orbitrap Elite instrument. For each run, 5 μg of a 1:1 K-Ras•GppNHp:Raf_{RBD} solution (5 μL injection volume) in 50 mM ammonium acetate containing 5 μM magnesium acetate (pH 7.8) was injected onto a 2.1 mm × 150 mm ACQUITY UPLC Protein BEH SEC column with a 200 Å pore size and 1.7 μm particle size (Waters, Milford, MA). An isocratic mobile phase of 50 mM ammonium acetate at pH

6.8 was flowed at a rate of 100 µL min^{-1}. The LC effluent was introduced into the MS using a HESI source with an applied voltage of 4 kV. ESI-MS spectra were collected with a resolving power of 240 K at *m*/*z* 400. Normalized relative abundances of K-Ras•GppNHp + Raf_{RBD} complexes were calculated from peak areas of EIC traces of *m*/*z* values corresponding to each species. MS/MS analysis of K-Ras•GppNHp + Raf_{RBD} heterodimers involved selection of the 12+ charge state of the complex using an isolation width of 20 *m*/*z* and activation with a single 3 mJ pulse. Each UVPD mass spectrum represents 500 transients with a scan range *m*/*z* 220-4000 using an AGC value of 5E5 and maximum ion time of 2 sec. For each K-Ras•GppNHp + Raf_{RBD} heterocomplex triplicate UVPD data was collected.

5.3.3 Data Analysis

For MS1 spectra, the amount of K-Ras homodimer formation was assessed by normalizing the summed abundances of all charge states corresponding to the observed dimer to the total ion current of the spectrum. UVPD MS/MS spectra were de-charged and de-isotoped using the Thermo Xtract algorithm (S/N ratio of 3, fit factor of 44%, remainder of 25%). Monoisotopic apo fragment ions were identified using ProSight Lite v1.4 which accounts for the nine ion types typically observed during UVPD (*a*, *a + 1*, *b*, *c*, *x*, *x + 1*, *y*, *y – 1*, *z*). Holo fragment ions were also identified by including mass shifts in the search corresponding to the GppNHp ligand, coordinating Mg^{2+} ion, and intact Raf_{RBD} subunit. Although Raf_{RBD} itself likely underwent fragmentation during UV activation, to streamline data interpretation this subunit was treated as a ligand bound to K-Ras and only the intact mass shift of Raf_{RBD} was searched. Confident identification of holo fragment ions containing a cleaved portion of K-Ras bound to a cleaved portion of Raf_{RBD} is impeded given the nearly unlimited array of possible fragment ion assignments that can arise from

combinations of partial protein sequence segments. Thus, assignment of these types of holo ions was not considered owing to low statistical confidence. Given that Raf_{RBD} is much smaller than K-Ras and has a different sequence, the unidentified fragments of Raf_{RBD} should not overlap significantly with the K-Ras fragments of interest. Specific mass additions included in the searches for holo ions are: 9952.879 – 9954.894 Da for Raf_{RBD} + GppNHp•Mg^{2+}, and 542.969 – 544.984 Da for GppNHp•Mg^{2+} alone. The divalent Mg^{2+} cofactor necessary to coordinate the GppNHp ligand contributed a +21.969 Da shift. The fragment abundance utility of UV-POSIT[70] was used to sum cleavage yields at each backbone position upon UVPD if the amino acids of a protein are numbered from 1 (N-terminus) to R (C-terminus) for a protein containing R amino acids. This Web-based program normalizes the abundances of identified holo and corresponding apo ions to the total ion current of the spectrum by collectively summing N-terminal product ions (a_n, b_n, c_n) arising from backbone cleavage C-terminal to a given amino acid, *n*, with C-terminal fragment ions (x_{R-n+1}, y_{R-n+1}, z_{R-n+1}) resulting from cleavage N-terminal to residue *n*.[70] This calculated value is used to convey the UVPD backbone cleavage efficiency adjacent to each amino acid throughout the protein. Student's *t*-test with pooled standard deviations was used to determine the statistical significance of differences in backbone cleavage efficiency upon UVPD for WT and G12X K-Ras•GppNHp + Raf_{RBD} heterocomplexes. A two-tailed test was assumed to determine *p*-values from calculated *t*-values. **Figure 5.2** gives graphs of the log of calculated *p*-values per residue for backbone cleavage efficiency of heterodimers of each G12X K-Ras variant compared to WT. The black dotted line represents a confidence threshold at 99%. A histogram of calculated *p*-values for the entire data set is shown in **Figure 5.2** demonstrating over 55% of measured UVPD backbone cleavage efficiencies within a triplicate measurement are statistically different for G12X variants from the measured average of the corresponding WT backbone position at the 99%

confidence level. For reference, **Figure 5.3** is the crystal structure of WT K-Ras bound to GppNHp and complexed with Raf_{RBD} (PDB ID: 4G0N)[71] with important helical and loop regions labelled and the two dimer interfaces highlighted.

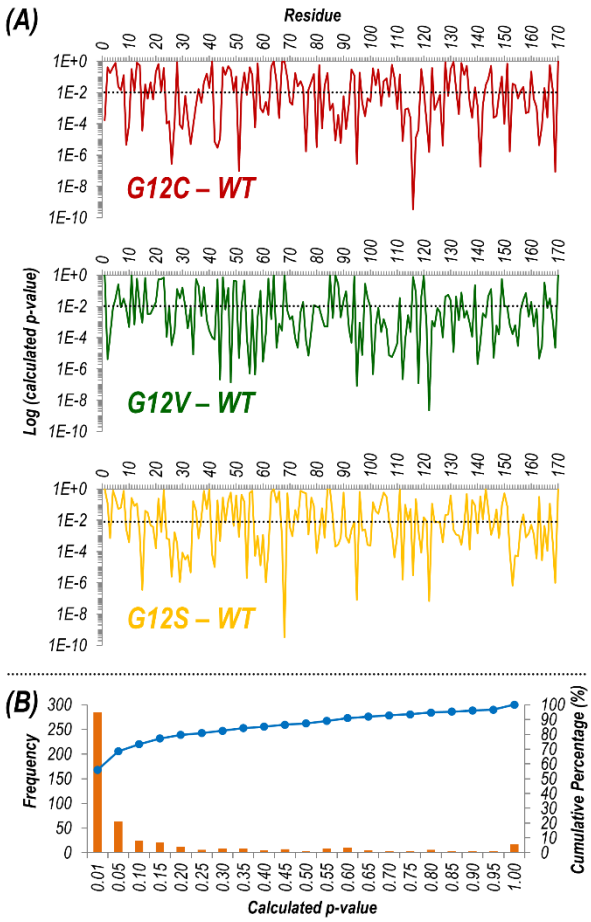

Figure 5.2: (A) Log of calculated *p*-values per residue for the differences plotted in Figure 5.19. The black dotted line represents a confidence threshold at 99%. (B) Histogram of all calculated *p*-values in (A-C) with the cumulative percentage shown in blue. Pooled standard deviations were used to perform Student's *t*-test for comparison of UVPD of each K-Ras variant to the WT. Assuming a two-tailed hypothesis, *p*-values were determined from calculated *t*-values. In summary, a *p*-value smaller than 0.01 at a given residue for a variant of K-Ras indicates that the average measured UVPD intensity within a triplicate measurement is statistically different from the measured average of the WT at the 99% confidence level.

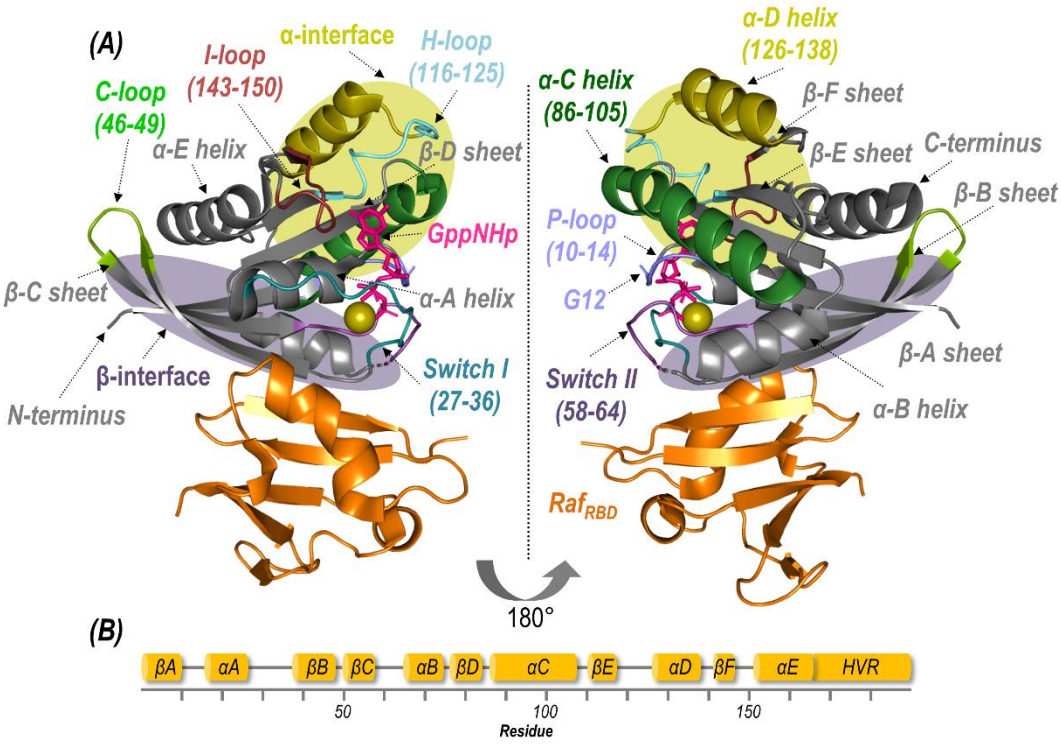

Figure 5.3: (A) Crystal structure of WT K-Ras bound to GppNHp and complexed with Raf_{RBD} (PDB ID: 4G0N) highlighting important loop and α-helical regions. The two possible dimer interfaces include the α-interface at α-C and α-D helices (shaded yellow) and β-interface at Switch I (shaded purple). Binding with most upstream or downstream effector proteins occurs at the stronger β-interface, but the α-interface might be used for homodimerization. (B) Secondary structure map of the catalytic domain of the Ras family of proteins. Isoforms are almost identical in these regions but differ significantly in the C-terminal hypervariable region (HVR). For this study, only residues 1-169 were examined.

Owing to the fact that UVPD-MS is a new approach for characterization of structural variations in protein complexes and providing insight into potential changes in conformation and binding motifs, there is need for critical evaluation of the method via appropriate controls and statistical tests. Some of the statistical tests and controls are described above and shown in **Figures 5.2**, **5.12** and **5.21**. Moreover, the K-Ras protein used in the present study was also the subject of a prior study (ref. 62). Additional controls

and statistical tests were performed previously, as provided in Figures S2–S4 in ref. 62, including the assessment of the statistical significance of backbone cleavage efficiency for K-Ras and the G12C, G12V, and G12S mutants, both as native-like and denatured forms. One relevant control entailed the examination of UVPD of the denatured proteins, confirming that the relative fragment ion abundances were identical for 166 out of 169 comparisons of specific backbone positions. In contrast, the UVPD fragment ion abundances of the native-like proteins showed numerous statistically significant differences in fragment ion abundances. These types of control experiments support the premise that UVPD is sensitive to protein structure.

5.4 Results and Discussion

5.4.1 Native MS to Detect GTP-Dependent Formation of K-Ras Homodimers

In addition to membrane localization and GTP-loading, recent studies posit the formation of homodimers as a significant factor in signaling output related to K-Ras.[23–29] Specifically, dimerization of K-Ras might promote self-association of downstream effectors necessary for their activation.[23,28] Consequently, defining the extent to which specific G12X mutations impact the formation of K-Ras homodimers when bound to either GDP or GTP is essential. ESI-mass spectra were collected under native conditions for WT, G12C, G12V, and G12S K-Ras sprayed with a 1:1 ratio of either GDP or GppNHp (the non-hydrolyzable analogue of the GTP ligand) at both a relatively standard (20 μM) and high (80 μM) protein concentration (**Figure 5.4**). In addition to the ligand-bound monomers (9+, 10+, 11+), homodimers (12+, 13+, 14+) were observed for all K-Ras protein except G12V at 20 μM. **Table 5.1** summarizes the measured intact masses for observed dimers containing two protein molecules and two ligands. Native MS represents a unique strategy to determine both stoichiometries and compositions of complexes. The

experimentally measured masses confirm that each subunit of the dimer is bound to the same ligand (GDP or GppNHp) as the other subunit (since the nucleotide exchange is 90-95% efficient, there is always a portion of GDP-bound K-Ras in solution). Other biochemical techniques have been used to demonstrate the existence of K-Ras dimers but lacked sufficient mass resolution to confirm their specific compositions.[23–29]

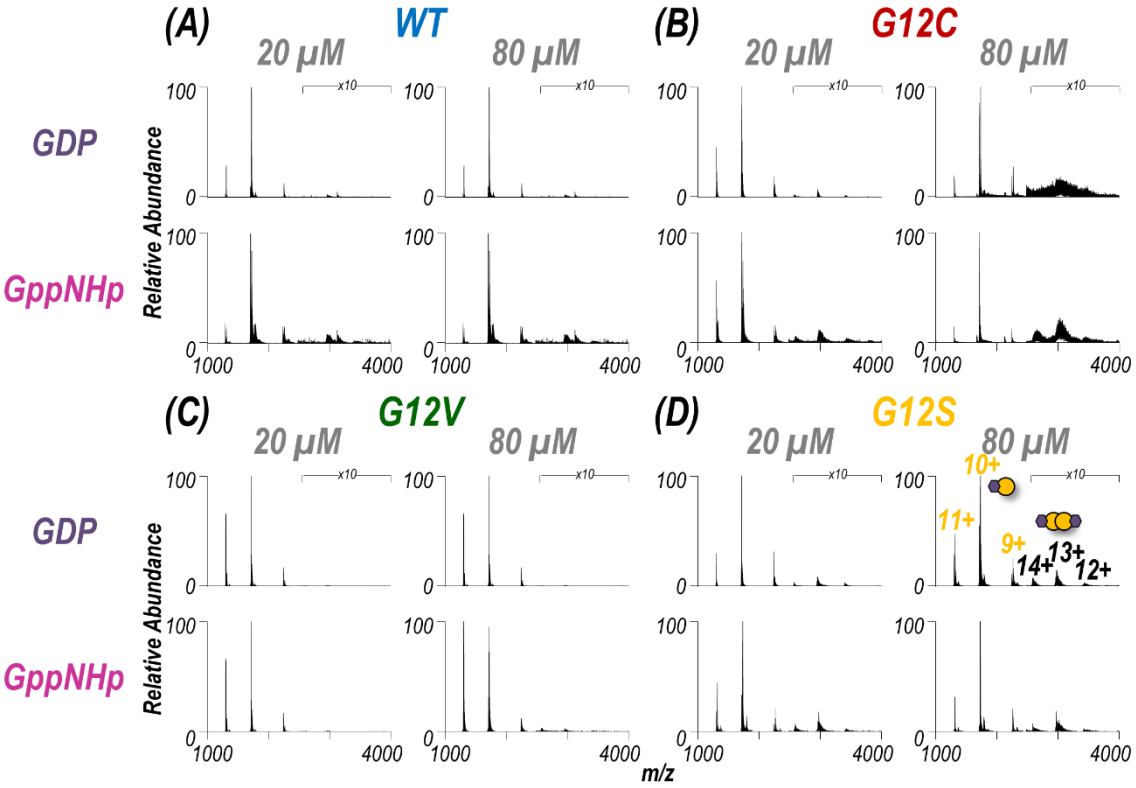

Figure 5.4: Native ESI mass spectra of (A) WT, (B) G12C, (C) G12V, and (D) G12S K-Ras bound to GDP (top) or GppNHp (bottom) (1:1 protein:ligand ratio) at a protein concentration of 20 μM or 80 μM. Observed species are labelled in panel (D, right-side) (9+, 10+, 11+ monomers and 12+, 13+, 14+ homodimers). A bar graph displaying the abundance of each observed homodimer normalized to the TIC is given in Figure 5.5. The theoretical and measured monoisotopic masses for each observed homodimer are reported in Table 5.1.

Table 5.1: Table of theoretical and measured monoisotopic masses for each observed dimer in Figure 5.4. All expected masses account for one divalent Mg^{2+} ion bound per monomer subunit. The reported standard deviations represent triplicate data.

Mass (Da)		GDP + GDP	GppNHp + GppNHp
WT	Theoretical	*39511.327*	*39669.292*
	Measured at 20 µM	*39513 ± 1*	*39668 ± 1*
	Measured at 80 µM	*39511.7 ± 0.4*	*39668.9 ± 0.8*
G12C	Theoretical	*39603.287*	*39761.252*
	Measured at 20 µM	*39603.7 ± 0.4*	*39761.6 ± 0.5*
	Measured at 80 µM	*39603.1 ± 0.5*	*39760.8 ± 0.9*
G12V	Theoretical	*39595.407*	*39753.372*
	Measured at 20 µM	-	-
	Measured at 80 µM	*39593 ± 2*	*39753.1 ± 0.9*
G12S	Theoretical	*39571.347*	*39729.312*
	Measured at 20 µM	*39571.3 ± 0.2*	*39729.1 ± 0.5*
	Measured at 80 µM	*39571.3 ± 0.6*	*39729.9 ± 0.7*

The distribution of homodimers versus monomers for each variant are estimated by comparing normalized abundances of the ions in the native ESI mass spectra shown in **Figure 5.4**. **Figure 5.5** illustrates the relative abundances of each observed K-Ras homodimer normalized to the total ion current for WT, G12C, G12V, and G12S K-Ras bound to GDP or GppNHp for protein concentrations of 20 or 80 µM. A larger bar indicates a greater portion of the dimeric form of the protein relative to the monomeric protein. GppNHp-bound WT K-Ras was observed to form significantly more abundant homodimers compared to its GDP-bound counterpart. This result is in line with the significant role of dimerization in the activation of K-Ras. The same general trend indicating enhanced formation of dimers containing GppNHp over GDP was observed for

both G12C and G12S K-Ras, and for each of these two variants the overall abundances of homodimers containing GDP or GppNHp were substantially higher than the abundances of WT homodimers. Since the G12C and G12S mutations result in constitutively active variants of K-Ras, higher abundances of the homodimers support the idea that oligomerization is important for activation of the enzyme. Interestingly, the abundances of G12V K-Ras homodimers were low in general and were only observed at the higher (80 µM) protein concentration, suggesting dimerization is not a significant factor in maintaining an active state when the bulky Val is substituted for Gly.

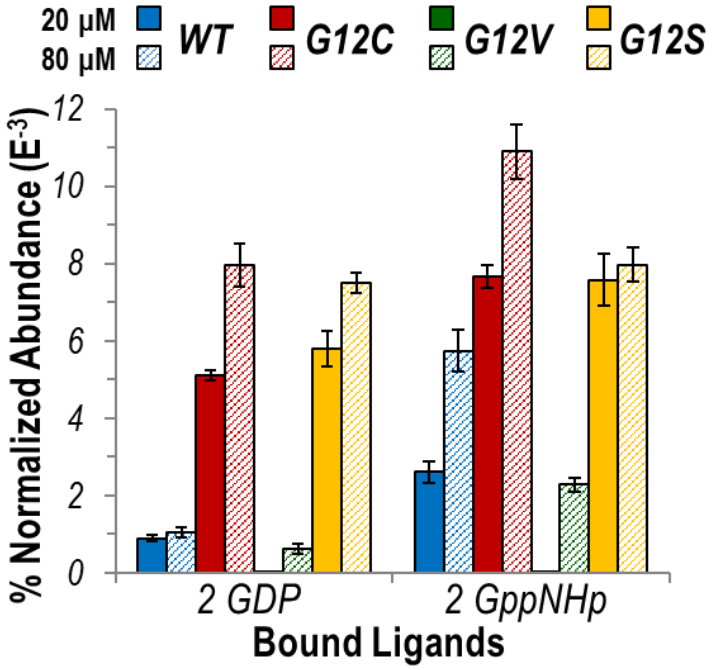

Figure 5.5: Graph displaying the abundance of each K-Ras homodimer normalized to the total ion current (TIC) for the native ESI mass spectra (Figure 5.4) for WT (blue), G12C (red), G12V (green), and G12S (yellow) bound to two GDP or two GppNHp (1:1 ratio) at a protein concentration of 20 µM (solid bars) or 80 µM (hashed bars). GppNHp is a non-hydrolyzable analogue of GTP and represents the active state ligand of K-Ras. The theoretical and measured monoisotopic masses for each observed homodimer are reported in Table 5.1.

In general, the relatively low percentage of dimers (<1% to 11% in **Figure 5.5**) compared to the corresponding monomers is not surprising given that the protein is in solution with no membrane localization to aid in self-assembly.[23,28] Previous dynamic light scattering experiments observed higher order oligomers only for K-Ras bound to another GTP-analogue, guanosine 5'-O-[γ-thio]triphosphate (GTP-γ-S), not GDP nor GppNHP.[26] Although GTP-γ-S is expected to be a better mimic of GTP, for the experimental conditions tested herein this compound hydrolyzed too quickly to allow confident measurements of protein complexation (**Figure 5.6**).

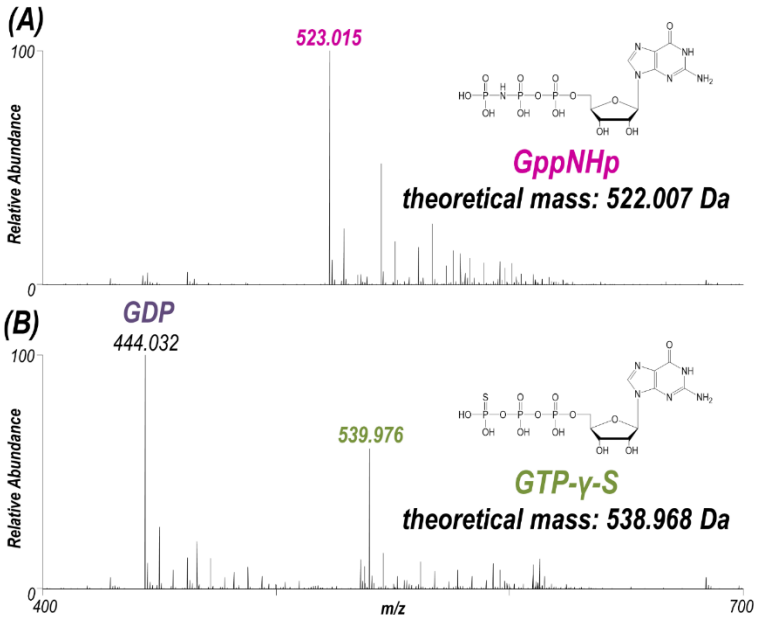

Figure 5.6: ESI mass spectra of the non-hydrolyzable mimics of GTP: (A) GppNHp and (B) GTP-γ-S sprayed in 50 mM ammonium acetate (pH 7.8). The spectrum for GTP-γ-S suggests the ligand is mostly hydrolyzed to GDP.

There is accumulating evidence that WT K-Ras can act as a tumor suppressor and counteract the activating effects of G12X mutations.[72] To mimic cells heterozygous for G12X mutations, each of the three mutants bound to GDP or GppNHp was mixed in a 1:1

ratio with WT K-Ras at 20 or 80 μM total protein concentration prior to ESI. No dimers were observed in the ESI-MS spectra, thus suggesting that homodimers composed of two protein variants (WT and G12X K-Ras) are less stable or membrane localization is required for formation (**Figure 5.7**).

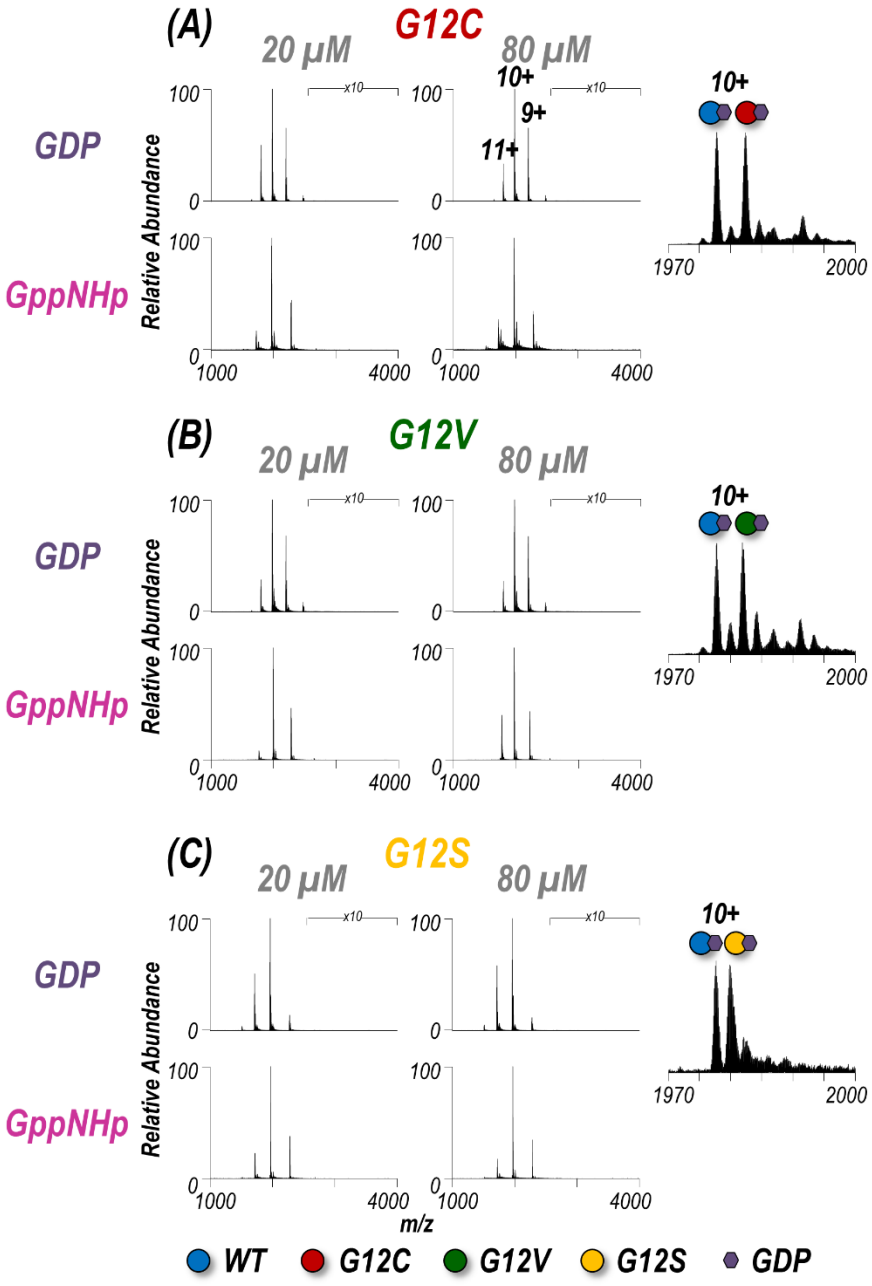

Figure 5.7: Native ESI mass spectra of (A) G12C, (B) G12V, and (C) G12S K-Ras bound to GDP (top) or GppNHp (bottom) (1:1 ratio) with an equimolar amount of WT K-Ras present in solution (total protein concentration of 20 µM or 80 µM). Observed species are labelled in panel (A, top right) (9+, 10+, 11+ monomers of each variant). No dimers were observed under these conditions. Insets show zoomed-in views of 10+ charge states of each variant of GDP-bound K-Ras (*m/z* 1970–2000).

5.4.2 Impact of G12X Mutations on K-Ras:Raf Heterodimer Formation

Understanding how specific G12X mutations in K-Ras affect interactions with downstream effectors is another piece of the puzzle encompassing the mechanism by which individual substitutions impact signaling.[65] Each of the four K-Ras variants bound to either GDP or GppNHp (the non-hydrolyzable analogue of GTP) was combined in a 1:1 ratio with the Ras binding domain of Raf (Raf_{RBD}) to determine the extent to which heterocomplexes are formed in solution. ESI-MS spectra are shown for WT K-Ras in **Figure 5.8** and for the three G12X variants in **Figure 5.9**. K-Ras:Raf_{RBD} heterodimers were observed only for GppNHp-bound K-Ras but not for GDP-bound K-Ras (**Figure 5.8**), a result consistent with the fact that only activated K-Ras (GTP-bound form) should bind Raf_{RBD}. The same outcome is true for the formation of heterodimers of the G12X variants in **Figure 5.9**: G12X:Raf_{RBD} heterodimers were only observed for solutions containing GppNHp, not GDP.

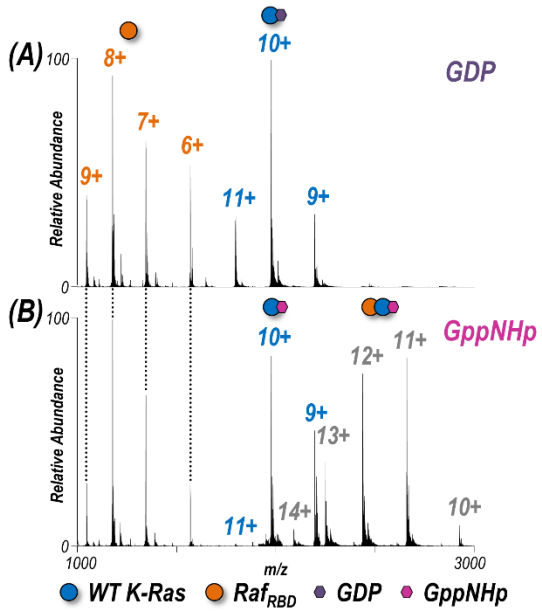

Figure 5.8: Native ESI mass spectra of 1:1 K-Ras:Raf_{RBD} solution of WT K-Ras bound to (A) GDP or (B) GppNHp (1:1 ratio). Observed species are labelled as colored circles (6+, 7+, 8+, 9+ Raf_{RBD} monomers, 9+, 10+, 11+ K-Ras monomers, and 10+, 11+, 12+, 13+, 14+ heterodimers). Corresponding spectra for G12C, G12V, and G12S K-Ras are shown in Figure 5.9. K-Ras:Raf_{RBD} heterodimers were only observed for solutions containing GppNHp (non-hydrolyzable analogue of GTP), not GDP. The relative abundances of each species are estimated from SEC-MS and reported in Figure 5.11 The 12+ heterodimer was selectively isolated and activated to yield the UVPD spectra shown in Figure 5.13.

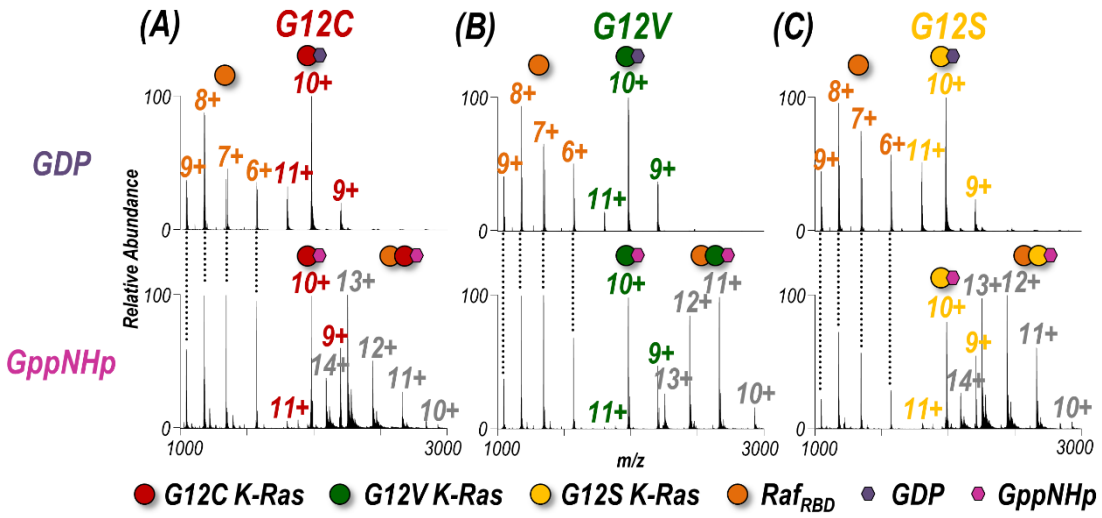

Figure 5.9: Native ESI mass spectra of 1:1 K-Ras:Raf_{RBD} solution of (A) G12C, (B) G12V, and (C) G12S K-Ras bound to GDP (top) or GppNHp (bottom) (1:1 ratio). Observed species are labelled as colored spheres (6+, 7+, 8+, 9+ Raf_{RBD} monomers, 9+, 10+, 11+ K-Ras monomers, and 10+, 11+, 12+, 13+, 14+ heterodimers). Corresponding spectra for WT K-Ras are given in Figure 5.8. K-Ras + Raf_{RBD} heterodimers were only observed for solutions containing GppNHp, not GDP. Very low abundances of G12C and G12S homodimers are also observed. The relative abundances of each species are estimated from SEC-MS and reported in Figure 5.11. The 12+ heterodimer was selectively isolated and activated to yield the UVPD spectra shown in Figure 5.13.

Given that the observed monomeric and dimeric protein complexes span a broad *m*/*z* range, on-line size-exclusion chromatography was used to separate the various complexes in order to allow optimization of MS tuning parameters and improve the accurate measurement of abundances. **Figure 5.10** illustrates extracted ion chromatograms (EICs) derived for the *m*/*z* values corresponding to each key species (K-Ras•GppNHp, Raf_{RBD}, and K-Ras•GppNHp + Raf_{RBD}). Peak areas from the EICs were used to estimate the distributions of the monomeric proteins (K-Ras•GppNHp and Raf_{RBD}) and heterodimers (K-Ras•GppNHp + Raf_{RBD}) for WT K-Ras and each of the three variants (**Figure 5.11**). The portions of K-Ras•GppNHp + Raf_{RBD} heterodimers (green segments)

are the focal point of **Figure 5.11**. G12V yields a significantly lower percentage of heterodimers than WT K-Ras, and conversely G12C and G12S display a larger percentage of heterodimers than WT K-Ras. This general trend in the formation of K-Ras•GppNHp + Raf_{RBD} heterodimers mirrors the results reported above for K-Ras homodimer formation. These results suggest that amino acid substitutions (G12C, G12S) that have enhanced hydrogen-bonding capabilities contribute to stabilizing the β-interface interactions with Raf. In contrast, the bulkier, hydrophobic G12V substitution causes destabilization of this interface.

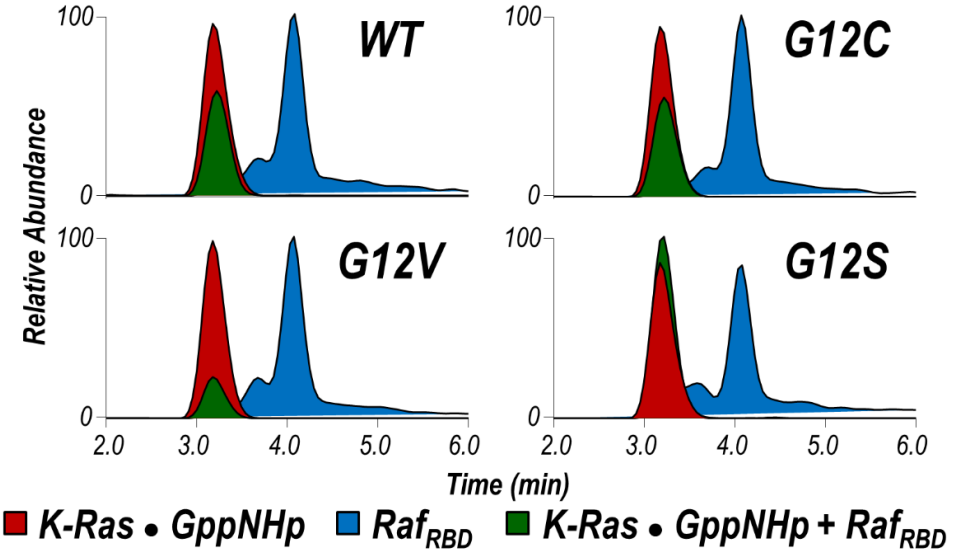

Figure 5.10: EIC traces (2.0–6.0 min) of the *m*/*z* values corresponding to K-Ras•GppNHp (red), Raf_{RBD} (blue), and K-Ras•GppNHp + Raf_{RBD} heterodimer (green) from on-line SEC of solutions containing WT, G12C, G12V, or G12S K-Ras•GppNHp with an equimolar amount of Raf_{RBD}. Peak areas were used to calculate the percent normalized relative abundance of each species reported in the bar graph in Figure 5.11.

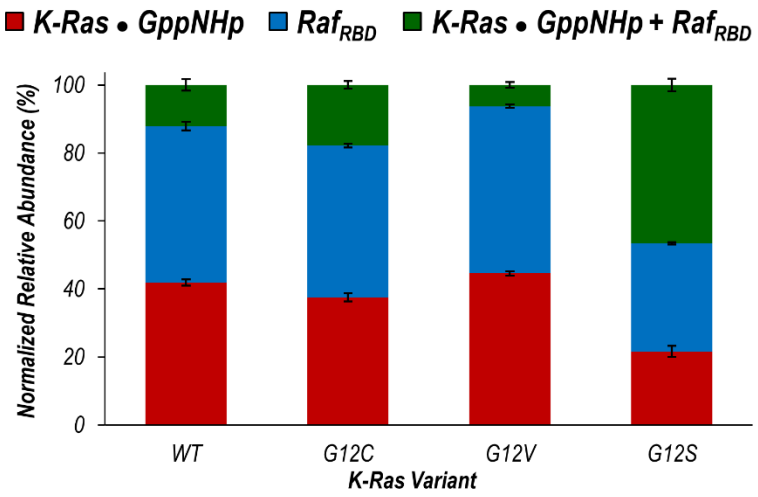

Figure 5.11: Distribution of the normalized relative abundances of K-Ras•GppNHp (red), Raf_{RBD} (blue), and K-Ras•GppNHp + Raf_{RBD} heterodimer (green) from on-line SEC of solutions containing WT, G12C, G12V, or G12S K-Ras•GppNHp with an equimolar amount of Raf_{RBD}. Peak areas of the EIC traces of *m*/*z* values corresponding to each species were used to calculate the reported percentages (Figure 5.10).

5.4.3 Analysis of UVPD Holo Fragment Ions to Examine K-Ras:Raf Heterodimer Interface

To further probe the differences in protein-protein interactions governing the binding of WT and G12X K-Ras to Raf_{RBD}, the most abundant charge state (12+) of each observed heterocomplex (K-Ras•GppNHp + Raf_{RBD}) was subjected to 193 nm UV photoactivation. Deconvoluted mass spectra of the isolated species are shown in **Figure 5.12** confirming that the isolated population is similar for WT and all three variants. **Figure 5.13** displays the UVPD MS/MS spectra for all four K-Ras•GppNHp + Raf_{RBD} complexes. In addition to disassembly of the complexes into their constituent subunits (K-Ras•GppNHp (9+) and Raf_{RBD} (3+)), UVPD also yields diagnostic sequence ions.[56] Deconvolution of the UVPD spectra allows identification of these fragment ions (**Figure 5.14**). Based on the fragmentation patterns from UVPD, sequence coverage maps for each

K-Ras variant are given in **Figure 5.15.** UVPD afforded 85-89% coverage of WT K-Ras or G12X for each of the four complexes.

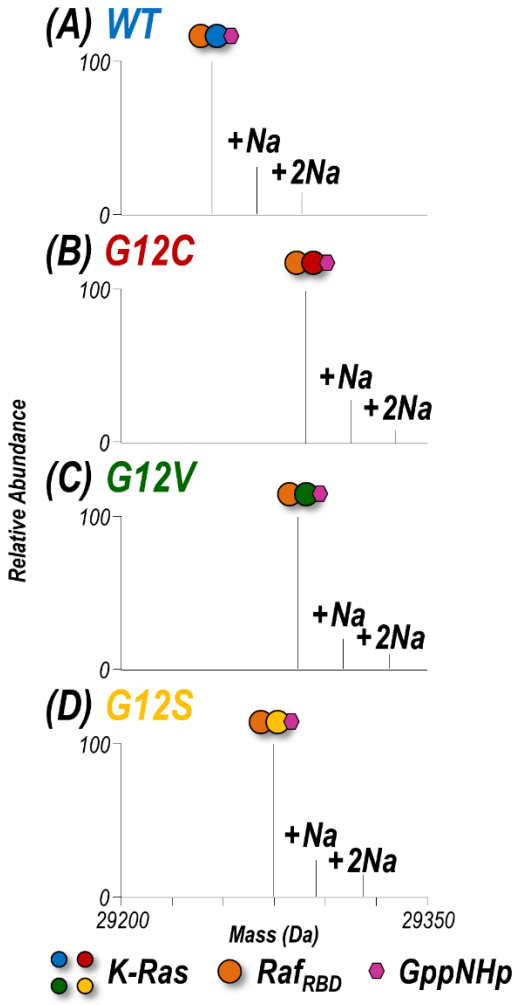

Figure 5.12: (A-D) Deconvoluted mass spectra of the K-Ras•GppNHp + Raf_{RBD} complexes (12+ charge state) selectively isolated for activation by UVPD. The isolated species activated are fairly homogenous with up to two Na adducts present for each variant.

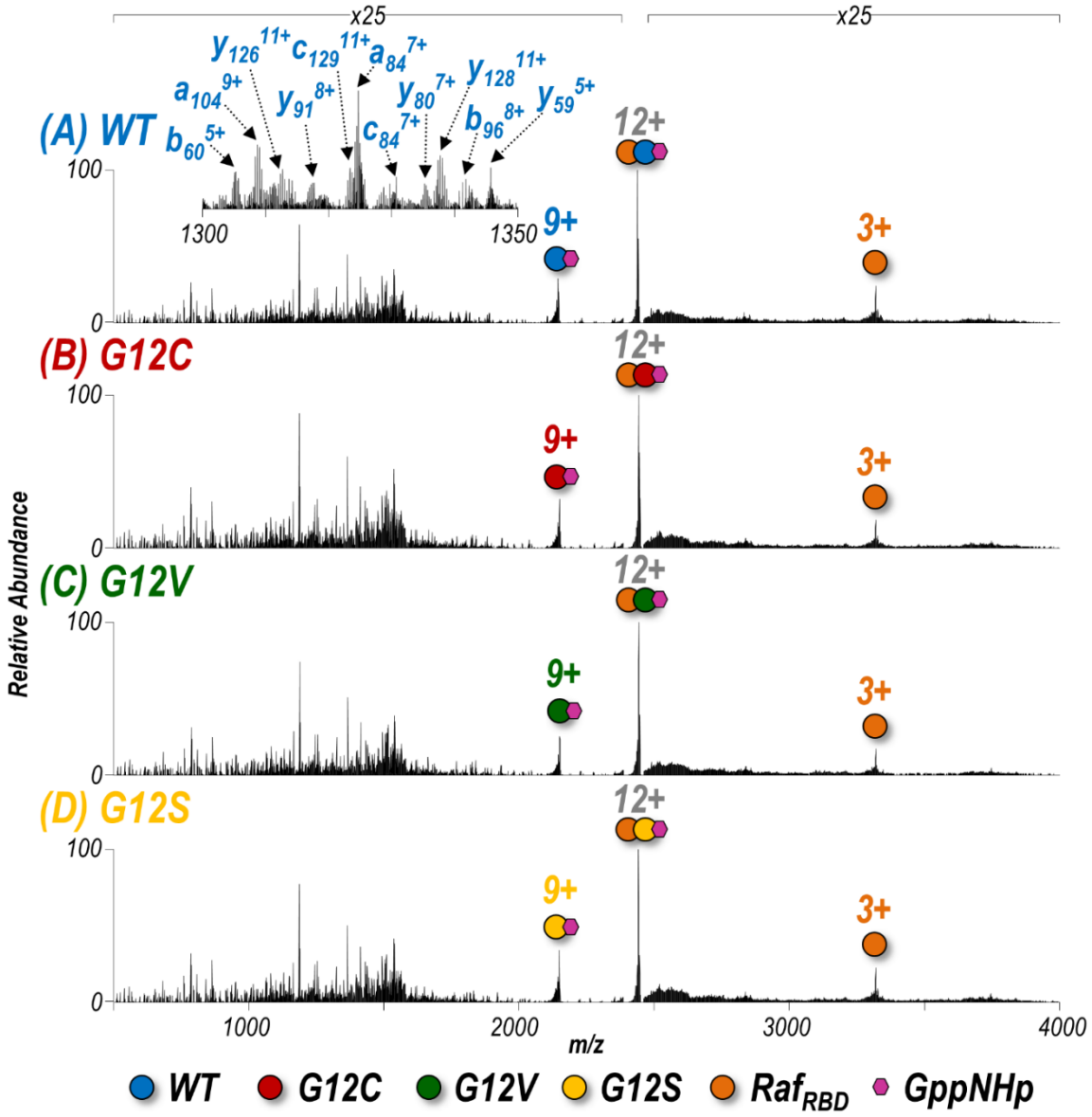

Figure 5.13: (A-D) UVPD mass spectra of the 12+ charge state of K-Ras•GppNHp + Raf_{RBD} heterodimers activated using a single 3 mJ pulse. Selected fragment ions are labelled in the expanded inset (*m/z* 1300-1350) in panel (A). Intact subunits are labelled for K-Ras•GppNHp in the 9+ charge state or Raf_{RBD} in the 3+ charge state.

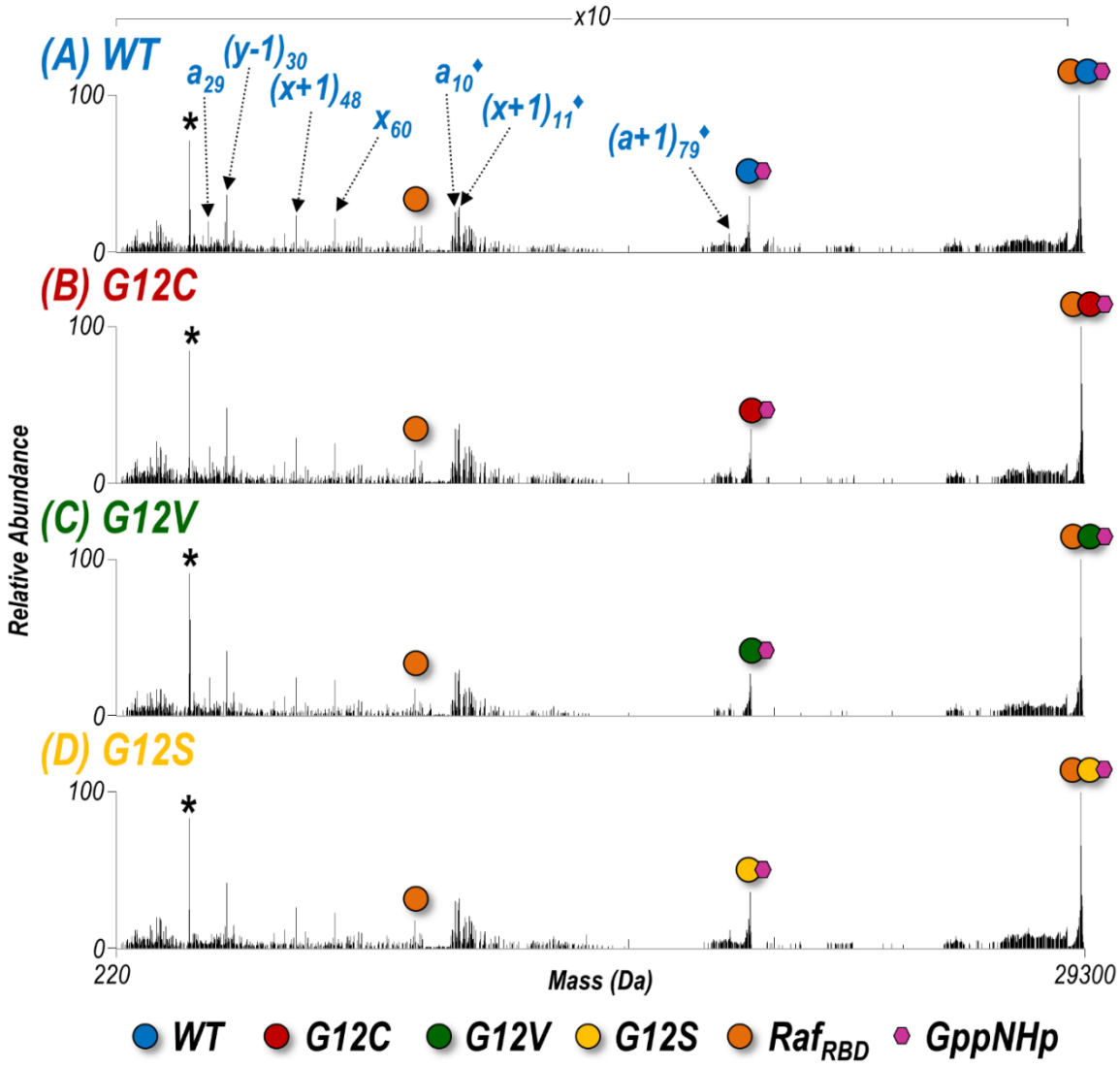

Figure 5.14: (A-D) Deconvoluted UVPD mass spectra (corresponding to the spectra in Figure 5.13) of all K-Ras•GppNHp + Raf_{RBD} complexes (12+ charge state) using one 193 nm pulse at 3 mJ. Several abundant fragment ions are labelled in (A). Holo fragment ions (K-Ras•GppNHp bound to intact Raf_{RBD}) are denoted with ♦. The asterisks represent surviving precursor ions (non-deconvoluted) as an artifact during deconvolution.

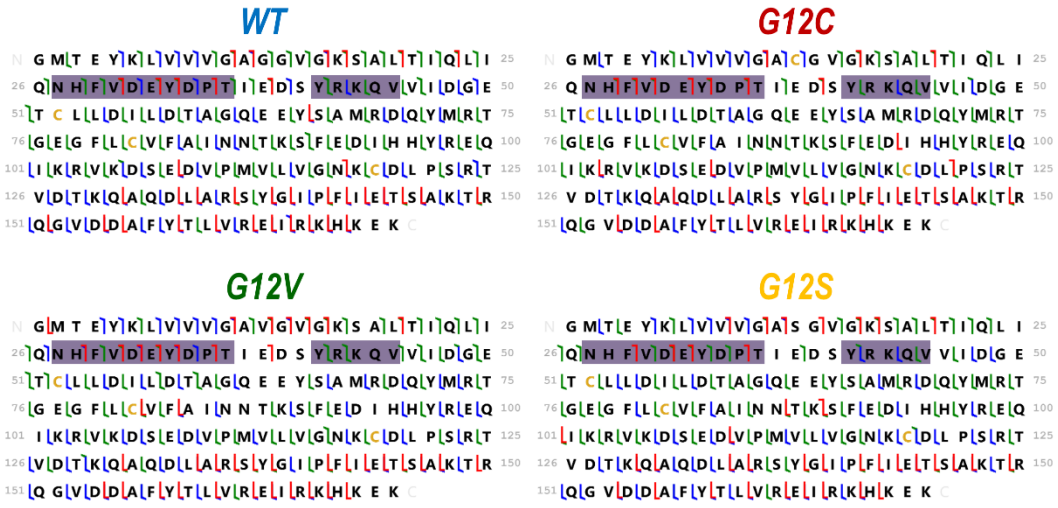

Figure 5.15: Sequence coverage maps of K-Ras based on identification of apo (ligand-free) fragment ions identified in the deconvoluted UVPD spectra shown in Figure 5.14 (12+ charge state of the K-Ras•GppNHp + Raf_{RBD} heterodimer). The β-interface is shaded in purple. The apo ion sequence coverage was 85–89% for K-Ras in all complexes.

The fragment ions generated upon UVPD can be further categorized as apo (Raf_{RBD}-free) or holo (containing Raf_{RBD}) product ions. While traditional HCD typically causes ejection of the intact ligand prior to backbone fragmentation owing to the preferential cleavage of non-covalent interactions during collisional activation, UV photoactivation of protein-ligand complexes yields diagnostic sequence ions that retain non-covalent interactions with the bound ligands, termed holo fragment ions.[55,60–62,73] HCD has been reported to yield holo ions consisting of a portion of a non-covalently bound nucleotide[74] but UVPD consistently allows retention of intact nucleotides like GTP or GppNHp.[62] The high energy imparted to a protein via absorption of 193 nm photons results in activation to excited electronic states and affords preferential cleavage of backbone bonds rather than disruption of electrostatic interactions with bound ligands. Consequently, mapping the location of observed holo ions along the protein backbone affords insight into

ligand-binding interfaces. **Figure 5.16A** displays the sequence of K-Ras with indicators above specific residues to show the sites of backbone cleavages that lead to production of holo ions. The indicators are color-coded to reflect whether the backbone cleavage sites correspond to formation of N-terminal ions (*a*,*b*,*c*), C-terminal ions (*x*,*y*,*z*), or bi-directional ions (i.e. backbone cleavages resulting in complementary N- and C-terminal holo ions). Although UVPD of the K-Ras•Raf_{RBD} complexes caused backbone fragmentation of both the K-Ras and Raf_{RBD} subunits, for streamlined data interpretation Raf_{RBD} was treated as one large ligand and only holo ions containing the intact Raf_{RBD} protein were considered. The crystal structure of K-Ras bound to Raf_{RBD} is shown in **Figure 5.16B** with residues corresponding to the observed sites of backbone cleavages color coded to aid in visualization for WT K-Ras (and corresponding structures for the three G12X mutants given in **Figure 5.17**).

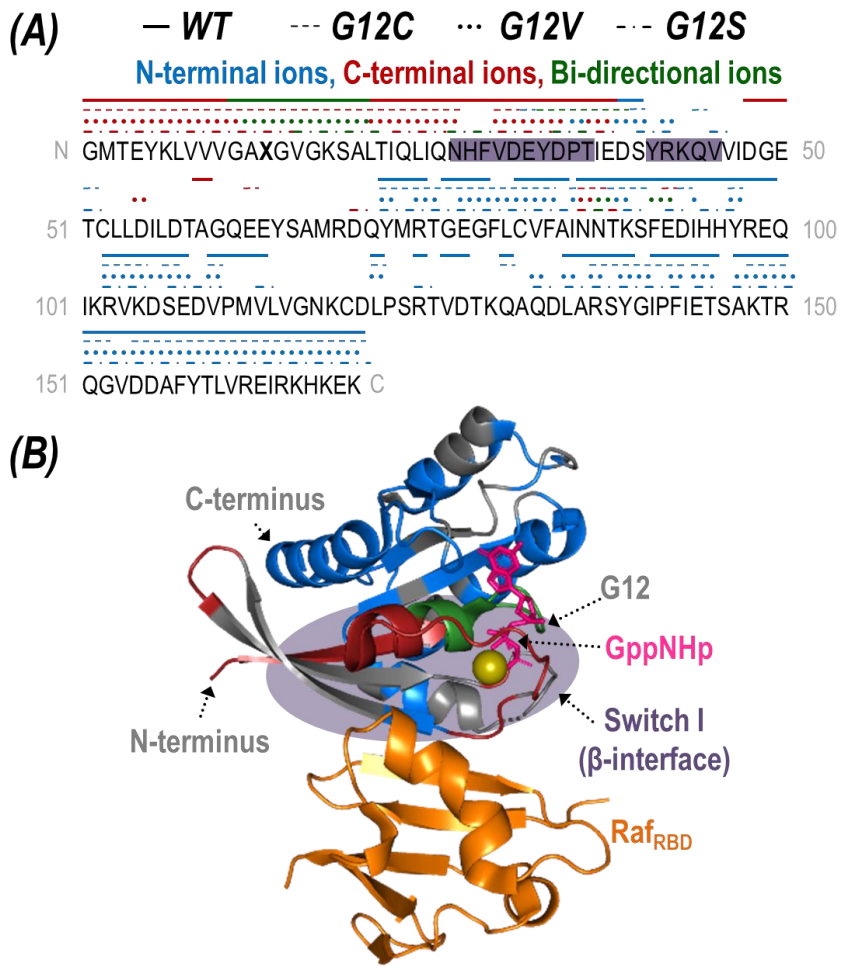

Figure 5.16: (A) The backbone cleavage sites upon UVPD of the K-Ras•GppNHp + Raf_{RBD} heterodimer (12+) are mapped above the sequence of K-Ras (X13 = G, C, V, or S) as lines or symbols for WT (solid), G12C (dashes), G12V (dots), and G12S (pattern). The backbone cleavages that result in N-terminal ions (a,b,c) are colored blue; those that result in C-terminal ions (x,y,z) are colored red; and those that yield complementary N-terminal and C-terminal ions are categorized as bi-directional and are colored green. The β-interface region is shaded in purple. (B) Crystal structure of K-Ras bound to GppNHp and complexed with Raf_{RBD} (PDB ID: 4G0N) with residues colored corresponding to N-terminal (*a*, *b*, *c*-type ions; blue), C-terminal (*x*, *y*, *z*-type ions; red), and bi-directional (green) holo fragment ions observed during UVPD of the 12+ WT heterodimer. Corresponding structures for the G12X mutants are given in Figure 5.17. The original UVPD spectra are shown in Figure 5.13. The GppNHp ligand (a non-hydrolyzable analogue of GTP) is shown as pink sticks and labelled in (B).

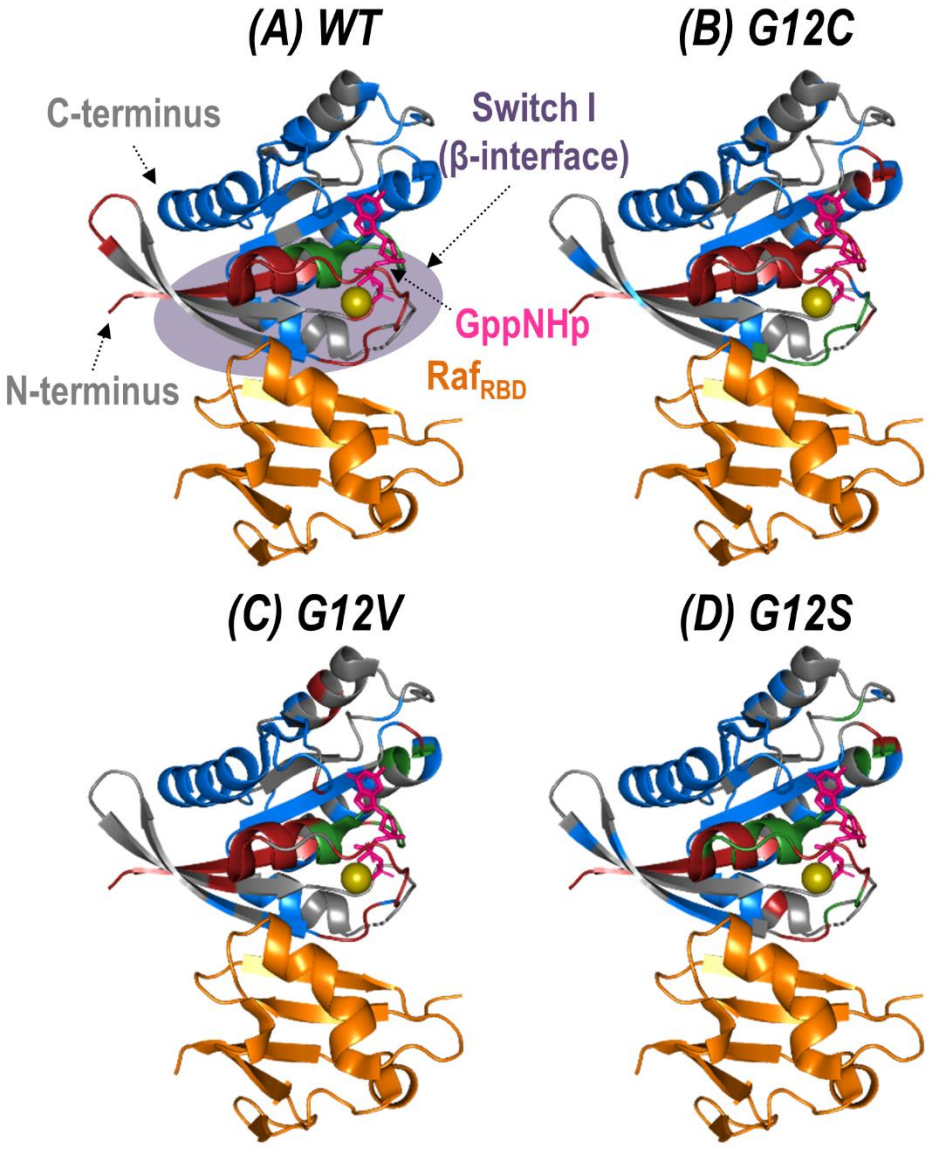

Figure 5.17: Crystal structures of K-Ras bound to GppNHp and complexed with Raf$_{RBD}$ (PDB ID: 4G0N) with residues colored corresponding to backbone cleavages that produce N-terminal (*a*, *b*, *c*-type ions; blue), C-terminal (*x*, *y*, *z*-type ions; red), and bi-directional (green) holo fragment ions observed during UVPD of the 12+ heterodimer formed between (A) WT, (B) G12C, (C) G12V, and (D) G12S K-Ras and Raf$_{RBD}$. These structures correspond with the sequence shown in Figure 5.16A. The original UVPD spectra are shown in Figure 5.13. The GppNHp ligand (a non-hydrolyzable analogue of GTP) is shown as pink sticks and is labelled in (A).

Of the two known interfaces along K-Ras (α- and β-interfaces), effector binding is expected to occur at the stronger β-interface containing Switch-I (residues 27-36, 41-45, shaded in **Figure 5.16A**).[26] The observed backbone cleavage sites that lead to Raf_{RBD}-bound holo ions upon UVPD of the K-Ras•Raf_{RBD} complexes support the β-interface as the primary binding region for WT K-Ras as well as for the three G12X mutants. In particular, backbone cleavages that result in C-terminal (*x*,*y*,*z*) holo ions only occur in the region of K-Ras that is N-terminal to the β-interface, and backbone cleavages that lead to N-terminal (*a*,*b*,*c*) ions occur exclusively in the region C-terminal to the β-interface (**Figure 5.16A**). Moreover, the bi-directional holo ions that result in complementary C-terminal and N-terminal product ions originate from backbone cleavages along or near this expected interface. Further evidence is provided by the apo sequence coverage maps (**Figure 5.15**) in which coverage of the β-interfacial region (shaded in purple) is relatively sparse, suggesting two possibilities. One possibility is that backbone cleavages in the β-interfacial region might instead preferentially produce the mass-shifted holo fragment ions showcased in **Figure 5.16A** (thus depleting the abundances of apo sequence ions). Alternatively, fragmentation along the β-interfacial region might be suppressed owing to its engagement in interactions with Raf_{RBD} (thus stabilizing the β-interfacial region and preventing separation of fragment ions).

Interestingly, there are several C-terminal and bi-directional holo fragment ions originating from backbone cleavages adjacent to residues N86-E92 (C-terminal to the β-interface) which are observed for all three G12X mutants but not WT K-Ras (**Figure 5.16A**). This region is part of the weaker α-interface (residues 86-105, 126-138) where K-Ras homodimerization is thought to occur.[16,26] Perhaps G12X mutants also use the α-interface to bind effector proteins and maintain an active state. However, the fact that fewer holo ions originate from this region suggests either it is a lower population effector binding

region compared to the β-interface or the non-covalent interactions stabilizing this alternative binding mode are too weak to survive photodissociation (thus preventing survival of holo ions). The observations about the involvement of the α-interface merit future investigation using other traditional biophysical methods.

5.4.4 Variations in UVPD Cleavage Efficiency for G12X K-Ras:Raf Heterodimers

Since the mutated G12 position is located along the outer surface of K-Ras, it is expected that the conformational changes induced by the substitution result in longer-range changes in regions of the protein involved in dimer formation.[62] UVPD has previously been demonstrated to be sensitive to these types of structural changes for other protein complexes.[59–62] Specifically, variations in the efficiency of backbone cleavage induced by UVPD relative to the same protein in a different state are determined for each residue. The extent to which a given region engages in stabilizing intramolecular interactions (i.e. protein organization and rigidity) can be inferred from enhancement or suppression in UVPD backbone cleavage efficiency.[59–62] Details are provided in the Experimental section on how backbone fragment ion abundances are summed and how cleavage efficiency is determined to generate the UVPD backbone cleavage efficiency plots shown in **Figure 5.18**. Comparisons of the backbone cleavage efficiencies of G12X mutants to WT K-Ras are best visualized as plots of the differences in UVPD backbone cleavage efficiency for each residue (i.e. backbone cleavage efficiency of WT subtracted from the backbone cleavage efficiency of each mutant at each position) (**Figure 5.19**). These differences are represented as a heat map in which suppression of UVPD (values that fall below the zero axis) or enhancement of UVPD (values that lie above the zero axis) compared to UVPD of WT K-Ras are highlighted in blue and red, respectively (**Figure 5.20A**). The heat map

values are imprinted on the crystal structure of K-Ras•GppNHp + Raf_{RBD} to aid in relating conformational changes to structural features of the protein (**Figure 5.20B-D**).

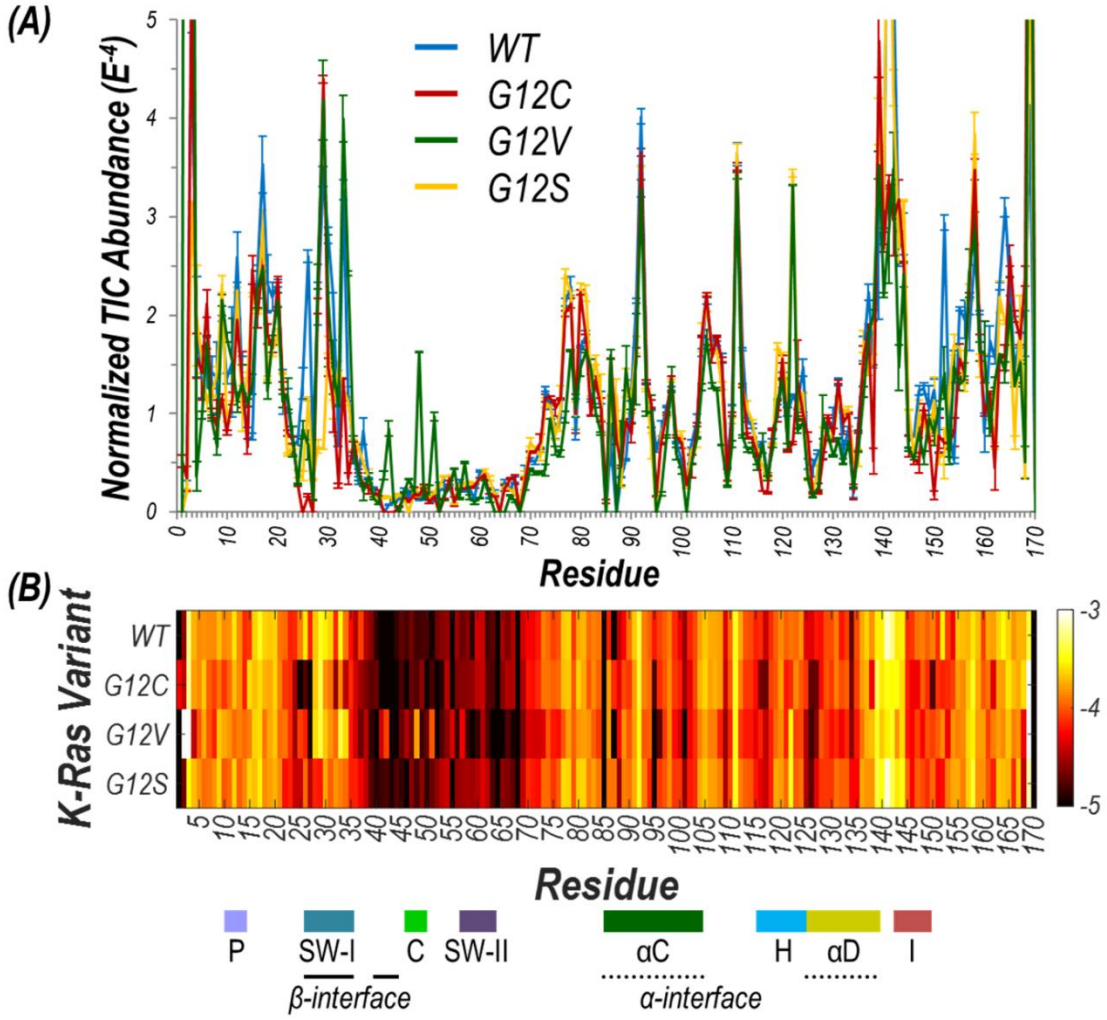

Figure 5.18: (A) Normalized TIC abundance of summed holo and apo product ions plotted per residue for each K-Ras•GppNHp + Raf_{RBD} heterodimer examined. These plots were used to create the difference plots shown in Figure 5.19 by subtraction of the values for each K-Ras variant from the corresponding values for WT K-Ras. (B) Heat map of the log of the values shown in (A). Relevant loops, α-helices, and interfaces are labelled underneath the *x*-axis.

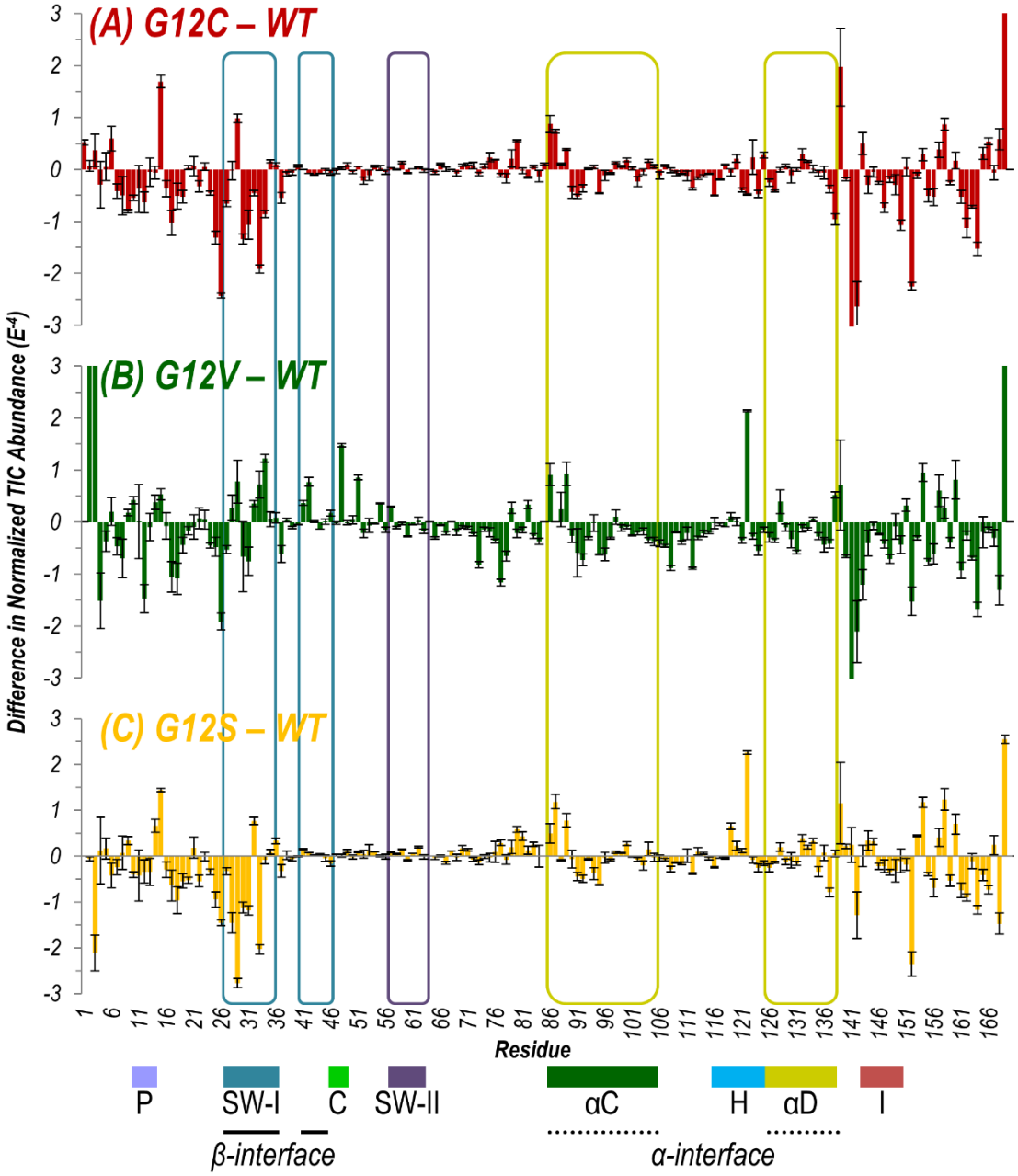

Figure 5.19: Difference plots showing the change in summed abundances of holo and apo fragment ions produced upon UVPD for Raf_{RBD}-bound heterodimers of (A) G12C, (B) G12V, and (C) G12S K-Ras variants compared to WT. The UVPD fragmentation plot for each of the complexes is shown in Figure 5.18. Relevant loops, α-helices, and interfaces are labelled underneath the *x*-axis, and the regions of particular interest (alpha interface, beta interface, and switch II) are bracketed for emphasis.

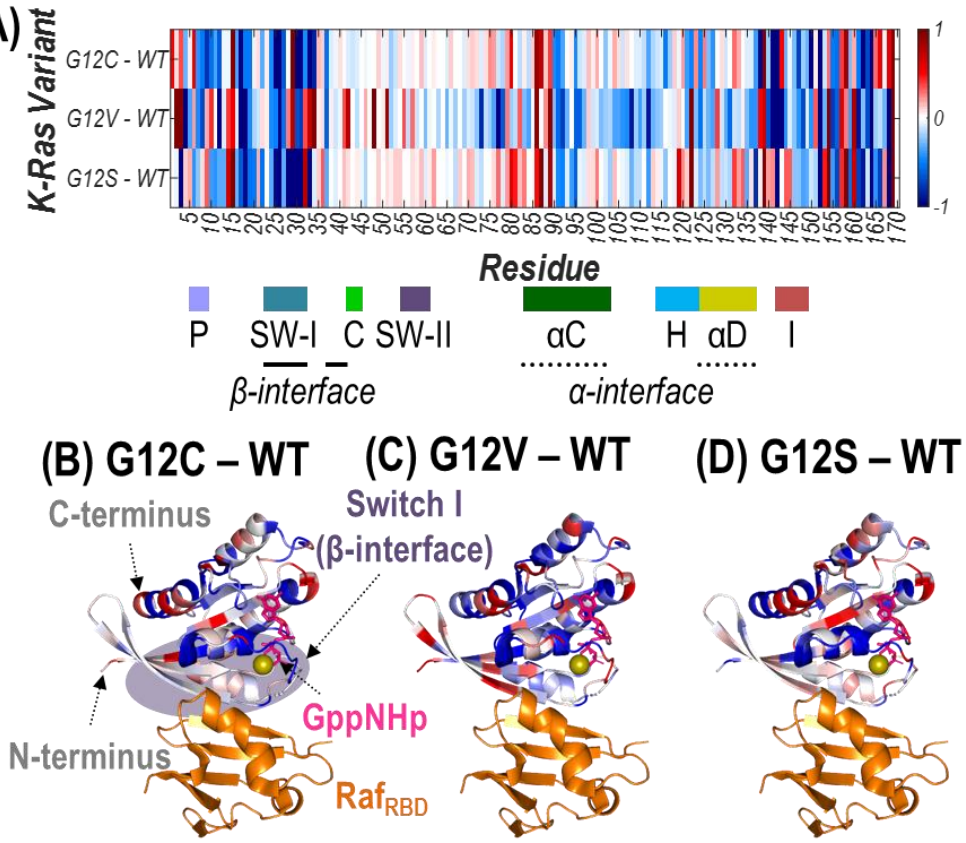

Figure 5.20: Heat maps of the enhancement (red) and suppression (blue) of UVPD for Raf_{RBD}-bound heterodimers shown as a linear map across the sequence (A) or displayed along the crystal structure of K-Ras bound to GppNHp (non-hydrolyzable analogue of GTP) and complexed with Raf_{RBD} for (B) G12C, (C) G12V, and (D) G12S K-Ras variants relative to WT K-Ras. These heat maps are difference plots: (i.e. G12X – WT). The colored regions represent statistically significant changes in cleavage efficiency of the protein backbone during UVPD based on the difference plots in Figure 5.19. The GppNHp ligand (pink) is shown as sticks and labelled in (B). The β-interface region is highlighted in purple in (B). Relevant loops, α-helices, and interfaces are labelled underneath the *x*-axis of (A).

To gain insight into how the identity of the G12X mutations impacts the effects on signaling, we focus on conformational differences observed in three key regions: β-interface (switch I: residues 27-36, 41-45), switch II (residues 58-64), and α-interface (α-

C and α-D helices: residues 86-105 and 126-138). Zoomed-in views for these three regions of the difference plots shown in **Figure 5.19** help to clarify the trends in UVPD backbone cleavage efficiency for each of the three variants compared to WT (**Figure 5.21**). **Figure 5.22** summarizes the observed enhancement or suppression in UVPD backbone cleavage efficiency of those three regions for Raf_{RBD}-bound heterodimers of G12C, G12V, and G12S compared to WT K-Ras. G12C and G12S result in similar changes in these regions, mainly stabilization of the β-interface (e.g., suppression of UVPD). Conversely the G12V substitution favors increased proximity of the helices in the α-interfacial region (observed as suppression of UVPD) and destabilization of the β-interface (resulting in enhancement of UVPD).

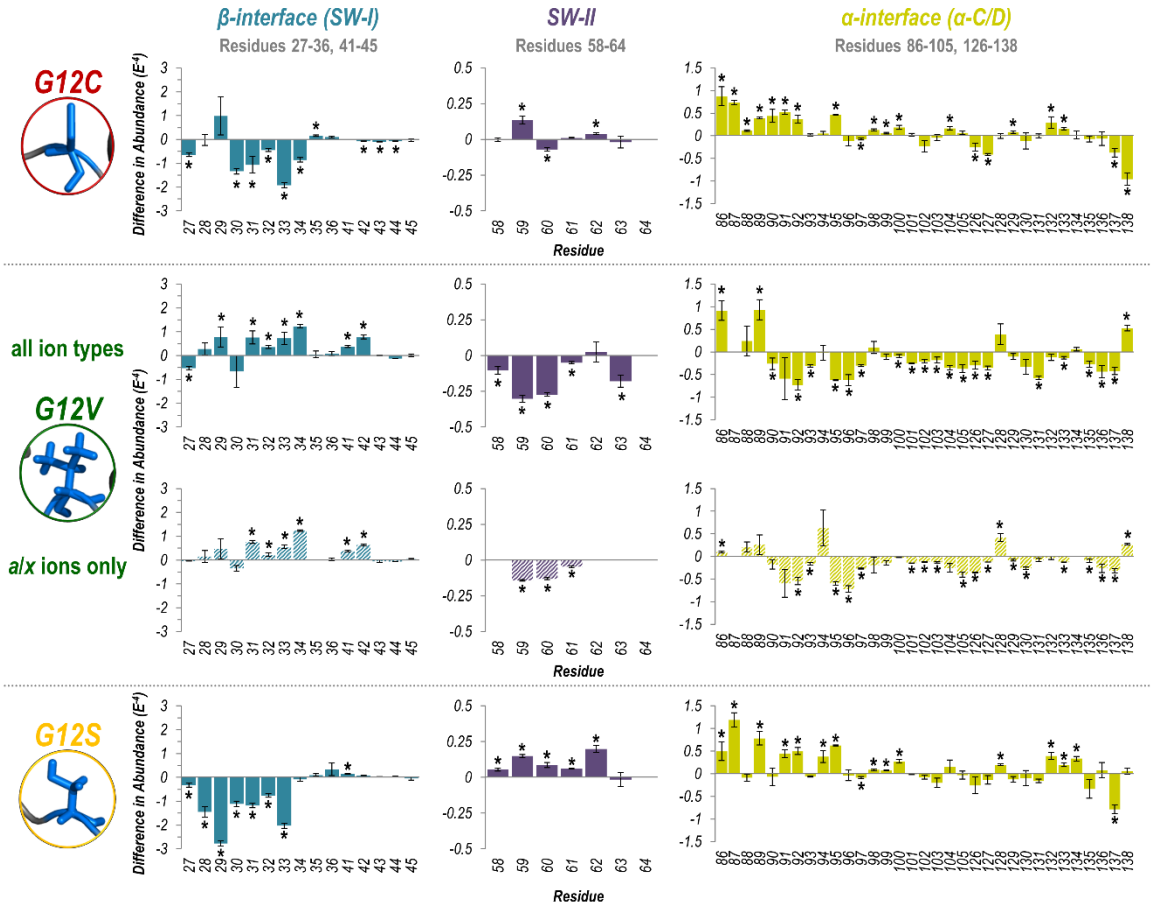

Figure 5.21: Difference plots shown in Figure 5.19 for Raf_{RBD}-bound heterodimers of G12C, G12V, and G12S K-Ras variants compared to WT zoomed-in on three key regions: β-interface (switch I), switch II, and α-interface (α-C and α-D helices). Asterisks indicate residues at which the summed intensity for the given variant is significantly different than WT at the 99% confidence level ($p \leq 0.01$). Figure 5.2 gives plots of calculated *p*-values for all residues. For the G12V variant, the difference plot is also shown considering only *a*/*x*-type fragment ions to demonstrate the same trends are observed when summing all ion types.

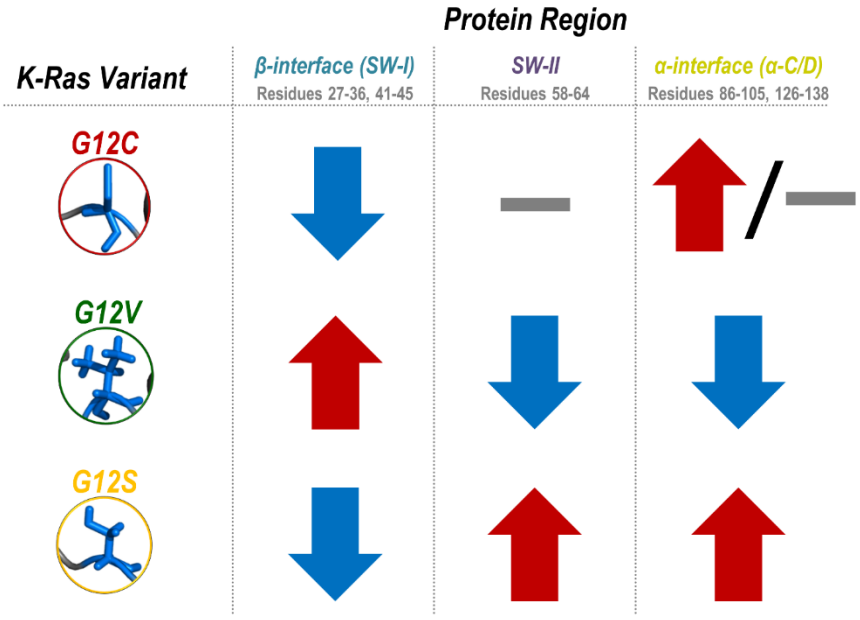

Figure 5.22: Summary of the observed enhancement (red) or suppression (blue) in UVPD backbone cleavage efficiency compared to the WT K-Ras for Raf_{RBD}-bound heterodimers of G12C, G12V, and G12S K-Ras in three key regions: β-interface (switch I), switch II, and α-interface (α-C and α-D helices). The difference plots from which these trends were determined are given in Figure 5.19.

These observations bring new light to a previous study that used UVPD-MS to evaluate conformational changes that occurred for K-Ras and its three G12X mutants during the GTP loading step of K-Ras activation.[62] In the previous study, a more stable α-helical region was inferred for G12C K-Ras in comparison to WT K-Ras based on suppression of UVPD in that region, whereas G12S K-Ras exhibited more flexibility in the β-interface region based on enhancement of UVPD.[62] Both of these findings are consistent with the adoption of a more stable β-interface upon Raf_{RBD} binding in the present study (i.e. given the β-interface was found to be more flexible, more intramolecular contacts could be formed upon Raf binding). For G12V K-Ras compared to WT K-Ras, the converse was observed previously: the β-interface appeared to be more rigid (stabilized by

more interactions; lower UVPD fragmentation efficiency) after substitution of GppNHp for GDP.[62] Again this finding correlates with the more stabilized α-interface of G12V after Raf_{RBD} binding as evidenced by the decreased UVPD fragmentation efficiency in the present study. This outcome implies engagement of fewer interactions between Raf_{RBD} and the β-interface, since G12V K-Ras was more rigidly pre-organized prior to effector binding. Collectively these results suggest that mutations of K-Ras which introduce hydrogen-bonding groups (G12C, G12S) result in a stabilized β-interface, although it is also acknowledged that thiols form weaker hydrogen bonds than alcohols.[75] In contrast, a bulkier, more hydrophobic substitution (G12V) relies preferentially on contacts along the α-interface for oncogenic activation of K-Ras.

5.5 CONCLUSION

Native MS and UVPD-MS were used to probe homo- and hetero-dimers of WT and G12X mutants of K-Ras, along with its effector protein Raf. K-Ras formed more homodimers when bound to a GTP-analogue compared to GDP for the WT, G12C, and G12S variants. G12V K-Ras only formed homodimers at a relatively high protein concentration. Similar results were observed for heterodimer formation between K-Ras and the Ras binding domain of effector protein Raf: compared to WT K-Ras, G12V K-Ras yielded less abundant heterodimers in contrast to G12C and G12S K-Ras. Characterization of the K-Ras•GppNHp + Raf_{RBD} heterocomplexes by UVPD revealed that all three G12X mutants prefer binding along the β-interface, which is the expected effector binding region for WT K-Ras. However, there is also evidence that the three mutants, but not WT K-Ras, can bind Raf along the weaker α-interface as well. Moreover, comparison of UVPD backbone cleavage efficiencies for the G12X mutants relative to WT K-Ras afforded insight into longer-range conformational changes responsible for observed differences in

downstream signaling. Specifically, the G12C and G12S substitutions (ones that introduce hydrogen-bonding groups) resulted in a stabilized β-interface, whereas the G12V mutation (a bulky, hydrophobic substitution) yielded tighter helical bundles along the α-interface. G-domain non-covalent interactions (α- and β-interfaces) are only one of the factors governing homo- and hetero-dimerization, along with membrane localization by post-translational modifications along the hypervariable region of K-Ras or other scaffold proteins. This work offers new insight into the seemingly complex mechanism relating the identity of G12X mutations to different downstream effects.

5.6 REFERENCES

(1) Colicelli, J. Human RAS Superfamily Proteins and Related GTPases. *Sci. STKE Signal Transduct. Knowl. Environ.* **2004**, *2004*, RE13.

(2) Lavoie, H.; Therrien, M. Regulation of RAF Protein Kinases in ERK Signalling. *Nat. Rev. Mol. Cell Biol.* **2015**, *16*, 281–298.

(3) Prior, I. A.; Muncke, C.; Parton, R. G.; Hancock, J. F. Direct Visualization of Ras Proteins in Spatially Distinct Cell Surface Microdomains. *J. Cell Biol.* **2003**, *160*, 165–170.

(4) Castellano, E.; Santos, E. Functional Specificity of Ras Isoforms. *Genes Cancer* **2011**, *2*, 216–231.

(5) Ntai, I.; Fornelli, L.; DeHart, C. J.; Hutton, J. E.; Doubleday, P. F.; LeDuc, R. D.; Nispen, A. J. van; Fellers, R. T.; Whiteley, G.; Boja, E. S.; Rodriguez, H.; Kelleher, N. L. Precise Characterization of KRAS4b Proteoforms in Human Colorectal Cells and Tumors Reveals Mutation/Modification Cross-Talk. *Proc. Natl. Acad. Sci.* **2018**, 201716122.

(6) Prior, I. A.; Lewis, P. D.; Mattos, C. A Comprehensive Survey of Ras Mutations in Cancer. *Cancer Res.* **2012**, *72*, 2457–2467.

(7) Rajalingam, K.; Schreck, R.; Rapp, U. R.; Albert, Š. Ras Oncogenes and Their Downstream Targets. *Biochim. Biophys. Acta BBA - Mol. Cell Res.* **2007**, *1773*, 1177–1195.

(8) Simanshu, D. K.; Nissley, D. V.; McCormick, F. RAS Proteins and Their Regulators in Human Disease. *Cell* **2017**, *170*, 17–33.

(9) Zimmermann, G.; Papke, B.; Ismail, S.; Vartak, N.; Chandra, A.; Hoffmann, M.; Hahn, S. A.; Triola, G.; Wittinghofer, A.; Bastiaens, P. I. H.; Waldmann, H. Small Molecule Inhibition of the KRAS–PDEδ Interaction Impairs Oncogenic KRAS Signaling. *Nature* **2013**, *497*, 638–642.

(10) Spoerner, M.; Nuehs, A.; Herrmann, C.; Steiner, G.; Kalbitzer, H. R. Slow Conformational Dynamics of the Guanine Nucleotide-Binding Protein Ras Complexed with the GTP Analogue GTPγS. *FEBS J.* **2007**, *274*, 1419–1433.
(11) Lim, S. M.; Westover, K. D.; Ficarro, S. B.; Harrison, R. A.; Choi, H. G.; Pacold, M. E.; Carrasco, M.; Hunter, J.; Kim, N. D.; Xie, T.; Sim, T.; Jänne, P. A.; Meyerson, M.; Marto, J. A.; Engen, J. R.; Gray, N. S. Therapeutic Targeting of Oncogenic K-Ras by a Covalent Catalytic Site Inhibitor. *Angew. Chem. Int. Ed.* **2014**, *53*, 199–204.
(12) Harrison, R. A.; Lu, J.; Carrasco, M.; Hunter, J.; Manandhar, A.; Gondi, S.; Westover, K. D.; Engen, J. R. Structural Dynamics in Ras and Related Proteins upon Nucleotide Switching. *J. Mol. Biol.* **2016**, *428*, 4723–4735.
(13) Hobbs, G. A.; Wittinghofer, A.; Der, C. J. Selective Targeting of the KRAS G12C Mutant: Kicking KRAS When It's Down. *Cancer Cell* **2016**, *29*, 251–253.
(14) Lu, S.; Jang, H.; Nussinov, R.; Zhang, J. The Structural Basis of Oncogenic Mutations G12, G13 and Q61 in Small GTPase K-Ras4B. *Sci. Rep.* **2016**, *6*, 21949.
(15) Ostrem, J. M. L.; Shokat, K. M. Direct Small-Molecule Inhibitors of KRAS: From Structural Insights to Mechanism-Based Design. *Nat. Rev. Drug Discov.* **2016**, *15*, 771–785.
(16) Spencer-Smith, R.; Koide, A.; Zhou, Y.; Eguchi, R. R.; Sha, F.; Gajwani, P.; Santana, D.; Gupta, A.; Jacobs, M.; Herrero-Garcia, E.; Cobbert, J.; Lavoie, H.; Smith, M.; Rajakulendran, T.; Dowdell, E.; Okur, M. N.; Dementieva, I.; Sicheri, F.; Therrien, M.; Hancock, J. F.; Ikura, M.; Koide, S.; O'Bryan, J. P. Inhibition of RAS Function through Targeting an Allosteric Regulatory Site. *Nat. Chem. Biol.* **2017**, *13*, 62–68.
(17) Welsch, M. E.; Kaplan, A.; Chambers, J. M.; Stokes, M. E.; Bos, P. H.; Zask, A.; Zhang, Y.; Sanchez-Martin, M.; Badgley, M. A.; Huang, C. S.; Tran, T. H.; Akkiraju, H.; Brown, L. M.; Nandakumar, R.; Cremers, S.; Yang, W. S.; Tong, L.; Olive, K. P.; Ferrando, A.; Stockwell, B. R. Multivalent Small-Molecule Pan-RAS Inhibitors. *Cell* **2017**, *168*, 878-889.e29.
(18) Ostrem, J. M.; Peters, U.; Sos, M. L.; Wells, J. A.; Shokat, K. M. K-Ras(G12C) Inhibitors Allosterically Control GTP Affinity and Effector Interactions. *Nature* **2013**, *503*, 548–551.
(19) Mazhab-Jafari, M. T.; Marshall, C. B.; Smith, M. J.; Gasmi-Seabrook, G. M. C.; Stathopulos, P. B.; Inagaki, F.; Kay, L. E.; Neel, B. G.; Ikura, M. Oncogenic and RASopathy-Associated K-RAS Mutations Relieve Membrane-Dependent Occlusion of the Effector-Binding Site. *Proc. Natl. Acad. Sci.* **2015**, *112*, 6625–6630.
(20) Marcus, K.; Mattos, C. Direct Attack on RAS: Intramolecular Communication and Mutation-Specific Effects. *Clin. Cancer Res.* **2015**, *21*, 1810–1818.
(21) Athuluri-Divakar, S. K.; Vasquez-Del Carpio, R.; Dutta, K.; Baker, S. J.; Cosenza, S. C.; Basu, I.; Gupta, Y. K.; Reddy, M. V. R.; Ueno, L.; Hart, J. R.; Vogt, P. K.; Mulholland, D.; Guha, C.; Aggarwal, A. K.; Reddy, E. P. A Small Molecule RAS-

Mimetic Disrupts RAS Association with Effector Proteins to Block Signaling. *Cell* **2016**, *165*, 643–655.
(22) Samatar, A. A.; Poulikakos, P. I. Targeting RAS-ERK Signalling in Cancer: Promises and Challenges. *Nat. Rev. Drug Discov.* **2014**, *13*, 928–942.
(23) Inouye, K.; Mizutani, S.; Koide, H.; Kaziro, Y. Formation of the Ras Dimer Is Essential for Raf-1 Activation. *J. Biol. Chem.* **2000**, *275*, 3737–3740.
(24) Güldenhaupt, J.; Rudack, T.; Bachler, P.; Mann, D.; Triola, G.; Waldmann, H.; Kötting, C.; Gerwert, K. N-Ras Forms Dimers at POPC Membranes. *Biophys. J.* **2012**, *103*, 1585–1593.
(25) Lin, W.-C.; Iversen, L.; Tu, H.-L.; Rhodes, C.; Christensen, S. M.; Iwig, J. S.; Hansen, S. D.; Huang, W. Y. C.; Groves, J. T. H-Ras Forms Dimers on Membrane Surfaces via a Protein–Protein Interface. *Proc. Natl. Acad. Sci.* **2014**, *111*, 2996–3001.
(26) Muratcioglu, S.; Chavan, T. S.; Freed, B. C.; Jang, H.; Khavrutskii, L.; Freed, R. N.; Dyba, M. A.; Stefanisko, K.; Tarasov, S. G.; Gursoy, A.; Keskin, O.; Tarasova, N. I.; Gaponenko, V.; Nussinov, R. GTP-Dependent K-Ras Dimerization. *Structure* **2015**, *23*, 1325–1335.
(27) Nickerson, A.; Huang, T.; Lin, L.-J.; Nan, X. Photoactivated Localization Microscopy with Bimolecular Fluorescence Complementation (BiFC-PALM) for Nanoscale Imaging of Protein-Protein Interactions in Cells. *PLOS ONE* **2014**, *9*, e100589.
(28) Nan, X.; Tamgüney, T. M.; Collisson, E. A.; Lin, L.-J.; Pitt, C.; Galeas, J.; Lewis, S.; Gray, J. W.; McCormick, F.; Chu, S. Ras-GTP Dimers Activate the Mitogen-Activated Protein Kinase (MAPK) Pathway. *Proc. Natl. Acad. Sci.* **2015**, *112*, 7996–8001.
(29) Ambrogio, C.; Köhler, J.; Zhou, Z.-W.; Wang, H.; Paranal, R.; Li, J.; Capelletti, M.; Caffarra, C.; Li, S.; Lv, Q.; Gondi, S.; Hunter, J. C.; Lu, J.; Chiarle, R.; Santamaría, D.; Westover, K. D.; Jänne, P. A. KRAS Dimerization Impacts MEK Inhibitor Sensitivity and Oncogenic Activity of Mutant KRAS. *Cell* **2018**, *172*, 857-868.e15.
(30) Cho, K.-J.; Hancock, J. F. Ras Nanoclusters. *Small GTPases* **2013**, *4*, 57–60.
(31) Zhou, Y.; Hancock, J. F. Ras Nanoclusters: Versatile Lipid-Based Signaling Platforms. *Biochim. Biophys. Acta BBA - Mol. Cell Res.* **2015**, *1853*, 841–849.
(32) Thompson, H. US National Cancer Institute's New Ras Project Targets an Old Foe. *Nat. Med.* **2013**, *19*, 949–950.
(33) Wu, H. Higher-Order Assemblies in a New Paradigm of Signal Transduction. *Cell* **2013**, *153*, 287–292.
(34) Santos, E. Dimerization Opens New Avenues into Ras Signaling Research. *Sci Signal* **2014**, *7*, pe12–pe12.
(35) Langeberg, L. K.; Scott, J. D. Signalling Scaffolds and Local Organization of Cellular Behaviour. *Nat. Rev. Mol. Cell Biol.* **2015**, *16*, 232–244.
(36) Chen, M.; Peters, A.; Huang, T.; Nan, X. Ras Dimer Formation as a New Signaling Mechanism and Potential Cancer Therapeutic Target. *Mini Rev. Med. Chem.* **2016**, *16*, 391–403.

(37) Liko, I.; Allison, T. M.; Hopper, J. T.; Robinson, C. V. Mass Spectrometry Guided Structural Biology. *Curr. Opin. Struct. Biol.* **2016**, *40*, 136–144.
(38) Leney, A. C.; Heck, A. J. R. Native Mass Spectrometry: What Is in the Name? *J. Am. Soc. Mass Spectrom.* **2017**, *28*, 5–13.
(39) Konermann, L.; Vahidi, S.; Sowole, M. A. Mass Spectrometry Methods for Studying Structure and Dynamics of Biological Macromolecules. *Anal. Chem.* **2014**, *86*, 213–232.
(40) Pirrone, G. F.; Iacob, R. E.; Engen, J. R. Applications of Hydrogen/Deuterium Exchange MS from 2012 to 2014. *Anal. Chem.* **2014**, *87*, 99–118.
(41) Cammarata, M.; Lin, K.-Y.; Pruet, J.; Liu, H.; Brodbelt, J. Probing the Unfolding of Myoglobin and Domain C of PARP-1 with Covalent Labeling and Top-Down Ultraviolet Photodissociation Mass Spectrometry. *Anal. Chem.* **2014**, *86*, 2534–2542.
(42) Breuker, K.; McLafferty, F. W. Stepwise Evolution of Protein Native Structure with Electrospray into the Gas Phase, 10−12 to 102 S. *Proc. Natl. Acad. Sci.* **2008**, *105*, 18145–18152.
(43) Bush, M. F.; Hall, Z.; Giles, K.; Hoyes, J.; Robinson, C. V.; Ruotolo, B. T. Collision Cross Sections of Proteins and Their Complexes: A Calibration Framework and Database for Gas-Phase Structural Biology. *Anal. Chem.* **2010**, *82*, 9557–9565.
(44) Benesch, J. L. P.; Aquilina, J. A.; Ruotolo, B. T.; Sobott, F.; Robinson, C. V. Tandem Mass Spectrometry Reveals the Quaternary Organization of Macromolecular Assemblies. *Chem. Biol.* **2006**, *13*, 597–605.
(45) Hall, Z.; Hernández, H.; Marsh, J. A.; Teichmann, S. A.; Robinson, C. V. The Role of Salt Bridges, Charge Density, and Subunit Flexibility in Determining Disassembly Routes of Protein Complexes. *Structure* **2013**, *21*, 1325–1337.
(46) Breuker, K.; Oh, H.; Horn, D. M.; Cerda, B. A.; McLafferty, F. W. Detailed Unfolding and Folding of Gaseous Ubiquitin Ions Characterized by Electron Capture Dissociation. *J. Am. Chem. Soc.* **2002**, *124*, 6407–6420.
(47) Zhang, H.; Cui, W.; Gross, M. L. Native Electrospray Ionization and Electron-Capture Dissociation for Comparison of Protein Structure in Solution and the Gas Phase. *Int. J. Mass Spectrom.* **2013**, *354–355*, 288–291.
(48) Li, H.; Wongkongkathep, P.; Orden, S. L. V.; Loo, R. R. O.; Loo, J. A. Revealing Ligand Binding Sites and Quantifying Subunit Variants of Noncovalent Protein Complexes in a Single Native Top-Down FTICR MS Experiment. *J. Am. Soc. Mass Spectrom.* **2014**, 1–9.
(49) Lermyte, F.; Sobott, F. Electron Transfer Dissociation Provides Higher-Order Structural Information of Native and Partially Unfolded Protein Complexes. *PROTEOMICS* **2015**, *15*, 2813–2822.
(50) Lermyte, F.; Williams, J. P.; Brown, J. M.; Martin, E. M.; Sobott, F. Extensive Charge Reduction and Dissociation of Intact Protein Complexes Following Electron Transfer on a Quadrupole-Ion Mobility-Time-of-Flight MS. *J. Am. Soc. Mass Spectrom.* **2015**, *26*, 1068–1076.

(51) Li, H.; Nguyen, H. H.; Ogorzalek Loo, R. R.; Campuzano, I. D. G.; Loo, J. A. An Integrated Native Mass Spectrometry and Top-down Proteomics Method That Connects Sequence to Structure and Function of Macromolecular Complexes. *Nat. Chem.* **2018**, *10*, 139–148.
(52) Zhou, M.; Wysocki, V. H. Surface Induced Dissociation: Dissecting Noncovalent Protein Complexes in the Gas Phase. *Acc. Chem. Res.* **2014**, *47*, 1010–1018.
(53) Sahasrabuddhe, A.; Hsia, Y.; Busch, F.; Sheffler, W.; King, N. P.; Baker, D.; Wysocki, V. H. Confirmation of Intersubunit Connectivity and Topology of Designed Protein Complexes by Native MS. *Proc. Natl. Acad. Sci.* **2018**, *115*, 1268–1273.
(54) Shaw, J. B.; Li, W.; Holden, D. D.; Zhang, Y.; Griep-Raming, J.; Fellers, R. T.; Early, B. P.; Thomas, P. M.; Kelleher, N. L.; Brodbelt, J. S. Complete Protein Characterization Using Top-Down Mass Spectrometry and Ultraviolet Photodissociation. *J. Am. Chem. Soc.* **2013**, *135*, 12646–12651.
(55) O'Brien, J. P.; Li, W.; Zhang, Y.; Brodbelt, J. S. Characterization of Native Protein Complexes Using Ultraviolet Photodissociation Mass Spectrometry. *J. Am. Chem. Soc.* **2014**, *136*, 12920–12928.
(56) Morrison, L. J.; Brodbelt, J. S. 193 Nm Ultraviolet Photodissociation Mass Spectrometry of Tetrameric Protein Complexes Provides Insight into Quaternary and Secondary Protein Topology. *J. Am. Chem. Soc.* **2016**, *138*, 10849–10859.
(57) Tamara, S.; Dyachenko, A.; Fort, K. L.; Makarov, A. A.; Scheltema, R. A.; Heck, A. J. R. Symmetry of Charge Partitioning in Collisional and UV Photon-Induced Dissociation of Protein Assemblies. *J. Am. Chem. Soc.* **2016**, *138*, 10860–10868.
(58) Julian, R. R. The Mechanism Behind Top-Down UVPD Experiments: Making Sense of Apparent Contradictions. *J. Am. Soc. Mass Spectrom.* **2017**, *28*, 1823–1826.
(59) Cammarata, M. B.; Brodbelt, J. S. Structural Characterization of Holo- and Apo-Myoglobin in the Gas Phase by Ultraviolet Photodissociation Mass Spectrometry. *Chem. Sci.* **2015**, *6*, 1324–1333.
(60) Cammarata, M. B.; Thyer, R.; Rosenberg, J.; Ellington, A.; Brodbelt, J. S. Structural Characterization of Dihydrofolate Reductase Complexes by Top-Down Ultraviolet Photodissociation Mass Spectrometry. *J. Am. Chem. Soc.* **2015**, *137*, 9128–9135.
(61) Mehaffey, M. R.; Cammarata, M. B.; Brodbelt, J. S. Tracking the Catalytic Cycle of Adenylate Kinase by Ultraviolet Photodissociation Mass Spectrometry. *Anal. Chem.* **2018**, *90*, 839–846.
(62) Cammarata, M. B.; Schardon, C. L.; Mehaffey, M. R.; Rosenberg, J.; Singleton, J.; Fast, W.; Brodbelt, J. S. Impact of G12 Mutations on the Structure of K-Ras Probed by Ultraviolet Photodissociation Mass Spectrometry. *J. Am. Chem. Soc.* **2016**, *138*, 13187–13196.
(63) Miller, M. S.; Miller, L. D. RAS Mutations and Oncogenesis: Not All RAS Mutations Are Created Equally. *Front. Genet.* **2012**, *2*.
(64) Rajakulendran, T.; Sahmi, M.; Lefrançois, M.; Sicheri, F.; Therrien, M. A Dimerization-Dependent Mechanism Drives RAF Catalytic Activation. *Nature* **2009**, *461*, 542–545.

(65) Ihle, N. T.; Byers, L. A.; Kim, E. S.; Saintigny, P.; Lee, J. J.; Blumenschein, G. R.; Tsao, A.; Liu, S.; Larsen, J. E.; Wang, J.; Diao, L.; Coombes, K. R.; Chen, L.; Zhang, S.; Abdelmelek, M. F.; Tang, X.; Papadimitrakopoulou, V.; Minna, J. D.; Lippman, S. M.; Hong, W. K.; Herbst, R. S.; Wistuba, I. I.; Heymach, J. V.; Powis, G. Effect of KRAS Oncogene Substitutions on Protein Behavior: Implications for Signaling and Clinical Outcome. *J. Natl. Cancer Inst.* **2012**, *104*, 228–239.

(66) Freeman, A. K.; Ritt, D. A.; Morrison, D. K. Effects of Raf Dimerization and Its Inhibition on Normal and Disease-Associated Raf Signaling. *Mol. Cell* **2013**, *49*, 751–758.

(67) Young, A.; Lou, D.; McCormick, F. Oncogenic and Wild-Type Ras Play Divergent Roles in the Regulation of Mitogen-Activated Protein Kinase Signaling. *Cancer Discov.* **2013**, *3*, 112–123.

(68) Hammond, D. E.; Mageean, C. J.; Rusilowicz, E. V.; Wickenden, J. A.; Clague, M. J.; Prior, I. A. Differential Reprogramming of Isogenic Colorectal Cancer Cells by Distinct Activating KRAS Mutations. *J. Proteome Res.* **2015**, *14*, 1535–1546.

(69) Gnad, F.; Doll, S.; Song, K.; Stokes, M. P.; Moffat, J.; Liu, B.; Arnott, D.; Wallin, J.; Friedman, L. S.; Hatzivassiliou, G.; Belvin, M. Phosphoproteome Analysis of the MAPK Pathway Reveals Previously Undetected Feedback Mechanisms. *PROTEOMICS* **2016**, *16*, 1998–2004.

(70) Rosenberg, J.; Parker, W. R.; Cammarata, M. B.; Brodbelt, J. S. UV-POSIT: Web-Based Tools for Rapid and Facile Structural Interpretation of Ultraviolet Photodissociation (UVPD) Mass Spectra. *J. Am. Soc. Mass Spectrom.* **2018**, *29*, 1323–1326.

(71) Fetics, S. K.; Guterres, H.; Kearney, B. M.; Buhrman, G.; Ma, B.; Nussinov, R.; Mattos, C. Allosteric Effects of the Oncogenic RasQ61L Mutant on Raf-RBD. *Structure* **2015**, *23*, 505–516.

(72) Bentley, C.; Jurinka, S. S.; Kljavin, N. M.; Vartanian, S.; Ramani, S. R.; Gonzalez, L. C.; Yu, K.; Modrusan, Z.; Du, P.; Bourgon, R.; Neve, R. M.; Stokoe, D. A Requirement for Wild-Type Ras Isoforms in Mutant KRas-Driven Signalling and Transformation. *Biochem. J.* **2013**, *452*, 313–320.

(73) Mehaffey, M. R.; Sanders, J. D.; Holden, D. D.; Nilsson, C. L.; Brodbelt, J. S. Multistage Ultraviolet Photodissociation Mass Spectrometry To Characterize Single Amino Acid Variants of Human Mitochondrial BCAT2. *Anal. Chem.* **2018**, *90*, 9904–9911.

(74) Yin, S.; Loo, J. A. Elucidating the Site of Protein-ATP Binding by Top-Down Mass Spectrometry. *J. Am. Soc. Mass Spectrom.* **2010**, *21*, 899–907.

(75) Lobo, I. A.; Robertson, P. A.; Villani, L.; Wilson, D. J. D.; Robertson, E. G. Thiols as Hydrogen Bond Acceptors and Donors: Spectroscopy of 2-Phenylethanethiol Complexes. *J. Phys. Chem. A* **2018**, *122*, 7171–7180.

Chapter 6: Mapping a Conformational Epitope of Hemagglutinin A Using Native MS and Ultraviolet Photodissociation[§]

6.1 Overview

As the importance of effective vaccines and the role of protein therapeutics in the drug industry continue to expand, alternative strategies to characterize protein complexes are needed. Mass spectrometry (MS) in conjunction with enzymatic digestion or chemical probes has been widely used for mapping binding epitopes at the molecular level. However, advances in instrumentation and application of activation methods capable of accessing higher energy dissociation pathways have recently allowed direct analysis of protein complexes. Here we demonstrate a workflow utilizing native MS and ultraviolet photodissociation (UVPD) to map the antigenic determinants of a model antibody-antigen complex involving hemagglutinin (HA), the primary immunogenic antigen of the influenza virus, and the D1 H1-17/H3-14 antibody which has shown to confer potent protection to lethal infection in mice despite lacking neutralization activity. Comparison of sequence coverages upon UV photoactivation of HA and of the HA•antibody complex indicates the elimination of some sequence ions that originate from backbone cleavages exclusively along the putative epitope regions of HA in the presence of the antibody. Mapping the number of sequence ions covering the HA antigen versus the HA•antibody complex highlights regions with suppressed backbone cleavage and allows elucidation of unknown epitopes. Moreover, examining the observed fragment ion types generated by UVPD demonstrates a loss in diversity exclusively along the antigenic determinants upon MS/MS

[§]Mehaffey, M. R.; Lee, J.; Jung, J.; Lanzillotti, M. B.; Escobar, E. E.; Morgenstern, K. R.; Georgiou, G.; Brodbelt, J. S. Mapping a Conformational Epitope of Hemagglutinin A Using Native MS and Ultraviolet Photodissociation. *Anal. Chem.* **2020**, doi: 10.1021/acs.analchem.0c02237.

JL and JJ expressed and purified the proteins for the study. MBL wrote a script to aid in data interpretation. EE assisted in sample preparation. KRM offered advice in regards to the sample preparation workflow. GG and JSB provided mentorship and reviewed the manuscript prior to publication.

of the antibody-antigen complex. UVPD-MS shows promise as a method to rapidly map epitope regions along antibody-antigen complexes as novel antibodies are discovered or developed.

6.2 INTRODUCTION

The design of immunotherapeutic drugs and vaccines relies on identification of the epitopes to which antibodies bind. The location within the intact antibody of corresponding paratopes comprising predominantly but not exclusively loops within the variable domain, *i.e.* the complementarity determining regions (CDRs), is very important for understanding antibody function and also for generating improved variants having higher antigen affinity or specificity.[1,2] Although structural biology approaches, namely X-ray crystallography, NMR spectroscopy, and cryo-electron microscopy, provide high resolution information on the residues at the antibody:antigen interface, alternative epitope/paratope mapping pipelines offer certain advantages including requiring lower quantities of proteins and allowing more rapid analysis.[3] Over the past three decades, mass spectrometry (MS) has emerged as a rapid and sensitive technique for determining the higher order structure of antibodies and identifying residues comprising the binding epitope and paratope.[4] Traditionally MS-based approaches to map antigenic epitopes involve formation of the complexes in solution followed by enzymatic digestion to preserve structural information prior to mass spectrometric read-out.[4] Proteolytic digestion of the antigen can occur before or after formation of the complex with the antibody, termed respectively epitope extraction and epitope excision, followed by washing of unbound peptides and MS analysis of epitope peptides.[4,5] More modern MS-based epitope and paratope mapping methods rely on hydrogen/deuterium exchange (HDX),[6–9] carboxyl footprinting,[10,11] or fast photochemical oxidation of proteins (FPOP)[12,13] to compare the uptake of unbound and bound antigens

and detect regions protected upon antibody binding. Chemical cross-linking of immune complexes has also been demonstrated for identifying antigenic determinants.[14]

With the advent of native MS, intact antibody-antigen complexes that have not been subjected to proteolytic digestion can now be interrogated directly.[15,16] The native MS approach utilizes electrospray ionization of analytes in solutions of high ionic strength to maintain non-covalent interactions and transfer intact proteins into the gas phase with architectures reminiscent of their solution structures.[17–19] While the absence of solvent certainly impacts structure to some extent, there is growing evidence that charged protein complexes maintain a large portion of the folded tertiary and quaternary structures adopted in solution.[20–22] An early experiment to address this issue involved electrospray ionization of the tobacco mosaic virus and subsequent capture of the sprayed protein by soft landing.[20] Visualization by transmission electron microscopy suggested the virus was still structurally viable, further demonstrated by its ability to infect tobacco plants after transition through the gas phase. More recently, ion mobility spectrometry (IMS) experiments have provided convincing evidence protein structures are partially retained based on gas-phase measurements of collision cross sections (CCS) that can be directly compared to solution-phase values. [21,22] Such analysis has demonstrated similarity between solution-phase CCS values for the *trp* RNA-binding protein, TRAP, as well as GroEL-GroES complexes with those measured in the absence of bulk water.[21,22] As such, the stoichiometry and higher order structures of antibodies and antibody-antigen complexes are now routinely detected with MS.[23–26] Notable improvements in instrumentation have focused on extending the observable mass range to allow detection of high MW complexes such as those involved in complement initiation by the classical pathway, specifically the interaction of hexameric immunoglobulin G (IgG) with C1q.[27,28] Most recently charge detection MS was utilized to probe virus-like particles conjugated to antibodies.[29] Additionally, utilizing native MS

streamlines sample handling for epitope extraction workflows by allowing analysis of antigen digest and antibody mixtures.[30,31] In this latter method, collisionally-activated separation of epitope peptides from the antibody-peptide complexes and subsequent sequencing of the peptides is carried out within the mass spectrometer.[31] Ion mobility mass spectrometry (IM-MS) has also demonstrated utility in defining antibody heterogeneity and detecting immune complexes.[26,32–34] Specifically, collision-induced unfolding (CIU) footprints can be used to distinguish antibodies with divergent higher order structures[34] or those bound to the same antigen along different epitopes.[33]

While collisional activation, including collision-induced dissociation (CID) and higher-energy collisional dissociation (HCD), is most commonly used to sequence resulting epitope or paratope peptides, studies aimed at detection of protected regions following antibody binding in the gas phase have opted for alternative MS/MS approaches.[35] In particular, electron-based activation methods, including electron transfer dissociation (ETD) and electron capture dissociation (ECD), afford higher sequence coverage of epitope/paratope regions, allowing utilization of middle-down or even top-down analysis to determine sites of chemical modification after HDX of antibody-antigen complexes or to characterize the amino acids along CDRs.[36,37] Moreover, native MS and ECD of an antigen bound to the Fab region of an antibody yielded sequence ions exclusively from flexible regions of the complexes,[38] a trend also commonly observed for ETD or ECD of protein complexes.[39,40] Similarly, UVPD[41] has afforded unsurpassed sequence coverage of CDRs for monoclonal antibody mixtures, but the feasibility of using UVPD for epitope mapping has not been reported.

Previous UVPD-MS workflows include modification of the CDR of a monoclonal antibody with a chromogenic, cysteine-selective tag and subsequent liquid chromatography (LC) MS/MS analysis with 351 nm UVPD,[42] and middle-down digestion of monoclonal

antibody mixtures followed by identification using 193 nm photoactivation.[43] A recent study demonstrated the utility of both ECD and 157 nm UVPD for determining heavy and light chain antibody pairing and successful sequencing of the CDR-H3.[44] Native MS/UVPD studies of other types of proteins and protein complexes have tracked suppression or enhancement of backbone cleavages as a means to characterize changes in non-covalent interactions and conformation, including loop movements and structural variations stemming from single point mutations.[41] Owing to the production of a wide array of fragment ions which afford high sequence coverages for increasingly large proteins[45–47] in combination with the apparent sensitivity of UVPD for profiling secondary and tertiary structures,[41,48] application of this frontier strategy for characterization of antibody-antigen complexes was warranted.

Here we explore the epitope mapping capabilities of 193 nm UVPD-MS for a recently identified antibody that recognizes influenza A hemagglutinin (HA). Despite widespread vaccination efforts, seasonal outbreaks of influenza A virus remain a major threat to public health and affect millions of people worldwide every year.[49] Along with the glycoside hydrolase neuraminidase (NA), HA resides on the surface of virus particles. It recognizes sialic acid moieties presented along the surfaces of target cells and facilitates fusion of the viral envelope with the host endosomal membrane.[50] Functioning as a homo-trimer, each HA protomer consists of two domains: HA1 and HA2.[51] Apart from residues along the receptor binding site, HA1 is subject to intense evolutionary pressure causing antigenic drift, while HA2 remains relatively conserved.[52–54] Vaccines must be updated continually to match predicted seasonal strains of influenza but are still ineffective against pandemic outbreaks resulting from more significant antigenic shift. Efforts to develop a prophylactic offering universal protection across influenza strains and subtypes rely on elucidation of the HA epitopes recognized by broadly protective antibodies.[55–57] As

illustrated in the present study, comparison of sequence coverages of the HA1 antigen upon UVPD of unbound HA1 and antibody-bound HA1 suggests the presence of the antibody curbs fragmentation specifically along the putative epitope regions of the antigen, resulting in an observed suppression in sequence coverage. Moreover, charting the sequence coverage per residue based on UVPD reveals attenuation of sequence ions specifically along the two epitope regions and provides a more general approach for elucidation of an unknown epitope.

6.3 EXPERIMENTAL

6.3.1 Sample Preparation

The D1 H1-17/H3-14 IgG monoclonal antibody and the monomeric HA1 domain (residues 57-267) of the corresponding HA protomer from H1N1 A/California/04/2009 were expressed and purified as described as follows (expressed protein sequences of the antibody and antigen are shown in **Figure 6.1)**. Genes for the antibody and antigen involved in the study were purchased as gBlocks (Integrated DNA Technologies) and cloned into the pcDNA3.4 vector (Invitrogen). For monoclonal antibody expression, heavy and light chain plasmids for D1 H1-17/H3-14 IgG were transfected into Expi293 cells (Invitrogen) at a 1:3 ratio. After incubating for 5 days at 37 °C with 8% CO_2, the supernatant containing secreted antibodies was collected by centrifugation at 500×g for 15 min at room temperature. Supernatant was passed over a column with 1 mL Protein A agarose resin (Thermo Scientific) three times to ensure efficient capture. After washing the column with 20 cv of PBS, antibodies were eluted with 3 mL of 100 mM glycine-HCl, pH 2.7 and immediately neutralized with 1 mL of 1 M Tris-HCl, pH 8.0. Antibodies were buffer-exchanged into PBS utilizing Amicon Ultra-30 centrifugal spin columns (Millipore). Similarly, for the HA1 antigen expression, after incubating for 5 days at 37 °C

with 8% CO_2, the supernatant containing secreted protein was collected by centrifugation at 500×g for 15 min at room temperature. Supernatant was passed over 2 mL Ni-NTA agarose (QIAGEN) affinity column in gravity mode. Flow-through sample was collected and passed through the column three times. The column was washed with 15 cv of 10 mM imidazole, 150 nM NaCl, 100 mM Tris-HCl, pH 7.5 prior to eluting with 5 cv of 250 mM imidazole, 150 nM NaCl, 100 mM Tris-HCl, pH 7.5. Eluates were then buffer-exchanged into PBS using Amicon Ultra-30 centrifugal spin columns (Millipore).

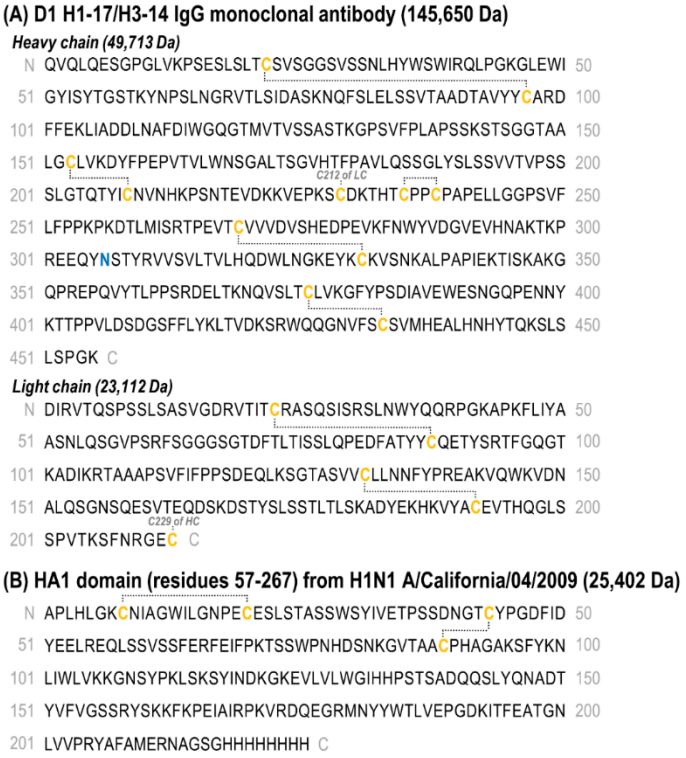

Figure 6.1: Expressed sequences of the (A) D1 H1-17/H3-14 IgG monoclonal antibody and (B) HA1 domain (residues 57-267) of the corresponding HA protomer from H1N1 A/California/04/2009 used for all experiments. Cysteine residues are shown in yellow font, and expected disulfide linkages are represented as dotted lines. Calculated average masses for each sequence account for disulfide bonds. A G0F glycan is expected to exist at N306 on the heavy chain of the antibody (highlighted in blue).

For glycan removal, 20 μg of the antigen was diluted in 50 mM sodium phosphate (pH 7.5) and incubated for 48 hours at room temperature with 1000 units of PNGase F (New England BioLabs Inc., Ipswich, MA). The antibody was then added to the antigen solution at a 1:2 or 1:20 antibody:antigen ratio, and the resulting solution was flash frozen in an effort to minimize deglycosylation of the antibody by PNGase F. Samples were desalted and exchanged into 20 mM ammonium acetate (pH 6.8) at 5-10 μM using 50 kDa molecular weight cut-off filters (MilliporeSigma, Burlington, MA) for MS analysis.

6.3.2 Mass Spectrometry & Data Analysis

MS experiments were performed on a Thermo Scientific Q Exactive UHMR (Bremen, Germany) modified as previously described[58] to allow photodissociation in the HCD cell through incorporation of a 193 nm ArF Coherent Excistar excimer laser (Santa Cruz, CA). Protein solutions were subjected to electrospray ionization using source voltages of 1.0-1.2 kV and a source temperature of 200 °C. Solutions were introduced via an offline nano-ESI source using borosilicate emitters fabricated in-house and coated with Au/Pd. The on-line size-exclusion chromatography experiments were performed using a Dionex LC system (Thermo Scientific) interfaced to the modified Q Exactive UHMR mass spectrometer. Separation was carried out on a 2.1 mm × 150 mm Waters ACQUITY UPLC Protein BEH SEC column with a 200 Å pore size and 1.7 μm particle size (Milford, MA). An isocratic mobile phase comprised of 20 mM ammonium acetate (pH 6.8) and flowing at 100 μL min^{-1} was used to elute a 5 μL injection of the 1:2 antibody:antigen sample (1 μg/μL) after deglycosylation. An applied voltage of 4 kV on the HESI source interfacing the LC to the MS was used to ionize the effluent. An in-source trapping value of -150 V allowed efficient desolvation of the antibody-antigen complex. ESI-MS were collected at a resolving power of 12500 at *m/z* 200.

In-source trapping (IST) provided low energy collisional activation to promote desolvation of the antibody or antibody-antigen complex with an optimal value of -100 V. All other ion optics were tuned to optimize transmission of the species of interest: the antigen (lower *m/z* region) or the antibody-antigen complex (higher *m/z* region). ESI mass spectra represent 60 transients collected at a resolving power of 12500 at *m/z* 200. For MS/MS spectra, a single charge state was isolated using a width of 10-15 *m/z* and activated in the HCD cell. A resolving power of 140K at *m/z* 200 was used while collecting 500 transients for each MS/MS spectrum. Collision energies of 200-300 eV/q were used for HCD spectra while UVPD spectra represent a single laser pulse at 3 mJ. Automated gain control (AGC) was turned off during collection of all MS and MS/MS data and instead the ion population was controlled by adjusting the ion time (IT). Specifically, IT values were set at 20 ms and 350 ms for MS and MS/MS spectra, respectively. Lowering the nitrogen bath gas pressure of the HCD cell from a corresponding pressure in the ultra-high vacuum (UHV) region of 1E-9 mbar to 1E-10 mbar aided in detection of fragments after photoactivation. However, for collisional activation a minimum UHV pressure of 4E-10 mbar was necessary for effective HCD to occur.

Lower resolution ESI-MS was used to assign average masses of the antigen, antibody, and antibody-antigen complex species using UniDec.[59] High resolution MS/MS spectra were de-charged and de-isotoped using the Xtract algorithm from Thermo Scientific (S/N ratio of 3, fit factor 44%, remainder 25%) to create lists of monoisotopic fragment ion masses that could be assigned as sequence ions using ProSight Lite v1.4. Identifications of HCD (*b*, *y*) and UVPD (*a*, *a+1*, *b*, *c*, *x*, *x+1*, *y*, *y-1*, *z*) sequence ions were made within ±10 ppm. All MS/MS spectra were collected in triplicate and only sequence ions identified in all three spectra are considered. For HCD or UVPD of the antibody-antigen complex in which sequence ions could arise from the antibody or antigen, there

were no overlapping masses in the assigned fragment ions. Sequence coverage maps were made using ProSight Lite in which sequence ion types are color coded as *a/x*-type green, *b/y*-type blue, *c/z*-type red. All cysteine residues in the antigen and antibody sequences were assumed to be disulfide bound and identifications accounted for the loss of a hydrogen at each cysteine (-1.0078 Da).

A custom script in R was used to calculate the number of sequence ions observed per residue for HCD or UVPD of the antigen and antibody-antigen complex. Briefly, for each amino acid the number of N-terminal product ions (*a, b, c*) resulting from cleavage of the backbone C-terminal to a given residue and C-terminal product ions (*x, y, z*) arising from backbone fragmentation N-terminal to that position were summed. Values are reported as a percentage of the total possible number of cleavages adjacent to a given residue (*i.e.* two for HCD and nine for UVPD, except residues at the N- and C-terminus). A crystal structure of the HA1 domain of an HA protomer bound to the antigen binding fragment (Fab) region of an IgG antibody (PDB ID: 6E4X)[60] is shown in **Figure 6.2**. Although not the same sequence as the D1 H1-17/H3-14 antibody, both IgGs are known to bind along the HA1 domain near the trimeric interface.[60,61] The two expected epitope regions are highlighted and, based on the HA protomer sequence, include: residues 90-109 and 213-233, herein referred to respectively as epitope regions 1 and 2. This corresponds to amino acids T35-R55 and F163-Y183 in the HA1 sequence expressed for this study.

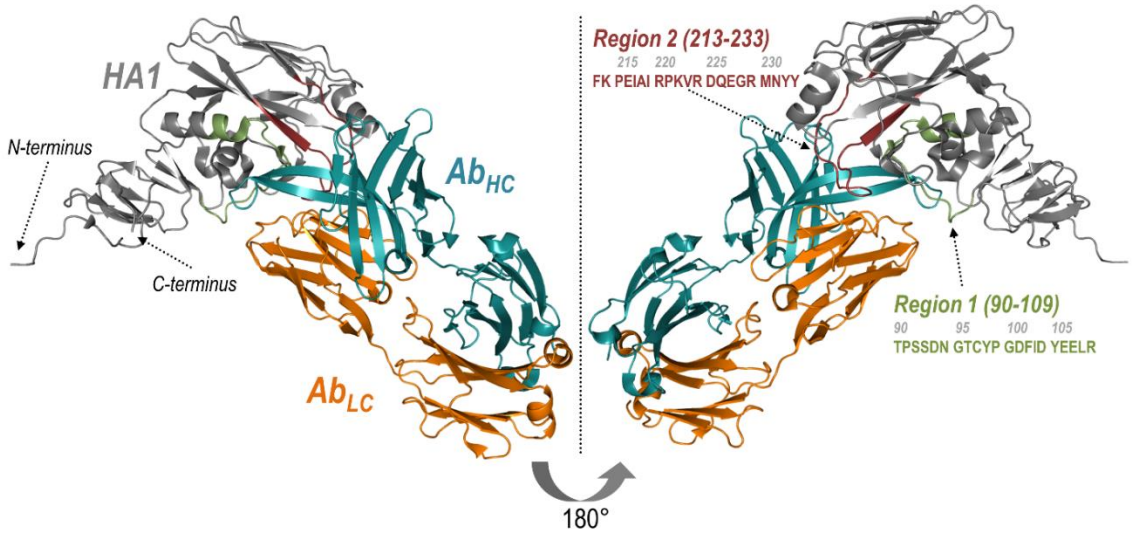

Figure 6.2: Crystal structure with a 180° view of the HA1 domain of an HA protomer (H3N2 A/Texas/50/2012) bound to the antigen binding fragment (Fab) region of the S5V2-29 IgG monoclonal antibody (PDB ID: 6E4X) with subunits labelled. The two epitope regions are highlighted (red, green) along the HA1 subunit (gray) with the corresponding epitope sequences from the HA strain expressed for this study shown (numbering is based on the HA protomer sequence; these residues correspond to T35-R55 and F163-Y193 in the expressed HA1 sequence shown in **Figure 6.1B**). The heavy chain (HC) and light chain (LC) of the antibody are colored separately (turquoise and orange, respectively).

6.4 Results and Discussion

6.4.1 Deglycosylation of HA1 Antigen for Improved MS Analysis

Previous analysis of the repertoire of monoclonal antibodies that comprise the serological response to influenza vaccination led to the identification of a set of antibodies showing broad binding to HA from divergent influenza virus strains.[61] In the present study, one such antibody (termed D1 H1-17/H3-14), which was shown to bind to the interface region of HA trimer via negative-stain EM, was expressed recombinantly to target the HA1 domain of HA from an H1N1 strain of influenza A virus responsible for a pandemic in 2009.[62] Without the HA2 domain to stabilize trimer formation, HA1 exists in solution as a

25.4 kDa monomer. ESI-MS of HA1 under native conditions yields low charge states (9+ – 11+) of eight proteoforms corresponding to the attachment of up to seven variations of sugars at an asparagine residue along the sequence (**Figures 6.3A**, **6.3B**). The locations of glycan modifications along the HA1 domain are known to vary by HA strain with the glycosylation sites likely evolving under selective pressure to provide steric blocking to antigenic sites and impede interaction with neutralizing antibodies.[63]

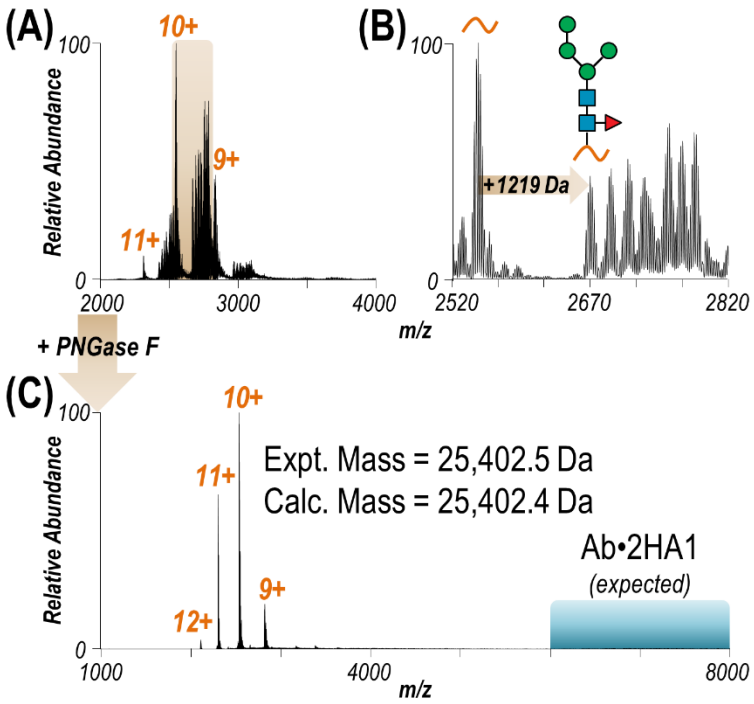

Figure 6.3: (A) ESI mass spectrum of HA1 sprayed in 20 mM ammonium acetate. (B) An expanded view of the region of the spectrum spanning *m/z* 2520-2820 reveals several proteoforms of the 10+ charge state resulting from glycosylation. Based on a mass shift of +1219 Da, one possible glycan structure is shown, with up to six additional sugars accounting for all observed glycoforms. (C) ESI mass spectrum of HA1 after glycan removal with PNGase F. Observed as a monomer, the experimental mass of deglycosylated HA1 matches the calculated mass accounting for two disulfide bonds. The *m/z* region in which antibody•HA1 complexes would be expected is highlighted in turquoise.

Although understanding HA glycosylation patterns can offer insight into viral mechanisms, the various glycoforms result in charge states overlapping with the unmodified protein of interest and hinder MS/MS analysis.[64,65] The amidase PNGase F was used to cleave N-linked glycosylations from HA1.[15] After the deglycosylation reaction, a substoichiometric amount of antibody was used to bind and isolate the antigen. The result is a simplified mass spectrum of the unmodified antigen with an intact mass matching the expected sequence, accounting for two disulfide bonds (**Figure 6.3C**). Owing to the lower concentration at which the antibody was present in solution compared to the antigen, the antibody-antigen complex is not observed under these conditions (*m/z* region of expected antibody-antigen complexes highlighted in turquoise in **Figure 6.3C**). The 10+ charge state of unmodified HA1 was selectively isolated and activated with HCD or UVPD (**Figure 6.4A**). Deconvolution of the MS/MS spectra allowed fragment ions to be assigned as backbone cleavage sites along the sequence of HA1 (**Figure 6.4B**). Sequence coverage maps shown in **Figure 6.4C** demonstrate that UVPD affords coverage of over twice as much of the protein sequence compared to HCD (60% and 27%, respectively). As expected, the presence of two disulfide bonds along the N-terminal region hampers production of informative fragments between those cysteine residues using HCD and to a lesser extent UVPD.[66,67]

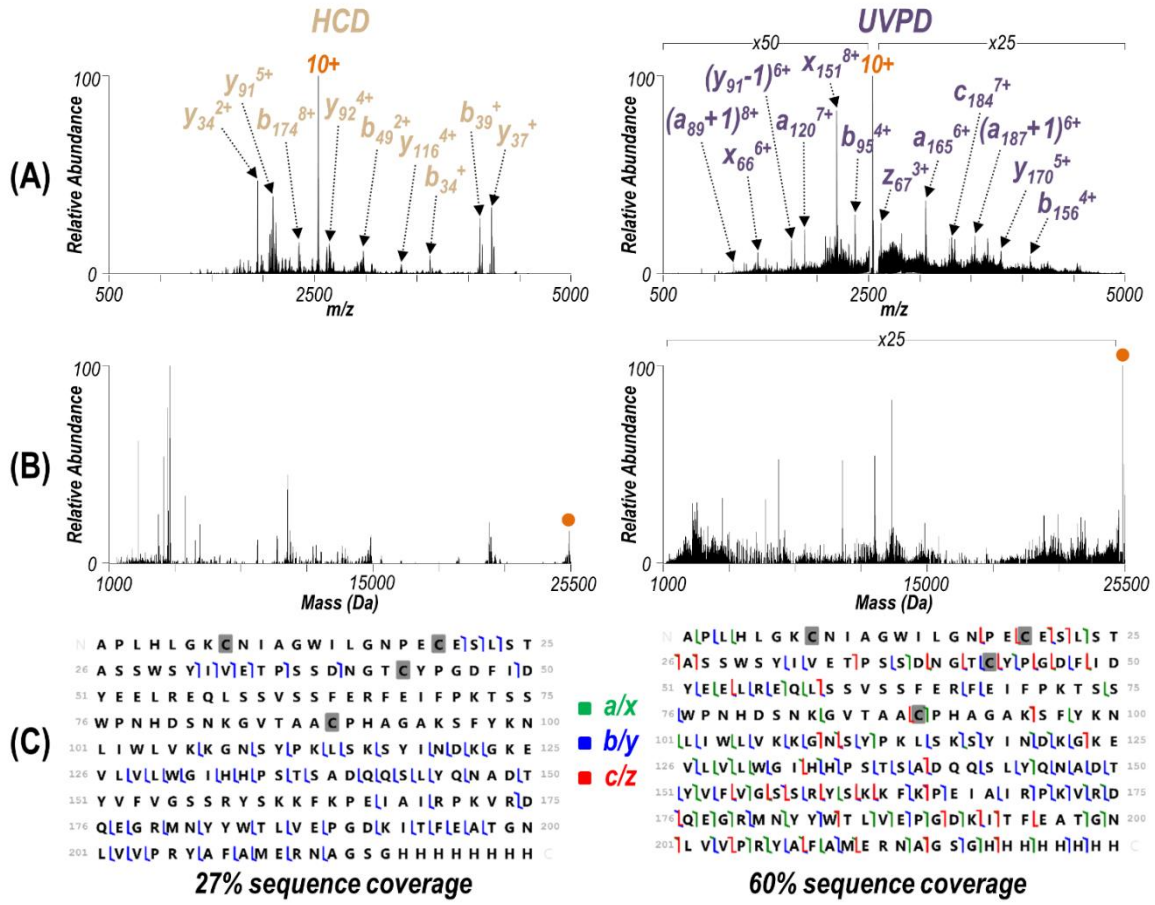

Figure 6.4: (A) MS/MS spectra resulting from activation of the 10+ charge state of HA1 with HCD (left) and UVPD (right). Several abundant fragment ions are identified and labelled. (B) Corresponding deconvoluted MS/MS spectra in which the precursor is denoted with a filled circle. Monoisotopic masses identified as assignable fragment ions originating from backbone cleavages of HA1 are used to create the sequence coverage maps in (C). Searches accounted for disulfide bonds at all four cysteine residues (highlighted in gray).

Given our workflow requires exposing the antibody to PNGase F as it is added to the deglycosylation reaction mixture to form the antibody-antigen complex and recover HA1, it is likely the amidase will also competitively cleave the G0F glycans present along the constant region (Fc) of the antibody. Glycosylation of the heavy chains alters the

affinity of Fc receptors but has little impact on antigen binding.[68] As such, the antibody was reacted with PNGase F separately, mirroring the conditions used when the antigen was present, to determine the extent of deglycosylation. The most abundant species in **Figure 6.5A** corresponds to removal of the glycan from each of the heavy chains. Nevertheless, the presence of the singly and doubly glycosylated antibody forms in the spectrum suggests the short reaction time in the presence of PNGase F prevented complete glycan removal. The 25+ charge state of the antibody with no glycans was subsequently isolated and activated using HCD or UVPD (**Figures 6.5B**, **6.5C**). Owing to the presence of one intermolecular and seven intramolecular disulfide bonds that preserve the overall structure of the antibody, the majority of fragment ions identified as portions of the sequences of the light or heavy chain are observed in the region encompassing *m/z* 500-4000. By matching fragment ions from the deconvoluted MS/MS spectra, the resulting sequence coverages were 6% each for the light and heavy chains using HCD, and 45% and 37% respectively for the light and heavy chains using UVPD (**Figure 6.6**). While the cysteine bridges significantly hinder analysis with HCD as evidenced by the low sequence coverages, the majority of observed light and heavy chain sequence ions upon UVPD occur along regions not restricted by disulfide bonds. Overall, UVPD affords moderate to high sequence coverage of the each of the separate components that form the antibody-antigen complex.

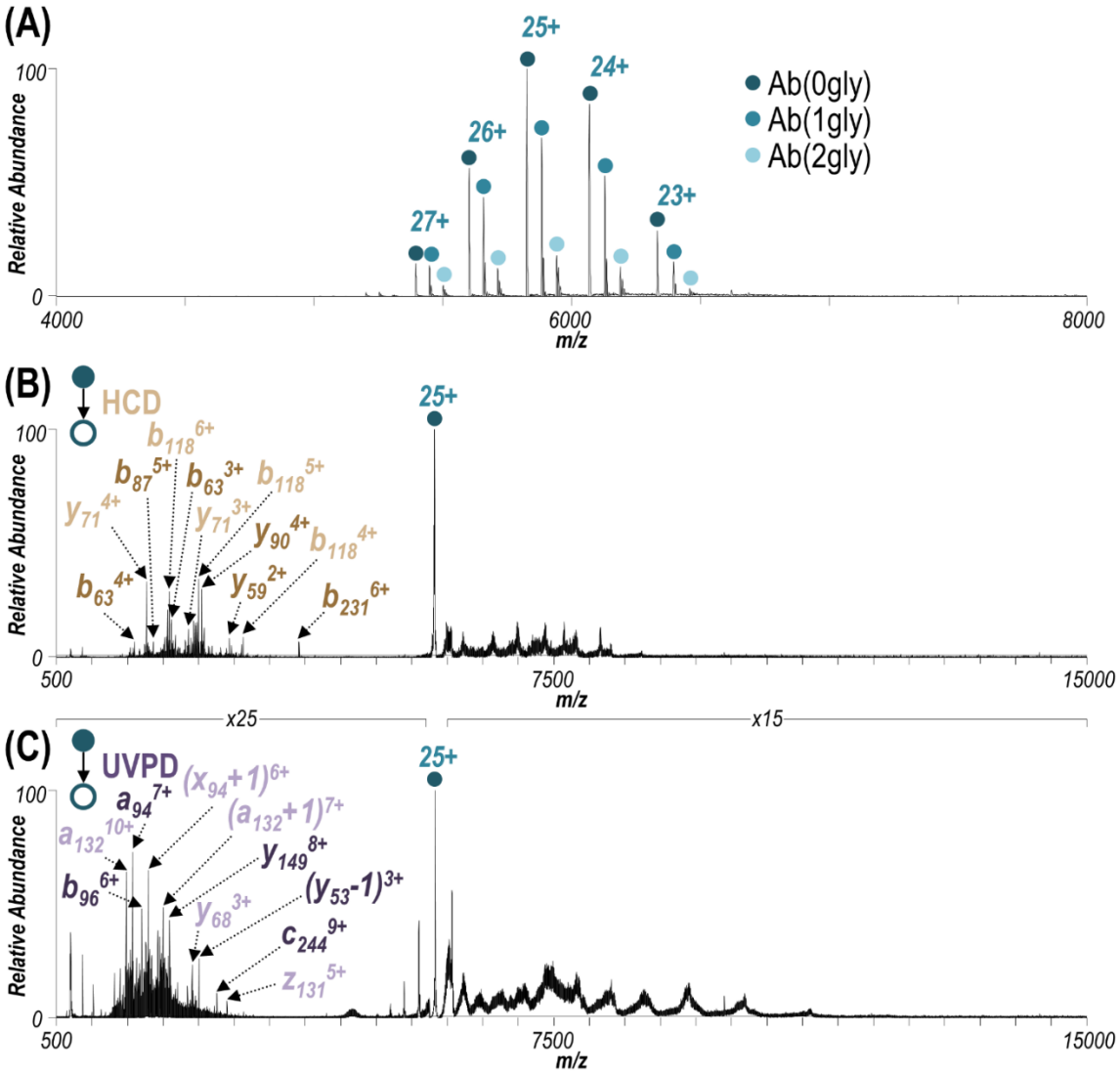

Figure 6.5: (A) ESI-MS of the D1 H1-17/H3-14 antibody in 20 mM ammonium acetate after reaction with PNGase F. Observed charge states are labelled and glycoforms are denoted with turquoise colored circles. Even with the short reaction time, the most abundant species corresponds to removal of the G0F glycan from both heavy chains. The 25+ charge state of the antibody without glycans was selectively isolated and activated with (B) HCD and (C) UVPD. Several abundant fragment ions resulting from HCD (tan) and UVPD (purple) are labelled corresponding to the sequences of the light chain (light color) or heavy chain (dark color).

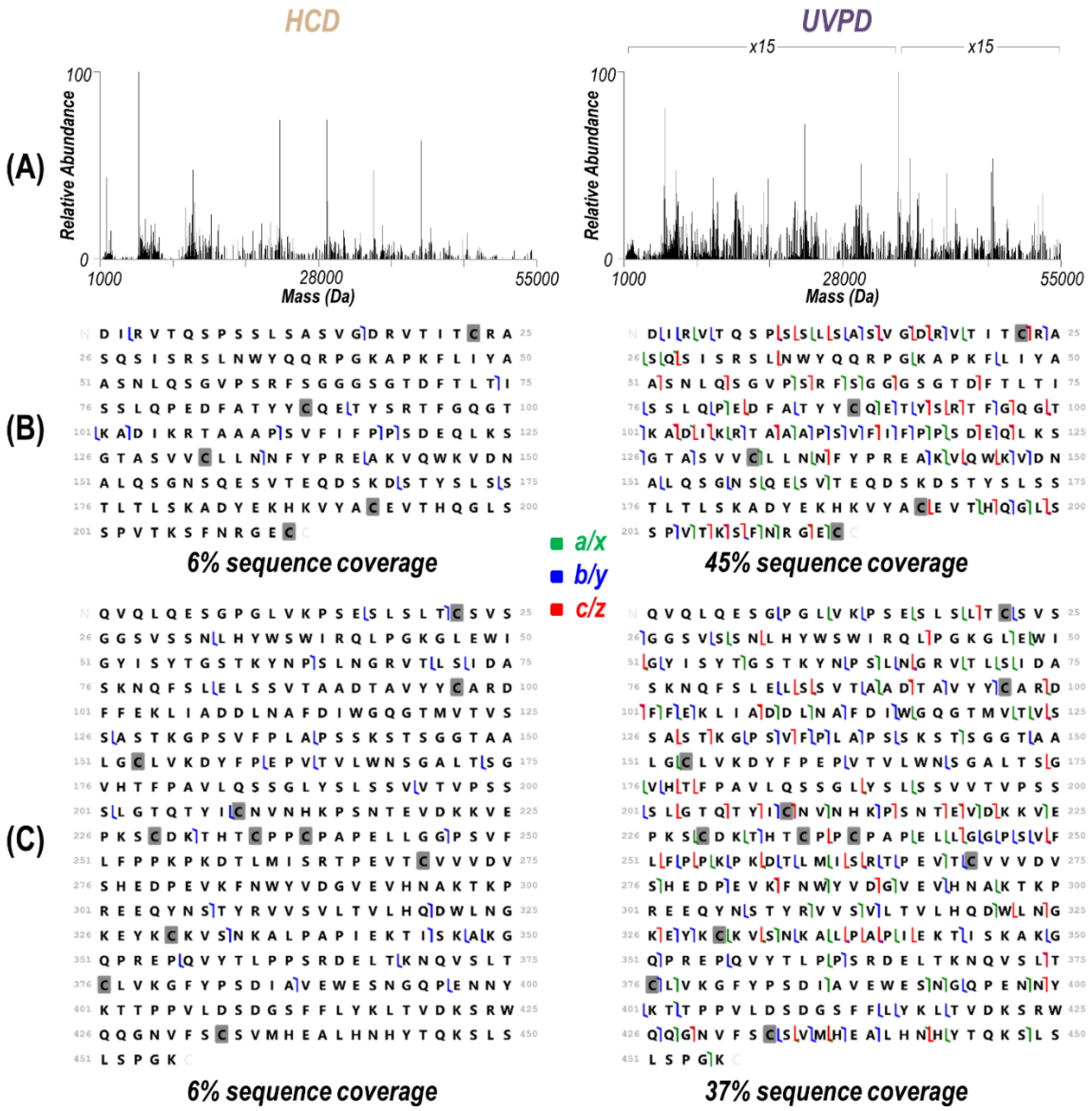

Figure 6.6: (A) Spectra resulting from deconvolution of the HCD and UVPD MS/MS spectra of the D1 H1-17/H3-14 antibody shown in Figure 6.5. Monoisotopic masses identified as assignable fragment ions originating from backbone cleavages of the (B) light chain and (C) heavy chain of the antibody are used to create the sequence coverage maps. The eight disulfide bonds that stabilize the antibody structure (highlighted in gray) were assumed to be intact for fragment ion identification.

6.4.2 Formation and MS Characterization of the Antibody-Antigen Complex

Size-exclusion chromatography (SEC) MS was used to confirm the expected 1:2 antibody:antigen stoichiometry after incubation of HA1 and the D1 H1-17/H3-14 antibody (**Figure 6.7**). The SEC trace shown in **Figure 6.7A** demonstrates one major species present in solution (RT 2.58 min) with a small amount of a second species (RT 3.56 min). Corresponding mass spectra confirm these species respectively as the antibody-antigen complex (**Figure 6.7B**) and unbound HA1 (**Figure 6.7C**). An inset of **Figure 6.7B** for the region encompassing *m/z* 6500 – 10000 shows the antibody-antigen complex was formed between the antibody retaining either 0, 1, or 2 G0F glycans (due to exposure of the antibody to PNGase F) and two HA1 subunits. In the mass spectrum of the complex, a 1:1 antibody:antigen species is also observed as well as unbound HA1 (**Figure 6.7B**). Extracted ion chromatograms of the *m/z* values corresponding to these three species highlight that unbound HA1 (*m/z* 3175 (7+ charge state)) elutes in two separate peaks while the antibody-antigen complexes (1:1 and 1:2, *m/z* 8185 (24+ charge state) and 13157 (13+ charge state)) elute simultaneously (**Figure 6.7A**). As such, the unbound HA1 and 1:1 antibody:antigen species co-eluting with the antibody-antigen complex (**Figure 6.7A**, RT 2.58 min) are likely due to disassembly of the 1:2 Ab:HA1 complexes as a result of in-source trapping (IST, a type of non-selective front-end collisional activation), a method typically used to desolvate large biomolecules in mass spectrometry workflows.[69] The use of higher IST parameters can cause disassembly of desired protein complexes. To demonstrate this outcome, mass spectra of the complex were collected using various IST values (-10 V to -250V) for comparison of the relative abundances of the three major species: unbound HA1, the Ab•2HA1 complex, and the Ab•HA1 complex (**Figure 6.8**). Specifically, at low IST values (*i.e.* -10 V) the complex is poorly desolvated and the quality of the MS1 spectrum is sub-par. As the applied voltage is increased, the adducts are

collisionally removed resulting in a cleaner spectrum of the antibody-antigen complex. However, at the same time the abundances of ejected unbound HA1 and the corresponding 1:1 antibody:antigen complex increase. While an IST value of -150 V was used during SEC-MS, an optimized value of -100 V was selected based on the trend in **Figure 6.8**, representing a justifiable compromise between removal of adducts and decomposition of intact Ab•2HA1 complexes. For the later eluting peak in the SEC trace (**Figure 6.7A**, RT 3.56 min, corresponding to free HA1), its narrower charge state distribution (7+ to 9+) compared to the HA1 ejected from the complex in **Figure 6.7B** (6+ to 11+) suggests the former HA1 species was unbound in solution and ionized separately from the complex.

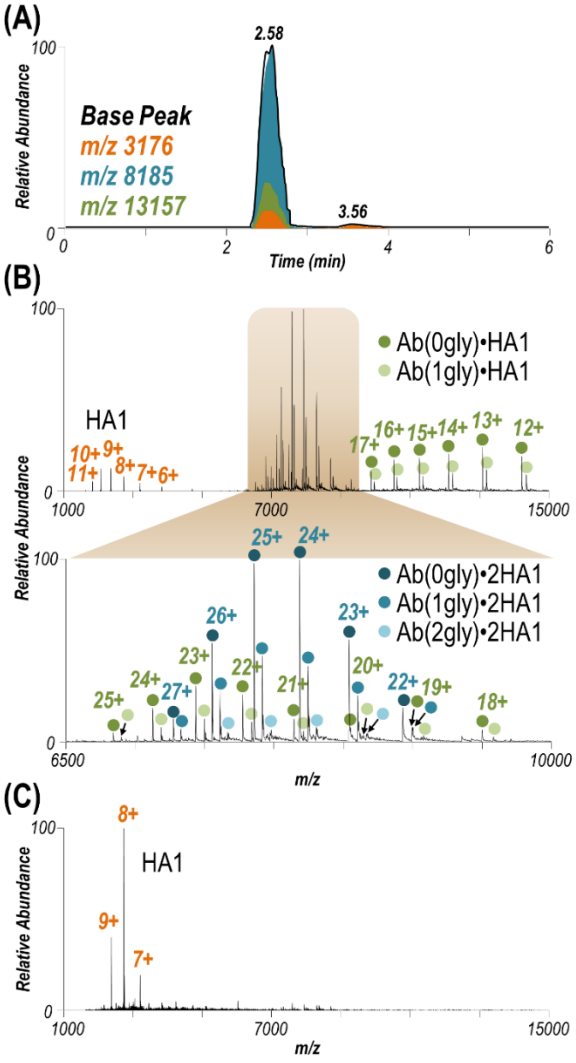

Figure 6.7: (A) SEC LC trace for HA1 with the antibody at a 1:2 antibody:antigen ratio. Extracted ion chromatograms of the *m/z* values corresponding to HA1 (orange), Ab•HA1 (green), and Ab•2HA1 (turquoise) are shown. (B) ESI mass spectrum collected at retention time 2.58 min along with an expanded view of the range spanning *m/z* 6500-10000. Observed species include HA1, Ab•HA1, and Ab•2HA1 with 0-2 glycans (gly) attached to the antibody (glycoforms are denoted with colored circles for the complex). In-source trapping (-150 V) necessary to desolvate the Ab•2HA1 complex causes ejection of one HA1, resulting in the observed Ab•HA1 species and unbound HA1. Mass spectra of the complexes obtained using various in-source trapping energies are shown in Figure 6.8. (C) ESI mass spectrum collected at retention time 3.56 min suggests a low abundance of unbound HA1 is in solution.

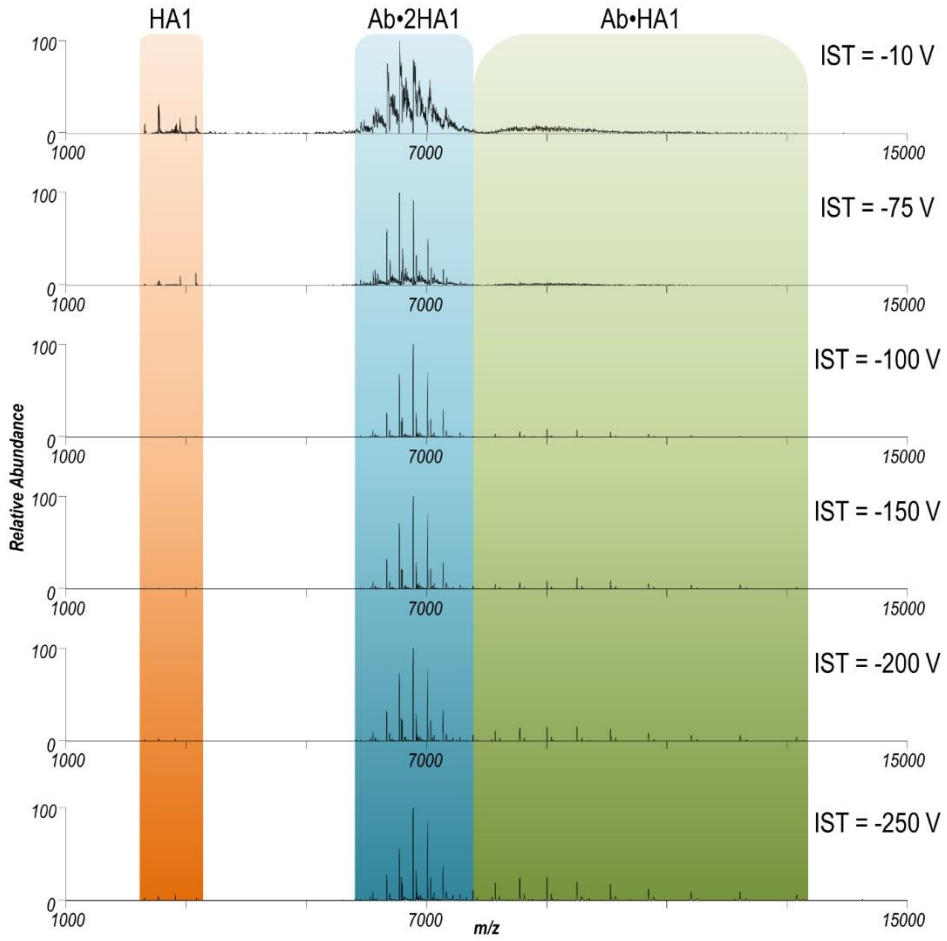

Figure 6.8: ESI-MS of the antibody-antigen complex collected using various in-source trapping energies (-10 V to -250 V) to determine the ideal value for analysis. Up to three species are observed including HA1 monomer (orange), 1:2 antibody:antigen complex (turquoise), and 1:1 antibody:antigen complex (green). At low IST values (top), the complex is poorly desolvated resulting in many adducts, while at high IST values (bottom) significant disruption of the complex and ejection of one HA monomer occurs.

Using these optimized conditions, the 1:2 antibody:antigen mixture was infused by nano-ESI and the 29+ charge state of the antibody-antigen complex (with no G0F glycans bound to antibody) was activated with HCD or UVPD (**Figure 6.9**). Ejection of one HA1 monomer to yield the 1:1 antibody:antigen complex was a dominant pathway following activation with HCD and to a lesser extent for UVPD (**Figures 6.9B**, **6.9C**). In addition to

production of intact protein subunits (unbound HA1 and Ab•HA1), both activation methods yielded a vast array of fragment ions that were deconvoluted and assigned as portions of the sequences of HA1 or the light and heavy chains of the antibody (**Figure 6.10**). Briefly, sequence coverages were 20% (HCD) and 49% (UVPD) for HA1, 9% (HCD) and 46% (UVPD) for the antibody light chain, and 6% (HCD) and 37% (UVPD) for the antibody heavy chain. Activation of the Ab•2HA1 complex compared to activation of unbound HA1 resulted in lower sequence coverage of HA1 using either HCD or UVPD (**Figure 6.11**) whereas the observed coverage of either chain of the antibody was not significantly impeded by the presence of the antigen (**Figures 6.6**, **6.10**).

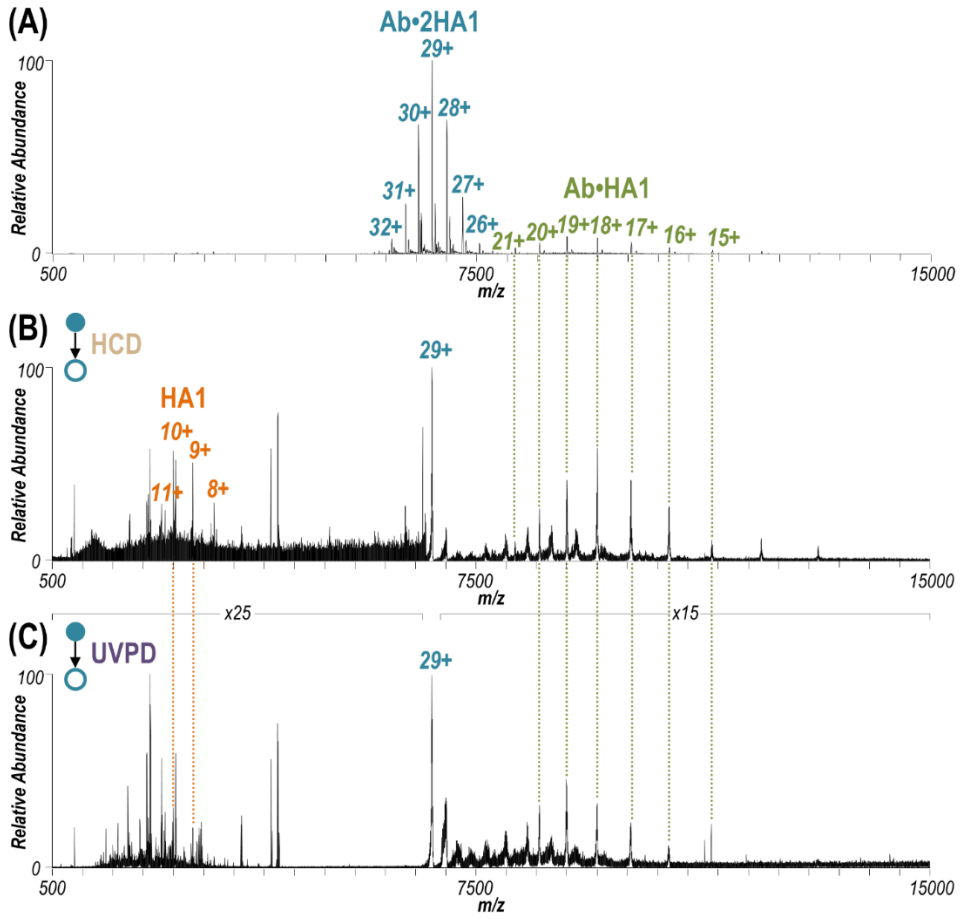

Figure 6.9: (A) ESI mass spectrum of a solution containing 1:2 antibody:antigen using an in-source trapping energy of -100 V. Charge states of the two observed species are labelled: Ab•2HA1 (turquoise) and Ab•HA1 (green). The 29+ charge state of the antibody-antigen complex was selectively isolated and activated with (B) HCD or (C) UVPD to yield the MS/MS spectra. Observed charge states of intact subunits of HA1 (orange) or Ab•HA1 (green) are identified, suggesting antigen ejection was a more favored fragmentation pathway for HCD compared to UVPD.

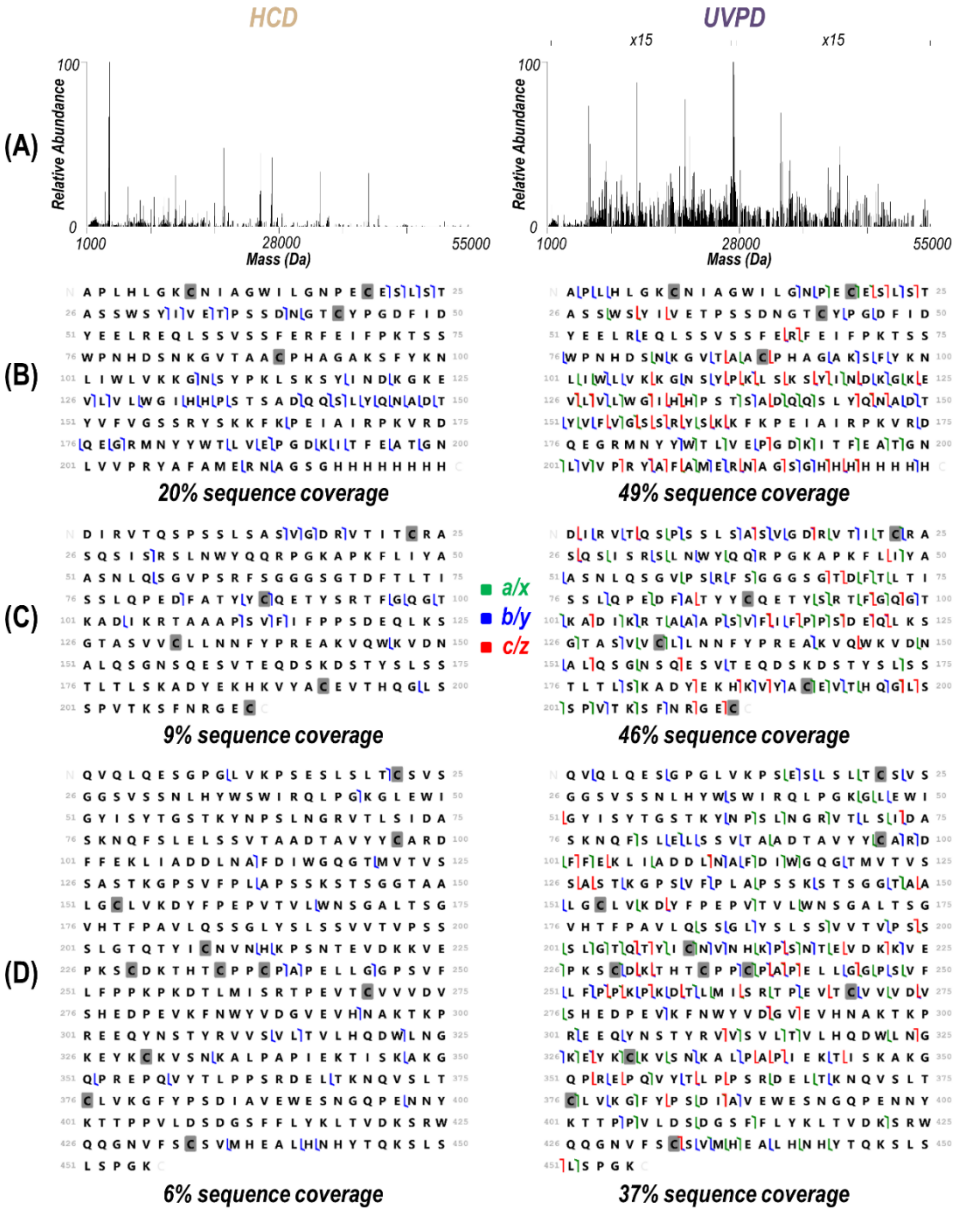

Figure 6.10: (A) Deconvoluted HCD (left) and UVPD (right) mass spectra corresponding to the MS/MS spectra of the antibody-antigen complex in Figure 6.9. Fragment ions originating from backbone cleavages were searched against the sequences of (B) HA1, (C) antibody light chain, and (D) antibody heavy chain to create the sequence coverage maps. All cysteine residues (highlighted in gray) were assumed to be disulfide bound. None of the observed fragment ions matched expected backbone cleavages for more than one of the three sequences. Sequence coverages are reported for each protein in the complex.

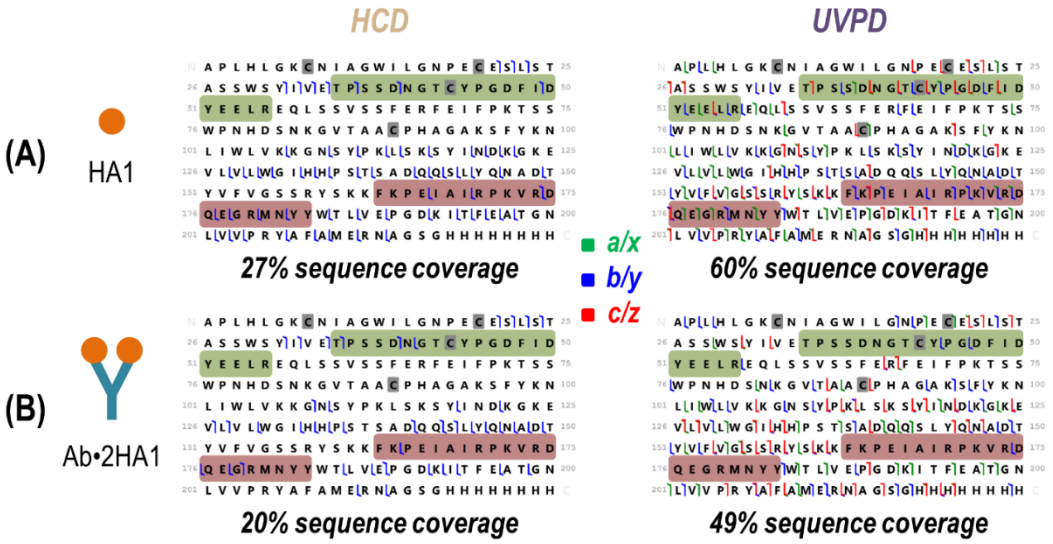

Figure 6.11: Comparison of the sequence coverage of HA1 afforded by HCD (left) and UVPD (right) for activation of (A) unbound HA1 and the (B) 1:2 antibody:antigen complex. Corresponding MS/MS spectra are shown in Figure 6.4 for unbound HA1 (10+) and Figure 6.9 for the complex (29+). Sequence coverages are reported below each map with the complex yielding lower sequence coverage than the unbound hemagglutinin A for both HCD and UVPD. The two epitope regions are highlighted: epitope region 1 (green) and epitope region 2 (red).

6.4.3 UVPD-MS for Epitope Mapping

Past studies leveraging UVPD-MS to probe protein-ligand and protein-protein complexes have relied on comparison of backbone cleavage propensities upon photoactivation of protein states of interest.[41] In essence, observed enhancement of backbone cleavages for a specific protein region upon UVPD correlates with an increase in flexibility or reduction in noncovalent interactions, while suppression of backbone cleavages suggests the formation of new or strengthened stabilizing interactions that hamper the separation/release of fragment ions and inhibits their detection.[41,70] As such, during UVPD experiments a decrease in the overall sequence coverage of HA1 upon complexation with the antibody is expected. Nevertheless, to be useful in mapping

antibody-antigen complex interactions, the reduction in backbone cleavages must occur specifically along the epitope regions of the antigen. The D1 H1-17/H3-14 antibody is known to bind a conformational epitope spanning two regions near the trimeric interface along the HA1 domain of H1 strains.[61] Although existence of epitopes at the contact surface between HA subunits is not intuitive, this interface is exposed post-fusion as well as by molecular breathing of the HA trimer.[60,71,72] A published crystal structure of the Fab fragment of the S5V2-29 antibody that binds similarly near the HA trimer interface (PDB ID: 6E4X) visualizes these two putative epitope regions for the HA1 domain of H3N2 A/Texas/50/2014 corresponding to residues 90-109 and 213-233 in the H1 strain used in this study (or residues 35-55 and 163-183 in the expressed HA1 sequence) (**Figure 6.2**).[60] These two regions are highlighted in green and red along the HCD and UVPD sequence coverage maps of unbound HA1 and the antibody-antigen complex in **Figure 6.11**. Although coverage is visibly curbed along these regions upon HCD and UVPD of the complex compared to the monomeric antigen, sequence coverage was plotted by protein region to better assess the corresponding changes in identified sequence ions for the rest of the protein.

Bar graphs of sequence coverages (*i.e.* the number of backbone cleavages as a percent of the total number of protein residues) are shown for HCD and UVPD of unbound HA1 versus the Ab•2HA1 complex for four different regions: entire protein, epitope region 1, epitope region 2, and the rest of the protein excluding the epitope regions (**Figure 6.12**). Both HCD and UVPD resulted in statistically significant lower sequence coverages along the entire protein for activation of the Ab•2HA1 complex. Along the two epitope regions, HCD resulted in a significant suppression in sequence coverage for only one of the regions while UVPD did for both. Comparison of coverage for the rest of the protein sequence excluding the two epitope regions for HCD showed significant suppression but for UVPD

remained the same for activation of unbound HA1 or the Ab•2HA1 complex. These results suggest the presence of the antibody prevents production/detection of fragments originating from backbone cleavages of the epitope regions of the antigen during UVPD, resulting in the observed suppression in sequence coverage. An analogous change in sequence coverage of the antibody was not observed upon HCD nor UVPD likely owing to the overall lower sequence coverage, extensive disulfide bonding, and size difference between the antibody and antigen (*e.g.* the antibody accounts for 75% of the mass of the Ab•2HA1complex).

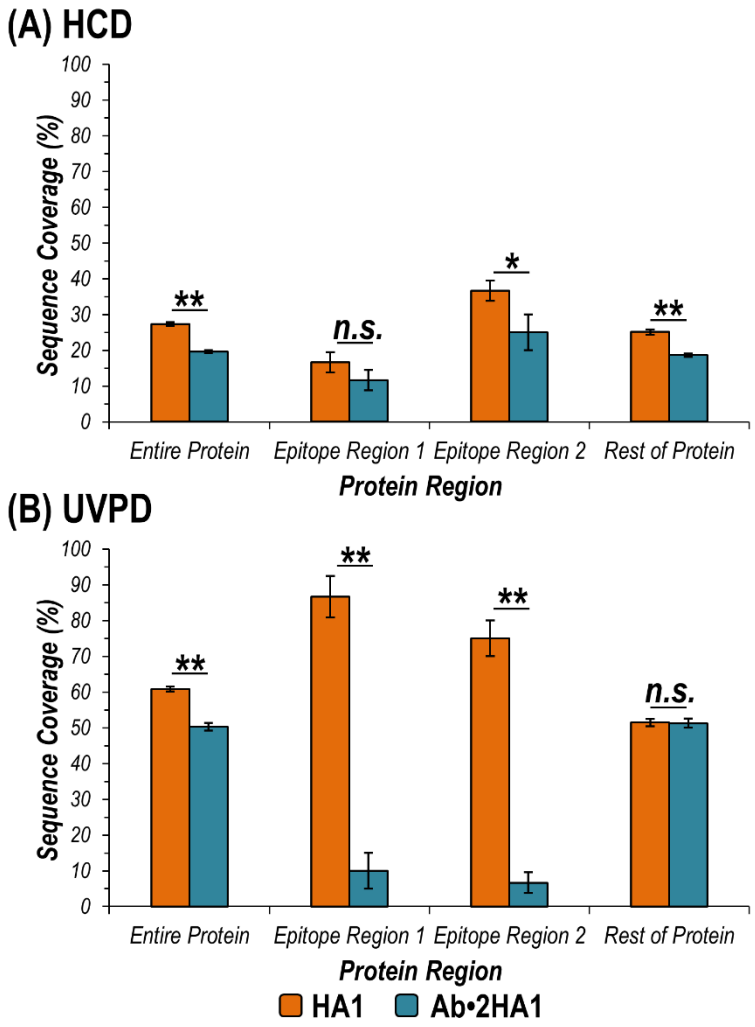

Figure 6.12: Graphs displaying sequence coverage of various regions of HA1 afforded by activation of HA1 (10+) (orange) or the Ab•2HA1 (29+) complex (turquoise) using (A) HCD and (B) UVPD. In the expressed HA1 sequence, epitope region 1 encompasses residues T35-R55, while epitope region 2 includes amino acids F163-Y183 (corresponding to residues 90-109 and 213-233 in the HA protomer). The rest of the protein is defined as the entire expressed HA1 protein sequence excluding the two epitope regions. Asterisks indicate statically significant differences in sequence coverage for the two precursors at a 95% or 99% confidence level (* p-value < 0.05, ** p-value < 0.01, n.s. not significant).

The distributions of fragment ion types for each of these four regions of HA1 were also plotted as a percentage of the total number of sequence ions identified upon HCD or UVPD of unbound HA1 or the Ab•2HA1 complex (**Figure 6.13**). While HCD typically yields only two ion types (*b*- and *y*-type from cleavage of the labile C-N amide backbone bond), UVPD produces up to nine different ion types from cleavage of different backbone bonds between pairs of amino acids (*a, a+1, x, x+1* from cleavage of C_α – C bonds, *b, y,* and *y-1* from C-N amide bonds, and *c, z* from N - C_α bonds).[41] For HCD generally more *b*-type ions (containing the N-terminus) were observed for activation of the Ab•2HA1 complex compared to the antigen alone, except along epitope region 1 spanning residues 35-55 (**Figure 6.13A**). For UVPD only *b*- and *y*-type fragment ions were observed in the epitope regions upon activation of the Ab•2HA1 complex, while the entire array of expected ion types (*a/x, b/y, c/z*) were produced for the free antigen (**Figure 6.13B**). Moreover, the diversity in the ion type distributions upon UVPD was maintained for the rest of the protein excluding the two epitope regions.

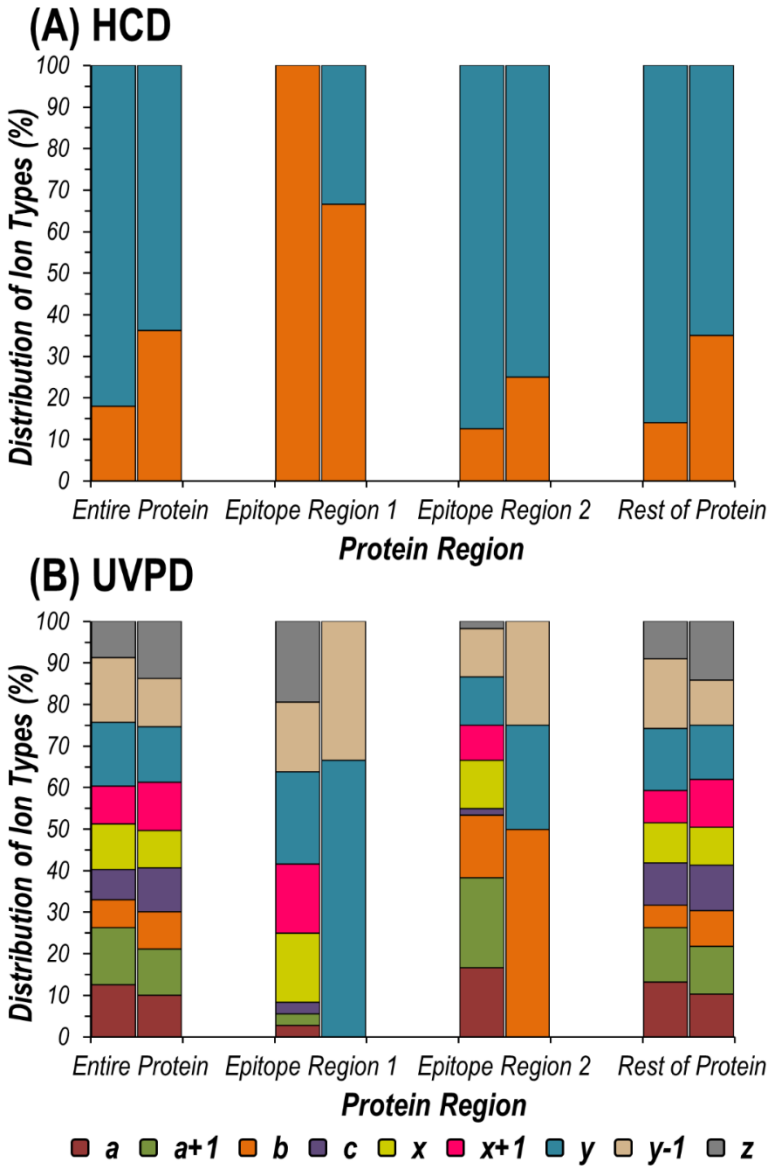

Figure 6.13: Bar graphs of the distribution of fragment ion types across several different regions of HA1 for (A) HCD and (B) UVPD showing pairs of stacked bars representing unbound HA1 (left bar) and the Ab•2HA1 complex (right bar), corresponding to the sequence coverages shown in Figure 6.12 for the entire protein, epitope region 1, epitope region 2 and the rest of the protein. Residues 35-55 and 163-183 of the expressed HA1 sequence encompass the two expected epitope regions (or residues 90-109 and 213-233 in the HA protomer sequence). The rest of the protein represents the entire sequence excluding those two regions.

While the complex mechanisms underlying UVPD of intact proteins have yet to be fully unraveled, the hypothesis that both direct fragmentation from excited states and dissociation from vibrationally excited ground states after internal conversion are at play is generally accepted.[73] The latter leads to fragmentation pathways similar to those that occur during collisional activation and produces *b*- and *y*-type ions.[74] The former describes direct cleavage of the backbone by excitation of an electron into an excited state orbital, typically yielding the other ion types observed upon UV photoactivation: *a/x* and *c/z*.[73] These considerations align with observation of exclusively *b*- and *y*-type ions upon UVPD of the Ab•2HA1 complex along epitope regions that produced the entire array of possible sequence ions in the absence of the antibody. In particular, upon formation of the Ab•2HA1 complex, it seems that the network of non-covalent interactions between the antibody and antigen suppresses direct dissociation pathways (*e.g.* formation and release of *a/x* or *c/z*-type ions) especially at residues involved in the protein-protein interface. However, the fragmentation pathways that proceed via redistribution of vibrational energy and disruption of weak non-covalent bonds result in cleavage of backbone bonds in the epitope region and concomitant release of *b/y* ions.

6.4.4 Approach for Elucidation of an Unknown Epitope using UVPD-MS

While the epitope regions for the model antibody-antigen system in the present study are reputed,[61] a similar UVPD-MS approach could be used to resolve disputed sites or even elucidate unknown antigenic determinants. Examining the number of observed sequence ions bracketing each individual residue of the antigen after UVPD of the Ab•2HA1 complex compared to the unbound antigen highlights possible epitope regions. Stretches of amino acids exhibiting suppressed or completely curbed backbone cleavage for the complexes relative to the free Ab or HA1 subunits suggest involvement in the

interface. Such analysis is demonstrated in **Figure 6.14** for the Ab•2HA1 complex. The number of observed HA1 sequence ions upon activation of the antibody-antigen complex or unbound antigen are graphed as a percentage of the total possible number of fragment ions per residue (*e.g.* two for HCD (*b/y*) and nine for UVPD (*a, a+1, b, c, x, x+1, y, y-1, z*)). Subtraction of the corresponding values for the Ab•2HA1 complex and monomeric antigen yields a difference plot and aids in visualization of changes (**Figure 6.15**). In short, for residues with values that lie below the *x*-axis, fewer sequence ions originated from backbone cleavage adjacent to that amino acid upon activation of the antibody-antigen complex compared to the unbound antigen. Conversely the production of more sequence ions arising from backbone cleavage adjacent to a given residue when comparing the Ab•2HA1 complex compared to HA1 is indicated by a value above the *x*-axis. For HCD there is no distinct pattern or specific region in which fewer sequence ions were observed (**Figure 6.15A**). On the contrary, for UVPD there are two main stretches of amino acids resulting in fewer sequence ions upon formation of the Ab•2HA1 complex: residues 35-59 and residues 163-188 of the expressed HA1 sequence (**Figure 6.15B**). These regions largely align with the presumed antigenic determinants for the specific antibody-antigen complex used in this study (T35-R55 and F163-Y183 or residues 90-109 and 213-233 of the HA protomer).[61]

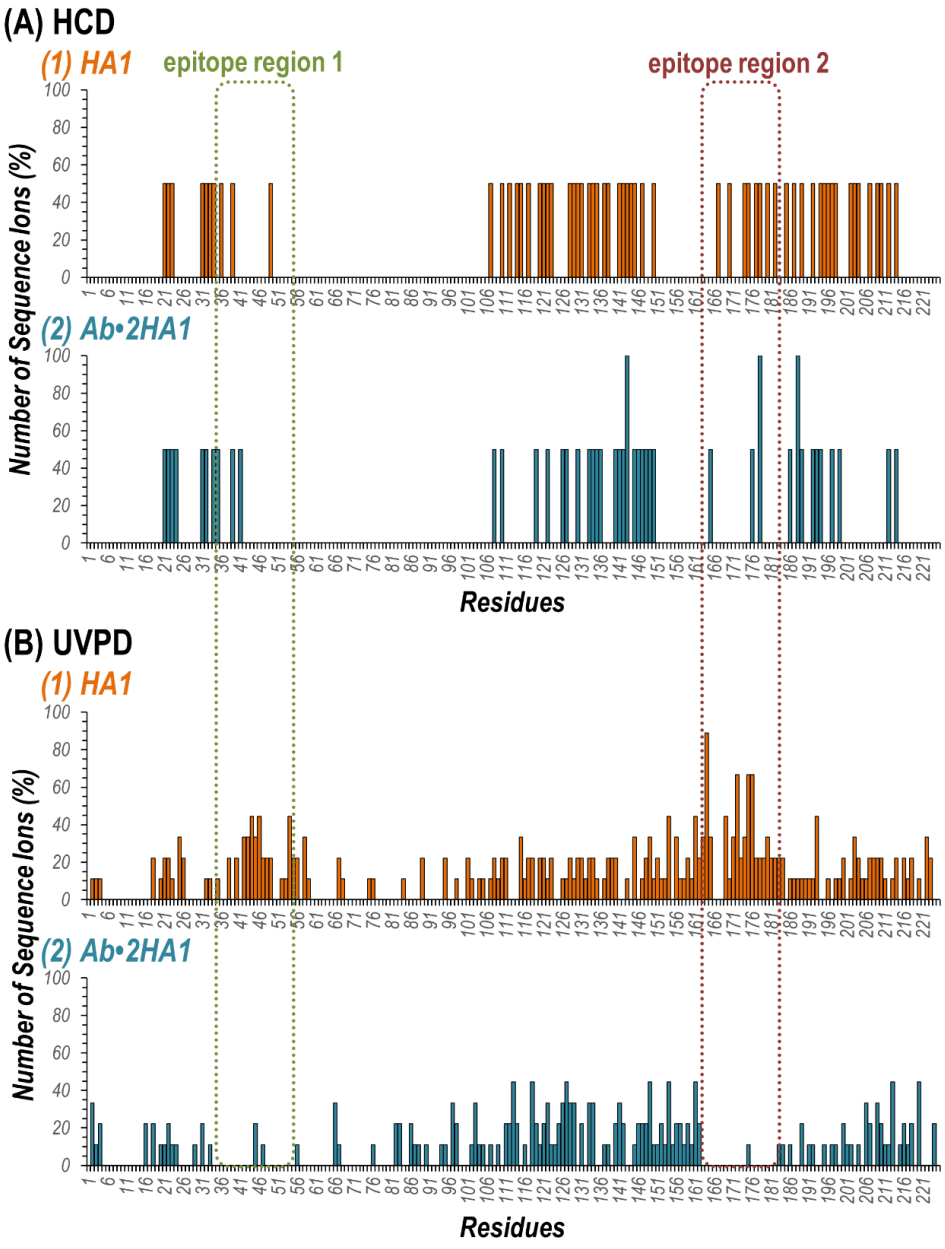

Figure 6.14: Plots of the number of HA1 sequence ions (originating from backbone cleavages along the protein sequence) as a percentage of the total number possible per residue resulting from activation of (1) unbound HA1 (10+) (orange) or (2) antibody-antigen Ab•2HA1 complex (29+) (turquoise) using (A) HCD and (B) UVPD. The two epitope regions (residues 90-109 and 213-233 in the HA protomer sequence, or 35-55 and 163-183 in the expressed sequence) are outlined with dashed lines. Subtraction of the corresponding values yielded the difference plots in Figure 6.15.

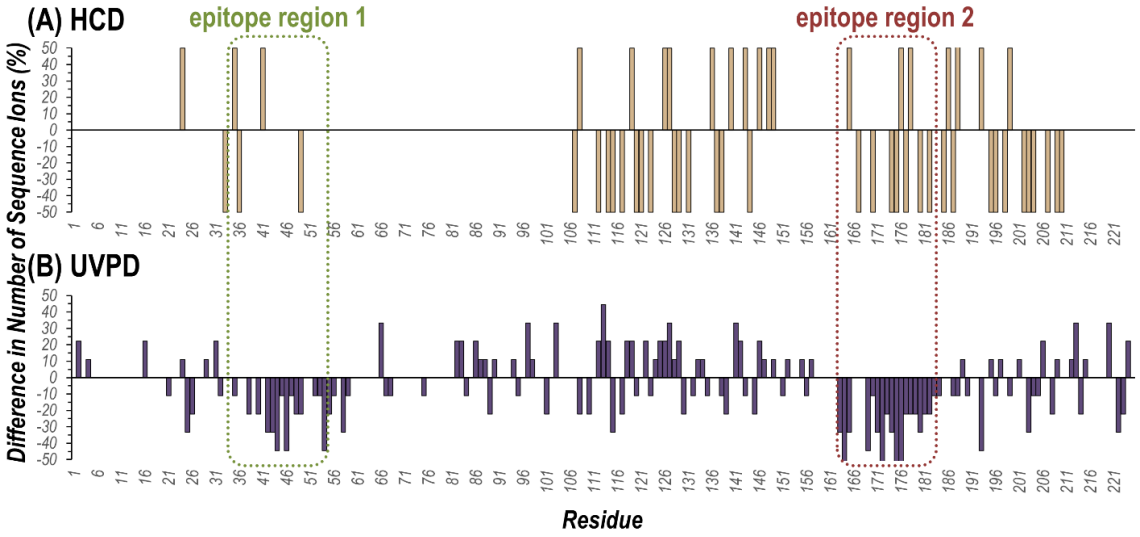

Figure 6.15: Difference plots representing the changes in the number of observed sequence ions produced by backbone cleavages that bracket each residue upon activation of the Ab•2HA1 antibody-antigen complex (29+) compared to unbound HA1 (10+) using (A) HCD and (B) UVPD. Values greater than zero mean more sequence ions were observed from cleavages adjacent to a given residue when activating the complex compared to the unbound antigen, while values less than zero mean fewer sequence ions were observed. The two known epitope regions of HA1 (residues 90-109 and 213-233 in the HA protomer sequence or 35-55 and 163-183 in the expressed HA1 sequence) are outlined with dashed lines. Plots of the number of sequence ions per residue as a percentage of the possible number of backbone cleavages are shown in Figure 6.14.

Moreover difference plot values can be represented as heatmaps by residue number or visualized along a crystal structure of HA1 bound to the Fab region of an antibody known to interact similarly with HA as D1 H1-17/H3-14 (PDB ID: 6E4X)[60] (**Figure 6.16**). Suppression (blue) or enhancement (red) in the number of observed sequence ions generated upon backbone cleavages bracketing each residue is shown for activation of the antibody-antigen complex compared to the antigen alone using HCD and UVPD. Residues demarcated in blue (**Figure 6.16A**) or shaded in blue (**Figure 6.16B**) signal likely involvement in the antibody-antigen complex interface. Conversely an increase in the

number of sequence ions produced adjacent to a given residue after formation of the antibody-antigen complex (colored red) can result from increased flexibility/fewer stabilizing interactions in that region or simply the redistribution of energy to dissociation pathways that were inaccessible in the unbound antigen. For the UVPD data, the majority of amino acids exhibiting suppressed cleavage (colored blue) are located along the interface with the Fab region of the antibody in the crystal structure (*e.g.* the epitope regions), whereas for the HCD data there is both suppression and enhancement of fragmentation along those regions (**Figure 6.16B**, **6.16C**). When a structure of the antibody-antigen complex is lacking, mapping differences in the number of UVPD cleavages adjacent to each residue along a high-resolution structure of an unbound antigen could help correlate observed changes in photodissociation with structural features of the protein and aid in localization of the epitopes. Lastly, plotting the observed fragment ion types per residue makes apparent a loss in diversity of observed sequence ions for activation of the antibody-antigen complex compared to the unbound antigen (**Figure 6.17**). In particular, the full array of UVPD ion types (*a/x*, *b/y*, *c/z*) cover the residues involved in the epitope regions upon activation of HA1, yet only *b*- and *y*-type ions are identified for those same regions upon UVPD of the antibody-antigen complex. Comparison of the number and type of sequence ions arising from backbone cleavages adjacent to individual residues upon UVPD of unbound antigens and antibody-antigen complexes offers an alternative approach for probing unidentified epitopes.

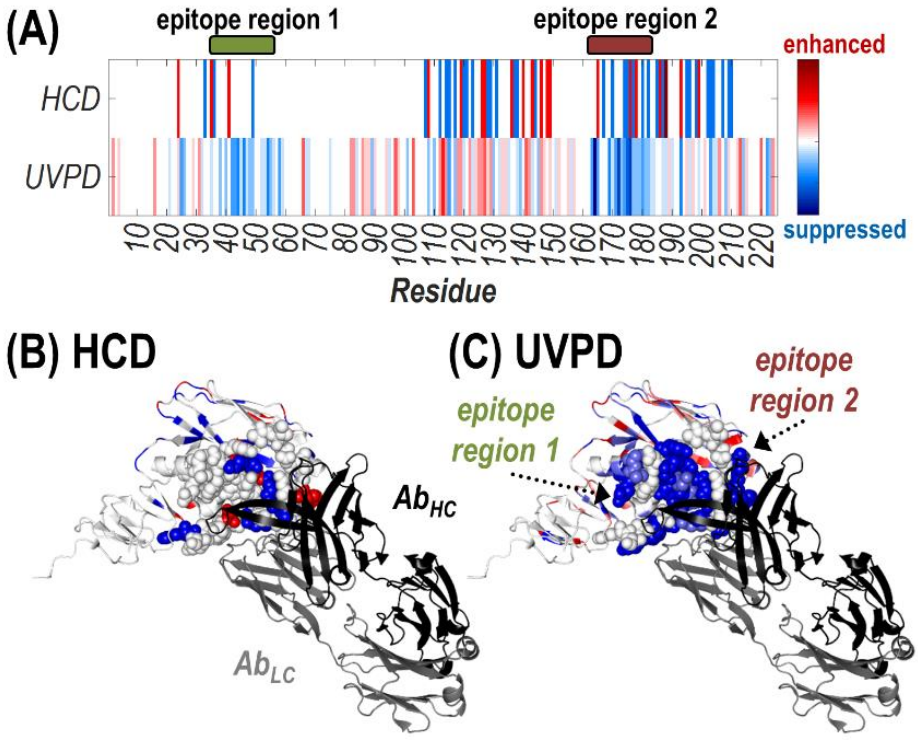

Figure 6.16: Heatmaps of the suppression (blue) or enhancement (red) in the number of observed sequence ions generated upon backbone cleavages bracketing each residue for activation of the Ab•2HA1 complex (29+) compared to the antigen alone (10+) using HCD and UVPD shown (A) for the HA1 sequence or (B, C) along the crystal structure of the HA1 domain of an HA protomer (H3N2 A/Texas/50/2012) bound to the antigen binding fragment (Fab) region of the S5V2-29 IgG monoclonal antibody (PDB ID: 6E4X). Residues encompassing the two epitope regions are shown as spheres, while the light chain (gray) and heavy chain (black) of the antibody are labelled in (B).

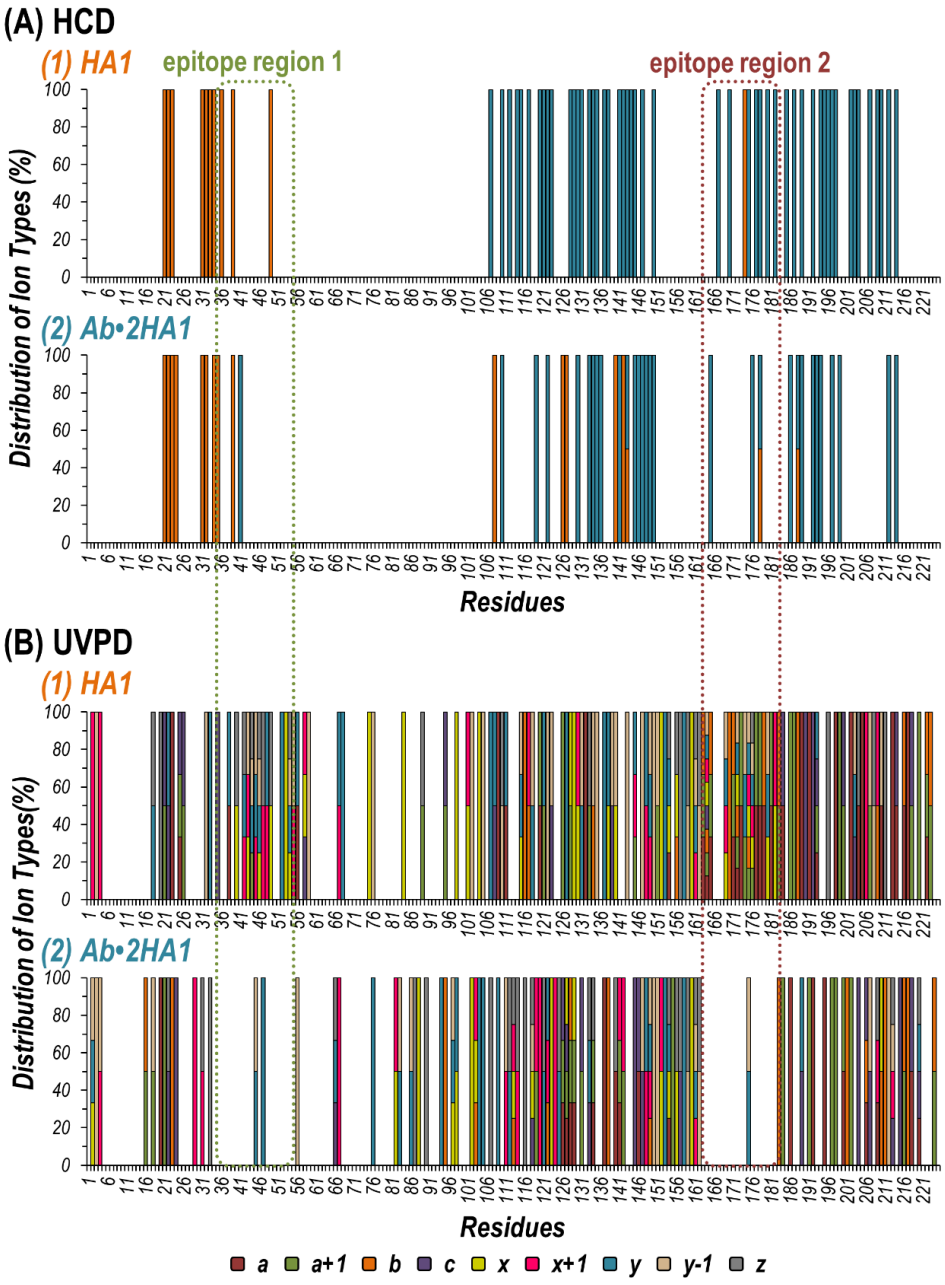

Figure 6.17: Distribution of ion types corresponding to the plots in Figure 6.14 of the number of sequence ions originating from backbone cleavages at each residue for activation with (A) HCD and (B) UVPD of (1) unbound HA1 and (2) antibody-antigen complex. The dashed lines highlight the two epitope regions.

6.5 CONCLUSION

Native MS in conjunction with 193 nm UVPD was utilized to probe the antigenic determinants of an antibody-antigen complex. Plotting sequence coverage revealed suppression of UVPD along the two expected epitope regions and provides an approach for elucidation of an unknown antigenic determinant. Moreover, comparing the sequence ion types produced upon UVPD of the antigen in the presence and absence of the antibody highlighted a loss in diversity of fragment ion types covering the epitope regions for the complex. This observation merits future investigation in which utilizing different laser wavelengths or intensities could provide insight into the timescales and extent to which individual processes govern UVPD. Additional information about the specific factors that influence the lack of fragmentation of specific regions of antibody-antigen complexes might be obtained by employing supplemental activation prior to and/or after UVPD. When integrated with electron activation methods, supplemental activation has proven effective for disruption of non-covalent interactions that prevent the separation and release of fragment ions.[75]

Further experiments are underway to apply this UVPD-MS workflow to a wider variety of antibody-antigen complexes to determine if there is an ideal size regime or limit for the antigen as well as if targets that exist as higher order oligomers can be probed. Additionally, MS analysis can be hampered by the presence of post-translational modifications along the antigen, as demonstrated by extensive glycosylation of HA1. Nevertheless, leveraging native MS along with structurally sensitive MS/MS techniques such as ECD or UVPD could further minimize sample handling and provide a new era of MS-based epitope mapping to aid in the discovery of novel therapeutics for use in passive immunotherapy or the identification of conserved epitopes for improved vaccine design.

6.6 REFERENCES

(1) Mahler, M.; Fritzler, M. J. Epitope Specificity and Significance in Systemic Autoimmune Diseases. *Ann. N. Y. Acad. Sci.* **2010**, *1183*, 267–287.

(2) Regenmortel, M. H. V. V. Specificity, Polyspecificity, and Heterospecificity of Antibody-Antigen Recognition. *J. Mol. Recognit.* **2014**, *27*, 627–639.

(3) Abbott, W. M.; Damschroder, M. M.; Lowe, D. C. Current Approaches to Fine Mapping of Antigen–Antibody Interactions. *Immunology* **2014**, *142*, 526–535.

(4) Opuni, K. F. M.; Al-Majdoub, M.; Yefremova, Y.; El-Kased, R. F.; Koy, C.; Glocker, M. O. Mass Spectrometric Epitope Mapping. *Mass Spectrom. Rev.* **2018**, *37*, 229–241.

(5) Stefanescu, R.; Iacob, R. E.; Damoc, E. N.; Marquardt, A.; Amstalden, E.; Manea, M.; Perdivara, I.; Maftei, M.; Paraschiv, G.; Przybylski, M. Mass Spectrometric Approaches for Elucidation of Antigen—Antibody Recognition Structures in Molecular Immunology. *Eur. J. Mass Spectrom.* **2007**, *13*, 69–75.

(6) Wei, H.; Mo, J.; Tao, L.; Russell, R. J.; Tymiak, A. A.; Chen, G.; Iacob, R. E.; Engen, J. R. Hydrogen/Deuterium Exchange Mass Spectrometry for Probing Higher Order Structure of Protein Therapeutics: Methodology and Applications. *Drug Discov. Today* **2014**, *19*, 95–102.

(7) Puchades, C.; Kűkrer, B.; Diefenbach, O.; Sneekes-Vriese, E.; Juraszek, J.; Koudstaal, W.; Apetri, A. Epitope Mapping of Diverse Influenza Hemagglutinin Drug Candidates Using HDX-MS. *Sci. Rep.* **2019**, *9*, 1–10.

(8) Zhu, S.; Liuni, P.; Ettorre, L.; Chen, T.; Szeto, J.; Carpick, B.; James, D. A.; Wilson, D. J. Hydrogen–Deuterium Exchange Epitope Mapping Reveals Distinct Neutralizing Mechanisms for Two Monoclonal Antibodies against Diphtheria Toxin. *Biochemistry* **2019**, *58*, 646–656.

(9) Huang, R. Y.-C.; Jr, S. R. K.; Felix, N.; Graziano, R. F.; Srinivasan, M.; Pashine, A.; Chen, G. Hydrogen/Deuterium Exchange Mass Spectrometry and Computational Modeling Reveal a Discontinuous Epitope of an Antibody/TL1A Interaction. *mAbs* **2018**, *10*, 95–103.

(10) Wecksler, A. T.; Kalo, M. S.; Deperalta, G. Mapping of Fab-1:VEGF Interface Using Carboxyl Group Footprinting Mass Spectrometry. *J. Am. Soc. Mass Spectrom.* **2015**, *26*, 2077–2080.

(11) Kaur, P.; Tomechko, S. E.; Kiselar, J.; Shi, W.; Deperalta, G.; Wecksler, A. T.; Gokulrangan, G.; Ling, V.; Chance, M. R. Characterizing Monoclonal Antibody Structure by Carboxyl Group Footprinting. *mAbs* **2015**, *7*, 540–552.

(12) Zhang, Y.; Rempel, D. L.; Zhang, H.; Gross, M. L. An Improved Fast Photochemical Oxidation of Proteins (FPOP) Platform for Protein Therapeutics. *J. Am. Soc. Mass Spectrom.* **2015**, *26*, 526–529.

(13) Zhang, Y.; Wecksler, A. T.; Molina, P.; Deperalta, G.; Gross, M. L. Mapping the Binding Interface of VEGF and a Monoclonal Antibody Fab-1 Fragment with Fast Photochemical Oxidation of Proteins (FPOP) and Mass Spectrometry. *J. Am. Soc. Mass Spectrom.* **2017**, *28*, 850–858.

(14) Pimenova, T.; Nazabal, A.; Roschitzki, B.; Seebacher, J.; Rinner, O.; Zenobi, R. Epitope Mapping on Bovine Prion Protein Using Chemical Cross-Linking and Mass Spectrometry. *J. Mass Spectrom.* **2008**, *43*, 185–195.
(15) Rosati, S.; Yang, Y.; Barendregt, A.; Heck, A. J. R. Detailed Mass Analysis of Structural Heterogeneity in Monoclonal Antibodies Using Native Mass Spectrometry. *Nat. Protoc.* **2014**, *9*, 967–976.
(16) Thompson, N. J.; Rosati, S.; Heck, A. J. R. Performing Native Mass Spectrometry Analysis on Therapeutic Antibodies. *Methods* **2014**, *65*, 11–17.
(17) Leney, A. C.; Heck, A. J. R. Native Mass Spectrometry: What Is in the Name? *J. Am. Soc. Mass Spectrom.* **2017**, *28*, 5–13.
(18) Eschweiler, J. D.; Kerr, R.; Rabuck-Gibbons, J.; Ruotolo, B. T. Sizing Up Protein–Ligand Complexes: The Rise of Structural Mass Spectrometry Approaches in the Pharmaceutical Sciences. *Annu. Rev. Anal. Chem.* **2017**, *10*, 25–44.
(19) Kaur, U.; Johnson, D. T.; Chea, E. E.; Deredge, D. J.; Espino, J. A.; Jones, L. M. Evolution of Structural Biology through the Lens of Mass Spectrometry. *Anal. Chem.* **2019**, *91*, 142–155.
(20) Siuzdak, G.; Bothner, B.; Yeager, M.; Brugidou, C.; Fauquet, C. M.; Hoey, K.; Change, C.-M. Mass Spectrometry and Viral Analysis. *Chem. Biol.* **1996**, *3*, 45–48.
(21) Ruotolo, B. T.; Giles, K.; Campuzano, I.; Sandercock, A. M.; Bateman, R. H.; Robinson, C. V. Evidence for Macromolecular Protein Rings in the Absence of Bulk Water. *Science* **2005**, *310*, 1658–1661.
(22) Duijn, E. van; Barendregt, A.; Synowsky, S.; Versluis, C.; Heck, A. J. R. Chaperonin Complexes Monitored by Ion Mobility Mass Spectrometry. *J. Am. Chem. Soc.* **2009**, *131*, 1452–1459.
(23) Tito, M. A.; Miller, J.; Walker, N.; Griffin, K. F.; Williamson, E. D.; Despeyroux-Hill, D.; Titball, R. W.; Robinson, C. V. Probing Molecular Interactions in Intact Antibody: Antigen Complexes, an Electrospray Time-of-Flight Mass Spectrometry Approach. *Biophys. J.* **2001**, *81*, 3503–3509.
(24) Haberger, M.; Leiss, M.; Heidenreich, A.-K.; Pester, O.; Hafenmair, G.; Hook, M.; Bonnington, L.; Wegele, H.; Haindl, M.; Reusch, D.; Bulau, P. Rapid Characterization of Biotherapeutic Proteins by Size-Exclusion Chromatography Coupled to Native Mass Spectrometry. *mAbs* **2015**, *8*, 331–339.
(25) Yang, Y.; Wang, G.; Song, T.; Lebrilla, C. B.; Heck, A. J. R. Resolving the Micro-Heterogeneity and Structural Integrity of Monoclonal Antibodies by Hybrid Mass Spectrometric Approaches. *mAbs* **2017**, *9*, 638–645.
(26) Tian, Y.; Ruotolo, B. T. The Growing Role of Structural Mass Spectrometry in the Discovery and Development of Therapeutic Antibodies. *Analyst* **2018**, *143*, 2459–2468.
(27) Dyachenko, A.; Wang, G.; Belov, M.; Makarov, A.; de Jong, R. N.; van den Bremer, E. T. J.; Parren, P. W. H. I.; Heck, A. J. R. Tandem Native Mass-Spectrometry on Antibody–Drug Conjugates and Submillion Da Antibody–Antigen Protein Assemblies on an Orbitrap EMR Equipped with a High-Mass Quadrupole Mass Selector. *Anal. Chem.* **2015**, *87*, 6095–6102.

(28) Wang, G.; de Jong, R. N.; van den Bremer, E. T. J.; Beurskens, F. J.; Labrijn, A. F.; Ugurlar, D.; Gros, P.; Schuurman, J.; Parren, P. W. H. I.; Heck, A. J. R. Molecular Basis of Assembly and Activation of Complement Component C1 in Complex with Immunoglobulin G1 and Antigen. *Mol. Cell* **2016**, *63*, 135–145.
(29) Bond, K. M.; Aanei, I. L.; Francis, M. B.; Jarrold, M. F. Determination of Antibody Population Distributions for Virus-Antibody Conjugates by Charge Detection Mass Spectrometry. *Anal. Chem.* **2020**, *92*, 1285–1291.
(30) Lu, X.; DeFelippis, M. R.; Huang, L. Linear Epitope Mapping by Native Mass Spectrometry. *Anal. Biochem.* **2009**, *395*, 100–107.
(31) Danquah, B. D.; Röwer, C.; Opuni, K. F. M.; El-Kased, R.; Frommholz, D.; Illges, H.; Koy, C.; Glocker, M. O. Intact Transition Epitope Mapping – Targeted High-Energy Rupture of Extracted Epitopes (ITEM-THREE). *Mol. Cell. Proteomics* **2019**, *18*, 1543–1555.
(32) Atmanene, C.; Wagner-Rousset, E.; Malissard, M.; Chol, B.; Robert, A.; Corvaïa, N.; Dorsselaer, A. V.; Beck, A.; Sanglier-Cianférani, S.-. Extending Mass Spectrometry Contribution to Therapeutic Monoclonal Antibody Lead Optimization: Characterization of Immune Complexes Using Noncovalent ESI-MS. *Anal. Chem.* **2009**, *81*, 6364–6373.
(33) Huang, Y.; Salinas, N. D.; Chen, E.; Tolia, N. H.; Gross, M. L. Native Mass Spectrometry, Ion Mobility, and Collision-Induced Unfolding Categorize Malaria Antigen/Antibody Binding. *J. Am. Soc. Mass Spectrom.* **2017**, *28*, 2515–2518.
(34) Ehkirch, A.; Goyon, A.; Hernandez-Alba, O.; Rouviere, F.; D'Atri, V.; Dreyfus, C.; Haeuw, J.-F.; Diemer, H.; Beck, A.; Heinisch, S.; Guillarme, D.; Cianferani, S. A Novel Online Four-Dimensional SEC×SEC-IM×MS Methodology for Characterization of Monoclonal Antibody Size Variants. *Anal. Chem.* **2018**, *90*, 13929–13937.
(35) Allison, T. M.; Bechara, C. Structural Mass Spectrometry Comes of Age: New Insight into Protein Structure, Function and Interactions. *Biochem. Soc. Trans.* **2019**, *47*, 317–327.
(36) Pan, J.; Zhang, S.; Chou, A.; Hardie, D. B.; Borchers, C. H. Fast Comparative Structural Characterization of Intact Therapeutic Antibodies Using Hydrogen–Deuterium Exchange and Electron Transfer Dissociation. *Anal. Chem.* **2015**, *87*, 5884–5890.
(37) Pan, J.; Zhang, S.; Chou, A.; H. Borchers, C. Higher-Order Structural Interrogation of Antibodies Using Middle-down Hydrogen/Deuterium Exchange Mass Spectrometry. *Chem. Sci.* **2016**, *7*, 1480–1486.
(38) Zhang, Y.; Cui, W.; Wecksler, A. T.; Zhang, H.; Molina, P.; Deperalta, G.; Gross, M. L. Native MS and ECD Characterization of a Fab–Antigen Complex May Facilitate Crystallization for X-Ray Diffraction. *J. Am. Soc. Mass Spectrom.* **2016**, *27*, 1139–1142.
(39) Lermyte, F.; Sobott, F. Electron Transfer Dissociation Provides Higher-Order Structural Information of Native and Partially Unfolded Protein Complexes. *PROTEOMICS* **2015**, *15*, 2813–2822.

(40) Li, H.; Nguyen, H. H.; Ogorzalek Loo, R. R.; Campuzano, I. D. G.; Loo, J. A. An Integrated Native Mass Spectrometry and Top-down Proteomics Method That Connects Sequence to Structure and Function of Macromolecular Complexes. *Nat. Chem.* **2018**, *10*, 139–148.
(41) Brodbelt, J. S.; Morrison, L. J.; Santos, I. Ultraviolet Photodissociation Mass Spectrometry for Analysis of Biological Molecules. *Chem. Rev.* **2019**.
(42) Cotham, V. C.; Wine, Y.; Brodbelt, J. S. Selective 351 Nm Photodissociation of Cysteine-Containing Peptides for Discrimination of Antigen-Binding Regions of IgG Fragments in Bottom-Up Liquid Chromatography–Tandem Mass Spectrometry Workflows. *Anal. Chem.* **2013**, *85*, 5577–5585.
(43) Cotham, V. C.; Horton, A. P.; Lee, J.; Georgiou, G.; Brodbelt, J. S. Middle-Down 193-Nm Ultraviolet Photodissociation for Unambiguous Antibody Identification and Its Implications for Immunoproteomic Analysis. *Anal. Chem.* **2017**, *89*, 6498–6504.
(44) Shaw, J. B.; Liu, W.; Vasil′ev, Y. V.; Bracken, C. C.; Malhan, N.; Guthals, A.; Beckman, J. S.; Voinov, V. G. Direct Determination of Antibody Chain Pairing by Top-down and Middle-down Mass Spectrometry Using Electron Capture Dissociation and Ultraviolet Photodissociation. *Anal. Chem.* **2020**, *92*, 766–773.
(45) Shaw, J. B.; Li, W.; Holden, D. D.; Zhang, Y.; Griep-Raming, J.; Fellers, R. T.; Early, B. P.; Thomas, P. M.; Kelleher, N. L.; Brodbelt, J. S. Complete Protein Characterization Using Top-Down Mass Spectrometry and Ultraviolet Photodissociation. *J. Am. Chem. Soc.* **2013**, *135*, 12646–12651.
(46) O'Brien, J. P.; Li, W.; Zhang, Y.; Brodbelt, J. S. Characterization of Native Protein Complexes Using Ultraviolet Photodissociation Mass Spectrometry. *J. Am. Chem. Soc.* **2014**, *136*, 12920–12928.
(47) Greisch, J.-F.; Tamara, S.; Scheltema, R. A.; Maxwell, H. W. R.; Fagerlund, R. D.; Fineran, P. C.; Tetter, S.; Hilvert, D.; Heck, A. J. R. Expanding the Mass Range for UVPD-Based Native Top-down Mass Spectrometry. *Chem. Sci.* **2019**, *10*, 7163–7171.
(48) Zhou, M.; Liu, W.; Shaw, J. B. Charge Movement and Structural Changes in the Gas-Phase Unfolding of Multimeric Protein Complexes Captured by Native Top-Down Mass Spectrometry. *Anal. Chem.* **2020**, *92*, 1788–1795.
(49) Krammer, F.; Palese, P. Advances in the Development of Influenza Virus Vaccines. *Nat. Rev. Drug Discov.* **2015**, *14*, 167–182.
(50) Gamblin, S. J.; Skehel, J. J. Influenza Hemagglutinin and Neuraminidase Membrane Glycoproteins. *J. Biol. Chem.* **2010**, *285*, 28403–28409.
(51) Wu, N. C.; Wilson, I. A. Structural Insights into the Design of Novel Anti-Influenza Therapies. *Nat. Struct. Mol. Biol.* **2018**, *25*, 115–121.
(52) Air, G. M. Sequence Relationships among the Hemagglutinin Genes of 12 Subtypes of Influenza A Virus. *Proc. Natl. Acad. Sci. U. S. A.* **1981**, *78*, 7639–7643.
(53) Brandenburg, B.; Koudstaal, W.; Goudsmit, J.; Klaren, V.; Tang, C.; Bujny, M. V.; Korse, H. J. W. M.; Kwaks, T.; Otterstrom, J. J.; Juraszek, J.; Oijen, A. M. van;

Vogels, R.; Friesen, R. H. E. Mechanisms of Hemagglutinin Targeted Influenza Virus Neutralization. *PLOS ONE* **2013**, *8*, e80034.

(54) Sparrow, E.; Friede, M.; Sheikh, M.; Torvaldsen, S.; Newall, A. T. Passive Immunization for Influenza through Antibody Therapies, a Review of the Pipeline, Challenges and Potential Applications. *Vaccine* **2016**, *34*, 5442–5448.

(55) Laursen, N. S.; Friesen, R. H. E.; Zhu, X.; Jongeneelen, M.; Blokland, S.; Vermond, J.; Eijgen, A. van; Tang, C.; Diepen, H. van; Obmolova, G.; Kolfschoten, M. van der N.; Zuijdgeest, D.; Straetemans, R.; Hoffman, R. M. B.; Nieusma, T.; Pallesen, J.; Turner, H. L.; Bernard, S. M.; Ward, A. B.; Luo, J.; Poon, L. L. M.; Tretiakova, A. P.; Wilson, J. M.; Limberis, M. P.; Vogels, R.; Brandenburg, B.; Kolkman, J. A.; Wilson, I. A. Universal Protection against Influenza Infection by a Multidomain Antibody to Influenza Hemagglutinin. *Science* **2018**, *362*, 598–602.

(56) Sautto, G. A.; Kirchenbaum, G. A.; Ross, T. M. Towards a Universal Influenza Vaccine: Different Approaches for One Goal. *Virol. J.* **2018**, *15*, 17.

(57) Zhang, Y.; Xu, C.; Zhang, H.; Liu, G. D.; Xue, C.; Cao, Y. Targeting Hemagglutinin: Approaches for Broad Protection against the Influenza A Virus. *Viruses* **2019**, *11*.

(58) Mehaffey, M. R.; Sanders, J. D.; Holden, D. D.; Nilsson, C. L.; Brodbelt, J. S. Multistage Ultraviolet Photodissociation Mass Spectrometry To Characterize Single Amino Acid Variants of Human Mitochondrial BCAT2. *Anal. Chem.* **2018**, *90*, 9904–9911.

(59) Marty, M. T.; Baldwin, A. J.; Marklund, E. G.; Hochberg, G. K. A.; Benesch, J. L. P.; Robinson, C. V. Bayesian Deconvolution of Mass and Ion Mobility Spectra: From Binary Interactions to Polydisperse Ensembles. *Anal. Chem.* **2015**, *87*, 4370–4376.

(60) Watanabe, A.; McCarthy, K. R.; Kuraoka, M.; Schmidt, A. G.; Adachi, Y.; Onodera, T.; Tonouchi, K.; Caradonna, T. M.; Bajic, G.; Song, S.; McGee, C. E.; Sempowski, G. D.; Feng, F.; Urick, P.; Kepler, T. B.; Takahashi, Y.; Harrison, S. C.; Kelsoe, G. Antibodies to a Conserved Influenza Head Interface Epitope Protect by an IgG Subtype-Dependent Mechanism. *Cell* **2019**, *177*, 1124-1135.e16.

(61) Lee, J.; Boutz, D. R.; Chromikova, V.; Joyce, M. G.; Vollmers, C.; Leung, K.; Horton, A. P.; DeKosky, B. J.; Lee, C.-H.; Lavinder, J. J.; Murrin, E. M.; Chrysostomou, C.; Hoi, K. H.; Tsybovsky, Y.; Thomas, P. V.; Druz, A.; Zhang, B.; Zhang, Y.; Wang, L.; Kong, W.-P.; Park, D.; Popova, L. I.; Dekker, C. L.; Davis, M. M.; Carter, C. E.; Ross, T. M.; Ellington, A. D.; Wilson, P. C.; Marcotte, E. M.; Mascola, J. R.; Ippolito, G. C.; Krammer, F.; Quake, S. R.; Kwong, P. D.; Georgiou, G. Molecular-Level Analysis of the Serum Antibody Repertoire in Young Adults before and after Seasonal Influenza Vaccination. *Nat. Med.* **2016**, *22*, 1456–1464.

(62) Garten, R. J.; Davis, C. T.; Russell, C. A.; Shu, B.; Lindstrom, S.; Balish, A.; Sessions, W. M.; Xu, X.; Skepner, E.; Deyde, V.; Okomo-Adhiambo, M.; Gubareva, L.; Barnes, J.; Smith, C. B.; Emery, S. L.; Hillman, M. J.; Rivailler, P.; Smagala, J.; Graaf, M. de; Burke, D. F.; Fouchier, R. A. M.; Pappas, C.; Alpuche-Aranda, C. M.; López-Gatell, H.; Olivera, H.; López, I.; Myers, C. A.; Faix, D.; Blair, P. J.; Yu, C.; Keene, K. M.; Dotson, P. D.; Boxrud, D.; Sambol, A. R.; Abid, S. H.; George, K.

S.; Bannerman, T.; Moore, A. L.; Stringer, D. J.; Blevins, P.; Demmler-Harrison, G. J.; Ginsberg, M.; Kriner, P.; Waterman, S.; Smole, S.; Guevara, H. F.; Belongia, E. A.; Clark, P. A.; Beatrice, S. T.; Donis, R.; Katz, J.; Finelli, L.; Bridges, C. B.; Shaw, M.; Jernigan, D. B.; Uyeki, T. M.; Smith, D. J.; Klimov, A. I.; Cox, N. J. Antigenic and Genetic Characteristics of Swine-Origin 2009 A(H1N1) Influenza Viruses Circulating in Humans. *Science* **2009**, *325*, 197–201.

(63) Tate, M. D.; Job, E. R.; Deng, Y.-M.; Gunalan, V.; Maurer-Stroh, S.; Reading, P. C. Playing Hide and Seek: How Glycosylation of the Influenza Virus Hemagglutinin Can Modulate the Immune Response to Infection. *Viruses* **2014**, *6*, 1294–1316.

(64) Wang, L.; Qin, Y.; Ilchenko, S.; Bohon, J.; Shi, W.; Cho, M. W.; Takamoto, K.; Chance, M. R. Structural Analysis of a Highly Glycosylated and Unliganded Gp120-Based Antigen Using Mass Spectrometry. *Biochemistry* **2010**, *49*, 9032–9045.

(65) Wohlschlager, T.; Scheffler, K.; Forstenlehner, I. C.; Skala, W.; Senn, S.; Damoc, E.; Holzmann, J.; Huber, C. G. Native Mass Spectrometry Combined with Enzymatic Dissection Unravels Glycoform Heterogeneity of Biopharmaceuticals. *Nat. Commun.* **2018**, *9*, 1713.

(66) Lioe, H.; O'Hair, R. A. J. A Novel Salt Bridge Mechanism Highlights the Need for Nonmobile Proton Conditions to Promote Disulfide Bond Cleavage in Protonated Peptides under Low-Energy Collisional Activation. *J. Am. Soc. Mass Spectrom.* **2007**, *18*, 1109–1123.

(67) Quick, M. M.; Crittenden, C. M.; Rosenberg, J. A.; Brodbelt, J. S. Characterization of Disulfide Linkages in Proteins by 193 Nm Ultraviolet Photodissociation (UVPD) Mass Spectrometry. *Anal. Chem.* **2018**, *90*, 8523–8530.

(68) Jennewein, M. F.; Alter, G. The Immunoregulatory Roles of Antibody Glycosylation. *Trends Immunol.* **2017**, *38*, 358–372.

(69) Fort, K. L.; Waterbeemd, M. van de; Boll, D.; Reinhardt-Szyba, M.; Belov, M. E.; Sasaki, E.; Zschoche, R.; Hilvert, D.; Makarov, A. A.; Heck, A. J. R. Expanding the Structural Analysis Capabilities on an Orbitrap-Based Mass Spectrometer for Large Macromolecular Complexes. *Analyst* **2017**, *143*, 100–105.

(70) Cammarata, M. B.; Brodbelt, J. S. Structural Characterization of Holo- and Apo-Myoglobin in the Gas Phase by Ultraviolet Photodissociation Mass Spectrometry. *Chem. Sci.* **2015**, *6*, 1324–1333.

(71) Bajic, G.; Maron, M. J.; Adachi, Y.; Onodera, T.; McCarthy, K. R.; McGee, C. E.; Sempowski, G. D.; Takahashi, Y.; Kelsoe, G.; Kuraoka, M.; Schmidt, A. G. Influenza Antigen Engineering Focuses Immune Responses to a Subdominant but Broadly Protective Viral Epitope. *Cell Host Microbe* **2019**, *25*, 827-835.e6.

(72) Bangaru, S.; Lang, S.; Schotsaert, M.; Vanderven, H. A.; Zhu, X.; Kose, N.; Bombardi, R.; Finn, J. A.; Kent, S. J.; Gilchuk, P.; Gilchuk, I.; Turner, H. L.; García-Sastre, A.; Li, S.; Ward, A. B.; Wilson, I. A.; Crowe, J. E. A Site of Vulnerability on the Influenza Virus Hemagglutinin Head Domain Trimer Interface. *Cell* **2019**, *177*, 1136-1152.e18.

(73) R. Julian, R. The Mechanism Behind Top-Down UVPD Experiments: Making Sense of Apparent Contradictions. *J. Am. Soc. Mass Spectrom.* **2017**, *28*, 1823–1826.

(74) Paizs, B.; Suhai, S. Fragmentation Pathways of Protonated Peptides. *Mass Spectrom. Rev.* **2005**, *24*, 508–548.
(75) Riley, N. M.; Coon, J. J. The Role of Electron Transfer Dissociation in Modern Proteomics. *Anal. Chem.* **2018**, *90*, 40–64.

Chapter 7: Multistage Ultraviolet Photodissociation Mass Spectrometry to Characterize Single Amino Acid Variants of Human Mitochondrial BCAT2[**]

7.1 Overview

Unraveling disease mechanisms requires a comprehensive understanding of how the interplay between higher-order structure and protein-ligand interactions impacts the function of a given protein. Recent advances in native mass spectrometry (MS) involving multi-modal or higher energy activation methods have allowed direct interrogation of intact protein complexes in the gas phase, allowing analysis of both composition and subunit connectivity. We report a multistage approach combining collisional activation and 193 nm ultraviolet photodissociation (UVPD) to characterize single amino acid variants of the human mitochondrial enzyme branched-chain amino acid transferase 2 (BCAT2), a protein implicated in chemotherapeutic resistance in glioblastoma tumors. Native electrospray ionization confirms that both proteins exist as homodimers. Front-end collisional activation disassembles the dimers into monomeric subunits that are further interrogated using UVPD to yield high sequence coverage of the mutated region. Additionally, holo (ligand-bound) fragment ions resulting from photodissociation reveal that the mutation causes destabilization of the interactions with a bound cofactor. This study demonstrates the unique advantages of implementing UVPD in a multistage MS approach for analyzing intact protein assemblies.

[**]Mehaffey, M. R.; Sanders, J. D.; Holden, D. D.; Nilsson, C. L.; Brodbelt, J. S. Multistage Ultraviolet Photodissociation Mass Spectrometry to Characterize Single Amino Acid Variants of Human Mitochondrial BCAT2. *Anal. Chem.* **2018**, *90*, 9904-9911.

JDS and DDH implemented UVPD on the Q Exactive UHMR. CLN provided access to BCAT2 samples. JSB provided mentorship and reviewed the manuscript prior to publication.

7.2 INTRODUCTION

Single amino acid variants that result in altered function are often associated with oncogenic potential.[1–3] Precision design of small molecule inhibitors or therapeutic antibodies to target protein variants and suppress cancer growth relies on a comprehensive understanding of the functional impact of the mutation.[3,4] Recently a proteogenomic screening of glioma stem cells from patient-derived glioblastoma tumors identified the T186R sequence variant of the human mitochondrial enzyme branched-chain amino acid transferase 2 (BCAT2) as a potential factor of resistance to standard treatments.[5] BCAT2 exists as a 83 kDa homodimer and, along with a pyridoxal phosphate (PLP) cofactor, degrades branched chain amino acids into branched chain α-keto acids.[6,7] Crystallographic experiments suggest R186 in the mutant repulses K59 in the other subunit of the dimer and impacts the electrostatic environment near the CXXC (C342 and C345) site. Both are perturbations which may destabilize the dimer and alter enzyme kinetics.[8] Consequently characterization of the structural and functional differences between the wild-type (WT) and mutant proteoforms is necessary for further pursuit of the variant as a precision drug target in glioblastoma.

Mass spectrometry (MS) has emerged as a rapid and sensitive approach to characterize protein complexes[9–11] in a manner complementary to traditional structural biology techniques that afford high-resolution three-dimensional structures, such as X-ray crystallography and NMR spectroscopy. Native MS experiments involving the transfer of intact protein complexes into the gas phase via electrospray ionization of volatile salt solutions allow the higher levels of protein organization to be probed, thus providing structural information including stoichiometry and spatial arrangement of subunits.[9–11] Traditionally quadrupole time-of-flight (Q-TOF) instruments have been used for native MS experiments due to the efficient transmission of high *m/z* ions.[12–16] However, significant

inroads in characterization of protein complexes have occurred with the development of extended mass range Orbitrap mass spectrometers.[17,18] Both proteoform differentiation and measurement of ligand binding to macromolecular complexes are possible owing to the increased effective resolution and greater *m/z* range of these instruments compared to previous generations of Orbitrap instruments.[19–22] Moreover, disassembling higher-order structures using tandem mass spectrometry (MS/MS) techniques can further probe the higher-order structures of protein complexes. Electron-based activation methods, such as electron transfer dissociation (ETD)[23] and electron capture dissociation (ECD)[24], yield sequence fragment ions from intact protein complexes that correlate with the exposed surfaces and provide insight into the higher-order structure. Surface-induced dissociation (SID) is another activation method that combined with ion mobility (IM) reveals the subunit architecture of protein-protein complexes.[15] Although ETD, ECD, and SID have not yet been reported on an extended mass range Orbitrap platform, they have been demonstrated on other instruments capable of analyzing species over *m/z* 4000.[15,23,24] Recently ultraviolet photodissociation (UVPD) provided feedback about both quaternary and secondary structures of multimeric protein complexes as well as limited primary sequence information, based on disassembly of the complexes when irradiated with 193 nm photons.[25–27] Typically, separate bottom-up or top-down proteomics experiments involving digestion or denaturation of the protein complexes to further interrogate the primary sequence, localize post-translation modifications (PTMs), and identify proteoforms are necessary to provide an all-encompassing view into the dynamics and functional role of protein complexation in disease mechanisms.[28,29]

Efforts to bridge the gap between obtaining primary sequence information and deciphering architectures of protein complexes have driven the development of new multi-modal and/or higher energy activation mass spectrometry methods.[30–36] Recently in-source

dissociation (ISD), collisional-induced dissociation (CID), and infrared multiphoton dissociation (IRMPD) were used in conjunction with ECD on a Fourier-transform ion cyclotron resonance (FTICR) MS to yield an integrated native top-down MS/MS approach.[36] This strategy allowed acquisition of sequence and higher-order structural information of native protein complexes. Alternatively, a multistage MS approach on an extended mass range Orbitrap platform has been reported that involved introducing intact protein complexes into the gas phase by native ESI methods, disassembling protein complexes into monomers using front-end collisional activation, referred to as in-source trapping (IST), isolating a specific monomer using a quadrupole mass filter, then further fragmenting the selected monomeric species with higher energy collisional dissociation (HCD). Using this platform, the resulting multiply charged fragment ions were detected at high resolution and mass accuracy in an Orbitrap mass analyzer.[18,30,32–35] This approach has been demonstrated for model protein complexes,[30] applied to uncover a novel layer of regulation in a key metabolic enzyme,[34] and implemented in a high-throughput manner to identify endogenous protein complexes.[35] While these studies represent a major breakthrough, fragmentation efficiency using HCD was found to be low throughout the middle of the protein monomer sequences and bottom-up experiments were necessary to completely localize PTMs.[30,34] In order to enhance sequence coverage in this type of advanced multistage strategy, integration with UVPD offers a compelling option. The high-energy excitation caused by absorption of 193 nm photons has consistently demonstrated unsurpassed levels of diagnostic backbone fragmentation for intact monomeric proteins sprayed under both denaturing and native conditions.[27,37–41] UVPD has demonstrated improved retention of labile PTMs, including phosphorylation[42] and sulfation[43], allowing better localization of modifications. Additionally, mapping holo (ligand-bound) fragment ions produced during photodissociation of native-like proteins has been used to elucidate

regions of interaction with a bound ligand.[39,44–46] These properties make UVPD an ideal activation method for characterization of protein complexes.

Here we report the use of a multistage native UVPD-MS approach implemented on a modified prototype of an extended mass range Orbitrap mass spectrometer instrument to elucidate the oligomeric state, localize a single amino acid mutation, and identify the bound cofactor for two single amino acid variants of BCAT2 in a single experiment. Each variant was sprayed using native ESI to determine the oligomeric state. In-source trapping was used to disassemble the complexes into composing subunits that were isolated with a quadrupole mass analyzer and subjected to 193 nm UVPD. A previous top-down study combined ETD and CID in a LC-FT-ICR MS at 21 T to confidently localize the BCAT2 amino acid variant to its position in the sequence.[8] In the present study, native ESI confirms that both WT and T186R BCAT2 exist as homodimers, even when the proteins are combined in solution. Gently activating the complexes in the front-end of the instrument using in-source trapping splits the dimers into monomeric subunits that are each non-covalently bound to a PLP cofactor. UVPD of the monomer affords the highest level of sequence coverage compared to HCD of the monomers. Tracking holo ions observed during photodissociation of the monomers indicates that the cofactor interacts with the loop containing K229 where the cofactor is known to bind.[7]

7.3 EXPERIMENTAL

7.3.1 Sample Preparation

Human hemoglobin (Sigma-Aldrich, St. Louis, MO), ammonium acetate (Sigma-Aldrich, St. Louis, MO), acetonitrile (EMD Millipore, Billerica, MA), and formic acid (Fisher Scientific, Hampton, NH) were purchased. Recombinant human WT and T186R BCAT2 (**Figure 7.1**) were expressed using purchased plasmids and purified as previously

described.[8] Protein samples were diluted to 40 µM (hemoglobin) or 20 µM (BCAT2) of the complex in 50 mM ammonium acetate at pH 6.8 and desalted using micro bio-spin P-6 gel columns (Bio-Rad Laboratories Inc., Hercules, CA) for MS analysis.

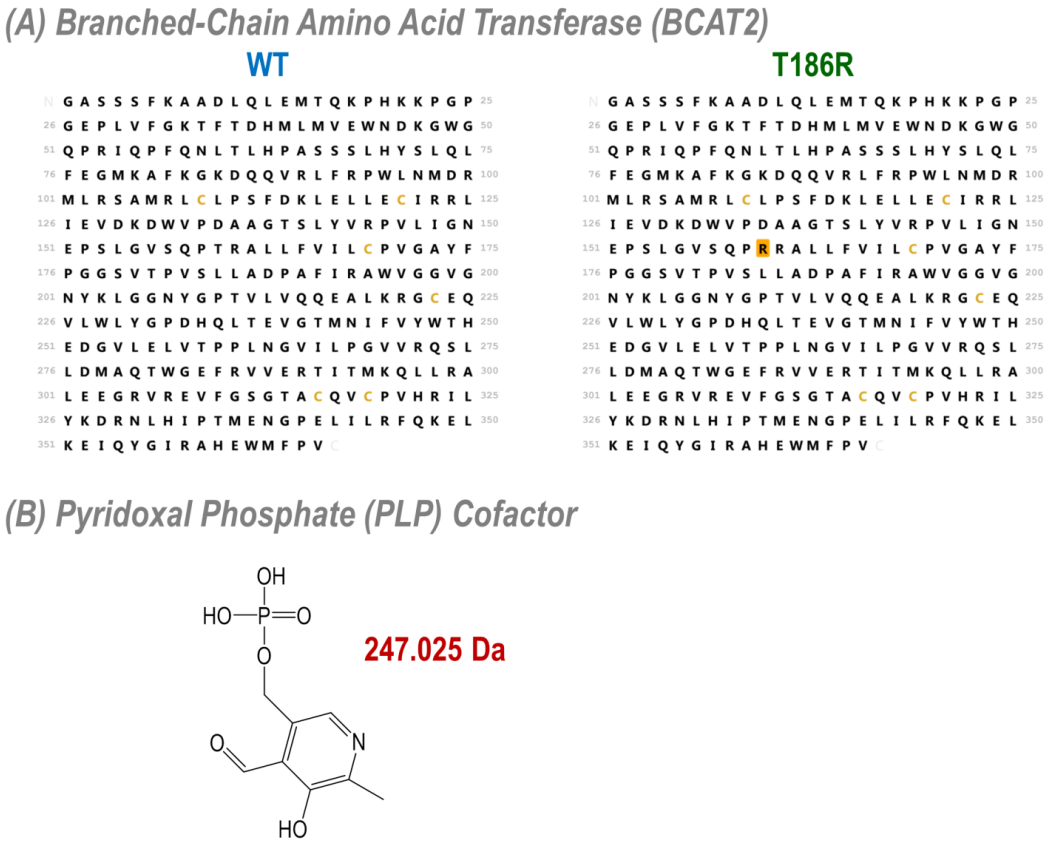

Figure 7.1: (A) Sequences of expressed WT and T186R protein constructs of BCAT2. The location of the variant amino acid is highlighted in yellow. The numbering system used to refer to the variant (T186R) and PLP binding site (K229) accounts for the 27 amino acid transit peptide that is not included in the expressed chain. (B) Structure of the pyridoxal phosphate (PLP) cofactor necessary for enzymatic action by BCAT2.

7.3.2 Mass Spectrometry

Hemoglobin samples at 40 µM in 50 mM ammonium acetate (pH 6.8) and BCAT2 samples diluted to 10 µM in 50:50 acetonitrile:water with 0.1% formic acid for MS analysis

under denaturing conditions were analyzed on a Thermo Scientific Orbitrap Elite mass spectrometer (Bremen, Germany) modified to enable photodissociation in the HCD cell with a Coherent Excistar 193 nm ArF excimer laser (Santa Cruz, CA), as previously described.[37] A gold-coated static tip nano-electrospray setup using an applied voltage of 1.0-1.1 kV and a heated capillary set at 275˚C were used to infuse protein samples. For MS1 spectra, sixty scans were averaged at a resolving power of 240K at *m/z* 400 and an automatic gain control setting of 1E6. Ion trap isolation with an isolation width of 15 *m/z* was used to select the 7+ charge states of the α– or β–chain of holo-hemoglobin, and the 27+ or 37+ charge state of BCAT2 for MS/MS analysis. HCD (15-20% NCE) and UVPD (1 pulse at 1.5 or 3 mJ) fragmentation spectra represent the average of 500 scans (over a range from *m/z* 220-4000) using an automatic gain control setting of 5E5 and maximum ion time of 2 sec. Three replicates of MS/MS spectra were collected for each protein.

A schematic of the modified prototype of a Thermo Scientific Q Exactive UHMR instrument (Bremen, Germany) used for all multistage experiments is given in **Figure 7.2**. The instrument was built on the basis of a standard Q Exactive Plus (Thermo Scientific, Bremen, Germany) and modified to optimize the analysis of ions up to 80,000 *m/z*, as described in references 18 and 22. Briefly, several customized boards to enable lowering of the RF frequency in the instrument's ion guides, a capillary to allow higher bath gas pressure in the HCD cell, and an S-lens exit lens with a smaller aperture (1 mm instead of 2 mm) were installed in place of standard parts. Additionally, pulsing of the electrical potentials within the injection flatapole and inter-flatapole lens allows implementation of in-source trapping (**Figure 7.2**).[18,22,30,32–35] UVPD was implemented in the HCD cell through incorporation of a Coherent Excistar 193 nm ArF excimer laser (Santa Cruz, CA).

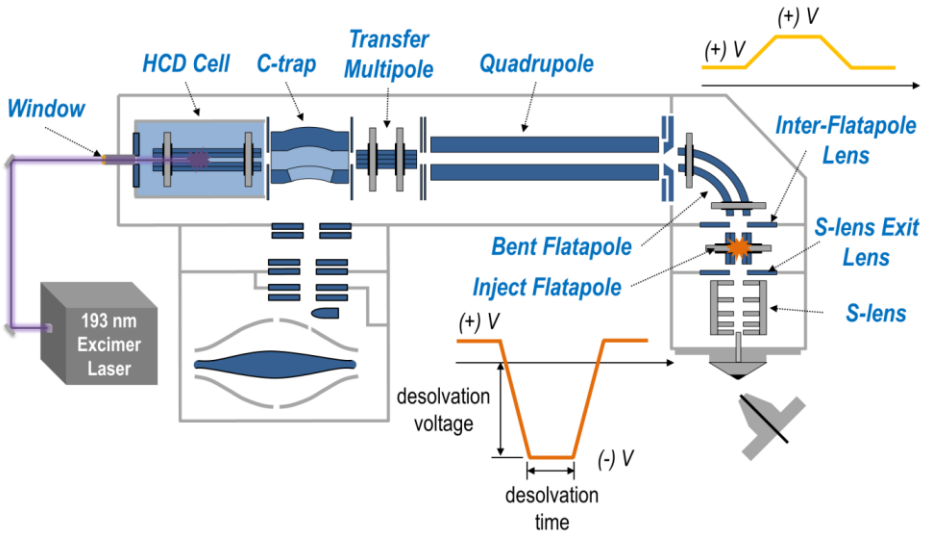

Figure 7.2: Schematic representation of implementation of UVPD in the HCD cell of a prototype of the Thermo Scientific Q Exactive UHMR mass spectrometer. Modified electronics allow the ion guides (bent flatapole, quadrupole, transfer multipole, C-trap) and HCD cell to operate at lower RF frequencies favoring the transmission of higher *m*/*z* ions. In-source trapping is enabled in the injection flatapole region by raising the bias of the inter-flatapole lens and trapping the ions in a potential well created between the S-lens exit lens and inject flatapole. The depth and duration of this potential well is set by the desolvation voltage and desolvation time, respectively.

Implementation of UVPD on the prototype Q Exactive Plus UHMR instrument required removal of the charge detector (electrometer, routinely used to aid in automatic gain control) to incorporate a fused silica optical window (Kurt J. Lesker Company, Hustings, England) and allow introduction of the laser beam concentric with the HCD cell. Removal of the electrometer breached the vacuum seal between the back of the HCD cell and high-vacuum chamber, causing increased flow of collision gas from the cell. To mitigate the resulting loss of pressure, a stainless steel tube (2 cm O.D × 13 cm long) with O-rings affixed to either end was inserted through a hole in a custom built vacuum flange so that it made contact with a Teflon washer mounted to the back of the HCD cell, thus preventing gas from leaking out. The fused silica window was mounted to the other end of

the tube using a custom-built holder. An optical periscope (Thorlabs, Newton, NJ) equipped with two 25 mm UV mirrors (Edmund Optics, Barrington, NJ) mounted at 45˚ with micropositioners was used to elevate and guide the laser beam coaxial to the HCD cell. Emission of the laser was triggered by a rise in the HCD multipole DC offset so that the laser was triggered after ions had cooled in the HCD and just prior to sending them to the C-trap. To bring the offset signal down to a 0-5 V range, it was modulated by a series of voltage dividers and diodes assembled in house. Following voltage division this signal was used to gate an Arduino Uno microcontroller programmed with a custom script to generate one or more TTL pulses, corresponding to the desired number of laser shots specified by the user, to trigger the laser.

A nano-electrospray setup with gold-coated borosilicate emitters operated at 1.0-1.2 kV was used to infuse protein solutions. A heated inlet capillary set at 200˚C aided in desolvation. The modified electronics on the instrument enabled transmission of higher *m*/*z* ions by operating at lower RF frequencies for the bent flatapole (1.1 MHz), transfer multipole (770 kHz), C-trap (2.1 MHz), and HCD cell (770 kHz). Additionally, control of the nitrogen bath gas pressure was adjusted during collection of MS1 (UHV pressure of 1.09E-9 mbar), in-source trapping (UHV pressure of 4.09E-10 mbar), HCD MS/MS (UHV pressure of 4.09E-10 mbar), UVPD MS/MS (UHV pressure of 1.28E-10 mbar) spectra to optimize signal intensity.

In-source trapping was enabled in the region of the injection flatapole. Specifically, the inter-flatapole lens is operated at an increased positive potential compared to the normal operating value to block the ions from exiting the injection flatapole. Simultaneously the injection flatapole is maintained at a negative voltage (up to -300 V), referred to as the desolvation voltage (**Figure 7.2**). During trapping, as ions exit the S-lens region they collide with background gas and settle at the bottom of a potential well created by the S-

lens exit lens and injection flatapole for a set amount of time termed the desolvation time (4 ms – 10 ms) (**Figure 7.2**). A 200 µs release event returns the inject flatapole and inter-flatapole lens biases to their set operating values (given in **Table 7.1**). Depending on protein size and flexibility, lower desolvation voltage values (-50 to -150 V) typically leave complexes intact and simply aid in desolvation while higher desolvation voltages (> -150 V) result in complex disassembly into constituent subunits.

Given that implementation of UVPD required removal of the electrometer, the automated gain control was turned off for all experiments. Instead the maximum inject time was optimized to control the number of ions analyzed. **Table 7.1** summarizes all other instrumental parameters used for each scan type: MS1, in-source trapping, and MS/MS. For MS1 and in-source trapping spectra, fifty scans were averaged while the MS/MS spectra represent the average of 500 scans. During collection of in-source trapping and MS/MS spectra, the RF amplitude of the bent flatapole and injection flatapole were dropped from 990 Vpp to 300 Vpp to favor the transfer of lower mass ions. For MS/MS analysis, the most intense monomeric charge state was selected after in-source trapping with an isolation width of ±15 *m*/*z* using a segmented quadrupole mass filter with a modified electronic board that featured a decreased RF frequency (278 kHz) allowing a mass-selection limit of up to 40,000 *m*/*z*. During MS/MS analysis, HCD collision energy was set to 225 eV or 160 eV for the activation of dimers and monomers, respectively. For UVPD MS/MS spectra, ions were activated by exposure to a single 1 mJ or 3 mJ pulse.

Table 7.1: Summary of instrumental parameters used for analysis of BCAT2 solutions.

Parameter	***Scan Type***		
	MS1	**IST**	**MS/MS**
Source Fragmentation (eV)	20	50	50
Desolvation Voltage (V)	-100	-250	-250
Desolvation Time (ms)	4	6	6
Source DC Offset (V)	3	3	3
Injection Flatapole DC (V)	10	9	9
Inter-Flatapole Lens (V)	8	8	8
Bent Flatapole DC (V)	7	7	7
Auto Transfer Multipole DC (V)	6.5	5.0	5.0
Auto C-Trap Entrance Lens Inject (V)	5.0	3.5	3.5
Resolving Power (at *m*/*z* 200)	10K	15K	140K
Max Inject Time (ms)	25	50	500
Scan Range (*m*/*z*)	1000-10000	1000-10000	500-8000

A Dionex LC system interfaced to the modified Thermo Scientific Q Exactive UHMR instrument described above was used to perform all size exclusion chromatography experiments. For each run, 5 µg of protein complex (5 µL injection volume) in 50 mM ammonium acetate (pH 6.8) was injected onto a 2.1 mm × 30 cm Zenix-C column with an 80 Å pore size and 3 µm particle size (Sepax Technologies, Newark, DE). An isocratic mobile phase comprised of 50 mM ammonium acetate at pH 6.8 was applied at a flow rate of 80 µL min^{-1}. A HESI source with an applied voltage of 4 kV was used to introduce the LC effluent into the MS. Data was collected using the parameters for MS1 spectra described above in **Table 7.1**.

7.3.3 Data Analysis

Intact molecular masses of protein complexes from MS1 and in-source trapping mass spectra were determined by taking the apex of the most abundant peak in the charge state distribution, manually calculating the charge state based on the spacing of the peaks, and calculating the molecular mass from the assigned charge state. All MS/MS spectra

were de-charged and de-isotoped using Xtract with a signal-to-noise ratio of 3, fit factor of 44%, and remainder of 25%. ProSight Lite v1.4 software was used to search monoisotopic fragment ions against the sequence of hemoglobin or BCAT2 and identify fragment ions (± 10 ppm) produced by HCD (*b*, *y*) or UVPD (*a*, $a^{\bullet}$, *b*, *c*, *x*, $x^{\bullet}$, *y*, *y*-1, *z*). Sequence coverage maps shown were created using ProSight Lite according to the following legend: *a/x*-type ions (green), *b/y*-type ions (blue), and *c/z*-type ions (red). Holo fragment ions resulting from UVPD were identified by searching the spectra for a mass shift corresponding to the heme in hemoglobin (615.170 Da) or PLP in BCAT2 (247.025 Da) fixed at the N- and C-terminus. For all MS/MS spectra, three replicates were collected. Only fragment ions (apo and holo) identified in all three replicates were considered confidently identified. All raw spectra are archived and available at: https://repository.jpostdb.org/ and accession numbers are PXD009447 for ProteomeXchange and JPST000410 for jPOST.

7.4 Results and Discussion

7.4.1 Multistage Native UVPD-MS for Complete Protein Complex Characterization

The recent development of Orbitrap mass spectrometers with extended mass range capabilities has enabled improved resolution and sensitivity in the analysis of protein complexes.[17–22,30–35] Specifically modification of the quadrupole RF drive allows selection of higher *m/z* species and implementation of a "trap and release" approach to convert the inject flatapole into a linear quadrupole trap affords high-efficiency desolvation and improved dissociation of assemblies into subunits.[18,30,32–35] By leveraging these key upgrades in instrumentation, we have further advanced the utility of a multistage approach for analysis of protein complexes by implementing UVPD for activation/fragmentation after disassembly of the complexes. To optimize and characterize the performance of this multistage approach, we first analyzed the heterotetramer hemoglobin (64 kDa).

Electrospray ionization of hemoglobin in a solution containing the volatile salt ammonium acetate allows efficient transfer of the intact heterotetramer into the gas phase (**Figure 7.3**). The 15+, 16+, and 17+ charge states of a complex comprised of two α-chains and two β-chains with each subunit non-covalently bound to a heme ligand were observed in the MS1 spectrum (**Figure 7.3A**). Increasing the applied desolvation voltage allows in-source trapping, resulting in dissociation of the tetramer into its constituent α- and β-chain monomers as well as some low abundance dimeric species (**Figure 7.3B**). Interestingly, the non-covalently bound heme is retained during this front-end low energy collisional activation, yielding the 7+ charge states of the α– and β–chains that can be selectively isolated using the quadrupole (**Figure 7.3C, 7.3D**) and subsequently activated with HCD or UVPD. The fragmentation patterns observed for the α- and β-chain monomers activated with HCD or 193 nm UVPD are shown in **Figure 7.4**. Important benchmark performance comparisons are facilitated by comparison of the sequence information obtained by this multistage approach (which allows dissection of multimers) to the sequence information obtained directly from monomeric forms of the protein. As extended mass range instruments are designed for analysis of large, multimeric complexes, the higher mass range is optimized at the expense of the lower mass range. To ensure this did not impede the efficient transmission of monomeric proteins, the sequence analysis of hemoglobin was undertaken using similar native MS conditions on a standard Orbitrap instrument (without extended mass range) outfitted with UVPD to enable direct analysis of monomers.[25,37–40,44–46] The 7+ charge state of α- and β-chain monomers were observed in the MS1 spectrum obtained on the Elite mass spectrometer, each of which could be isolated using the ion trap and activated with HCD or UVPD (**Figure 7.4**). Identifying the fragment ions and mapping these along the sequences confirms that the multistage approach on the extended mass range Orbitrap instrument yields comparable or higher sequence coverage of the α- and β-

chains of hemoglobin for both HCD and UVPD (**Figure 7.4**). Additionally, holo (ligand-bound) fragment ions originated from the same regions of the protein using the multistage approach on the mass spectrometer with the extended mass range compared to the direct analysis of monomers on the standard Orbitrap mass spectrometer, suggesting that sufficient electrostatic contacts between the ligand and protein side-chains are maintained during in-source trapping to allow retention of binding site information. This optimized multistage approach involving native MS, in-source trapping, and UVPD provides an ideal platform to interrogate the differences in fragmentation of dimeric BCAT2 complexes containing the WT and T186R variants.

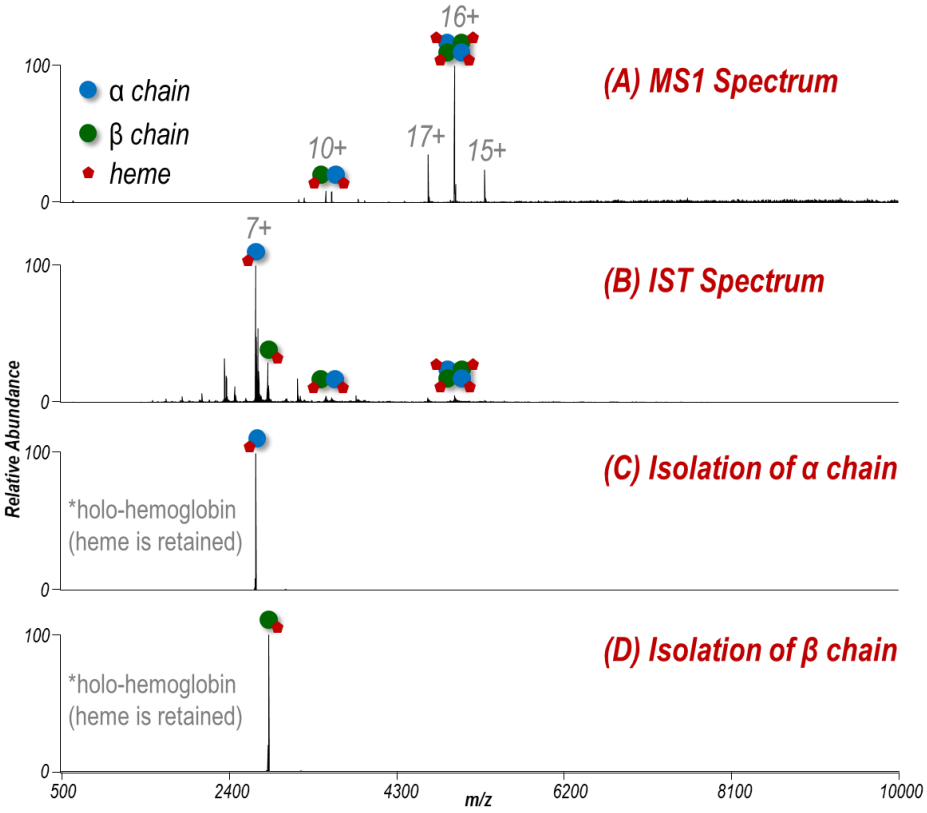

Figure 7.3: (A) ESI mass spectra (*m/z* 500-10,000) of hemoglobin sprayed in 50 mM ammonium acetate (pH 6.8). Each species observed is identified by colored circles. (B) IST ejects the 7+ monomers of the α and β chains in which the heme is retained. (C, D) Using the quadrupole, each chain can be selectively isolated for MS/MS analysis.

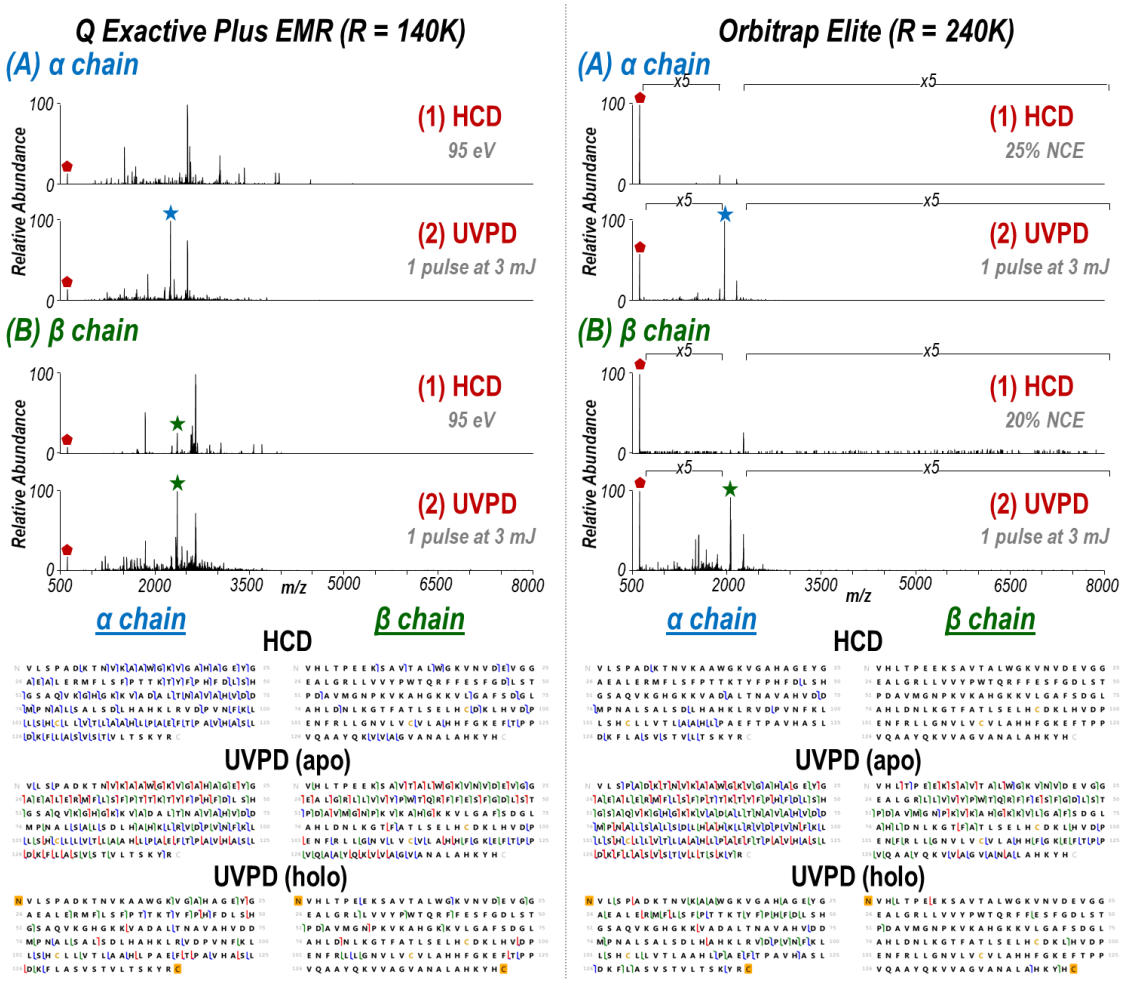

Figure 7.4: Direct comparison of (1) HCD and (2) UVPD mass spectra of the 7+ charge state of the monomeric (A) α and (B) β chains of holo hemoglobin collected on the Q Exactive UHMR (left) and Orbitrap Elite (right). The precursor species was observed after IST on the UHMR and in the MS1 spectra on the Elite. Surviving precursors are indicated with a star in the MS/MS spectra and the ejected heme is identified with a red pentagon. Sequence coverage maps for HCD and UVPD (apo and holo fragment ions separately) of the α and β chains are shown beneath the spectra (± 10 ppm tolerance). Holo fragment ions were identified by searching for a +615.170 Da shift fixed at the N- and C-terminus to encompass all mass-shifted product ions. The holo ions observed for both chains are similar for each mass spectrometer. The heme is known directly interact with H58 and H87 for the α-chain, and H63 and H92 for the β-chain.

7.4.2 Native MS1 and Size-Exclusion Chromatography of BCAT2

Spraying WT and T186R BCAT2 under native conditions provides insight into the oligomeric state of each variant, thus revealing the highest level of protein structure. The MS1 spectra of WT and T186R BCAT2 indicate that each protein exists as a homodimer (**Figure 7.5A**, **7.5B**). Although previous crystallographic experiments[8] indicate that R186 in the mutant repulses K59 in the other subunit, this effect is insufficient to completely destabilize the dimer. Heterodimers were not observed after simply mixing the variants; a co-folding experiment would be necessary to investigate more explicitly the potential formation of WT and T186R heterodimers (**Figure 7.5C**). The observed masses of the dimers were 497 Da greater than the theoretical masses (**Figure 7.5**), suggesting that one or more ligands are non-covalently bound to the proteins. Conversely, when the proteins are sprayed from denaturing solutions, no mass shift is observed for the unfolded monomeric proteins (**Figure 7.6**). Sequence coverages were 11% (27+, denatured) and 7% (37+, denatured) from HCD, and 36% (27+, denatured) and 34% (37+, denatured) from UVPD for WT and T186R BCAT2, respectively. The mass shift for the dimers is attributed to the non-covalent binding of one PLP cofactor (247.025 Da) to each subunit of the dimer. A PLP cofactor is necessary for the enzymatic action of the protein.[7] On-line size-exclusion chromatography was used to confirm the results observed for the MS1 spectra (**Figure 7.7**). The proteins were injected individually and as a mixture after incubation for 120 minutes. Each variant eluted as a homodimer containing two molecules of PLP. Extracted ion chromatograms confirmed that no heterodimers were observed, nor were any dimers containing a single or no cofactors (**Figure 7.7**).

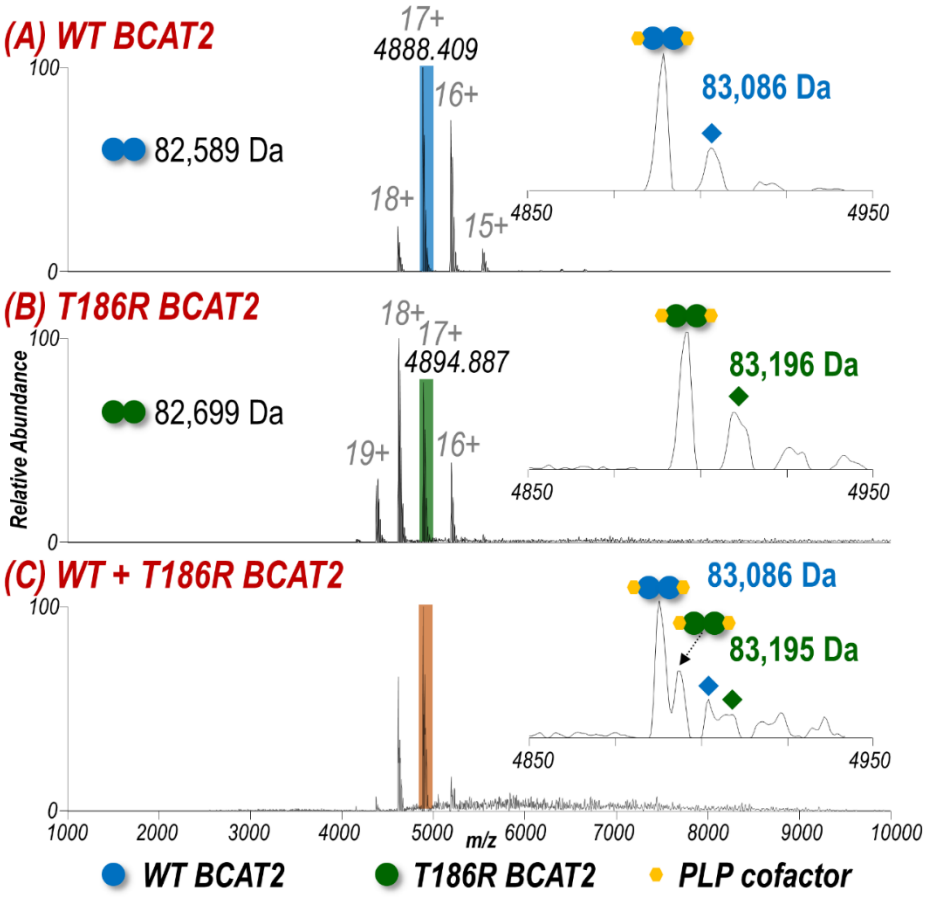

(D)

BCAT2 Variant	Theoretical Mass of Dimer (Da)	Measured Mass of Dimer (Da)
WT	*82,589*	*83,086*
T186R	*82,699*	*83,196*

Figure 7.5: ESI mass spectra (*m/z* 1,000-10,000) of (A) WT, (B) T186R, and (C) WT+T186R BCAT2 sprayed in 50 mM ammonium acetate (pH 6.8). Each species observed is identified by colored circles in an expanded view (insets) of the 17+ charge state of the homodimer (*m/z* 4,850-4,950). The peaks denoted by diamonds (♦) represent the corresponding Na-adducted species. The experimentally measured masses are 497 Da larger than the expected masses for both WT and T186R BCAT2. This mass shift is attributed to a PLP cofactor bound to each subunit of the dimer. As demonstrated in (C), combining the protein variants in solution only yields homodimers. SEC confirms that these are the oligomeric states that exist in solution (Figure 7.7). The table in (D) summarizes theoretical and measured masses for the dimers.

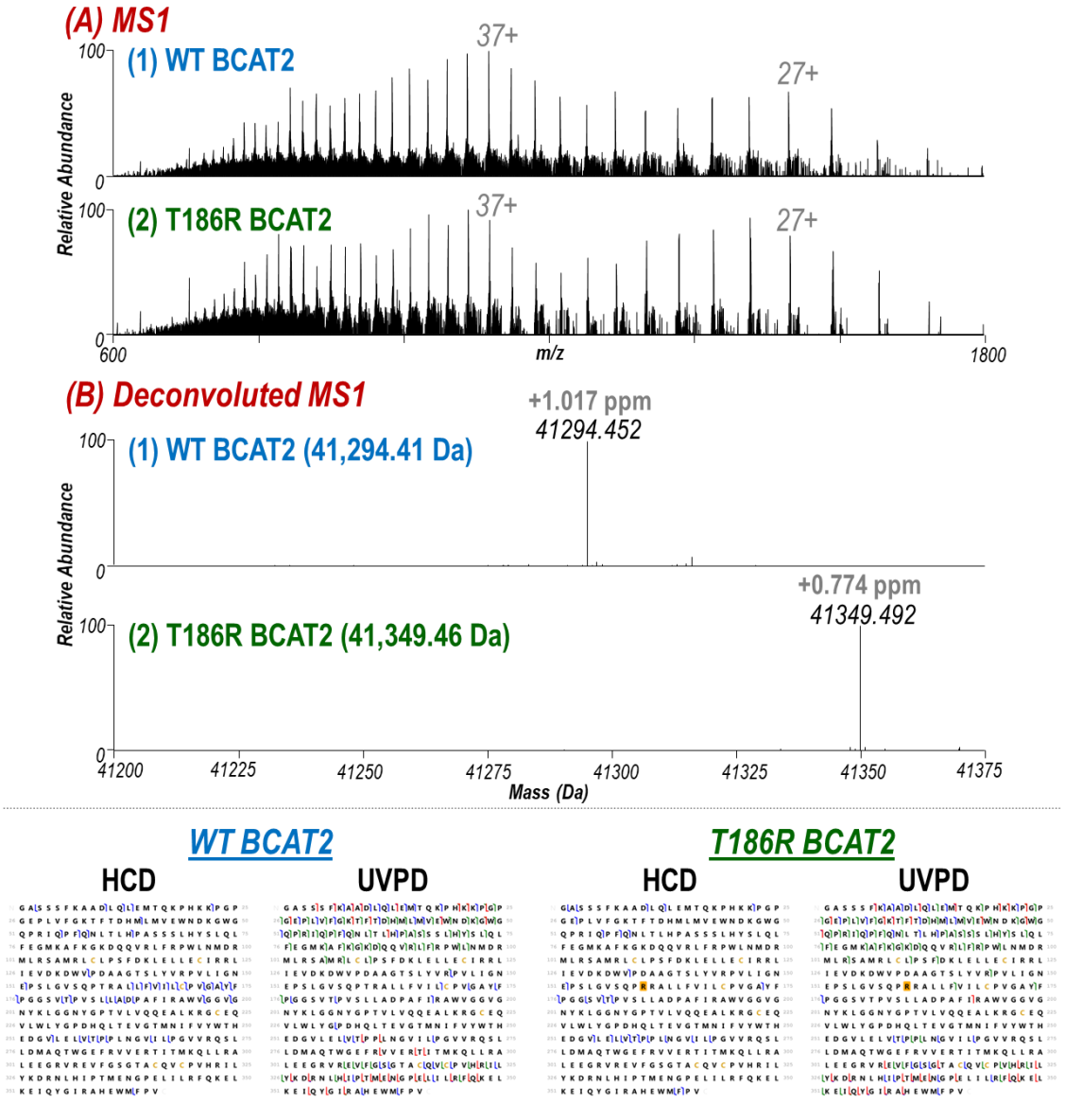

Figure 7.6: (A) ESI mass spectra collected on the Orbitrap Elite (*m/z* 600-1,800) of (1) WT and (2) T186R BCAT2 sprayed under denaturing conditions (50:50 ACN:H_2O w/ 0.1% formic acid). (B) Deconvoluted ESI mass spectra of (1) WT and (2) T186R BCAT2 confirming that the intact masses are within 2 ppm of the expected masses for both protein variants without any cofactor bound. Combined HCD (15% NCE) or UVPD (1 pulse at 2 mJ) sequence coverage maps of the 27+ and 37+ charge states of each variant are shown beneath the spectra. Sequence coverages were 11% and 7% from HCD, and 36% and 34% from UVPD for WT and T186R BCAT2, respectively.

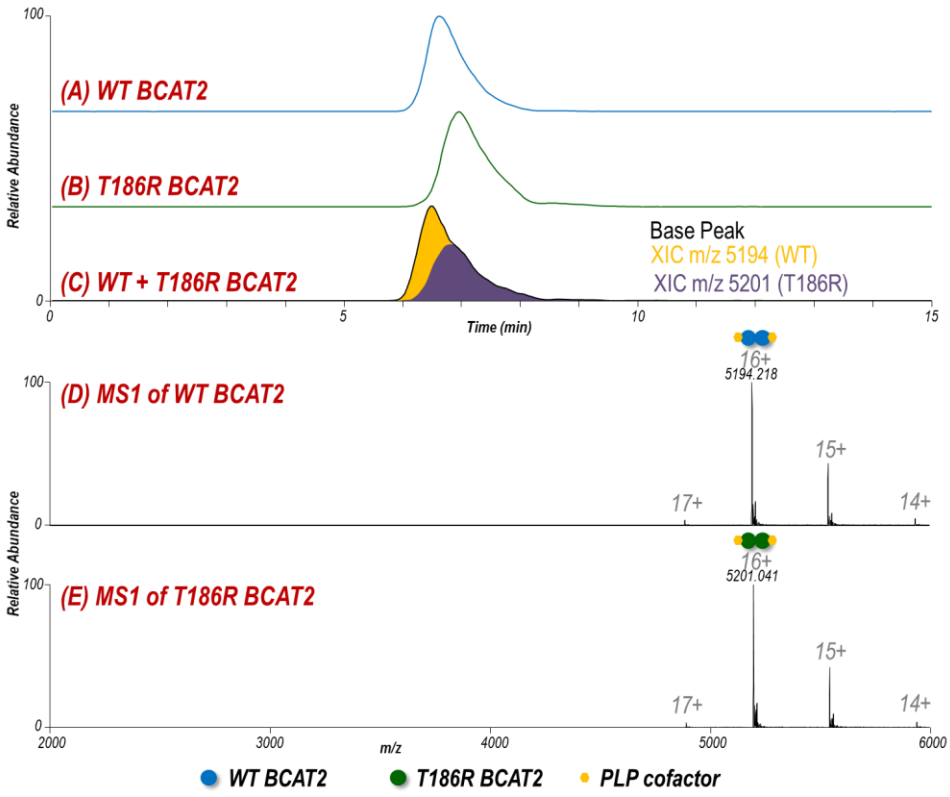

Figure 7.7: (A-C) SEC base peak LC traces of (A) WT, (B) T186R, and (C) WT+T186R BCAT2. For the combined sample in (C), XIC traces of the m/z values corresponding to the homodimer of each variant are shown. (D, E) ESI mass spectra (*m/z* 2,000-6,000) collected at RT 6.60 min in (A) and 6.95 min in (B) confirm that both variants exist as homodimers in solution with each subunit bound to a PLP cofactor.

7.4.3 In-Source Trapping and UVPD for Improved Localization of T186R Mutation in BCAT2

Identification of the protein sequences requires activation and disassembly of the dimeric complexes. Irradiation of protein complexes in the gas phase with 193 nm photons has been demonstrated to release the constituent subunits as well as diagnostic backbone fragment ions.[25,26] Isolation and activation of the homodimers of WT and T186R BCAT2 (17+ charge state with two PLP cofactors per dimer) by HCD or UVPD produces the MS/MS spectra shown in **Figure 7.8**. Both activation methods result in backbone cleavages

that result in production of diagnostic sequence ions (**Figure 7.8**). UVPD outperforms HCD for both protein variants, yielding higher sequence coverage deeper into the protein sequence. Sequence coverages were 12% and 16% from HCD, and 21% and 28% from UVPD for WT and T186R BCAT2, respectively. This improved coverage is attributed to the access to excited electronic states and thus higher energy fragmentation pathways upon absorption of 193 nm photons.[25,26,37,38,41] Additionally, the pressure of the nitrogen bath gas in the trapping cell used for ion activation was significantly reduced during UVPD, resulting in a slower transient decay and higher resolution frequency measurements and improved sensitivity as a result of fewer collisions during ion ejection from the C-trap into the mass analyzer and during analysis in the Orbitrap.[47,48] The use of reduced pressure has no impact on the fragmentation efficiency of UVPD but is detrimental for the performance of HCD.

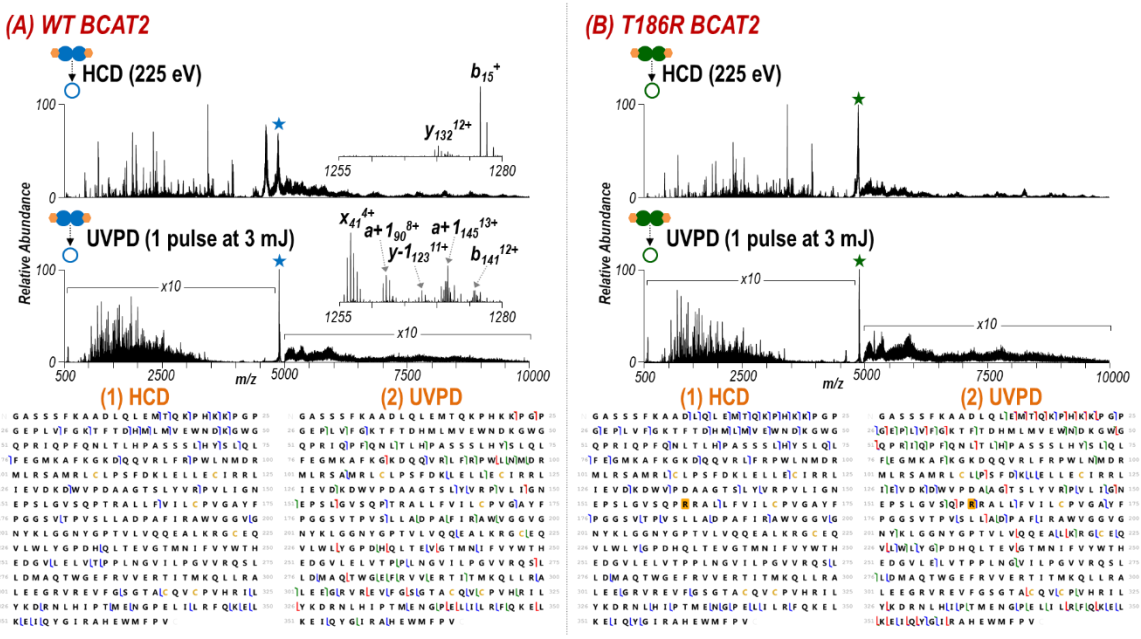

Figure 7.8: HCD and UVPD mass spectra of the 17+ charge state of the homodimer of (A) WT and (B) T186R BCAT2. Expanded views (*m/z* 1,255-1,280) in panel (A) show selected fragment ions labelled. The precursors are indicated with a star in the MS/MS spectra. Sequence coverage maps for (1) HCD and (2) UVPD of (A) WT and (B) T186R BCAT2 are shown beneath the spectra. Sequence coverages were 12% and 16% from HCD, and 21% and 28% from UVPD for WT and T186R BCAT2, respectively. The Thr residue mutated to an Arg is shaded in gold in panel (B).

When protein complexes are subjected to UVPD, sequence ions that retain the PLP cofactor or portions of other subunits are produced, in addition to the diagnostic apo (ligand-free) fragment ions. The formation of such holo (ligand-bound) fragment ions has been observed previously for UVPD.[39,44–46] Conversely, HCD causes ejection of ligands and results exclusively in formation of apo fragment ions. In the case of the BCAT2, the sequence coverage achieved with UVPD would be even further improved if the holo fragment ions bound to the PLP cofactor could be identified and contribute in a meaningful way to the net sequence coverage. Confident identification of holo ions at this time is challenging for a protein complex of this size given the nearly unlimited array of possible

fragment ion assignments that can arise from combinations of partial protein sequence segments and the PLP cofactor. In essence, "mass shifted" fragment ions could be falsely attributed to the presence of the PLP cofactor when in reality the mass shift arises from a portion of the protein from the other subunit with the same exact mass as the cofactor. By utilizing a multistage approach, however, monomers can be separated from the dimeric complexes at the front-end of the mass spectrometer prior to MS/MS analysis, thus alleviating the ambiguity in the origin and identities of holo fragment ions.[30,32–35] For implementation of the multistage strategy, the in-source trapping parameters were optimized to cause subunit ejection and yield the mass spectra shown in **Figure 7.9**. The bound PLP ligands are retained as the subunits are disassembled. A mass shift of +249 Da corresponding to a single PLP cofactor bound to a monomeric subunit of the protein is observed for both variants. In-source trapping of the solution containing both the WT and T186R proteins yields PLP-bound monomers of each (**Figure 7.9C**).

The 12+ charge state monomer of each variant bound to a PLP cofactor resulting from in-source trapping of the observed homodimer was selectively isolated and activated with HCD or UVPD, resulting in the MS/MS spectra in **Figure 7.10**. Identified sequence ions are mapped on to the known protein sequences (**Figure 7.10**). As evident in the UVPD spectra, lower energy laser pulses (1 mJ) yielded larger fragments corresponding to cleavage in the central region of the protein. Conversely, using a higher energy per laser pulse (3 mJ) resulted in smaller fragments originating from the termini of the protein. The UVPD sequence maps shown in **Figure 7.10** represent the combined coverage for identified apo and holo (ligand-bound) fragment ions for the spectra collected using 1 mJ and 3 mJ per pulse. For comparison, **Figure 7.11** gives sequence coverage maps based solely on the apo fragment ions obtained from UVPD.

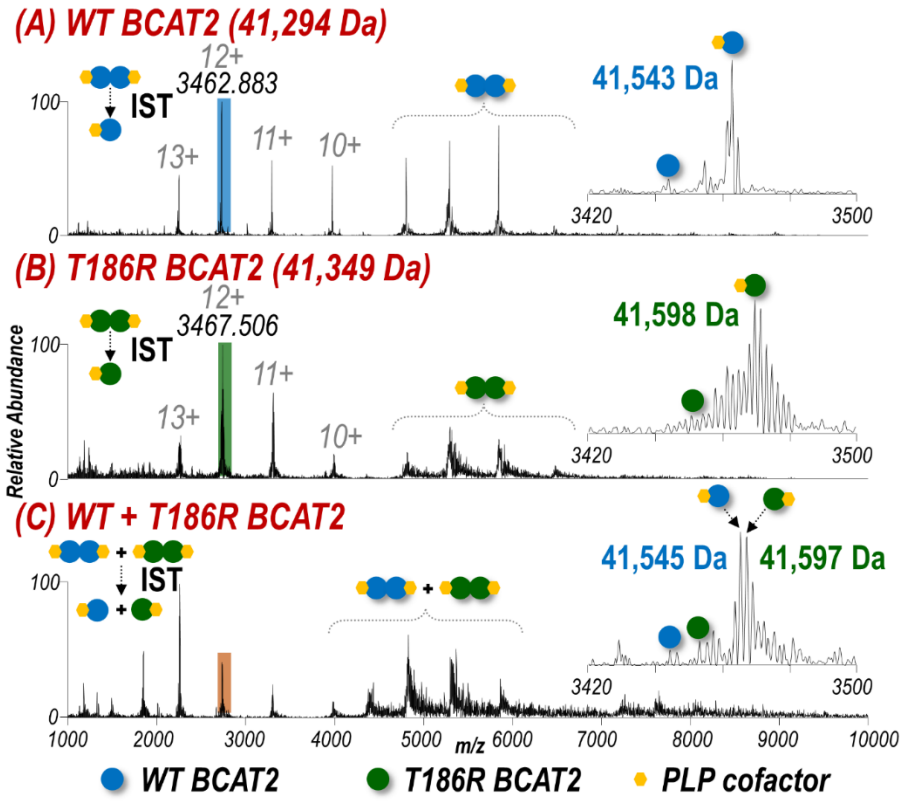

(D)

BCAT2 Variant	Theoretical Mass of Monomer (Da)	Measured Mass of Monomer (Da)
WT	*41,294*	*41,543*
T186R	*41,349*	*41,598*

Figure 7.9: In-source trapping mass spectra (*m/z* 1,000-10,000) of (A) WT, (B) T186R, and (C) WT+T186R BCAT2. Each species observed is identified by colored circles in an expanded view (insets) of the 12+ charge state of the monomer (*m/z* 3,420-3,500). The experimentally measured monomeric masses are 249 Da larger than the expected masses for both WT and T186R BCAT2. This mass shift is attributed to a PLP cofactor bound to each monomer. Given that in-source trapping occurs at the front of the instrument, each monomeric species of interest can be isolated and subjected to MS/MS analysis (Figure 7.10). The table in (D) summarizes theoretical and measured masses for the monomers.

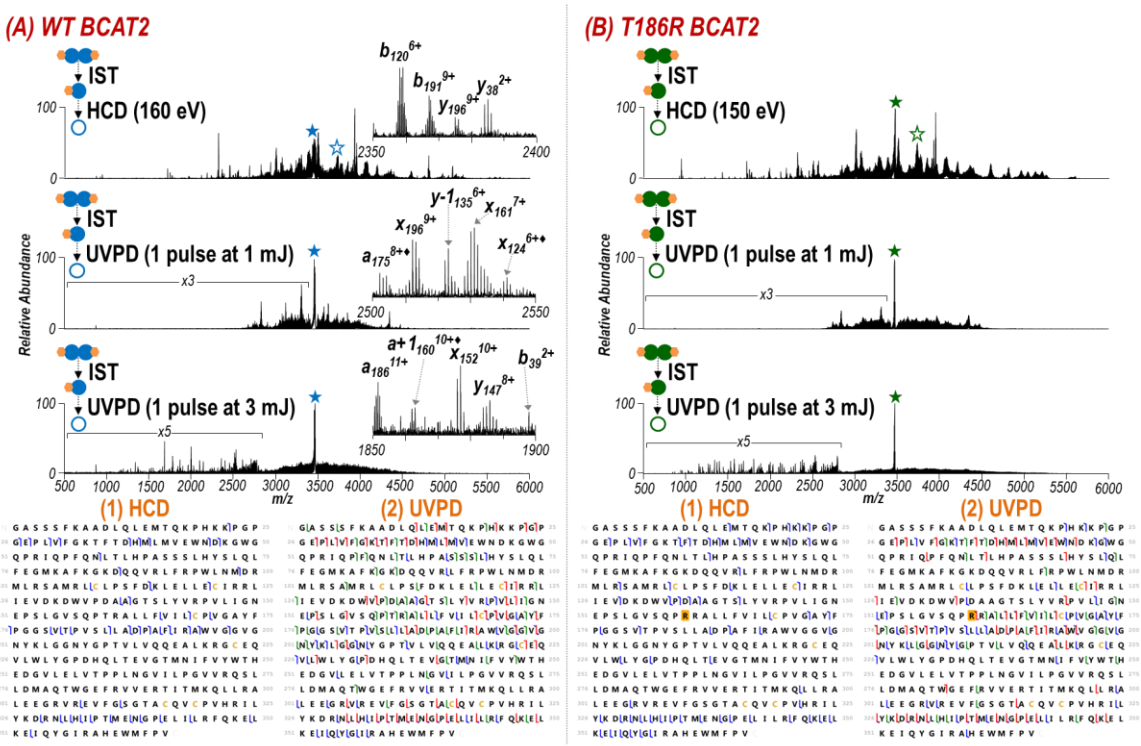

Figure 7.10: HCD and UVPD mass spectra of the 12+ charge state monomer of (A) WT and (B) T186R BCAT2 observed after in-source trapping. Expanded views (insets) in panel (A) show selected fragment ions labelled. Holo fragment ions that contain the PLP cofactor are denoted by a diamond. The precursors are indicated with a filled star in the MS/MS spectra. The unfilled star denotes the charge-reduced precursor (11+) as the PLP cofactor is ejected during HCD. Sequence coverage maps for (1) HCD and (2) UVPD of (A) WT and (B) T186R BCAT2 are shown beneath the spectra. The UVPD sequence maps represent the combined coverage for identified apo and holo fragment ions for the spectra collected using 1 mJ and 3 mJ per pulse. Apo ion only sequence coverage maps are given in Figure 7.11. Sequence coverages were 13% and 18% from HCD, and 45% and 37% from UVPD for WT and T186R BCAT2, respectively. The Thr residue mutated to an Arg is shaded in gold in panel (B).

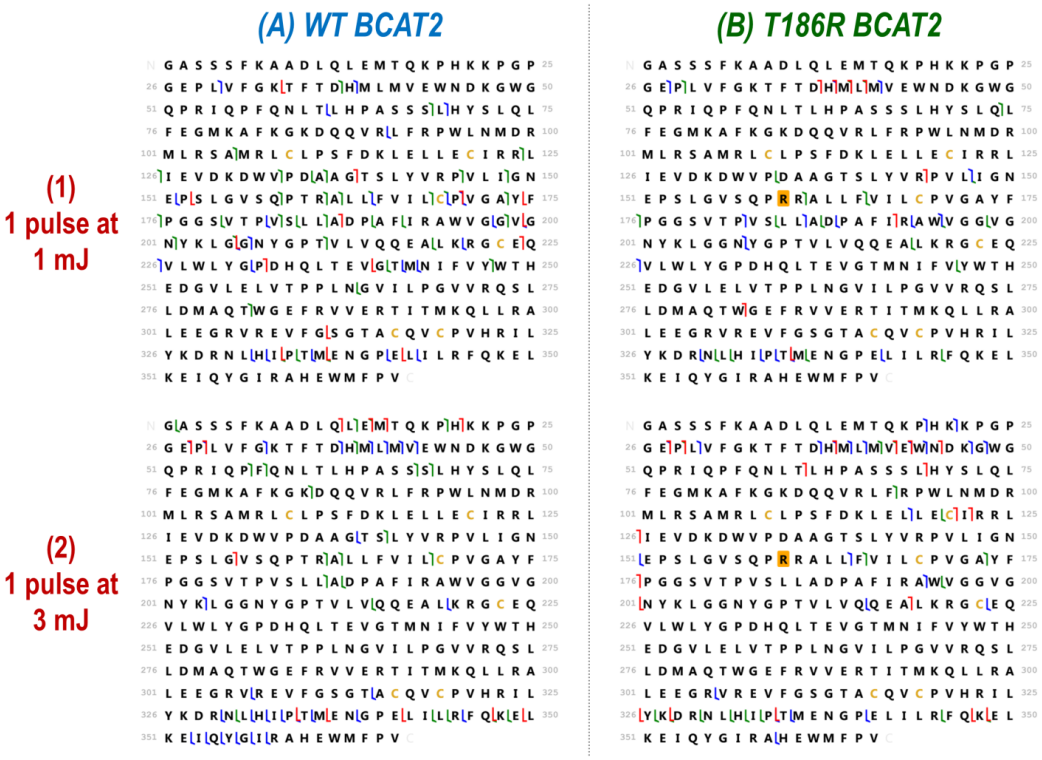

Figure 7.11: Sequence coverage maps based on apo fragment ions only produced by UVPD using 1 pulse at (1) 1 mJ or (2) 3 mJ of the 12+ monomer of (A) WT and (B) T186R BCAT2. Sequence coverages were 18% and 10% using 1 mJ pulses, and 15% and 14% using 3 mJ pulses for WT and T186R BCAT2, respectively. The Thr residue mutated to an Arg is highlighted in yellow in panel (B).

UVPD affords higher sequence coverage (45% and 37% for WT and T186R BCAT2, respectively) compared to HCD (13% and 18% for WT and T186R BCAT2, respectively) and more effectively spans the central region of the protein where the mutation is located. These sequence coverages obtained by UVPD are higher than or comparable to those found for denatured BCAT proteins, as reported above for the 27+ and 37+ charge states. HCD of the monomers ejected from the dimeric complexes afforded only a 1-2% increase in sequence coverage compared to HCD of the dimers. UVPD of the monomers ejected from the dimers give significantly higher sequence coverage compared

to UVPD of the intact dimers (e.g. increasing from 21% to 45% for WT BCAT2). The holo (PLP-containing) sequence ions contributed significantly to the gain in sequence coverage achieved by UVPD. **Figure 7.12** summarizes the sequence coverage afforded by HCD and UVPD. In general, substantial improvements in sequence coverage and localization of the mutation in BCAT2 were obtained by disassembling the dimer and selecting a single charge state of the monomer for subsequent UV photoactivation.

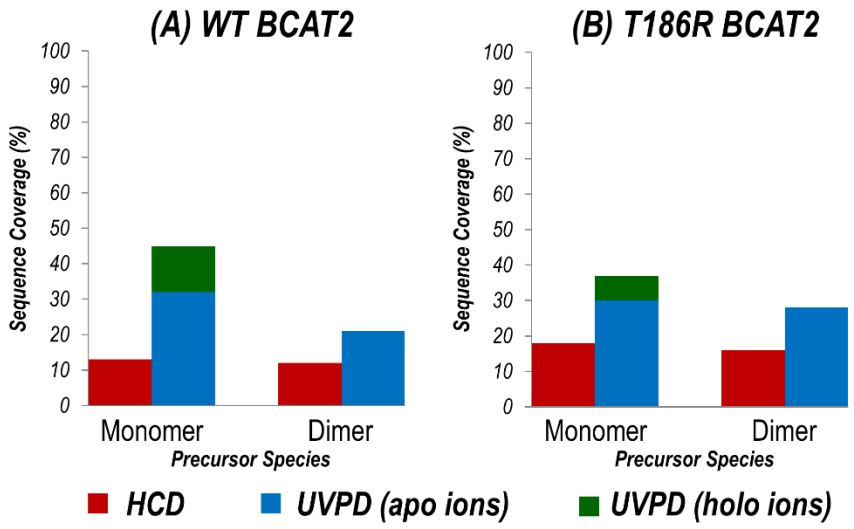

Figure 7.12: Graphs summarizing the sequence coverage afforded by HCD and UVPD (apo and holo ions) for activation of the monomer ejected by IST vs. direct interrogation of the intact dimer for (A) WT and (B) T186R BCAT2.

7.4.4 Mapping UVPD Holo Fragment Ions to Examine the Cofactor Binding Site along BCAT2

Identifying PLP-bound holo ions produced upon photodissociation not only adds to the sequence coverage but also sheds light on the binding site based on the pattern of apo versus holo fragment ions. The high energy deposited during absorption of 193 nm photons by the protein backbone favors preferential cleavage of backbone bonds rather than disruption of the electrostatic interactions with a bound ligand.[39,44–46] **Figure 7.13**

gives the sequence of BCAT2 with the regions of the protein demarcated where backbone cleavages occurred to produce holo fragment ions upon UVPD. For both variants, the majority of holo ions are bi-directional (i.e. holo ions for which both N-terminal and C-terminal fragment ions retain the ligands and share overlapping residues) and cover regions in the middle (V205-Y233) of the protein. Those residues which are consistently included in bi-directional holo fragment ions expected to be those that interact with the cofactor.[39,44–46,49] To aid in visualization, space-filling models of the crystal structures of WT (PDB ID: 5CR5)[50] and T186R (PDB ID: 5MPR)[8] BCAT2 with the residues corresponding to holo fragment ions produced by UVPD represented as colored spheres are shown in **Figure 7.13**.

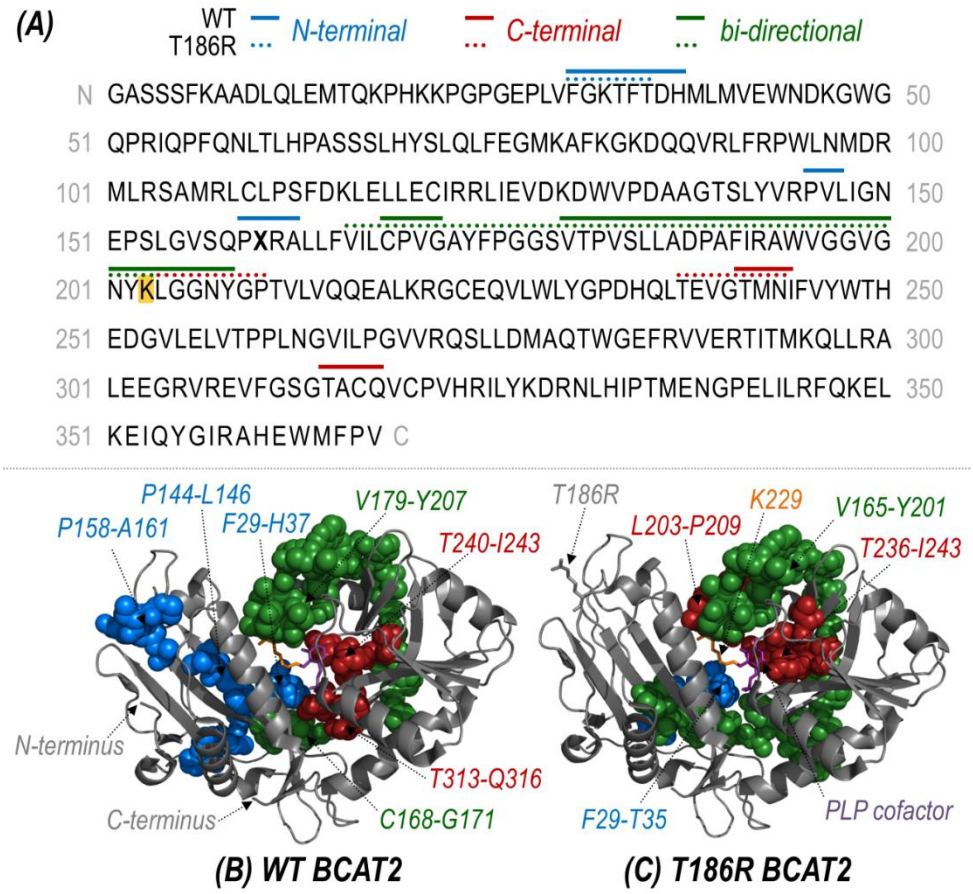

Figure 7.13: (A) Sequence of BCAT2 (X160 = T for WT or R for T186R in bold font) with the observed N-terminal (blue), C-terminal (red), and bi-directional (green) PLP cofactor-bound holo fragment ions observed during UVPD of the 12+ monomer (combined from 1 mJ and 3 mJ) mapped above for WT (solid line) and T186R (dotted line). Bi-directional fragmentation indicates complementary N- and C-terminal ions occurring at the same backbone position. The known binding site of the PLP cofactor is K229 shown highlighted in yellow. Note that the numbering system used to refer to the variant (T186R) and PLP binding site (K229) accounts for the 27 amino acid transit peptide that is not included in the expressed chain. (B, C) Space-filling models of the crystal structures of WT (PDB ID: 5CR5) and T186R (PDB ID: 5MPR) BCAT2 with the residues corresponding to holo fragment ions produced by UVPD represented as colored spheres. The PLP cofactor (purple) and residue K229 (orange) are shown as sticks and labelled in (C).

BCAT2 is dependent on a PLP cofactor to catalyze the transfer of an amino group from the donor branched-chain amino acid to α-ketoglutarate. This ligand is known to bind at active site residue K229.[7] The observation that the bi-directional holo ions generally contain K229 is consistent with the prevailing understanding of the structure of BCAT2. Furthermore, the N-terminal holo ions are only observed C-terminal to the first loop that is in proximity to K229 (F29-H37) and the active site (**Figure 7.13B, 7.13C**). Both variants yielded holo ions from the same regions with the exception of P144-L146 and P158-A161 which were only observed for the wild-type protein. The T186R substitution occurs in this region suggesting that the mutation may destabilize electrostatic interactions between amino acids along that area of the protein and the PLP cofactor, a hypothesis that merits further confirmation using ancillary structural and biophysical methods, as well additional supporting examples from future UVPD-MS studies. This finding agrees with previous electrostatic free energy calculations suggesting that the substitution of Thr for Arg at residue 186 induces a sufficiently large pKa shift of nearby Cys residues in the other subunit of the dimer that influences the Cys protonation state, and prevents the substrate and PLP cofactor from orienting correctly.[5] Obtaining this type of insight on the ligand binding sites by mapping holo fragment ions is an advantage of UVPD in a multistage MS approach.

7.5 Conclusion

In addition to establishing T186R BCAT2 exists as a dimer in solution and identifying a bound PLP cofactor, our study demonstrates the general utility of incorporating 193 nm UVPD into a multistage MS approach for complete characterization of protein complexes from the oligomeric state down to the primary sequence. The first stage (MS1) provided a comprehensive view of the oligomeric state adopted by each

BCAT2 protein and aided in the identification of a bound PLP cofactor based on the measured intact mass. Direct interrogation of the BCAT2 dimers by UVPD afforded moderate sequence coverage and yielded holo product ions that could not be confidently assigned owing to the large number of possible compositional combinations. To mitigate the ambiguous identification of key PLP-containing holo fragment ions, in-source trapping was used to eject a PLP-bound BCAT2 monomer which was subsequently subjected to UVPD. The ability to confidently identify holo ions contributed significantly to the sequence coverage achieved, and mapping the origin of observed holo ions along the sequence provided insight into the binding of PLP in the T186R mutant of BCAT2 compared to the WT protein. In summary, by increasing the diversity of sequence ions observed and producing assignable holo ions that reveal information about bound ligands, the incorporation of UVPD advances the utility of a multistage MS approach for complete characterization of intact protein complexes.

7.6 REFERENCES

(1) Erichsen, H. C.; Chanock, S. J. SNPs in Cancer Research and Treatment. *Br. J. Cancer* **2004**, *90*, 747–751.

(2) Wood, L. D.; Parsons, D. W.; Jones, S.; Lin, J.; Sjöblom, T.; Leary, R. J.; Shen, D.; Boca, S. M.; Barber, T.; Ptak, J.; Silliman, N.; Szabo, S.; Dezso, Z.; Ustyanksky, V.; Nikolskaya, T.; Nikolsky, Y.; Karchin, R.; Wilson, P. A.; Kaminker, J. S.; Zhang, Z.; Croshaw, R.; Willis, J.; Dawson, D.; Shipitsin, M.; Willson, J. K. V.; Sukumar, S.; Polyak, K.; Park, B. H.; Pethiyagoda, C. L.; Pant, P. V. K.; Ballinger, D. G.; Sparks, A. B.; Hartigan, J.; Smith, D. R.; Suh, E.; Papadopoulos, N.; Buckhaults, P.; Markowitz, S. D.; Parmigiani, G.; Kinzler, K. W.; Velculescu, V. E.; Vogelstein, B. The Genomic Landscapes of Human Breast and Colorectal Cancers. *Science* **2007**, *318*, 1108–1113.

(3) Rossi, E. D.; Martini, M.; Bizzarro, T.; Schmitt, F.; Longatto-Filho, A.; Larocca, L. M. Somatic Mutations in Solid Tumors: A Spectrum at the Service of Diagnostic Armamentarium or an Indecipherable Puzzle? The Morphological Eyes Looking for BRAF and Somatic Molecular Detections on Cyto-Histological Samples. *Oncotarget* **2016**, *8*, 3746–3760.

(4) Vogelstein, B.; Kinzler, K. W. Cancer Genes and the Pathways They Control. *Nat. Med.* **2004**, *10*, 789–799.

(5) Lichti, C. F.; Mostovenko, E.; Wadsworth, P. A.; Lynch, G. C.; Pettitt, B. M.; Sulman, E. P.; Wang, Q.; Lang, F. F.; Rezeli, M.; Marko-Varga, G.; Végvári, Á.; Nilsson, C. L. Systematic Identification of Single Amino Acid Variants in Glioma Stem-Cell-Derived Chromosome 19 Proteins. *J. Proteome Res.* **2015**, *14*, 778–786.
(6) Ichihara, A. Isozyme Patterns of Branched-Chain Amino Acid Transaminase During Cellular Differentiation and Carcinogenesis. *Ann. N. Y. Acad. Sci.* **1975**, *259*, 347–354.
(7) Hutson, S. Structure and Function of Branched Chain Aminotransferases. *Prog. Nucleic Acid Res. Mol. Biol.* **2001**, *70*, 175–206.
(8) Anderson, L. C.; Håkansson, M.; Walse, B.; Nilsson, C. L. Intact Protein Analysis at 21 Tesla and X-Ray Crystallography Define Structural Differences in Single Amino Acid Variants of Human Mitochondrial Branched-Chain Amino Acid Aminotransferase 2 (BCAT2). *J. Am. Soc. Mass Spectrom.* **2017**, *28*, 1796–1804.
(9) Sharon, M.; Robinson, C. V. The Role of Mass Spectrometry in Structure Elucidation of Dynamic Protein Complexes. *Annu. Rev. Biochem.* **2007**, *76*, 167–193.
(10) Heck, A. J. R. Native Mass Spectrometry: A Bridge between Interactomics and Structural Biology. *Nat. Methods* **2008**, *5*, 927–933.
(11) Konermann, L.; Vahidi, S.; Sowole, M. A. Mass Spectrometry Methods for Studying Structure and Dynamics of Biological Macromolecules. *Anal. Chem.* **2014**, *86*, 213–232.
(12) Lomeli, S. H.; Yin, S.; Ogorzalek Loo, R. R.; Loo, J. A. Increasing Charge While Preserving Noncovalent Protein Complexes for ESI-MS. *J. Am. Soc. Mass Spectrom.* **2009**, *20*, 593–596.
(13) Bush, M. F.; Hall, Z.; Giles, K.; Hoyes, J.; Robinson, C. V.; Ruotolo, B. T. Collision Cross Sections of Proteins and Their Complexes: A Calibration Framework and Database for Gas-Phase Structural Biology. *Anal. Chem.* **2010**, *82*, 9557–9565.
(14) Snijder, J.; Rose, R. J.; Veesler, D.; Johnson, J. E.; Heck, A. J. R. Studying 18 Mega Dalton Virus Assemblies with Native Mass Spectrometry. *Angew. Chem. Int. Ed Engl.* **2013**, *52*, 4020–4023.
(15) Zhou, M.; Wysocki, V. H. Surface Induced Dissociation: Dissecting Noncovalent Protein Complexes in the Gas Phase. *Acc. Chem. Res.* **2014**, *47*, 1010–1018.
(16) Lermyte, F.; Williams, J. P.; Brown, J. M.; Martin, E. M.; Sobott, F. Extensive Charge Reduction and Dissociation of Intact Protein Complexes Following Electron Transfer on a Quadrupole-Ion Mobility-Time-of-Flight MS. *J. Am. Soc. Mass Spectrom.* **2015**, *26*, 1068–1076.
(17) Rose, R. J.; Damoc, E.; Denisov, E.; Makarov, A.; Heck, A. J. R. High-Sensitivity Orbitrap Mass Analysis of Intact Macromolecular Assemblies. *Nat. Methods* **2012**, *9*, 1084–1086.
(18) Fort, K. L.; Waterbeemd, M. van de; Boll, D.; Reinhardt-Szyba, M.; Belov, M. E.; Sasaki, E.; Zschoche, R.; Hilvert, D.; Makarov, A. A.; Heck, A. J. R. Expanding the Structural Analysis Capabilities on an Orbitrap-Based Mass Spectrometer for Large Macromolecular Complexes. *Analyst* **2017**, *143*, 100–105.

(19) Snijder, J.; van de Waterbeemd, M.; Damoc, E.; Denisov, E.; Grinfeld, D.; Bennett, A.; Agbandje-McKenna, M.; Makarov, A.; Heck, A. J. R. Defining the Stoichiometry and Cargo Load of Viral and Bacterial Nanoparticles by Orbitrap Mass Spectrometry. *J. Am. Chem. Soc.* **2014**, *136*, 7295–7299.
(20) Dyachenko, A.; Wang, G.; Belov, M.; Makarov, A.; de Jong, R. N.; van den Bremer, E. T. J.; Parren, P. W. H. I.; Heck, A. J. R. Tandem Native Mass-Spectrometry on Antibody–Drug Conjugates and Submillion Da Antibody–Antigen Protein Assemblies on an Orbitrap EMR Equipped with a High-Mass Quadrupole Mass Selector. *Anal. Chem.* **2015**, *87*, 6095–6102.
(21) Gault, J.; Donlan, J. A. C.; Liko, I.; Hopper, J. T. S.; Gupta, K.; Housden, N. G.; Struwe, W. B.; Marty, M. T.; Mize, T.; Bechara, C.; Zhu, Y.; Wu, B.; Kleanthous, C.; Belov, M.; Damoc, E.; Makarov, A.; Robinson, C. V. High-Resolution Mass Spectrometry of Small Molecules Bound to Membrane Proteins. *Nat. Methods* **2016**, *13*, 333–336.
(22) Waterbeemd, M. van de; Fort, K. L.; Boll, D.; Reinhardt-Szyba, M.; Routh, A.; Makarov, A.; Heck, A. J. R. High-Fidelity Mass Analysis Unveils Heterogeneity in Intact Ribosomal Particles. *Nat. Methods* **2017**, *14*, 283.
(23) Lermyte, F.; Sobott, F. Electron Transfer Dissociation Provides Higher-Order Structural Information of Native and Partially Unfolded Protein Complexes. *PROTEOMICS* **2015**, *15*, 2813–2822.
(24) Li, H.; Wongkongkathep, P.; Orden, S. L. V.; Loo, R. R. O.; Loo, J. A. Revealing Ligand Binding Sites and Quantifying Subunit Variants of Noncovalent Protein Complexes in a Single Native Top-Down FTICR MS Experiment. *J. Am. Soc. Mass Spectrom.* **2014**, *25*, 2060–2068.
(25) Morrison, L. J.; Brodbelt, J. S. 193 Nm Ultraviolet Photodissociation Mass Spectrometry of Tetrameric Protein Complexes Provides Insight into Quaternary and Secondary Protein Topology. *J. Am. Chem. Soc.* **2016**, *138*, 10849–10859.
(26) Tamara, S.; Dyachenko, A.; Fort, K. L.; Makarov, A. A.; Scheltema, R. A.; Heck, A. J. R. Symmetry of Charge Partitioning in Collisional and UV Photon-Induced Dissociation of Protein Assemblies. *J. Am. Chem. Soc.* **2016**, *138*, 10860–10868.
(27) Julian, R. R. The Mechanism Behind Top-Down UVPD Experiments: Making Sense of Apparent Contradictions. *J. Am. Soc. Mass Spectrom.* **2017**, *28*, 1823–1826.
(28) Smith, L. M.; Kelleher, N. L.; Proteomics, T. C. for T. D.; Linial, M.; Goodlett, D.; Langridge-Smith, P.; Goo, Y. A.; Safford, G.; Bonilla, L.; Kruppa, G.; Zubarev, R.; Rontree, J.; Chamot-Rooke, J.; Garavelli, J.; Heck, A.; Loo, J.; Penque, D.; Hornshaw, M.; Hendrickson, C.; Pasa-Tolic, L.; Borchers, C.; Chan, D.; Young, N.; Agar, J.; Masselon, C.; Gross, M.; McLafferty, F.; Tsybin, Y.; Ge, Y.; Sanders, I.; Langridge, J.; Whitelegge, J.; Marshall, A. Proteoform: A Single Term Describing Protein Complexity. *Nat. Methods* **2013**, *10*, 186–187.
(29) Savaryn, J. P.; Catherman, A. D.; Thomas, P. M.; Abecassis, M. M.; Kelleher, N. L. The Emergence of Top-down Proteomics in Clinical Research. *Genome Med.* **2013**, *5*, 53.

(30) Belov, M. E.; Damoc, E.; Denisov, E.; Compton, P. D.; Horning, S.; Makarov, A. A.; Kelleher, N. L. From Protein Complexes to Subunit Backbone Fragments: A Multi-Stage Approach to Native Mass Spectrometry. *Anal. Chem.* **2013**, *85*, 11163–11173.
(31) Konijnenberg, A.; Bannwarth, L.; Yilmaz, D.; Koçer, A.; Venien-Bryan, C.; Sobott, F. Top-down Mass Spectrometry of Intact Membrane Protein Complexes Reveals Oligomeric State and Sequence Information in a Single Experiment. *Protein Sci.* **2015**, *24*, 1292–1300.
(32) Belov, M. Method and Apparatus for Mass Spectrometry of Macromolecular Complexes. U.S. Patent 9,887,074, February 6, 2018.
(33) Skinner, O. S.; Havugimana, P. C.; Haverland, N. A.; Fornelli, L.; Early, B. P.; Greer, J. B.; Fellers, R. T.; Durbin, K. R.; Do Vale, L. H. F.; Melani, R. D.; Seckler, H. S.; Nelp, M. T.; Belov, M. E.; Horning, S. R.; Makarov, A. A.; LeDuc, R. D.; Bandarian, V.; Compton, P. D.; Kelleher, N. L. An Informatic Framework for Decoding Protein Complexes by Top-down Mass Spectrometry. *Nat. Methods* **2016**, *13*, 237–240.
(34) Ben-Nissan, G.; Belov, M. E.; Morgenstern, D.; Levin, Y.; Dym, O.; Arkind, G.; Lipson, C.; Makarov, A. A.; Sharon, M. Triple-Stage Mass Spectrometry Unravels the Heterogeneity of an Endogenous Protein Complex. *Anal. Chem.* **2017**, *89*, 4708–4715.
(35) Skinner, O. S.; Haverland, N. A.; Fornelli, L.; Melani, R. D.; Do Vale, L. H. F.; Seckler, H. S.; Doubleday, P. F.; Schachner, L. F.; Srzentić, K.; Kelleher, N. L.; Compton, P. D. Top-down Characterization of Endogenous Protein Complexes with Native Proteomics. *Nat. Chem. Biol.* **2018**, *14*, 36–41.
(36) Li, H.; Nguyen, H. H.; Ogorzalek Loo, R. R.; Campuzano, I. D. G.; Loo, J. A. An Integrated Native Mass Spectrometry and Top-down Proteomics Method That Connects Sequence to Structure and Function of Macromolecular Complexes. *Nat. Chem.* **2018**, *10*, 139–148.
(37) Shaw, J. B.; Li, W.; Holden, D. D.; Zhang, Y.; Griep-Raming, J.; Fellers, R. T.; Early, B. P.; Thomas, P. M.; Kelleher, N. L.; Brodbelt, J. S. Complete Protein Characterization Using Top-Down Mass Spectrometry and Ultraviolet Photodissociation. *J. Am. Chem. Soc.* **2013**, *135*, 12646–12651.
(38) Cannon, J. R.; Cammarata, M. B.; Robotham, S. A.; Cotham, V. C.; Shaw, J. B.; Fellers, R. T.; Early, B. P.; Thomas, P. M.; Kelleher, N. L.; Brodbelt, J. S. Ultraviolet Photodissociation for Characterization of Whole Proteins on a Chromatographic Time Scale. *Anal. Chem.* **2014**, *86*, 2185–2192.
(39) O'Brien, J. P.; Li, W.; Zhang, Y.; Brodbelt, J. S. Characterization of Native Protein Complexes Using Ultraviolet Photodissociation Mass Spectrometry. *J. Am. Chem. Soc.* **2014**, *136*, 12920–12928.
(40) Cammarata, M. B.; Brodbelt, J. S. Structural Characterization of Holo- and Apo-Myoglobin in the Gas Phase by Ultraviolet Photodissociation Mass Spectrometry. *Chem. Sci.* **2015**, *6*, 1324–1333.

(41) Cleland, T. P.; DeHart, C. J.; Fellers, R. T.; VanNispen, A. J.; Greer, J. B.; LeDuc, R. D.; Parker, W. R.; Thomas, P. M.; Kelleher, N. L.; Brodbelt, J. S. High-Throughput Analysis of Intact Human Proteins Using UVPD and HCD on an Orbitrap Mass Spectrometer. *J. Proteome Res.* **2017**, *16*, 2072–2079.
(42) Robinson, M. R.; Taliaferro, J. M.; Dalby, K. N.; Brodbelt, J. S. 193 Nm Ultraviolet Photodissociation Mass Spectrometry for Phosphopeptide Characterization in the Positive and Negative Ion Modes. *J. Proteome Res.* **2016**, *15*, 2739–2748.
(43) Robinson, M. R.; Moore, K. L.; Brodbelt, B. Direct Identification of Tyrosine Sulfation by Using Ultraviolet Photodissociation Mass Spectrometry. *J. Am. Soc. Mass Spectrom.* **2014**, *25*, 1461–1471.
(44) Cammarata, M. B.; Thyer, R.; Rosenberg, J.; Ellington, A.; Brodbelt, J. S. Structural Characterization of Dihydrofolate Reductase Complexes by Top-Down Ultraviolet Photodissociation Mass Spectrometry. *J. Am. Chem. Soc.* **2015**, *137*, 9128–9135.
(45) Cammarata, M. B.; Schardon, C. L.; Mehaffey, M. R.; Rosenberg, J.; Singleton, J.; Fast, W.; Brodbelt, J. S. Impact of G12 Mutations on the Structure of K-Ras Probed by Ultraviolet Photodissociation Mass Spectrometry. *J. Am. Chem. Soc.* **2016**, *138*, 13187–13196.
(46) Mehaffey, M. R.; Cammarata, M. B.; Brodbelt, J. S. Tracking the Catalytic Cycle of Adenylate Kinase by Ultraviolet Photodissociation Mass Spectrometry. *Anal. Chem.* **2018**, *90*, 839–846.
(47) Makarov, A.; Denisov, E. Dynamics of Ions of Intact Proteins in the Orbitrap Mass Analyzer. *J. Am. Soc. Mass Spectrom.* **2009**, *20*, 1486–1495.
(48) Shaw, J. B.; Brodbelt, J. S. Extending the Isotopically Resolved Mass Range of Orbitrap Mass Spectrometers. *Anal. Chem.* **2013**, *85*, 8313–8318.
(49) Enyenihi, A. A.; Yang, H.; Ytterberg, A. J.; Lyutvinskiy, Y.; Zubarev, R. A. Heme Binding in Gas-Phase Holo-Myoglobin Cations: Distal Becomes Proximal? *J. Am. Soc. Mass Spectrom.* **2011**, *22*.
(50) Deng, H.; Zhou, J.; Sundersingh, F. S.; Summerfield, J.; Somers, D.; Messer, J. A.; Satz, A. L.; Ancellin, N.; Arico-Muendel, C. C.; Sargent Bedard, K. L.; Beljean, A.; Belyanskaya, S. L.; Bingham, R.; Smith, S. E.; Boursier, E.; Carter, P.; Centrella, P. A.; Clark, M. A.; Chung, C.; Davie, C. P.; Delorey, J. L.; Ding, Y.; Franklin, G. J.; Grady, L. C.; Herry, K.; Hobbs, C.; Kollmann, C. S.; Morgan, B. A.; Pothier Kaushansky, L. J.; Zhou, Q. Discovery, SAR, and X-Ray Binding Mode Study of BCATm Inhibitors from a Novel DNA-Encoded Library. *ACS Med. Chem. Lett.* **2015**, *6*, 919–924.

Chapter 8: Uniting Native Capillary Electrophoresis and Multistage Ultraviolet Photodissociation Mass Spectrometry for On-line Separation and Characterization of *E. Coli* Ribosomal Proteins and Protein Complexes

8.1 Overview

With an overarching goal of characterizing the structure of every protein within a cell, identifying its interacting partners, and quantifying the dynamics of the states in which it exists, key developments are still necessary to achieve comprehensive native proteomics by mass spectrometry. In practice, much work remains to optimize reliable on-line separation methods that are compatible with native mass spectrometry (MS), as well as improve tandem MS (MS/MS) approaches with respect to when and how energy is deposited into proteins of interest. Herein we utilize native capillary zone electrophoresis (CE) coupled with MS to characterize the proteoforms in the *E. coli* 70S ribosome. The capabilities of 193 nm ultraviolet photodissociation (UVPD) to yield informative backbone sequence ions are compared to those of higher-energy collisional dissociation (HCD). To further improve sequence coverage values, a multistage MS/MS approach is implemented involving front-end collisional activation to disassemble protein complexes into constituent subunits that are subsequently individually isolated and activated by HCD or UVPD. In total, 48 of the 55 known *E. coli* ribosomal proteins are identified as 84 unique proteoforms included 22 protein-metal complexes and 10 protein-protein complexes. Additionally, mapping metal-bound holo fragment ions resulting from UVPD of protein-metal complexes offers insight into the metal binding sites.

8.2 INTRODUCTION

Owing to the prevalence of noncovalent interactions between proteins and metals, ligands, or other proteins, the definition of such networks is necessary to fully understand cellular processes or elucidate disease mechanisms.[1] Preservation of such interactions and characterization of the protein-protein and protein-ligand partners poses a significant problem, especially in the quest to analyze more elaborate mixtures of proteins that are better representative of a biological system. Numerous strategies have been developed to evaluate protein interactions, ranging from spectroscopic to microscopic to mass spectrometric to other molecular biology methods.[2,3] Mass spectrometry (MS) in particular offers the potential both to identify individual proteins via various proteomic techniques and to characterize interactions via application of native-MS methods that allow preservation of non-covalent interactions of the protein-protein and protein-ligand partners.[4–6] However, despite substantial inroads in the performance of mass spectrometric methods, characterization of mixtures of protein complexes remains challenging. Bottom-up MS-based proteomics provides a robust method for characterization of the primary sequences of proteins but is less suitable for mapping protein interactions due to the use of denaturing conditions and proteolytic digestion of proteins into peptides.[7] Alternative top-down methods enable direct analysis of intact proteins, now successfully demonstrated even for complex mixtures.[8] As such top-down proteomics uniquely offers the potential to derive a complete picture of all of the combinations of molecular forms in which a protein resulting from a single gene exists (*i.e.* caused by genetic variation, alternative splicing, and PTM), referred to as proteoforms.[9] However, the wealth of information related to noncovalent interactions is typically not retained owing to the use of denaturing solvents that facilitate conventional reversed phase liquid chromatography necessary for efficient protein separations but disrupt all levels of higher order structure. An alternative approach,

native MS, involves the use of volatile salts during electrospray ionization (ESI) to efficiently transfer proteins into the gas phase while maintaining noncovalent interactions. This method allows analysis of multi-protein complexes that retain both metals and ligands with higher order structures reminiscent of those adopted in solution.[4–6] While this technique has become widely used in studies aimed at probing secondary, tertiary, and quaternary protein structure, it is generally limited to highly purified single proteins or simple protein mixtures.[10,11] Achieving more comprehensive characterization of the proteoforms present in multimeric macromolecules in complex biological mixtures requires technical advances in two primary areas: (1) robust, high-resolution separation methods compatible with the volatile salts necessary for native MS, and (2) MS instrumentation capable of detecting high *m/z* species as well as enabling proficient tandem mass spectrometry to allow identification of the constituent proteins.

Several separation techniques have been adapted to be compatible with native MS conditions, including size exclusion chromatography (SEC),[12–14] ion exchange chromatography (IEX),[15,16] hydrophobic interaction chromatography (HIC),[17] and electrophoresis methods.[18–24] While SEC is routinely used to separate higher order structure variants or aggregates of antibodies under native MS conditions,[12–14] the simplicity of this method often yields relatively low-resolution separations insufficient to distinguish the subtle differences between various proteoforms of a single protein. IEX and HIC have demonstrated superior resolving powers in the analysis of computationally designed oligomers,[15] biopharmaceutical protein products,[16] and antibody-drug conjugates.[17] However, both of these methods operate on principles requiring relatively high salt concentrations which can cause disruption of weak noncovalent interactions. Additionally, the amenability of these separation methods (SEC, IEX, HIC) to nanoscale flow rates has yet to be demonstrated. In this regard, they require significantly larger

sample quantities, may cause sample dilution, and ultimately result in lower sensitivity compared to conventional reversed-phase LC approaches used for bottom-up and top-down proteomics. In contrast to such techniques that rely on interactions of analytes with a solid phase, electrophoresis methods utilizing a high electric field to separate molecules based on charge and size have become attractive options for performing native separations.[18–24] Isoforms and subcomplexes of relatively stable protein-protein complexes have been separated by capillary isoelectric focusing (cIEF).[18,19] However, this method requires denaturing sheath flow buffers to maintain stable ESI, potentially causing protein unfolding. Additionally, native gel-eluted liquid fraction entrapment electrophoresis (GELFrEE) has been used for off-line separation of endogenous protein complexes but has not yet been coupled on-line to a mass spectrometer owing to the use of non-MS compatible detergents and salts.[20,21] Stemming from its ability to achieve high-resolution separations using negligible quantities of sample and buffer under both denaturing and native conditions, capillary zone electrophoresis (CE) has emerged as a top contender for facilitating analysis of protein complexes in conjunction with native MS.[22–27] Although non-MS compatible buffers are typically used as the background electrolyte (BGE) in CE, volatile salts such as ammonium acetate or ammonium formate are easily substituted. Additionally, commercially available MS sources (both sheath flow and sheathless) circumvent initial issues with completing the electrical circuit for separation while simultaneously maintaining appropriate voltages necessary for ESI.[28,29]

Two key features of native MS, the deposition of less charge during the ESI process and the retention of noncovalent interaction partners, result in the production of high *m/z* ions that demand mass analyzers with extended mass ranges. This is why initial native MS studies were generally limited to time-of-flight (TOF) or Fourier-transform ion cyclotron resonance (FT-ICR) instruments.[30–33] More recently the development of Orbitrap

instruments with ultra-high mass range (UHMR) capabilities has provided a new high performance platform for native MS.[34] With respect to MS/MS capabilities, collisional activation, including collisional-induced dissociation (CID) and higher-energy collisional dissociation (HCD), has proven proficient for disassembly of protein complexes into subunits or even monomeric proteins, but the low degree of backbone cleavages results in limited sequence coverage of proteins, impeding both identification and characterization.[35] Several ion activation methods based on alternative mechanisms and/or offering higher energy deposition have been developed for the characterization of intact protein complexes.[36] Electron-based methods, including electron-transfer dissociation (ETD), electron-capture dissociation (ECD), and electron ionization dissociation (EID), offer improved sequence coverage of the proteins within protein complexes.[37–40] Conversely surface-induced dissociation (SID) mainly causes disruption of multimeric complexes into constituent protein subcomplexes and individual subunits, thus affording a remarkable new strategy for probing architectures of protein assemblies.[41] Another high energy activation method, ultraviolet photodissociation (UVPD), produces both intact subunits and extensive series of sequence ions resulting from backbone cleavages.[42–44] In addition to returning unsurpassed sequence coverages and retention of labile PTMs even for high-throughput workflows,[45–48] UVPD maintains non-covalent interactions, thus resulting in metal- or ligand-bound holo fragment ions that offer insight into binding sites.[49]

While these alternative MS/MS methods provide high sequence coverages and impressive characterization of increasingly large protein complexes,[50] signal averaging of several minutes may be required to achieve sufficient resolution and signal-to-noise necessary for identifying backbone cleavage sites. Thus, the amenability to high-throughput workflows is limited. Several recent studies posit a multistage MS approach in which an initial stage of collisional activation of intact protein complexes (referred to as

in-source trapping (IST)) is used to disassemble oligomeric proteins into constituent monomeric subunits.[51,52] The resulting monomeric species are then individually isolated and activated using HCD or UVPD. These successful multistage MS/MS approaches (IST-HCD or IST-UVPD) have afforded higher sequence coverages compared to single step activation methods and improved characterization of model protein complexes,[51] enzymes implicated in either metabolism[53] or chemotherapeutic resistance of glioblastoma tumors,[54] and protein complexes in a human cell lysate pre-fractionated off-line.[21] More recently, endogenous lipids bound to membrane proteins were identified using a strategy that integrated native MS of intact protein-lipid complexes, collisional activation to separate the lipids from the protein, and subsequent HCD or 213 nm UVPD of the lipids.[55]

Here we unite CE with a multistage IST-UVPD approach to characterize the proteins comprising the *E. coli* 70S ribosome. The tolerance for high salt concentrations characteristic of CE allows up to 500 μM magnesium acetate to be included in the background electrolyte (BGE) solution and results in the observation of the intact 30S and 50S subunits. By strategically reducing the magnesium concentration in the BGE and removing the ribosomal RNA, subcomplexes and/or single proteins are generated for subsequent MS/MS characterization. HCD and UVPD as well as multistage IST-HCD and IST-UVPD methods are used to characterize the ribosomal proteins and protein complexes. PTMs, including methylation, acetylation and phosphorylation, are identified in addition to noncovalently bound metal cofactors (Mg^{2+} and Zn^{2+}). UVPD consistently yields higher sequence coverages of the ribosomal proteins, protein-metal, and protein-protein complexes compared to HCD. Incorporating front-end collisional activation (IST-UVPD) further improves the protein characterization capabilities of UVPD, yielding significantly higher sequence coverage and offering insight into metal-binding sites based on mapping holo fragment ions. The demonstration of CE in conjunction with a multistage MS/MS

approach represents a significant advance in establishing a robust pipeline for native proteomics studies.

8.3 EXPERIMENTAL

8.3.1 Ribosomal Sample Preparation

E. coli 70S ribosomes were purchased from New England BioLabs (Ipswich, MA) and exchanged into 25 mM ammonium acetate (pH 6.8) containing 1 mM magnesium acetate using 10 kDa molecular weight cutoff filters (MilliporeSigma, Burlington, MA) for CE-MS analysis using a BGE containing a high magnesium concentration. Alternatively, ribosomal nucleic acids were precipitated as previously described.[56] Briefly, 1:4 (*v:v*) 100 mM magnesium acetate:ribosome and 1:1 (v:v) glacial acetic acid:ribosome were added to the ribosome suspension. The sample was incubated at 4 °C for 1 hr before centrifugation at 10000 RPM for 5 min. The resultant supernatant was removed and exchanged into 25 mM ammonium acetate (pH 6.8) containing 0 or 100 μM magnesium acetate for CE-MS analysis.

8.3.2 Native Capillary Electrophoresis

Ribosomal samples prepared at ~30 μg/μL were hydrodynamically injected at 5 psi for 30-45 sec using a CMP Scientific (Brooklyn, NY) ECE-001 capillary electrophoresis autosampler into a 100 cm capillary (50 μm inner diameter) coated with linear polyacrylamide (LPA) as previously described.[24] In short, a bare fused silica was flushed successively with 1 M hydrochloric acid, water, 1 M sodium hydroxide, water, and methanol prior to exposure to 3-(trimethoxysilyl) propyl methacrylate to introduce carbon-carbon double bonds along the capillary wall. An aqueous acrylamide solution containing ammonium persulfate was used to fill the treated capillary before incubation at 50 °C for 2

hrs. Extensive flushing with water removed unreacted reagents, and introduction of the background electrolyte (BGE) solution (25 mM ammonium acetate, pH 6.8, containing no, 100, or 500 μM magnesium acetate) conditioned the capillary. CE separations were achieved using a +30 kV separation voltage with 0.5 psi of pressure applied throughout the separation. An electrokinetically pumped sheath flow interface (CMP Scientific, Brooklyn, NY) allowed coupling of the CE capillary with the mass spectrometer. ESI emitters (~20 μm tip opening, 4 cm length) were fabricated using a Sutter Instrument (Novato, CA) P-1000 micropipette puller from borosilicate capillaries (1.0 mm outer dimeter, 0.75 mm inner diameter) for the CE-MS interface. Following CE separation, on-line ionization of proteins was carried out using ESI spray voltages of 2.4-2.6 kV.

8.3.3 Mass Spectrometry

A Thermo Scientific Q Exactive UHMR mass spectrometer (Bremen, Germany) previously modified[54] to perform UVPD in the HCD cell by a Coherent ExciStar XS 500 (Santa Clara, CA) pulsed excimer laser operating at 193 nm (ArF gas) was used for all CE-MS experiments. The source temperature was set at 200 °C, and all ion optics were optimized for the transmission of species of interest. Specifically, for CE conditions with high magnesium acetate concentrations (100 and 500 μM), values were tuned to transfer higher *m/z* species, whereas for CE-MS without magnesium acetate present in the BGE solution, parameters were adjusted for lower *m/z* species. During ribosomal analysis, ESI mass spectra, without and with IST, were collected at a resolving power of 6250. MS/MS spectra were acquired at a resolving power of 140K for the top three most abundant precursors in a data dependent manner. For all spectra, the ion population was controlled by the ion time (IT) as automated gain control (AGC) was turned off during CE-MS analysis. MS spectra represent two averages using an IT of 20 ms, and MS/MS spectra are

based on 10 averages with an IT of 300 ms. HCD spectra were collected using collision energies of 200-250 eV/q, and a single laser pulse at 3 mJ was used for UVPD spectra. For multistage analyses (IST-HCD and IST-UVPD), the desolvation voltage was increased from -25 V to -225 V (*i.e.* resulting in disassembly of protein complexes instead of simply desolvation). The nitrogen bath gas pressure of the HCD cell was lowered for CE-MS analysis using none or 100 μM in the BGE solution. Specifically, the value was adjusted from a pressure corresponding to 1E-9 to 4E-10 mbar or 1E-10 mbar in the ultra-high vacuum (UHV) region for HCD and UVPD, respectively.

8.3.4 Data Analysis

Triplicate CE-MS runs were collected each using HCD, UVPD, IST-HCD and IST-UVPD for solutions containing no and 100 μM magnesium acetate in the BGE. ProSight Native was used to de-charge low resolution ESI and IST mass spectra and deconvolute corresponding high resolution MS/MS spectra. Lists of the average masses observed in the ESI mass spectra (acquired with and without IST) were assigned as 70S ribosomal proteins or protein-protein complexes within ±3 Da. Searches included methylation (+14.0 Da), acetylation (+42.0 Da), and phosphorylation (+80.0 Da) as possible PTMs. The presence of metal cofactors was identified by a mass difference corresponding to Mg^{2+} (+22.3 Da) or Zn^{2+} (+63.4 Da). Fragment ion matches were made using a tolerance of ±15 ppm. For HCD mass spectra, only *b*- and *y*-type ions were considered, whereas for UVPD mass spectra, nine ion types were searched (*a, a+1, b, c, x, x+1, y, y-1, z*). **Table 8.1** summarizes the observed average mass, sequence coverage, and P-score (Poisson-based score) for each identified ribosomal protein and protein complex based on CE-MS analysis in the absence of magnesium acetate ((-) Mg^{2+}) or containing 100 μM magnesium acetate in the BGE. Holo fragment ions (bound to Mg^{2+} or Zn^{2+}) produced upon UVPD were identified by

inclusion of the corresponding mass shifts at the N- and C-terminus. All reported sequence coverages derived from UVPD include both holo (metal-bound) and apo (metal-free) fragment ions. Only holo fragment ions identified in all three replicates at a given magnesium acetate concentration in the BGE were considered confidently identified and reported.

Table 8.1: List of all proteoforms identified by CE-MS in conjunction with HCD, UVPD, IST-HCD, or IST-UVPD using no (turquoise) or 100 μM (orange) magnesium acetate in the background electrolyte (BGE) solution. In addition to individual proteins (unmodified or post-translationally modified), several protein-metal and protein-protein complexes were characterized. For each identified proteoform the protein name, Uniprot protein accession number, sequence (accounting for initiator Met removal), covalent modifications (Me = methylation (+14.0 Da), Ac = acetylation (+42.0 Da), Ph = phosphorylation (+80.0 Da)) with the localized site in parenthesis, theoretical average mass (accounting for covalent modifications), attached metal cofactors, observed average mass, difference in observed and theoretical average mass (+22 Da corresponds to a Mg^{2+} cofactor and +64 Da results from a Zn^{2+} cofactor), sequence coverage (resulting from HCD, UVPD, IST-HCD, or IST-UVPD), and the corresponding Poisson-based P-score value (lower values indicate better characterization of a given proteoform). Identified protein-protein complexes are listed in the furthest left column with the observed average mass of the intact complex listed. Blank spaces indicate that a given proteoform was not identified using that combination of BGE solution conditions (no or 100 μM magnesium acetate) and MS/MS method (HCD, UVPD, IST-HCD, or IST-UVPD).

Protein-Protein Complex	Obs $M_{r(1)}$ of Protein-Protein Complex (Da)	Protein Name	Uniprot Protein Accession Number	Sequence	Covalent Modification	Theo $M_{r(1)}$ (Da)	Metal Cofactor	*i) 1 Mg^{2+}*												*ii) 100 μM Mg^{2+}*											
								HCD				IST-HCD				UVPD				IST-UVPD				HCD				IST-HCD			
								Obs $M_{r(1)}$ (Da)	Diff $M_{r(1)}$ (Da)	Seq Cov (%)	P-score

8.4 RESULTS AND DISCUSSION

8.4.1 Separation of Ribosomal Proteins by Native CE using Various Mg2+ Concentrations

Comprised of 55 proteins held together by three ribosomal RNA strands, the *E. coli* 70S ribosome requires a minimum concentration (10 mM) of Mg^{2+} to maintain its intact 2.3 MDa structure.[57,58] At lower concentrations (< 1 mM), this macromolecular complex dissociates into 50S (1.4 MDa, composed of 33 proteins) and 30S (850 kDa, consisting of 22 proteins) subunits.[59] The dependence of subunit association and activity on the presence and concentration of Mg^{2+} suggests this metal cofactor intricately governs the dynamics of the ribosome by controlling the balance between flexibility and stability.[60,61] The Mg^{2+}-dependent reorganization of the ribosome has been studied by hydrogen/deuterium exchange (HDX) and MALDI TOF-MS to localize regions impacted by varying magnesium concentrations.[62,63] Additionally, intact *E. coli* ribosomes have been previously detected by native MS[64] and the heterogeneity of such macromolecules studied using various concentrations of magnesium acetate in the ESI spray solution.[65] Similarly, native MS in conjunction with top-down and bottom-up MS methods have been used to dissect ribosomal protein complexes and define the ribosomal proteoforms present across the kingdoms of life, including bacteria, plants, and humans.[66] These prior studies relied on denaturation of the ribosomal proteins to delineate the proteoforms present based on application of bottom-up or top-down MS techniques. In the present study, the use of CE for front-end separation facilitates the characterization of the ribosomal proteins and protein complexes present at various magnesium concentrations under native conditions.

Base peak electropherograms for the CE-MS analysis of ribosomal proteins with various concentrations of magnesium acetate (no, 100, and 500 μM) in the BGE solution

are shown in **Figure 8.1**. Although CE is typically tolerant of salts, inclusion of greater than 500 μM magnesium acetate in the BGE resulted in poor spray stability and low MS signal. Nevertheless, two dominant multimeric species were observed in the presence of 500 μM magnesium acetate (**Figure 8.1A**). Intact masses in the ESI mass spectra shown in **Figure 8.1B** allow these species to be identified as the 30S (RT 53.72 min, 850.1 ± 0.2 kDa) and 50S (RT 65.41 min, 1450.4 ± 0.9 kDa) subunits. Decreasing the magnesium concentration of the BGE alone failed to result in production and detection of significantly more subcomplexes or individual proteins. However, removal of the ribosomal RNA by precipitation, as described in the Experimental section, yielded the electropherograms in **Figure 8.1C** and **8.1D**. After removal of the nucleic acids scaffolding the complex, a variety of proteins and protein complexes were present in solution for characterization by MS/MS methods.

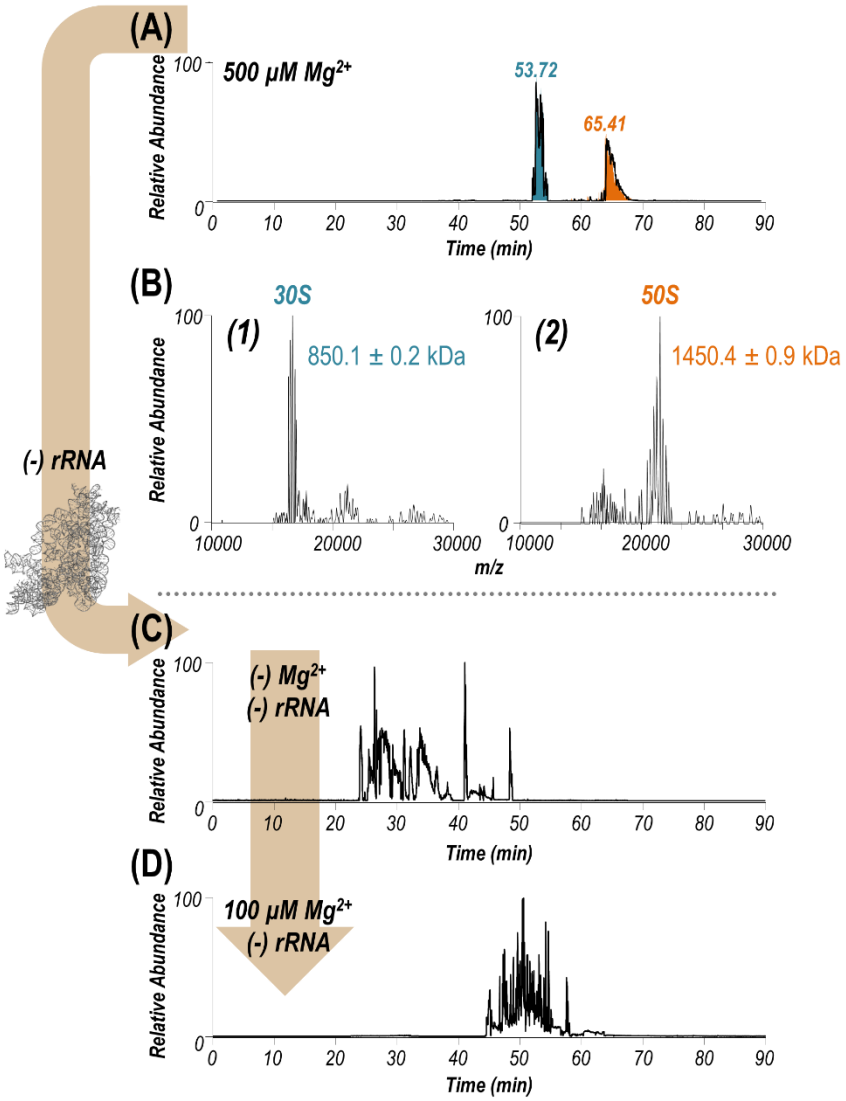

Figure 8.1: (A) Base peak electropherogram of *E. coli* ribosomal proteins containing 500 μM magnesium acetate in the background electrolyte solution. (B) Experimental masses of the dominant species in the ESI mass spectra collected at retention times of (1) 53.72 and (2) 65.41 min with a high Mg^{2+} concentration (500 μM) correspond to the theoretical masses of intact 30S and 50S subunits. Extracted ion chromatograms for observed *m/z* values of the 30S (turquoise) and 50S (orange) subunits are overlaid with the base peak electropherogram in (A). Removal of ribosomal RNA (rRNA) allowed separation of smaller subcomplexes and individual proteins shown as the base peak electropherograms in (C) no Mg^{2+} and (D) 100 μM Mg^{2+} in the BGE. Table 8.1 summarizes all species identified under these latter two conditions.

8.4.2 MS/MS Methods for the Analysis of Ribosomal Proteins

The absorption of 193 nm photons by the protein backbone results in direct dissociation from excited states and allows access to more fragmentation pathways during UVPD compared to collisional activation methods.[44] Owing to its higher energy deposition, UVPD has consistently yielded greater levels of sequence coverage for intact proteins under denaturing[45–48] and native[42,43,50,54] conditions alike. For proteomics applications, higher sequence coverage generally affords better characterization of the various proteoforms present.[47] HCD and UVPD mass spectra were collected in a data dependent manner after CE separation of ribosomal proteins with no or 100 μM magnesium acetate present in the BGE solution. Additionally, increasing the in-source trapping (IST) voltage enabled implementation of a multistage MS/MS approach (referred to as IST-HCD and IST-UVPD) for protein characterization.

Table 8.1 summarizes the sequence coverage values and P-scores for all identified proteoforms using each of the four activation methods (HCD, UVPD, IST-HCD, and IST-UVPD) obtained for both CE separation conditions (*e.g.*, no and 100 μM magnesium acetate). Representative MS and MS/MS spectra are shown in **Figure 8.2** for three proteoforms containing covalent modifications (RL7 (Me, Ph) • Mg^{2+}, RS16 (Ac) • Mg^{2+}, and RS11 (Me)) confidently identified and characterized using IST-UVPD. Identified proteoforms are categorized into three groups: individual proteins, protein-metal complexes, and protein-protein complexes (**Figure 8.3**). In the absence of magnesium acetate during CE separation, HCD and IST-HCD resulted in the identification of the same 54 proteoforms, whereas UVPD alone confirmed the presence of 61 proteoforms and IST-UVPD allowed assignment of 62 proteoforms. Almost half of the species identified by both HCD and UVPD corresponded to protein-metal complexes with only 3 protein-protein complexes confirmed by each of the four MS/MS approaches. As expected, inclusion of

100 μM magnesium acetate in the BGE for the CE separation resulted in the identification of significantly more protein-protein complexes (10 each for HCD and UVPD). The identification of an overall lower number of proteoforms for CE-MS with 100 μM magnesium acetate in the BGE solution compared to no magnesium acetate is attributed to the signal suppression and MS peak broadening caused by the presence of a high concentration of Mg^{2+}, a trend commonly noted in native MS studies.[65,67]

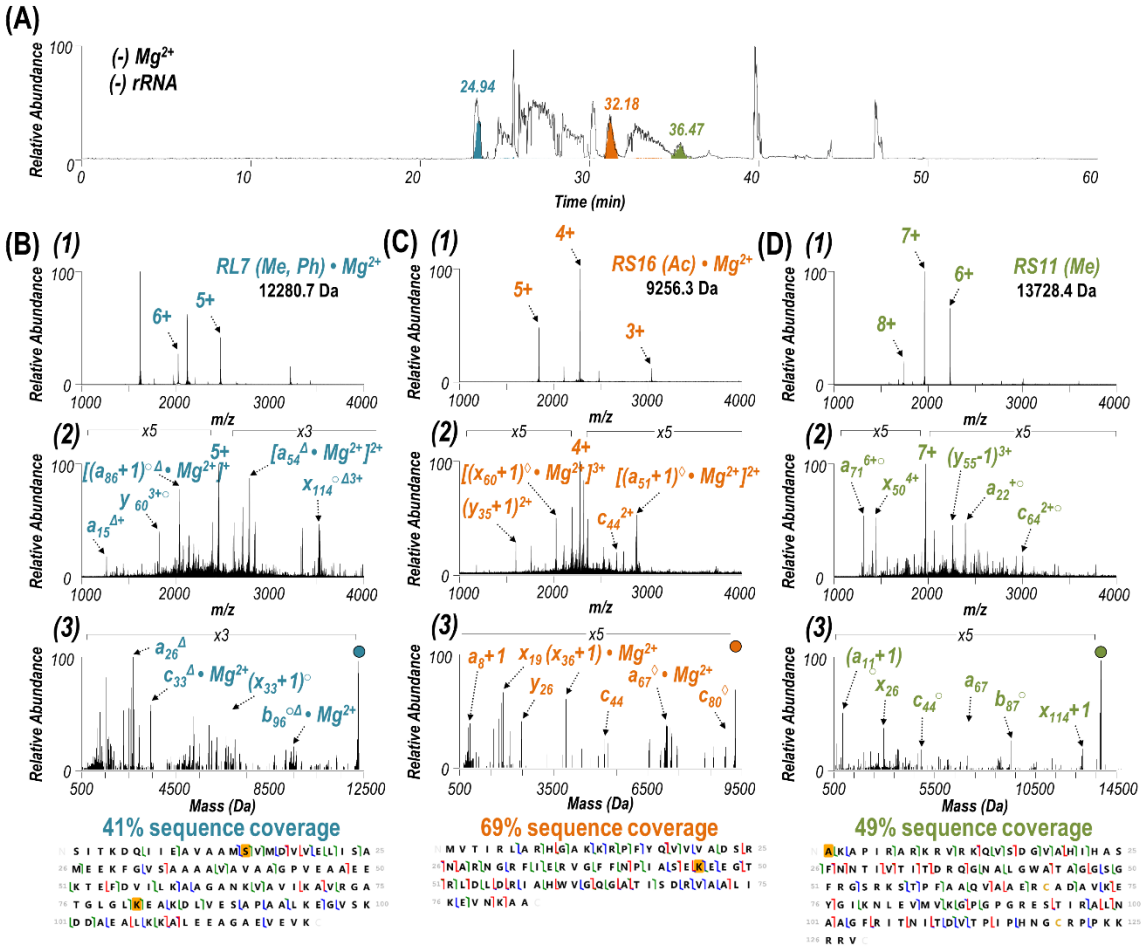

Figure 8.2: (A) Base peak electropherogram for IST-UPVD analysis of *E. coli* ribosomal proteins containing no magnesium acetate in the background electrolyte solution. Extracted ion chromatograms are shown in (A) for *m/z* values corresponding to (B) RL7 (Me, Ph) • Mg^{2+} (*m/z* 2457, turquoise), (B) RS16 (Ac) • Mg^{2+} (*m/z* 2315, orange), and (C) RS11 (Me) (*m/z* 1962, green). (B-D) For each of these three identified proteoforms containing covalent modifications the (1) in-source trapping MS spectrum, (2) UVPD mass spectrum, and (3) deconvoluted UVPD mass spectrum are shown. Observed charge states of the identified proteoforms are labelled in each IST-MS spectrum. UVPD mass spectra are the result of activating the most abundant charge state of the corresponding proteoform in (1) (5+ for RL7 (Me, Ph) • Mg^{2+}, 4+ for RS16 (Ac) • Mg^{2+}, and 7+ for RS11 (Me)). Select identified fragment ions are labelled in (2) and (3) with retention of the covalent modifications denoted as (○) for methylation, (◊) for acetylation, and (Δ) for phosphorylation. Additionally, metal-bound holo fragment ions containing Mg^{2+} are labelled as such. Surviving precursor is indicated as a filled circle in (3). UVPD sequence coverage maps and values (accounting for both apo and Mg^{2+}-bound holo fragment ions) are shown at the bottom with the fragment ion types indicated as: *a/x* (green), *b/y* (blue), and *c/z* (red). Residues with localized covalent modifications are highlighted in yellow including (B) phosphorylation (+80.0 Da) at S15 and methylation (+14.0 Da) at K82, (C) acetylation (+42.0 Da) at K46, and (D) methylation (+14.0 Da) at A2.

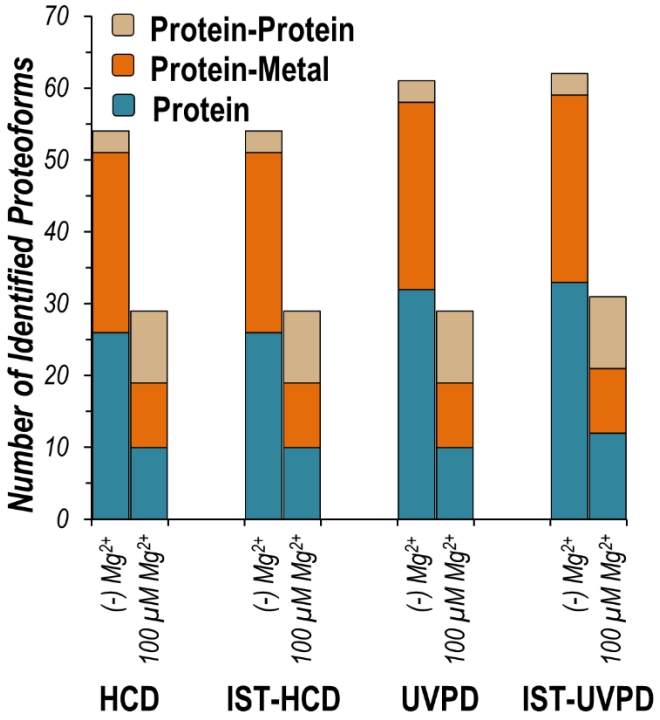

Figure 8.3: Graph displaying the total number of *E. coli* ribosomal proteoforms identified using HCD, IST-HCD, UVPD, or IST-UVPD to activate proteins after CE separation with no (left) or 100 µM (right) magnesium acetate present in the background electrolyte solution. Identified proteoforms are divided into three categories: protein (turquoise), protein-metal complex (orange), or protein-protein complex (tan). A complete list of identified proteoforms is shown in Table 8.1.

While there is significant agreement between the overall number of proteoforms identified by HCD and UVPD (**Figure 8.4**), examination of sequence coverage values confirm that UVPD generally offers better characterization of a given proteoform. **Figure 8.5A** displays the sequence coverages obtained by HCD and UVPD for all identified proteoforms for the CE-MS analysis of the ribosome containing no magnesium acetate. Corresponding bar graphs for IST-HCD vs. IST-UVPD in the absence of magnesium acetate in the BGE solution and all activation methods (HCD vs. UVPD and IST-HCD vs. IST-UVPD) for CE-MS using 100 µM magnesium acetate are shown in **Figure 8.6**. With

the exception of a proteoforms of lower molecular weight (< 10 kDa), UVPD resulted in higher sequence coverage values across the board. Plots of the differences in sequence coverages for HCD vs. UVPD and IST-HCD vs. IST-UVPD for both CE conditions (no and 100 μM magnesium acetate) highlight this trend (**Figure 8.5B**). A list detailing the ranked proteoform pairs is shown in **Table 8.2**. The orange dots and triangles indicate those proteoforms in common for which greater sequence coverage (> 2%) was afforded by UVPD or IST-UVPD compared to HCD or IST-HCD. The turquoise dots and triangles denote the opposite outcome with higher sequence coverages for HCD or IST-HCD compared to UVPD or IST-UVPD. Under both CE conditions (no and 100 μM magnesium acetate in the BGE), over 75% of the dots/triangles are orange which suggests sequence coverages produced by UVPD and IST-UVPD are consistently higher than those resulting from HCD and IST-HCD for native protein complexes analyzed in a high-throughput manner by CE-MS. Greater sequence coverages of *E. coli* ribosomal proteins (unmodified or carbamylated) by UVPD compared to HCD have also been previously using denaturing LC-MS/MS for analysis.[46,68] In general, UVPD sequence coverages reported here using native CE-MS are somewhat lower (by ~10-15%) than six similar ribosomal proteins reported in a previous study (RS19, RL15, RL18, RL24, RL34, RL36),[68] an outcome attributed to the fact the MS parameters in the present study were optimized for identification of multimeric protein complexes (*i.e.*, higher *m/z* species).

A comparison of the sequence coverage values associated with UVPD and IST-UVPD is also shown for both CE conditions (no and 100 μM magnesium acetate in BGE) in **Figure 8.5C**. Again, orange dots denote proteoforms in common whose sequence coverages using IST-UVPD were higher compared to UVPD, while turquoise dots and triangles indicate higher sequence coverage values resulting from UVPD compared to IST-UVPD. In the absence of magnesium acetate, there is minimal improvement in sequence

coverage when using the multistage approach (IST-UVPD) relative to UVPD. However, at a magnesium acetate concentration of 100 μM (favoring the survival of more multimeric protein-protein complexes), IST-UVPD resulted in higher sequence coverage than UVPD for over two-thirds of the proteoforms.

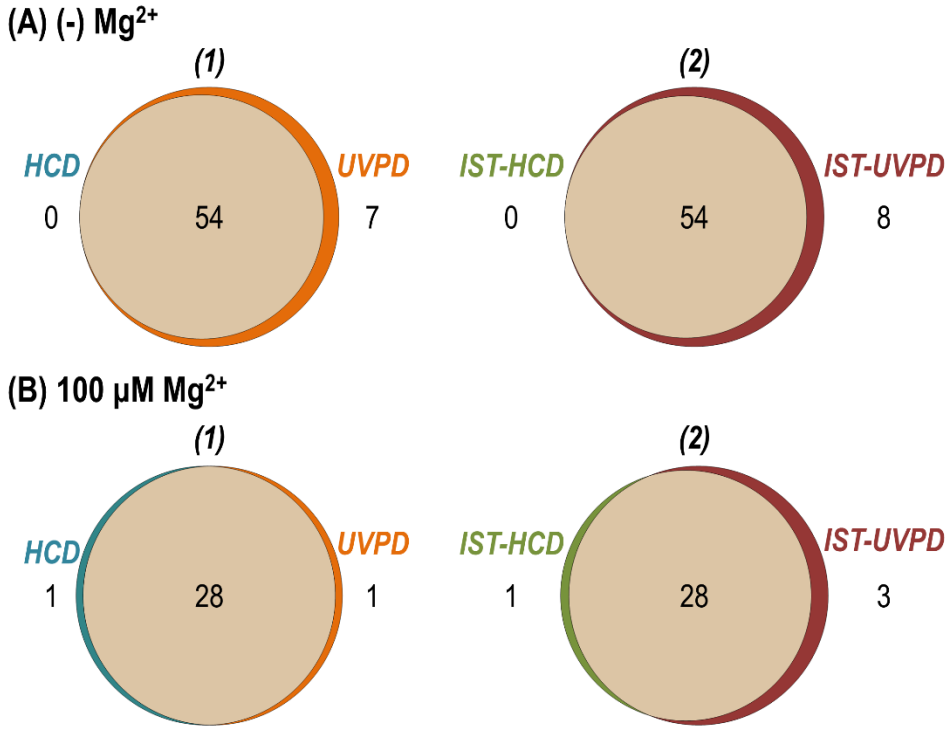

Figure 8.4: Venn diagrams showing the overlap in identified proteoforms (including individual proteins, protein-metal complexes, and protein-protein complexes) between (1) HCD and UVPD or (2) IST-HCD and IST-UVPD for CE-MS analysis of ribosomal proteins using (A) no or (B) 100 μM magnesium acetate in the BGE solution.

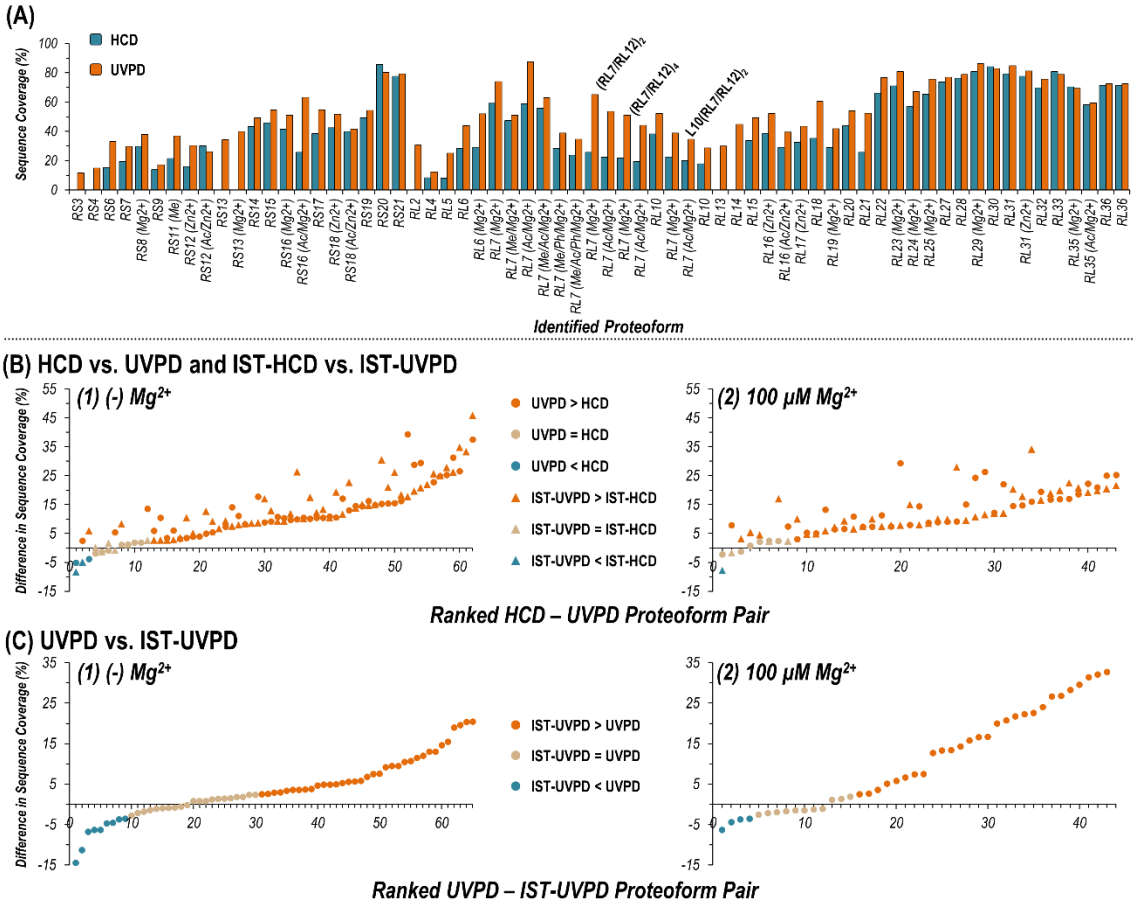
(A)
HCD
UVPD
Sequence Coverage (%)
(RL7/RL12)2
(RL7/RL12)4
L10/(RL7/RL12)2
Identified Proteoform
(B) HCD vs. UVPD and IST-HCD vs. IST-UVPD
(1) (-) Mg2+
(2) 100 μM Mg2+
Difference in Sequence Coverage (%)
UVPD > HCD
UVPD = HCD
UVPD < HCD
IST-UVPD > IST-HCD
IST-UVPD = IST-HCD
IST-UVPD < IST-HCD
Ranked HCD – UVPD Proteoform Pair
(C) UVPD vs. IST-UVPD
(1) (-) Mg2+
(2) 100 μM Mg2+
Difference in Sequence Coverage (%)
IST-UVPD > UVPD
IST-UVPD = UVPD
IST-UVPD < UVPD
Ranked UVPD – IST-UVPD Proteoform Pair

Figure 8.5: (A) Bar graph depicting sequence coverages afforded by HCD (turquoise) and UVPD (orange) for each *E. coli* ribosome proteoform identified after CE separation with no magnesium acetate in the background electrolyte solution. The floating labels correspond to the proteoforms of the subunits comprising the identified protein-protein complexes. Corresponding graphs for IST-HCD and IST-UVPD as well as for the separation containing 100 μM magnesium acetate using each activation method are shown in Figure 8.6. The differences in sequence coverage of proteoforms identified in common are shown for (B) HCD vs. UVPD (dots) and IST-HCD vs. IST-UVPD (triangles), and (C) UVPD vs. IST-UVPD. Proteoforms were ranked by increasing difference in coverage. Lists of ranked proteoform pairs are included in Table 8.2. In (B), orange indicates proteoforms for which UVPD (dots) or IST-UVPD (triangles) generated greater sequence coverage than HCD (dots) or IST-HCD (triangles) by more than 2%, turquoise highlights proteoforms for which HCD (dots) or IST-HCD (triangles) yielded higher sequence coverage than UVPD (dots) or IST-UVPD (triangles) by more than 2%, and tan indicates proteoforms for which the sequence coverage differed by less than 2%. Similarly, in (C) orange denotes proteoforms for which IST-UVPD afforded greater sequence coverage than UVPD (> 2%), turquoise indicates proteoforms for which UVPD resulted in higher sequence coverage than IST-UVPD (> 2%), and tan identifies proteoforms for which the sequence coverage differed by less than 2%. Note that the y-axis for (1) (-) Mg^{2+} and (2) 100 μM Mg^{2+} in (C) is scaled differently than (B) (maximum value of 35% instead of 55%) since the differences in sequence coverages between UVPD and IST-UVPD for corresponding proteoforms were smaller. Sequence coverages for all identified proteoforms are listed in Table 8.1.

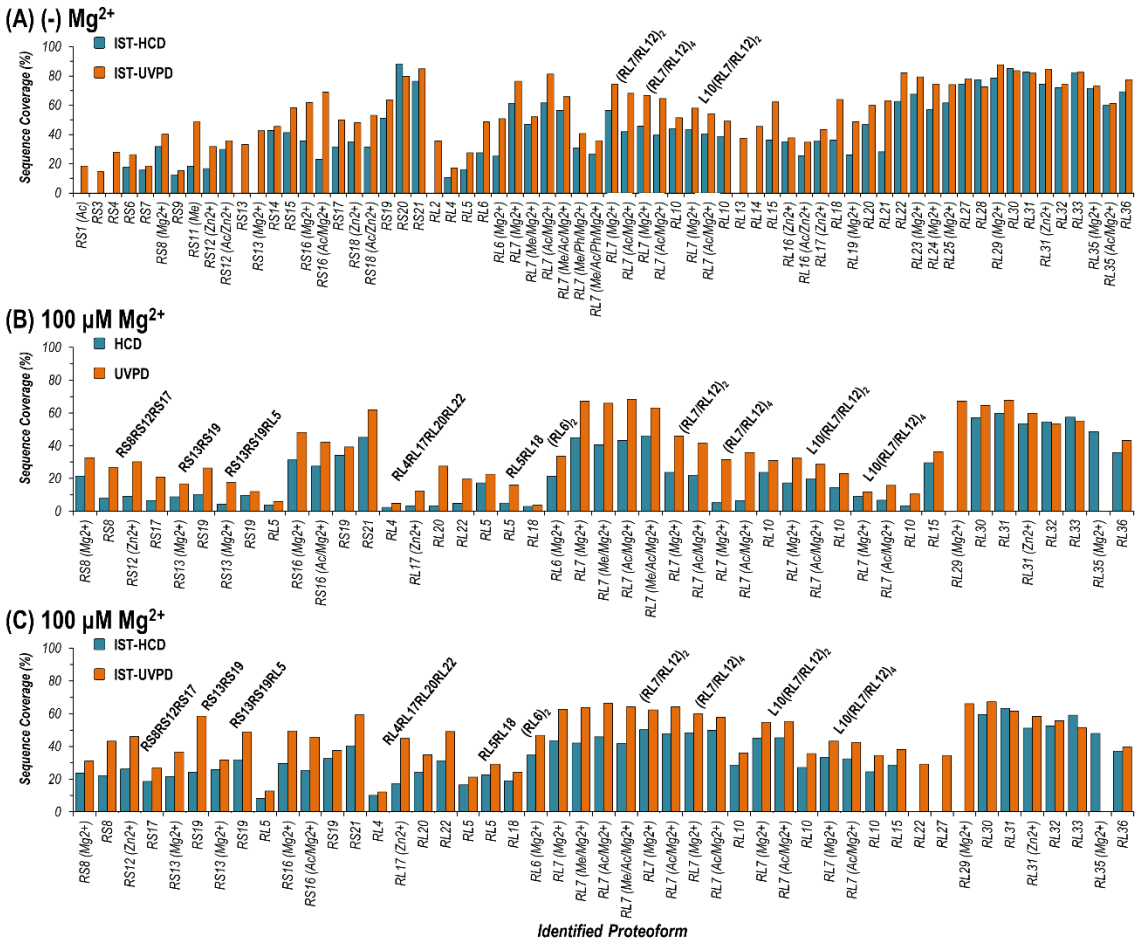

Figure 8.6: Bar graphs illustrating sequence coverages afforded by HCD or IST-HCD (turquoise) and UVPD or IST-UVPD (orange) for each *E. coli* ribosome proteoform identified after CE separation with (A) no or (B, C) 100 µM magnesium acetate in the background electrolyte solution. Identified protein-protein complexes are labelled above the bars of corresponding proteoforms.

Table 8.2: Table detailing the ranked proteoform pairs (for HCD vs. UVPD (and IST-HCD vs. IST-UVPD), and UVPD vs. IST-UVPD using no (turquoise) or 100 μM (orange) magnesium acetate in the BGE solution during CE-MS) corresponding to Figure 8.5B, 8.5C. Covalent modifications are included (Me = methylation, Ac = acetylation, and Ph = phosphorylation) as well as noncovalently bound metals (Mg2+ or Zn2+). Subunits constituting oligomeric protein-protein complexes are labelled as such.

	(-) Mg^{2+}		*100 μM Mg^{2+}*	
Proteoform Rank	HCD vs. UVPD and IST-HCD vs. IST-UVPD	UVPD vs. IST-UVPD	HCD vs. UVPD and IST-HCD vs. IST-UVPD	UVPD vs. IST-UVPD
1	RS20	RL16 Zn2+	RL33	RL31
2	RL28	RS7	RL31	RL7 Mg2+
3	RS12(Ac) Zn2+	RS6	RL32	RL33
4	RL33	RL7(Ac) Mg2+	RL18 from RL5RL18	RL36
5	RL30	RL28	RL5 from RS13RS19RL5	RS21
6	RL35 Mg2+	RS17	RL4 from RL4RL17RL20RL22	RL7(Me) Mg2+
7	RL31	RL16(Ac) Zn2+	RS19 from RS13RS19RL5	RL7(Ac) Mg2+
8	RL36	RS14	RL36	RS19
9	RL35(Ac) Mg2+	RS18 Zn2+	RL7 Mg2+ from RL10(RL7/RL12)4	RS8 Mg2+
10	RS18(Ac) Zn2+	RL31	RL5	RL31 Zn2+
11	RS21	RS9	RS19	RL5
12	RL16 Zn2+	RL25 Mg2+	RS13 Mg2+ from RS13RS19RL5	RL29 Mg2+
13	RS7	RL23 Mg2+	RL31 Zn2+	RL7(Me, Ac) Mg2+
14	RS9	RL6 Mg2+	RL15	RS16 Mg2+
15	RL32	RL32	RL5 from RL5RL18	RL15
16	RS14	RS13	RL10	RL32
17	RL27	RL10	RL10 from RL10(RL7/RL12)4	RL30
18	RL31 Zn2+	RS20	RS8 Mg2+	RS16(Ac) Mg2+
19	RL7(Me) Mg2+	RL17 Zn2+	RL30	RL10
20	RL4	RL7(Me) Mg2+	RL7(Ac) Mg2+ from (RL7/RL12)4	RS17 from RS8RS12RS17
21	RS19	RL14	RS13 Mg2+ from RS13RS19	RL5 from RS13RS19RL5
22	RL29 Mg2+	RL30	RS17 from RS8RS12RS17	RL4 from RL4RL17RL20RL22
23	RL7(Me, Ac) Mg2+	RL7(Me, Ac, Ph) Mg2+	RL10 from RL10(RL7/RL12)2	RL20 from RL4RL17RL20RL22
24	RL10	RL27	RL7(Ac) Mg2+ from RL10(RL7/RL12)4	RL10 from RL10(RL7/RL12)2
25	RL17 Zn2+	RS12 Zn2+	RL7(Ac) Mg2+ from RL10(RL7/RL12)2	RL5 from RL5RL18
26	RS8 Mg2+	RL29 Mg2+	RL17 Zn2+ from RL4RL17RL20RL22	RL6 Mg2+ from (RL6)2
27	RS6	RL7(Me, Ph) Mg2+	RL7 Mg2+ from RL10(RL7/RL12)2	RS13 Mg2+ from RS13RS19RL5
28	RS15	RL35(Ac) Mg2+	RL20 from RL4RL17RL20RL22	RS12 Zn2+ from RS8RS12RS17
29	RS18 Zn2+	RS8 Mg2+	RL7 Mg2+ from (RL7/RL12)4	RL7 Mg2+ from (RL7/RL12)2
30	RL7(Me, Ac, Ph) Mg2+	RL7 Mg2+	RL6 Mg2+ from (RL6)2	RS8 from RS8RS12RS17
31	RL16(Ac) Zn2+	RS13 Mg2+	RL7 Mg2+ from (RL7/RL12)2	RS13 Mg2+ from RS13RS19
32	RL23 Mg2+	RL5	RS16(Ac) Mg2+	RL18 from RL5RL18
33	RS16 Mg2+	RL7(Me, Ac) Mg2+	RL22 from RL4RL17RL20RL22	RL7(Ac) Mg2+ from (RL7/RL12)4
34	RL24 Mg2+	RS3	RS19 from RS13RS19	RL7 Mg2+ from RL10(RL7/RL12)2
35	RL7(Me, Ph) Mg2+	RL18	RS7(Ac) Mg2+ from (R7/R12)2	RL7(Ac) Mg2+ from (RL7/RL12)2
36	RL20	RS15	RS21	RL10 from RL10(RL7/RL12)4
37	RL25 Mg2+	RL31 Zn2+	RS16 Mg2+	RL7(Ac) Mg2+ from RL10(RL7/RL12)2
38	RL10 from RL10(RL7/RL12)2	RL33	RL7(Me, Ac) Mg2+	RL7(Ac) Mg2+ from RL10(RL7/RL12)4
39	RL22	RL35 Mg2+	RS8 from RS8RS12RS17	RL7 Mg2+ from (RL7/RL12)4
40	RL5	RL6	RL7 Mg2+	RL22 from RL4RL17RL20RL22
41	RL19 Mg2+	RL2	RS12 Zn2+ from RS8RS12RS17	RL7 Mg2+ from RL10(RL7/RL12)4
42	RL7(Ac) Mg2+ from RL10(RL7/RL12)2	RL4	RL7(Ac) Mg2+	RS19 from RS13RS19
43	RS12 Zn2+	RL36	RL7 (Me) Mg2+	RL17 Zn2+ from RL4RL17RL20RL22
44	RL7 Mg2+ from RL10(RL7/RL12)2	RL22		RS19 from RS13RS19RL5
45	RL7 Mg2+	RS21		
46	RS11 (Me)	RS16(Ac) Mg2+		
47	RL6	RL20		
48	RL15	RL19 Mg2+		
49	RS17	RL24 Mg2+		
50	RL7 Mg2+ from (RL7/RL12)2	RL13		
51	RL7(Ac) Mg2+	RL7 Mg2+ from (RL7/RL12)2		
52	RL7 Mg2+ from (RL7/RL12)4	RS12(Ac) Zn2+		
53	RL6 Mg2+	RS19		
54	RL7(Ac) Mg2+ from (RL7/RL12)4	RL21		
55	RL18	RS16 Mg2+		
56	RL7(Ac) Mg2+ from (RL7/RL12)2	RS18(Ac) Zn2+		
57	RL21	RS11 (Me)		
58	RS13 Mg2+	RS4		
59	RS16(Ac) Mg2+	RL15		
60	RS13	RL7(Ac) Mg2+ from (RL7/RL12)2		
61		RL7 Mg2+ from (RL7/RL12)4		
62		RL7 Mg2+ from RL10(RL7/RL12)2		
63		RL7(Ac) Mg2+ from RL10(RL7/RL12)2		
64		RL7(Ac) Mg2+ from (RL7/RL12)4		
65		RL10 from RL10(RL7/RL12)2		

8.4.3 Multistage MS/MS Approach for the Improved Characterization of Ribosomal Protein Complexes

As demonstrated in **Figure 8.5C**, a multistage MS/MS approach is particularly beneficial for improved characterization of protein-protein complexes compared to HCD or UVPD alone. Closer examination of the largest protein-protein complex (66.4 kDa) identified at no or 100 μM magnesium concentrations further demonstrates this trend. The heteropentameric RL8 complex (consisting of RL10(RL7/RL12)$_4$) comprises the stalk of the ribosomal complex.[69] Owing to its role in promoting translation factors to the ribosome, it remains highly mobile and is absent from most crystal structures of the ribosome.[57,58,69] As such, the development of alternative structural biology methods in which this protein complex can be reliably detected as part of the ribosome are important. While subcomplexes of this assembly were detected in the absence of magnesium acetate in the BGE during CE separation (*i.e.*, (RL7/RL12)$_2$, (RL7/RL12)$_4$, and RL10(RL7/RL12)$_2$), the intact complex was only identified at the higher magnesium acetate concentration (100 μM). The ESI mass spectra collected at a retention time of 61.81 min during the CE separation performed with 100 μM magnesium acetate in the BGE (**Figure 8.1D**) is shown in **Figure 8.7A**. The 14+ – 16+ charge states of the pentameric RL10(RL7/RL12)$_4$ complex bound to four equivalents of Mg^{2+} (observed average mass: 66325 ± 9 Da; theoretical average mass: 66409.7 Da) were detected. Increasing the desolvation voltage (-225 V) for a multistage MS/MS approach yields the in-source trapping (IST) mass spectrum displayed in **Figure 8.7B** in which the monomeric subunits corresponding to each individual protein are observed (6+, 7+ charge states of RL7/RL12 • Mg^{2+}; 5+, 6+ charge states of RL7/RL12 (Ac) • Mg^{2+}; and 6+ – 8+ charge states of RL10).

The UVPD mass spectrum of the 15+ charge state of the pentameric RL10(RL7/RL12)$_4$ complex and IST-UVPD mass spectra of each individual subunit (7+

charge state of RL7/RL12 • Mg^{2+}, 6+ charge state of RL7/RL12 (Ac) • Mg^{2+}, 7+ charge state of RL10) and the corresponding deconvoluted MS/MS spectra are shown in **Figure 8.8.** The sequence coverage maps and sequence coverages corresponding to each of the three proteins contained in the complex demonstrate several remarkable features (**Figure 8.7C**). First, UVPD (without IST) of the pentameric complex yields a modest number of diagnostic fragment ions of each of the constituent proteins, yielding 11% to 16% sequence coverage. More notably, the multistage IST-UVPD approach results in significantly better characterization of the proteoforms constituting this complex (**Figure 8.7C-2**). In particular, sequence coverage values using IST-UVPD increased to 43% for RL7/RL12 • Mg^{2+}, 43% for RL7/RL12 (Ac) • Mg^{2+}, and 35% for RL10. These improvements are attributed to the simplification of the UVPD spectra owing to disassembly of the pentamer and activation of the subunits individually instead of activation of the pentameric complex. Fewer averages are necessary to achieve quality MS/MS spectra for the subunits than the multi-protein complex making the multistage approach more amenable for the high-throughput analysis of protein-protein complexes.

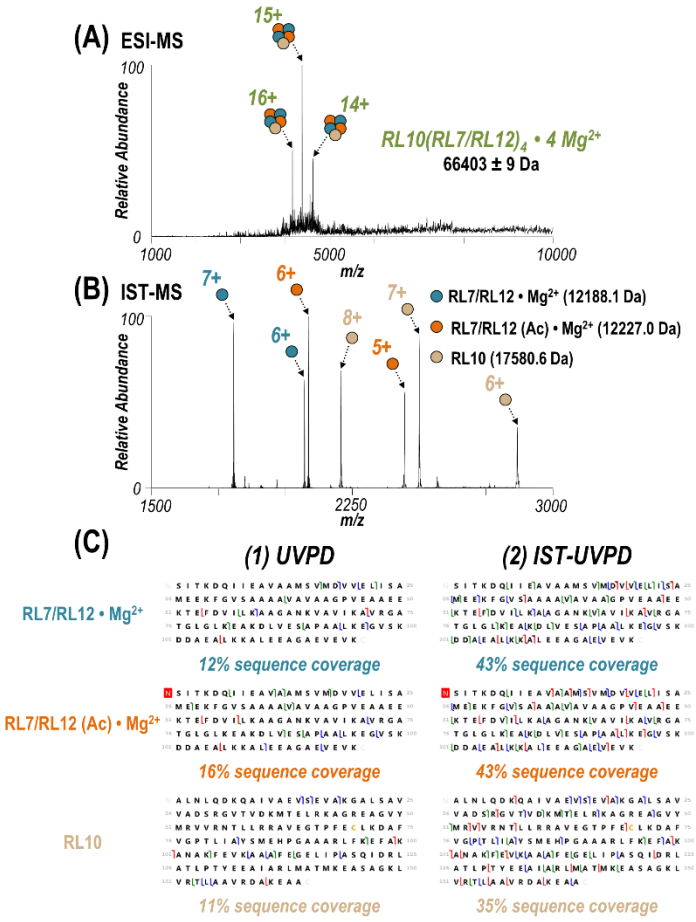

Figure 8.7: (A) ESI mass spectrum collected at a retention time of 61.81 min during on-line CE separation of *E. coli* ribosomal proteins using a background electrolyte solution containing 100 μM magnesium acetate (base peak electropherogram shown in Figure 8.1D). The 14+ – 16+ charge states of the pentameric RL10(RL7/RL12)$_4$ • 4Mg^{2+} complex are labelled. (B) In-source trapping spectrum, collected at a retention time of 61.27 min during CE separation with 100 μM magnesium acetate in the BGE, resulting from disassembly of the protein-protein complex observed in (A) into its constituent monomeric subunits: RL7/RL12 • Mg^{2+} (6+, 7+ charge states labelled in turquoise), RL7/RL12 (Ac) • Mg^{2+} (5+, 6+ charge states labelled in orange), and RL10 (6+ – 8+ charge states labelled in tan). (C) Maps and sequence coverage values for each protein comprising the complex afforded by (1) UVPD of the 15+ charge state of the pentamer or (2) IST-UVPD of each individual subunit (7+ charge state of RL7/RL12 • Mg^{2+}, 6+ charge state of RL7/RL12 (Ac) • Mg^{2+}, 7+ charge state of RL10). Observed fragment ion types are labelled as: *a/x* (green), *b/y* (blue), and *c/z* (red). MS/MS spectra for each of the maps shown in (C) are included in Figure 8.8.

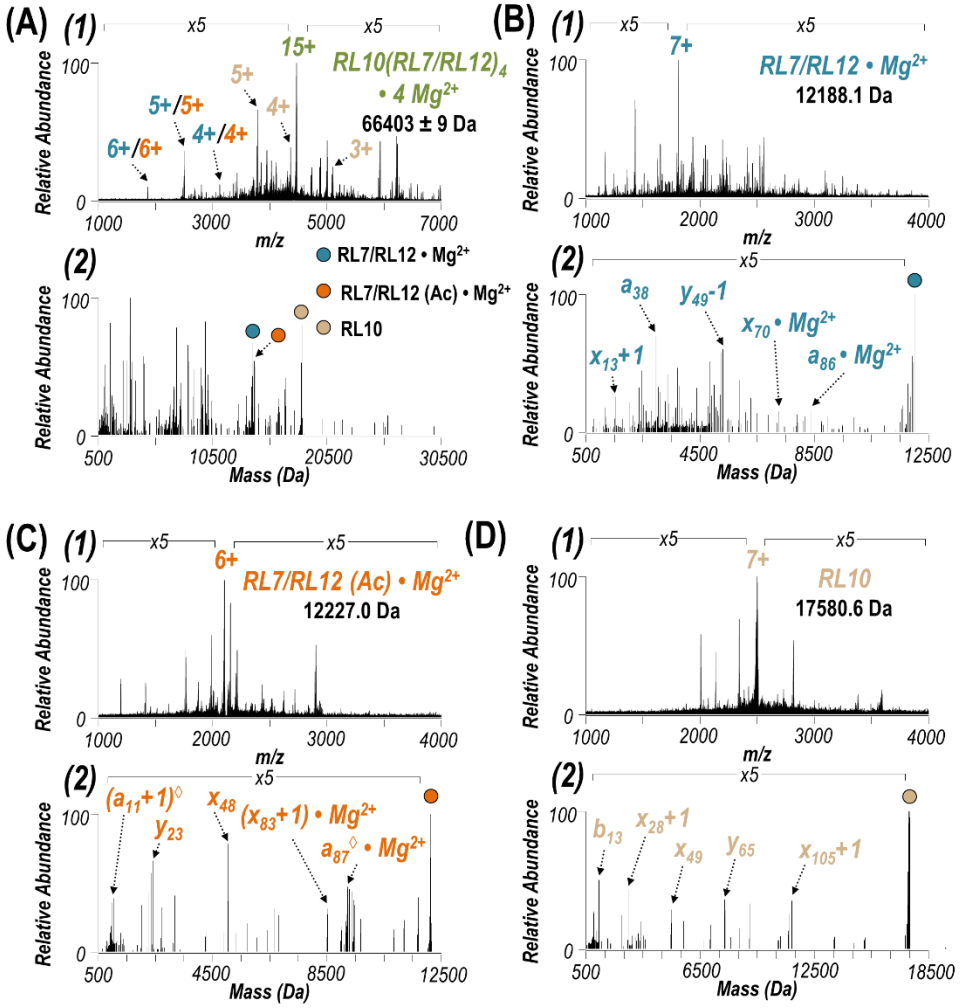

Figure 8.8: (1) MS/MS spectrum and (2) deconvoluted MS/MS spectrum resulting from (A) UVPD of the 15+ charge state of the RL8 stalk complex ($RL10(RL7/RL12)_4 \bullet 4Mg^{2+}$) or IST-UVPD of (B) the 7+ charge state of RL7/RL12 • Mg^{2+}, (C) the 6+ charge state of RL7/Rl2 (Ac) • Mg^{2+}, and (D) the 7+ charge state of RL10 collected during CE-MS analysis of *E. coli* ribosomes using 100 μM magnesium acetate in the background electrolyte. The ESI-MS and IST-MS spectra are shown in Figure 8.7. In (A), intact subunits are observed and the corresponding charge states are labelled for RL7/RL12 • Mg^{2+} (turquoise), RL7/Rl2 (Ac) • Mg^{2+} (orange), and RL10 (tan). Representative apo and holo (Mg^{2+}-bound) fragment ions are labelled in (2) for (B-C) with fragment ions retaining the acetylation in (C) indicated by ◊ and any surviving precursor denoted with a filled circle. Corresponding sequence coverage maps and values are shown in Figure 8.7.

8.4.4 Mapping UVPD Holo Fragment Ions to Examine Metal Cofactor Binding to Ribosomal Proteins

In addition to higher sequence coverages, the accessibility to higher energy fragmentation pathways allows the preservation of non-covalent interactions between the protein and metals or ligands during cleavage of covalent backbone bonds of the protein, a phenomenon reported for UV photoactivation of protein-metal and protein-ligand complexes.[49,54,70–72] This counter-intuitive outcome is rationalized by the fast cleavage of the polypeptide backbone occurring from ions in excited states prior to vibrational energy redistribution which favors disruption of lower energy covalent or noncovalent bonds.[44] In practice, mapping these ligand- or metal-retaining holo fragment ions generated during UVPD has offered insight into the residues involved in ligand binding for a wide variety of protein-ligand complexes such as an NADPH cofactor and inhibitor methotrexate bound to dihydrofolate reductase (DHFR),[70] GDP or a GTP-analogue within the oncogenic rat sarcoma protein K-Ras,[71] adenosine phosphate ligands interacting with the phosphotransferase enzyme adenylate kinase,[72] and a PLP cofactor pulled down with branched-chain amino acid transferase 2 (BCAT2).[54]

Two specific examples of UVPD holo fragment ion mapping are shown in **Figure 8.9** for the protein-metal complexes RL29 • Mg^{2+} and RL31 • Zn^{2+} identified by IST-UVPD in the CE separation of ribosomal proteins with no magnesium acetate present in the BGE. The backbone cleavage sites that lead to holo fragment ions are represented either as lines above the protein sequence or colored along the corresponding crystal structure of the proteins (PDB ID: 4V4Q).[73] Backbone cleavages that result in N-terminal-containing holo fragment ions (*a, b, c*) are colored turquoise, C-terminal-containing holo fragment ions (*x, y, z*) are shaded orange, and backbone cleavages that produce complementary N-terminal- and C-terminal-containing ions ("bi-directional" holo fragment ions) are shown in dark

red. Corresponding IST-MS spectra and IST-UVPD MS/MS spectra for both protein-metal complexes are shown in **Figure 8.10**. For RL29, the Mg^{2+} ion is expected to interact with acidic residues (D or E) which correlates with the interaction site identified by mapping holo fragment ions (L22-Q25). Similarly, the putative binding site of Zn^{2+} in RL31 is C16. This aligns with the binding region elucidated from tracking the holo fragment ions (S15-N20). These types of holo ions are not generally created upon HCD as collisional activation tends to disrupt electrostatic interactions preferentially relative to cleavage of backbone bonds of the protein.

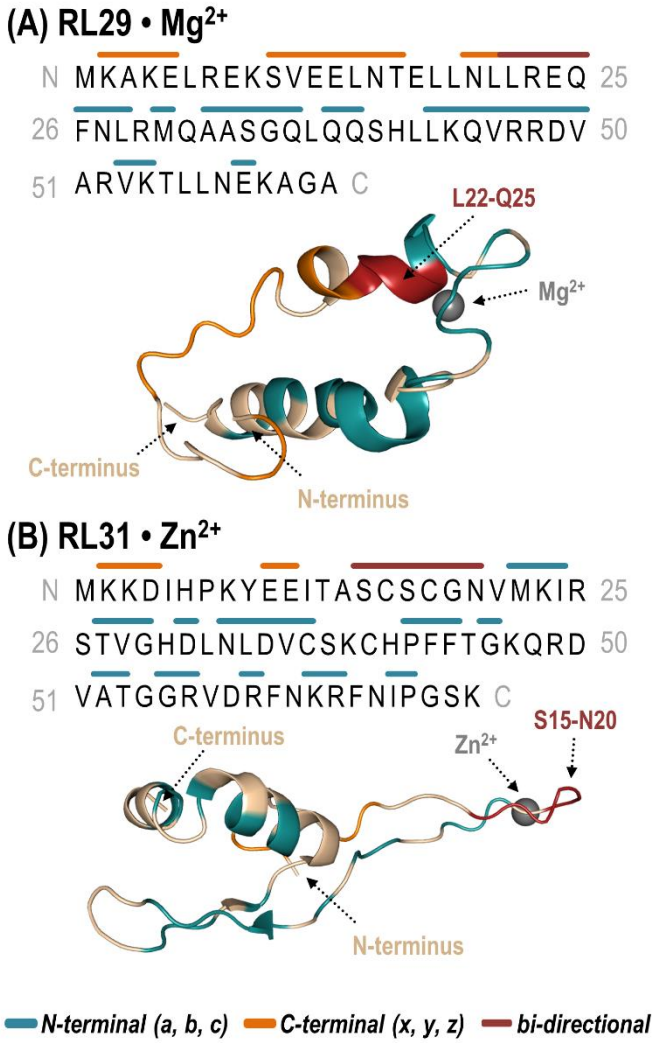

Figure 8.9: Backbone cleavage sites of holo (Mg^{2+}- or Zn^{2+}-containing) fragment ions observed upon IST-UVPD of (A) RL29 • Mg^{2+} and (B) RL31 • Zn^{2+} following on-line CE separation of *E. coli* ribosomal proteins using no magnesium acetate in the background electrolyte solution represented as lines above the corresponding sequences or colored along a crystal structure of the protein (PDB ID: 4V4Q). Cleavage that results in N-terminal holo fragment ions (*a*, *b*, *c*) are colored turquoise, C-terminal holo fragment ions (*x*, *y*, *z*) are shaded orange, or complementary N-terminal and C-terminal ions (bi-directional holo fragment ions) are shown in pink. Corresponding ESI-MS spectra, UVPD MS/MS spectra, and sequence coverage maps including apo (metal-free) fragment ions are shown in Figure 8.10.

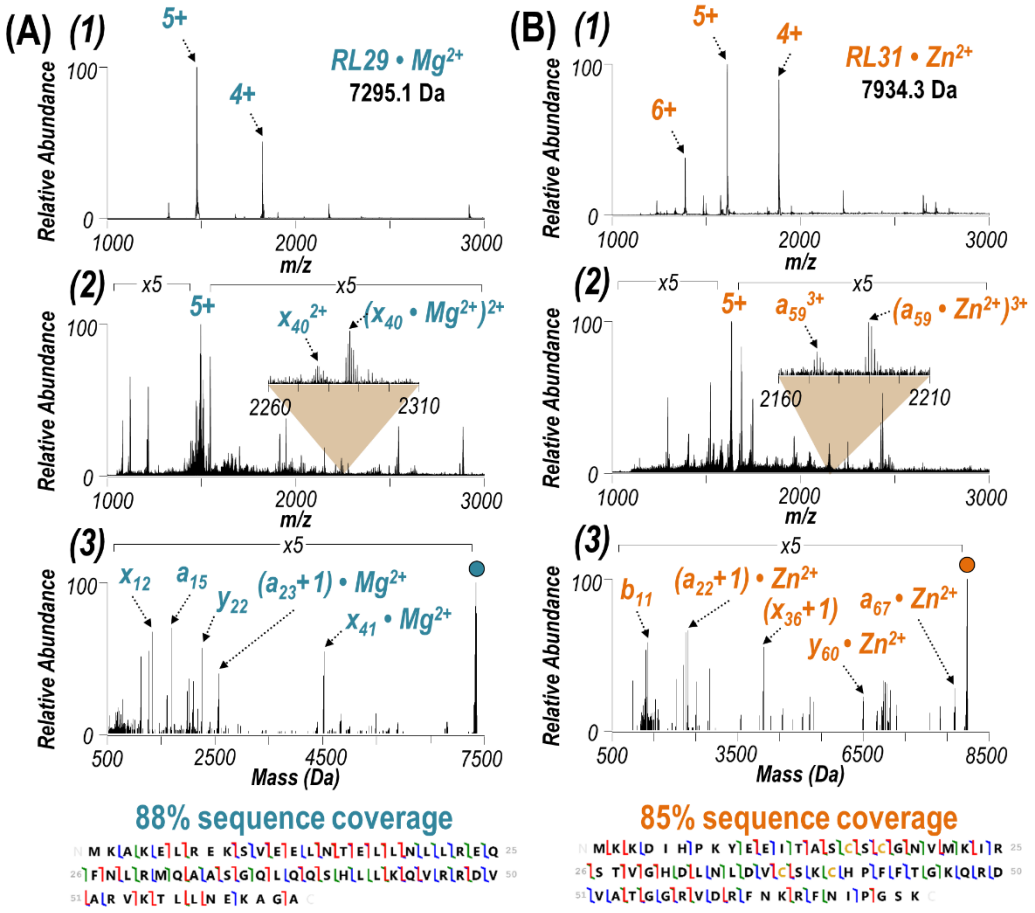

Figure 8.10: (1) In-source trapping mass spectrum, (2) IST-UVPD mass spectrum, and (3) deconvoluted IST-UVPD mass spectrum for (A) RL29 • Mg^{2+} and (B) RL31 • Zn^{2+} collected during CE-MS analysis of *E. coli* ribosomes using no magnesium acetate in the background electrolyte solution and IST-UVPD for ion activation (at retention times of 27.57 min (RL29 • Mg^{2+}) and 28.31 min (RL31 • Zn^{2+}) in Figure 8.1C). Observed charge states are labelled in the respective IST-MS spectra. Activation of the most abundant charge state of each protein in (1) resulted in the UVPD mass spectra shown in (2) (5+ for RL29 • Mg^{2+} and 5+ for RL31 • Zn^{2+}). Zoom views in (2) show an example apo (metal-free) and holo (bound to Mg^{2+} or Zn^{2+}) fragment ion. Several identified apo and holo fragment ions are labelled in (3). The surviving precursor is denoted with a filled circle in (3). Sequence coverage maps and values (accounting for both apo and metal-bound holo fragment ions) are shown at the bottom (fragment ion types are indicated as *a/x* (green), *b/y* (blue), and *c/z* (red)). Corresponding maps of holo fragment ions only are shown in Figure 8.9.

8.5 CONCLUSION

Characterization of *E. coli* 70S ribosomes at various Mg^{2+} concentrations is successfully accomplished by coupling native CE with a UHMR mass spectrometer equipped with UVPD. The capabilities of this instrument for detecting high *m/z* species mitigates bias evident in previous studies towards the identification of lower mass complexes (< 30 kDa) and enables identification of protein-protein complexes (up to 66.4 kDa) larger than previously reported using a native high-throughput workflow.[23,24] Additionally, the ability to access different structural states of a macromolecular complex through adjustment of the salt concentration of the BGE solution posits CE as a versatile separation partner for MS. Four different MS/MS approaches are compared, with UVPD consistently outperforming HCD in the characterization of ribosomal proteoforms across individual protein, protein-metal complexes, and protein-protein complexes. Incorporation of a multistage approach (IST-HCD and IST-UVPD) further increases observed sequence coverage values, particularly for protein-protein complexes owing to the simplification of the precursor species. Although previous studies using native MS in conjunction with denaturing top-down and bottom-up LC-MS/MS[66] or CE-MS/MS under denaturing and native conditions[23] to analyze *E. coli* 70S ribosomes both resulted in the identification of more proteoforms, the current study was designed specifically to improve the characterization of intact protein-protein complexes (higher *m/z* species). Additionally, mapping holo fragment ions generated by UVPD offers further confirmation of putative binding sites for protein-metal complexes. Such fragment ions provide another layer of information relevant for deciphering the organization of protein complexes containing metals or small molecule ligands. As this multistage native CE/UVPD-MS approach is further scaled up, the high-throughput analysis of more complex samples such as the endogenous proteins in cell lysates represents the next frontier.

8.6 REFERENCES

(1) Savaryn, J. P.; Catherman, A. D.; Thomas, P. M.; Abecassis, M. M.; Kelleher, N. L. The Emergence of Top-down Proteomics in Clinical Research. *Genome Med.* **2013**, *5*, 53.

(2) Xing, S.; Wallmeroth, N.; Berendzen, K. W.; Grefen, C. Techniques for the Analysis of Protein-Protein Interactions in Vivo. *Plant Physiol.* **2016**, *171*, 727–758.

(3) Hayes, S.; Malacrida, B.; Kiely, M.; Kiely, P. A. Studying Protein–Protein Interactions: Progress, Pitfalls and Solutions. *Biochem. Soc. Trans.* **2016**, *44*, 994–1004.

(4) Leney, A. C.; Heck, A. J. R. Native Mass Spectrometry: What Is in the Name? *J. Am. Soc. Mass Spectrom.* **2017**, *28*, 5–13.

(5) Allison, T. M.; Bechara, C. Structural Mass Spectrometry Comes of Age: New Insight into Protein Structure, Function and Interactions. *Biochem. Soc. Trans.* **2019**, *47*, 317–327.

(6) Kaur, U.; Johnson, D. T.; Chea, E. E.; Deredge, D. J.; Espino, J. A.; Jones, L. M. Evolution of Structural Biology through the Lens of Mass Spectrometry. *Anal. Chem.* **2019**, *91*, 142–155.

(7) Gillet, L. C.; Leitner, A.; Aebersold, R. Mass Spectrometry Applied to Bottom-Up Proteomics: Entering the High-Throughput Era for Hypothesis Testing. *Annu. Rev. Anal. Chem.* **2016**, *9*, 449–472.

(8) Donnelly, D. P.; Rawlins, C. M.; DeHart, C. J.; Fornelli, L.; Schachner, L. F.; Lin, Z.; Lippens, J. L.; Aluri, K. C.; Sarin, R.; Chen, B.; Lantz, C.; Jung, W.; Johnson, K. R.; Koller, A.; Wolff, J. J.; Campuzano, I. D. G.; Auclair, J. R.; Ivanov, A. R.; Whitelegge, J. P.; Paša-Tolić, L.; Chamot-Rooke, J.; Danis, P. O.; Smith, L. M.; Tsybin, Y. O.; Loo, J. A.; Ge, Y.; Kelleher, N. L.; Agar, J. N. Best Practices and Benchmarks for Intact Protein Analysis for Top-down Mass Spectrometry. *Nat. Methods* **2019**, *16*, 587–594.

(9) Smith, L. M.; Kelleher, N. L.; Proteomics, T. C. for T. D.; Linial, M.; Goodlett, D.; Langridge-Smith, P.; Goo, Y. A.; Safford, G.; Bonilla, L.; Kruppa, G.; Zubarev, R.; Rontree, J.; Chamot-Rooke, J.; Garavelli, J.; Heck, A.; Loo, J.; Penque, D.; Hornshaw, M.; Hendrickson, C.; Pasa-Tolic, L.; Borchers, C.; Chan, D.; Young, N.; Agar, J.; Masselon, C.; Gross, M.; McLafferty, F.; Tsybin, Y.; Ge, Y.; Sanders, I.; Langridge, J.; Whitelegge, J.; Marshall, A. Proteoform: A Single Term Describing Protein Complexity. *Nat. Methods* **2013**, *10*, 186–187.

(10) Hyung, S.-J.; Ruotolo, B. T. Integrating Mass Spectrometry of Intact Protein Complexes into Structural Proteomics. *Proteomics* **2012**, *12*, 1547–1564.

(11) Ngounou Wetie, A. G.; Sokolowska, I.; Woods, A. G.; Roy, U.; Loo, J. A.; Darie, C. C. Investigation of Stable and Transient Protein-Protein Interactions: Past, Present, and Future. *Proteomics* **2013**, *13*, 538–557.

(12) Kükrer, B.; Filipe, V.; van Duijn, E.; Kasper, P. T.; Vreeken, R. J.; Heck, A. J. R.; Jiskoot, W. Mass Spectrometric Analysis of Intact Human Monoclonal Antibody Aggregates Fractionated by Size-Exclusion Chromatography. *Pharm. Res.* **2010**, *27*, 2197–2204.

(13) Muneeruddin, K.; Thomas, J. J.; Salinas, P. A.; Kaltashov, I. A. Characterization of Small Protein Aggregates and Oligomers Using Size Exclusion Chromatography with Online Detection by Native Electrospray Ionization Mass Spectrometry. *Anal. Chem.* **2014**, *86*, 10692–10699.
(14) Haberger, M.; Leiss, M.; Heidenreich, A.-K.; Pester, O.; Hafenmair, G.; Hook, M.; Bonnington, L.; Wegele, H.; Haindl, M.; Reusch, D.; Bulau, P. Rapid Characterization of Biotherapeutic Proteins by Size-Exclusion Chromatography Coupled to Native Mass Spectrometry. *mAbs* **2015**, *8*, 331–339.
(15) Sahasrabuddhe, A.; Hsia, Y.; Busch, F.; Sheffler, W.; King, N. P.; Baker, D.; Wysocki, V. H. Confirmation of Intersubunit Connectivity and Topology of Designed Protein Complexes by Native MS. *Proc. Natl. Acad. Sci.* **2018**, *115*, 1268–1273.
(16) Muneeruddin, K.; Nazzaro, M.; Kaltashov, I. A. Characterization of Intact Protein Conjugates and Biopharmaceuticals Using Ion-Exchange Chromatography with Online Detection by Native Electrospray Ionization Mass Spectrometry and Top-Down Tandem Mass Spectrometry. *Anal. Chem.* **2015**, *87*, 10138–10145.
(17) Debaene, F.; Bœuf, A.; Wagner-Rousset, E.; Colas, O.; Ayoub, D.; Corvaïa, N.; Van Dorsselaer, A.; Beck, A.; Cianférani, S. Innovative Native MS Methodologies for Antibody Drug Conjugate Characterization: High Resolution Native MS and IM-MS for Average DAR and DAR Distribution Assessment. *Anal. Chem.* **2014**, *86*, 10674–10683.
(18) Martinović, S.; Berger, S. J.; Paša-Tolić, L.; Smith, R. D. Separation and Detection of Intact Noncovalent Protein Complexes from Mixtures by On-Line Capillary Isoelectric Focusing-Mass Spectrometry. *Anal. Chem.* **2000**, *72*, 5356–5360.
(19) Fonslow, B. R.; Kang, S. A.; Gestaut, D. R.; Graczyk, B.; Davis, T. N.; Sabatini, D. M.; Yates III, J. R. Native Capillary Isoelectric Focusing for the Separation of Protein Complex Isoforms and Subcomplexes. *Anal. Chem.* **2010**, *82*, 6643–6651.
(20) Skinner, O. S.; Do Vale, L. H. F.; Catherman, A. D.; Havugimana, P. C.; Sousa, M. V. de; Compton, P. D.; Kelleher, N. L. Native GELFrEE: A New Separation Technique for Biomolecular Assemblies. *Anal. Chem.* **2015**, *87*, 3032–3038.
(21) Skinner, O. S.; Haverland, N. A.; Fornelli, L.; Melani, R. D.; Do Vale, L. H. F.; Seckler, H. S.; Doubleday, P. F.; Schachner, L. F.; Srzentić, K.; Kelleher, N. L.; Compton, P. D. Top-down Characterization of Endogenous Protein Complexes with Native Proteomics. *Nat. Chem. Biol.* **2018**, *14*, 36–41.
(22) Han, X.; Wang, Y.; Aslanian, A.; Fonslow, B.; Graczyk, B.; Davis, T. N.; Yates, J. R. In-Line Separation by Capillary Electrophoresis Prior to Analysis by Top-Down Mass Spectrometry Enables Sensitive Characterization of Protein Complexes. *J. Proteome Res.* **2014**, *13*, 6078–6086.
(23) Belov, A. M.; Viner, R.; Santos, M. R.; Horn, D. M.; Bern, M.; Karger, B. L.; Ivanov, A. R. Analysis of Proteins, Protein Complexes, and Organellar Proteomes Using Sheathless Capillary Zone Electrophoresis - Native Mass Spectrometry. *J. Am. Soc. Mass Spectrom.* **2017**, *28*, 2614–2634.

(24) Shen, X.; Kou, Q.; Guo, R.; Yang, Z.; Chen, D.; Liu, X.; Hong, H.; Sun, L. Native Proteomics in Discovery Mode Using Size-Exclusion Chromatography–Capillary Zone Electrophoresis–Tandem Mass Spectrometry. *Anal. Chem.* **2018**, *90*, 10095–10099.
(25) McCool, E. N.; Lubeckyj, R. A.; Shen, X.; Chen, D.; Kou, Q.; Liu, X.; Sun, L. Deep Top-Down Proteomics Using Capillary Zone Electrophoresis-Tandem Mass Spectrometry: Identification of 5700 Proteoforms from the Escherichia Coli Proteome. *Anal. Chem.* **2018**, *90*, 5529–5533.
(26) Lubeckyj, R. A.; Basharat, A. R.; Shen, X.; Liu, X.; Sun, L. Large-Scale Qualitative and Quantitative Top-Down Proteomics Using Capillary Zone Electrophoresis-Electrospray Ionization-Tandem Mass Spectrometry with Nanograms of Proteome Samples. *J. Am. Soc. Mass Spectrom.* **2019**.
(27) McCool, E. N.; Lodge, J. M.; Basharat, A. R.; Liu, X.; Coon, J. J.; Sun, L. Capillary Zone Electrophoresis-Tandem Mass Spectrometry with Activated Ion Electron Transfer Dissociation for Large-Scale Top-down Proteomics. *J. Am. Soc. Mass Spectrom.* **2019**.
(28) Shen, X.; Yang, Z.; McCool, E. N.; Lubeckyj, R. A.; Chen, D.; Sun, L. Capillary Zone Electrophoresis-Mass Spectrometry for Top-down Proteomics. *TrAC Trends Anal. Chem.* **2019**, *120*, 115644.
(29) Kristoff, C. J.; Bwanali, L.; Veltri, L. M.; Gautam, G. P.; Rutto, P. K.; Newton, E. O.; Holland, L. A. Challenging Bioanalyses with Capillary Electrophoresis. *Anal. Chem.* **2020**, *92*, 49–66.
(30) Lössl, P.; Snijder, J.; Heck, A. J. R. Boundaries of Mass Resolution in Native Mass Spectrometry. *J. Am. Soc. Mass Spectrom.* **2014**, *25*, 906–917.
(31) Robinson, C. V.; Chung, E. W.; Kragelund, B. B.; Knudsen, J.; Aplin, R. T.; Poulsen, F. M.; Dobson, C. M. Probing the Nature of Noncovalent Interactions by Mass Spectrometry. A Study of Protein−CoA Ligand Binding and Assembly. *J. Am. Chem. Soc.* **1996**, *118*, 8646–8653.
(32) Li, H.; Wolff, J. J.; Van Orden, S. L.; Loo, J. A. Native Top-Down Electrospray Ionization-Mass Spectrometry of 158 KDa Protein Complex by High-Resolution Fourier Transform Ion Cyclotron Resonance Mass Spectrometry. *Anal. Chem.* **2014**, *86*, 317–320.
(33) Li, H.; Nguyen, H. H.; Ogorzalek Loo, R. R.; Campuzano, I. D. G.; Loo, J. A. An Integrated Native Mass Spectrometry and Top-down Proteomics Method That Connects Sequence to Structure and Function of Macromolecular Complexes. *Nat. Chem.* **2018**, *10*, 139–148.
(34) Fort, K. L.; Waterbeemd, M. van de; Boll, D.; Reinhardt-Szyba, M.; Belov, M. E.; Sasaki, E.; Zschoche, R.; Hilvert, D.; Makarov, A. A.; Heck, A. J. R. Expanding the Structural Analysis Capabilities on an Orbitrap-Based Mass Spectrometer for Large Macromolecular Complexes. *Analyst* **2017**, *143*, 100–105.
(35) Hall, Z.; Hernández, H.; Marsh, J. A.; Teichmann, S. A.; Robinson, C. V. The Role of Salt Bridges, Charge Density, and Subunit Flexibility in Determining Disassembly Routes of Protein Complexes. *Structure* **2013**, *21*, 1325–1337.

(36) Macias, L. A.; Santos, I. C.; Brodbelt, J. S. Ion Activation Methods for Peptides and Proteins. *Anal. Chem.* **2020**, *92*, 227–251.
(37) Zhang, H.; Cui, W.; Wen, J.; Blankenship, R. E.; Gross, M. L. Native Electrospray and Electron-Capture Dissociation FTICR Mass Spectrometry for Top-down Studies of Protein Assemblies. *Anal. Chem.* **2011**, *83*, 5598–5606.
(38) Lermyte, F.; Sobott, F. Electron Transfer Dissociation Provides Higher-Order Structural Information of Native and Partially Unfolded Protein Complexes. *PROTEOMICS* **2015**, *15*, 2813–2822.
(39) Li, H.; Sheng, Y.; McGee, W.; Cammarata, M.; Holden, D.; Loo, J. A. Structural Characterization of Native Proteins and Protein Complexes by Electron Ionization Dissociation-Mass Spectrometry. *Anal. Chem.* **2017**, *89*, 2731–2738.
(40) Lermyte, F.; Valkenborg, D.; Loo, J. A.; Sobott, F. Radical Solutions: Principles and Application of Electron-Based Dissociation in Mass Spectrometry-Based Analysis of Protein Structure. *Mass Spectrom. Rev.* **2018**, *37*, 750–771.
(41) Zhou, M.; Wysocki, V. H. Surface Induced Dissociation: Dissecting Noncovalent Protein Complexes in the Gas Phase. *Acc. Chem. Res.* **2014**, *47*, 1010–1018.
(42) Morrison, L. J.; Brodbelt, J. S. 193 Nm Ultraviolet Photodissociation Mass Spectrometry of Tetrameric Protein Complexes Provides Insight into Quaternary and Secondary Protein Topology. *J. Am. Chem. Soc.* **2016**, *138*, 10849–10859.
(43) Tamara, S.; Dyachenko, A.; Fort, K. L.; Makarov, A. A.; Scheltema, R. A.; Heck, A. J. R. Symmetry of Charge Partitioning in Collisional and UV Photon-Induced Dissociation of Protein Assemblies. *J. Am. Chem. Soc.* **2016**, *138*, 10860–10868.
(44) Brodbelt, J. S.; Morrison, L. J.; Santos, I. Ultraviolet Photodissociation Mass Spectrometry for Analysis of Biological Molecules. *Chem. Rev.* **2019**.
(45) Shaw, J. B.; Li, W.; Holden, D. D.; Zhang, Y.; Griep-Raming, J.; Fellers, R. T.; Early, B. P.; Thomas, P. M.; Kelleher, N. L.; Brodbelt, J. S. Complete Protein Characterization Using Top-Down Mass Spectrometry and Ultraviolet Photodissociation. *J. Am. Chem. Soc.* **2013**, *135*, 12646–12651.
(46) Cannon, J. R.; Cammarata, M. B.; Robotham, S. A.; Cotham, V. C.; Shaw, J. B.; Fellers, R. T.; Early, B. P.; Thomas, P. M.; Kelleher, N. L.; Brodbelt, J. S. Ultraviolet Photodissociation for Characterization of Whole Proteins on a Chromatographic Time Scale. *Anal. Chem.* **2014**, *86*, 2185–2192.
(47) Cleland, T. P.; DeHart, C. J.; Fellers, R. T.; VanNispen, A. J.; Greer, J. B.; LeDuc, R. D.; Parker, W. R.; Thomas, P. M.; Kelleher, N. L.; Brodbelt, J. S. High-Throughput Analysis of Intact Human Proteins Using UVPD and HCD on an Orbitrap Mass Spectrometer. *J. Proteome Res.* **2017**, *16*, 2072–2079.
(48) Greer, S. M.; Brodbelt, J. S. Top-Down Characterization of Heavily Modified Histones Using 193 Nm Ultraviolet Photodissociation Mass Spectrometry. *J. Proteome Res.* **2018**, *17*, 1138–1145.
(49) O'Brien, J. P.; Li, W.; Zhang, Y.; Brodbelt, J. S. Characterization of Native Protein Complexes Using Ultraviolet Photodissociation Mass Spectrometry. *J. Am. Chem. Soc.* **2014**, *136*, 12920–12928.

(50) Greisch, J.-F.; Tamara, S.; Scheltema, R. A.; Maxwell, H. W. R.; Fagerlund, R. D.; Fineran, P. C.; Tetter, S.; Hilvert, D.; Heck, A. J. R. Expanding the Mass Range for UVPD-Based Native Top-down Mass Spectrometry. *Chem. Sci.* **2019**, *10*, 7163–7171.
(51) Belov, M. E.; Damoc, E.; Denisov, E.; Compton, P. D.; Horning, S.; Makarov, A. A.; Kelleher, N. L. From Protein Complexes to Subunit Backbone Fragments: A Multi-Stage Approach to Native Mass Spectrometry. *Anal. Chem.* **2013**, *85*, 11163–11173.
(52) Konijnenberg, A.; Bannwarth, L.; Yilmaz, D.; Koçer, A.; Venien-Bryan, C.; Sobott, F. Top-down Mass Spectrometry of Intact Membrane Protein Complexes Reveals Oligomeric State and Sequence Information in a Single Experiment. *Protein Sci.* **2015**, *24*, 1292–1300.
(53) Ben-Nissan, G.; Belov, M. E.; Morgenstern, D.; Levin, Y.; Dym, O.; Arkind, G.; Lipson, C.; Makarov, A. A.; Sharon, M. Triple-Stage Mass Spectrometry Unravels the Heterogeneity of an Endogenous Protein Complex. *Anal. Chem.* **2017**, *89*, 4708–4715.
(54) Mehaffey, M. R.; Sanders, J. D.; Holden, D. D.; Nilsson, C. L.; Brodbelt, J. S. Multistage Ultraviolet Photodissociation Mass Spectrometry To Characterize Single Amino Acid Variants of Human Mitochondrial BCAT2. *Anal. Chem.* **2018**, *90*, 9904–9911.
(55) Gault, J.; Liko, I.; Landreh, M.; Shutin, D.; Bolla, J. R.; Jefferies, D.; Agasid, M.; Yen, H.-Y.; Ladds, M. J. G. W.; Lane, D. P.; Khalid, S.; Mullen, C.; Remes, P. M.; Huguet, R.; McAlister, G.; Goodwin, M.; Viner, R.; Syka, J. E. P.; Robinson, C. V. Combining Native and 'Omics' Mass Spectrometry to Identify Endogenous Ligands Bound to Membrane Proteins. *Nat. Methods* **2020**, *17*, 505–508.
(56) Hardy, S. J. S.; Kurland, C. G.; Voynow, P.; Mora, G. Ribosomal Proteins of Escherichia Coli. I. Purification of the 30 S Ribosomal Proteins. *Biochemistry* **1969**, *8*, 2897–2905.
(57) Ban, N.; Nissen, P.; Hansen, J.; Moore, P. B.; Steitz, T. A. The Complete Atomic Structure of the Large Ribosomal Subunit at 2.4 Å Resolution. *Science* **2000**, *289*, 905–920.
(58) Noeske, J.; Wasserman, M. R.; Terry, D. S.; Altman, R. B.; Blanchard, S. C.; Cate, J. H. D. High-Resolution Structure of the Escherichia Coli Ribosome. *Nat. Struct. Mol. Biol.* **2015**, *22*, 336–341.
(59) Wimberly, B. T.; Brodersen, D. E.; Clemons, W. M.; Morgan-Warren, R. J.; Carter, A. P.; Vonrhein, C.; Hartsch, T.; Ramakrishnan, V. Structure of the 30S Ribosomal Subunit. *Nature* **2000**, *407*, 327–339.
(60) Valle, M.; Zavialov, A.; Sengupta, J.; Rawat, U.; Ehrenberg, M.; Frank, J. Locking and Unlocking of Ribosomal Motions. *Cell* **2003**, *114*, 123–134.
(61) Zhang, W.; Dunkle, J. A.; Cate, J. H. D. Structures of the Ribosome in Intermediate States of Ratcheting. *Science* **2009**, *325*, 1014–1017.

(62) Yamamoto, T.; Izumi, S.; Gekko, K. Mass Spectrometry of Hydrogen/Deuterium Exchange in 70S Ribosomal Proteins from E. Coli. *FEBS Lett.* **2006**, *580*, 3638–3642.
(63) Yamamoto, T.; Shimizu, Y.; Ueda, T.; Shiro, Y. Mg2+ Dependence of 70 S Ribosomal Protein Flexibility Revealed by Hydrogen/Deuterium Exchange and Mass Spectrometry. *J. Biol. Chem.* **2010**, *285*, 5646–5652.
(64) Benjamin, D. R.; Robinson, C. V.; Hendrick, J. P.; Hartl, F. U.; Dobson, C. M. Mass Spectrometry of Ribosomes and Ribosomal Subunits. *Proc. Natl. Acad. Sci.* **1998**, *95*, 7391–7395.
(65) Waterbeemd, M. van de; Fort, K. L.; Boll, D.; Reinhardt-Szyba, M.; Routh, A.; Makarov, A.; Heck, A. J. R. High-Fidelity Mass Analysis Unveils Heterogeneity in Intact Ribosomal Particles. *Nat. Methods* **2017**, *14*, 283.
(66) van de Waterbeemd, M.; Tamara, S.; Fort, K. L.; Damoc, E.; Franc, V.; Bieri, P.; Itten, M.; Makarov, A.; Ban, N.; Heck, A. J. R. Dissecting Ribosomal Particles throughout the Kingdoms of Life Using Advanced Hybrid Mass Spectrometry Methods. *Nat. Commun.* **2018**, *9*, 1–12.
(67) Gülbakan, B.; Barylyuk, K.; Schneider, P.; Pillong, M.; Schneider, G.; Zenobi, R. Native Electrospray Ionization Mass Spectrometry Reveals Multiple Facets of Aptamer–Ligand Interactions: From Mechanism to Binding Constants. *J. Am. Chem. Soc.* **2018**, *140*, 7486–7497.
(68) Greer, S. M.; Holden, D. D.; Fellers, R.; Kelleher, N. L.; Brodbelt, J. S. Modulation of Protein Fragmentation Through Carbamylation of Primary Amines. *J. Am. Soc. Mass Spectrom.* **2017**, *28*, 1587–1599.
(69) Diaconu, M.; Kothe, U.; Schlünzen, F.; Fischer, N.; Harms, J. M.; Tonevitsky, A. G.; Stark, H.; Rodnina, M. V.; Wahl, M. C. Structural Basis for the Function of the Ribosomal L7/12 Stalk in Factor Binding and GTPase Activation. *Cell* **2005**, *121*, 991–1004.
(70) Cammarata, M. B.; Thyer, R.; Rosenberg, J.; Ellington, A.; Brodbelt, J. S. Structural Characterization of Dihydrofolate Reductase Complexes by Top-Down Ultraviolet Photodissociation Mass Spectrometry. *J. Am. Chem. Soc.* **2015**, *137*, 9128–9135.
(71) Cammarata, M. B.; Schardon, C. L.; Mehaffey, M. R.; Rosenberg, J.; Singleton, J.; Fast, W.; Brodbelt, J. S. Impact of G12 Mutations on the Structure of K-Ras Probed by Ultraviolet Photodissociation Mass Spectrometry. *J. Am. Chem. Soc.* **2016**, *138*, 13187–13196.
(72) Mehaffey, M. R.; Cammarata, M. B.; Brodbelt, J. S. Tracking the Catalytic Cycle of Adenylate Kinase by Ultraviolet Photodissociation Mass Spectrometry. *Anal. Chem.* **2018**, *90*, 839–846.
(73) Schuwirth, B. S.; Borovinskaya, M. A.; Hau, C. W.; Zhang, W.; Vila-Sanjurjo, A.; Holton, J. M.; Cate, J. H. D. Structures of the Bacterial Ribosome at 3.5 Å Resolution. *Science* **2005**, *310*, 827–834.

Chapter 9: Conclusions

9.1 Summary of Chapters

Significant advances with regards to covalent labeling workflows, instrumentation, and ion activation methods have already solidified a spot for MS in the structural biology toolbox as a rapid, sensitive alternative to supplement traditional methods in defining the higher order structures of biomolecules. Nevertheless, many opportunities to extend the versatility of MS approaches for structural biology applications still remain. Specifically, the work presented in this dissertation sought to further develop native MS and 193 nm UVPD for probing conformational changes in protein-ligand and protein-protein complexes, as well as lay the groundwork for scaling up this analysis to more complex biological samples in a high-throughput workflow.

Although the capabilities of UVPD-MS for elucidating ligand binding sites and detecting changes in secondary/tertiary structure resulting from enzymatic processes, ligand exchange, or single point mutation in protein-ligand complexes had been previously established, further studies were still necessary to establish the sensitivity of this approach and demonstrate applicability to larger protein complexes. Tracking variations in UVPD backbone cleavage efficiency for the phosphotransferase AK throughout its catalytic cycle, as described in Chapter 3, highlighted the utility of this approach for offering information on how structural dynamics, metal cofactors, and side-chain chemistries each contribute to enzyme catalysis. Specifically, UVPD-MS pinpointed five main regions (three α-helices of the AMP binding domain and the adenosine binding regions of AMP and ATP) undergoing such movements to facilitate a global open-to-closed transition and optimize the environment for phosphoryl transfer. As such, this study demonstrated the application

of UVPD-MS to detect structural changes on several different scales ranging from global movements down to conformational fluctuations of single residues for active enzymes.

In Chapter 4, UVPD-MS offered critical insights into structural variations induced by inhibitor binding or mutation of the MBL enzyme NDM that have remained elusive using other biochemical techniques. Both Lys and Cys specific covalent inhibitors were studied in addition to clinical single amino acid variants, demonstrating the versatility of UVPD-MS. The detection of the closure of a beta-hairpin loop near the active site upon inhibitor binding and elucidation of the individual contributions to metal affinity of the six Zn-binding residues in clinical variants are both important to designing potent inhibitors of this enzyme. Previous spectroscopic studies aimed at studying NDM-inhibitor complexes relied on labelling the protein or using non-native metalloforms both of which can artificially perturb the system. Studies such as this further establish UVPD-MS as a sensitive and versatile structural biology tool.

Owing to the fact that an estimated 86% of proteins exist as higher order oligomers, scaling up the UVPD-MS approach to protein-protein complexes was necessary to exhibit utility in establishing a comprehensive picture of interaction networks and disease mechanisms. Previously published UVPD studies of protein-protein complexes utilized model proteins and focused on defining favored dissociation pathways. Instead, Chapter 5 detailed structural changes resulting from the most common genetic alterations in human cancers, G12X mutations in the GTPase enzyme K-Ras. Probing complexes formed between K-Ras variants and the downstream effector protein Raf revealed hydrogen-bonding substitutions resulted in a stabilized β-interface of the Ras-Raf heterodimer, whereas a bulky, hydrophobic mutation yielded tighter helical bundles instead along the α-interface.

Another important subset of protein-protein complexes was analyzed by UVPD-MS in Chapter 6, antibody-antigen complexes. Specifically, the epitope mapping capabilities of UVPD were demonstrated for hemagglutinin (HA), the primary immunogenic antigen of the influenza virus, and the D1 H1-17/H3-14 antibody based on the suppression of UVPD sequence ions. As no crystal structure for this specific antibody-antigen complex exists, confirmation of the putative epitope regions elevates both the UVPD-MS approach and previous literature.

Aimed at enabling native MS and UVPD for the structural analysis of complex biological mixtures in a high-throughput, Chapter 7 demonstrated the application of a multistage MS/MS approach to characterize single amino acid variants of BCAT2. Disassembly of the homodimer into constituent subunits by IST and subsequent UVPD of the monomer afforded significantly higher sequence coverage (increasing from 21% to 45% for WT BCAT2) as well as enabled confident identification of PLP-bound holo ions. Additionally, mapping the origin of observed holo ions along the sequence provided insight into the destabilization of interactions with the PLP cofactor resulting from a single point mutation (T186R). This study established the utility in incorporating UVPD in a multistage MS/MS workflow to improve structural characterization of protein-protein complexes via the production of a more diverse set of sequence ions, including assignable holo ions that provide insight into ligand interactions.

The work presented in Chapter 8 harnessed these developments to improve structural characterization of ribosomal proteins introduced by on-line CE-MS. Owing to the operating principles of CE, this separation method was fully compatible with native MS and separated a variety of protein-protein, protein-ligand, and protein-metal complexes for subsequent MS analysis. Additionally, tuning the magnesium acetate concentration of the BGE yielded substructures of the ribosome (at high concentrations) or disassembled

monomers (at low concentrations). UVPD consistently outperformed HCD regarding the structural characterization of protein complexes and implementation of the multistage MS/MS workflow afforded the highest sequence coverages and allowed tracking of holo ions to define ligand interactions. While this work was limited to the analysis of ~50 proteins, it established an experimental workflow that can be scaled up to more complex samples.

9.2 Future Directions

As the world currently waits at the time of writing this for the development of an effective vaccine to end a global pandemic caused by a novel coronavirus (COVID-19), the need for rapid, sensitive approaches to identify antigenic epitopes has become abundantly clear. Accordingly, further studies are already underway aimed at using the UVPD-MS workflow for epitope mapping of a wider variety of antibody-antigen complexes. Owing to the adoption of a trimeric structure by the spike proteins on the surfaces of most viruses, an important avenue of this future work is determining if the antigenic determinants of targets that exist as higher order oligomers can be successfully probed. Additionally, it is necessary to establish an ideal antigen size regime or upper limit for epitope mapping by UVPD-MS. One anticipated technical hurdle in the analysis of more structurally complex antigens is confident assignment of fragment ions in the resulting MS/MS spectra. One possible workaround includes using single chain variable fragments (scFv) to bind corresponding antigens, as opposed to entire antibodies. These fusion proteins retain the specificity of the original antibody but are significantly smaller (30 kDa), which could reduce the complexity of resulting UVPD spectra and streamline the epitope mapping process.

While the use of CE in conjunction with multistage UVPD in Chapter 8 to probe ribosomal protein complexes under native MS conditions represents a significant advance, much work remains to make this type of analysis routine for complex endogenous samples. A logical next step towards this goal would be application of this approach to analyze a pre-fractionated lysate for which a workflow is proposed in **Figure 9.1**. Briefly, lysis of *E. coli* cells and subsequent SEC pre-fractionation would result in 8-10 samples containing ~200 proteins each for CE-MS analysis. Currently, a major technical challenge with this approach is maintaining samples at high enough concentrations during pre-fractionation for subsequent CE, owing to the low loading capacity of this electrophoretic separation technique. Nevertheless, several pre-concentration methods have been developed including field-amplified sample stacking (FASS), transient isotachophoresis (tITP), and dynamic pH junction. Although these techniques typically require denaturing solvents, developments focused on substituting in native MS solvents could significantly improve the CE loading capacity and allow routine injection of less concentrated samples.

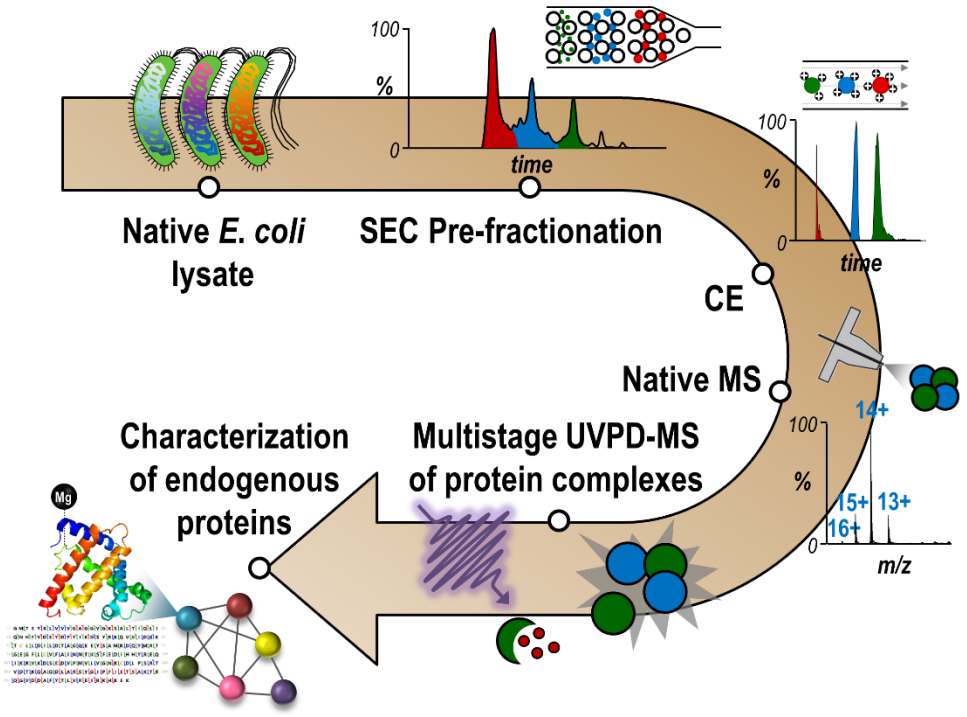

Figure 9.1: Proposed workflow for the analysis of endogenous protein complexes in *E. coli* cells by CE in conjunction with multistage UVPD-MS.

References

CHAPTER 1

(1) Baker, D.; Sali, A. Protein Structure Prediction and Structural Genomics. *Science* **2001**, *294*, 93–96.

(2) Forster, M. J. Molecular Modelling in Structural Biology. *Micron* **2002**, *33*, 365–384.

(3) Shi, Y. A Glimpse of Structural Biology through X-Ray Crystallography. *Cell* **2014**, *159*, 995–1014.

(4) Ameh, E. S. A Review of Basic Crystallography and X-Ray Diffraction Applications. *Int. J. Adv. Manuf. Technol.* **2019**, *105*, 3289–3302.

(5) Wüthrich, K. The Way to NMR Structures of Proteins. *Nat. Struct. Mol. Biol.* **2001**, *8*, 923–925.

(6) Cavalli, A.; Salvatella, X.; Dobson, C. M.; Vendruscolo, M. Protein Structure Determination from NMR Chemical Shifts. *Proc. Natl. Acad. Sci.* **2007**, *104*, 9615–9620.

(7) Bai, X.; McMullan, G.; Scheres, S. H. W. How Cryo-EM Is Revolutionizing Structural Biology. *Trends Biochem. Sci.* **2015**, *40*, 49–57.

(8) Fernández, C.; Jahnke, W. New Approaches for NMR Screening in Drug Discovery. *Drug Discov. Today Technol.* **2004**, *1*, 277–283.

(9) Søndergaard, C. R.; Garrett, A. E.; Carstensen, T.; Pollastri, G.; Nielsen, J. E. Structural Artifacts in Protein−Ligand X-Ray Structures: Implications for the Development of Docking Scoring Functions. *J. Med. Chem.* **2009**, *52*, 5673–5684.

(10) Niedzialkowska, E.; Gasiorowska, O.; Handing, K. B.; Majorek, K. A.; Porebski, P. J.; Shabalin, I. G.; Zasadzinska, E.; Cymborowski, M.; Minor, W. Protein Purification and Crystallization Artifacts: The Tale Usually Not Told. *Protein Sci.* **2016**, *25*, 720–733.

(11) Glaeser, R. M.; Hall, R. J. Reaching the Information Limit in Cryo-EM of Biological Macromolecules: Experimental Aspects. *Biophys. J.* **2011**, *100*, 2331–2337.

(12) Benesch, J. L.; Ruotolo, B. T. Mass Spectrometry: Come of Age for Structural and Dynamical Biology. *Curr. Opin. Struct. Biol.* **2011**, *21*, 641–649.

(13) Liko, I.; Allison, T. M.; Hopper, J. T.; Robinson, C. V. Mass Spectrometry Guided Structural Biology. *Curr. Opin. Struct. Biol.* **2016**, *40*, 136–144.

(14) Allison, T. M.; Bechara, C. Structural Mass Spectrometry Comes of Age: New Insight into Protein Structure, Function and Interactions. *Biochem. Soc. Trans.* **2019**, *47*, 317–327.

(15) Marcoux, J.; Robinson, C. V. Twenty Years of Gas Phase Structural Biology. *Structure* **2013**, *21*, 1541–1550.

(16) Lössl, P.; Waterbeemd, M. van de; Heck, A. J. The Diverse and Expanding Role of Mass Spectrometry in Structural and Molecular Biology. *EMBO J.* **2016**, *35*, 2634–2657.

(17) Konermann, L.; Vahidi, S.; Sowole, M. A. Mass Spectrometry Methods for Studying Structure and Dynamics of Biological Macromolecules. *Anal. Chem.* **2014**, *86*, 213–232.
(18) Heck, A. J. R. Native Mass Spectrometry: A Bridge between Interactomics and Structural Biology. *Nat. Methods* **2008**, *5*, 927–933.
(19) Leney, A. C.; Heck, A. J. R. Native Mass Spectrometry: What Is in the Name? *J. Am. Soc. Mass Spectrom.* **2017**, *28*, 5–13.
(20) Zhong, Y.; Hyung, S.-J.; Ruotolo, B. T. Ion Mobility–Mass Spectrometry for Structural Proteomics. *Expert Rev. Proteomics* **2012**, *9*, 47–58.
(21) Mendoza, V. L.; Vachet, R. W. Probing Protein Structure by Amino Acid-Specific Covalent Labeling and Mass Spectrometry. *Mass Spectrom. Rev.* **2009**, *28*, 785–815.
(22) O'Brien, J. P.; Pruet, J. M.; Brodbelt, J. S. Chromogenic Chemical Probe for Protein Structural Characterization via Ultraviolet Photodissociation Mass Spectrometry. *Anal. Chem.* **2013**, *85*, 7391–7397.
(23) Zhou, Y.; Vachet, R. W. Increased Protein Structural Resolution from Diethylpyrocarbonate-Based Covalent Labeling and Mass Spectrometric Detection. *J. Am. Soc. Mass Spectrom.* **2012**, *23*, 708–717.
(24) Zhang, H.; Gau, B. C.; Jones, L. M.; Vidavsky, I.; Gross, M. L. Fast Photochemical Oxidation of Proteins for Comparing Structures of Protein−Ligand Complexes: The Calmodulin−Peptide Model System. *Anal. Chem.* **2011**, *83*, 311–318.
(25) Zhang, B.; Rempel, D. L.; Gross, M. L. Protein Footprinting by Carbenes on a Fast Photochemical Oxidation of Proteins (FPOP) Platform. *J. Am. Soc. Mass Spectrom.* **2016**, *27*, 552–555.
(26) Madsen, J. A.; Yin, Y.; Qiao, J.; Gill, V.; Renganathan, K.; Fu, W.-Y.; Smith, S.; Anderson, J. Covalent Labeling Denaturation Mass Spectrometry for Sensitive Localized Higher Order Structure Comparisons. *Anal. Chem.* **2016**, *88*, 2478–2488.
(27) Benhaim, M.; Lee, K. K.; Guttman, M. Tracking Higher Order Protein Structure by Hydrogen-Deuterium Exchange Mass Spectrometry. *Protein Pept. Lett.* **2019**, *26*, 16–26.
(28) Pirrone, G. F.; Iacob, R. E.; Engen, J. R. Applications of Hydrogen/Deuterium Exchange MS from 2012 to 2014. *Anal. Chem.* **2014**, *87*, 99–118.
(29) Zhang, Y.; Rempel, D. L.; Zhang, J.; Sharma, A. K.; Mirica, L. M.; Gross, M. L. Pulsed Hydrogen–Deuterium Exchange Mass Spectrometry Probes Conformational Changes in Amyloid Beta (Aβ) Peptide Aggregation. *Proc. Natl. Acad. Sci.* **2013**, *110*, 14604–14609.
(30) Malito, E.; Faleri, A.; Surdo, P. L.; Veggi, D.; Maruggi, G.; Grassi, E.; Cartocci, E.; Bertoldi, I.; Genovese, A.; Santini, L.; Romagnoli, G.; Borgogni, E.; Brier, S.; Passo, C. L.; Domina, M.; Castellino, F.; Felici, F.; Veen, S. van der; Johnson, S.; Lea, S. M.; Tang, C. M.; Pizza, M.; Savino, S.; Norais, N.; Rappuoli, R.; Bottomley, M. J.; Masignani, V. Defining a Protective Epitope on Factor H Binding Protein, a Key Meningococcal Virulence Factor and Vaccine Antigen. *Proc. Natl. Acad. Sci.* **2013**, *110*, 3304–3309.

(31) Sinz, A. Chemical Cross-Linking and Mass Spectrometry to Map Three-Dimensional Protein Structures and Protein–Protein Interactions. *Mass Spectrom. Rev.* **2006**, *25*, 663–682.
(32) Schmidt, C.; Robinson, C. V. A Comparative Cross-Linking Strategy to Probe Conformational Changes in Protein Complexes. *Nat. Protoc.* **2014**, *9*, 2224–2236.
(33) Liu, F.; Rijkers, D. T. S.; Post, H.; Heck, A. J. R. Proteome-Wide Profiling of Protein Assemblies by Cross-Linking Mass Spectrometry. *Nat. Methods* **2015**, *12*, 1179–1184.
(34) Pham, N. D.; Parker, R. B.; Kohler, J. J. Photocrosslinking Approaches to Interactome Mapping. *Curr. Opin. Chem. Biol.* **2013**, *17*, 90–101.
(35) Hage, C.; Iacobucci, C.; Rehkamp, A.; Arlt, C.; Sinz, A. The First Zero-Length Mass Spectrometry-Cleavable Cross-Linker for Protein Structure Analysis. *Angew. Chem.* **2017**, *129*, 14743–14747.
(36) Trester-Zedlitz, M.; Kamada, K.; Burley, S. K.; Fenyö, D.; Chait, B. T.; Muir, T. W. A Modular Cross-Linking Approach for Exploring Protein Interactions. *J. Am. Chem. Soc.* **2003**, *125*, 2416–2425.
(37) Kao, A.; Chiu, C.; Vellucci, D.; Yang, Y.; Patel, V. R.; Guan, S.; Randall, A.; Baldi, P.; Rychnovsky, S. D.; Huang, L. Development of a Novel Cross-Linking Strategy for Fast and Accurate Identification of Cross-Linked Peptides of Protein Complexes. *Mol. Cell. Proteomics* **2011**, *10*, M110.002212.
(38) Kruppa, G. H.; Schoeniger, J.; Young, M. M. A Top down Approach to Protein Structural Studies Using Chemical Cross-Linking and Fourier Transform Mass Spectrometry. *Rapid Commun. Mass Spectrom.* **2003**, *17*, 155–162.
(39) Cammarata, M. B.; Brodbelt, J. S. Characterization of Intra- and Intermolecular Protein Crosslinking by Top Down Ultraviolet Photodissociation Mass Spectrometry. *ChemistrySelect* **2016**, *1*, 590–593.
(40) Loo, J. A. Studying Noncovalent Protein Complexes by Electrospray Ionization Mass Spectrometry. *Mass Spectrom. Rev.* **1997**, *16*, 1–23.
(41) Konermann, L.; Ahadi, E.; Rodriguez, A. D.; Vahidi, S. Unraveling the Mechanism of Electrospray Ionization. *Anal. Chem.* **2013**, *85*, 2–9.
(42) Konermann, L. Addressing a Common Misconception: Ammonium Acetate as Neutral PH “Buffer” for Native Electrospray Mass Spectrometry. *J. Am. Soc. Mass Spectrom.* **2017**, *28*, 1827–1835.
(43) Lössl, P.; Snijder, J.; Heck, A. J. R. Boundaries of Mass Resolution in Native Mass Spectrometry. *J. Am. Soc. Mass Spectrom.* **2014**, *25*, 906–917.
(44) Robinson, C. V.; Chung, E. W.; Kragelund, B. B.; Knudsen, J.; Aplin, R. T.; Poulsen, F. M.; Dobson, C. M. Probing the Nature of Noncovalent Interactions by Mass Spectrometry. A Study of Protein−CoA Ligand Binding and Assembly. *J. Am. Chem. Soc.* **1996**, *118*, 8646–8653.
(45) Li, H.; Wolff, J. J.; Van Orden, S. L.; Loo, J. A. Native Top-Down Electrospray Ionization-Mass Spectrometry of 158 KDa Protein Complex by High-Resolution Fourier Transform Ion Cyclotron Resonance Mass Spectrometry. *Anal. Chem.* **2014**, *86*, 317–320.

(46) Li, H.; Nguyen, H. H.; Ogorzalek Loo, R. R.; Campuzano, I. D. G.; Loo, J. A. An Integrated Native Mass Spectrometry and Top-down Proteomics Method That Connects Sequence to Structure and Function of Macromolecular Complexes. *Nat. Chem.* **2018**, *10*, 139–148.
(47) Rose, R. J.; Damoc, E.; Denisov, E.; Makarov, A.; Heck, A. J. R. High-Sensitivity Orbitrap Mass Analysis of Intact Macromolecular Assemblies. *Nat. Methods* **2012**, *9*, 1084–1086.
(48) Fort, K. L.; Waterbeemd, M. van de; Boll, D.; Reinhardt-Szyba, M.; Belov, M. E.; Sasaki, E.; Zschoche, R.; Hilvert, D.; Makarov, A. A.; Heck, A. J. R. Expanding the Structural Analysis Capabilities on an Orbitrap-Based Mass Spectrometer for Large Macromolecular Complexes. *Analyst* **2017**, *143*, 100–105.
(49) Sharon, M.; Robinson, C. V. The Role of Mass Spectrometry in Structure Elucidation of Dynamic Protein Complexes. *Annu. Rev. Biochem.* **2007**, *76*, 167–193.
(50) Schmidt, C.; Zhou, M.; Marriott, H.; Morgner, N.; Politis, A.; Robinson, C. V. Comparative Cross-Linking and Mass Spectrometry of an Intact F-Type ATPase Suggest a Role for Phosphorylation. *Nat. Commun.* **2013**, *4*, 1985.
(51) Waterbeemd, M. van de; Fort, K. L.; Boll, D.; Reinhardt-Szyba, M.; Routh, A.; Makarov, A.; Heck, A. J. R. High-Fidelity Mass Analysis Unveils Heterogeneity in Intact Ribosomal Particles. *Nat. Methods* **2017**, *14*, 283.
(52) Snijder, J.; Rose, R. J.; Veesler, D.; Johnson, J. E.; Heck, A. J. R. Studying 18 Mega Dalton Virus Assemblies with Native Mass Spectrometry. *Angew. Chem. Int. Ed Engl.* **2013**, *52*, 4020–4023.
(53) Snijder, J.; van de Waterbeemd, M.; Damoc, E.; Denisov, E.; Grinfeld, D.; Bennett, A.; Agbandje-McKenna, M.; Makarov, A.; Heck, A. J. R. Defining the Stoichiometry and Cargo Load of Viral and Bacterial Nanoparticles by Orbitrap Mass Spectrometry. *J. Am. Chem. Soc.* **2014**, *136*, 7295–7299.
(54) Schmidt, C.; Robinson, C. V. Dynamic Protein Ligand Interactions – Insights from MS. *FEBS J.* **2014**, *281*, 1950–1964.
(55) Kitova, E. N.; El-Hawiet, A.; Schnier, P. D.; Klassen, J. S. Reliable Determinations of Protein–Ligand Interactions by Direct ESI-MS Measurements. Are We There Yet? *J. Am. Soc. Mass Spectrom.* **2012**, *23*, 431–441.
(56) Laganowsky, A.; Reading, E.; Allison, T. M.; Ulmschneider, M. B.; Degiacomi, M. T.; Baldwin, A. J.; Robinson, C. V. Membrane Proteins Bind Lipids Selectively to Modulate Their Structure and Function. *Nature* **2014**, *510*, 172–175.
(57) Gault, J.; Donlan, J. A. C.; Liko, I.; Hopper, J. T. S.; Gupta, K.; Housden, N. G.; Struwe, W. B.; Marty, M. T.; Mize, T.; Bechara, C.; Zhu, Y.; Wu, B.; Kleanthous, C.; Belov, M.; Damoc, E.; Makarov, A.; Robinson, C. V. High-Resolution Mass Spectrometry of Small Molecules Bound to Membrane Proteins. *Nat. Methods* **2016**, *13*, 333–336.
(58) Cubrilovic, D.; Haap, W.; Barylyuk, K.; Ruf, A.; Badertscher, M.; Gubler, M.; Tetaz, T.; Joseph, C.; Benz, J.; Zenobi, R. Determination of Protein–Ligand Binding

Constants of a Cooperatively Regulated Tetrameric Enzyme Using Electrospray Mass Spectrometry. *ACS Chem. Biol.* **2014**, *9*, 218–226.
(59) Cong, X.; Liu, Y.; Liu, W.; Liang, X.; Russell, D. H.; Laganowsky, A. Determining Membrane Protein–Lipid Binding Thermodynamics Using Native Mass Spectrometry. *J. Am. Chem. Soc.* **2016**, *138*, 4346–4349.
(60) Moghadamchargari, Z.; Huddleston, J.; Shirzadeh, M.; Zheng, X.; Clemmer, D. E.; M. Raushel, F.; Russell, D. H.; Laganowsky, A. Intrinsic GTPase Activity of K-RAS Monitored by Native Mass Spectrometry. *Biochemistry* **2019**, *58*, 3396–3405.
(61) Lanucara, F.; Holman, S. W.; Gray, C. J.; Eyers, C. E. The Power of Ion Mobility-Mass Spectrometry for Structural Characterization and the Study of Conformational Dynamics. *Nat. Chem.* **2014**, *6*, 281–294.
(62) Uetrecht, C.; Rose, R. J.; Duijn, E. van; Lorenzen, K.; Heck, A. J. R. Ion Mobility Mass Spectrometry of Proteins and Protein Assemblies. *Chem. Soc. Rev.* **2010**, *39*, 1633–1655.
(63) Jurneczko, E.; E. Barran, P. How Useful Is Ion Mobility Mass Spectrometry for Structural Biology? The Relationship between Protein Crystal Structures and Their Collision Cross Sections in the Gas Phase. *Analyst* **2011**, *136*, 20–28.
(64) Konijnenberg, A.; Butterer, A.; Sobott, F. Native Ion Mobility-Mass Spectrometry and Related Methods in Structural Biology. *Biochim. Biophys. Acta BBA - Proteins Proteomics* **2013**, *1834*, 1239–1256.
(65) Ben-Nissan, G.; Sharon, M. The Application of Ion-Mobility Mass Spectrometry for Structure/Function Investigation of Protein Complexes. *Curr. Opin. Chem. Biol.* **2018**, *42*, 25–33.
(66) Eschweiler, J. D.; Frank, A. T.; Ruotolo, B. T. Coming to Grips with Ambiguity: Ion Mobility-Mass Spectrometry for Protein Quaternary Structure Assignment. *J. Am. Soc. Mass Spectrom.* **2017**, *28*, 1991–2000.
(67) Breuker, K.; McLafferty, F. W. Stepwise Evolution of Protein Native Structure with Electrospray into the Gas Phase, 10−12 to 102 S. *Proc. Natl. Acad. Sci.* **2008**, *105*, 18145–18152.
(68) Vahidi, S.; Stocks, B. B.; Konermann, L. Partially Disordered Proteins Studied by Ion Mobility-Mass Spectrometry: Implications for the Preservation of Solution Phase Structure in the Gas Phase. *Anal. Chem.* **2013**, *85*, 10471–10478.
(69) Devine, P. W. A.; Fisher, H. C.; Calabrese, A. N.; Whelan, F.; Higazi, D. R.; Potts, J. R.; Lowe, D. C.; Radford, S. E.; Ashcroft, A. E. Investigating the Structural Compaction of Biomolecules Upon Transition to the Gas-Phase Using ESI-TWIMS-MS. *J. Am. Soc. Mass Spectrom.* **2017**, *28*, 1855–1862.
(70) Williams, J. P.; Giles, K.; Green, B. N.; Scrivens, J. H.; Bateman, R. H. Ion Mobility Augments the Utility of Mass Spectrometry in the Identification of Human Hemoglobin Variants. *Rapid Commun. Mass Spectrom.* **2008**, *22*, 3179–3186.
(71) Vakhrushev, S. Y.; Langridge, J.; Campuzano, I.; Hughes, C.; Peter-Katalinić, J. Ion Mobility Mass Spectrometry Analysis of Human Glycourinome. *Anal. Chem.* **2008**, *80*, 2506–2513.

(72) Smith, D. P.; Giles, K.; Bateman, R. H.; Radford, S. E.; Ashcroft, A. E. Monitoring Copopulated Conformational States during Protein Folding Events Using Electrospray Ionization-Ion Mobility Spectrometry-Mass Spectrometry. *J. Am. Soc. Mass Spectrom.* **2007**, *18*, 2180–2190.
(73) Ashcroft, A. E. Mass Spectrometry and the Amyloid Problem—How Far Can We Go in the Gas Phase? *J. Am. Soc. Mass Spectrom.* **2010**, *21*, 1087–1096.
(74) Bush, M. F.; Hall, Z.; Giles, K.; Hoyes, J.; Robinson, C. V.; Ruotolo, B. T. Collision Cross Sections of Proteins and Their Complexes: A Calibration Framework and Database for Gas-Phase Structural Biology. *Anal. Chem.* **2010**, *82*, 9557–9565.
(75) Shepherd, D. A.; Marty, M. T.; Giles, K.; Baldwin, A. J.; Benesch, J. L. P. Combining Tandem Mass Spectrometry with Ion Mobility Separation to Determine the Architecture of Polydisperse Proteins. *Int. J. Mass Spectrom.* **2015**, *377*, 663–671.
(76) Zheng, X.; Wojcik, R.; Zhang, X.; Ibrahim, Y. M.; Burnum-Johnson, K. E.; Orton, D. J.; Monroe, M. E.; Moore, R. J.; Smith, R. D.; Baker, E. S. Coupling Front-End Separations, Ion Mobility Spectrometry, and Mass Spectrometry For Enhanced Multidimensional Biological and Environmental Analyses. *Annu. Rev. Anal. Chem.* **2017**, *10*, 71–92.
(77) Lermyte, F.; Tsybin, Y. O.; O'Connor, P. B.; Loo, J. A. Top or Middle? Up or Down? Toward a Standard Lexicon for Protein Top-Down and Allied Mass Spectrometry Approaches. *J. Am. Soc. Mass Spectrom.* **2019**, *30*, 1149–1157.
(78) Brodbelt, J. S.; Morrison, L. J.; Santos, I. Ultraviolet Photodissociation Mass Spectrometry for Analysis of Biological Molecules. *Chem. Rev.* **2019**.
(79) Macias, L. A.; Santos, I. C.; Brodbelt, J. S. Ion Activation Methods for Peptides and Proteins. *Anal. Chem.* **2020**, *92*, 227–251.
(80) Roepstorff, P.; Fohlman, J. Proposal for a Common Nomenclature for Sequence Ions in Mass Spectra of Peptides. *Biomed. Mass Spectrom.* **1984**, *11*, 601.
(81) Paizs, B.; Suhai, S. Fragmentation Pathways of Protonated Peptides. *Mass Spectrom. Rev.* **2005**, *24*, 508–548.
(82) McLuckey, S. A. Principles of Collisional Activation in Analytical Mass Spectrometry. *J. Am. Soc. Mass Spectrom.* **1992**, *3*, 599–614.
(83) Hall, Z.; Hernández, H.; Marsh, J. A.; Teichmann, S. A.; Robinson, C. V. The Role of Salt Bridges, Charge Density, and Subunit Flexibility in Determining Disassembly Routes of Protein Complexes. *Structure* **2013**, *21*, 1325–1337.
(84) Yin, S.; Loo, J. A. Elucidating the Site of Protein-ATP Binding by Top-Down Mass Spectrometry. *J. Am. Soc. Mass Spectrom.* **2010**, *21*, 899–907.
(85) Yin, S.; Loo, J. A. Top-down Mass Spectrometry of Supercharged Native Protein–Ligand Complexes. *Int. J. Mass Spectrom.* **2011**, *300*, 118–122.
(86) Dixit, S. M.; Polasky, D. A.; Ruotolo, B. T. Collision Induced Unfolding of Isolated Proteins in the Gas Phase: Past, Present, and Future. *Curr. Opin. Chem. Biol.* **2018**, *42*, 93–100.
(87) Zubarev, R. A.; Horn, D. M.; Fridriksson, E. K.; Kelleher, N. L.; Kruger, N. A.; Lewis, M. A.; Carpenter, B. K.; McLafferty, F. W. Electron Capture Dissociation

for Structural Characterization of Multiply Charged Protein Cations. *Anal. Chem.* **2000**, *72*, 563–573.
(88) Zubarev, R. A. Electron-Capture Dissociation Tandem Mass Spectrometry. *Curr. Opin. Biotechnol.* **2004**, *15*, 12–16.
(89) Syka, J. E. P.; Coon, J. J.; Schroeder, M. J.; Shabanowitz, J.; Hunt, D. F. Peptide and Protein Sequence Analysis by Electron Transfer Dissociation Mass Spectrometry. *Proc. Natl. Acad. Sci.* **2004**, *101*, 9528–9533.
(90) Li, H.; Sheng, Y.; McGee, W.; Cammarata, M.; Holden, D.; Loo, J. A. Structural Characterization of Native Proteins and Protein Complexes by Electron Ionization Dissociation-Mass Spectrometry. *Anal. Chem.* **2017**, *89*, 2731–2738.
(91) Zubarev, R. A.; Kelleher, N. L.; McLafferty, F. W. Electron Capture Dissociation of Multiply Charged Protein Cations. A Nonergodic Process. *J. Am. Chem. Soc.* **1998**, *120*, 3265–3266.
(92) Breuker, K.; Oh, H.; Horn, D. M.; Cerda, B. A.; McLafferty, F. W. Detailed Unfolding and Folding of Gaseous Ubiquitin Ions Characterized by Electron Capture Dissociation. *J. Am. Chem. Soc.* **2002**, *124*, 6407–6420.
(93) Breuker, K.; Oh, H.; Lin, C.; Carpenter, B. K.; McLafferty, F. W. Nonergodic and Conformational Control of the Electron Capture Dissociation of Protein Cations. *Proc. Natl. Acad. Sci.* **2004**, *101*, 14011–14016.
(94) Lermyte, F.; Valkenborg, D.; Loo, J. A.; Sobott, F. Radical Solutions: Principles and Application of Electron-Based Dissociation in Mass Spectrometry-Based Analysis of Protein Structure. *Mass Spectrom. Rev.* **2018**, *37*, 750–771.
(95) Lermyte, F.; Sobott, F. Electron Transfer Dissociation Provides Higher-Order Structural Information of Native and Partially Unfolded Protein Complexes. *PROTEOMICS* **2015**, *15*, 2813–2822.
(96) Zhang, H.; Cui, W.; Wen, J.; Blankenship, R. E.; Gross, M. L. Native Electrospray and Electron-Capture Dissociation FTICR Mass Spectrometry for Top-down Studies of Protein Assemblies. *Anal. Chem.* **2011**, *83*, 5598–5606.
(97) Li, H.; Wongkongkathep, P.; Van Orden, S. L.; Ogorzalek Loo, R. R.; Loo, J. A. Revealing Ligand Binding Sites and Quantifying Subunit Variants of Noncovalent Protein Complexes in a Single Native Top-Down FTICR MS Experiment. *J. Am. Soc. Mass Spectrom.* **2014**, *25*, 2060–2068.
(98) Zhou, M.; Wysocki, V. H. Surface Induced Dissociation: Dissecting Noncovalent Protein Complexes in the Gas Phase. *Acc. Chem. Res.* **2014**, *47*, 1010–1018.
(99) Sahasrabuddhe, A.; Hsia, Y.; Busch, F.; Sheffler, W.; King, N. P.; Baker, D.; Wysocki, V. H. Confirmation of Intersubunit Connectivity and Topology of Designed Protein Complexes by Native MS. *Proc. Natl. Acad. Sci.* **2018**, *115*, 1268–1273.
(100) Busch, F.; VanAernum, Z. L.; Ju, Y.; Yan, J.; Gilbert, J. D.; Quintyn, R. S.; Bern, M.; Wysocki, V. H. Localization of Protein Complex Bound Ligands by Surface-Induced Dissociation High-Resolution Mass Spectrometry. *Anal. Chem.* **2018**, *90*, 12796–12801.

(101) Dunbar, R. C. Photodissociation of the Methyl Chloride (CH3Cl+) and Nitrous Oxide (N2O+) Cations. *J. Am. Chem. Soc.* **1971**, *93*, 4354–4358.
(102) Tecklenburg, R. E.; Miller, M. N.; Russell, D. H. Laser Ion Beam Photodissociation Studies of Model Amino Acids and Peptides. *J. Am. Chem. Soc.* **1989**, *111*, 1161–1171.
(103) Canon, F.; Milosavljević, A. R.; van der Rest, G.; Réfrégiers, M.; Nahon, L.; Sarni-Manchado, P.; Cheynier, V.; Giuliani, A. Photodissociation and Dissociative Photoionization Mass Spectrometry of Proteins and Noncovalent Protein–Ligand Complexes. *Angew. Chem. Int. Ed.* **2013**, *52*, 8377–8381.
(104) Shaw, J. B.; Li, W.; Holden, D. D.; Zhang, Y.; Griep-Raming, J.; Fellers, R. T.; Early, B. P.; Thomas, P. M.; Kelleher, N. L.; Brodbelt, J. S. Complete Protein Characterization Using Top-Down Mass Spectrometry and Ultraviolet Photodissociation. *J. Am. Chem. Soc.* **2013**, *135*, 12646–12651.
(105) O'Brien, J. P.; Li, W.; Zhang, Y.; Brodbelt, J. S. Characterization of Native Protein Complexes Using Ultraviolet Photodissociation Mass Spectrometry. *J. Am. Chem. Soc.* **2014**, *136*, 12920–12928.
(106) Zabuga, A. V.; Kamrath, M. Z.; Boyarkin, O. V.; Rizzo, T. R. Fragmentation Mechanism of UV-Excited Peptides in the Gas Phase. *J. Chem. Phys.* **2014**, *141*, 154309.
(107) R. Julian, R. The Mechanism Behind Top-Down UVPD Experiments: Making Sense of Apparent Contradictions. *J. Am. Soc. Mass Spectrom.* **2017**, *28*, 1823–1826.
(108) Pereverzev, A. Y.; Koczor-Benda, Z.; Saparbaev, E.; Kopysov, V. N.; Rosta, E.; Boyarkin, O. V. Spectroscopic Evidence for Peptide-Bond-Selective Ultraviolet Photodissociation. *J. Phys. Chem. Lett.* **2020**, *11*, 206–209.
(109) Sipe, S. N.; Patrick, J. W.; Laganowsky, A.; Brodbelt, J. S. Enhanced Characterization of Membrane Protein Complexes by Ultraviolet Photodissociation Mass Spectrometry. *Anal. Chem.* **2020**, *92*, 899–907.
(110) Robinson, M. R.; Moore, K. L.; Brodbelt, B. Direct Identification of Tyrosine Sulfation by Using Ultraviolet Photodissociation Mass Spectrometry. *J. Am. Soc. Mass Spectrom.* **2014**, *25*, 1461–1471.
(111) Fort, K. L.; Dyachenko, A.; Potel, C. M.; Corradini, E.; Marino, F.; Barendregt, A.; Makarov, A. A.; Scheltema, R. A.; Heck, A. J. R. Implementation of Ultraviolet Photodissociation on a Benchtop Q Exactive Mass Spectrometer and Its Application to Phosphoproteomics. *Anal. Chem.* **2016**, *88*, 2303–2310.
(112) Robinson, M. R.; Taliaferro, J. M.; Dalby, K. N.; Brodbelt, J. S. 193 Nm Ultraviolet Photodissociation Mass Spectrometry for Phosphopeptide Characterization in the Positive and Negative Ion Modes. *J. Proteome Res.* **2016**, *15*, 2739–2748.
(113) Cammarata, M. B.; Thyer, R.; Rosenberg, J.; Ellington, A.; Brodbelt, J. S. Structural Characterization of Dihydrofolate Reductase Complexes by Top-Down Ultraviolet Photodissociation Mass Spectrometry. *J. Am. Chem. Soc.* **2015**, *137*, 9128–9135.
(114) Cammarata, M. B.; Schardon, C. L.; Mehaffey, M. R.; Rosenberg, J.; Singleton, J.; Fast, W.; Brodbelt, J. S. Impact of G12 Mutations on the Structure of K-Ras Probed

by Ultraviolet Photodissociation Mass Spectrometry. *J. Am. Chem. Soc.* **2016**, *138*, 13187–13196.
(115) Cammarata, M. B.; Brodbelt, J. S. Structural Characterization of Holo- and Apo-Myoglobin in the Gas Phase by Ultraviolet Photodissociation Mass Spectrometry. *Chem. Sci.* **2015**, *6*, 1324–1333.
(116) Zhou, M.; Liu, W.; Shaw, J. B. Charge Movement and Structural Changes in the Gas-Phase Unfolding of Multimeric Protein Complexes Captured by Native Top-Down Mass Spectrometry. *Anal. Chem.* **2020**, *92*, 1788–1795.
(117) Warnke, S.; von Helden, G.; Pagel, K. Analyzing the Higher Order Structure of Proteins with Conformer-Selective Ultraviolet Photodissociation. *PROTEOMICS* **2015**, *15*, 2804–2812.
(118) Cammarata, M.; Thyer, R.; Lombardo, M.; Anderson, A.; Wright, D.; Ellington, A.; Brodbelt, J. S. Characterization of Trimethoprim Resistant E. Coli Dihydrofolate Reductase Mutants by Mass Spectrometry and Inhibition by Propargyl-Linked Antifolates. *Chem. Sci.* **2017**, *8*, 4062–4072.
(119) Crittenden, C. M.; Novelli, E. T.; Mehaffey, M. R.; Xu, G. N.; Giles, D. H.; Fies, W. A.; Dalby, K. N.; Webb, L. J.; Brodbelt, J. S. Structural Evaluation of Protein/Metal Complexes via Native Electrospray Ultraviolet Photodissociation Mass Spectrometry. *J. Am. Soc. Mass Spectrom.* **2020**, *31*, 1140–1150.
(120) Morrison, L. J.; Brodbelt, J. S. 193 Nm Ultraviolet Photodissociation Mass Spectrometry of Tetrameric Protein Complexes Provides Insight into Quaternary and Secondary Protein Topology. *J. Am. Chem. Soc.* **2016**, *138*, 10849–10859.
(121) Tamara, S.; Dyachenko, A.; Fort, K. L.; Makarov, A. A.; Scheltema, R. A.; Heck, A. J. R. Symmetry of Charge Partitioning in Collisional and UV Photon-Induced Dissociation of Protein Assemblies. *J. Am. Chem. Soc.* **2016**, *138*, 10860–10868.
(122) Greisch, J.-F.; Tamara, S.; Scheltema, R. A.; Maxwell, H. W. R.; Fagerlund, R. D.; Fineran, P. C.; Tetter, S.; Hilvert, D.; Heck, A. J. R. Expanding the Mass Range for UVPD-Based Native Top-down Mass Spectrometry. *Chem. Sci.* **2019**, *10*, 7163–7171.
(123) Sipe, S. N.; Brodbelt, J. S. Impact of Charge State on 193 Nm Ultraviolet Photodissociation of Protein Complexes. *Phys. Chem. Chem. Phys.* **2019**, *21*, 9265–9276.
(124) Skinner, O. S.; Haverland, N. A.; Fornelli, L.; Melani, R. D.; Do Vale, L. H. F.; Seckler, H. S.; Doubleday, P. F.; Schachner, L. F.; Srzentić, K.; Kelleher, N. L.; Compton, P. D. Top-down Characterization of Endogenous Protein Complexes with Native Proteomics. *Nat. Chem. Biol.* **2018**, *14*, 36–41.
(125) Gault, J.; Liko, I.; Landreh, M.; Shutin, D.; Bolla, J. R.; Jefferies, D.; Agasid, M.; Yen, H.-Y.; Ladds, M. J. G. W.; Lane, D. P.; Khalid, S.; Mullen, C.; Remes, P. M.; Huguet, R.; McAlister, G.; Goodwin, M.; Viner, R.; Syka, J. E. P.; Robinson, C. V. Combining Native and 'Omics' Mass Spectrometry to Identify Endogenous Ligands Bound to Membrane Proteins. *Nat. Methods* **2020**, *17*, 505–508.

(126) Savaryn, J. P.; Catherman, A. D.; Thomas, P. M.; Abecassis, M. M.; Kelleher, N. L. The Emergence of Top-down Proteomics in Clinical Research. *Genome Med.* **2013**, *5*, 53.
(127) Belov, A. M.; Viner, R.; Santos, M. R.; Horn, D. M.; Bern, M.; Karger, B. L.; Ivanov, A. R. Analysis of Proteins, Protein Complexes, and Organellar Proteomes Using Sheathless Capillary Zone Electrophoresis - Native Mass Spectrometry. *J. Am. Soc. Mass Spectrom.* **2017**, *28*, 2614–2634.
(128) Kükrer, B.; Filipe, V.; van Duijn, E.; Kasper, P. T.; Vreeken, R. J.; Heck, A. J. R.; Jiskoot, W. Mass Spectrometric Analysis of Intact Human Monoclonal Antibody Aggregates Fractionated by Size-Exclusion Chromatography. *Pharm. Res.* **2010**, *27*, 2197–2204.
(129) Muneeruddin, K.; Thomas, J. J.; Salinas, P. A.; Kaltashov, I. A. Characterization of Small Protein Aggregates and Oligomers Using Size Exclusion Chromatography with Online Detection by Native Electrospray Ionization Mass Spectrometry. *Anal. Chem.* **2014**, *86*, 10692–10699.
(130) Muneeruddin, K.; Nazzaro, M.; Kaltashov, I. A. Characterization of Intact Protein Conjugates and Biopharmaceuticals Using Ion-Exchange Chromatography with Online Detection by Native Electrospray Ionization Mass Spectrometry and Top-Down Tandem Mass Spectrometry. *Anal. Chem.* **2015**, *87*, 10138–10145.
(131) Debaene, F.; Bœuf, A.; Wagner-Rousset, E.; Colas, O.; Ayoub, D.; Corvaïa, N.; Van Dorsselaer, A.; Beck, A.; Cianférani, S. Innovative Native MS Methodologies for Antibody Drug Conjugate Characterization: High Resolution Native MS and IM-MS for Average DAR and DAR Distribution Assessment. *Anal. Chem.* **2014**, *86*, 10674–10683.
(132) Han, X.; Wang, Y.; Aslanian, A.; Fonslow, B.; Graczyk, B.; Davis, T. N.; Yates, J. R. In-Line Separation by Capillary Electrophoresis Prior to Analysis by Top-Down Mass Spectrometry Enables Sensitive Characterization of Protein Complexes. *J. Proteome Res.* **2014**, *13*, 6078–6086.
(133) Shen, X.; Kou, Q.; Guo, R.; Yang, Z.; Chen, D.; Liu, X.; Hong, H.; Sun, L. Native Proteomics in Discovery Mode Using Size-Exclusion Chromatography–Capillary Zone Electrophoresis–Tandem Mass Spectrometry. *Anal. Chem.* **2018**, *90*, 10095–10099.
(134) Shen, X.; Yang, Z.; McCool, E. N.; Lubeckyj, R. A.; Chen, D.; Sun, L. Capillary Zone Electrophoresis-Mass Spectrometry for Top-down Proteomics. *TrAC Trends Anal. Chem.* **2019**, *120*, 115644.
(135) Kristoff, C. J.; Bwanali, L.; Veltri, L. M.; Gautam, G. P.; Rutto, P. K.; Newton, E. O.; Holland, L. A. Challenging Bioanalyses with Capillary Electrophoresis. *Anal. Chem.* **2020**, *92*, 49–66.
(136) Fonslow, B. R.; Kang, S. A.; Gestaut, D. R.; Graczyk, B.; Davis, T. N.; Sabatini, D. M.; Yates III, J. R. Native Capillary Isoelectric Focusing for the Separation of Protein Complex Isoforms and Subcomplexes. *Anal. Chem.* **2010**, *82*, 6643–6651.

(137) Skinner, O. S.; Do Vale, L. H. F.; Catherman, A. D.; Havugimana, P. C.; Sousa, M. V. de; Compton, P. D.; Kelleher, N. L. Native GELFrEE: A New Separation Technique for Biomolecular Assemblies. *Anal. Chem.* **2015**, *87*, 3032–3038.
(138) Belov, M. E.; Damoc, E.; Denisov, E.; Compton, P. D.; Horning, S.; Makarov, A. A.; Kelleher, N. L. From Protein Complexes to Subunit Backbone Fragments: A Multi-Stage Approach to Native Mass Spectrometry. *Anal. Chem.* **2013**, *85*, 11163–11173.
(139) Ben-Nissan, G.; Belov, M. E.; Morgenstern, D.; Levin, Y.; Dym, O.; Arkind, G.; Lipson, C.; Makarov, A. A.; Sharon, M. Triple-Stage Mass Spectrometry Unravels the Heterogeneity of an Endogenous Protein Complex. *Anal. Chem.* **2017**, *89*, 4708–4715.

CHAPTER 2

(1) Fenn, J. B.; Mann, M.; Meng, C. K.; Wong, S. F.; Whitehouse, C. M. Electrospray Ionization for Mass Spectrometry of Large Biomolecules. *Science* **1989**, *246*, 64–71.
(2) Cech, N. B.; Enke, C. G. Practical Implications of Some Recent Studies in Electrospray Ionization Fundamentals. *Mass Spectrom. Rev.* **2001**, *20*, 362–387.
(3) Schwartz, J. C.; Senko, M. W.; Syka, J. E. P. A Two-Dimensional Quadrupole Ion Trap Mass Spectrometer. *J. Am. Soc. Mass Spectrom.* **2002**, *13*, 659–669.
(4) Makarov, A. Electrostatic Axially Harmonic Orbital Trapping: A High-Performance Technique of Mass Analysis. *Anal. Chem.* **2000**, *72*, 1156–1162.
(5) Michalski, A.; Damoc, E.; Lange, O.; Denisov, E.; Nolting, D.; Müller, M.; Viner, R.; Schwartz, J.; Remes, P.; Belford, M.; Dunyach, J.-J.; Cox, J.; Horning, S.; Mann, M.; Makarov, A. Ultra High Resolution Linear Ion Trap Orbitrap Mass Spectrometer (Orbitrap Elite) Facilitates Top Down LC MS/MS and Versatile Peptide Fragmentation Modes. *Mol. Cell. Proteomics* **2012**, *11*.
(6) Fort, K. L.; Waterbeemd, M. van de; Boll, D.; Reinhardt-Szyba, M.; Belov, M. E.; Sasaki, E.; Zschoche, R.; Hilvert, D.; Makarov, A. A.; Heck, A. J. R. Expanding the Structural Analysis Capabilities on an Orbitrap-Based Mass Spectrometer for Large Macromolecular Complexes. *Analyst* **2017**, *143*, 100–105.
(7) Shaw, J. B.; Li, W.; Holden, D. D.; Zhang, Y.; Griep-Raming, J.; Fellers, R. T.; Early, B. P.; Thomas, P. M.; Kelleher, N. L.; Brodbelt, J. S. Complete Protein Characterization Using Top-Down Mass Spectrometry and Ultraviolet Photodissociation. *J. Am. Chem. Soc.* **2013**, *135*, 12646–12651.
(8) Shen, X.; Kou, Q.; Guo, R.; Yang, Z.; Chen, D.; Liu, X.; Hong, H.; Sun, L. Native Proteomics in Discovery Mode Using Size-Exclusion Chromatography–Capillary Zone Electrophoresis–Tandem Mass Spectrometry. *Anal. Chem.* **2018**, *90*, 10095–10099.
(9) Fellers, R. T.; Greer, J. B.; Early, B. P.; Yu, X.; LeDuc, R. D.; Kelleher, N. L.; Thomas, P. M. ProSight Lite: Graphical Software to Analyze Top-down Mass Spectrometry Data. *PROTEOMICS* **2015**, *15*, 1235–1238.

(10) Rosenberg, J.; Parker, W. R.; Cammarata, M. B.; Brodbelt, J. S. UV-POSIT: Web-Based Tools for Rapid and Facile Structural Interpretation of Ultraviolet Photodissociation (UVPD) Mass Spectra. *J. Am. Soc. Mass Spectrom.* **2018**, *29*, 1323–1326.

CHAPTER 3

(1) Daniel, R. M.; Dunn, R. V.; Finney, J. L.; Smith, J. C. The Role of Dynamics in Enzyme Activity. *Annu. Rev. Biophys. Biomol. Struct.* **2003**, *32*, 69–92.
(2) Henzler-Wildman, K. A.; Thai, V.; Lei, M.; Ott, M.; Wolf-Watz, M.; Fenn, T.; Pozharski, E.; Wilson, M. A.; Petsko, G. A.; Karplus, M.; Hübner, C. G.; Kern, D. Intrinsic Motions along an Enzymatic Reaction Trajectory. *Nature* **2007**, *450*, 838–844.
(3) Henzler-Wildman, K. A.; Lei, M.; Thai, V.; Kerns, S. J.; Karplus, M.; Kern, D. A Hierarchy of Timescales in Protein Dynamics Is Linked to Enzyme Catalysis. *Nature* **2007**, *450*, 913–916.
(4) Kamerlin, S. C. L.; Warshel, A. At the Dawn of the 21st Century: Is Dynamics the Missing Link for Understanding Enzyme Catalysis? *Proteins Struct. Funct. Bioinforma.* **2010**, *78*, 1339–1375.
(5) Vonrhein, C.; Schlauderer, G. J.; Schulz, G. E. Movie of the Structural Changes during a Catalytic Cycle of Nucleoside Monophosphate Kinases. *Structure* **1995**, *3*, 483–490.
(6) Noda, L. Adenosine Triphosphate-Adenosine Monophosphate Transphosphorylase Iii. Kinetic Studies. *J. Biol. Chem.* **1958**, *232*, 237–250.
(7) Abele, U.; Schulz, G. E. High-Resolution Structures of Adenylate Kinase from Yeast Ligated with Inhibitor Ap5A, Showing the Pathway of Phosphoryl Transfer. *Protein Sci.* **1995**, *4*, 1262–1271.
(8) Sinev, M. A.; Sineva, E. V.; Ittah, V.; Haas, E. Domain Closure in Adenylate Kinase. *Biochemistry* **1996**, *35*, 6425–6437.
(9) Sheng, X. R.; Li, X.; Pan, X. M. An Iso-Random Bi Bi Mechanism for Adenylate Kinase. *J. Biol. Chem.* **1999**, *274*, 22238–22242.
(10) Miyashita, O.; Onuchic, J. N.; Wolynes, P. G. Nonlinear Elasticity, Proteinquakes, and the Energy Landscapes of Functional Transitions in Proteins. *Proc. Natl. Acad. Sci.* **2003**, *100*, 12570–12575.
(11) Krishnamurthy, H.; Lou, H.; Kimple, A.; Vieille, C.; Cukier, R. I. Associative Mechanism for Phosphoryl Transfer: A Molecular Dynamics Simulation of Escherichia Coli Adenylate Kinase Complexed with Its Substrates. *Proteins Struct. Funct. Bioinforma.* **2005**, *58*, 88–100.
(12) Bae, E.; Phillips, G. N. Roles of Static and Dynamic Domains in Stability and Catalysis of Adenylate Kinase. *Proc. Natl. Acad. Sci. U. S. A.* **2006**, *103*, 2132–2137.
(13) Ådén, J.; Wolf-Watz, M. NMR Identification of Transient Complexes Critical to Adenylate Kinase Catalysis. *J. Am. Chem. Soc.* **2007**, *129*, 14003–14012.

(14) Arora, K.; Brooks, C. L. Large-Scale Allosteric Conformational Transitions of Adenylate Kinase Appear to Involve a Population-Shift Mechanism. *Proc. Natl. Acad. Sci.* **2007**, *104*, 18496–18501.
(15) Hanson, J. A.; Duderstadt, K.; Watkins, L. P.; Bhattacharyya, S.; Brokaw, J.; Chu, J.-W.; Yang, H. Illuminating the Mechanistic Roles of Enzyme Conformational Dynamics. *Proc. Natl. Acad. Sci.* **2007**, *104*, 18055–18060.
(16) Whitford, P. C.; Miyashita, O.; Levy, Y.; Onuchic, J. N. Conformational Transitions of Adenylate Kinase: Switching by Cracking. *J. Mol. Biol.* **2007**, *366*, 1661–1671.
(17) Schrank, T. P.; Bolen, D. W.; Hilser, V. J. Rational Modulation of Conformational Fluctuations in Adenylate Kinase Reveals a Local Unfolding Mechanism for Allostery and Functional Adaptation in Proteins. *Proc. Natl. Acad. Sci.* **2009**, *106*, 16984–16989.
(18) Daily, M. D.; Phillips Jr., G. N.; Cui, Q. Many Local Motions Cooperate to Produce the Adenylate Kinase Conformational Transition. *J. Mol. Biol.* **2010**, *400*, 618–631.
(19) Olsson, U.; Wolf-Watz, M. Overlap between Folding and Functional Energy Landscapes for Adenylate Kinase Conformational Change. *Nat. Commun.* **2010**, *1*, 111.
(20) Ådén, J.; Verma, A.; Schug, A.; Wolf-Watz, M. Modulation of a Pre-Existing Conformational Equilibrium Tunes Adenylate Kinase Activity. *J. Am. Chem. Soc.* **2012**, *134*, 16562–16570.
(21) Rao, V. V. H. G.; Gosavi, S. In the Multi-Domain Protein Adenylate Kinase, Domain Insertion Facilitates Cooperative Folding While Accommodating Function at Domain Interfaces. *PLOS Comput. Biol.* **2014**, *10*, e1003938.
(22) Kerns, S. J.; Agafonov, R. V.; Cho, Y.-J.; Pontiggia, F.; Otten, R.; Pachov, D. V.; Kutter, S.; Phung, L. A.; Murphy, P. N.; Thai, V.; Alber, T.; Hagan, M. F.; Kern, D. The Energy Landscape of Adenylate Kinase during Catalysis. *Nat. Struct. Mol. Biol.* **2015**, *22*, 124–131.
(23) Ferreiro, D. U.; Hegler, J. A.; Komives, E. A.; Wolynes, P. G. On the Role of Frustration in the Energy Landscapes of Allosteric Proteins. *Proc. Natl. Acad. Sci.* **2011**, *108*, 3499–3503.
(24) Warshel, A.; Bora, R. P. Perspective: Defining and Quantifying the Role of Dynamics in Enzyme Catalysis. *J. Chem. Phys.* **2016**, *144*, 180901.
(25) Konermann, L.; Vahidi, S.; Sowole, M. A. Mass Spectrometry Methods for Studying Structure and Dynamics of Biological Macromolecules. *Anal. Chem.* **2014**, *86*, 213–232.
(26) Konermann, L.; Tong, X.; Pan, Y. Protein Structure and Dynamics Studied by Mass Spectrometry: H/D Exchange, Hydroxyl Radical Labeling, and Related Approaches. *J. Mass Spectrom.* **2008**, *43*, 1021–1036.
(27) Fitzgerald, M. C.; West, G. M. Painting Proteins with Covalent Labels: What's In the Picture? *J. Am. Soc. Mass Spectrom.* **2009**, *20*, 1193–1206.
(28) Cammarata, M.; Lin, K.-Y.; Pruet, J.; Liu, H.; Brodbelt, J. Probing the Unfolding of Myoglobin and Domain C of PARP-1 with Covalent Labeling and Top-Down

Ultraviolet Photodissociation Mass Spectrometry. *Anal. Chem.* **2014**, *86*, 2534–2542.
(29) Pirrone, G. F.; Iacob, R. E.; Engen, J. R. Applications of Hydrogen/Deuterium Exchange MS from 2012 to 2014. *Anal. Chem.* **2014**, *87*, 99–118.
(30) Sharon, M.; Robinson, C. V. The Role of Mass Spectrometry in Structure Elucidation of Dynamic Protein Complexes. *Annu. Rev. Biochem.* **2007**, *76*, 167–193.
(31) Heck, A. J. R. Native Mass Spectrometry: A Bridge between Interactomics and Structural Biology. *Nat. Methods* **2008**, *5*, 927–933.
(32) Hopper, J. T. S.; Oldham, N. J. Collision Induced Unfolding of Protein Ions in the Gas Phase Studied by Ion Mobility-Mass Spectrometry: The Effect of Ligand Binding on Conformational Stability. *J. Am. Soc. Mass Spectrom.* **2009**, *20*, 1851–1858.
(33) Konermann, L.; Ahadi, E.; Rodriguez, A. D.; Vahidi, S. Unraveling the Mechanism of Electrospray Ionization. *Anal. Chem.* **2012**, *85*, 2–9.
(34) Schennach, M.; Breuker, K. Proteins with Highly Similar Native Folds Can Show Vastly Dissimilar Folding Behavior When Desolvated. *Angew. Chem. Int. Ed.* **2014**, *53*, 164–168.
(35) Cubrilovic, D.; Haap, W.; Barylyuk, K.; Ruf, A.; Badertscher, M.; Gubler, M.; Tetaz, T.; Joseph, C.; Benz, J.; Zenobi, R. Determination of Protein–Ligand Binding Constants of a Cooperatively Regulated Tetrameric Enzyme Using Electrospray Mass Spectrometry. *ACS Chem. Biol.* **2014**, *9*, 218–226.
(36) Li, H.; Wongkongkathep, P.; Orden, S. L. V.; Loo, R. R. O.; Loo, J. A. Revealing Ligand Binding Sites and Quantifying Subunit Variants of Noncovalent Protein Complexes in a Single Native Top-Down FTICR MS Experiment. *J. Am. Soc. Mass Spectrom.* **2014**, *25*, 2060–2068.
(37) Li, H.; Wolff, J. J.; Van Orden, S. L.; Loo, J. A. Native Top-Down Electrospray Ionization-Mass Spectrometry of 158 KDa Protein Complex by High-Resolution Fourier Transform Ion Cyclotron Resonance Mass Spectrometry. *Anal. Chem.* **2014**, *86*, 317–320.
(38) O'Brien, J. P.; Li, W.; Zhang, Y.; Brodbelt, J. S. Characterization of Native Protein Complexes Using Ultraviolet Photodissociation Mass Spectrometry. *J. Am. Chem. Soc.* **2014**, *136*, 12920–12928.
(39) Cammarata, M. B.; Brodbelt, J. S. Structural Characterization of Holo- and Apo-Myoglobin in the Gas Phase by Ultraviolet Photodissociation Mass Spectrometry. *Chem. Sci.* **2015**, *6*, 1324–1333.
(40) Cammarata, M. B.; Thyer, R.; Rosenberg, J.; Ellington, A.; Brodbelt, J. S. Structural Characterization of Dihydrofolate Reductase Complexes by Top-Down Ultraviolet Photodissociation Mass Spectrometry. *J. Am. Chem. Soc.* **2015**, *137*, 9128–9135.
(41) Cammarata, M. B.; Schardon, C. L.; Mehaffey, M. R.; Rosenberg, J.; Singleton, J.; Fast, W.; Brodbelt, J. S. Impact of G12 Mutations on the Structure of K-Ras Probed by Ultraviolet Photodissociation Mass Spectrometry. *J. Am. Chem. Soc.* **2016**, *138*, 13187–13196.

(42) Zechel, D. L.; Konermann, L.; Withers, S. G.; Douglas, D. J. Pre-Steady State Kinetic Analysis of an Enzymatic Reaction Monitored by Time-Resolved Electrospray Ionization Mass Spectrometry. *Biochemistry* **1998**, *37*, 7664–7669.
(43) Li, Z.; Sau, A. K.; Shen, S.; Whitehouse, C.; Baasov, T.; Anderson, K. S. A Snapshot of Enzyme Catalysis Using Electrospray Ionization Mass Spectrometry. *J. Am. Chem. Soc.* **2003**, *125*, 9938–9939.
(44) Liuni, P.; Jeganathan, A.; Wilson, D. J. Conformer Selection and Intensified Dynamics During Catalytic Turnover in Chymotrypsin. *Angew. Chem. Int. Ed.* **2012**, *51*, 9666–9669.
(45) Lermyte, F.; Sobott, F. Electron Transfer Dissociation Provides Higher-Order Structural Information of Native and Partially Unfolded Protein Complexes. *PROTEOMICS* **2015**, *15*, 2813–2822.
(46) Breuker, K.; Oh, H.; Horn, D. M.; Cerda, B. A.; McLafferty, F. W. Detailed Unfolding and Folding of Gaseous Ubiquitin Ions Characterized by Electron Capture Dissociation. *J. Am. Chem. Soc.* **2002**, *124*, 6407–6420.
(47) Breuker, K.; McLafferty, F. W. Stepwise Evolution of Protein Native Structure with Electrospray into the Gas Phase, 10−12 to 102 S. *Proc. Natl. Acad. Sci.* **2008**, *105*, 18145–18152.
(48) Zhang, H.; Cui, W.; Wen, J.; Blankenship, R. E.; Gross, M. L. Native Electrospray and Electron-Capture Dissociation in FTICR Mass Spectrometry Provide Top-down Sequencing of a Protein Component in an Intact Protein Assembly. *J. Am. Soc. Mass Spectrom.* **2010**, *21*, 1966–1968.
(49) Zhang, H.; Cui, W.; Gross, M. L.; Blankenship, R. E. Native Mass Spectrometry of Photosynthetic Pigment–Protein Complexes. *FEBS Lett.* **2013**, *587*, 1012–1020.
(50) Zhang, H.; Cui, W.; Gross, M. L. Native Electrospray Ionization and Electron-Capture Dissociation for Comparison of Protein Structure in Solution and the Gas Phase. *Int. J. Mass Spectrom.* **2013**, *354–355*, 288–291.
(51) Zhou, M.; Wysocki, V. H. Surface Induced Dissociation: Dissecting Noncovalent Protein Complexes in the Gas Phase. *Acc. Chem. Res.* **2014**, *47*, 1010–1018.
(52) Shaw, J. B.; Li, W.; Holden, D. D.; Zhang, Y.; Griep-Raming, J.; Fellers, R. T.; Early, B. P.; Thomas, P. M.; Kelleher, N. L.; Brodbelt, J. S. Complete Protein Characterization Using Top-Down Mass Spectrometry and Ultraviolet Photodissociation. *J. Am. Chem. Soc.* **2013**, *135*, 12646–12651.
(53) Cannon, J. R.; Cammarata, M. B.; Robotham, S. A.; Cotham, V. C.; Shaw, J. B.; Fellers, R. T.; Early, B. P.; Thomas, P. M.; Kelleher, N. L.; Brodbelt, J. S. Ultraviolet Photodissociation for Characterization of Whole Proteins on a Chromatographic Time Scale. *Anal. Chem.* **2014**, *86*, 2185–2192.
(54) Brodbelt, J. S. Ion Activation Methods for Peptides and Proteins. *Anal. Chem.* **2016**, *88*, 30–51.
(55) Warnke, S.; Baldauf, C.; Bowers, M. T.; Pagel, K.; von Helden, G. Photodissociation of Conformer-Selected Ubiquitin Ions Reveals Site-Specific Cis/Trans Isomerization of Proline Peptide Bonds. *J. Am. Chem. Soc.* **2014**, *136*, 10308–10314.

(56) Warnke, S.; von Helden, G.; Pagel, K. Analyzing the Higher Order Structure of Proteins with Conformer-Selective Ultraviolet Photodissociation. *PROTEOMICS* **2015**, *15*, 2804–2812.
(57) Briand, G.; Perrier, V.; Kouach, M.; Takahashi, M.; Gilles, A. M.; Bârzu, O. Characterization of Metal and Nucleotide Liganded Forms of Adenylate Kinase by Electrospray Ionization Mass Spectrometry. *Arch. Biochem. Biophys.* **1997**, *339*, 291–297.
(58) Daniel, J. M.; McCombie, G.; Wendt, S.; Zenobi, R. Mass Spectrometric Determination of Association Constants of Adenylate Kinase with Two Noncovalent Inhibitors. *J. Am. Soc. Mass Spectrom.* **2003**, *14*, 442–448.
(59) Yin, S.; Loo, J. A. Elucidating the Site of Protein-ATP Binding by Top-Down Mass Spectrometry. *J. Am. Soc. Mass Spectrom.* **2010**, *21*, 899–907.
(60) Bunkoczi, G.; Filippakopoulos, P.; Jansson, A.; Longman, E.; Von Delft, F.; Edwards, A.; Arrowsmith, C.; Sundstrom, M.; Weigelt, J.; Knapp, S. Structure of Adenylate Kinase 1 in Complex with P1, P4-Di(Adenosine)Tetraphosphate, **2017**, to be submitted for publication.
(61) Yin, S.; Loo, J. A. Top-Down Mass Spectrometry of Supercharged Native Protein-Ligand Complexes. *Int. J. Mass Spectrom.* **2011**, *300*, 118–122.
(62) Pai, E. F.; Sachsenheimer, W.; Schirmer, R. H.; Schulz, G. E. Substrate Positions and Induced-Fit in Crystalline Adenylate Kinase. *J. Mol. Biol.* **1977**, *114*, 37–45.
(63) Schulz, G. E.; Müller, C. W.; Diederichs, K. Induced-Fit Movements in Adenylate Kinases. *J. Mol. Biol.* **1990**, *213*, 627–630.
(64) Tsai, M. D.; Yan, H. Mechanism of Adenylate Kinase: Site-Directed Mutagenesis versus x-Ray and NMR. *Biochemistry* **1991**, *30*, 6806–6818.
(65) Müller, C. W.; Schulz, G. E. Structure of the Complex between Adenylate Kinase from Escherichia Coli and the Inhibitor Ap5A Refined at 1.9 Å Resolution. *J. Mol. Biol.* **1992**, *224*, 159–177.
(66) Rogne, P.; Wolf-Watz, M. Urea-Dependent Adenylate Kinase Activation Following Redistribution of Structural States. *Biophys. J.* **2016**, *111*, 1385–1395.
(67) Kern, P.; Brunne, R. M.; Folkers, G. Nucleotide-Binding Properties of Adenylate Kinase from Escherichia Coli: A Molecular Dynamics Study in Aqueous and Vacuum Environments. *J. Comput. Aided Mol. Des.* **1994**, *8*, 367–388.
(68) Elamrani, S.; Berry, M. B.; Phillips, G. N.; McCammon, J. A. Study of Global Motions in Proteins by Weighted Masses Molecular Dynamics: Adenylate Kinase as a Test Case. *Proteins Struct. Funct. Bioinforma.* **1996**, *25*, 79–88.
(69) Orzechowski, M.; Tama, F. Flexible Fitting of High-Resolution X-Ray Structures into Cryoelectron Microscopy Maps Using Biased Molecular Dynamics Simulations. *Biophys. J.* **2008**, *95*, 5692–5705.
(70) Baxter, N. J.; Blackburn, G. M.; Marston, J. P.; Hounslow, A. M.; Cliff, M. J.; Bermel, W.; Williams, N. H.; Hollfelder, F.; Wemmer, D. E.; Waltho, J. P. Anionic Charge Is Prioritized over Geometry in Aluminum and Magnesium Fluoride Transition State Analogs of Phosphoryl Transfer Enzymes. *J. Am. Chem. Soc.* **2008**, *130*, 3952–3958.

(71) Yan, H.; Tsai, M.-D. Nucleoside Monophosphate Kinases: Structure, Mechanism, and Substrate Specificity. In *Advances in Enzymology and Related Areas of Molecular Biology*; Purich, D. L., Ed.; John Wiley & Sons, Inc.: Hoboken, NJ, USA, 1999; pp 103–134.
(72) Fried, S. D.; Boxer, S. G. Measuring Electric Fields and Noncovalent Interactions Using the Vibrational Stark Effect. *Acc. Chem. Res.* **2015**, *48*, 998–1006.

CHAPTER 4

(1) Centers for Disease Control and Prevention (CDC). *Antibiotic Resistance Threats in the United States, 2019*; Centers for Disease Control and Prevention (U.S.): Atlanta, 2019.
(2) Papp-Wallace, K. M.; Endimiani, A.; Taracila, M. A.; Bonomo, R. A. Carbapenems: Past, Present, and Future. *Antimicrob. Agents Chemother.* **2011**, *55*, 4943–4960.
(3) Thomas, P. W.; Zheng, M.; Wu, S.; Guo, H.; Liu, D.; Xu, D.; Fast, W. Characterization of Purified New Delhi Metallo-β-Lactamase-1. *Biochemistry* **2011**, *50*, 10102–10113.
(4) Ju, L.-C.; Cheng, Z.; Fast, W.; Bonomo, R. A.; Crowder, M. W. The Continuing Challenge of Metallo-β-Lactamase Inhibition: Mechanism Matters. *Trends Pharmacol. Sci.* **2018**, *39*, 635–647.
(5) Toney, J. H.; Fitzgerald, P. M. D.; Grover-Sharma, N.; Olson, S. H.; May, W. J.; Sundelof, J. G.; Vanderwall, D. E.; Cleary, K. A.; Grant, S. K.; Wu, J. K.; Kozarich, J. W.; Pompliano, D. L.; Hammond, G. G. Antibiotic Sensitization Using Biphenyl Tetrazoles as Potent Inhibitors of Bacteroides Fragilis Metallo-β-Lactamase. *Chem. Biol.* **1998**, *5*, 185–196.
(6) Moali, C.; Anne, C.; Lamotte-Brasseur, J.; Groslambert, S.; Devreese, B.; Van Beeumen, J.; Galleni, M.; Frère, J.-M. Analysis of the Importance of the Metallo-β-Lactamase Active Site Loop in Substrate Binding and Catalysis. *Chem. Biol.* **2003**, *10*, 319–329.
(7) Scrofani, S. D. B.; Chung, J.; Huntley, J. J. A.; Benkovic, S. J.; Wright, P. E.; Dyson, H. J. NMR Characterization of the Metallo-β-Lactamase from Bacteroides Fragilis and Its Interaction with a Tight-Binding Inhibitor: Role of an Active-Site Loop. *Biochemistry* **1999**, *38*, 14507–14514.
(8) Huntley, J. J. A.; Scrofani, S. D. B.; Osborne, M. J.; Wright, P. E.; Dyson, H. J. Dynamics of the Metallo-β-Lactamase from Bacteroides Fragilis in the Presence and Absence of a Tight-Binding Inhibitor. *Biochemistry* **2000**, *39*, 13356–13364.
(9) Huntley, J. J. A.; Fast, W.; Benkovic, S. J.; Wright, P. E.; Dyson, H. J. Role of a Solvent-Exposed Tryptophan in the Recognition and Binding of Antibiotic Substrates for a Metallo-β-Lactamase. *Protein Sci.* **2003**, *12*, 1368–1375.
(10) Fast, W.; Sutton, L. D. Metallo-β-Lactamase: Inhibitors and Reporter Substrates. *Biochim. Biophys. Acta BBA - Proteins Proteomics* **2013**, *1834*, 1648–1659.

(11) Chiou, J.; Leung, T. Y.-C.; Chen, S. Molecular Mechanisms of Substrate Recognition and Specificity of New Delhi Metallo-β-Lactamase. *Antimicrob. Agents Chemother.* **2014**, *58*, 5372–5378.
(12) Palacios, A. R.; Mojica, M. F.; Giannini, E.; Taracila, M. A.; Bethel, C. R.; Alzari, P. M.; Otero, L. H.; Klinke, S.; Llarrull, L. I.; Bonomo, R. A.; Vila, A. J. The Reaction Mechanism of Metallo-β-Lactamases Is Tuned by the Conformation of an Active-Site Mobile Loop. *Antimicrob. Agents Chemother.* **2019**, *63*.
(13) Aitha, M.; Moritz, L.; Sahu, I. D.; Sanyurah, O.; Roche, Z.; McCarrick, R.; Lorigan, G. A.; Bennett, B.; Crowder, M. W. Conformational Dynamics of Metallo-β-Lactamase CcrA during Catalysis Investigated by Using DEER Spectroscopy. *J. Biol. Inorg. Chem.* **2015**, *20*, 585–594.
(14) Rydzik, A. M.; Brem, J.; van Berkel, S. S.; Pfeffer, I.; Makena, A.; Claridge, T. D. W.; Schofield, C. J. Monitoring Conformational Changes in the NDM-1 Metallo-β-Lactamase by 19F NMR Spectroscopy. *Angew. Chem. Int. Ed.* **2014**, *53*, 3129–3133.
(15) Stewart, A. C.; Bethel, C. R.; VanPelt, J.; Bergstrom, A.; Cheng, Z.; Miller, C. G.; Williams, C.; Poth, R.; Morris, M.; Lahey, O.; Nix, J. C.; Tierney, D. L.; Page, R. C.; Crowder, M. W.; Bonomo, R. A.; Fast, W. Clinical Variants of New Delhi Metallo-β-Lactamase Are Evolving To Overcome Zinc Scarcity. *ACS Infect. Dis.* **2017**, *3*, 927–940.
(16) Bahr, G.; Vitor-Horen, L.; Bethel, C. R.; Bonomo, R. A.; González, L. J.; Vila, A. J. Clinical Evolution of New Delhi Metallo-β-Lactamase (NDM) Optimizes Resistance under Zn(II) Deprivation. *Antimicrob. Agents Chemother.* **2018**, *62*, e01849-17.
(17) Cheng, Z.; Thomas, P. W.; Ju, L.; Bergstrom, A.; Mason, K.; Clayton, D.; Miller, C.; Bethel, C. R.; VanPelt, J.; Tierney, D. L.; Page, R. C.; Bonomo, R. A.; Fast, W.; Crowder, M. W. Evolution of New Delhi Metallo-β-Lactamase (NDM) in the Clinic: Effects of NDM Mutations on Stability, Zinc Affinity, and Mono-Zinc Activity. *J. Biol. Chem.* **2018**, *293*, 12606–12618.
(18) Makena, A.; Brem, J.; Pfeffer, I.; Geffen, R. E. J.; Wilkins, S. E.; Tarhonskaya, H.; Flashman, E.; Phee, L. M.; Wareham, D. W.; Schofield, C. J. Biochemical Characterization of New Delhi Metallo-β-Lactamase Variants Reveals Differences in Protein Stability. *J. Antimicrob. Chemother.* **2015**, *70*, 463–469.
(19) Konermann, L.; Ahadi, E.; Rodriguez, A. D.; Vahidi, S. Unraveling the Mechanism of Electrospray Ionization. *Anal. Chem.* **2013**, *85*, 2–9.
(20) Leney, A. C.; Heck, A. J. R. Native Mass Spectrometry: What Is in the Name? *J. Am. Soc. Mass Spectrom.* **2017**, *28*, 5–13.
(21) Allison, T. M.; Bechara, C. Structural Mass Spectrometry Comes of Age: New Insight into Protein Structure, Function and Interactions. *Biochem. Soc. Trans.* **2019**, *47*, 317–327.
(22) Macias, L. A.; Santos, I. C.; Brodbelt, J. S. Ion Activation Methods for Peptides and Proteins. *Anal. Chem.* **2020**, *92*, 227–251.

(23) Lermyte, F.; Sobott, F. Electron Transfer Dissociation Provides Higher-Order Structural Information of Native and Partially Unfolded Protein Complexes. *PROTEOMICS* **2015**, *15*, 2813–2822.
(24) Zhang, H.; Cui, W.; Wen, J.; Blankenship, R. E.; Gross, M. L. Native Electrospray and Electron-Capture Dissociation FTICR Mass Spectrometry for Top-Down Studies of Protein Assemblies. *Anal. Chem.* **2011**, *83*, 5598–5606.
(25) Zhang, J.; Malmirchegini, G. R.; Clubb, R. T.; Loo, J. A. Native Top-down Mass Spectrometry for the Structural Characterization of Human Hemoglobin. *Eur. J. Mass Spectrom.* **2015**, *21*, 221–231.
(26) Wongkongkathep, P.; Han, J. Y.; Choi, T. S.; Yin, S.; Kim, H. I.; Loo, J. A. Native Top-Down Mass Spectrometry and Ion Mobility MS for Characterizing the Cobalt and Manganese Metal Binding of α-Synuclein Protein. *J. Am. Soc. Mass Spectrom.* **2018**, *29*, 1870–1880.
(27) Li, H.; Sheng, Y.; McGee, W.; Cammarata, M.; Holden, D.; Loo, J. A. Structural Characterization of Native Proteins and Protein Complexes by Electron Ionization Dissociation-Mass Spectrometry. *Anal. Chem.* **2017**, *89*, 2731–2738.
(28) Li, H.; Nguyen, H. H.; Ogorzalek Loo, R. R.; Campuzano, I. D. G.; Loo, J. A. An Integrated Native Mass Spectrometry and Top-down Proteomics Method That Connects Sequence to Structure and Function of Macromolecular Complexes. *Nat. Chem.* **2018**, *10*, 139–148.
(29) Shaw, J. B.; Li, W.; Holden, D. D.; Zhang, Y.; Griep-Raming, J.; Fellers, R. T.; Early, B. P.; Thomas, P. M.; Kelleher, N. L.; Brodbelt, J. S. Complete Protein Characterization Using Top-Down Mass Spectrometry and Ultraviolet Photodissociation. *J. Am. Chem. Soc.* **2013**, *135*, 12646–12651.
(30) O'Brien, J. P.; Li, W.; Zhang, Y.; Brodbelt, J. S. Characterization of Native Protein Complexes Using Ultraviolet Photodissociation Mass Spectrometry. *J. Am. Chem. Soc.* **2014**, *136*, 12920–12928.
(31) Cammarata, M. B.; Brodbelt, J. S. Structural Characterization of Holo- and Apo-Myoglobin in the Gas Phase by Ultraviolet Photodissociation Mass Spectrometry. *Chem. Sci.* **2015**, *6*, 1324–1333.
(32) Robinson, M. R.; Taliaferro, J. M.; Dalby, K. N.; Brodbelt, J. S. 193 Nm Ultraviolet Photodissociation Mass Spectrometry for Phosphopeptide Characterization in the Positive and Negative Ion Modes. *J. Proteome Res.* **2016**, *15*, 2739–2748.
(33) Sipe, S. N.; Brodbelt, J. S. Impact of Charge State on 193 Nm Ultraviolet Photodissociation of Protein Complexes. *Phys. Chem. Chem. Phys.* **2019**, *21*, 9265–9276.
(34) Cammarata, M. B.; Thyer, R.; Rosenberg, J.; Ellington, A.; Brodbelt, J. S. Structural Characterization of Dihydrofolate Reductase Complexes by Top-Down Ultraviolet Photodissociation Mass Spectrometry. *J. Am. Chem. Soc.* **2015**, *137*, 9128–9135.
(35) Cammarata, M. B.; Schardon, C. L.; Mehaffey, M. R.; Rosenberg, J.; Singleton, J.; Fast, W.; Brodbelt, J. S. Impact of G12 Mutations on the Structure of K-Ras Probed by Ultraviolet Photodissociation Mass Spectrometry. *J. Am. Chem. Soc.* **2016**, *138*, 13187–13196.

(36) Mehaffey, M. R.; Schardon, C. L.; Novelli, E. T.; Cammarata, M. B.; Webb, L. J.; Fast, W.; Brodbelt, J. S. Investigation of GTP-Dependent Dimerization of G12X K-Ras Variants Using Ultraviolet Photodissociation Mass Spectrometry. *Chem. Sci.* **2019**, *10*, 8025–8034.
(37) Cammarata, M.; Thyer, R.; Lombardo, M.; Anderson, A.; Wright, D.; Ellington, A.; Brodbelt, J. S. Characterization of Trimethoprim Resistant E. Coli Dihydrofolate Reductase Mutants by Mass Spectrometry and Inhibition by Propargyl-Linked Antifolates. *Chem. Sci.* **2017**, *8*, 4062–4072.
(38) Mehaffey, M. R.; Cammarata, M. B.; Brodbelt, J. S. Tracking the Catalytic Cycle of Adenylate Kinase by Ultraviolet Photodissociation Mass Spectrometry. *Anal. Chem.* **2018**, *90*, 839–846.
(39) Kurosaki, H.; Yamaguchi, Y.; Higashi, T.; Soga, K.; Matsueda, S.; Yumoto, H.; Misumi, S.; Yamagata, Y.; Arakawa, Y.; Goto, M. Irreversible Inhibition of Metallo-β-Lactamase (IMP-1) by 3-(3-Mercaptopropionylsulfanyl)Propionic Acid Pentafluorophenyl Ester. *Angew. Chem. Int. Ed.* **2005**, *44*, 3861–3864.
(40) Tilvawala, R.; Cammarata, M.; Adediran, S. A.; Brodbelt, J. S.; Pratt, R. F. A New Covalent Inhibitor of Class C β-Lactamases Reveals Extended Active Site Specificity. *Biochemistry* **2015**, *54*, 7375–7384.
(41) Thomas, P. W.; Cammarata, M.; Brodbelt, J. S.; Monzingo, A. F.; Pratt, R. F.; Fast, W. A Lysine-Targeted Affinity Label for Serine-β-Lactamase Also Covalently Modifies New Delhi Metallo-β-Lactamase-1 (NDM-1). *Biochemistry* **2019**, *58*, 2834–2843.
(42) Chiou, J.; Wan, S.; Chan, K.-F.; So, P.-K.; He, D.; Chan, E. W.; Chan, T.; Wong, K.; Tao, J.; Chen, S. Ebselen as a Potent Covalent Inhibitor of New Delhi Metallo-β-Lactamase (NDM-1). *Chem. Commun.* **2015**, *51*, 9543–9546.
(43) Rosenberg, J.; Parker, W. R.; Cammarata, M. B.; Brodbelt, J. S. UV-POSIT: Web-Based Tools for Rapid and Facile Structural Interpretation of Ultraviolet Photodissociation (UVPD) Mass Spectra. *J. Am. Soc. Mass Spectrom.* **2018**, *29*, 1323–1326.
(44) King, D.; Strynadka, N. Crystal Structure of New Delhi Metallo-β-Lactamase Reveals Molecular Basis for Antibiotic Resistance. *Protein Sci.* **2011**, *20*, 1484–1491.
(45) Chen, A. Y.; Thomas, C.; Thomas, P. W.; Yang, K.; Cheng, Z.; Fast, W.; Crowder, M. W.; Cohen, S. M. Iminodiacetic Acid as a Novel Metal-Binding Pharmacophore for New Delhi Metallo-β-Lactamase Inhibitor Development. *ChemMedChem* **2020**, *10.1002/cmdc.202000123*.
(46) Xu, K.; Zhang, Y.; Tang, B.; Laskin, J.; Roach, P. J.; Chen, H. Study of Highly Selective and Efficient Thiol Derivatization Using Selenium Reagents by Mass Spectrometry. *Anal. Chem.* **2010**, *82*, 6926–6932.
(47) Chen, C.; Xiang, Y.; Yang, K.-W.; Zhang, Y.; Wang, W.-M.; Su, J.-P.; Ge, Y.; Liu, Y. A Protein Structure-Guided Covalent Scaffold Selectively Targets the B1 and B2 Subclass Metallo-β-Lactamases. *Chem. Commun.* **2018**, *54*, 4802–4805.

(48) Guo, Y.; Wang, J.; Niu, G.; Shui, W.; Sun, Y.; Zhou, H.; Zhang, Y.; Yang, C.; Lou, Z.; Rao, Z. A Structural View of the Antibiotic Degradation Enzyme NDM-1 from a Superbug. *Protein Cell* **2011**, *2*, 384–394.
(49) Boyd, S. E.; Livermore, D. M.; Hooper, D. C.; Hope, W. W. Metallo-β-Lactamases: Structure, Function, Epidemiology, Treatment Options, and the Development Pipeline. *Antimicrob. Agents Chemother.* **2020**, *10.1128/AAC.00397-20*.

CHAPTER 5

(1) Colicelli, J. Human RAS Superfamily Proteins and Related GTPases. *Sci. STKE Signal Transduct. Knowl. Environ.* **2004**, *2004*, RE13.
(2) Lavoie, H.; Therrien, M. Regulation of RAF Protein Kinases in ERK Signalling. *Nat. Rev. Mol. Cell Biol.* **2015**, *16*, 281–298.
(3) Prior, I. A.; Muncke, C.; Parton, R. G.; Hancock, J. F. Direct Visualization of Ras Proteins in Spatially Distinct Cell Surface Microdomains. *J. Cell Biol.* **2003**, *160*, 165–170.
(4) Castellano, E.; Santos, E. Functional Specificity of Ras Isoforms. *Genes Cancer* **2011**, *2*, 216–231.
(5) Ntai, I.; Fornelli, L.; DeHart, C. J.; Hutton, J. E.; Doubleday, P. F.; LeDuc, R. D.; Nispen, A. J. van; Fellers, R. T.; Whiteley, G.; Boja, E. S.; Rodriguez, H.; Kelleher, N. L. Precise Characterization of KRAS4b Proteoforms in Human Colorectal Cells and Tumors Reveals Mutation/Modification Cross-Talk. *Proc. Natl. Acad. Sci.* **2018**, 201716122.
(6) Prior, I. A.; Lewis, P. D.; Mattos, C. A Comprehensive Survey of Ras Mutations in Cancer. *Cancer Res.* **2012**, *72*, 2457–2467.
(7) Rajalingam, K.; Schreck, R.; Rapp, U. R.; Albert, Š. Ras Oncogenes and Their Downstream Targets. *Biochim. Biophys. Acta BBA - Mol. Cell Res.* **2007**, *1773*, 1177–1195.
(8) Simanshu, D. K.; Nissley, D. V.; McCormick, F. RAS Proteins and Their Regulators in Human Disease. *Cell* **2017**, *170*, 17–33.
(9) Zimmermann, G.; Papke, B.; Ismail, S.; Vartak, N.; Chandra, A.; Hoffmann, M.; Hahn, S. A.; Triola, G.; Wittinghofer, A.; Bastiaens, P. I. H.; Waldmann, H. Small Molecule Inhibition of the KRAS–PDEδ Interaction Impairs Oncogenic KRAS Signaling. *Nature* **2013**, *497*, 638–642.
(10) Spoerner, M.; Nuehs, A.; Herrmann, C.; Steiner, G.; Kalbitzer, H. R. Slow Conformational Dynamics of the Guanine Nucleotide-Binding Protein Ras Complexed with the GTP Analogue GTPγS. *FEBS J.* **2007**, *274*, 1419–1433.
(11) Lim, S. M.; Westover, K. D.; Ficarro, S. B.; Harrison, R. A.; Choi, H. G.; Pacold, M. E.; Carrasco, M.; Hunter, J.; Kim, N. D.; Xie, T.; Sim, T.; Jänne, P. A.; Meyerson, M.; Marto, J. A.; Engen, J. R.; Gray, N. S. Therapeutic Targeting of Oncogenic K-Ras by a Covalent Catalytic Site Inhibitor. *Angew. Chem. Int. Ed.* **2014**, *53*, 199–204.

(12) Harrison, R. A.; Lu, J.; Carrasco, M.; Hunter, J.; Manandhar, A.; Gondi, S.; Westover, K. D.; Engen, J. R. Structural Dynamics in Ras and Related Proteins upon Nucleotide Switching. *J. Mol. Biol.* **2016**, *428*, 4723–4735.
(13) Hobbs, G. A.; Wittinghofer, A.; Der, C. J. Selective Targeting of the KRAS G12C Mutant: Kicking KRAS When It's Down. *Cancer Cell* **2016**, *29*, 251–253.
(14) Lu, S.; Jang, H.; Nussinov, R.; Zhang, J. The Structural Basis of Oncogenic Mutations G12, G13 and Q61 in Small GTPase K-Ras4B. *Sci. Rep.* **2016**, *6*, 21949.
(15) Ostrem, J. M. L.; Shokat, K. M. Direct Small-Molecule Inhibitors of KRAS: From Structural Insights to Mechanism-Based Design. *Nat. Rev. Drug Discov.* **2016**, *15*, 771–785.
(16) Spencer-Smith, R.; Koide, A.; Zhou, Y.; Eguchi, R. R.; Sha, F.; Gajwani, P.; Santana, D.; Gupta, A.; Jacobs, M.; Herrero-Garcia, E.; Cobbert, J.; Lavoie, H.; Smith, M.; Rajakulendran, T.; Dowdell, E.; Okur, M. N.; Dementieva, I.; Sicheri, F.; Therrien, M.; Hancock, J. F.; Ikura, M.; Koide, S.; O'Bryan, J. P. Inhibition of RAS Function through Targeting an Allosteric Regulatory Site. *Nat. Chem. Biol.* **2017**, *13*, 62–68.
(17) Welsch, M. E.; Kaplan, A.; Chambers, J. M.; Stokes, M. E.; Bos, P. H.; Zask, A.; Zhang, Y.; Sanchez-Martin, M.; Badgley, M. A.; Huang, C. S.; Tran, T. H.; Akkiraju, H.; Brown, L. M.; Nandakumar, R.; Cremers, S.; Yang, W. S.; Tong, L.; Olive, K. P.; Ferrando, A.; Stockwell, B. R. Multivalent Small-Molecule Pan-RAS Inhibitors. *Cell* **2017**, *168*, 878-889.e29.
(18) Ostrem, J. M.; Peters, U.; Sos, M. L.; Wells, J. A.; Shokat, K. M. K-Ras(G12C) Inhibitors Allosterically Control GTP Affinity and Effector Interactions. *Nature* **2013**, *503*, 548–551.
(19) Mazhab-Jafari, M. T.; Marshall, C. B.; Smith, M. J.; Gasmi-Seabrook, G. M. C.; Stathopulos, P. B.; Inagaki, F.; Kay, L. E.; Neel, B. G.; Ikura, M. Oncogenic and RASopathy-Associated K-RAS Mutations Relieve Membrane-Dependent Occlusion of the Effector-Binding Site. *Proc. Natl. Acad. Sci.* **2015**, *112*, 6625–6630.
(20) Marcus, K.; Mattos, C. Direct Attack on RAS: Intramolecular Communication and Mutation-Specific Effects. *Clin. Cancer Res.* **2015**, *21*, 1810–1818.
(21) Athuluri-Divakar, S. K.; Vasquez-Del Carpio, R.; Dutta, K.; Baker, S. J.; Cosenza, S. C.; Basu, I.; Gupta, Y. K.; Reddy, M. V. R.; Ueno, L.; Hart, J. R.; Vogt, P. K.; Mulholland, D.; Guha, C.; Aggarwal, A. K.; Reddy, E. P. A Small Molecule RAS-Mimetic Disrupts RAS Association with Effector Proteins to Block Signaling. *Cell* **2016**, *165*, 643–655.
(22) Samatar, A. A.; Poulikakos, P. I. Targeting RAS-ERK Signalling in Cancer: Promises and Challenges. *Nat. Rev. Drug Discov.* **2014**, *13*, 928–942.
(23) Inouye, K.; Mizutani, S.; Koide, H.; Kaziro, Y. Formation of the Ras Dimer Is Essential for Raf-1 Activation. *J. Biol. Chem.* **2000**, *275*, 3737–3740.
(24) Güldenhaupt, J.; Rudack, T.; Bachler, P.; Mann, D.; Triola, G.; Waldmann, H.; Kötting, C.; Gerwert, K. N-Ras Forms Dimers at POPC Membranes. *Biophys. J.* **2012**, *103*, 1585–1593.

(25) Lin, W.-C.; Iversen, L.; Tu, H.-L.; Rhodes, C.; Christensen, S. M.; Iwig, J. S.; Hansen, S. D.; Huang, W. Y. C.; Groves, J. T. H-Ras Forms Dimers on Membrane Surfaces via a Protein–Protein Interface. *Proc. Natl. Acad. Sci.* **2014**, *111*, 2996–3001.
(26) Muratcioglu, S.; Chavan, T. S.; Freed, B. C.; Jang, H.; Khavrutskii, L.; Freed, R. N.; Dyba, M. A.; Stefanisko, K.; Tarasov, S. G.; Gursoy, A.; Keskin, O.; Tarasova, N. I.; Gaponenko, V.; Nussinov, R. GTP-Dependent K-Ras Dimerization. *Structure* **2015**, *23*, 1325–1335.
(27) Nickerson, A.; Huang, T.; Lin, L.-J.; Nan, X. Photoactivated Localization Microscopy with Bimolecular Fluorescence Complementation (BiFC-PALM) for Nanoscale Imaging of Protein-Protein Interactions in Cells. *PLOS ONE* **2014**, *9*, e100589.
(28) Nan, X.; Tamgüney, T. M.; Collisson, E. A.; Lin, L.-J.; Pitt, C.; Galeas, J.; Lewis, S.; Gray, J. W.; McCormick, F.; Chu, S. Ras-GTP Dimers Activate the Mitogen-Activated Protein Kinase (MAPK) Pathway. *Proc. Natl. Acad. Sci.* **2015**, *112*, 7996–8001.
(29) Ambrogio, C.; Köhler, J.; Zhou, Z.-W.; Wang, H.; Paranal, R.; Li, J.; Capelletti, M.; Caffarra, C.; Li, S.; Lv, Q.; Gondi, S.; Hunter, J. C.; Lu, J.; Chiarle, R.; Santamaría, D.; Westover, K. D.; Jänne, P. A. KRAS Dimerization Impacts MEK Inhibitor Sensitivity and Oncogenic Activity of Mutant KRAS. *Cell* **2018**, *172*, 857-868.e15.
(30) Cho, K.-J.; Hancock, J. F. Ras Nanoclusters. *Small GTPases* **2013**, *4*, 57–60.
(31) Zhou, Y.; Hancock, J. F. Ras Nanoclusters: Versatile Lipid-Based Signaling Platforms. *Biochim. Biophys. Acta BBA - Mol. Cell Res.* **2015**, *1853*, 841–849.
(32) Thompson, H. US National Cancer Institute's New Ras Project Targets an Old Foe. *Nat. Med.* **2013**, *19*, 949–950.
(33) Wu, H. Higher-Order Assemblies in a New Paradigm of Signal Transduction. *Cell* **2013**, *153*, 287–292.
(34) Santos, E. Dimerization Opens New Avenues into Ras Signaling Research. *Sci Signal* **2014**, *7*, pe12–pe12.
(35) Langeberg, L. K.; Scott, J. D. Signalling Scaffolds and Local Organization of Cellular Behaviour. *Nat. Rev. Mol. Cell Biol.* **2015**, *16*, 232–244.
(36) Chen, M.; Peters, A.; Huang, T.; Nan, X. Ras Dimer Formation as a New Signaling Mechanism and Potential Cancer Therapeutic Target. *Mini Rev. Med. Chem.* **2016**, *16*, 391–403.
(37) Liko, I.; Allison, T. M.; Hopper, J. T.; Robinson, C. V. Mass Spectrometry Guided Structural Biology. *Curr. Opin. Struct. Biol.* **2016**, *40*, 136–144.
(38) Leney, A. C.; Heck, A. J. R. Native Mass Spectrometry: What Is in the Name? *J. Am. Soc. Mass Spectrom.* **2017**, *28*, 5–13.
(39) Konermann, L.; Vahidi, S.; Sowole, M. A. Mass Spectrometry Methods for Studying Structure and Dynamics of Biological Macromolecules. *Anal. Chem.* **2014**, *86*, 213–232.
(40) Pirrone, G. F.; Iacob, R. E.; Engen, J. R. Applications of Hydrogen/Deuterium Exchange MS from 2012 to 2014. *Anal. Chem.* **2014**, *87*, 99–118.

(41) Cammarata, M.; Lin, K.-Y.; Pruet, J.; Liu, H.; Brodbelt, J. Probing the Unfolding of Myoglobin and Domain C of PARP-1 with Covalent Labeling and Top-Down Ultraviolet Photodissociation Mass Spectrometry. *Anal. Chem.* **2014**, *86*, 2534–2542.
(42) Breuker, K.; McLafferty, F. W. Stepwise Evolution of Protein Native Structure with Electrospray into the Gas Phase, 10−12 to 102 S. *Proc. Natl. Acad. Sci.* **2008**, *105*, 18145–18152.
(43) Bush, M. F.; Hall, Z.; Giles, K.; Hoyes, J.; Robinson, C. V.; Ruotolo, B. T. Collision Cross Sections of Proteins and Their Complexes: A Calibration Framework and Database for Gas-Phase Structural Biology. *Anal. Chem.* **2010**, *82*, 9557–9565.
(44) Benesch, J. L. P.; Aquilina, J. A.; Ruotolo, B. T.; Sobott, F.; Robinson, C. V. Tandem Mass Spectrometry Reveals the Quaternary Organization of Macromolecular Assemblies. *Chem. Biol.* **2006**, *13*, 597–605.
(45) Hall, Z.; Hernández, H.; Marsh, J. A.; Teichmann, S. A.; Robinson, C. V. The Role of Salt Bridges, Charge Density, and Subunit Flexibility in Determining Disassembly Routes of Protein Complexes. *Structure* **2013**, *21*, 1325–1337.
(46) Breuker, K.; Oh, H.; Horn, D. M.; Cerda, B. A.; McLafferty, F. W. Detailed Unfolding and Folding of Gaseous Ubiquitin Ions Characterized by Electron Capture Dissociation. *J. Am. Chem. Soc.* **2002**, *124*, 6407–6420.
(47) Zhang, H.; Cui, W.; Gross, M. L. Native Electrospray Ionization and Electron-Capture Dissociation for Comparison of Protein Structure in Solution and the Gas Phase. *Int. J. Mass Spectrom.* **2013**, *354–355*, 288–291.
(48) Li, H.; Wongkongkathep, P.; Orden, S. L. V.; Loo, R. R. O.; Loo, J. A. Revealing Ligand Binding Sites and Quantifying Subunit Variants of Noncovalent Protein Complexes in a Single Native Top-Down FTICR MS Experiment. *J. Am. Soc. Mass Spectrom.* **2014**, 1–9.
(49) Lermyte, F.; Sobott, F. Electron Transfer Dissociation Provides Higher-Order Structural Information of Native and Partially Unfolded Protein Complexes. *PROTEOMICS* **2015**, *15*, 2813–2822.
(50) Lermyte, F.; Williams, J. P.; Brown, J. M.; Martin, E. M.; Sobott, F. Extensive Charge Reduction and Dissociation of Intact Protein Complexes Following Electron Transfer on a Quadrupole-Ion Mobility-Time-of-Flight MS. *J. Am. Soc. Mass Spectrom.* **2015**, *26*, 1068–1076.
(51) Li, H.; Nguyen, H. H.; Ogorzalek Loo, R. R.; Campuzano, I. D. G.; Loo, J. A. An Integrated Native Mass Spectrometry and Top-down Proteomics Method That Connects Sequence to Structure and Function of Macromolecular Complexes. *Nat. Chem.* **2018**, *10*, 139–148.
(52) Zhou, M.; Wysocki, V. H. Surface Induced Dissociation: Dissecting Noncovalent Protein Complexes in the Gas Phase. *Acc. Chem. Res.* **2014**, *47*, 1010–1018.
(53) Sahasrabuddhe, A.; Hsia, Y.; Busch, F.; Sheffler, W.; King, N. P.; Baker, D.; Wysocki, V. H. Confirmation of Intersubunit Connectivity and Topology of Designed Protein Complexes by Native MS. *Proc. Natl. Acad. Sci.* **2018**, *115*, 1268–1273.

(54) Shaw, J. B.; Li, W.; Holden, D. D.; Zhang, Y.; Griep-Raming, J.; Fellers, R. T.; Early, B. P.; Thomas, P. M.; Kelleher, N. L.; Brodbelt, J. S. Complete Protein Characterization Using Top-Down Mass Spectrometry and Ultraviolet Photodissociation. *J. Am. Chem. Soc.* **2013**, *135*, 12646–12651.
(55) O'Brien, J. P.; Li, W.; Zhang, Y.; Brodbelt, J. S. Characterization of Native Protein Complexes Using Ultraviolet Photodissociation Mass Spectrometry. *J. Am. Chem. Soc.* **2014**, *136*, 12920–12928.
(56) Morrison, L. J.; Brodbelt, J. S. 193 Nm Ultraviolet Photodissociation Mass Spectrometry of Tetrameric Protein Complexes Provides Insight into Quaternary and Secondary Protein Topology. *J. Am. Chem. Soc.* **2016**, *138*, 10849–10859.
(57) Tamara, S.; Dyachenko, A.; Fort, K. L.; Makarov, A. A.; Scheltema, R. A.; Heck, A. J. R. Symmetry of Charge Partitioning in Collisional and UV Photon-Induced Dissociation of Protein Assemblies. *J. Am. Chem. Soc.* **2016**, *138*, 10860–10868.
(58) Julian, R. R. The Mechanism Behind Top-Down UVPD Experiments: Making Sense of Apparent Contradictions. *J. Am. Soc. Mass Spectrom.* **2017**, *28*, 1823–1826.
(59) Cammarata, M. B.; Brodbelt, J. S. Structural Characterization of Holo- and Apo-Myoglobin in the Gas Phase by Ultraviolet Photodissociation Mass Spectrometry. *Chem. Sci.* **2015**, *6*, 1324–1333.
(60) Cammarata, M. B.; Thyer, R.; Rosenberg, J.; Ellington, A.; Brodbelt, J. S. Structural Characterization of Dihydrofolate Reductase Complexes by Top-Down Ultraviolet Photodissociation Mass Spectrometry. *J. Am. Chem. Soc.* **2015**, *137*, 9128–9135.
(61) Mehaffey, M. R.; Cammarata, M. B.; Brodbelt, J. S. Tracking the Catalytic Cycle of Adenylate Kinase by Ultraviolet Photodissociation Mass Spectrometry. *Anal. Chem.* **2018**, *90*, 839–846.
(62) Cammarata, M. B.; Schardon, C. L.; Mehaffey, M. R.; Rosenberg, J.; Singleton, J.; Fast, W.; Brodbelt, J. S. Impact of G12 Mutations on the Structure of K-Ras Probed by Ultraviolet Photodissociation Mass Spectrometry. *J. Am. Chem. Soc.* **2016**, *138*, 13187–13196.
(63) Miller, M. S.; Miller, L. D. RAS Mutations and Oncogenesis: Not All RAS Mutations Are Created Equally. *Front. Genet.* **2012**, *2*.
(64) Rajakulendran, T.; Sahmi, M.; Lefrançois, M.; Sicheri, F.; Therrien, M. A Dimerization-Dependent Mechanism Drives RAF Catalytic Activation. *Nature* **2009**, *461*, 542–545.
(65) Ihle, N. T.; Byers, L. A.; Kim, E. S.; Saintigny, P.; Lee, J. J.; Blumenschein, G. R.; Tsao, A.; Liu, S.; Larsen, J. E.; Wang, J.; Diao, L.; Coombes, K. R.; Chen, L.; Zhang, S.; Abdelmelek, M. F.; Tang, X.; Papadimitrakopoulou, V.; Minna, J. D.; Lippman, S. M.; Hong, W. K.; Herbst, R. S.; Wistuba, I. I.; Heymach, J. V.; Powis, G. Effect of KRAS Oncogene Substitutions on Protein Behavior: Implications for Signaling and Clinical Outcome. *J. Natl. Cancer Inst.* **2012**, *104*, 228–239.
(66) Freeman, A. K.; Ritt, D. A.; Morrison, D. K. Effects of Raf Dimerization and Its Inhibition on Normal and Disease-Associated Raf Signaling. *Mol. Cell* **2013**, *49*, 751–758.

(67) Young, A.; Lou, D.; McCormick, F. Oncogenic and Wild-Type Ras Play Divergent Roles in the Regulation of Mitogen-Activated Protein Kinase Signaling. *Cancer Discov.* **2013**, *3*, 112–123.
(68) Hammond, D. E.; Mageean, C. J.; Rusilowicz, E. V.; Wickenden, J. A.; Clague, M. J.; Prior, I. A. Differential Reprogramming of Isogenic Colorectal Cancer Cells by Distinct Activating KRAS Mutations. *J. Proteome Res.* **2015**, *14*, 1535–1546.
(69) Gnad, F.; Doll, S.; Song, K.; Stokes, M. P.; Moffat, J.; Liu, B.; Arnott, D.; Wallin, J.; Friedman, L. S.; Hatzivassiliou, G.; Belvin, M. Phosphoproteome Analysis of the MAPK Pathway Reveals Previously Undetected Feedback Mechanisms. *PROTEOMICS* **2016**, *16*, 1998–2004.
(70) Rosenberg, J.; Parker, W. R.; Cammarata, M. B.; Brodbelt, J. S. UV-POSIT: Web-Based Tools for Rapid and Facile Structural Interpretation of Ultraviolet Photodissociation (UVPD) Mass Spectra. *J. Am. Soc. Mass Spectrom.* **2018**, *29*, 1323–1326.
(71) Fetics, S. K.; Guterres, H.; Kearney, B. M.; Buhrman, G.; Ma, B.; Nussinov, R.; Mattos, C. Allosteric Effects of the Oncogenic RasQ61L Mutant on Raf-RBD. *Structure* **2015**, *23*, 505–516.
(72) Bentley, C.; Jurinka, S. S.; Kljavin, N. M.; Vartanian, S.; Ramani, S. R.; Gonzalez, L. C.; Yu, K.; Modrusan, Z.; Du, P.; Bourgon, R.; Neve, R. M.; Stokoe, D. A Requirement for Wild-Type Ras Isoforms in Mutant KRas-Driven Signalling and Transformation. *Biochem. J.* **2013**, *452*, 313–320.
(73) Mehaffey, M. R.; Sanders, J. D.; Holden, D. D.; Nilsson, C. L.; Brodbelt, J. S. Multistage Ultraviolet Photodissociation Mass Spectrometry To Characterize Single Amino Acid Variants of Human Mitochondrial BCAT2. *Anal. Chem.* **2018**, *90*, 9904–9911.
(74) Yin, S.; Loo, J. A. Elucidating the Site of Protein-ATP Binding by Top-Down Mass Spectrometry. *J. Am. Soc. Mass Spectrom.* **2010**, *21*, 899–907.
(75) Lobo, I. A.; Robertson, P. A.; Villani, L.; Wilson, D. J. D.; Robertson, E. G. Thiols as Hydrogen Bond Acceptors and Donors: Spectroscopy of 2-Phenylethanethiol Complexes. *J. Phys. Chem. A* **2018**, *122*, 7171–7180.

CHAPTER 6

(1) Mahler, M.; Fritzler, M. J. Epitope Specificity and Significance in Systemic Autoimmune Diseases. *Ann. N. Y. Acad. Sci.* **2010**, *1183*, 267–287.
(2) Regenmortel, M. H. V. V. Specificity, Polyspecificity, and Heterospecificity of Antibody-Antigen Recognition. *J. Mol. Recognit.* **2014**, *27*, 627–639.
(3) Abbott, W. M.; Damschroder, M. M.; Lowe, D. C. Current Approaches to Fine Mapping of Antigen–Antibody Interactions. *Immunology* **2014**, *142*, 526–535.
(4) Opuni, K. F. M.; Al-Majdoub, M.; Yefremova, Y.; El-Kased, R. F.; Koy, C.; Glocker, M. O. Mass Spectrometric Epitope Mapping. *Mass Spectrom. Rev.* **2018**, *37*, 229–241.

(5) Stefanescu, R.; Iacob, R. E.; Damoc, E. N.; Marquardt, A.; Amstalden, E.; Manea, M.; Perdivara, I.; Maftei, M.; Paraschiv, G.; Przybylski, M. Mass Spectrometric Approaches for Elucidation of Antigen—Antibody Recognition Structures in Molecular Immunology. *Eur. J. Mass Spectrom.* **2007**, *13*, 69–75.
(6) Wei, H.; Mo, J.; Tao, L.; Russell, R. J.; Tymiak, A. A.; Chen, G.; Iacob, R. E.; Engen, J. R. Hydrogen/Deuterium Exchange Mass Spectrometry for Probing Higher Order Structure of Protein Therapeutics: Methodology and Applications. *Drug Discov. Today* **2014**, *19*, 95–102.
(7) Puchades, C.; Kűkrer, B.; Diefenbach, O.; Sneekes-Vriese, E.; Juraszek, J.; Koudstaal, W.; Apetri, A. Epitope Mapping of Diverse Influenza Hemagglutinin Drug Candidates Using HDX-MS. *Sci. Rep.* **2019**, *9*, 1–10.
(8) Zhu, S.; Liuni, P.; Ettorre, L.; Chen, T.; Szeto, J.; Carpick, B.; James, D. A.; Wilson, D. J. Hydrogen–Deuterium Exchange Epitope Mapping Reveals Distinct Neutralizing Mechanisms for Two Monoclonal Antibodies against Diphtheria Toxin. *Biochemistry* **2019**, *58*, 646–656.
(9) Huang, R. Y.-C.; Jr, S. R. K.; Felix, N.; Graziano, R. F.; Srinivasan, M.; Pashine, A.; Chen, G. Hydrogen/Deuterium Exchange Mass Spectrometry and Computational Modeling Reveal a Discontinuous Epitope of an Antibody/TL1A Interaction. *mAbs* **2018**, *10*, 95–103.
(10) Wecksler, A. T.; Kalo, M. S.; Deperalta, G. Mapping of Fab-1:VEGF Interface Using Carboxyl Group Footprinting Mass Spectrometry. *J. Am. Soc. Mass Spectrom.* **2015**, *26*, 2077–2080.
(11) Kaur, P.; Tomechko, S. E.; Kiselar, J.; Shi, W.; Deperalta, G.; Wecksler, A. T.; Gokulrangan, G.; Ling, V.; Chance, M. R. Characterizing Monoclonal Antibody Structure by Carboxyl Group Footprinting. *mAbs* **2015**, *7*, 540–552.
(12) Zhang, Y.; Rempel, D. L.; Zhang, H.; Gross, M. L. An Improved Fast Photochemical Oxidation of Proteins (FPOP) Platform for Protein Therapeutics. *J. Am. Soc. Mass Spectrom.* **2015**, *26*, 526–529.
(13) Zhang, Y.; Wecksler, A. T.; Molina, P.; Deperalta, G.; Gross, M. L. Mapping the Binding Interface of VEGF and a Monoclonal Antibody Fab-1 Fragment with Fast Photochemical Oxidation of Proteins (FPOP) and Mass Spectrometry. *J. Am. Soc. Mass Spectrom.* **2017**, *28*, 850–858.
(14) Pimenova, T.; Nazabal, A.; Roschitzki, B.; Seebacher, J.; Rinner, O.; Zenobi, R. Epitope Mapping on Bovine Prion Protein Using Chemical Cross-Linking and Mass Spectrometry. *J. Mass Spectrom.* **2008**, *43*, 185–195.
(15) Rosati, S.; Yang, Y.; Barendregt, A.; Heck, A. J. R. Detailed Mass Analysis of Structural Heterogeneity in Monoclonal Antibodies Using Native Mass Spectrometry. *Nat. Protoc.* **2014**, *9*, 967–976.
(16) Thompson, N. J.; Rosati, S.; Heck, A. J. R. Performing Native Mass Spectrometry Analysis on Therapeutic Antibodies. *Methods* **2014**, *65*, 11–17.
(17) Leney, A. C.; Heck, A. J. R. Native Mass Spectrometry: What Is in the Name? *J. Am. Soc. Mass Spectrom.* **2017**, *28*, 5–13.

(18) Eschweiler, J. D.; Kerr, R.; Rabuck-Gibbons, J.; Ruotolo, B. T. Sizing Up Protein–Ligand Complexes: The Rise of Structural Mass Spectrometry Approaches in the Pharmaceutical Sciences. *Annu. Rev. Anal. Chem.* **2017**, *10*, 25–44.
(19) Kaur, U.; Johnson, D. T.; Chea, E. E.; Deredge, D. J.; Espino, J. A.; Jones, L. M. Evolution of Structural Biology through the Lens of Mass Spectrometry. *Anal. Chem.* **2019**, *91*, 142–155.
(20) Siuzdak, G.; Bothner, B.; Yeager, M.; Brugidou, C.; Fauquet, C. M.; Hoey, K.; Change, C.-M. Mass Spectrometry and Viral Analysis. *Chem. Biol.* **1996**, *3*, 45–48.
(21) Ruotolo, B. T.; Giles, K.; Campuzano, I.; Sandercock, A. M.; Bateman, R. H.; Robinson, C. V. Evidence for Macromolecular Protein Rings in the Absence of Bulk Water. *Science* **2005**, *310*, 1658–1661.
(22) Duijn, E. van; Barendregt, A.; Synowsky, S.; Versluis, C.; Heck, A. J. R. Chaperonin Complexes Monitored by Ion Mobility Mass Spectrometry. *J. Am. Chem. Soc.* **2009**, *131*, 1452–1459.
(23) Tito, M. A.; Miller, J.; Walker, N.; Griffin, K. F.; Williamson, E. D.; Despeyroux-Hill, D.; Titball, R. W.; Robinson, C. V. Probing Molecular Interactions in Intact Antibody: Antigen Complexes, an Electrospray Time-of-Flight Mass Spectrometry Approach. *Biophys. J.* **2001**, *81*, 3503–3509.
(24) Haberger, M.; Leiss, M.; Heidenreich, A.-K.; Pester, O.; Hafenmair, G.; Hook, M.; Bonnington, L.; Wegele, H.; Haindl, M.; Reusch, D.; Bulau, P. Rapid Characterization of Biotherapeutic Proteins by Size-Exclusion Chromatography Coupled to Native Mass Spectrometry. *mAbs* **2015**, *8*, 331–339.
(25) Yang, Y.; Wang, G.; Song, T.; Lebrilla, C. B.; Heck, A. J. R. Resolving the Micro-Heterogeneity and Structural Integrity of Monoclonal Antibodies by Hybrid Mass Spectrometric Approaches. *mAbs* **2017**, *9*, 638–645.
(26) Tian, Y.; Ruotolo, B. T. The Growing Role of Structural Mass Spectrometry in the Discovery and Development of Therapeutic Antibodies. *Analyst* **2018**, *143*, 2459–2468.
(27) Dyachenko, A.; Wang, G.; Belov, M.; Makarov, A.; de Jong, R. N.; van den Bremer, E. T. J.; Parren, P. W. H. I.; Heck, A. J. R. Tandem Native Mass-Spectrometry on Antibody–Drug Conjugates and Submillion Da Antibody–Antigen Protein Assemblies on an Orbitrap EMR Equipped with a High-Mass Quadrupole Mass Selector. *Anal. Chem.* **2015**, *87*, 6095–6102.
(28) Wang, G.; de Jong, R. N.; van den Bremer, E. T. J.; Beurskens, F. J.; Labrijn, A. F.; Ugurlar, D.; Gros, P.; Schuurman, J.; Parren, P. W. H. I.; Heck, A. J. R. Molecular Basis of Assembly and Activation of Complement Component C1 in Complex with Immunoglobulin G1 and Antigen. *Mol. Cell* **2016**, *63*, 135–145.
(29) Bond, K. M.; Aanei, I. L.; Francis, M. B.; Jarrold, M. F. Determination of Antibody Population Distributions for Virus-Antibody Conjugates by Charge Detection Mass Spectrometry. *Anal. Chem.* **2020**, *92*, 1285–1291.
(30) Lu, X.; DeFelippis, M. R.; Huang, L. Linear Epitope Mapping by Native Mass Spectrometry. *Anal. Biochem.* **2009**, *395*, 100–107.

(31) Danquah, B. D.; Röwer, C.; Opuni, K. F. M.; El-Kased, R.; Frommholz, D.; Illges, H.; Koy, C.; Glocker, M. O. Intact Transition Epitope Mapping – Targeted High-Energy Rupture of Extracted Epitopes (ITEM-THREE). *Mol. Cell. Proteomics* **2019**, *18*, 1543–1555.
(32) Atmanene, C.; Wagner-Rousset, E.; Malissard, M.; Chol, B.; Robert, A.; Corvaïa, N.; Dorsselaer, A. V.; Beck, A.; Sanglier-Cianférani, S.-. Extending Mass Spectrometry Contribution to Therapeutic Monoclonal Antibody Lead Optimization: Characterization of Immune Complexes Using Noncovalent ESI-MS. *Anal. Chem.* **2009**, *81*, 6364–6373.
(33) Huang, Y.; Salinas, N. D.; Chen, E.; Tolia, N. H.; Gross, M. L. Native Mass Spectrometry, Ion Mobility, and Collision-Induced Unfolding Categorize Malaria Antigen/Antibody Binding. *J. Am. Soc. Mass Spectrom.* **2017**, *28*, 2515–2518.
(34) Ehkirch, A.; Goyon, A.; Hernandez-Alba, O.; Rouviere, F.; D'Atri, V.; Dreyfus, C.; Haeuw, J.-F.; Diemer, H.; Beck, A.; Heinisch, S.; Guillarme, D.; Cianferani, S. A Novel Online Four-Dimensional SEC×SEC-IM×MS Methodology for Characterization of Monoclonal Antibody Size Variants. *Anal. Chem.* **2018**, *90*, 13929–13937.
(35) Allison, T. M.; Bechara, C. Structural Mass Spectrometry Comes of Age: New Insight into Protein Structure, Function and Interactions. *Biochem. Soc. Trans.* **2019**, *47*, 317–327.
(36) Pan, J.; Zhang, S.; Chou, A.; Hardie, D. B.; Borchers, C. H. Fast Comparative Structural Characterization of Intact Therapeutic Antibodies Using Hydrogen–Deuterium Exchange and Electron Transfer Dissociation. *Anal. Chem.* **2015**, *87*, 5884–5890.
(37) Pan, J.; Zhang, S.; Chou, A.; H. Borchers, C. Higher-Order Structural Interrogation of Antibodies Using Middle-down Hydrogen/Deuterium Exchange Mass Spectrometry. *Chem. Sci.* **2016**, *7*, 1480–1486.
(38) Zhang, Y.; Cui, W.; Wecksler, A. T.; Zhang, H.; Molina, P.; Deperalta, G.; Gross, M. L. Native MS and ECD Characterization of a Fab–Antigen Complex May Facilitate Crystallization for X-Ray Diffraction. *J. Am. Soc. Mass Spectrom.* **2016**, *27*, 1139–1142.
(39) Lermyte, F.; Sobott, F. Electron Transfer Dissociation Provides Higher-Order Structural Information of Native and Partially Unfolded Protein Complexes. *PROTEOMICS* **2015**, *15*, 2813–2822.
(40) Li, H.; Nguyen, H. H.; Ogorzalek Loo, R. R.; Campuzano, I. D. G.; Loo, J. A. An Integrated Native Mass Spectrometry and Top-down Proteomics Method That Connects Sequence to Structure and Function of Macromolecular Complexes. *Nat. Chem.* **2018**, *10*, 139–148.
(41) Brodbelt, J. S.; Morrison, L. J.; Santos, I. Ultraviolet Photodissociation Mass Spectrometry for Analysis of Biological Molecules. *Chem. Rev.* **2019**.
(42) Cotham, V. C.; Wine, Y.; Brodbelt, J. S. Selective 351 Nm Photodissociation of Cysteine-Containing Peptides for Discrimination of Antigen-Binding Regions of

IgG Fragments in Bottom-Up Liquid Chromatography–Tandem Mass Spectrometry Workflows. *Anal. Chem.* **2013**, *85*, 5577–5585.
(43) Cotham, V. C.; Horton, A. P.; Lee, J.; Georgiou, G.; Brodbelt, J. S. Middle-Down 193-Nm Ultraviolet Photodissociation for Unambiguous Antibody Identification and Its Implications for Immunoproteomic Analysis. *Anal. Chem.* **2017**, *89*, 6498–6504.
(44) Shaw, J. B.; Liu, W.; Vasil′ev, Y. V.; Bracken, C. C.; Malhan, N.; Guthals, A.; Beckman, J. S.; Voinov, V. G. Direct Determination of Antibody Chain Pairing by Top-down and Middle-down Mass Spectrometry Using Electron Capture Dissociation and Ultraviolet Photodissociation. *Anal. Chem.* **2020**, *92*, 766–773.
(45) Shaw, J. B.; Li, W.; Holden, D. D.; Zhang, Y.; Griep-Raming, J.; Fellers, R. T.; Early, B. P.; Thomas, P. M.; Kelleher, N. L.; Brodbelt, J. S. Complete Protein Characterization Using Top-Down Mass Spectrometry and Ultraviolet Photodissociation. *J. Am. Chem. Soc.* **2013**, *135*, 12646–12651.
(46) O'Brien, J. P.; Li, W.; Zhang, Y.; Brodbelt, J. S. Characterization of Native Protein Complexes Using Ultraviolet Photodissociation Mass Spectrometry. *J. Am. Chem. Soc.* **2014**, *136*, 12920–12928.
(47) Greisch, J.-F.; Tamara, S.; Scheltema, R. A.; Maxwell, H. W. R.; Fagerlund, R. D.; Fineran, P. C.; Tetter, S.; Hilvert, D.; Heck, A. J. R. Expanding the Mass Range for UVPD-Based Native Top-down Mass Spectrometry. *Chem. Sci.* **2019**, *10*, 7163–7171.
(48) Zhou, M.; Liu, W.; Shaw, J. B. Charge Movement and Structural Changes in the Gas-Phase Unfolding of Multimeric Protein Complexes Captured by Native Top-Down Mass Spectrometry. *Anal. Chem.* **2020**, *92*, 1788–1795.
(49) Krammer, F.; Palese, P. Advances in the Development of Influenza Virus Vaccines. *Nat. Rev. Drug Discov.* **2015**, *14*, 167–182.
(50) Gamblin, S. J.; Skehel, J. J. Influenza Hemagglutinin and Neuraminidase Membrane Glycoproteins. *J. Biol. Chem.* **2010**, *285*, 28403–28409.
(51) Wu, N. C.; Wilson, I. A. Structural Insights into the Design of Novel Anti-Influenza Therapies. *Nat. Struct. Mol. Biol.* **2018**, *25*, 115–121.
(52) Air, G. M. Sequence Relationships among the Hemagglutinin Genes of 12 Subtypes of Influenza A Virus. *Proc. Natl. Acad. Sci. U. S. A.* **1981**, *78*, 7639–7643.
(53) Brandenburg, B.; Koudstaal, W.; Goudsmit, J.; Klaren, V.; Tang, C.; Bujny, M. V.; Korse, H. J. W. M.; Kwaks, T.; Otterstrom, J. J.; Juraszek, J.; Oijen, A. M. van; Vogels, R.; Friesen, R. H. E. Mechanisms of Hemagglutinin Targeted Influenza Virus Neutralization. *PLOS ONE* **2013**, *8*, e80034.
(54) Sparrow, E.; Friede, M.; Sheikh, M.; Torvaldsen, S.; Newall, A. T. Passive Immunization for Influenza through Antibody Therapies, a Review of the Pipeline, Challenges and Potential Applications. *Vaccine* **2016**, *34*, 5442–5448.
(55) Laursen, N. S.; Friesen, R. H. E.; Zhu, X.; Jongeneelen, M.; Blokland, S.; Vermond, J.; Eijgen, A. van; Tang, C.; Diepen, H. van; Obmolova, G.; Kolfschoten, M. van der N.; Zuijdgeest, D.; Straetemans, R.; Hoffman, R. M. B.; Nieusma, T.; Pallesen, J.; Turner, H. L.; Bernard, S. M.; Ward, A. B.; Luo, J.; Poon, L. L. M.; Tretiakova,

A. P.; Wilson, J. M.; Limberis, M. P.; Vogels, R.; Brandenburg, B.; Kolkman, J. A.; Wilson, I. A. Universal Protection against Influenza Infection by a Multidomain Antibody to Influenza Hemagglutinin. *Science* **2018**, *362*, 598–602.

(56) Sautto, G. A.; Kirchenbaum, G. A.; Ross, T. M. Towards a Universal Influenza Vaccine: Different Approaches for One Goal. *Virol. J.* **2018**, *15*, 17.

(57) Zhang, Y.; Xu, C.; Zhang, H.; Liu, G. D.; Xue, C.; Cao, Y. Targeting Hemagglutinin: Approaches for Broad Protection against the Influenza A Virus. *Viruses* **2019**, *11*.

(58) Mehaffey, M. R.; Sanders, J. D.; Holden, D. D.; Nilsson, C. L.; Brodbelt, J. S. Multistage Ultraviolet Photodissociation Mass Spectrometry To Characterize Single Amino Acid Variants of Human Mitochondrial BCAT2. *Anal. Chem.* **2018**, *90*, 9904–9911.

(59) Marty, M. T.; Baldwin, A. J.; Marklund, E. G.; Hochberg, G. K. A.; Benesch, J. L. P.; Robinson, C. V. Bayesian Deconvolution of Mass and Ion Mobility Spectra: From Binary Interactions to Polydisperse Ensembles. *Anal. Chem.* **2015**, *87*, 4370–4376.

(60) Watanabe, A.; McCarthy, K. R.; Kuraoka, M.; Schmidt, A. G.; Adachi, Y.; Onodera, T.; Tonouchi, K.; Caradonna, T. M.; Bajic, G.; Song, S.; McGee, C. E.; Sempowski, G. D.; Feng, F.; Urick, P.; Kepler, T. B.; Takahashi, Y.; Harrison, S. C.; Kelsoe, G. Antibodies to a Conserved Influenza Head Interface Epitope Protect by an IgG Subtype-Dependent Mechanism. *Cell* **2019**, *177*, 1124-1135.e16.

(61) Lee, J.; Boutz, D. R.; Chromikova, V.; Joyce, M. G.; Vollmers, C.; Leung, K.; Horton, A. P.; DeKosky, B. J.; Lee, C.-H.; Lavinder, J. J.; Murrin, E. M.; Chrysostomou, C.; Hoi, K. H.; Tsybovsky, Y.; Thomas, P. V.; Druz, A.; Zhang, B.; Zhang, Y.; Wang, L.; Kong, W.-P.; Park, D.; Popova, L. I.; Dekker, C. L.; Davis, M. M.; Carter, C. E.; Ross, T. M.; Ellington, A. D.; Wilson, P. C.; Marcotte, E. M.; Mascola, J. R.; Ippolito, G. C.; Krammer, F.; Quake, S. R.; Kwong, P. D.; Georgiou, G. Molecular-Level Analysis of the Serum Antibody Repertoire in Young Adults before and after Seasonal Influenza Vaccination. *Nat. Med.* **2016**, *22*, 1456–1464.

(62) Garten, R. J.; Davis, C. T.; Russell, C. A.; Shu, B.; Lindstrom, S.; Balish, A.; Sessions, W. M.; Xu, X.; Skepner, E.; Deyde, V.; Okomo-Adhiambo, M.; Gubareva, L.; Barnes, J.; Smith, C. B.; Emery, S. L.; Hillman, M. J.; Rivailler, P.; Smagala, J.; Graaf, M. de; Burke, D. F.; Fouchier, R. A. M.; Pappas, C.; Alpuche-Aranda, C. M.; López-Gatell, H.; Olivera, H.; López, I.; Myers, C. A.; Faix, D.; Blair, P. J.; Yu, C.; Keene, K. M.; Dotson, P. D.; Boxrud, D.; Sambol, A. R.; Abid, S. H.; George, K. S.; Bannerman, T.; Moore, A. L.; Stringer, D. J.; Blevins, P.; Demmler-Harrison, G. J.; Ginsberg, M.; Kriner, P.; Waterman, S.; Smole, S.; Guevara, H. F.; Belongia, E. A.; Clark, P. A.; Beatrice, S. T.; Donis, R.; Katz, J.; Finelli, L.; Bridges, C. B.; Shaw, M.; Jernigan, D. B.; Uyeki, T. M.; Smith, D. J.; Klimov, A. I.; Cox, N. J. Antigenic and Genetic Characteristics of Swine-Origin 2009 A(H1N1) Influenza Viruses Circulating in Humans. *Science* **2009**, *325*, 197–201.

(63) Tate, M. D.; Job, E. R.; Deng, Y.-M.; Gunalan, V.; Maurer-Stroh, S.; Reading, P. C. Playing Hide and Seek: How Glycosylation of the Influenza Virus Hemagglutinin Can Modulate the Immune Response to Infection. *Viruses* **2014**, *6*, 1294–1316.

(64) Wang, L.; Qin, Y.; Ilchenko, S.; Bohon, J.; Shi, W.; Cho, M. W.; Takamoto, K.; Chance, M. R. Structural Analysis of a Highly Glycosylated and Unliganded Gp120-Based Antigen Using Mass Spectrometry. *Biochemistry* **2010**, *49*, 9032–9045.
(65) Wohlschlager, T.; Scheffler, K.; Forstenlehner, I. C.; Skala, W.; Senn, S.; Damoc, E.; Holzmann, J.; Huber, C. G. Native Mass Spectrometry Combined with Enzymatic Dissection Unravels Glycoform Heterogeneity of Biopharmaceuticals. *Nat. Commun.* **2018**, *9*, 1713.
(66) Lioe, H.; O'Hair, R. A. J. A Novel Salt Bridge Mechanism Highlights the Need for Nonmobile Proton Conditions to Promote Disulfide Bond Cleavage in Protonated Peptides under Low-Energy Collisional Activation. *J. Am. Soc. Mass Spectrom.* **2007**, *18*, 1109–1123.
(67) Quick, M. M.; Crittenden, C. M.; Rosenberg, J. A.; Brodbelt, J. S. Characterization of Disulfide Linkages in Proteins by 193 Nm Ultraviolet Photodissociation (UVPD) Mass Spectrometry. *Anal. Chem.* **2018**, *90*, 8523–8530.
(68) Jennewein, M. F.; Alter, G. The Immunoregulatory Roles of Antibody Glycosylation. *Trends Immunol.* **2017**, *38*, 358–372.
(69) Fort, K. L.; Waterbeemd, M. van de; Boll, D.; Reinhardt-Szyba, M.; Belov, M. E.; Sasaki, E.; Zschoche, R.; Hilvert, D.; Makarov, A. A.; Heck, A. J. R. Expanding the Structural Analysis Capabilities on an Orbitrap-Based Mass Spectrometer for Large Macromolecular Complexes. *Analyst* **2017**, *143*, 100–105.
(70) Cammarata, M. B.; Brodbelt, J. S. Structural Characterization of Holo- and Apo-Myoglobin in the Gas Phase by Ultraviolet Photodissociation Mass Spectrometry. *Chem. Sci.* **2015**, *6*, 1324–1333.
(71) Bajic, G.; Maron, M. J.; Adachi, Y.; Onodera, T.; McCarthy, K. R.; McGee, C. E.; Sempowski, G. D.; Takahashi, Y.; Kelsoe, G.; Kuraoka, M.; Schmidt, A. G. Influenza Antigen Engineering Focuses Immune Responses to a Subdominant but Broadly Protective Viral Epitope. *Cell Host Microbe* **2019**, *25*, 827-835.e6.
(72) Bangaru, S.; Lang, S.; Schotsaert, M.; Vanderven, H. A.; Zhu, X.; Kose, N.; Bombardi, R.; Finn, J. A.; Kent, S. J.; Gilchuk, P.; Gilchuk, I.; Turner, H. L.; García-Sastre, A.; Li, S.; Ward, A. B.; Wilson, I. A.; Crowe, J. E. A Site of Vulnerability on the Influenza Virus Hemagglutinin Head Domain Trimer Interface. *Cell* **2019**, *177*, 1136-1152.e18.
(73) R. Julian, R. The Mechanism Behind Top-Down UVPD Experiments: Making Sense of Apparent Contradictions. *J. Am. Soc. Mass Spectrom.* **2017**, *28*, 1823–1826.
(74) Paizs, B.; Suhai, S. Fragmentation Pathways of Protonated Peptides. *Mass Spectrom. Rev.* **2005**, *24*, 508–548.
(75) Riley, N. M.; Coon, J. J. The Role of Electron Transfer Dissociation in Modern Proteomics. *Anal. Chem.* **2018**, *90*, 40–64.

CHAPTER 7

(1) Erichsen, H. C.; Chanock, S. J. SNPs in Cancer Research and Treatment. *Br. J. Cancer* **2004**, *90*, 747–751.

(2) Wood, L. D.; Parsons, D. W.; Jones, S.; Lin, J.; Sjöblom, T.; Leary, R. J.; Shen, D.; Boca, S. M.; Barber, T.; Ptak, J.; Silliman, N.; Szabo, S.; Dezso, Z.; Ustyanksky, V.; Nikolskaya, T.; Nikolsky, Y.; Karchin, R.; Wilson, P. A.; Kaminker, J. S.; Zhang, Z.; Croshaw, R.; Willis, J.; Dawson, D.; Shipitsin, M.; Willson, J. K. V.; Sukumar, S.; Polyak, K.; Park, B. H.; Pethiyagoda, C. L.; Pant, P. V. K.; Ballinger, D. G.; Sparks, A. B.; Hartigan, J.; Smith, D. R.; Suh, E.; Papadopoulos, N.; Buckhaults, P.; Markowitz, S. D.; Parmigiani, G.; Kinzler, K. W.; Velculescu, V. E.; Vogelstein, B. The Genomic Landscapes of Human Breast and Colorectal Cancers. *Science* **2007**, *318*, 1108–1113.

(3) Rossi, E. D.; Martini, M.; Bizzarro, T.; Schmitt, F.; Longatto-Filho, A.; Larocca, L. M. Somatic Mutations in Solid Tumors: A Spectrum at the Service of Diagnostic Armamentarium or an Indecipherable Puzzle? The Morphological Eyes Looking for BRAF and Somatic Molecular Detections on Cyto-Histological Samples. *Oncotarget* **2016**, *8*, 3746–3760.

(4) Vogelstein, B.; Kinzler, K. W. Cancer Genes and the Pathways They Control. *Nat. Med.* **2004**, *10*, 789–799.

(5) Lichti, C. F.; Mostovenko, E.; Wadsworth, P. A.; Lynch, G. C.; Pettitt, B. M.; Sulman, E. P.; Wang, Q.; Lang, F. F.; Rezeli, M.; Marko-Varga, G.; Végvári, Á.; Nilsson, C. L. Systematic Identification of Single Amino Acid Variants in Glioma Stem-Cell-Derived Chromosome 19 Proteins. *J. Proteome Res.* **2015**, *14*, 778–786.

(6) Ichihara, A. Isozyme Patterns of Branched-Chain Amino Acid Transaminase During Cellular Differentiation and Carcinogenesis. *Ann. N. Y. Acad. Sci.* **1975**, *259*, 347–354.

(7) Hutson, S. Structure and Function of Branched Chain Aminotransferases. *Prog. Nucleic Acid Res. Mol. Biol.* **2001**, *70*, 175–206.

(8) Anderson, L. C.; Håkansson, M.; Walse, B.; Nilsson, C. L. Intact Protein Analysis at 21 Tesla and X-Ray Crystallography Define Structural Differences in Single Amino Acid Variants of Human Mitochondrial Branched-Chain Amino Acid Aminotransferase 2 (BCAT2). *J. Am. Soc. Mass Spectrom.* **2017**, *28*, 1796–1804.

(9) Sharon, M.; Robinson, C. V. The Role of Mass Spectrometry in Structure Elucidation of Dynamic Protein Complexes. *Annu. Rev. Biochem.* **2007**, *76*, 167–193.

(10) Heck, A. J. R. Native Mass Spectrometry: A Bridge between Interactomics and Structural Biology. *Nat. Methods* **2008**, *5*, 927–933.

(11) Konermann, L.; Vahidi, S.; Sowole, M. A. Mass Spectrometry Methods for Studying Structure and Dynamics of Biological Macromolecules. *Anal. Chem.* **2014**, *86*, 213–232.

(12) Lomeli, S. H.; Yin, S.; Ogorzalek Loo, R. R.; Loo, J. A. Increasing Charge While Preserving Noncovalent Protein Complexes for ESI-MS. *J. Am. Soc. Mass Spectrom.* **2009**, *20*, 593–596.

(13) Bush, M. F.; Hall, Z.; Giles, K.; Hoyes, J.; Robinson, C. V.; Ruotolo, B. T. Collision Cross Sections of Proteins and Their Complexes: A Calibration Framework and Database for Gas-Phase Structural Biology. *Anal. Chem.* **2010**, *82*, 9557–9565.

(14) Snijder, J.; Rose, R. J.; Veesler, D.; Johnson, J. E.; Heck, A. J. R. Studying 18 Mega Dalton Virus Assemblies with Native Mass Spectrometry. *Angew. Chem. Int. Ed Engl.* **2013**, *52*, 4020–4023.
(15) Zhou, M.; Wysocki, V. H. Surface Induced Dissociation: Dissecting Noncovalent Protein Complexes in the Gas Phase. *Acc. Chem. Res.* **2014**, *47*, 1010–1018.
(16) Lermyte, F.; Williams, J. P.; Brown, J. M.; Martin, E. M.; Sobott, F. Extensive Charge Reduction and Dissociation of Intact Protein Complexes Following Electron Transfer on a Quadrupole-Ion Mobility-Time-of-Flight MS. *J. Am. Soc. Mass Spectrom.* **2015**, *26*, 1068–1076.
(17) Rose, R. J.; Damoc, E.; Denisov, E.; Makarov, A.; Heck, A. J. R. High-Sensitivity Orbitrap Mass Analysis of Intact Macromolecular Assemblies. *Nat. Methods* **2012**, *9*, 1084–1086.
(18) Fort, K. L.; Waterbeemd, M. van de; Boll, D.; Reinhardt-Szyba, M.; Belov, M. E.; Sasaki, E.; Zschoche, R.; Hilvert, D.; Makarov, A. A.; Heck, A. J. R. Expanding the Structural Analysis Capabilities on an Orbitrap-Based Mass Spectrometer for Large Macromolecular Complexes. *Analyst* **2017**, *143*, 100–105.
(19) Snijder, J.; van de Waterbeemd, M.; Damoc, E.; Denisov, E.; Grinfeld, D.; Bennett, A.; Agbandje-McKenna, M.; Makarov, A.; Heck, A. J. R. Defining the Stoichiometry and Cargo Load of Viral and Bacterial Nanoparticles by Orbitrap Mass Spectrometry. *J. Am. Chem. Soc.* **2014**, *136*, 7295–7299.
(20) Dyachenko, A.; Wang, G.; Belov, M.; Makarov, A.; de Jong, R. N.; van den Bremer, E. T. J.; Parren, P. W. H. I.; Heck, A. J. R. Tandem Native Mass-Spectrometry on Antibody–Drug Conjugates and Submillion Da Antibody–Antigen Protein Assemblies on an Orbitrap EMR Equipped with a High-Mass Quadrupole Mass Selector. *Anal. Chem.* **2015**, *87*, 6095–6102.
(21) Gault, J.; Donlan, J. A. C.; Liko, I.; Hopper, J. T. S.; Gupta, K.; Housden, N. G.; Struwe, W. B.; Marty, M. T.; Mize, T.; Bechara, C.; Zhu, Y.; Wu, B.; Kleanthous, C.; Belov, M.; Damoc, E.; Makarov, A.; Robinson, C. V. High-Resolution Mass Spectrometry of Small Molecules Bound to Membrane Proteins. *Nat. Methods* **2016**, *13*, 333–336.
(22) Waterbeemd, M. van de; Fort, K. L.; Boll, D.; Reinhardt-Szyba, M.; Routh, A.; Makarov, A.; Heck, A. J. R. High-Fidelity Mass Analysis Unveils Heterogeneity in Intact Ribosomal Particles. *Nat. Methods* **2017**, *14*, 283.
(23) Lermyte, F.; Sobott, F. Electron Transfer Dissociation Provides Higher-Order Structural Information of Native and Partially Unfolded Protein Complexes. *PROTEOMICS* **2015**, *15*, 2813–2822.
(24) Li, H.; Wongkongkathep, P.; Orden, S. L. V.; Loo, R. R. O.; Loo, J. A. Revealing Ligand Binding Sites and Quantifying Subunit Variants of Noncovalent Protein Complexes in a Single Native Top-Down FTICR MS Experiment. *J. Am. Soc. Mass Spectrom.* **2014**, *25*, 2060–2068.
(25) Morrison, L. J.; Brodbelt, J. S. 193 Nm Ultraviolet Photodissociation Mass Spectrometry of Tetrameric Protein Complexes Provides Insight into Quaternary and Secondary Protein Topology. *J. Am. Chem. Soc.* **2016**, *138*, 10849–10859.

(26) Tamara, S.; Dyachenko, A.; Fort, K. L.; Makarov, A. A.; Scheltema, R. A.; Heck, A. J. R. Symmetry of Charge Partitioning in Collisional and UV Photon-Induced Dissociation of Protein Assemblies. *J. Am. Chem. Soc.* **2016**, *138*, 10860–10868.
(27) Julian, R. R. The Mechanism Behind Top-Down UVPD Experiments: Making Sense of Apparent Contradictions. *J. Am. Soc. Mass Spectrom.* **2017**, *28*, 1823–1826.
(28) Smith, L. M.; Kelleher, N. L.; Proteomics, T. C. for T. D.; Linial, M.; Goodlett, D.; Langridge-Smith, P.; Goo, Y. A.; Safford, G.; Bonilla, L.; Kruppa, G.; Zubarev, R.; Rontree, J.; Chamot-Rooke, J.; Garavelli, J.; Heck, A.; Loo, J.; Penque, D.; Hornshaw, M.; Hendrickson, C.; Pasa-Tolic, L.; Borchers, C.; Chan, D.; Young, N.; Agar, J.; Masselon, C.; Gross, M.; McLafferty, F.; Tsybin, Y.; Ge, Y.; Sanders, I.; Langridge, J.; Whitelegge, J.; Marshall, A. Proteoform: A Single Term Describing Protein Complexity. *Nat. Methods* **2013**, *10*, 186–187.
(29) Savaryn, J. P.; Catherman, A. D.; Thomas, P. M.; Abecassis, M. M.; Kelleher, N. L. The Emergence of Top-down Proteomics in Clinical Research. *Genome Med.* **2013**, *5*, 53.
(30) Belov, M. E.; Damoc, E.; Denisov, E.; Compton, P. D.; Horning, S.; Makarov, A. A.; Kelleher, N. L. From Protein Complexes to Subunit Backbone Fragments: A Multi-Stage Approach to Native Mass Spectrometry. *Anal. Chem.* **2013**, *85*, 11163–11173.
(31) Konijnenberg, A.; Bannwarth, L.; Yilmaz, D.; Koçer, A.; Venien-Bryan, C.; Sobott, F. Top-down Mass Spectrometry of Intact Membrane Protein Complexes Reveals Oligomeric State and Sequence Information in a Single Experiment. *Protein Sci.* **2015**, *24*, 1292–1300.
(32) Belov, M. Method and Apparatus for Mass Spectrometry of Macromolecular Complexes. U.S. Patent 9,887,074, February 6, 2018.
(33) Skinner, O. S.; Havugimana, P. C.; Haverland, N. A.; Fornelli, L.; Early, B. P.; Greer, J. B.; Fellers, R. T.; Durbin, K. R.; Do Vale, L. H. F.; Melani, R. D.; Seckler, H. S.; Nelp, M. T.; Belov, M. E.; Horning, S. R.; Makarov, A. A.; LeDuc, R. D.; Bandarian, V.; Compton, P. D.; Kelleher, N. L. An Informatic Framework for Decoding Protein Complexes by Top-down Mass Spectrometry. *Nat. Methods* **2016**, *13*, 237–240.
(34) Ben-Nissan, G.; Belov, M. E.; Morgenstern, D.; Levin, Y.; Dym, O.; Arkind, G.; Lipson, C.; Makarov, A. A.; Sharon, M. Triple-Stage Mass Spectrometry Unravels the Heterogeneity of an Endogenous Protein Complex. *Anal. Chem.* **2017**, *89*, 4708–4715.
(35) Skinner, O. S.; Haverland, N. A.; Fornelli, L.; Melani, R. D.; Do Vale, L. H. F.; Seckler, H. S.; Doubleday, P. F.; Schachner, L. F.; Srzentić, K.; Kelleher, N. L.; Compton, P. D. Top-down Characterization of Endogenous Protein Complexes with Native Proteomics. *Nat. Chem. Biol.* **2018**, *14*, 36–41.
(36) Li, H.; Nguyen, H. H.; Ogorzalek Loo, R. R.; Campuzano, I. D. G.; Loo, J. A. An Integrated Native Mass Spectrometry and Top-down Proteomics Method That Connects Sequence to Structure and Function of Macromolecular Complexes. *Nat. Chem.* **2018**, *10*, 139–148.

(37) Shaw, J. B.; Li, W.; Holden, D. D.; Zhang, Y.; Griep-Raming, J.; Fellers, R. T.; Early, B. P.; Thomas, P. M.; Kelleher, N. L.; Brodbelt, J. S. Complete Protein Characterization Using Top-Down Mass Spectrometry and Ultraviolet Photodissociation. *J. Am. Chem. Soc.* **2013**, *135*, 12646–12651.
(38) Cannon, J. R.; Cammarata, M. B.; Robotham, S. A.; Cotham, V. C.; Shaw, J. B.; Fellers, R. T.; Early, B. P.; Thomas, P. M.; Kelleher, N. L.; Brodbelt, J. S. Ultraviolet Photodissociation for Characterization of Whole Proteins on a Chromatographic Time Scale. *Anal. Chem.* **2014**, *86*, 2185–2192.
(39) O'Brien, J. P.; Li, W.; Zhang, Y.; Brodbelt, J. S. Characterization of Native Protein Complexes Using Ultraviolet Photodissociation Mass Spectrometry. *J. Am. Chem. Soc.* **2014**, *136*, 12920–12928.
(40) Cammarata, M. B.; Brodbelt, J. S. Structural Characterization of Holo- and Apo-Myoglobin in the Gas Phase by Ultraviolet Photodissociation Mass Spectrometry. *Chem. Sci.* **2015**, *6*, 1324–1333.
(41) Cleland, T. P.; DeHart, C. J.; Fellers, R. T.; VanNispen, A. J.; Greer, J. B.; LeDuc, R. D.; Parker, W. R.; Thomas, P. M.; Kelleher, N. L.; Brodbelt, J. S. High-Throughput Analysis of Intact Human Proteins Using UVPD and HCD on an Orbitrap Mass Spectrometer. *J. Proteome Res.* **2017**, *16*, 2072–2079.
(42) Robinson, M. R.; Taliaferro, J. M.; Dalby, K. N.; Brodbelt, J. S. 193 Nm Ultraviolet Photodissociation Mass Spectrometry for Phosphopeptide Characterization in the Positive and Negative Ion Modes. *J. Proteome Res.* **2016**, *15*, 2739–2748.
(43) Robinson, M. R.; Moore, K. L.; Brodbelt, B. Direct Identification of Tyrosine Sulfation by Using Ultraviolet Photodissociation Mass Spectrometry. *J. Am. Soc. Mass Spectrom.* **2014**, *25*, 1461–1471.
(44) Cammarata, M. B.; Thyer, R.; Rosenberg, J.; Ellington, A.; Brodbelt, J. S. Structural Characterization of Dihydrofolate Reductase Complexes by Top-Down Ultraviolet Photodissociation Mass Spectrometry. *J. Am. Chem. Soc.* **2015**, *137*, 9128–9135.
(45) Cammarata, M. B.; Schardon, C. L.; Mehaffey, M. R.; Rosenberg, J.; Singleton, J.; Fast, W.; Brodbelt, J. S. Impact of G12 Mutations on the Structure of K-Ras Probed by Ultraviolet Photodissociation Mass Spectrometry. *J. Am. Chem. Soc.* **2016**, *138*, 13187–13196.
(46) Mehaffey, M. R.; Cammarata, M. B.; Brodbelt, J. S. Tracking the Catalytic Cycle of Adenylate Kinase by Ultraviolet Photodissociation Mass Spectrometry. *Anal. Chem.* **2018**, *90*, 839–846.
(47) Makarov, A.; Denisov, E. Dynamics of Ions of Intact Proteins in the Orbitrap Mass Analyzer. *J. Am. Soc. Mass Spectrom.* **2009**, *20*, 1486–1495.
(48) Shaw, J. B.; Brodbelt, J. S. Extending the Isotopically Resolved Mass Range of Orbitrap Mass Spectrometers. *Anal. Chem.* **2013**, *85*, 8313–8318.
(49) Enyenihi, A. A.; Yang, H.; Ytterberg, A. J.; Lyutvinskiy, Y.; Zubarev, R. A. Heme Binding in Gas-Phase Holo-Myoglobin Cations: Distal Becomes Proximal? *J. Am. Soc. Mass Spectrom.* **2011**, *22*.
(50) Deng, H.; Zhou, J.; Sundersingh, F. S.; Summerfield, J.; Somers, D.; Messer, J. A.; Satz, A. L.; Ancellin, N.; Arico-Muendel, C. C.; Sargent Bedard, K. L.; Beljean, A.;

Belyanskaya, S. L.; Bingham, R.; Smith, S. E.; Boursier, E.; Carter, P.; Centrella, P. A.; Clark, M. A.; Chung, C.; Davie, C. P.; Delorey, J. L.; Ding, Y.; Franklin, G. J.; Grady, L. C.; Herry, K.; Hobbs, C.; Kollmann, C. S.; Morgan, B. A.; Pothier Kaushansky, L. J.; Zhou, Q. Discovery, SAR, and X-Ray Binding Mode Study of BCATm Inhibitors from a Novel DNA-Encoded Library. *ACS Med. Chem. Lett.* **2015**, *6*, 919–924.

CHAPTER 8

(1) Savaryn, J. P.; Catherman, A. D.; Thomas, P. M.; Abecassis, M. M.; Kelleher, N. L. The Emergence of Top-down Proteomics in Clinical Research. *Genome Med.* **2013**, *5*, 53.

(2) Xing, S.; Wallmeroth, N.; Berendzen, K. W.; Grefen, C. Techniques for the Analysis of Protein-Protein Interactions in Vivo. *Plant Physiol.* **2016**, *171*, 727–758.

(3) Hayes, S.; Malacrida, B.; Kiely, M.; Kiely, P. A. Studying Protein–Protein Interactions: Progress, Pitfalls and Solutions. *Biochem. Soc. Trans.* **2016**, *44*, 994–1004.

(4) Leney, A. C.; Heck, A. J. R. Native Mass Spectrometry: What Is in the Name? *J. Am. Soc. Mass Spectrom.* **2017**, *28*, 5–13.

(5) Allison, T. M.; Bechara, C. Structural Mass Spectrometry Comes of Age: New Insight into Protein Structure, Function and Interactions. *Biochem. Soc. Trans.* **2019**, *47*, 317–327.

(6) Kaur, U.; Johnson, D. T.; Chea, E. E.; Deredge, D. J.; Espino, J. A.; Jones, L. M. Evolution of Structural Biology through the Lens of Mass Spectrometry. *Anal. Chem.* **2019**, *91*, 142–155.

(7) Gillet, L. C.; Leitner, A.; Aebersold, R. Mass Spectrometry Applied to Bottom-Up Proteomics: Entering the High-Throughput Era for Hypothesis Testing. *Annu. Rev. Anal. Chem.* **2016**, *9*, 449–472.

(8) Donnelly, D. P.; Rawlins, C. M.; DeHart, C. J.; Fornelli, L.; Schachner, L. F.; Lin, Z.; Lippens, J. L.; Aluri, K. C.; Sarin, R.; Chen, B.; Lantz, C.; Jung, W.; Johnson, K. R.; Koller, A.; Wolff, J. J.; Campuzano, I. D. G.; Auclair, J. R.; Ivanov, A. R.; Whitelegge, J. P.; Paša-Tolić, L.; Chamot-Rooke, J.; Danis, P. O.; Smith, L. M.; Tsybin, Y. O.; Loo, J. A.; Ge, Y.; Kelleher, N. L.; Agar, J. N. Best Practices and Benchmarks for Intact Protein Analysis for Top-down Mass Spectrometry. *Nat. Methods* **2019**, *16*, 587–594.

(9) Smith, L. M.; Kelleher, N. L.; Proteomics, T. C. for T. D.; Linial, M.; Goodlett, D.; Langridge-Smith, P.; Goo, Y. A.; Safford, G.; Bonilla, L.; Kruppa, G.; Zubarev, R.; Rontree, J.; Chamot-Rooke, J.; Garavelli, J.; Heck, A.; Loo, J.; Penque, D.; Hornshaw, M.; Hendrickson, C.; Pasa-Tolic, L.; Borchers, C.; Chan, D.; Young, N.; Agar, J.; Masselon, C.; Gross, M.; McLafferty, F.; Tsybin, Y.; Ge, Y.; Sanders, I.; Langridge, J.; Whitelegge, J.; Marshall, A. Proteoform: A Single Term Describing Protein Complexity. *Nat. Methods* **2013**, *10*, 186–187.

(10) Hyung, S.-J.; Ruotolo, B. T. Integrating Mass Spectrometry of Intact Protein Complexes into Structural Proteomics. *Proteomics* **2012**, *12*, 1547–1564.
(11) Ngounou Wetie, A. G.; Sokolowska, I.; Woods, A. G.; Roy, U.; Loo, J. A.; Darie, C. C. Investigation of Stable and Transient Protein-Protein Interactions: Past, Present, and Future. *Proteomics* **2013**, *13*, 538–557.
(12) Kükrer, B.; Filipe, V.; van Duijn, E.; Kasper, P. T.; Vreeken, R. J.; Heck, A. J. R.; Jiskoot, W. Mass Spectrometric Analysis of Intact Human Monoclonal Antibody Aggregates Fractionated by Size-Exclusion Chromatography. *Pharm. Res.* **2010**, *27*, 2197–2204.
(13) Muneeruddin, K.; Thomas, J. J.; Salinas, P. A.; Kaltashov, I. A. Characterization of Small Protein Aggregates and Oligomers Using Size Exclusion Chromatography with Online Detection by Native Electrospray Ionization Mass Spectrometry. *Anal. Chem.* **2014**, *86*, 10692–10699.
(14) Haberger, M.; Leiss, M.; Heidenreich, A.-K.; Pester, O.; Hafenmair, G.; Hook, M.; Bonnington, L.; Wegele, H.; Haindl, M.; Reusch, D.; Bulau, P. Rapid Characterization of Biotherapeutic Proteins by Size-Exclusion Chromatography Coupled to Native Mass Spectrometry. *mAbs* **2015**, *8*, 331–339.
(15) Sahasrabuddhe, A.; Hsia, Y.; Busch, F.; Sheffler, W.; King, N. P.; Baker, D.; Wysocki, V. H. Confirmation of Intersubunit Connectivity and Topology of Designed Protein Complexes by Native MS. *Proc. Natl. Acad. Sci.* **2018**, *115*, 1268–1273.
(16) Muneeruddin, K.; Nazzaro, M.; Kaltashov, I. A. Characterization of Intact Protein Conjugates and Biopharmaceuticals Using Ion-Exchange Chromatography with Online Detection by Native Electrospray Ionization Mass Spectrometry and Top-Down Tandem Mass Spectrometry. *Anal. Chem.* **2015**, *87*, 10138–10145.
(17) Debaene, F.; Bœuf, A.; Wagner-Rousset, E.; Colas, O.; Ayoub, D.; Corvaïa, N.; Van Dorsselaer, A.; Beck, A.; Cianférani, S. Innovative Native MS Methodologies for Antibody Drug Conjugate Characterization: High Resolution Native MS and IM-MS for Average DAR and DAR Distribution Assessment. *Anal. Chem.* **2014**, *86*, 10674–10683.
(18) Martinović, S.; Berger, S. J.; Paša-Tolić, L.; Smith, R. D. Separation and Detection of Intact Noncovalent Protein Complexes from Mixtures by On-Line Capillary Isoelectric Focusing-Mass Spectrometry. *Anal. Chem.* **2000**, *72*, 5356–5360.
(19) Fonslow, B. R.; Kang, S. A.; Gestaut, D. R.; Graczyk, B.; Davis, T. N.; Sabatini, D. M.; Yates III, J. R. Native Capillary Isoelectric Focusing for the Separation of Protein Complex Isoforms and Subcomplexes. *Anal. Chem.* **2010**, *82*, 6643–6651.
(20) Skinner, O. S.; Do Vale, L. H. F.; Catherman, A. D.; Havugimana, P. C.; Sousa, M. V. de; Compton, P. D.; Kelleher, N. L. Native GELFrEE: A New Separation Technique for Biomolecular Assemblies. *Anal. Chem.* **2015**, *87*, 3032–3038.
(21) Skinner, O. S.; Haverland, N. A.; Fornelli, L.; Melani, R. D.; Do Vale, L. H. F.; Seckler, H. S.; Doubleday, P. F.; Schachner, L. F.; Srzentić, K.; Kelleher, N. L.; Compton, P. D. Top-down Characterization of Endogenous Protein Complexes with Native Proteomics. *Nat. Chem. Biol.* **2018**, *14*, 36–41.

(22) Han, X.; Wang, Y.; Aslanian, A.; Fonslow, B.; Graczyk, B.; Davis, T. N.; Yates, J. R. In-Line Separation by Capillary Electrophoresis Prior to Analysis by Top-Down Mass Spectrometry Enables Sensitive Characterization of Protein Complexes. *J. Proteome Res.* **2014**, *13*, 6078–6086.
(23) Belov, A. M.; Viner, R.; Santos, M. R.; Horn, D. M.; Bern, M.; Karger, B. L.; Ivanov, A. R. Analysis of Proteins, Protein Complexes, and Organellar Proteomes Using Sheathless Capillary Zone Electrophoresis - Native Mass Spectrometry. *J. Am. Soc. Mass Spectrom.* **2017**, *28*, 2614–2634.
(24) Shen, X.; Kou, Q.; Guo, R.; Yang, Z.; Chen, D.; Liu, X.; Hong, H.; Sun, L. Native Proteomics in Discovery Mode Using Size-Exclusion Chromatography–Capillary Zone Electrophoresis–Tandem Mass Spectrometry. *Anal. Chem.* **2018**, *90*, 10095–10099.
(25) McCool, E. N.; Lubeckyj, R. A.; Shen, X.; Chen, D.; Kou, Q.; Liu, X.; Sun, L. Deep Top-Down Proteomics Using Capillary Zone Electrophoresis-Tandem Mass Spectrometry: Identification of 5700 Proteoforms from the Escherichia Coli Proteome. *Anal. Chem.* **2018**, *90*, 5529–5533.
(26) Lubeckyj, R. A.; Basharat, A. R.; Shen, X.; Liu, X.; Sun, L. Large-Scale Qualitative and Quantitative Top-Down Proteomics Using Capillary Zone Electrophoresis-Electrospray Ionization-Tandem Mass Spectrometry with Nanograms of Proteome Samples. *J. Am. Soc. Mass Spectrom.* **2019**.
(27) McCool, E. N.; Lodge, J. M.; Basharat, A. R.; Liu, X.; Coon, J. J.; Sun, L. Capillary Zone Electrophoresis-Tandem Mass Spectrometry with Activated Ion Electron Transfer Dissociation for Large-Scale Top-down Proteomics. *J. Am. Soc. Mass Spectrom.* **2019**.
(28) Shen, X.; Yang, Z.; McCool, E. N.; Lubeckyj, R. A.; Chen, D.; Sun, L. Capillary Zone Electrophoresis-Mass Spectrometry for Top-down Proteomics. *TrAC Trends Anal. Chem.* **2019**, *120*, 115644.
(29) Kristoff, C. J.; Bwanali, L.; Veltri, L. M.; Gautam, G. P.; Rutto, P. K.; Newton, E. O.; Holland, L. A. Challenging Bioanalyses with Capillary Electrophoresis. *Anal. Chem.* **2020**, *92*, 49–66.
(30) Lössl, P.; Snijder, J.; Heck, A. J. R. Boundaries of Mass Resolution in Native Mass Spectrometry. *J. Am. Soc. Mass Spectrom.* **2014**, *25*, 906–917.
(31) Robinson, C. V.; Chung, E. W.; Kragelund, B. B.; Knudsen, J.; Aplin, R. T.; Poulsen, F. M.; Dobson, C. M. Probing the Nature of Noncovalent Interactions by Mass Spectrometry. A Study of Protein−CoA Ligand Binding and Assembly. *J. Am. Chem. Soc.* **1996**, *118*, 8646–8653.
(32) Li, H.; Wolff, J. J.; Van Orden, S. L.; Loo, J. A. Native Top-Down Electrospray Ionization-Mass Spectrometry of 158 KDa Protein Complex by High-Resolution Fourier Transform Ion Cyclotron Resonance Mass Spectrometry. *Anal. Chem.* **2014**, *86*, 317–320.
(33) Li, H.; Nguyen, H. H.; Ogorzalek Loo, R. R.; Campuzano, I. D. G.; Loo, J. A. An Integrated Native Mass Spectrometry and Top-down Proteomics Method That

Connects Sequence to Structure and Function of Macromolecular Complexes. *Nat. Chem.* **2018**, *10*, 139–148.
(34) Fort, K. L.; Waterbeemd, M. van de; Boll, D.; Reinhardt-Szyba, M.; Belov, M. E.; Sasaki, E.; Zschoche, R.; Hilvert, D.; Makarov, A. A.; Heck, A. J. R. Expanding the Structural Analysis Capabilities on an Orbitrap-Based Mass Spectrometer for Large Macromolecular Complexes. *Analyst* **2017**, *143*, 100–105.
(35) Hall, Z.; Hernández, H.; Marsh, J. A.; Teichmann, S. A.; Robinson, C. V. The Role of Salt Bridges, Charge Density, and Subunit Flexibility in Determining Disassembly Routes of Protein Complexes. *Structure* **2013**, *21*, 1325–1337.
(36) Macias, L. A.; Santos, I. C.; Brodbelt, J. S. Ion Activation Methods for Peptides and Proteins. *Anal. Chem.* **2020**, *92*, 227–251.
(37) Zhang, H.; Cui, W.; Wen, J.; Blankenship, R. E.; Gross, M. L. Native Electrospray and Electron-Capture Dissociation FTICR Mass Spectrometry for Top-down Studies of Protein Assemblies. *Anal. Chem.* **2011**, *83*, 5598–5606.
(38) Lermyte, F.; Sobott, F. Electron Transfer Dissociation Provides Higher-Order Structural Information of Native and Partially Unfolded Protein Complexes. *PROTEOMICS* **2015**, *15*, 2813–2822.
(39) Li, H.; Sheng, Y.; McGee, W.; Cammarata, M.; Holden, D.; Loo, J. A. Structural Characterization of Native Proteins and Protein Complexes by Electron Ionization Dissociation-Mass Spectrometry. *Anal. Chem.* **2017**, *89*, 2731–2738.
(40) Lermyte, F.; Valkenborg, D.; Loo, J. A.; Sobott, F. Radical Solutions: Principles and Application of Electron-Based Dissociation in Mass Spectrometry-Based Analysis of Protein Structure. *Mass Spectrom. Rev.* **2018**, *37*, 750–771.
(41) Zhou, M.; Wysocki, V. H. Surface Induced Dissociation: Dissecting Noncovalent Protein Complexes in the Gas Phase. *Acc. Chem. Res.* **2014**, *47*, 1010–1018.
(42) Morrison, L. J.; Brodbelt, J. S. 193 Nm Ultraviolet Photodissociation Mass Spectrometry of Tetrameric Protein Complexes Provides Insight into Quaternary and Secondary Protein Topology. *J. Am. Chem. Soc.* **2016**, *138*, 10849–10859.
(43) Tamara, S.; Dyachenko, A.; Fort, K. L.; Makarov, A. A.; Scheltema, R. A.; Heck, A. J. R. Symmetry of Charge Partitioning in Collisional and UV Photon-Induced Dissociation of Protein Assemblies. *J. Am. Chem. Soc.* **2016**, *138*, 10860–10868.
(44) Brodbelt, J. S.; Morrison, L. J.; Santos, I. Ultraviolet Photodissociation Mass Spectrometry for Analysis of Biological Molecules. *Chem. Rev.* **2019**.
(45) Shaw, J. B.; Li, W.; Holden, D. D.; Zhang, Y.; Griep-Raming, J.; Fellers, R. T.; Early, B. P.; Thomas, P. M.; Kelleher, N. L.; Brodbelt, J. S. Complete Protein Characterization Using Top-Down Mass Spectrometry and Ultraviolet Photodissociation. *J. Am. Chem. Soc.* **2013**, *135*, 12646–12651.
(46) Cannon, J. R.; Cammarata, M. B.; Robotham, S. A.; Cotham, V. C.; Shaw, J. B.; Fellers, R. T.; Early, B. P.; Thomas, P. M.; Kelleher, N. L.; Brodbelt, J. S. Ultraviolet Photodissociation for Characterization of Whole Proteins on a Chromatographic Time Scale. *Anal. Chem.* **2014**, *86*, 2185–2192.
(47) Cleland, T. P.; DeHart, C. J.; Fellers, R. T.; VanNispen, A. J.; Greer, J. B.; LeDuc, R. D.; Parker, W. R.; Thomas, P. M.; Kelleher, N. L.; Brodbelt, J. S. High-

Throughput Analysis of Intact Human Proteins Using UVPD and HCD on an Orbitrap Mass Spectrometer. *J. Proteome Res.* **2017**, *16*, 2072–2079.
(48) Greer, S. M.; Brodbelt, J. S. Top-Down Characterization of Heavily Modified Histones Using 193 Nm Ultraviolet Photodissociation Mass Spectrometry. *J. Proteome Res.* **2018**, *17*, 1138–1145.
(49) O'Brien, J. P.; Li, W.; Zhang, Y.; Brodbelt, J. S. Characterization of Native Protein Complexes Using Ultraviolet Photodissociation Mass Spectrometry. *J. Am. Chem. Soc.* **2014**, *136*, 12920–12928.
(50) Greisch, J.-F.; Tamara, S.; Scheltema, R. A.; Maxwell, H. W. R.; Fagerlund, R. D.; Fineran, P. C.; Tetter, S.; Hilvert, D.; Heck, A. J. R. Expanding the Mass Range for UVPD-Based Native Top-down Mass Spectrometry. *Chem. Sci.* **2019**, *10*, 7163–7171.
(51) Belov, M. E.; Damoc, E.; Denisov, E.; Compton, P. D.; Horning, S.; Makarov, A. A.; Kelleher, N. L. From Protein Complexes to Subunit Backbone Fragments: A Multi-Stage Approach to Native Mass Spectrometry. *Anal. Chem.* **2013**, *85*, 11163–11173.
(52) Konijnenberg, A.; Bannwarth, L.; Yilmaz, D.; Koçer, A.; Venien-Bryan, C.; Sobott, F. Top-down Mass Spectrometry of Intact Membrane Protein Complexes Reveals Oligomeric State and Sequence Information in a Single Experiment. *Protein Sci.* **2015**, *24*, 1292–1300.
(53) Ben-Nissan, G.; Belov, M. E.; Morgenstern, D.; Levin, Y.; Dym, O.; Arkind, G.; Lipson, C.; Makarov, A. A.; Sharon, M. Triple-Stage Mass Spectrometry Unravels the Heterogeneity of an Endogenous Protein Complex. *Anal. Chem.* **2017**, *89*, 4708–4715.
(54) Mehaffey, M. R.; Sanders, J. D.; Holden, D. D.; Nilsson, C. L.; Brodbelt, J. S. Multistage Ultraviolet Photodissociation Mass Spectrometry To Characterize Single Amino Acid Variants of Human Mitochondrial BCAT2. *Anal. Chem.* **2018**, *90*, 9904–9911.
(55) Gault, J.; Liko, I.; Landreh, M.; Shutin, D.; Bolla, J. R.; Jefferies, D.; Agasid, M.; Yen, H.-Y.; Ladds, M. J. G. W.; Lane, D. P.; Khalid, S.; Mullen, C.; Remes, P. M.; Huguet, R.; McAlister, G.; Goodwin, M.; Viner, R.; Syka, J. E. P.; Robinson, C. V. Combining Native and 'Omics' Mass Spectrometry to Identify Endogenous Ligands Bound to Membrane Proteins. *Nat. Methods* **2020**, *17*, 505–508.
(56) Hardy, S. J. S.; Kurland, C. G.; Voynow, P.; Mora, G. Ribosomal Proteins of Escherichia Coli. I. Purification of the 30 S Ribosomal Proteins. *Biochemistry* **1969**, *8*, 2897–2905.
(57) Ban, N.; Nissen, P.; Hansen, J.; Moore, P. B.; Steitz, T. A. The Complete Atomic Structure of the Large Ribosomal Subunit at 2.4 Å Resolution. *Science* **2000**, *289*, 905–920.
(58) Noeske, J.; Wasserman, M. R.; Terry, D. S.; Altman, R. B.; Blanchard, S. C.; Cate, J. H. D. High-Resolution Structure of the Escherichia Coli Ribosome. *Nat. Struct. Mol. Biol.* **2015**, *22*, 336–341.

(59) Wimberly, B. T.; Brodersen, D. E.; Clemons, W. M.; Morgan-Warren, R. J.; Carter, A. P.; Vonrhein, C.; Hartsch, T.; Ramakrishnan, V. Structure of the 30S Ribosomal Subunit. *Nature* **2000**, *407*, 327–339.
(60) Valle, M.; Zavialov, A.; Sengupta, J.; Rawat, U.; Ehrenberg, M.; Frank, J. Locking and Unlocking of Ribosomal Motions. *Cell* **2003**, *114*, 123–134.
(61) Zhang, W.; Dunkle, J. A.; Cate, J. H. D. Structures of the Ribosome in Intermediate States of Ratcheting. *Science* **2009**, *325*, 1014–1017.
(62) Yamamoto, T.; Izumi, S.; Gekko, K. Mass Spectrometry of Hydrogen/Deuterium Exchange in 70S Ribosomal Proteins from E. Coli. *FEBS Lett.* **2006**, *580*, 3638–3642.
(63) Yamamoto, T.; Shimizu, Y.; Ueda, T.; Shiro, Y. Mg2+ Dependence of 70 S Ribosomal Protein Flexibility Revealed by Hydrogen/Deuterium Exchange and Mass Spectrometry. *J. Biol. Chem.* **2010**, *285*, 5646–5652.
(64) Benjamin, D. R.; Robinson, C. V.; Hendrick, J. P.; Hartl, F. U.; Dobson, C. M. Mass Spectrometry of Ribosomes and Ribosomal Subunits. *Proc. Natl. Acad. Sci.* **1998**, *95*, 7391–7395.
(65) Waterbeemd, M. van de; Fort, K. L.; Boll, D.; Reinhardt-Szyba, M.; Routh, A.; Makarov, A.; Heck, A. J. R. High-Fidelity Mass Analysis Unveils Heterogeneity in Intact Ribosomal Particles. *Nat. Methods* **2017**, *14*, 283.
(66) van de Waterbeemd, M.; Tamara, S.; Fort, K. L.; Damoc, E.; Franc, V.; Bieri, P.; Itten, M.; Makarov, A.; Ban, N.; Heck, A. J. R. Dissecting Ribosomal Particles throughout the Kingdoms of Life Using Advanced Hybrid Mass Spectrometry Methods. *Nat. Commun.* **2018**, *9*, 1–12.
(67) Gülbakan, B.; Barylyuk, K.; Schneider, P.; Pillong, M.; Schneider, G.; Zenobi, R. Native Electrospray Ionization Mass Spectrometry Reveals Multiple Facets of Aptamer–Ligand Interactions: From Mechanism to Binding Constants. *J. Am. Chem. Soc.* **2018**, *140*, 7486–7497.
(68) Greer, S. M.; Holden, D. D.; Fellers, R.; Kelleher, N. L.; Brodbelt, J. S. Modulation of Protein Fragmentation Through Carbamylation of Primary Amines. *J. Am. Soc. Mass Spectrom.* **2017**, *28*, 1587–1599.
(69) Diaconu, M.; Kothe, U.; Schlünzen, F.; Fischer, N.; Harms, J. M.; Tonevitsky, A. G.; Stark, H.; Rodnina, M. V.; Wahl, M. C. Structural Basis for the Function of the Ribosomal L7/12 Stalk in Factor Binding and GTPase Activation. *Cell* **2005**, *121*, 991–1004.
(70) Cammarata, M. B.; Thyer, R.; Rosenberg, J.; Ellington, A.; Brodbelt, J. S. Structural Characterization of Dihydrofolate Reductase Complexes by Top-Down Ultraviolet Photodissociation Mass Spectrometry. *J. Am. Chem. Soc.* **2015**, *137*, 9128–9135.
(71) Cammarata, M. B.; Schardon, C. L.; Mehaffey, M. R.; Rosenberg, J.; Singleton, J.; Fast, W.; Brodbelt, J. S. Impact of G12 Mutations on the Structure of K-Ras Probed by Ultraviolet Photodissociation Mass Spectrometry. *J. Am. Chem. Soc.* **2016**, *138*, 13187–13196.

(72) Mehaffey, M. R.; Cammarata, M. B.; Brodbelt, J. S. Tracking the Catalytic Cycle of Adenylate Kinase by Ultraviolet Photodissociation Mass Spectrometry. *Anal. Chem.* **2018**, *90*, 839–846.
(73) Schuwirth, B. S.; Borovinskaya, M. A.; Hau, C. W.; Zhang, W.; Vila-Sanjurjo, A.; Holton, J. M.; Cate, J. H. D. Structures of the Bacterial Ribosome at 3.5 Å Resolution. *Science* **2005**, *310*, 827–834.

Vita

Megan Rachel Mehaffey was born during September of 1992 in Asheville, NC and grew up in nearby Clyde, NC. She spent the summer of 2009 attending the prestigious Governor's School of North Carolina at Meredith College in Raleigh, NC. In 2010, she graduated valedictorian from Tuscola High School after which she moved to Greenville, NC to pursue higher-level education at East Carolina University. In 2013 she carried out over 900 hours of volunteer service for AmeriCorps as a Project Heart tutor. She graduated in May 2014 at the top of her class with a B.S. in Chemistry, B.S in Applied Physics, and minor in Hispanic Studies. At graduation she was awarded the Robert H. Wright Leadership Award recognizing academic achievement, service, and leadership qualities. While earning her degree, she completed one year of undergraduate research under the guidance of Dr. Allison Danell. During this time, she utilized mass spectrometry to detect damage along DNA strands caused by a xenobiotic. In the summer of 2014, she began her graduate studies under the supervision of Dr. Jennifer Brodbelt at the University of Texas at Austin where she has continued to develop mass spectrometry as an analytical tool to tackle challenging problems in structural biology.

Permanent email address: meganrachelmehaffey@gmail.com

This dissertation was typed by the author.